NASA/TM–20230014536
NESC-RP-18-01317

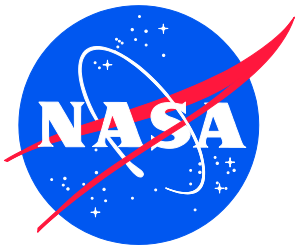

Assessment of Electrical, Electronic, and Electromechanical (EEE) Parts Copper Wire Bonds for Space Programs

Robert F. Hodson/NESC
Langley Research Center, Hampton, Virginia

Linda Y. Del Castillo
Jet Propulsion Laboratory, Pasadena, California

Yuan Chen
Langley Research Center, Hampton, Virginia

Reza Ghaffarian
Jet Propulsion Laboratory, Pasadena, California

Lyudmyla P. Ochs
Goddard Space Flight Center, Greenbelt, Maryland

Eric M. Galloway
Science Systems and Applications, Inc., Lanham, Maryland

October 2023

NASA STI Program Report Series

Since its founding, NASA has been dedicated to the advancement of aeronautics and space science. The NASA scientific and technical information (STI) program plays a key part in helping NASA maintain this important role.

The NASA STI program operates under the auspices of the Agency Chief Information Officer. It collects, organizes, provides for archiving, and disseminates NASA's STI. The NASA STI program provides access to the NTRS Registered and its public interface, the NASA Technical Reports Server, thus providing one of the largest collections of aeronautical and space science STI in the world. Results are published in both non-NASA channels and by NASA in the NASA STI Report Series, which includes the following report types:

- TECHNICAL PUBLICATION. Reports of completed research or a major significant phase of research that present the results of NASA Programs and include extensive data or theoretical analysis. Includes compilations of significant scientific and technical data and information deemed to be of continuing reference value. NASA counterpart of peer-reviewed formal professional papers but has less stringent limitations on manuscript length and extent of graphic presentations.

- TECHNICAL MEMORANDUM. Scientific and technical findings that are preliminary or of specialized interest, e.g., quick release reports, working papers, and bibliographies that contain minimal annotation. Does not contain extensive analysis.

- CONTRACTOR REPORT. Scientific and technical findings by NASA-sponsored contractors and grantees.

- CONFERENCE PUBLICATION. Collected papers from scientific and technical conferences, symposia, seminars, or other meetings sponsored or co-sponsored by NASA.

- SPECIAL PUBLICATION. Scientific, technical, or historical information from NASA programs, projects, and missions, often concerned with subjects having substantial public interest.

- TECHNICAL TRANSLATION. English-language translations of foreign scientific and technical material pertinent to NASA's mission.

Specialized services also include organizing and publishing research results, distributing specialized research announcements and feeds, providing information desk and personal search support, and enabling data exchange services.

For more information about the NASA STI program, see the following:

- Access the NASA STI program home page at http://www.sti.nasa.gov

- Help desk contact information:

https://www.sti.nasa.gov/sti-contact-form/
and select the "General" help request type.

NASA/TM–20230014536
NESC-RP-18-01317

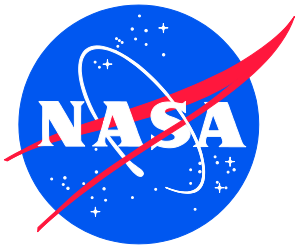

Assessment of Electrical, Electronic, and Electromechanical (EEE) Parts Copper Wire Bonds for Space Programs

Robert F. Hodson/NESC
Langley Research Center, Hampton, Virginia

Linda Y. Del Castillo
Jet Propulsion Laboratory, Pasadena, California

Yuan Chen
Langley Research Center, Hampton, Virginia

Reza Ghaffarian
Jet Propulsion Laboratory, Pasadena, California

Lyudmyla P. Ochs
Goddard Space Flight Center, Greenbelt, Maryland

Eric M. Galloway
Science Systems and Applications, Inc., Lanham, Maryland

National Aeronautics and
Space Administration

Langley Research Center
Hampton, Virginia 23681-2199

October 2023

Acknowledgments

Special thanks to the Goddard Space Flight Center (GSFC) Parts Analysis Laboratory, Jet Propulsion Laboratory (JPL) Analysis and Test Laboratory, and JPL Analytical Chemistry Laboratory.

The assessment team also thanks peer reviewers Shri Agarwal, Tim Brady, Andrew Chaloupka, Steve Gentz, Bryan McEnerny, Jesse Leitner, Carlton S. Faller, Kuok Y. Ling, Susana P. Douglas, Peter J. Majewicz, and Don Parker.

Available from:

NASA STI Program / Mail Stop 148
NASA Langley Research Center
Hampton, VA 23681-2199
Fax: 757-864-6500

NASA Engineering and Safety Center
Technical Assessment Report

Assessment of Electrical, Electronic, and Electromechanical (EEE) Parts Copper Wire Bonds for Space Programs

TI-18-01317

Dr. Robert F. Hodson

NESC Lead

Dr. Linda Del Castillo

Technical Lead

August 29, 2023

Report Approval and Revision History

NOTE: This document was approved at the August 29, 2023, NRB.

Approved:	*Original signature on file.*	
	NESC Director	

Version	Description of Revision	Office of Primary Responsibility	Effective Date
1.0	Initial Release	Dr. Robert F. Hodson, NASA Technical Fellow for Avionics, LaRC	August 29, 2023

Table of Contents

List of Figures

List of Tables

Technical Assessment Report

1.0 Notification and Authorization

Mr. Mike Sampson, NASA Electronic Parts and Packaging Program co-manager, requested the NASA Engineering and Safety Center (NESC) to compile a body of publicly available knowledge on copper (Cu) wire bonds and perform reliability testing and analysis on these bonds, including environment tests, sample destructive physical analysis (DPA), and bond pull/shear tests during environment test intervals. The goal is to understand the risks of using Cu wire bonds for space applications and develop guidelines on Cu bond pull/shear limits for NASA applications.

The key stakeholders for this assessment are Dr. Peter Majewicz, NASA Electronic Parts and Packaging Program Manager; NASA center and program/project EEE parts managers and leads; NASA projects using parts with Cu wire bonds; and the NESC.

2.0 Signatures

Submitted by: NESC Lead

Original signatures on file.

Dr. Robert F. Hodson

Significant Contributors:

Dr. Linda Y. Del Castillo

Dr. Yuan Chen

Dr. Reza Ghaffarian

Ms. Lyudmyla P. Ochs

Mr. Eric M. Galloway

Signatories declare the findings, observations, and NESC recommendations compiled in the report are factually based on data extracted from program/project documents, contractor reports, and open literature, and/or generated from independently conducted tests, analyses, and inspections.

3.0 Team Members

Name	Discipline	Organization
Core Team		
Bob Hodson	NASA Technical Fellow for Avionics. NESC Lead	NESC
Yuan Chen	Technical Lead 2018-2020	LaRC
Linda Del Castillo	Assessment Technical Lead 2020-2023	JPL
Reza Ghaffarian	Packaging	JPL
Lyudmyla P. Ochs	Failure Analysis	GSFC
Eric Galloway	Failure Analysis	GSFC
Consultants		
Ed Rutkowski	Reliability	GSFC
Susana Douglas	Parts Engineering/NASA EEE Parts Manager	GSFC
Carlton Faller	Parts Engineering	JSC
Jonathan Pellish	Parts Radiation/NASA EEE Parts Manager	GSFC
Richard Russell	Materials Technical Fellow	KSC
Dwayne Morgan	Avionics	WFF
Scott Gore	Parts Engineering	JPL
Ron Hodge	Parts/Packaging/Failure Analysis	MSFC
Thomas Miccolis	Parts Assurance	GSFC
Chris Green	Parts Engineering	GSFC
Michael Sampson	Parts Engineering	OSMA
Miguel Moe	Materials/Reliability	GSFC
Peter Majewicz	Parts Assurance & Reliability/NEPP Program Manager	GSFC
Business Management		
Becki Hendricks	Program Analyst	LaRC/MTSO
Assessment Support		
Melinda Meredith	Project Coordinator	LaRC/RSES
Linda Burgess	Planning and Control Analyst	LaRC/RSES
Jenny DeVasher	Technical Editor	LaRC/RSES

3.1 Acknowledgments

Special thanks to the Goddard Space Flight Center (GSFC) Parts Analysis Laboratory, Jet Propulsion Laboratory (JPL) Analysis and Test Laboratory, and JPL Analytical Chemistry Laboratory.

The assessment team also thanks peer reviewers Shri Agarwal, Tim Brady, Andrew Chaloupka, Steve Gentz, Bryan McEnerny, Jesse Leitner, Carlton S. Faller, Kuok Y. Ling, Susana P. Douglas, Peter J. Majewicz, and Don Parker.

4.0 Executive Summary

Traditionally, interconnects between silicon (Si) dice and electronic packages have been made using gold (Au) wire bonds. Semiconductor manufacturers are rapidly adopting copper (Cu) wire bonds for commercial components, due to cost as well as improved physical and mechanical properties. When compared to Au, Cu has approximately 25% lower electrical resistivity, 30% higher thermal conductivity, and 45% higher modulus of elasticity. A significant portion of commercial off-the-shelf (COTS) parts are bonded using Cu wire with or without a thin coating. The most commonly used coatings are palladium (Pd) alone or Pd with a layer of Au (Au flash). Although Cu wire bonding has matured significantly, reliability concerns remain due to the narrow bonding process window, oxidation during storage or processing, wire hardness, and corrosion at the bonded joint during operation or testing due to halides in the encapsulant. It is worth noting that several manufacturers use halide-free molding compounds. Military-specified components have not adopted Cu wire bonding, and there is no military standard for qualification of parts with Cu wire bonds. Additionally, no NASA-wide practice exists for addressing the use of Cu wire-bonded parts, and no NASA standards specify Cu wire bonds. The only commercial qualification requirements document on Cu wire is Automotive Electronics Council (AEC)-Q006, which does not provide bond pull/shear limits. The goals of this assessment were therefore to understand the risks and/or impact of using Cu wire-bonded components for space applications and to develop Cu bond assessment guidelines for NASA missions with risk classifications of A through D and human-rated missions, as defined in NASA Procedural Requirements (NPR) 8705.4, Risk Classification for NASA Payloads [ref. 1].

Although the selection of parts for the Cu wire bond assessment predates the NESC Technical Assessment Phase II report, “Recommendations on the Use of Commercial-Off-The-Shelf (COTS) Electrical, Electronic, and Electromechanical (EEE) Parts for NASA Missions” [ref. 2], the selection process was in line with that discussed for “Established COTS parts” from Industry Leading Parts Manufacturers (ILPM). The Cu wire bond assessment team identified hundreds of parts from well-known manufacturers following discussions with representatives from each NASA center, interested groups in various government agencies, and commercial aerospace companies. The team thoroughly reviewed all datasheets and down selected components on the basis of part type, package type, manufacturer, wire diameter, wire material, and wire count.

The reliability tests for this assessment were selected not only to determine the reliability of Cu wire-bonded plastic encapsulated microcircuits (PEMs), but also to envelop the requirements of most NASA mission environments under thermal fluctuations. The NESC assessment team considered mission, environment, application, and lifetime (MEAL) [ref. 3] to project thermal cycle (TC) life requirements at the assembly level for future NASA missions using PEMs with Cu wire bonds. Therefore, reliability testing was performed on parts assembled onto a printed circuit board (PCB). Assembly-level reliability of electronics is affected by part characteristics, including Cu wire bonds, PCB, and solder joints. The weakest link among the interconnections determines the first thermomechanical cycles to failure (CTF). In most cases, PCB assembly solder joints are the weakest links under TC fatigue. If solder joints are also the weakest link for failure of assemblies with Cu wire bond parts, then the use of existing analysis methods to project MEAL for NASA missions is valid. However, if Cu wire bonds become the weakest link, then new analysis methods must be developed because existing models have yet to address this aspect of fatigue failure. Highly accelerated stress testing (HAST), more specifically biased HAST (bHAST), was additionally performed to identify potential corrosion related failures.

The NESC assessment team used existing MEAL projection models, based on fatigue damage accumulation models for solder joints, to determine fatigue test conditions that encompass the widest range of applicable NASA mission conditions. TC and bHAST conditions of -55 to 125 ℃ for 2000 cycles, and 500 hours (hr) at 85% relative humidity (RH) and 110 ℃ were selected. All parts were rated to 110 ℃ or greater and data sheets indicated that these environmental conditions would be tolerable. It should be noted that the maximum junction temperature for PN M5-MCK-SOIC8-01 may have been exceeded by 3 ℃ at the maximum thermal cycling temperature. Shock and vibration testing were not performed because wire bonds in PEMs are encapsulated and are robust under mechanical loading in contrast to hermetically sealed parts with floating wire-bonds.

Upon receipt, each part type underwent construction analysis (CA), including X-ray, scanning acoustic microscopy (SAM), cross-section inspection, decapsulation, wire bond pull, and ball shear. Post-exposure evaluation (PEVAL) included SAM, decapsulation, visual inspection, wire bond pull, and ball shear. CA was critical in establishing Cu wire bond workmanship conditions. Cross-section evaluation was used to identify parts with significant aluminum (Al) bond pad displacement (i.e., splash), bond anomalies, and fractured Si underneath the bond pad (i.e., cratering). Decapsulation prior to bond pull and ball shear required optimization for each part and condition to obtain reliable, repeatable results. This was vital, since pull strengths for Cu wire bonds following decapsulation are highly dependent upon decapsulation processes. A combination of laser milling and chemical decapsulation was used. Decapsulation of multi-tier devices was challenging due to the range of bond heights and potential trapping of acid between inner and outer wire bond rings.

Thermal cycling and bHAST were monitored during testing, with no apparent electrical failures. Bond pull and ball shear testing were performed before and after environmental exposure. Wire bond pull and ball shear testing are the most often used methods of identify manufacturing process issues or degradation of the bond interface after reliability testing. Understanding the level of degradation and quality allows manufacturers and users to quantify assembly life. While electrical evaluation of parts with margin for the end use condition provides valuable information for that component, it does not provide sufficient information to determine the applicability of this technology for other missions with different MEAL requirements. Therefore, bond pull strengths and failure modes were assessed for each part to identify outliers, determine failure mechanisms, and evaluate statistical variations among conditions. Most parts exhibited failure either within the wire span or at the neck-down region, but cratering was observed for select parts following bond pull and shear testing. Multi-tiered components exhibited a relatively wide range of pull strength values. Stitch bond heel cracking was exhibited by one Cu and the only Au wire-bonded component following TC.

Statistical significance and trend determination were performed on pull and shear strength data for each part in the as-received condition as well as after TC and bHAST, using Analysis of Variance (ANOVA) and Student’s t-test. These analyses revealed that TC and bond pull testing were better differentiators for environmentally assisted damage to Cu wire bonds than bHAST or ball shear testing. Weibull distribution was used to evaluate pull and shear strength distributions for Cu wires as a function of wire diameter and part type. The 1-percentile pull strength values obtained through this assessment for Cu wire bonds were compared with MIL-STD-883, Method 2011 [ref. 4]. Cu wire bond pull strengths were found to be significantly higher for 1-mil (.001 in.) and 2-mil wire bonds, but approached the values for Au at lower diameters. These

results are supported by unbonded wire data plotted from literature, which exhibited a similar trend.

Since no electrical failures were observed due to Cu wire bonds under the harsh environmental conditions selected for this evaluation, the use of existing solder fatigue based analysis methods to project MEAL at the board level for various NASA missions was determined to be valid. The NESC assessment team identified four environmental conditions and mission durations to encompass a range of NASA flight conditions based on existing models.

The NESC Cu wire bond assessment team agrees with the NESC COTS Parts assessment Phase II report recommendations regarding COTS parts selection for NASA missions with risk classifications of A through D and human-rated missions [ref. 2]. Additionally, the Cu wire bond assessment team independently performed qualification at part-and board-level using a process similar to the recommendations in reference 2 for "Established COTS" from ILPMs. Based on the selection and evaluation process, the guidelines provided in this report are focused primarily on evaluation criteria for Established COTS parts with Cu wire bonds, with non-established COTS parts being used in only select circumstances. The Cu wire bond assessment builds upon the recommendations for using Established COTS parts from ILPMs for NASA Missions and provides criteria for part and board level verification of COTS parts with Cu wire bonds. As such, the team defined screening and lot acceptance testing (LAT) guidelines for Cu wire bonds in PEMs for a range of NASA flight conditions and mission risk classifications. In addition to the notion of using Established COTS, these guidelines include a combination of destructive physical analysis/CA (DPA/CA), outlier analysis, statistical analysis (e.g., Weibull), environmental testing (e.g, thermal cycling), and destructive bond pull testing to determine the reliability of Cu wire-bonds at the part- and board-level. The NESC assessment team additionally highlights the importance of obtaining bond pull data from the manufacturer prior to encapsulation. The importance of wire decapsulation process development is stressed for NASA Class categories requiring DPA/CA.

5.0 Assessment Plan

The specific assessment tasks requested were to:

1. Compile NASA's body of knowledge on Cu wire bonds, including publicly available knowledge gained from other government agencies.
2. Compare Cu wire bond DPA results, including bond pull/ball shear data to Au wire bond data, through researching databases at NASA and other government agencies.
3. Select representative Cu wire bond technologies and perform reliability testing and analysis on the Cu wire bonds. The reliability testing and analysis included environment testing, sample DPA, and bond pull/shear tests during environment testing intervals.

The goal was to understand the risks and/or impact of using Cu wire bonds for space applications and develop guidelines on Cu bond pull limits for NASA applications.

6.0 Problem Description and Background

In the past, commercial semiconductor manufacturers have used Au and Al wires to connect the semiconductor die to the leadframe and external pins. However, economics as well as the thermal and electrical properties of Cu wire have been the driving incentive for manufacturers to replace Au wire bonds with Cu wire bonds in the majority of commercial semiconductor devices, especially for the latest technologies including ball grid arrays (BGAs). When compared with Au, Cu is more economical and has approximately 25% lower electrical resistivity, 30% higher thermal conductivity, 75% higher tensile strength, and 45% higher modulus of elasticity. Cu also has 70% higher thermal conductivity and 60% higher electrical conductivity than Al. In addition, the growth rate of intermetallic compounds (IMCs) between Cu wires bonded on Al bond pads is approximately 100 times slower than that of Au wires on Al pads, which means less tendency to initiate voids during aging processes, resulting in wire bond failure.

However, Cu wire's increased hardness can cause cratering during the bonding process, which requires redesign and optimization of bond pads and bonding processes. Cu wires are prone to oxidation, which requires more cautious handling and storage and different kinds of inert gas flow during the bonding process depending on whether the Cu wires are coated with Pd. Therefore, different semiconductor manufacturers may have different types of Cu wire bonds and wire bonding processes.

There is no military standard for Cu bond wire qualification. The only commercial qualification requirements document on Cu wire is AEC-Q006, Qualification Requirements for Components Using Copper Wire Interconnections, which does not provide bond pull/shear limits. Recently, the Joint Electron Device Engineering Council (JEDEC) released two test methods: JESD22-B120 Wire Bond Pull Test Methods [ref. 5] and JESD22-B116B Wire Bond Shear Test Method [ref. 6]. Both methods include the evaluation of Cu wire bonds. Although Cu wire bond designs are moving forward for commercial applications, there are concerns regarding quality and reliability in high-reliability applications with long mission lifetimes.

7.0 Cu Wire Bond Assessment and NESC Recommendations

As part of this assessment, the NESC assessment team reviewed the current status of Cu wire bond technologies for space and military applications. The team then selected 17 PEMs with Cu wire bonds and one Au wire bond component to represent a cross-section of devices that are relevant for space applications and include important aspects of this technology. The parts were then evaluated through CA, decapsulation, mechanical evaluation, and reliability testing at the board-assembly level. The reliability testing and analysis included environment tests and sample post-exposure evaluation, including bond pull and ball shear tests, following environmental exposure.

7.1 Background

The adoption of Cu wire-bonded components for high-reliability NASA applications with long mission lifetimes requires a thorough understanding of Cu wire bond reliability. Part failures due to wire bond failure were common for Au wire bonds before temperature limits were identified and test methods determined. For Cu wire bonds in NASA applications, data is limited. Known issues related to workmanship have progressed significantly in recent years. Bond corrosion issues are still an area of active study. The impact of prolonged cryogenic exposure is not known. This reliability can be impacted by material properties, wire processing, bonding processes, and degradation mechanisms for the resulting joints following processing, qualification, and application. This section summarizes the assessment team's findings from lessons learned on Cu wire bonds via literature survey and reliability evaluation of numerous devices from small- to large-leaded, as well as BGA electronic packaging technologies. Appendix A presents detailed information on molding compounds and component soldering, as well as environmental testing and final application conditions, that can affect failure mechanisms. It also discusses screening and LAT on Cu wire bonds to ensure NASA mission reliability requirements are met, with comparison to various standards in use for Au wire bonds and consideration of differences in material properties and degradation mechanisms. This testing was performed to better understand thermomechanical fatigue of Cu wire bonded parts in the assembled condition. The results of testing can then be used for packaging qualification and verification evaluation of assemblies. Additional failure mechanisms include corrosion of the bond interface due to molding compound composition and this issue was evaluated through bHAST testing.

Manufacturers are able to optimize bond wires for specific applications through a combination of compositional optimization, wire processing, and annealing. Considerable work has been performed to optimize Cu wire bond performance and processability since wire strength, hardness, and oxidation behavior can all influence the reliability of a Cu wire bond and the resulting processing window. The effect of wire composition, processing, and microstructure on wire properties is discussed in detail in Appendix A. Figure 7.1-1 provides a plot of maximum and minimum breaking loads, obtained from manufacturer data sheets for a selection of commercially available Au and Cu bond wires, as a function of wire diameter. The curve entitled, Poly. (883-Au PreSeal) approximates the MIL-STD-883, Method 2011 Figure 2011-2 plot of minimum bond pull limits for Au in the Pre-Seal condition. [ref. 4] Since bond pull limits for Cu wires have not been established, several manufacturers and end users compare Cu wire pull strengths to the limits for Au. For this reason, the assessment team used the limits for Au as a basis for comparison. Figure 7.1-1 summarizes the impact of wire processing on resulting pull strength properties. Since bulk Cu has a higher strength and hardness than bulk Au, the goals of

microstructural optimization differ. Cu bond wires tend to have a higher purity, to minimize strengthening through alloying. Additionally, Cu wires tend to be more highly annealed, to minimize grain size strengthening. The impact of grain size and coatings on the tensile strength of thin Cu wires is discussed in Appendix A.1.1.

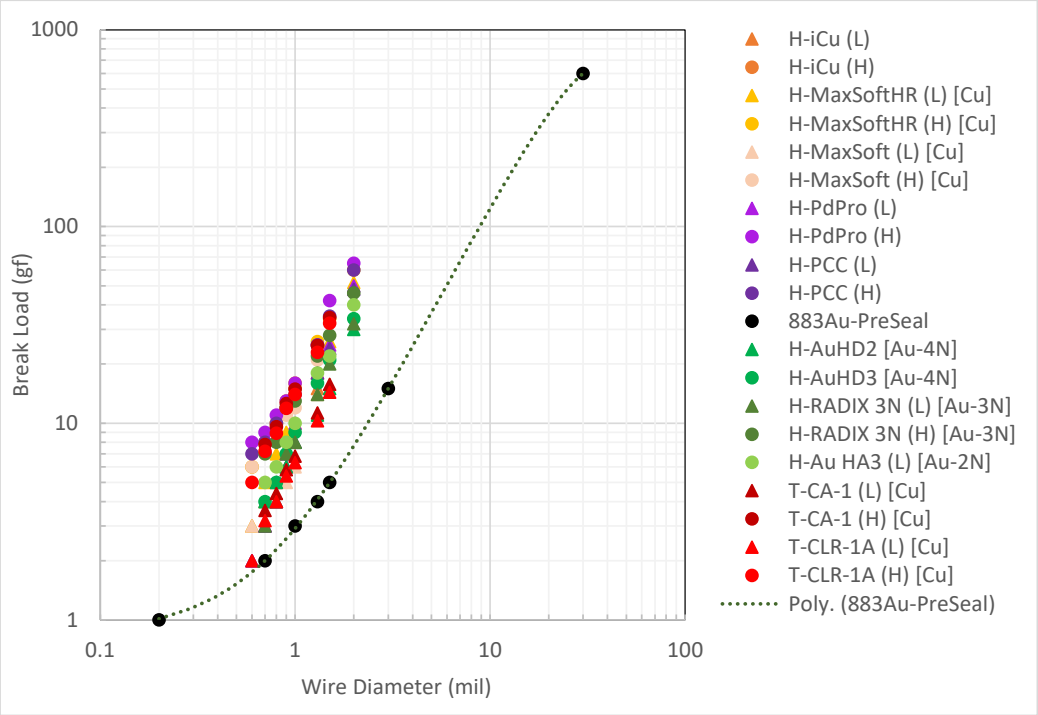

Figure 7.1-1. Break Load as Function of Wire Diameter for Commercial Cu and Au Wires. Data obtained from Heraeus and Tanaka wire specification sheets.

The wire bonding process and parameters are discussed in Appendix A.1.2. Although literature varies regarding the relative impact of ultrasonic energy, temperature, bond time, and pressure on specific bond properties, several facts are universally accepted. Cu wire is more likely than Au to oxidize during free air ball (FAB) formation, resulting in the need for cover gas. The higher thermal conductivity of Cu results in a smaller heat-affected zone (HAZ) than that of Au and the larger grain size of Cu wire prior to bonding minimizes the microstructural difference between the parent wire, HAZ and FAB. Because of this, Cu tends to have a less significant reduction in strength for the FAB and HAZ compared to the parent wire. Increased Cu hardness, compared with that of Au, increases the likelihood of damage to the Al bond pad (e.g., splash and cratering) and underlying device circuitry. Greater strain hardening of Cu wires is likely to occur during bond formation, compared with Au wires. Finally, Cu wire bonds have a narrower processing window than Au wire bonds. Figure 7.1-2 [ref. 7] provides an image of Au wire ball bonds on a semiconductor device, and Figure 7.1-3 [ref. 8] provides a general illustration of the wire ball bonding process.

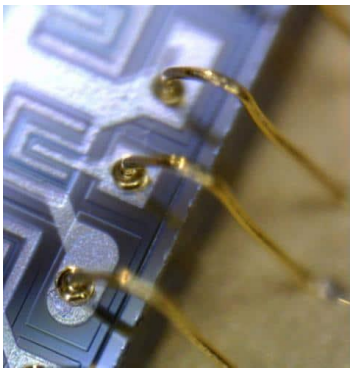

Figure 7.1-2. Image of Au Wire Bonds

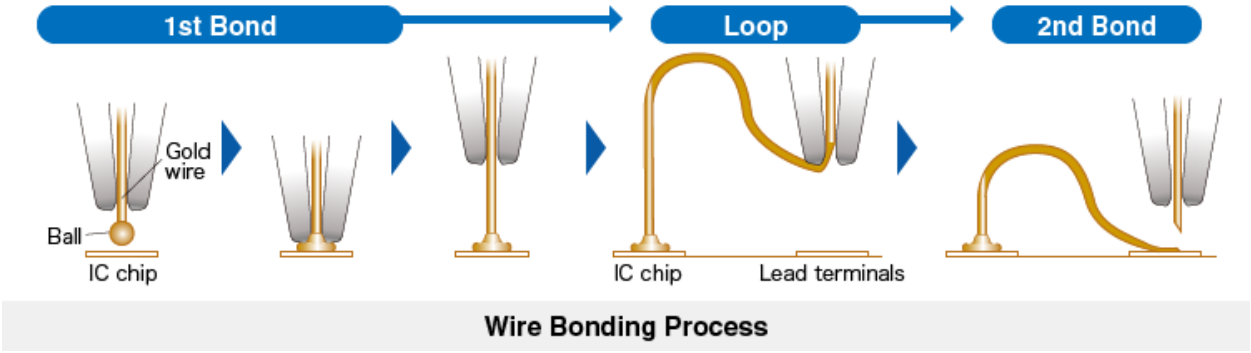

Figure 7.1-3. Schematic Illustration of Wire Ball Bonding Process

High wire count devices present unique challenges for Cu and Au wires (see Appendix A.1.3). Additionally, the molding compounds applied to PEMs after bonding present different challenges to Cu and Au bond wires. Au wire bonds tend to be affected by high curing temperatures, while Cu wire bonds are more susceptible to damage resulting from chemical composition.

IMC formation, growth, and reliability for Cu-Al and Au-Al bonds are detailed in Appendix A.1.4.1. The section discusses growth kinetics, activation energies, failure mechanisms, and the mechanical and physical properties of Cu-Al and Au-Al IMCs. IMCs begin to form at the interface through the bonding processes and continue to grow during molding compound curing, part screening, qualification, and operation. For example, the Au-Al IMC layer has been found to be 20 times thicker than that of Cu-Al in the as-bonded condition, and Au-Al IMCs grow at a significantly higher rate during aging.

A detailed discussion regarding the impact of molding compounds on corrosion of Cu ball bonds is provided in Appendix A.1.4.2. Investigations on the susceptibility of Cu wire bonds to corrosion indicate that the presence of bromine (Br-) or chlorine (Cl-) ions in molding compounds significantly increases corrosion issues for Cu wire-bonded joints. Close inspection of joint microstructure indicates that cracks form and propagate within the IMC layers, with the most significant corrosion occurring within the solid solution and Cu_9Al_4 phase. Consumption of this phase initiates cracks that can ultimately lead to electrical opens.

Assessment of the mechanical quality and reliability of bonded joints following initial processing and environmental exposure is most commonly performed using the destructive bond pull test [ref. 4] and wire bond shear test [ref. 6]. Section 7.1 details the history of the bond pull test

method and limits, as well as the test parameters. Additionally, details of the bond shear test method and a comparison of bond pull and shear test results for Cu and Au bonded joints are discussed in Appendix A.2.2. In general, pull testing of an Au wire bond will often result in failure within the HAZ. Due to the greater stiffness and strength of the Cu ball and reduced impact of a HAZ for Cu wires, a greater load is applied to the joint and the pad metallization. An Au ball bond will tend to shear within the ball, but a Cu bond is more likely to shear within the Al bond pad due to the increased Cu ball strength. Figure 7.1-4 provides a schematic illustration of the wire bond pull test and the wire bond shear test [ref. 9].

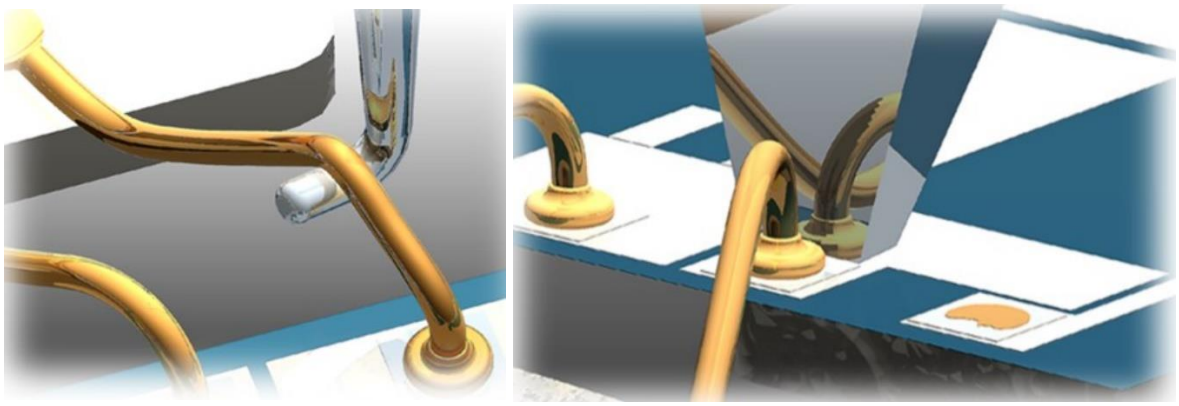

Figure 7.1-4. Schematic Illustrations of Wire Bond Pull Test and Wire Bond Shear Test

To better understand the reliability of Cu wire-bonded parts for NASA missions, the NESC assessment team considered the assembly-level reliability of these components. As discussed in Appendix A.2.3, assembly-level reliability under thermal stress depends on the reliability of constituent elements and global/local interfaces (i.e., attachments). Any of these elements, including Cu wire bonds, can become potential sources of the weakest link for reliability. Failure mechanisms under thermal cycling are complex, and a combination of parameters, including glass transition temperature (T_g), coefficient of thermal expansion (CTE) mismatches, and modulus, affect failure and mechanism. Each of these parameters are addressed through this assessment. Additionally, corrosion related mechanisms were addressed through HAST testing.

7.2 Experimental Test Plan

As of June 2023, no NASA-wide practice addresses the use of Cu wire bond parts, and no NASA standards, including the draft NASA-STD-8739.11, *EEE Parts Selection, Screening, Qualification & Derating*, specifically mention Cu wire bonds. There are no MIL-PRF-38534 or MIL-PRF-38535 products with Cu wire bonds. In situations where an application requires the use of COTS, NASA-STD-8739.10, *Electrical, Electronic, and Electromechanical (EEE) Parts Assurance Standard*, Section 5.1.1.4, requires NASA programs/projects to identify mitigating actions for approval based on the program or project EEE Parts Management and Control Plan. Several NASA centers use EEE-INST-002: Instructions for EEE Parts Selection, Screening, Qualification, and Derating, as the basis for those plans. Program assurance levels 1, 2, and 3 submit parts for DPA, where, per MIL-STD-1580, wire material is identified, and bond pull strength for Cu wire is judged against MIL-STD-883 limits for Au. No mention is made of whether to use pre- or post-seal bond pull limits from MIL-STD-883.

With respect to commercial standards, manufacturers can perform qualification per AEC Q006 [ref. 10], which contains tests and minimum requirements to qualify Cu wire-bonded parts for

use in automotive electronics. Although the standard replicates AEC-Q100/Q101 tests, AEC Q006 highlights different test conditions and durations needed to ensure the reliability of Cu wire bond parts. It does not provide minimum pull strength requirements for Cu wire bonds. Multiple documents cite AEC Q006 compliance for Cu wire bond use in avionics or space applications. These include MIL-STD-1580, IEC 62239-1, and SAE ARP6379. The recently released JEDEC JESD22-B120 [ref. 5] and JESD22-B116B [ref. 6] are applicable to pre- and post-encapsulated devices as well as Au alloy, Cu alloy, and Ag alloy wire bonds. Both methods provide information regarding decapsulation, failure modes, and details on how to perform the test, but not minimum pull or shear strengths. Minimum strength limits, combined with an assessment of outliers, allow manufacturers and end users to assess as-bonded and long-term reliability.

A summary of standards and specifications relevant to the use of Cu wire bonds for NASA applications is provided in Table 7.2-1. Appendix B.1 provides a more detailed discussion regarding current standards and specifications relevant to NASA use of Cu wire bonds. Process specifications for Cu wire bonding are not available. The impact of specific bonding parameters varies and it is highly dependent upon wire material, bond pad geometry, bond pad stack up, bond pad material, and tooling. Manufacturers are highly guarded with respect to process specifics and bond pull data. Specification and Standard developers are often unable to acquire bond pull strengths from manufacturers and end users in order to develop such specifications.

Table 7.2-1. Specifications and Standards Relevant to NASA Use of Cu Wire-Bonded Parts

Document	Source	Note	Cu Wire Bond DPA	Cu Wire Bond Pull Strength Limit
MIL-PRF-38534	DLA	No Cu wire bond parts	N/A	N/A
MIL-PRF-38535	DLA	No Cu wire bond parts	N/A	N/A
VID	DLA	No Cu wire bond parts	N/A	N/A
NASA-STD-8739.10	NASA	Does not specifically address Cu wire bonds; for commercial parts determine if DPA required	Mentions DPA but does not call out a specific standard	No pull limits
EEE-INST-002	NASA	Non-QML parts on Class A, B, C DPA per MIL-STD 1580	DPA per S-311-M-70	No pull limits
S-311-M-70	NASA GSFC	Requires identification of wire material; perform bond strength tests; ref. MIL-STD-1580 for DPA	Bond pull per MIL-STD-1580	No pull limits
MIL-STD-1580	DLA	References AEC Q006 Requirements for PEMS in military and space applications	- Identify wire material - Decapsulation methods discussed - Perform bond pull per MIL-STD-750 Method 2037 or MIL-STD-883 Method 2011 - Wire bond shear for PEMS per JESD22-B116	Bond pull strength for Cu wire is judged against MIL-STD-883 limits for Au
AEC Q006	AEC	Qualification requirements for Cu wire bonds defined	- Pull test method not referenced - Carefully decapsulate to avoid damage but enough to reliably test - Hook as close as possible to bond under test	Compare pull results with production or qualification data to assess degradation level in data distribution

MIL-STD-883	DLA	Test Method 2011 – Destructive bond pull test has no Cu wire bond strength limits	Test method is for hermetic parts (no decapsulation)	No Cu wire bond pull strength limits defined
MIL-STD-750	DLA	Test Method 2037 – Destructive bond pull test has no Cu wire bond strength limits	Test method is for hermetic parts (no decapsulation)	No Cu wire bond pull strength limits defined
JESD22-B120	JEDEC	Wire bond pull test method includes Cu wire bonds	Detailed decapsulation discussion provided	No minimum pull strength provided; stresses use of statistical process control per JESD557 and JESD50
JESD22-B116	JEDEC	Wire bond shear test method includes Cu wire bonds	Detailed decapsulation discussion provided	N/A

This assessment considered each of the Table 7.2-1 standards and test methods for the evaluation of Cu wire bonded components, with the goal of establishing guidelines for the acceptance of Cu wire bonded parts for future NASA missions. This includes determining which tests were most relevant in the evaluation of Cu wire bonds for NASA applications as well as the acceptance level for tests performed. The assessment was designed to not only determine the reliability of Cu wire-bonded PEMs, but also to develop a test plan that envelops the requirements of most NASA mission environments. MEAL guidelines [ref. 3] were used to project TC life requirements for future NASA missions that intend to use PEMs with Cu wire bonds. The assembly-level reliability of electronics is affected by package characteristics, including Cu wire bonds, PCB, and solder joint interconnections. These characteristics need to be combined with mission environmental conditions, design life, and acceptance failure probability to determine the life cycle for a NASA mission. The test plan was therefore tailored to include package-level test types known to impact device reliability, as well as assembly-level testing that envelops most NASA MEAL requirements.

The assessment started with the selection of relevant devices. High-quality parts of interest to the space and military communities were identified through discussions with representatives from each NASA center, interested groups in various government agencies, and commercial aerospace companies. Parts from this extensive list were down-selected based on the following:

- Part type – electrically erasable programmable read-only memory (EEPROM), Schottky diode, system-on-chip, operational amplifier (op amp), low-dropout (LDO) regulator, microprocessor, field programmable gate array (FPGA), shunt voltage reference, pulse width modulation (PWM) controller, driver, transistor, and/or transient voltage suppressor (TVS) diode array.
- Package type – Small outline integrated circuit (SOIC), small outline transistor (SOT), quad flat pack (QFP), thin QFP (TQFP), low-profile flat pack (LQFP), ball grid array (BGA), fine-pitch BGA (FBGA), low-profile FBGA (LFBGA), very-thin shrink small-outline package (VSSOP), and/or small outline diode (SOD).
- Wire count – 1 to 332.
- Wire composition – Cu, Pd-coated Cu (PCC), Au-coated PCC, and/or Au (for comparison).
- Wire diameter – 0.7, 0.8, 1.0, and 2.0 mil.
- Component manufacturer – 11 separate manufacturers.

The NESC assessment team members selected the parts of greatest interest, providing criteria for selection of each component and voting on which to include in the assessment. Based on ranking and applicability, the 18 components listed in Table 7.2-2 were ultimately selected. Every effort was made to identify relevant test data and discuss lessons learned from parties with experience in the evaluation of Cu wire-bonded components for high-reliability applications.

Table 7.2-2. Summary of Components for Cu Wire Bond Study

Part Number	Part Category	Part Description	Package	Wire Count	Halide, Halogen or Sb/Br Free Note
M10-D-SOD323-01	Discrete	Schottky Diode	SOD323	1	No
M10-D-SOT1061-01	Discrete	Schottky Diode	SOT-1061	2	No
M2-D-SOT233-01	Discrete	Schottky Diode	SOT-23-3	2	Yes
M2-D-SOT233-02	Discrete	Schottky Diode	SOT-23-3	2	Yes
M5-D-SOT233-01	Discrete	Shunt Voltage Reference	SOT-23-3	2	Yes
M5-MCK-SOT235-01	Microcircuit	Driver	SOT-23-5	4	Yes
M6-D-SOT235-01	Discrete	TVS Diode Array	SOT-23	5	No
M5-MCK-WSON6-01	Microcircuit	LDO	6-WSON	6	Yes
M1-MCK-SOIC8-01	Microcircuit	EEPROM	8-SOIC	7	Yes
M5-MCK-VSSOP8-01	Microcircuit	Op Amp	8-VSSOP	8	Yes
M9-D-Custom-01	Discrete	Transistor	Custom	9	Yes
M5-MCK-SOIC8-01	Microcircuit	PWM Controller	8-SOIC	11	Yes
M3-MCK-TQFP100-01	Microcircuit	Program System-on-Chip	100-TQFP	108	No
M8-MCK-LQFP100-01	Microcircuit	Microcontroller	100LQFP	144	Unclear
M11-MCK-TQFP144-01	Microcircuit	FPGA	TQFP144	151	No
M1-MCK-LFBGA144-01	Microcircuit	Microprocessor	144LFBGA	198	Unclear
M4-MCK-FBGA256-01	Microcircuit	Op Amp	256FBGA	272	No
M7-MCK-LFBGA169-01	Microcircuit	FPGA	169-LFBGA	332	Yes

Upon receipt, all parts were inspected and each part type underwent CA, including X-ray, SAM, cross-section inspection, decapsulation, wire pull, and ball shear, as described in Appendix B.2.1. Additionally, molding compounds were analyzed as detailed in Appendix B.2.1.2. Since environmental testing was performed at the assembly level, parts were exposed to relevant processing parameters, including two reflow cycles representing double-sided assembly. Soldering iron touch-up was performed to simulate local rework conditions prior to environmental testing. Design, fabrication, and assembly of PCB test vehicles are detailed in Appendix B.5. The selected components were assembled onto two differently designed PCBs and biased during environmental exposure. Table 7.2-3 describes onto which PCB each part was assembled, the number of parts per board, the number of boards assembled, part moisture sensitivity level, bake conditions, and bias conditions (e.g., power pins).

A total of 16 PCBs (8 PCB1 and 8 PCB2) were subjected to environmental testing following assembly, rework, and inspection. Qualification test conditions were selected to be significantly harsher than most applications meeting the hierarchy of package, subsystem (module/assembly), and system (box). Details of test plan development and exposure conditions are provided in Appendix B.5. Interconnection failure within the package should also be considered in the overall system life cycle projection. A review of available specifications and standards for the

use of PEMs with Cu wire bonds revealed the importance of highly accelerated stress testing (HAST), as well as thermal cycling to the reliability of such devices.

Synergism of HAST and TCs was evaluated by subjecting a limited number of assemblies first to HAST and then to thermal cycling. The weakest link among the interconnections determines the first thermomechanical CTF. In most cases, solder joints onto a board constitute the weakest link under TC fatigue. If solder joints become the weakest link for failure of assemblies with Cu wire bond parts, then the use of current analysis methods to project MEAL for various NASA missions is valid. However, if Cu wire bond interconnections become the weakest link, then new analysis methods must be developed because this aspect of fatigue failures has yet to be addressed in heritage MEAL projection models. This moves beyond the scope of this assessment, since HAST/cycles-to-failure correlations require the establishment of failure mechanisms internally within chip-level interfaces and externally for packaging materials and solder joints. The correlation may include an established relationship between the internal shear/tensile strengths of Cu wire bonds and associated IMCs and external packaging materials, including the Tg and chemical composition of molding compounds.

Table 7.2-3. 18 Parts Distributed Between Boards

Part Number	PCB #	PCB Qty	Parts/PCB	MSL	Bake (◦C)	Bias on Board (V)
M1-MCK-SOIC8-01	1	10	20	1	-	3.3
M5-MCK-SOIC8-01	1	10	20	1	-	18
M5-MCK-VSSOP8-01	1	10	20	1	-	18
M5-MCK-WSON6-01	1	10	40	1	-	3.3
M5-MCK-SOT235-01	1	10	20	1	-	3.3
M5-D-SOT-233-01	1	10	40	1	-	3.3
M4-MCK-FBGA256-01 (only sublot 1)	1	7	5	3	125	3.3
M3-MCK-TQFP100-01	1	10	10	3	125	3.3
M7-MCK-LFBGA169-01	1	10	10	3	125	3.3
M2-D-SOT233-02	2	10	40	1	-	18
M2-D-SOT233-01	2	10	40	1	-	18
M6-D-SOT-235-01	2	10	40	1	-	3.3
M9-D-CUSTOM-01	2	10	40	1	-	18
M10-D-SOD323-01	2	10	40	1	-	18
M10-D-SOT1061-01	2	10	40	1	-	18
M1-MCK-LFBGA144-01	2	10	10	3	125	3.3
M8-MCK-LQFP100-01	2	10	10	3	125	3.3
M11-MCK-TQFP144-01	2	10	10	3	125	3.3 and 1.2

Includes moisture sensitivity level (MSL), bake-out information and biasing voltage during test

Failure of solder joints on PCB assemblies occurs due to workmanship issues (e.g., early failures) or solder joint fatigue resulting from strain induced by temperature gradients and CTE mismatches. A detailed discussion on fatigue of solder joints and Cu wire bonds is provided in Appendix B.4.2. As discussed in section B.4.2.2, CTF can be determined using the Coffin-

Manson relationship, which relates CTF to plastic strain amplitude and fatigue ductility coefficient and exponent. The Norris-Landzberg model, a modified version of the Coffin-Manson model that includes the effects of frequency and temperature, has been applied to project thermal CTF for conventional and advanced packaging assemblies based on accelerated test data. These projections can be applied to various MEAL scenarios and exposure conditions. To encompass the widest range of conditions, a temperature range of -55 °C to 125 °C and 2000 TCs was selected for this assessment.

A schematic illustration of the experimental plan is provided in Figure 7.2-3. Upon receipt, a selection of components for each of the 18 selected parts underwent visual inspection, X-ray photoelectron spectroscopy (XPS), and X-ray imaging to confirm that they had Cu wire bonds. Each part type underwent CA, including cross-section inspection of the joint, decapsulation, SAM, scanning electron microscopy (SEM), destructive wire bond pull, and ball shear. Decapsulation was a critical part of this assessment, and the process used to evaluate decapsulation methods is outlined in Appendix B.2.1.3. Mold compounds were analyzed via differential scanning calorimetry (DSC) to determine the Tg.

Following design, fabrication, and assembly, PCB assemblies were subjected to post-assembly soldering iron touch-up, X-ray inspection and infrared (IR) inspection. The assemblies were then placed in their selected environmental test conditions, including bHAST and thermal cycling. Figure 7.2-3 shows when parts were placed in the chambers and removed, as well as detailing which conditions underwent destructive analysis following exposure. A detailed discussion on the selection of individual boards for each exposure condition is discussed in Appendix B.5.

PEVAL included SAM, decapsulation, visual inspection, destructive wire bond pull, and ball shear. Statistical analyses were performed on the results of bond pull testing and ball shear testing to determine whether exposure to thermal cycling and/or HAST resulted in significant differences in strength relative to baseline or within environmental conditions. Cu wire pull strengths were also compared with MIL-STD-883L, Method 2011.10 graphs [ref. 4] for Au wire bond pull strengths (pre-seal condition). TC and HAST data, failure mechanisms, and Cu-wire COTS packaging technologies were categorized based on MEAL conditions.

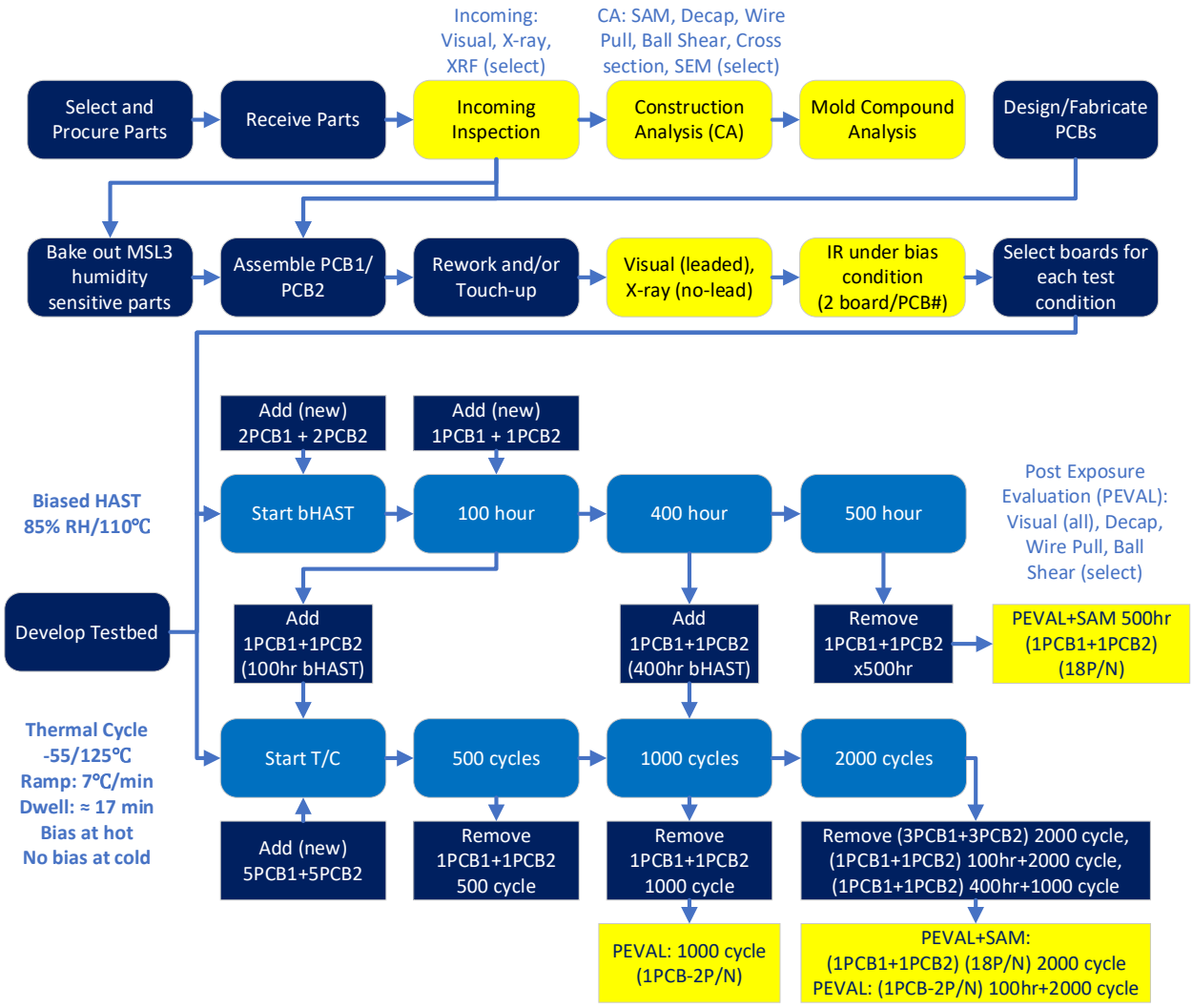

Figure 7.2-3. Schematic Illustration of Cu Wire Test Plan

7.3 Test Results

This section summarizes the results of CA, decapsulation, environmental testing, post-environmental evaluation, and mechanical evaluation of wire bonds, including destructive wire bond pull tests and ball shear tests. Failure modes and strength distributions are discussed for both mechanical test methods. Statistical analyses were performed on resulting bond pull and ball shear strengths. The relative impact of different test conditions and part configurations are discussed.

7.3.1 CA and Mold Compound Analysis

Upon receipt, representative parts from each part type were subjected to radiographic analysis. Preliminarily assessment of base material composition, prior to decapsulation, was performed by comparing these representative parts to a known plastic encapsulated device with Au wire bonds, under the same inspection conditions. Radiographic analysis was performed at 55 kV and 30 µA. Samples appeared homogenous in bond wire material using radiographic analysis. Wires of the representative devices appeared less dense than those of the known Au device, suggesting that

the bonds were made using Cu wires. Figure 7.3-1 shows X-ray images of the known Au wire bonded component and M3-MCK-TQFP100-01. Cu and Al wire bonds were not compared in this assessment. Al wires are less dense than Cu and could potentially be identified using X-ray analysis as well.

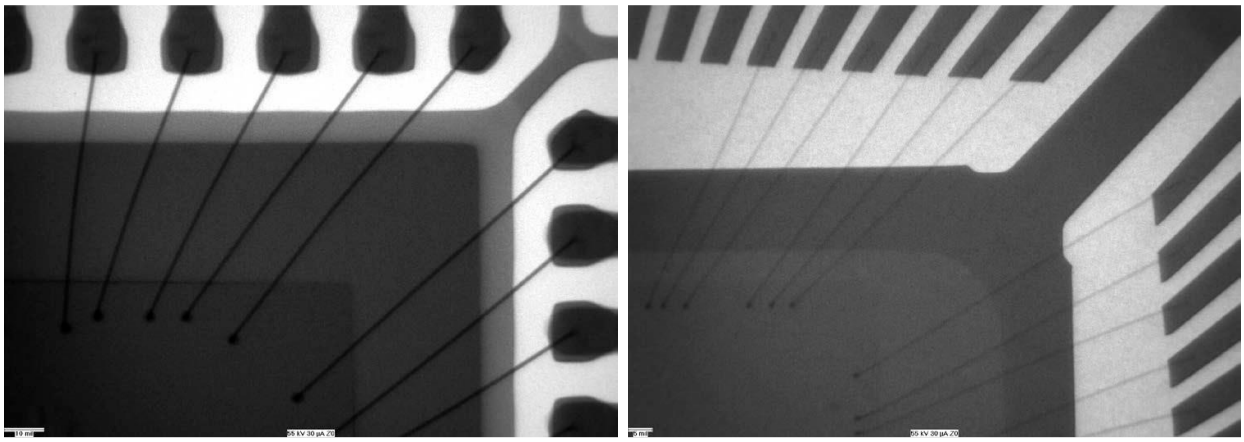

Figure 7.3-1. X-ray Images of Known Au Wire-bonded Device (left) and M3-MCK-TQFP100-01 (right). X-ray Inspection was performed at 55kV and 30 µA.

CA was performed on each of the 18 part types prior to environmental testing. Physical properties for each device are summarized in Table 7.3-1. It is convention in the United States to measure wire diameters in English units and device dimensions in metric units. As such, mils are used for wires and microns are used for the bond pad and device dimensions. X-ray images of the overall package from the top and side, optical micrographs and SEM micrographs of bond cross-sections, optical images (with measurements) of decapsulated bond wires on the package, as well as SEM backscatter electron (BSE) energy dispersive X-ray spectroscopy (EDS) compositional maps of ball bond cross-sections, stitch bond cross-sections, and decapsulated bond wires are provided in Appendix C.1 for each of the 18 part numbers. Representative images are included in Figure 7.3-2 for part number M3-MCK-TQFP100-01. These images provide information on the part configuration, wire bond shape, bond interface (e.g., splash of bond pad and distribution of Pd within the ball bond), bond pad geometry, leadframe composition (Ag plating), wire composition (Pd/Cu), and mold compound.

Molding compounds for the 18 part types were evaluated using DSC and thermogravimetric analysis (TGA) to determine the T_g and decomposition temperature. Details of this evaluation are provided in Appendix C.1. The T_g is provided in Table 7.3-1 for each part evaluated. Attempts were made to determine the CTE of the different molding compounds using a Thermomechanical Analyzer (TMA); however insufficient material was available after the device and lead frame were removed. Due to the small amount of molding compound and the significant proportion of silica filler, the team was unable to obtain reliable chemical analysis for halide content. Finally, nano-indentation was used to obtain the modulus of the molding compound. Results of this evaluation were inconclusive due to the high level of silica fillers and their impact on measurements.

Table 7.3-1. CA Summary

Part Number	Package Size (mm^3)	Wire Count	Wire (mil)	Ball Area (mil^2)	Bond Pad (um)	Splash (um)	Under Ball (um)	Wire Type	Lead Frame metallization	T_g (°C)
M10-D-SOD323-01	1.251.7x0.95	1	2.00	23.20	1.30	4.00	0.60	Cu	Ag/Cu	155.8
M2-D-SOT233-01	1.3x2.9x1	2	0.80	5.37	2.60	5.07	1.00	Cu	Cu/FeNi	126.0
M5-D-SOT233-01	1.3x2.9x0.95	2	1.00	3.06	1.43	2.33	0.28	Cu	Ag/Cu	109.0
M2-D-SOT233-02	1.3x2.9x1	2	0.80	7.38	2.00	5.50	0.90	Cu	Cu/FeNi	140.0
M10-D-SOT1061-01	2x2x0.65	2	2.00	18.60	1.72	4.88	0.68	Cu	Pd/Ni/Cu	126.9
M5-MCK-SOT235-01	1.6x2.9x1.1	4	0.80	4.44	1.40	2.80	1.50	Au	Ni/Cu	121.7
M6-D-SOT235-01	1.6x2.9x1.15	5	1.00	6.63	4.00	9.00	0.00	PCC (Pd/Cu)	Ag/Cu	123.3
M5-MCK-WSON6-01	2.02x2.5x0.8	6	0.80	2.56	1.10	3.40	0.00	PCC (Au/Pd/Cu)	Ag/Cu	139.8
M1-MCK-SOIC8-01	3.9x4.9x1.25	7	1.00	5.4	0.54	3.05	0.91	PCC (Au/Pd/Cu)	Ni/Cu	115.6
M5-MCK-VSSOP8-01	3x3x1.1	8	1.00	3.84	1.46	1.54	0.50	Cu	Ag/Cu	111.8
M9-D-CUSTOM-01	3x3x1	9	2.00	21.20	4.00	8.00	2.00	Cu	Ag/Cu	120.1
M5-MCK-SOIC8-01	3.9x4.9x1.5	11	1.00	4.70	2.9	8.80	0.70	Cu	Ni/CuFe	114.8
M3-MCK-TQFP100-01	14x14x1.4	108	0.80	2.56	0.85	4.00	0.50	PCC (Pd/Cu)	Ag/Cu	121.0
M8-MCK-LQFP100-01	10x10x0.96	144	1.00	3.28	2.80	0.00	2.80	PCC (Au/Pd/Cu)	Ag/Cu	119.6
M11-MCK-TQFP144-01	20x20x1.4	151	0.80	2.07	1.50	3.30	0.50	PCC (Au/Pd/Cu)	Ag/Cu	111.2
M1-MCK-LFBGA144-01	11x11x1	198	0.70	1.92	1.68	3.37	0.51	PCC (Au/Pd/Cu)	Au/Ni/Cu	153.7
M4-MCK-FBGA256-01	11x11x1	272	0.80	3.21	0.97	2.20	0.50	Cu	Au/Ni/Cu	130.6
M7-MCK-LFBGA169-01	14x14x1.4	332	0.70	1.42	2.70	5.10	0.90	PCC (Pd/Cu)	Au/Ni/Cu	110.3

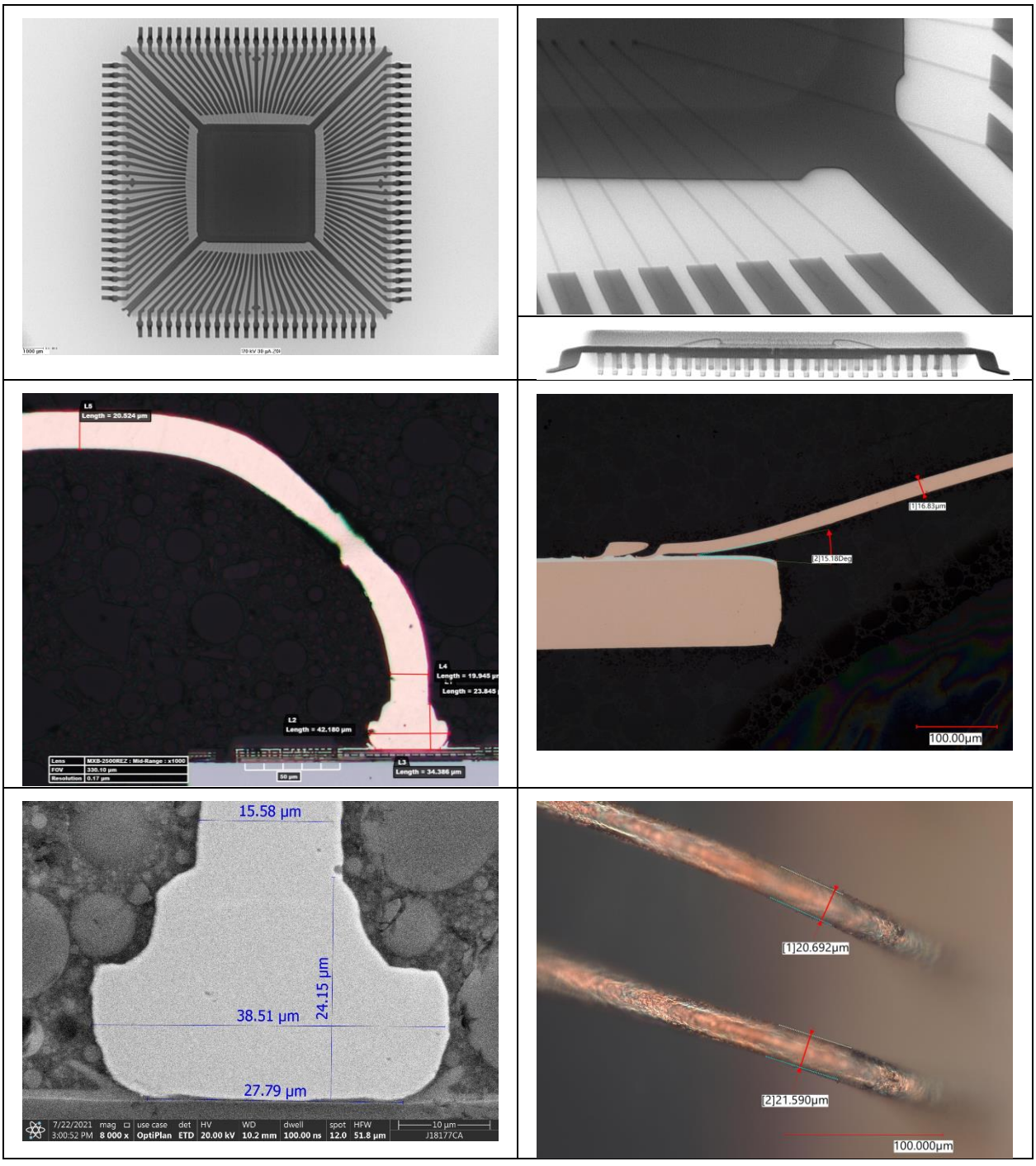

Figure 7.3-2a. CA Images for Part Number M3-MCK-TQFP100-01.
Component X-ray images, ball bond cross-section optical image, stitch bond cross-section optical image, ball bond cross-section SEM micrograph and optical image of decapsulated wires.

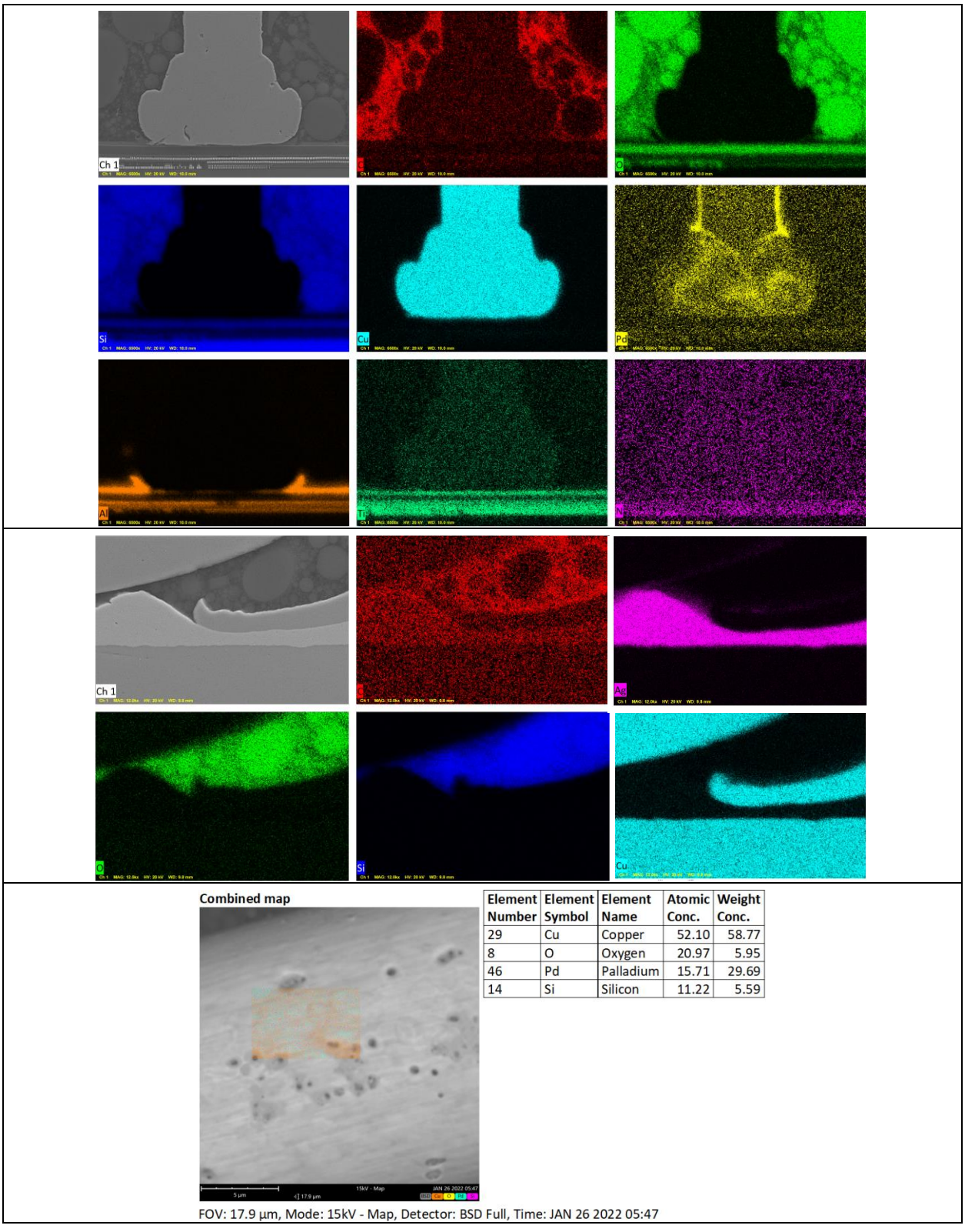

Element Number	Element Symbol	Element Name	Atomic Conc.	Weight Conc.
29	Cu	Copper	52.10	58.77
8	O	Oxygen	20.97	5.95
46	Pd	Palladium	15.71	29.69
14	Si	Silicon	11.22	5.59

Figure 7.3-2b. SEM EDS Composition Maps of Ball Bond and Stitch Bond Cross-Sections and Decapsulated Wire Bond for Part Number M3-MCK-TQFP100-01

7.3.1.2 Decapsulation Assessment

A combination of laser milling and chemical decapsulation was used for this investigation to minimize damage to Cu wire bonds and bond pads on the Si die and leadframe. The details of the decapsulation process development are provided in Appendix C.2. Laser decapsulation was used to reduce the amount of mold compound left to be removed by chemical decapsulation, which also helped mitigate undesired etching of key metallic features. Decapsulation with acid alone caused excessive etching of the Cu wire and metal leadframe, while decapsulation with laser alone caused excessive degradation of the Si die surface and bond pads. Figure 7.3-3 illustrates the difference in damage to the die surface and Cu bond wires for parts decapsulated using laser decapsulation alone and combined with chemical decapsulation to minimize damage to the die surface. Since this assessment focused on the evaluation of Cu wire bonds, including die and leadframe bonding surfaces, a combination of laser and chemical decapsulation was used to lessen damage to the die bond pads. Limited degradation to the die surface was allowed since no electrical part evaluation was planned post-decapsulation. This allowed more laser passes to remove molding compound and reduced chemical degradation of wires. Decapsulation guidelines provided in JESD22-B120 and JESD22-B116B were helpful in the development of the decapsulation method; however, a library of images indicating unacceptable and acceptable level of wire degradation would have been extremely useful.

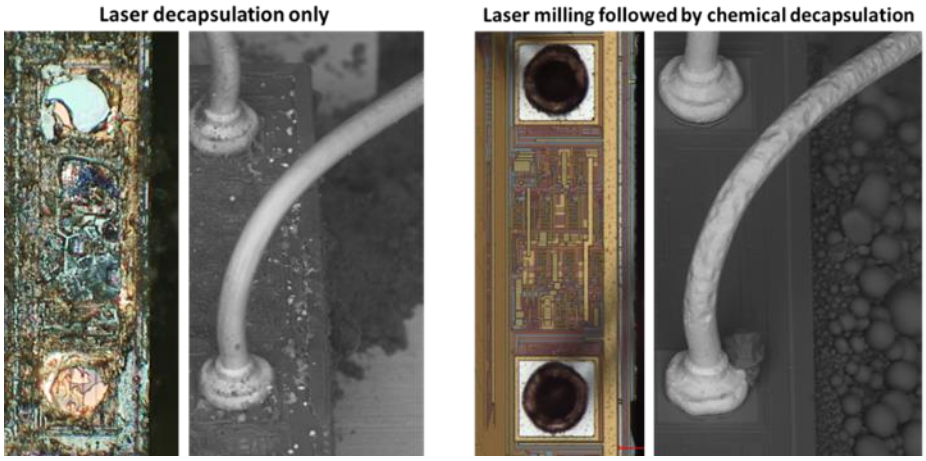

Figure 7.3-3. (Left) Using an IR Laser Decapsulation System to Fully Decapsulate Sample Protects Cu Wires but Causes Severe Damage to Die Features. (Right) Using laser to reduce mold compound, then finishing with acids, protects the die but can affect Cu wire integrity.

Unintended chemical etching of Cu wire occurs to a varying extent based on several parameters, including the procedures used. For high-wire-count and multiple-wire-tier parts, large segments of mold compound are blocked from quick laser or chemical decapsulation due to occlusion from densely packed wires. It was determined that agitation of the acid (vortex decapsulation) for multi-tier parts was detrimental to the integrity of exposed wires. This was due to the acid exposure duration required to etch the mold compound and fully expose dense groupings or lower tiers of wires. While in the submerged vortex, acid can seep into mold compound that has not completely dissolved, during which etching of Cu wire occurs before the mold compound washes away. The wire segments with the best appearance were those exposed beforehand by laser decapsulation. Figure 7.3-4 illustrates a multi-tier part that underwent this decapsulation process, with laser milling followed by chemical decapsulation with an acid vortex and final laser milling to the leadframe.

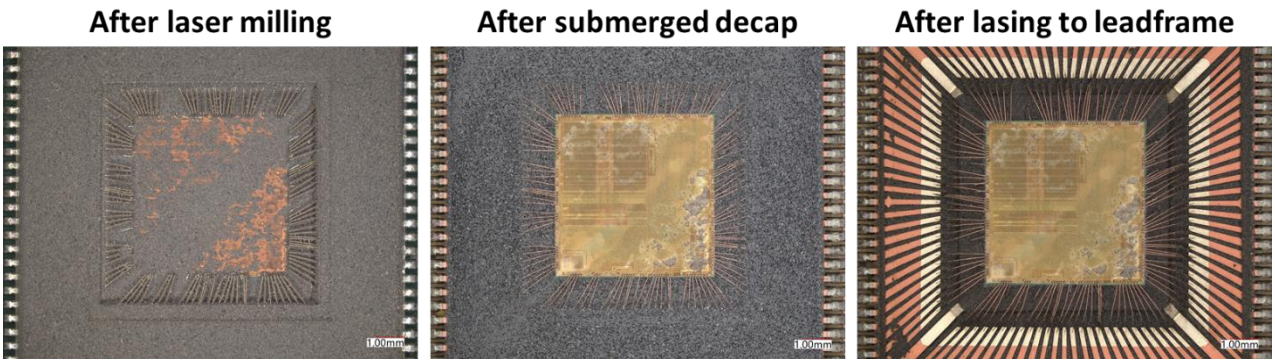

Figure 7.3-4. Images Representing Stages of Decapsulation for Multi-Tier Parts

Rinsing and Cleaning

This process was developed because the Cu bond wires of select parts used in this assessment exhibited a tendency to retain acid, causing continued Cu etching over hours or days, despite being rinsed and cleaned after decapsulation. Testing was performed to determine how to best preserve these wires after decapsulation, which included various baking durations and soaking in still and stirred acetone. Results are shown in Figure 7.3-5. The best results were obtained by soaking the decapsulated units in a stirred acetone bath. The acetone acts to neutralize and dehydrate the acids, while the stirring vortex continuously displaces acids released from the wires during the soak. Testing suggests that the units should remain in the acetone vortex for no less than one hour. After that, the parts underwent the complete rinsing and drying cycle again. Examination and bond testing of these parts were performed within one day of decapsulation.

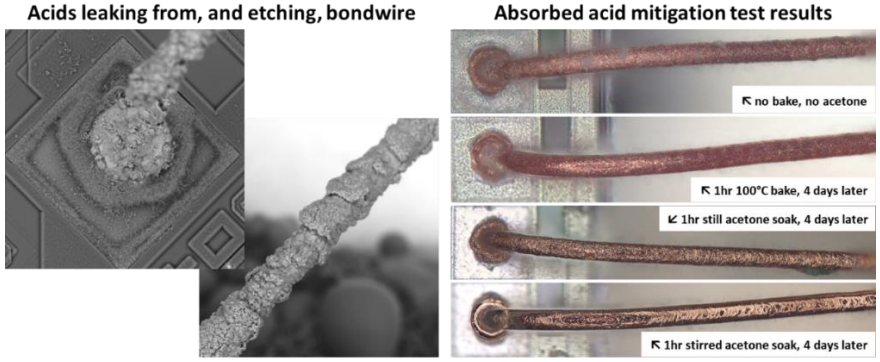

Figure 7.3-5. (Left) Images of Representative Bond Wire from Part That Absorbed Acid During Decapsulation and Continued Etching Over Time. (Right) Examination and bond testing of units after variety of mitigation techniques indicated stirred acetone yielded best results.

7.3.2. Environmental Test Results

TC and bHAST were monitored during environmental testing, with no apparent electrical failures. The levels of degradations and changes in failure mechanisms were evaluated using wire bond pull and shear strengths as well as characterization with optical microscopy and SEM. Strength integrity is affected by decapsulation approaches. Therefore, significant time was allocated to optimize mold removal, as discussed in Section 7.3.1. In weekly meetings, the NESC assessment team reviewed results and discussed suspicious wire bond strengths and failure mechanisms.

7.3.2.1 SAM Results

SAM was performed on individual components in the as-received condition. Following environmental exposure, PCB assemblies were cut into sections, mounted, and inspected using SAM. Representative SAM images are provided in Appendix C.3.1 and Table 7.3-2. These images represent a selection of parts with significant, minor, and no delamination. A summary of inspection results is provided in Figure 7.3-5. In certain cases, no parts were available following exposure due to location, availability, or part configuration.

Delaminations were ranked using the following:

- Significant = Delamination that covered an entire leadframe or die.
- Moderate = Delamination that covered part of the leadframe or die.
- Minor = Delamination that was not near a wire bond or die.
- None = No delaminations.
- N/A = SAM could not be performed because the part was destroyed during processing or had "deadbug" internal construction that could not be examined in SAM.

Table 7.3-2. SAM Representative Images

M5-MCK-VSSOP8-01	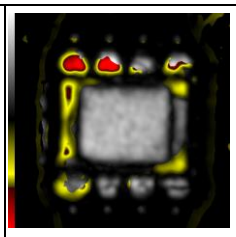 Incoming Inspection	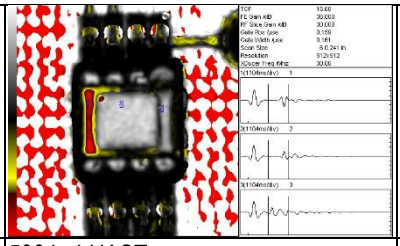 500 hr bHAST	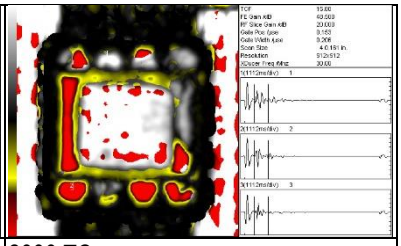 2000 TCs
M8-MCK-LQFP100-01	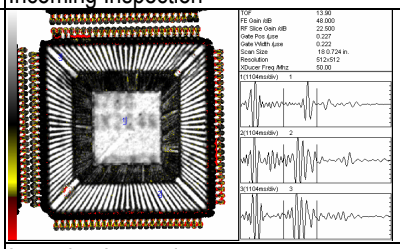 Incoming Inspection	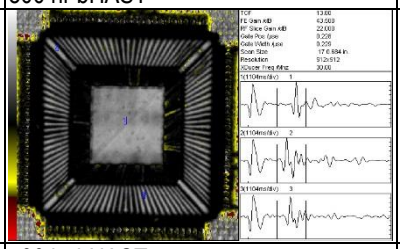 500 hr bHAST	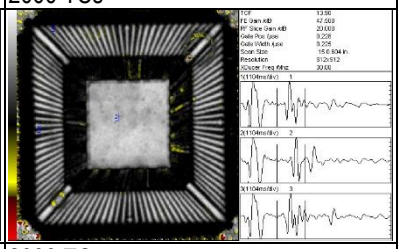 2000 TCs
M11-MCK-TQFP144-01	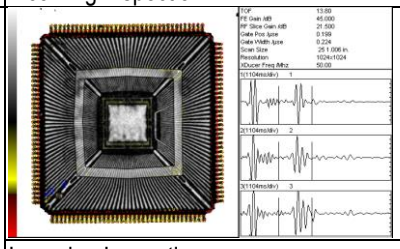 Incoming Inspection	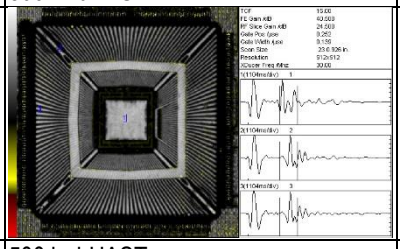 500 hr bHAST	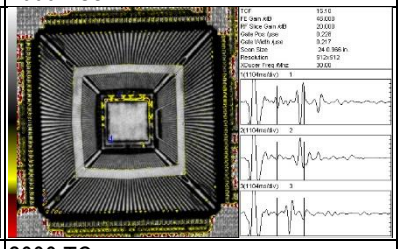 2000 TCs

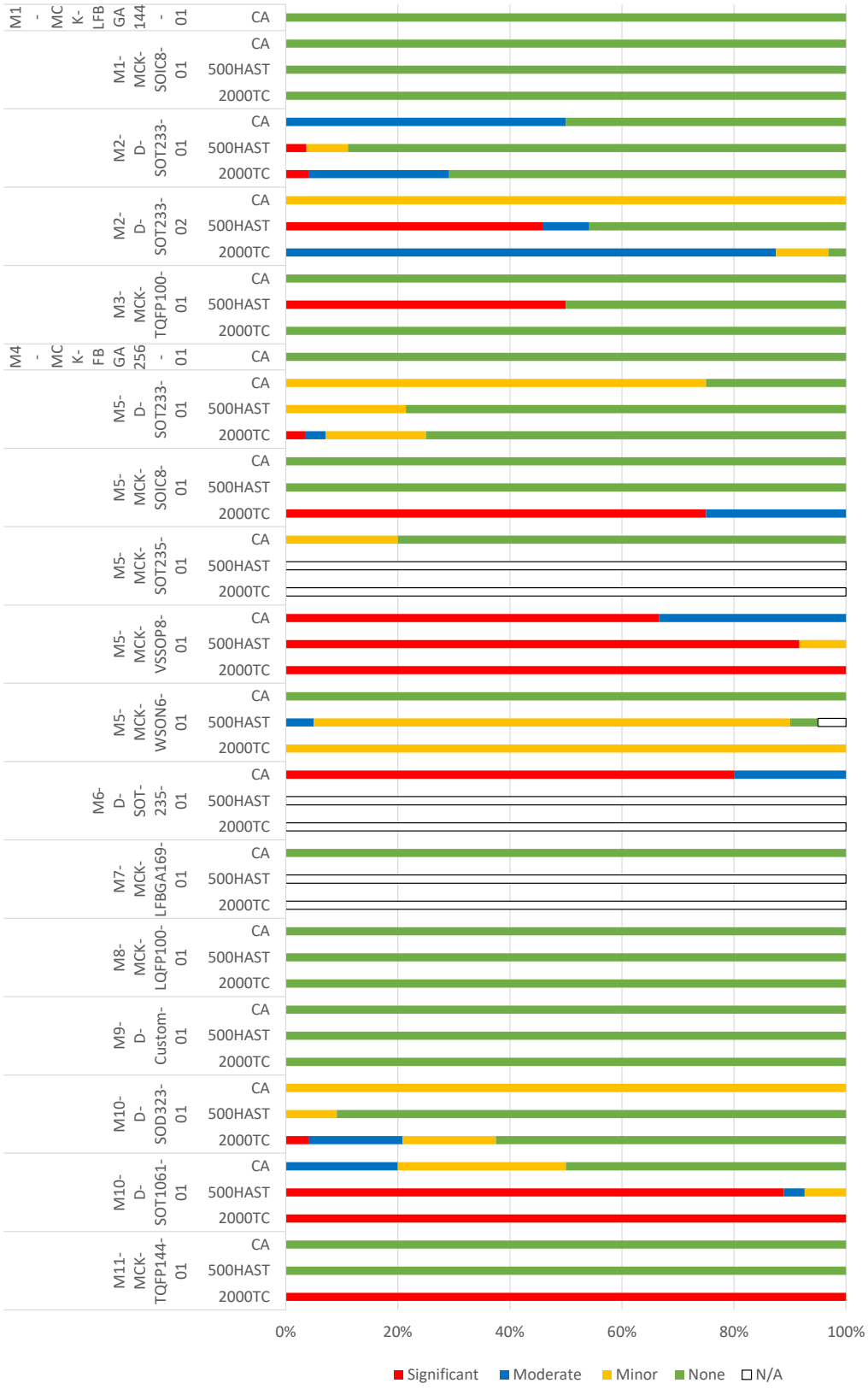

Figure 7.3-6. Plot Summarizing SAM Inspection Results for Each of 18 Part Numbers As-Received, Following 500 hr of bHAST and 2000 TCs

7.3.2.2 Cu Wire Bond Pull Test Results

Wire bond pull tests were performed in the as-received condition, after 500 hours of bHAST exposure and after 2000 TCs for all part types. Due to indications of possible TC-related wire fatigue damage, two parts were selected for decapsulation and wire pull following 1000 TCs. Additionally, two large-wire-count components were selected for decapsulation and wire pull following the combined exposure of 400 hours of bHAST and 1000 TCs. Figure 7.3-7 provides the cumulative bond pull strength for each wire diameter, regardless of Cu wire composition, part number, or environmental exposure condition. This method of plotting was used to more clearly identify individual outliers rather than binning of bond pull strengths. A summary of bond pull failure modes [ref. 4] for each part type and condition is provided in Figure 7.3-8. A detailed presentation of cumulative bond pull strength and associated failure mode for each part type and condition is provided in Appendix C.3.2. An example of these plots for M1-MCK-SOIC8-01 is provided in Figure 7.3-9. These plots were used to better understand the correlation between pull strength, failure mode, and root cause for bonds with outlier pull strengths.

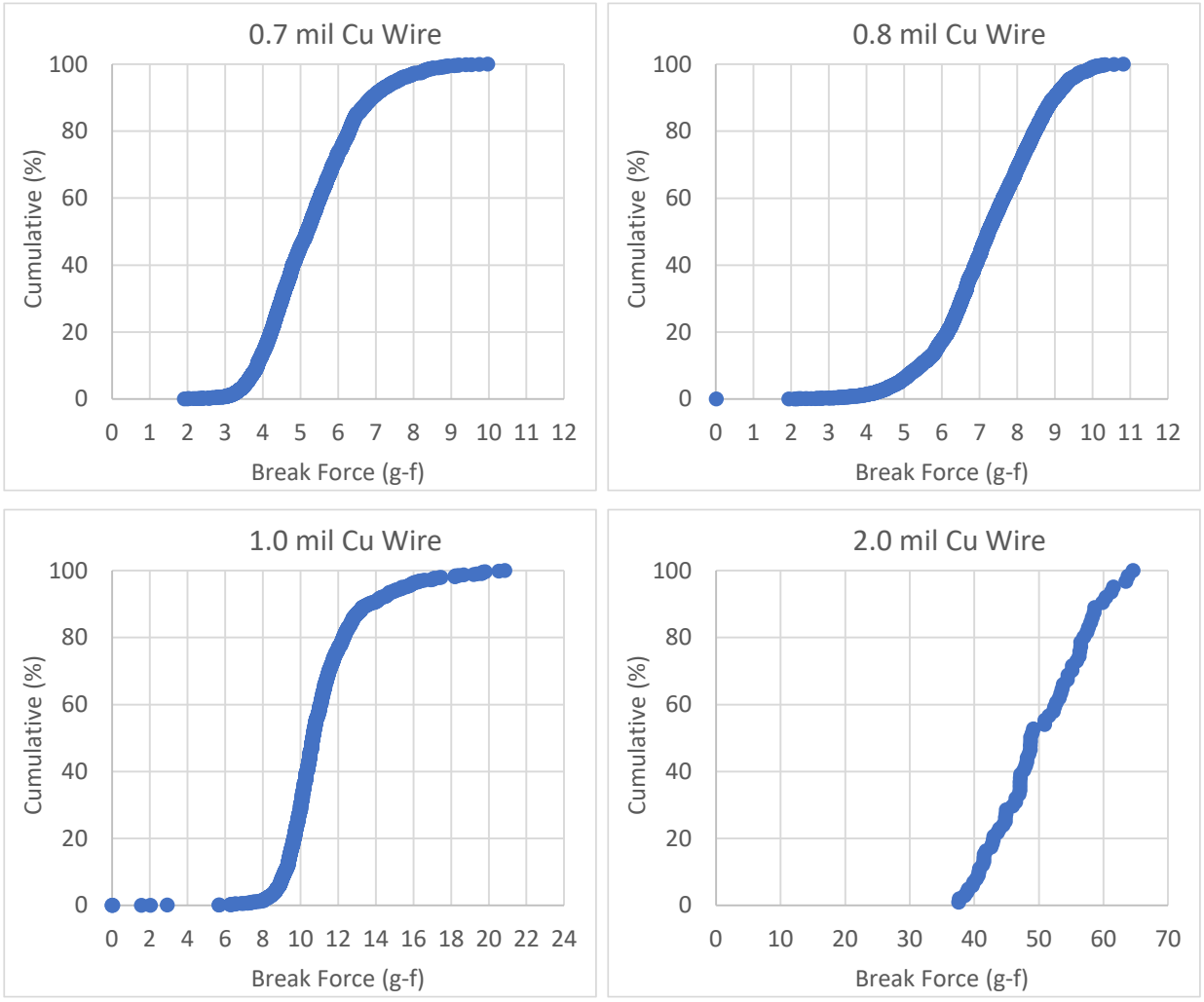

Figure 7.3-7. Cumulative Pull Strength for Each Cu Wire Diameter

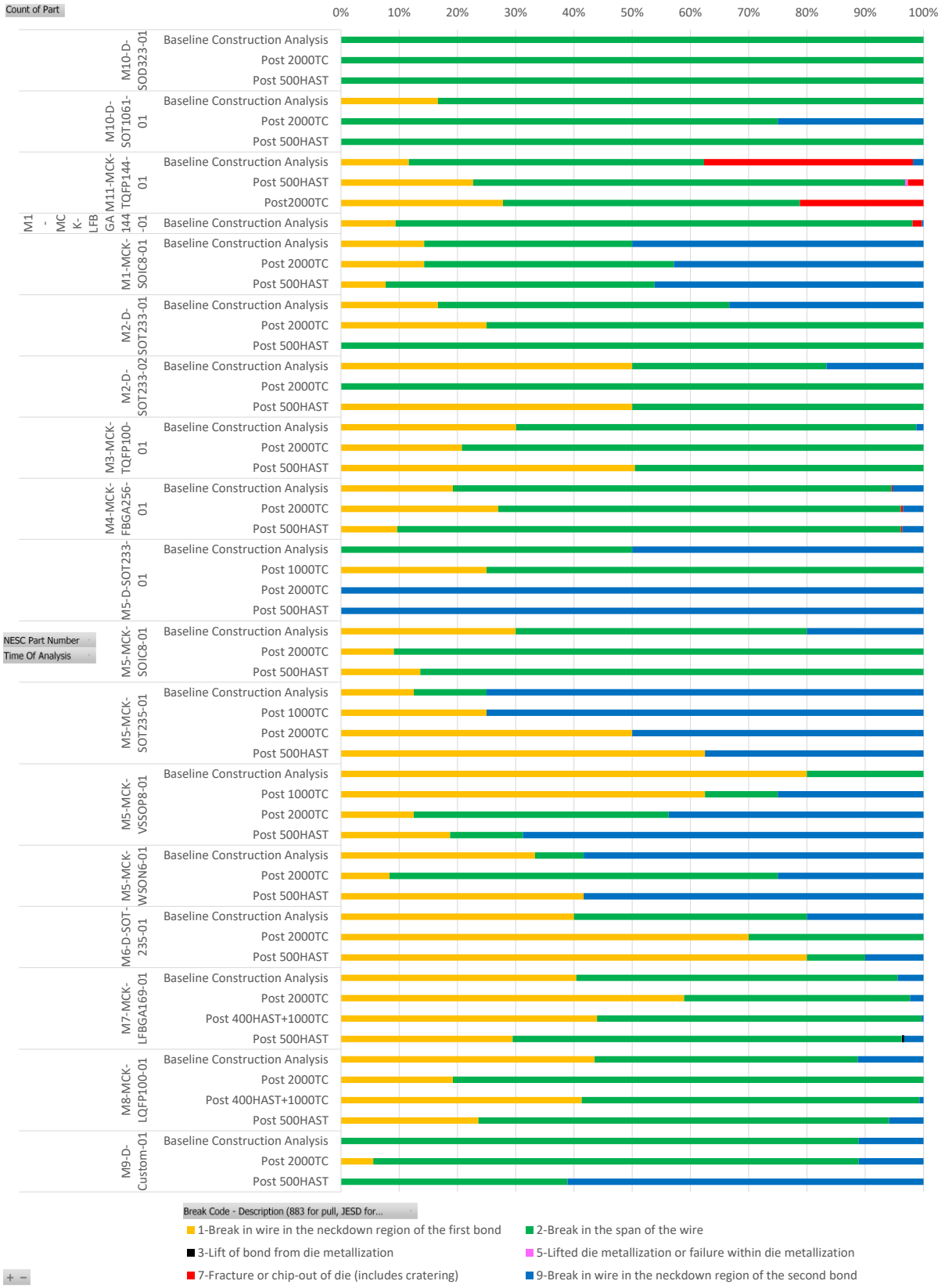

Figure 7.3-8. Plot of Destructive Bond Pull Test Failure Modes for Each Part Type and Condition

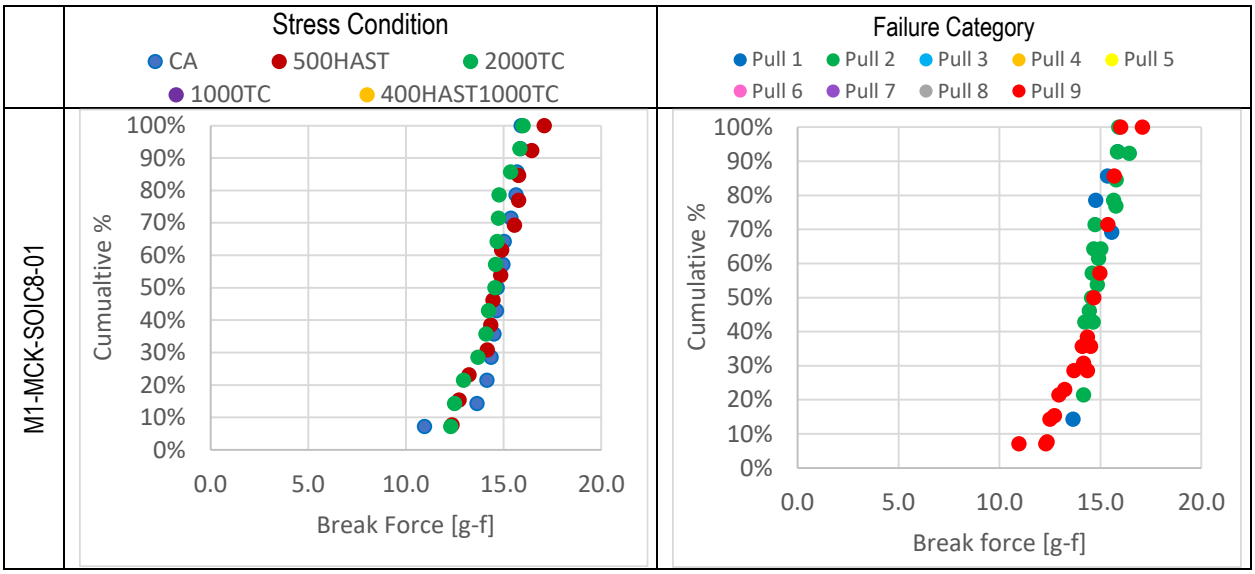

Figure 7.3-9. Plots of Cumulative Bond Pull Strengths and Associated Break Codes for M1-MCK-SOIC8-01 Under Each Exposure Condition

Bond Pull Issues Observed

Although most bonds exhibited wire breaks within the span or the neck-down region, select parts exhibited cratering or lifting of the die metallization. Additionally, certain wires exhibited low strengths (stitch heel break) possibly due to fatigue of the wire during thermal cycling. One Cu wire-bonded part and one Au wire-bonded part exhibited this failure mode. Parts with greater than 100 wire bonds and multiple tiers of bonds presented challenges during decapsulation. These challenges may have resulted in etch variability between the upper and lowest tiers, which could have contributed to reduced pull strength values for these parts. A discussion of these issues follows.

Cratering

As discussed, the higher hardness of Cu (compared to Al) and its propensity to increase hardness following thermosonic bonding can lead to cratering in Cu wire-bonded parts. Cratering, or fracture of the Si die beneath the Al bond pad, can result in electrical failure of the device. In certain cases, manufacturers minimize the impact of cratering by including protective structures within the device layer, such as an array of vias underneath the bondpad. It is worth noting that a combination of molding compound holding the parts together and bond pad design resulted in no electrical failures being observed, even in the case of cratered bond pads, for this assessment. Cratering was observed for three of the 17 Cu wire bonded parts investigated. Two parts (M1-MCK-LFBGA144-01 and M4-MCK-FBGA256-01) exhibited limited cratering (< 1%), while one part (M11-MCK-TQFP144-01) exhibited significant cratering (up to 35%, depending upon condition). Each of these parts had wires in the 0.7 to 0.8 mil range. Figure 7.3-10 provides example images of M11-MCK-TQFP144-01 bonds that exhibited cratering following decapsulation and bond pull. Figures showing multiple cratered parts under multiple exposure conditions are provided in Appendix C.3.2.1. Additionally, Figure 7.3-11 provides bond pull strengths and associated failure codes for the part that exhibited significant cratering. For this plot, Pull is used to refer to Break Code [ref. 4].

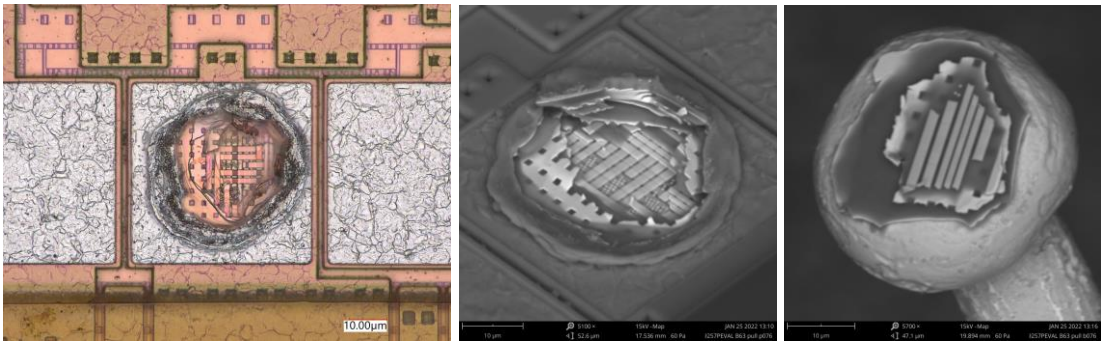

Figure 7.3-10. M11-MCK-TQFP144-01 Exhibited Extensive Cratering in As-Received, Post-bHAST and Post-Thermal Cycling Conditions. Representative optical and SEM images of ball bonds and bond pads exhibiting cratering following bond pull shown for post-thermal cycling condition.

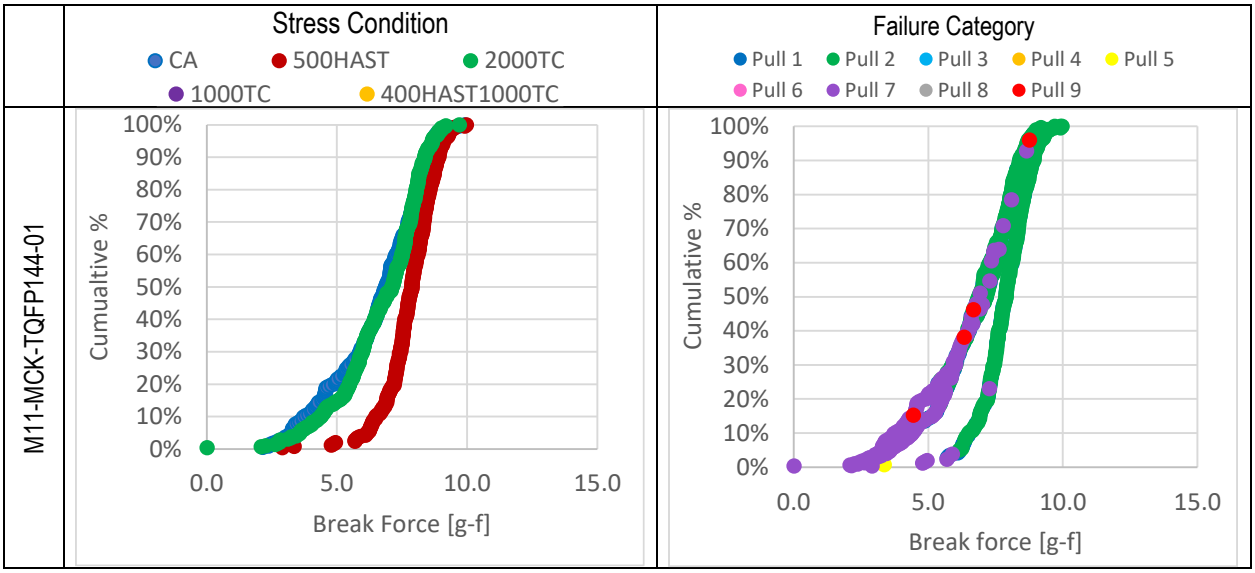

Figure 7.3-11. Plots of Cumulative Bond Pull Strengths and Associated Failure Modes for M11-MCK-TQFP144-01 Following Each Environmental Exposure Condition. Pull 7 refers to Break Code 7-die fracture beneath bond pad.

Bond Lift

Lifted ball bonds are associated with weak bonds between the wire and the bond pad or poor adhesion between the bond pad metallization and the device. M7-MCK-LFBGA169-01 and M11-MCK-TQFP144-01 exhibited a limited number of lifted ball bonds. Figure 7.3-12 provides SEM images and compositional analysis for the bond pad and associated lifted bond wire on M7-MCK-LFBGA169-01. Additional images of these conditions are provided in Appendix C.3.2.1.

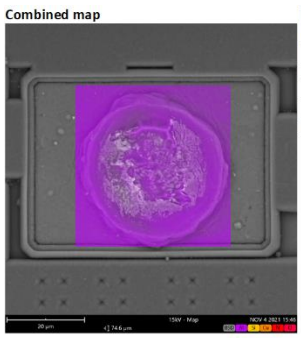

Element Number	Element Symbol	Element Name	Atomic Conc.	Weight Conc.
13	Al K	Aluminium	76.46	75.66
14	Si	Silicon	10.57	10.88
29	Cu	Copper	3.63	8.47
7	N	Nitrogen	6.71	3.45
8	O	Oxygen	2.62	1.54

FOV: 74.6 µm, Mode: 15kV - Map, Detector: BSD Full, Time: NOV 4 2021 15:46

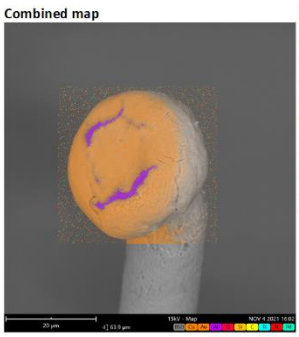

Element Number	Element Symbol	Element Name	Atomic Conc.	Weight Conc.
29	Cu	Copper	62.48	50.98
79	Au	Gold	16.81	42.51
13	Al K	Aluminium	15.18	5.26
8	O	Oxygen	3.53	0.72
14	Si	Silicon	0.97	0.35
6	C	Carbon	0.99	0.15
22	Ti	Titanium	0.04	0.02
7	N	Nitrogen	0.00	0.00
46	Pd	Palladium	0.00	0.00

FOV: 63.9 µm, Mode: 15kV - Map, Detector: BSD Full, Time: NOV 4 2021 16:02

Figure 7.3-12. M7-MCK-LFBGA169-01 Exhibited Lifting of Bond Pad Metallization. SEM images and energy dispersive X-ray analysis of bond composition are shown. No contamination or corrosion was detected.

Multi-Tier Package

Devices with greater than 100 wires (see Figure 7.3-13a) and multi-tier wire bonding patterns were especially challenging for decapsulation. During process development, the use of laser decapsulation was maximized to reduce chemical exposure. Initial experiments resulted in broken bonds (e.g., etched wires), as indicated in Figure 7.3-13b. Although every effort was made to minimize the impact of etchant on wire integrity, differences in pull strengths for different wires could be affected by etch duration and bond geometry. Finally, the strengthening mechanism provided by Pd coating of Cu wire would no longer be present if the Pd coating were etched away during decapsulation.

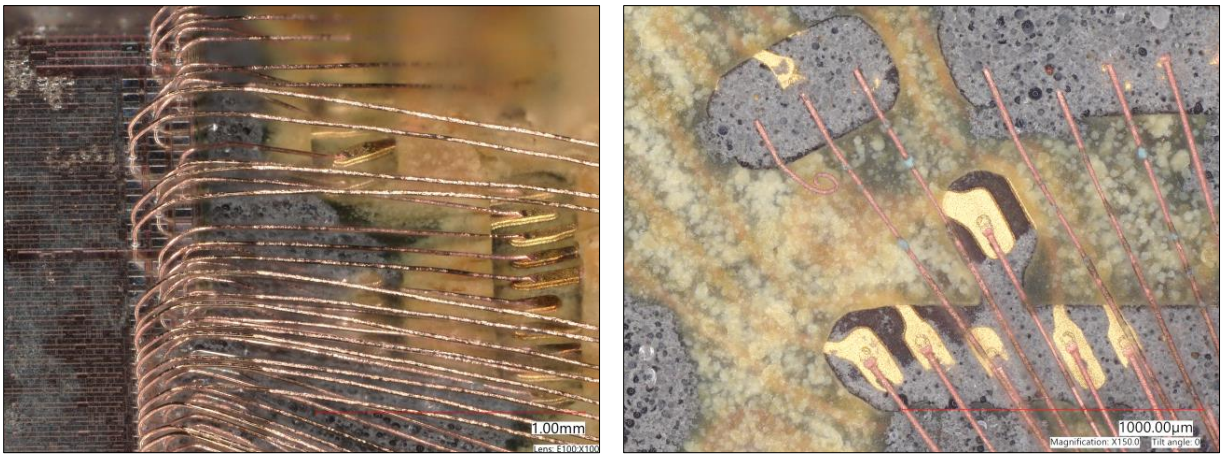

Figure 7.3-13. (a) Representative Optical Image of Multi-Tier Component (M7-MCK-LFBGA169-01); (b) Optical Image Showing Broken Bonds Following Decapsulation

Heel Cracking

Thermomechanical fatigue of bond wires resulting from thermal cycling can lead to electrical opens during thermal cycling or poor bond pull strength following decapsulation. Additionally, tearing can occur at the stitch bond and reduce pull strength. Heel cracks can occur for fatigue and tearing conditions. M5-MCK-VSSOP8-01 and M5-MCK-SOT235-01 (Au) exhibited cracked stitch bonds following decapsulation as well as low bond pull strength (with failure occurring in the neck-down region above the stitch bond) in the post-2000 and post-1000 TC conditions. Heel cracks were also observed in the as-received condition for the Au wire part and post bHAST for Cu and Au wire parts. Figure 7.3-14 provides optical and SEM images of the

fatigued stitch bonds and post-bond pull fracture surfaces for M5-MCK-VSSOP8-01. Figure 7.3-15 provides plots of bond pull strengths for M5-MCK-VSSOP8-01. The significant drop in strength following thermal cycling is clearly visible.

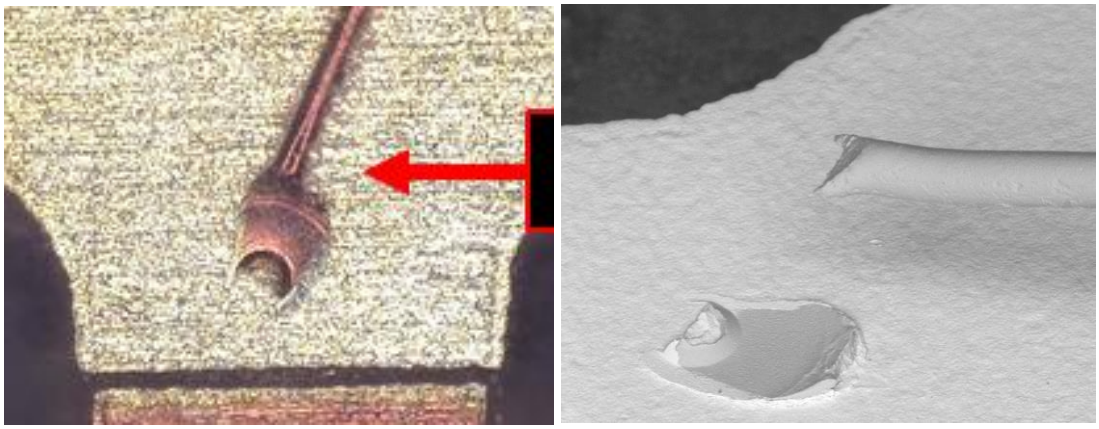

Figure 7.3-14. Optical and SEM Images Showing Representative Wire That Broke with Low Force (out-of-family) on M5-MCK-VSSOP8-01 Following Decapsulation and Bond Pull in Post-2000 TC Condition

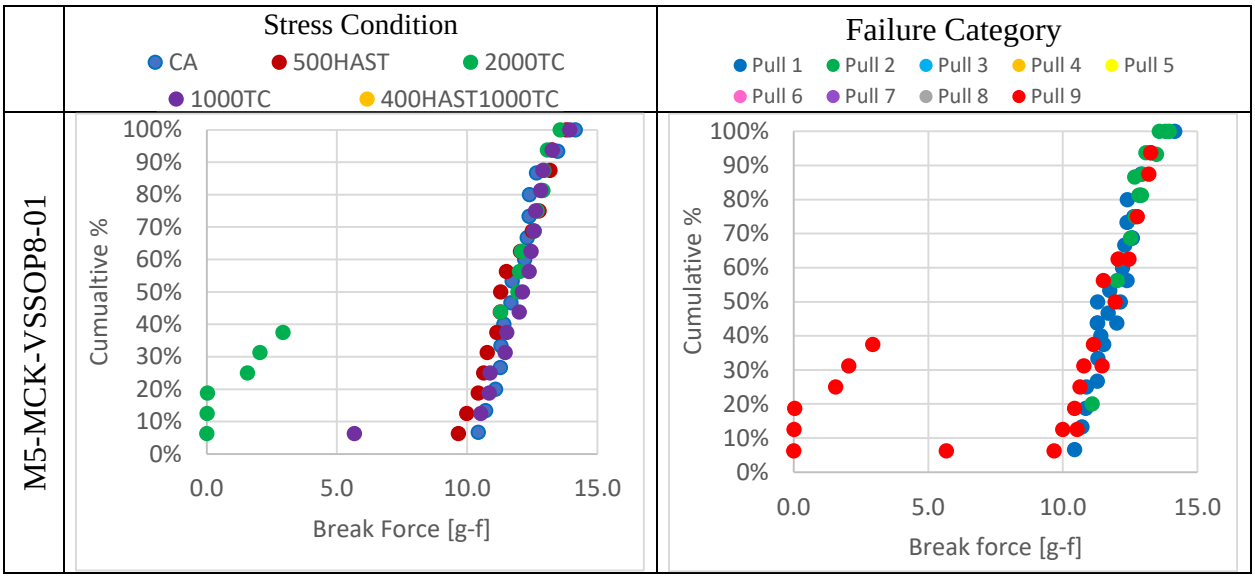

Figure 7.3-15. Plots of Cumulative Bond Pull Strengths and Associated Failure Modes for M5-MCK-VSSOP8-01 Following Each Environmental Exposure Condition. Break code 9 refers to break at neck-down region of second bond. The anomalously low pull values correspond with fatigue failures.

7.3.2.3 Cu Wire Bond Shear Test Results

Wire bond shear tests were performed in the as-received condition, after 500 hr of bHAST exposure and after 2000 TCs for all part types. Due to indications of possible TC-related fatigue damage of wires following bond pull testing, two parts were selected for decapsulation and mechanical evaluation following 1000 TCs. Additionally, two large-wire-count components were selected for decapsulation and ball shear following the combined exposure of 400 hr of bHAST and 1000 TCs. Figure 7.3-16 provides the cumulative ball shear strength for each wire diameter, regardless of Cu wire composition, part number, or environmental exposure condition.

For the 2.0 mil wire parts, one part exhibited a higher shear strength than the other two. The higher strength part was from a different manufacturer. A summary of ball shear failure modes [ref. 6] for each part type and condition is provided in Figure 7.3-17. A detailed presentation of cumulative ball shear strength and associated failure mode for each part type and condition is provided in Appendix C.3.3. These plots were used to better understand the correlation between ball shear strength, failure mode, and root cause for bonds with outlier shear strengths.

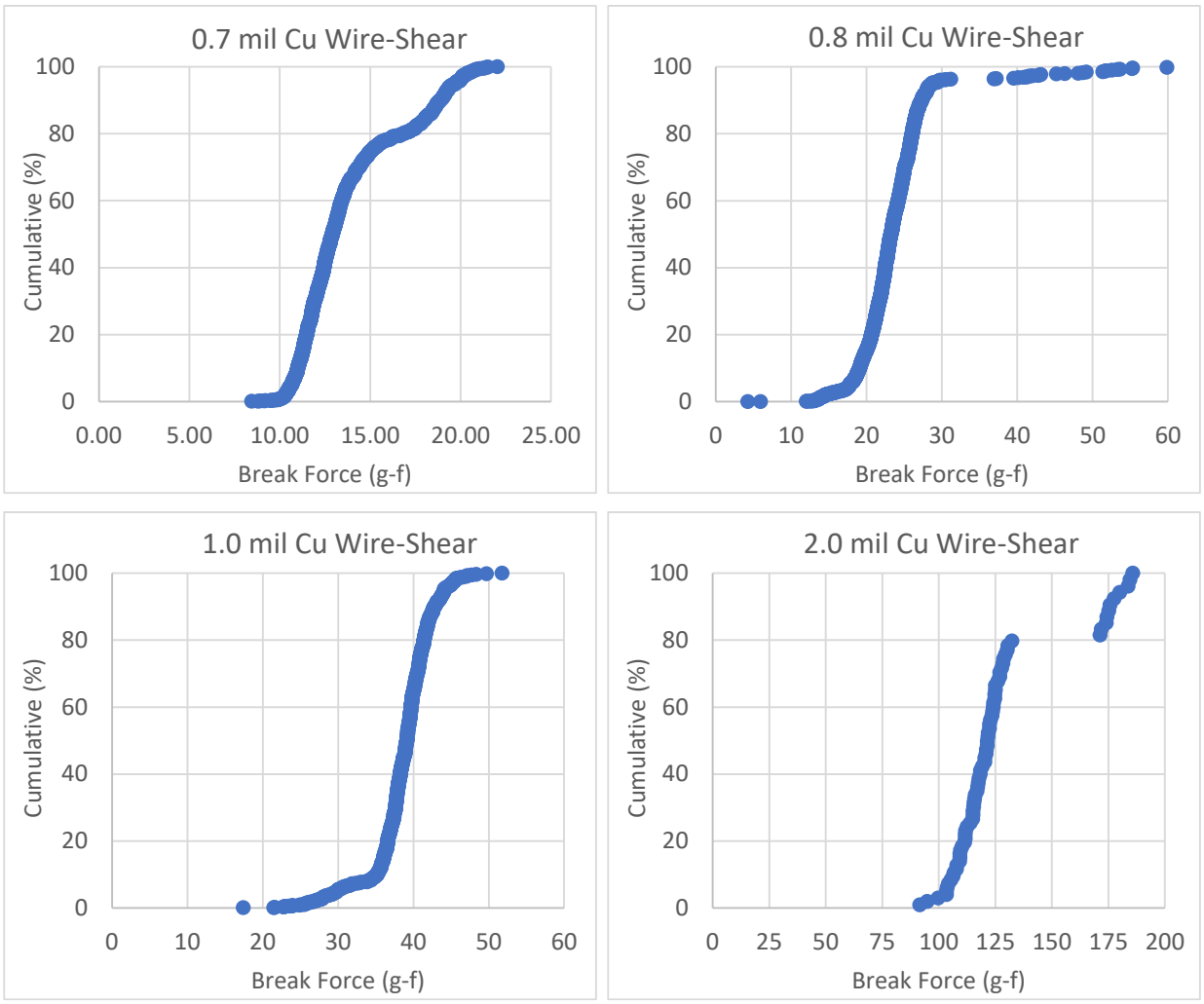

Figure 7.3-16. Plots of Cumulative Ball Shear Strength for Each Wire Diameter, Regardless of Cu Wire Composition, Part Number, or Environmental Exposure Condition

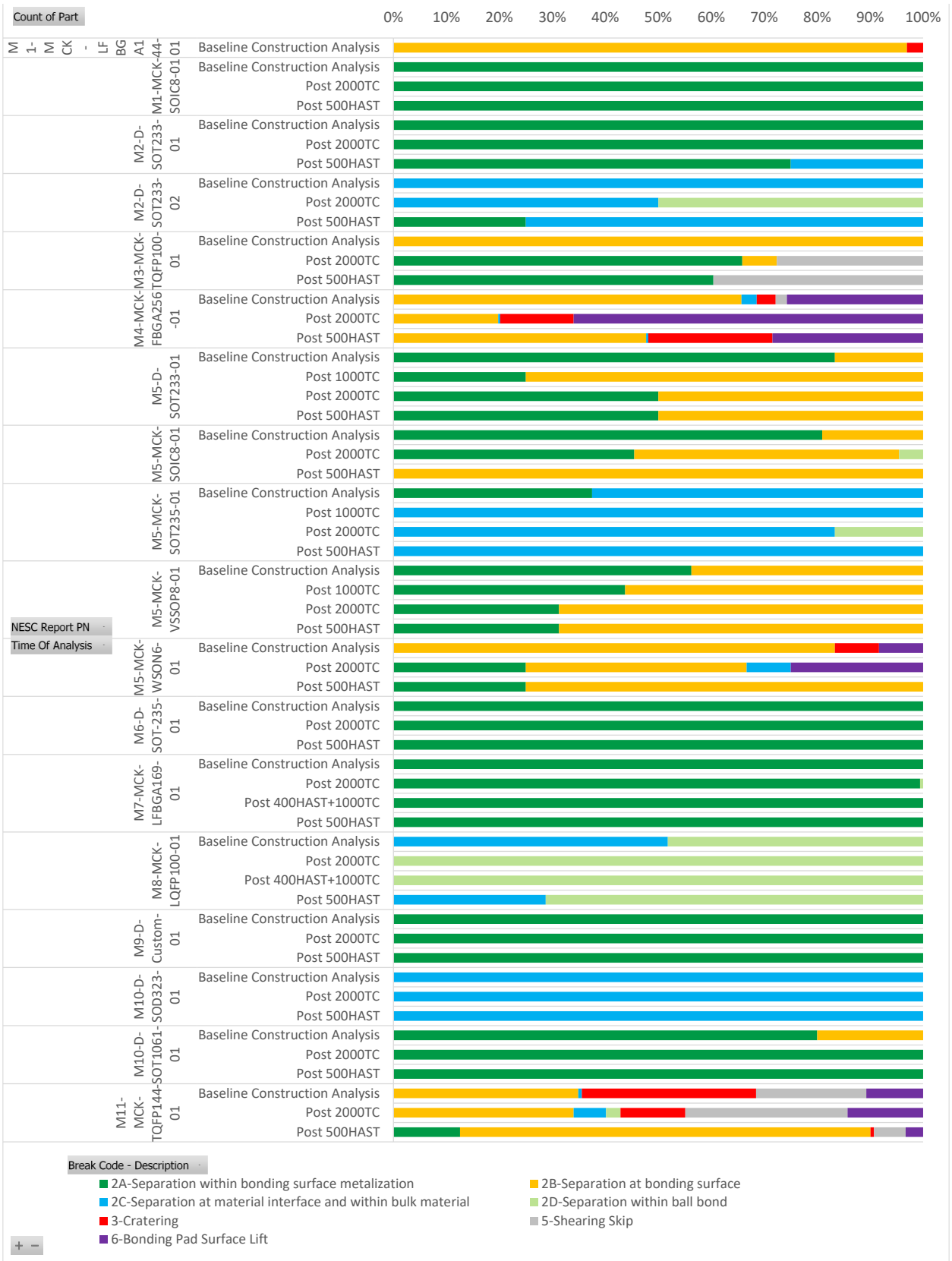

Figure 7.3-17. Plot Summarizing Ball Shear Test Failure Modes for Each Part Type and Condition

Ball Shear Issues Observed

The main issues observed following ball shear testing of all samples included cratering and shear skipping due to polyimide passivation on certain devices. Cratering was observed following ball shear for M4-MCK-FBGA256-01, M1-MCK-LFBGA144-01, and M11-MCK-TQFP144-01. One cratered bond was also observed for M5-MCK-WSON6-01. Fracture surfaces for representative cratered ball bonds are shown in Appendix C.3.3.1. One representative image is provided in Figure 7.3-18 for M4-MCK-FBGA256-01.

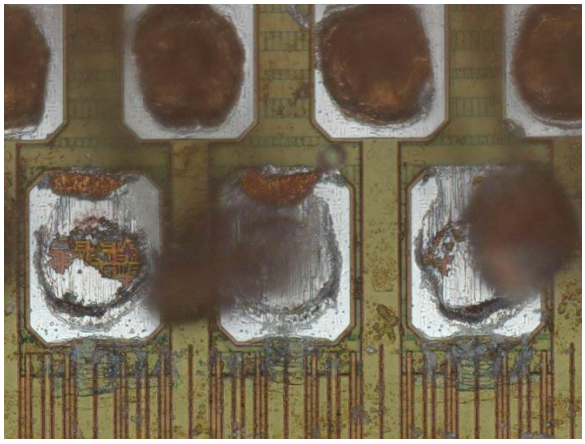

Figure 7.3-18. Optical Image of M4-MCK-FBGA256-01 in As-Received Condition Representing Code 3 Cratering (left) and Code 6 Bond Pad Lift (right) Ball Bond Shear Results

Polyimide passivation layers were present on M8-MCK-LQFP100-01, M3-MCK-TQFP100-01, and M11-MCK-TQFP144-01. The thickness of this layer requires that the ball shear tool be set to a higher position than other components to avoid contact with the polyimide surface. This causes the shear tool to contact some ball bonds above the centerline, which can result in shear skip. Regarding the impact of performing shear tests with the tool above the center line, JEDEC JESD-B116 states, “It is not recommended to attempt to perform quantitative comparisons between different shear test runs, but the results may be used for qualitative purposes” [ref. 6]. M11-MCK-TQFP144-01 had variable ball heights, as shown in Figure 7.3-19. Variable ball height resulted in a wider distribution of shear strengths for this device. A more detailed discussion of this issue is provided in Appendix C.3.3.1.

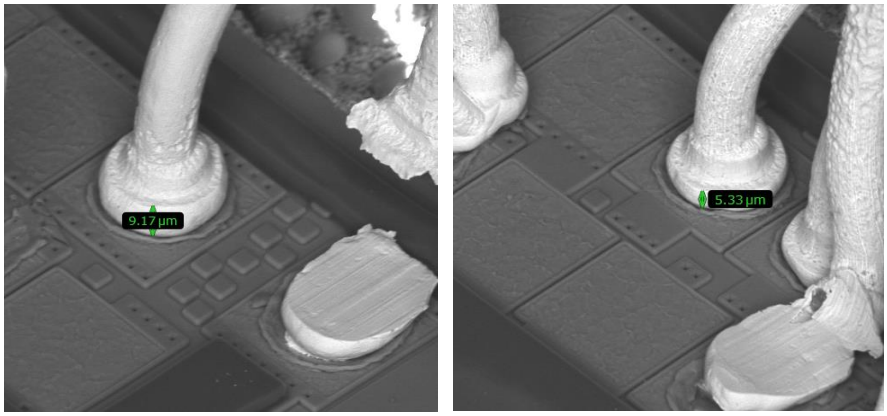

Figure 7.3-19. SEM Images of M11-MCK-TQFP144-01 Wires Illustrating Ball Bond Height Variation. A lower individual bond can result in the shear tool impacting above the centerline.

7.3.3 Statistical Analysis of Bond Pull and Ball Shear

Initial data evaluation indicated trends and allowed assessment of apparent outliers, but could not be evaluated for statistical significance. Statistical significance and trend determination were performed using ANOVA and Student's t-Test [refs. 11, 12]. Initial trend analyses include all test data irrespective of as-received failure condition. Later, the NESC assessment team discussed the effect of unacceptable failure types identified by CA. First, statistical analyses were performed for pull/shear strengths for each part and its associated results after TC and HAST environmental exposures. Then significance in trends was compared by combining SOT part strength values. Finally, the assessment team revisited results and removed those with indeterminate failure to better narrow trends and comparison to Military standard plots and industry data.

Adding all SOTs with fewer than 20 wire bonds allowed a sample size increase for wire diameter and better comparison to a single leaded part having 100 or more wire bonds. The results were compared with the trends for each BGA having more than 100 wire bonds. These trend evaluations also allowed to fit data into a Weibull distribution for ease of comparing data for various wire bond diameters and types and extrapolating to a lower failure percentile. Weibull parameters were calculated and presented. A detailed discussion of the statistical analysis methods used, along with several representative examples of the analyses and their statistical significances, is provided in Appendix C.4. This section provides a high-level overview and a subset of examples.

7.3.3.1 Statistical Analyses: Student's t-test (T test) and ANOVA

Statistical analyses were performed on pull and shear strength data for each part in the as-received condition after thermal cycling and bHAST environmental exposures. Their significances first required analysis using ANOVA for more than two conditions, generation of statistical parameters and standard deviations, and ultimately application of Student's t-test (also called T test) for acceptance/rejection between two conditions using applicable standard deviation. Conditions were: 1) as-received, 2) 2000 TCs, 3) 500 hr HAST, 4) 1000 TCs, and 5) other combined conditions.

The T test is a statistical test frequently used for assessing the difference between two independent sample means. It calculates means from assuming "t" or normal populations with populations having the same variance. For more than two parameters, however, standard deviations are compared to determine significance using F ratio (i.e., ANOVA). If F, which is the square between divided by the mean squared within, is ≤ 1, then do not reject null hypothesis. Null hypothesis assumes all means are equal (i.e., H0 : $\mu 1 = \mu 2 = \mu 3$), whereas the alternative hypothesis assumes the means are not equal (i.e., H1 : $\mu 1 \neq \mu 2 \neq \mu 3$).

Table 7.3-3 presents an example to elucidate the use of this method. An example of ANOVA analysis for wire pull strengths (i.e., baseline, post-2000 TCs, and post-500 hr bHAST) is illustrated in the left three columns. The right rows and columns show the ANOVA summary results for the three values. The overall F ratio is 3.24, which is >1. Therefore, do not reject the null hypothesis (H0: $\mu 1 = \mu 2 = \mu 3$). This means that for this specific case, either 2000 TCs or 500 hr bHAST have negligible degradation effects.

Table 7.3-3. Example of ANOVA Statistical Analysis

Pull Strenght M1-MCK-SOIC8-01			SUMMARY: ANOVA Single Factor							
Baseline-Pull	**2000TC**	**500HAST**	*Groups*	*Count*	*Sum*	*Average*	*Variance*	*STD Error*	*Condition*	*Average*
10.96	12.3	12.36	Baseline Construction Analysis	14	205.46	14.67571429	1.608641758	0.338973425	Baseline	14.68
13.64	12.5	12.73	Post 2000TC	14	200.35	14.31071429	1.276745604	0.301986944	2000TC	14.31
14.16	12.95	13.23	Post 500HAST	13	191.7	14.74615385	1.983992308	0.390659433	500HAST	14.75
14.36	13.7	14.17								
14.52	14.11	14.35								
14.64	14.23	14.46	ANOVA							
14.67	14.56	14.85	*Source of Variation*	*SS*	*df*	*MS*	*F*	*P-value*	*F crit*	
14.98	14.6	14.91	Between Groups	1.500578545	2	0.750289272	0.464969808	0.631680491	3.244818361	
15.03	14.68	15.56	Within Groups	61.31794341	38	1.61363009				
15.38	14.74	15.77								
15.65	14.77	15.78	Total	62.81852195	40					
15.69	15.36	16.44								
15.87	15.84	17.09								
15.91	16.01									

Left columns show raw pull strength data; right side shows various statistical ANOVA parameters

To determine significance between two means, a Student's t-test could be used. The only difference from previous equations is the use of mean square within different rather than pooled standard deviation, which is assumed to have come from populations with a common standard deviation. Table 7.3-4 shows the T test equation used to compare between two means of pull strength, e.g., between as-received (AS) and 2000 TCs. Then, statistical significance "p" was calculated to determine hypothesis type. The "p" lower than set Alpha (α) value (i.e., 0.05) is considered a significant difference.

Table 7.3-4. Student's t-test Analysis to Determine Significance for Each Mean as "Reject" or "Do Not Reject" Null Hypothesis

	AS/2000TC	**AS/500HAST**	**HAST/TC**
	1	1	0
	-1	0	1
	0	-1	-1
Num	0.365	-0.070	-0.435
Den	0.480	0.489	0.489
T-Test	0.760	-0.144	-0.890
p	0.452	0.886	0.379
	Do Not Reject Null Hypothesis	Do Not Reject Null Hypothesis	Do Not Reject Null Hypothesis

$$t = \frac{(1)\bar{X}_A + (-1)\bar{X}_B + (0)\bar{X}_C + (0)\bar{X}_D}{\sqrt{MS_{Within}\left[\frac{(1)^2}{n_A} + \frac{(-1)^2}{n_B} + \frac{(0)^2}{n_C} + \frac{(0)^2}{n_D}\right]}}$$

7.3.3.2 Cu Wire Bond Pull Strengths for Different Package Types

All wire bond pull strengths were subjected to ANOVA and T test statistical analyses to determine whether "null hypothesis" could be rejected. Figure 7.3-20 shows the test results for M1-MCK-SOIC8-01 with 14 wire-bond pull strength values. The bottom plot shows the strength values versus the number of wire bonds pull tested, and the middle plot shows the average values with the assumption of normal distribution. Finally, the top table shows calculation for T test and

"p" values. The statistical analysis appears to be consistent with closeness of strength distribution and average values. For all three compared cases, i.e., AS/2000TC (as-received vs. 2000 TCs), AS/500HAST (as-received vs. 500 hr HAST), and TC/HAST (2000 TCs vs. 500 hr HAST), the "p" values are larger than 0.05. Therefore, the conclusion is do not reject null hypothesis.

	AS/2000TC	AS/500HAST	HAST/TC
	1	1	0
	-1	0	1
	0	-1	-1
Num	0.365	-0.070	-0.435
Den	0.480	0.489	0.489
T-Test	0.760	-0.144	-0.890
p	0.452	0.886	0.379
	Do Not Reject Null Hypothesis	Do Not Reject Null Hypothesis	Do Not Reject Null Hypothesis

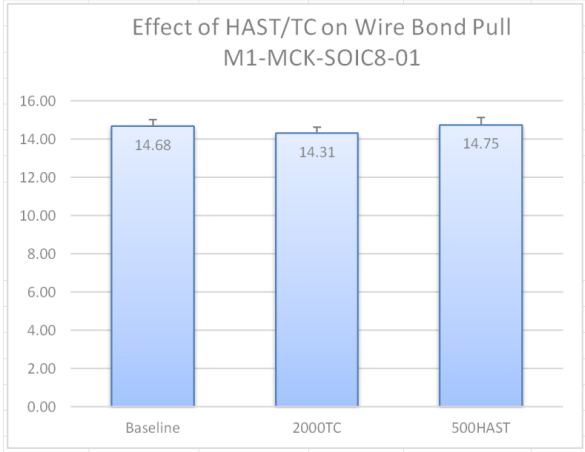

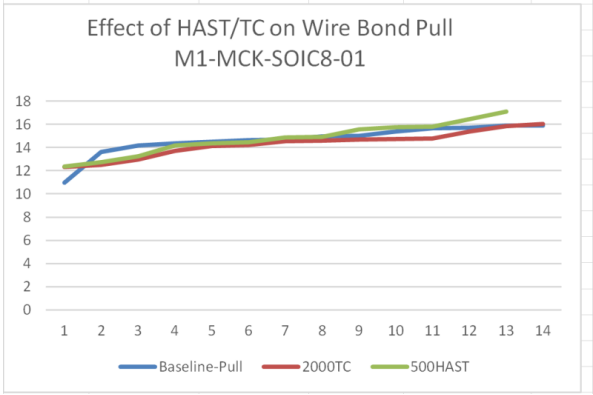

Figure 7.3-20. Pull Strength Plots (bottom), Mean Value Charts, and Table Show Student's t-test Analysis for M1-MCK-SOIC8-01 Part, Which Shows Statistical Significance for Each Mean as "Reject" or "Do Not Reject" Null Hypothesis

Table 7.3-5 provides a summary of significances; reject (Y) or do not reject (N) null hypothesis; for all parts with wire bond under pull loading. Two key categories were identified. For parts with a large number of wire bonds, significances are better narrowed under TC and HAST conditions. The results mostly showed significances among these conditions. This was not the case for SOTs with small numbers of wire bonds, which had mixed significance results. This was due to the effect of variation outliers, including decapsulation and wire bond length, on the standard deviation. Pooled standard deviation is less affected by outliers for parts with a larger

number of wire bonds, whereas parts with a few wire bonds are significantly affected. In subsequent pull strength analyses, SOT parts with a low number of wire bonds, but with one wire diameter, were added together and categorized as SOTs. This allowed better comparison for Weibull and statistical analysis under various conditions.

For SOTs, 8 of 12 parts showed significance after 2000 TCs, whereas 4 of 12 showed significance after 500 hr bHAST. It appears, therefore, that thermal cycling is a better discriminator for SOTs. Note that thermal cycling was performed at the assembly level, which induces additional fatigue stress due to CTE mismatches between the part and the PCB. The increased stress from greater CTE mismatches combined with a higher exposure temperature for thermal cycling (125 ℃) compared with that of bHAST (110 ℃) could have affected this result.

Table 7.3-5. Summary of Statistical Significances of Pull Strength for All Parts with "Y" Means "Reject Null Hypothesis"

Bond Pull Strength Part ID Test	Wire Diameter (mil)	Composition	Package Type	AS/2000TC Significance	AS/500HAST Significance	TC/HAST Significance	AS/1000TC Significance
M7-MCK-LFBGA169-01	0.7	PCC (Pd/Cu)	169-LFBGA	Y	Y	Y	
M11-MCK-TQFP144-01	0.8	PCC (Au/Pd/Cu)	TQFP144	N	Y	Y	
M3-MCK-TQFP100-01	0.8	PCC (Pd/Cu)	100-TQFP	Y	Y	N	
M4-MCK-FBGA256-01	0.8	Cu	256FBGA	Y	Y	Y	
M5-MCK-SOT235-01	0.8	Au	SOT23-5	N	N	N	N
M2-D-SOT233-02	0.8	Cu	SOT23-3	Y	Y	N	
M5-MCK-WSON6-01	0.8	PCC (Au/Pd/Cu)	6-WSON	Y	Y	N	
M2-D-SOT233-01	0.8	Cu	SOT-23-3	Y	Y	N	
M8-MCK-LQFP100-01	1	PCC(Au/Pd/Cu)	100LQFP	Y	Y	Y	
M5-MCK-SOIC8-01	1	Cu	8-SOIC	N	N	N	
M6-D-SOT-235-01	1	PCC (Pd/Cu)	SOT-23	Y	N	N	
M5-MCK-VSSOP8-01	1	Cu	8-VSSOP	Y	N	Y	N
M5-D-SOT233-01	1	Cu	SOT-23-3	Y	Y	Y	N
M1-MCK-SOIC8-01	1	PCC (Au/Pd/Cu)	8-SOIC	N	N	N	
M10-D-SOT1061-01	2	Cu	SOT1061	Y	N	Y	
M10-D-SOD323-01	2	Cu	SOD323	Y	N	Y	
M9-D-Custom-01	2	Cu	Custom	N	N	N	

7.3.3.3 Cu Wire Bond Shear Strength

Similar to the previous section on statistical analysis for wire bond pull strength, all wire bond shear strengths were subjected to ANOVA and T test evaluation. Table 7.3-6 presents a summary of significances; reject (Y) or do not reject (N) null hypothesis; for all parts under shear loading. Two key categories were identified: For parts with a large number of wire bonds, all showed significances under TC and bHAST conditions. This was not the case for SOTs with only a few wire bonds. The results for significance are mixed, due to the effect of variation outliers including decapsulation and wire bond area on the standard deviation. Pooled standard deviation is less affected by outliers for parts with larger numbers of wire bonds, whereas it significantly affects parts with few wire bonds. In subsequent strength analyses, parts such as SOTs with a low number of wire bonds) were combined for a single wire diameter to better compare Weibull and statistical results.

Note that for SOTs, 2 of 12 parts showed significance after 2000 TCs, whereas 3 of 12 showed significance after 500 hr bHAST. Therefore, it appears that neither 2000 TCs nor 500 hr bHAST is a good discriminator for SOTs under shear testing. It appears shear strengths were not affected by PCB CTE mismatches under thermal cycling. However, this was not the case for wire bond pull strengths.

Table 7.3-6. Summary of Statistical Significances of Shear Strengths for All Parts with "Y" Means "Reject Null Hypothesis"

Shear Strength Part ID Test	Wire Diameter (mil)	Composition	Package Type	AS/2000TC Significance	AS/500HAST Significance	TC/HAST Significance	AS/1000TC Significance
M7-MCK-LFBGA169-01	0.7	PCC (Pd/Cu)	169-LFBGA	Y	Y	Y	
M11-MCK-TQFP144-01	0.8	PCC (Au/Pd/Cu)	TQFP144	Y	Y	Y	
M3-MCK-TQFP100-01	0.8	PCC (Pd/Cu)	100-TQFP	Y	Y	Y	
M4-MCK-FBGA256-01	0.8	Cu	256FBGA	Y	Y	Y	
M5-MCK-SOT235-01	0.8	Au	SOT23-5	Y	N	N	N
M2-D-SOT233-02	0.8	Cu	SOT23-3	N	N	N	
M5-MCK-WSON6-01	0.8	PCC (Au/Pd/Cu)	6-WSON	Y	Y	N	
M2-D-SOT233-01	0.8	Cu	SOT-23-3	N	N	N	
M8-MCK-LQFP100-01	1	PCC(Au/Pd/Cu)	100LQFP	Y	Y	Y	
M5-MCK-SOIC8-01	1	Cu	8-SOIC	N	N	N	
M6-D-SOT-235-01	1	PCC (Pd/Cu)	SOT-23	N	Y	Y	
M5-MCK-VSSOP8-01	1	Cu	8-VSSOP	N	N	N	Y
M5-D-SOT233-01	1	Cu	SOT-23-3	N	N	N	N
M1-MCK-SOIC8-01	1	PCC (Au/Pd/Cu)	8-SOIC	Y	Y	Y	
M10-D-SOT1061-01	2	Cu	SOT1061	N	N	N	
M10-D-SOD323-01	2	Cu	SOD323	N	N	N	
M9-D-Custom-01	2	Cu	Custom	N	N	Y	

7.3.4 Summary of Experimental Results

1) CA was critical in establishing Cu wire bond workmanship conditions. The team did not have access to manufacturing process parameters to include in the establishment of optimal workmanship.
2) Pull strengths for Cu wire bonds following decapsulation are highly dependent upon decapsulation processes. Over-etched wires can lead to low or near-zero pull strength. Bond pull strengths of Cu wire bonds may be higher prior to encapsulation.
3) The decapsulation processes used during this assessment required significant optimization for each part and condition to obtain reliable, repeatable results. Results were dependent not only upon the method used (laser decapsulation or chemical decapsulation), but also upon time, temperature, specific acid chemical composition and age, time between processes, and part configuration.
4) Chemical wet etch of multi-tier devices presents unique challenges and dangers. Longer wires with loops that are above the other wire bonds may be exposed to acid for longer periods of time and result in greater material removal. Similarly, acid may be trapped between different tiers of wire bonds, resulting in local over-etching. Such over-etching could result in pull strength outliers for a device. Therefore, a wider Weibull distribution is expected for multi-tier wire bond devices.

5) JESD22-B120, Wire Bond Pull Test Method, and JESD22-B116B, Wire Bond Shear Test Method, provide general guidelines regarding decapsulation of PEMs with Cu wire bonds. These guidelines are helpful, but not sufficient.
6) The level of acceptable wire etching is not well-defined in applicable standards. This effect may be more critical for fine wire bonds due to the relatively large surface area compared with nominal diameter wire. It is not clear how much reduction in area is permissible.
7) Obtaining pre-molded wire bond pull strength values from the manufacturer would help in determining the acceptable level of etching.
8) Wire bond coatings (Pd or Pd/Au) are often removed during chemical decapsulation, but preserved during laser and microwave plasma decapsulation. Removal of Pd coating during decapsulation can affect the resulting wire bond pull strength. Literature suggests that the thin Pd coating could influence the grain size effect on fine wire bonds. If the coating is totally or partially removed through etching, then this additional strengthening effect would no longer be present and the wire would fail at the same strength as uncoated wire [ref. 13].
9) The impact of chemical manufacturer, age of chemicals, and composition of nitric and sulfuric acids (e.g., nitric acid in water versus nitric acid in dissolved nitrides) was not studied. These parameters may affect the efficiency of the decapsulation process and the quality of decapsulated wires.
10) For this assessment, no corrosion was observed on the bonds or bond pads following decapsulation of parts after environmental exposure. If corrosion was not significant enough to cause failure below the ball bond, it may have been present but not observed.
11) Cross-sections of the joints were only taken as part of CA in the as-received condition and cross-sections following environmental exposure were beyond the scope of this assessment. Therefore, measurement of intermetallic thickness or determination of wire bond joint degradation was not performed following environmental exposure.
12) Literature clearly indicates that the mechanical and chemical properties of epoxy molding compounds can have a significant effect on the reliability of Cu wire bonds. Access to the chemical and mechanical properties of molding compounds can be useful in the determination of root cause for failed Cu wire bonds. However, acquiring molding compound properties after encapsulation is challenging due to the small amount of available epoxy material and the high level of silica fillers (up to 85%) [refs. 14, 15, 16].
    a. No clear correlation between T_g and failure was observed.
    b. Determination of the molding compound modulus was attempted using nano-indentation. Results were inconclusive due to the high level of silica fillers and their impact on measurements.
    c. Chemical analysis using inductively coupled plasma mass spectrometry (ICP-MS) was attempted following thermogravimetric analysis (TGA), but an insufficient amount of epoxy and the high level of silica filler complicated the measurement and yielded unreliable results.
    d. Insufficient material was available to reliably measure CTE using a Thermomechanical Analyzer (TMA).
13) Cratering was observed for 3 of 17 Cu wire bonded parts investigated. Two parts (M1-MCK-LFBGA144-01 and M4-MCK-FBGA256-01) exhibited limited cratering (<1%), while one

(M11-MCK-TQFP144-01) exhibited significant cratering (up to 35%, depending upon condition). Each of these parts had wires in the 0.7 to 0.8 mil range.

14) Fatigue life of Cu wire bonds could not be determined since no electrical failures for various wire diameters and packaging configurations occurred after exposures to 2000 TCs (−55/125 °C) or 500 hr HAST (85 RH & 110 °C). Electrical monitoring was limited during environmental tests, with few parameters monitored. Fatigue life is assumed to be at least as long as the testing performed. Following destructive wire bond pull testing, M5-MCK-VSSOP8-1 (Cu wire bond) and M5-MCK-SOT235-01 (Au wire bond) exhibited evidence of heel cracking at the stitch bond. M5-MCK-VSSOP8-1 exhibited a statistically significant increase in bond pull failures in the thermally cycled condition (2000 TCs), but M5-MCK-SOT235-01 did not.
15) The level of solder joint cracking was not examined as part of this assessment, but no apparent open-circuit failures of solder joints were observed for these packages after exposure to 2000 TCs (−55/125 °C) or 500 hr HAST (85% RH &110 °C). Due to no-failure condition, the effect of lead touch-up with soldering iron could not be determined. However, it can be stated that touch-up did not cause an early failure.
16) For SOT pull strengths, it appears that generally the 2000 TCs for 0.8 and 2 mil diameters have more degradation effect than 500 hours of HAST. This does not show a clear statistical trend for 1 mil diameter Cu wires.
17) Pull strength results indicate that for SOT-23-5 with 0.8 mil Au wire bonds, statistically there are no significant changes for as-received bond pull strengths versus 2000 TCs (−55/125 °C) or 500 hr HAST (85 RH & 110 °C). This was not the case for two SOT23-3s (M2-D-SOT233-02 and M2-D-SOT233-01), which showed statistically significant changes in bond pull strength between as-received and post-environmental exposure for the AS and TC conditions.
18) In contrast to pull strengths, no apparent trend was observed for shear strength values under these conditions (thermal cycling or HAST). Therefore, this team is proposing to use pull strength along with thermal cycling to discriminate for workmanship deficiencies.
19) Shear strength results indicate that for SOT-23-5 with 0.8 mil Au wire bonds, statistically there were no significant changes for as-received bond shear strengths versus 2000 TCs (−55/125 °C) or 500 hr HAST (85 RH &110 °C). This was not the case for two SOT23-3s (M2-D-SOT233-02 & M2-D-SOT233-01), which showed significance for the AS and TC exposures.
20) All leaded parts with 100 and 144 leads showed statistical significance for 500 hr HAST and 2000 TCs, with the exception of the TQFP package following 2000 TCs. Non-significance for the TQFP was possibly due to initial pad cratering and low bond pull strengths, which were detected during CA.
21) Two BGAs (169LFBGA and 256FBGA) showed statistical significance on pull strengths for both exposures, even though 256FBGA had pad cratering issues. Strength significance alone may not indicate an issue with pad workmanship. Therefore, CA with failure mechanism would be required to determine the possibility of a latent failure.
22) Literature suggests that wires with fewer than 10 grains across the diameter may exhibit a grain size effect. This would be more significant for finer wires. The reduced strength value for Cu wires with diameters of 1 mil and lower may correlate with this phenomenon. Microstructural analysis of wire cross-sections was beyond the scope of this assessment.

Therefore, grain size and number within the cross-section were not determined [refs. 13, 17-22].

23) Degradation of Cu wire bonds following exposure to heat and humidity is different from that of Au wire bonds, based on review of available literature. Au-Al bonds tend to fail due to extensive intermetallic formation and Kirkendall voiding when thermally stressed above their maximum use temperature. Cu-Al bonds, alternatively, exhibit significantly less intermetallic formation, but such intermetallics are more susceptible to corrosion. Halide chemicals within molding compounds can potentially lead to corrosion of Cu-Al intermetallic compounds at elevated temperatures and elevated humidity levels. Such degradation may affect joint properties and can lead to premature failure. No corrosion-related failures were observed in this assessment. Manufacturer information on molding compound chemistry was listed as green compound, halide free or halogen free.

24) Although Cu wire bonding processes have been around for several years, the reduced process window compared with that of Au, modification of bond pads using different means to accommodate the increased hardness of Cu, and tooling differences may yield greater variability in results. Literature reveals that the impact of different bonding parameters, wire types, and resulting properties are inconsistent [ref. 23]. Some of these inconsistencies may be due to doping, processing, and microstructure. In addition, small differences in molding compound composition may influence properties.

7.4 Discussion

7.4.1 Cu Wire Bond Pull and Shear Limits

In Section 7.3, normal distribution parameters were used to compare significances in mean and standard deviation differences by T test and ANOVA. The Weibull distribution is often considered for failures, but also applied for the analysis of materials, including size effect on unidirectional composites [ref. 24] and strengths of pure Cu [ref. 25]. In this section, Weibull distribution will be used for pull and shear strength distributions of Cu and Au wire bonds. This distribution is expected to provide a better fit to strength data due to the possibility of using a broad range of distribution shapes included in the Weibull family [ref. 26]. Many other distributions are included in the Weibull family, exactly or approximately, including normal, exponential, Rayleigh, and sometimes Poisson and binomial. Moderate size samples (i.e., 20 or more failures) are needed to accurately discriminate between Weibull and other distributions. With less than 20 sample size, Weibull is the best choice and best practice.

To generate Weibull plots, wire strength values were ranked from low to high and used to calculate strength distribution percentiles for a total of N sample size. The percentiles were approximated using median plotting position (i.e., Benard's approximation of $F_i = (i-0.3)/(N+0.4)$), which increased from 1 to N [ref. 26]. Two-parameter Weibull distribution was used to characterize Cu wire bond pull and shear strength values and projections for a low probability of strength value, e.g., F(0.1%). Projections were made by fitting the cumulative ranked percentiles and strength values to two-parameter Weibull distribution. For this case, the Weibull could be written as:

$$F(s) = 1- \exp\left(-(s/\eta)^{\beta}\right)$$

Where:

- F(*s*) is the cumulative strength distribution function.
- (*s*) is the pull or shear strength value.
- η is a scale parameter commonly referred to as characteristic strength (i.e., S_0), or the strength value with 63.2% percentile.
- β is the shape parameter or module, *m*, which is inversely proportional to the coefficient of variation. As β increases, the spread in strength values decreases.

This equation, in double logarithm format, results in a straight line. The slope of the line will define the Weibull shape parameter. The ranking and strength data in log-log were fitted to a straight line, and the two Weibull parameters were calculated.

7.4.2 Weibull Strength Distributions for Package Type and Cu Wire Diameter

To determine the effect of Cu wire diameter on strengths and distributions, the strength test results were first narrowed based on package type only. Values were added for SOTs with fewer than 20 wire bonds, leaded packages with 100 or more wire bonds, and finally BGAs with up to 256 wire bonds. This approach enables distribution outliers to be determined first and raw test data to be scrutinized if needed. Lessons learned from CA were applied to strength results and distribution. These included the removal of COTS molding compounds (a combination of laser and chemical removal), the existence of a polyimide coating layer that added uncertainty in shear test values in a few cases, metallization thickness and pad lift, as well as length and looping of wire bonds and locations.

Strength data for parts with low wire bond numbers were combined to increase wire-bond sample size; these are categorized as SOTs. Figure 7.4-1 shows the Cu wire bond pull strength distribution for SOTs with wire diameters of 0.8, 1, and 2 mils. The results for Au wire bonds will be separated when discussing the tail end of Weibull distribution. The table in Figure 7.4-1 lists the Weibull parameters, η and β values, and the fit correlation R (R2). The β distribution scatter increases as wire diameter decreases, even though this is not apparent visually from the plots. As expected, the η strength value decreases as wire diameter decreases.

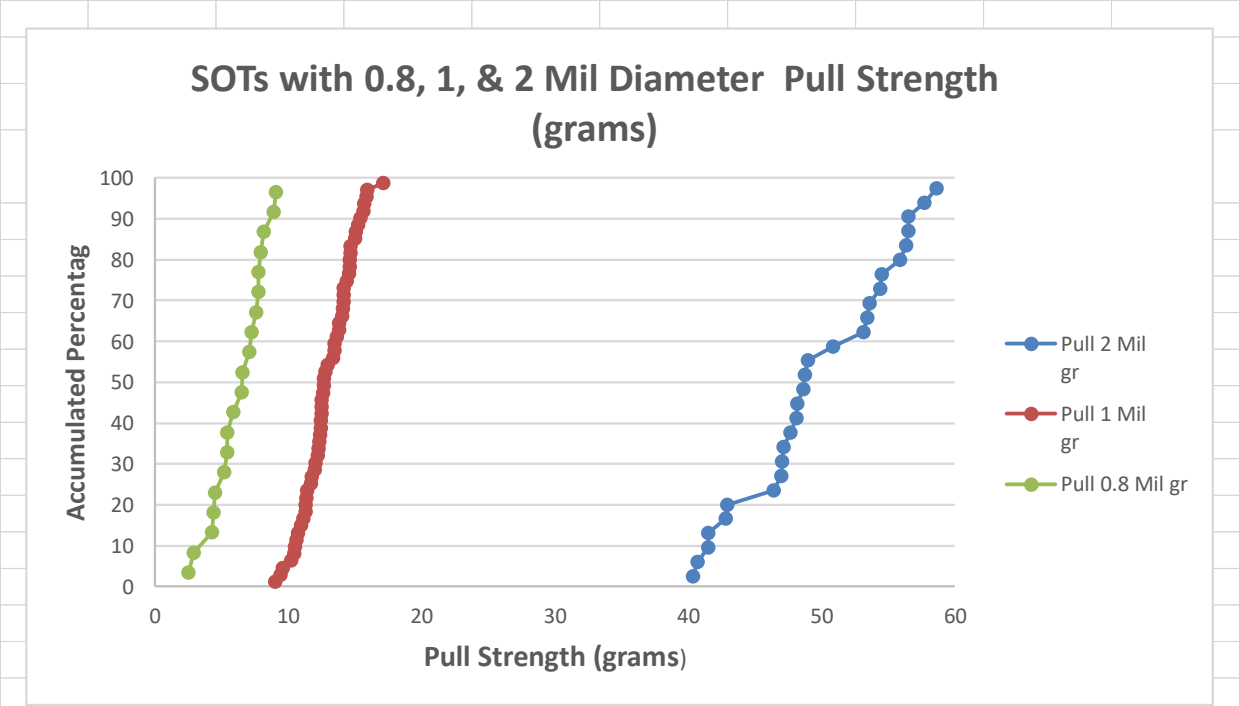

Weibull for 0.8 Mil Diameter		Weibull for 1 Mil Diameter		Weibull for 2 Mil Diameter	
β=	**3.353**	β=	**8.600**	β=	**10.780**
η=	**6.953**	η=	**13.677**	η=	**51.880**
R2 =	**0.9748**	R2 =	**0.9762**	R2 =	**0.9340**

Figure 7.4-1. Accumulative Percentage vs. Pull Strength (grams) Plots (top) with Calculated Weibull Parameters for 0.8, 1, and 2 mil Diameter Cu Wire Diameters and 1 mil Diameter Au Wire Bonds (M5-MCK-SOT235-01).

Figure 7.4-2 compares the Cu wire bond strength distribution for SOTs with QFP leaded parts having 100 and 144 leads and 1 and 0.8 mil diameters. The table in this figure lists the two Weibull parameters, η and β values, and the fit correlation R (R2). The β distribution for TQFP144, 0.8 mil diameter, followed the SOT slopes rather than other high-leaded parts. The NESC assessment team postulated that this discrepancy may have been caused by preferential wire etching during decapsulation of multi-tier components. This part exhibited cratering following bond pull testing under all exposure conditions. Therefore, an independent Weibull analysis of data enabled the assessment team to delineate decapsulation issues that could be addressed through further review of such results. As expected, the η strength value decreased as wire diameter decreased from 1 to 0.8 mil diameter.

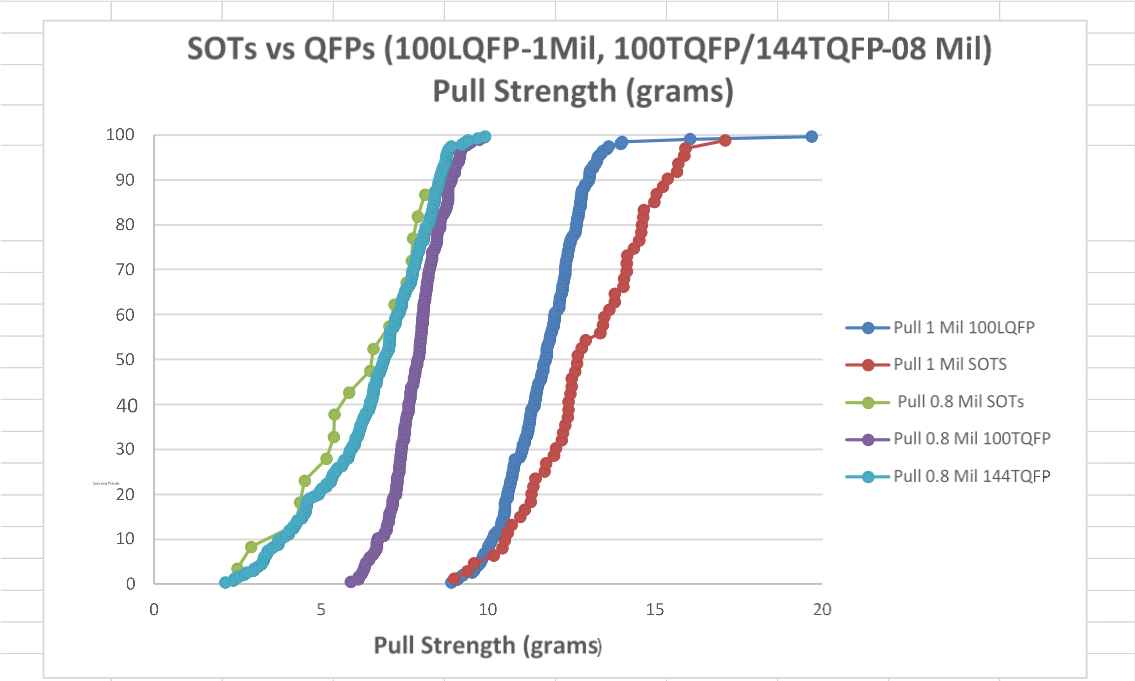

Weibull for 144TQFP 0.8 Mil Dia	
β=	4.046
η=	7.241
R2 =	0.9572

Weibull for 100TQFP 0.8 Mil Dia	
β=	12.312
η=	8.183
R2 =	0.9174

Weibull for 100LQFP 1 Mil Dia	
β=	12.668
η=	12.142
R2 =	0.9651

Figure 7.4-2. Comparison of Accumulative Percentage vs. Pull Strength (grams) Plots (top) and Calculated Weibull Parameters (bottom) for 3 Leaded QFPs with 0.8 and 1 mil Diameter vs. SOT with 1 mil Diameter

Figure 7.4-3 compares the Cu wire bond strength distribution for QFP versus BGA parts with 169 and 256 balls with 0.7 and 0.8 mil wire diameter, respectively. The table in this figure lists the two Weibull parameters, η and β values, as well as the fit correlation square (R^2). The β distribution for BGA169 and 100QFP follows the similar trend for slope, which is different for BGA256 input/output (I/O) with possibly two distribution slopes. The η strength value decrease was not appreciable when wire diameter decreased from 0.8 to 0.7 mil.

Initially, it was postulated that preferential test data could have been caused by decapsulation and anomalies. Furthermore, recent in-depth review of bond pull and shear test results indicated that 256 BGA with 0.8 mil, 169 LFBGA with 0.7 mil, and 144 TQFP with 0.8 mil diameter wire exhibited unacceptable failure modes. Most data for 0.7 and 0.8 mil wire are for leaded or BGAs with a large number of wires with decapsulation and cratering failure issues, and therefore scatter data in the tail ends of the Weibull with two parameter distributions.

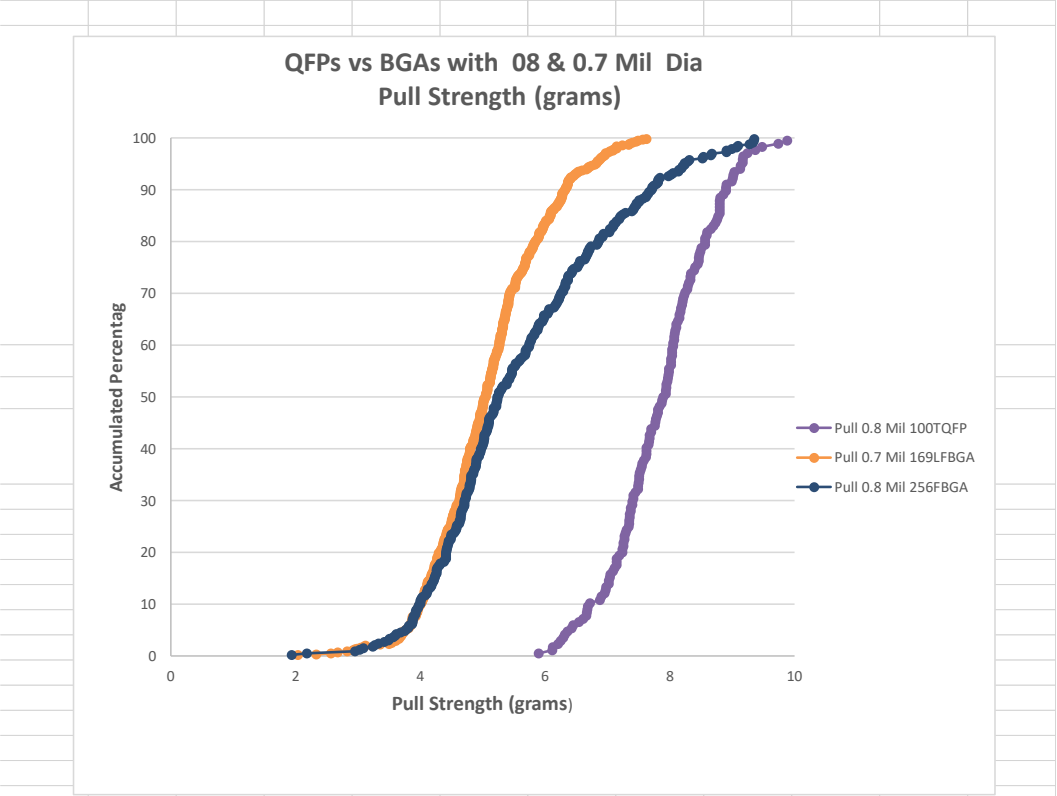

Weibull for 169 LFBGA 0.7 Mil Dia		Weibull for 256FPGA 0.8 Mil Dia	
β=	6.952	β=	5.122
η=	5.438	η=	6.062
R2 =	0.9728	R2 =	0.9412

Figure 7.4-3. Comparison of Accumulative Percentage vs. Pull Strength (grams) Plots (top) and Weibull Parameters (bottom) for Two BGA Packages with 0.7 and 0.8 mil Diameter vs. Leaded QFP with 0.8 mil Diameter

7.4.3 Projected Cu Wire Bond Pull Strength Comparison with Current Limits

The goal of this section is to plot a number of discrete Cu pull strength values obtained onto the MIL-STD-883 graphs [ref. 4] for Au wire bond minimum acceptable pull strength (pre-seal condition) to provide a quantitative visual comparison. An extrapolation of Weibull pull strength data points with projected values for specific percentiles, including low percentile values (e.g., 1 and 0.1), will be presented. These values were plotted with dot plots for Au wire bond values from MIL-STD-883 for a wider comparison. Weibull projections will be expanded for shear strength results. Finally, pull strength will be compared with published data for Au and Cu wire bonds.

In Section 7.4.2, Weibull distributions and parameters for various Cu wire bond diameters were presented. It was shown that the pull strength values and distributions depend not only on wire diameter and length, but also on the package type, decapsulation method, and failure mechanisms. For the MIL-STD-883 comparison, four packages with apparent low average and low tail pull strength values were further analyzed. This evaluation was performed using an open-source web tool for generation of Weibull plots with less data plotting flexibility. This allowed the NESC assessment team to verify the previous Weibull results and gain further

confidence in the analysis approach using Microsoft Excel formulas. These four plots with the Weibull parameters are shown in Figure 7.4-4 [ref. 27].

The figure also shows fitted Weibull lines with a 95% confidence level. When compared with Excel results, the calculated η and β values are slightly different. This difference is possibly due to using median ranking in the Excel approach. The reduction in strength from 2 to 1 mil wire diameter is clear, whereas for 0.8 to 0.7 mil diameters are inconsistent, possibly due to a wider spread in test data (β) for 0.8 mil diameter and pad cratering for 0.8 and 0.7 mil wire diameters.

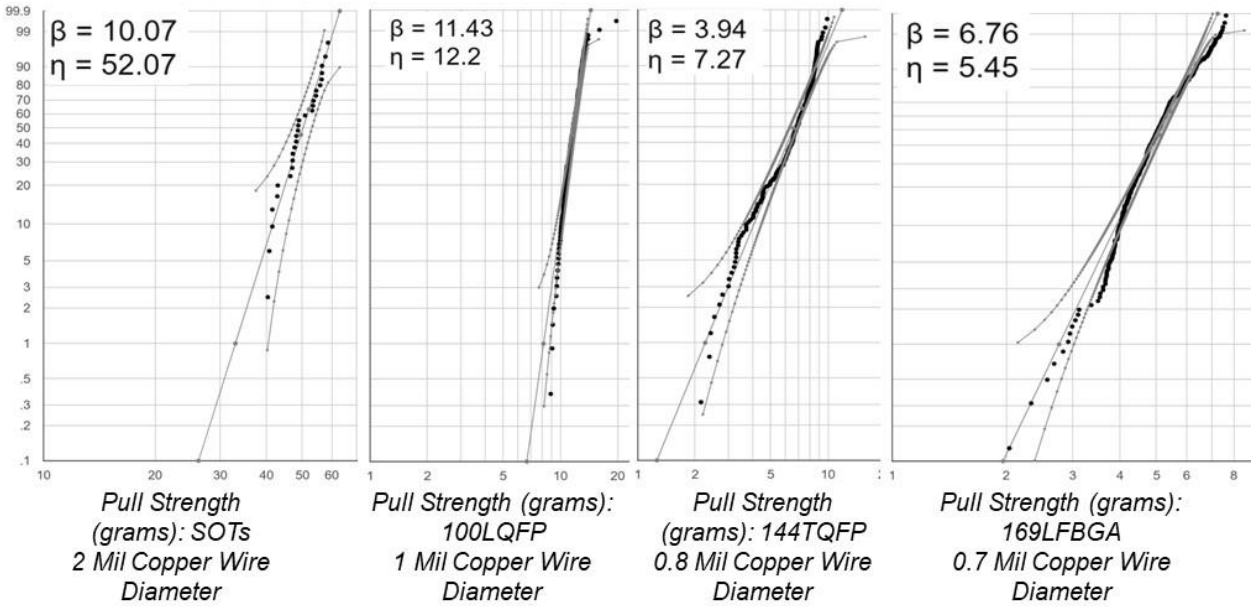

Figure 7.4-4. Comparison of Accumulative Percentage vs. Pull Strength (grams) Plots with Weibull Fit and Parameters for Four Select Parts (SOTs, LQFP, TQFP, BGA) with 2, 1, 0.8, and 0.7 mil Diameter

For comparison, the Cu pull strength values for 1 percentile, F(1%), were added to the MIL-STD-833 graph (see Figure 7.4-5). The pull strength percentiles used for these graphs are not stated, but the red dots for Cu wire bonds show a higher pull strength value for 1 and 2 mil diameters, but the value is slightly lower or higher for 0.7 and 0.8 mil diameters. The lowest value for 0.8 mil diameter was 1.77 gram-force (gf) of pull strength for SOTs, 2.3 gf for 144 TQFP, and 2.5 gf for 256FBGA, the latter two of which showed failure anomalies for the as-received condition.

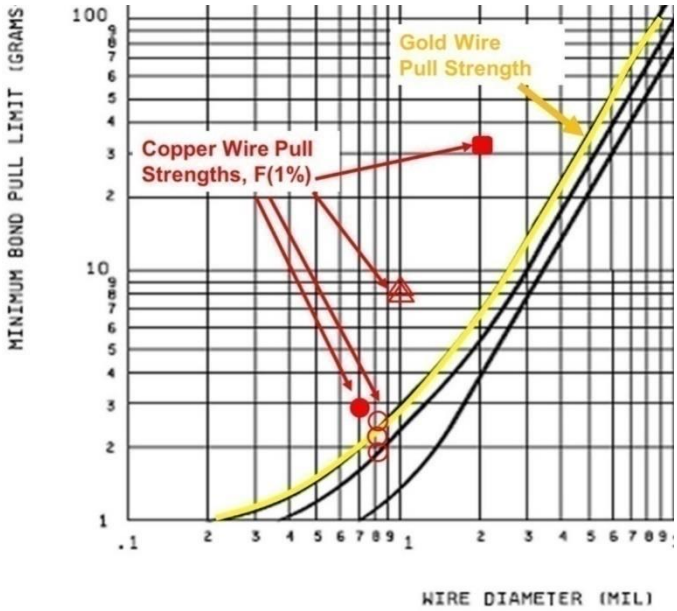

Figure 7.4-5. MIL-STD-883 for Au Wire Bond Pull Strength in Comparison to F(1) Percentage of Cu Wire Bond Pull Strengths (red dots) for Selected Parts with 2, 1, and 0.8 mil Diameter

Table 7.4-1 lists the Cu wire bond pull strengths, wire diameters, and Weibull parameters for all part types from the Excel data fit. This data fit is used due to the greater flexibility in assessing multiple variables and data subsets. The data includes SOTs, all parts with fewer than 20 wire bonds, leaded packages with 100 or more wire bonds, and BGAs with up to 256 wire bonds. SOTs included a part with Au wire bonds. From the Weibull parameters, the NESC assessment team estimated Cu wire strength values for 0.1, 1, 10, 50, and 63.2 percentiles. Figure 7.4-6 shows the F(t) values in logarithmic scale and wire diameter in linear scale for 0.7, 0.8, 1, and 2 mils. The scatter data for pull strength were also added by reading the MIL-STD-883 graphs for 0.2 [ref. 4], 0.7, 1, and 2 mil diameters, along with their associated pre-seal strengths of 1, 2, 3, and 7 grams, respectively. The plot clearly shows higher strength values for larger diameter Cu wire bonds, but this is not as clear for 0.7 and 0.8 mil diameters, which depend on package type and percentile. It should be noted that the parts that exhibited cratering had either 0.8 mil or 0.7 mil diameter Cu wires.

Table 7.4-1. Weibull Parameters for All Parts, Used to Calculate Cu Pull Strengths for Various Percentages, e.g., F(1%)

Weibull Parameters F(X)	Pull for SOTs 0.8 mil	Pull for SOTs 1 mil	Pull for SOTs 2 mil	Pull for 144TQFP 0.8 mil	Pull for 100TQFP 0.8 mil	Pull for 100TLQFP 1 mil	Pull for 169LFBGA 0.7 mil	Pull for 256FBGA 0.8 mil
β=	3.353	8.600	10.780	4.046	12.312	12.668	6.952	5.122
η=	6.953	13.677	51.880	7.241	8.183	12.142	5.438	6.062
R^2=	0.9748	0.9762	0.9340	0.9572	0.9174	0.9651	0.9728	0.9412
D=	0.8	1	2	0.8	0.8	1	0.7	0.8
F(63.2)=	6.953	13.677	51.878	7.241	8.182	12.141	5.438	6.062
F(50)=	6.233	13.107	50.146	6.614	7.943	11.795	5.159	5.644
F(10)=	3.554	10.528	42.105	4.152	6.816	10.165	3.934	3.907
F(1)=	1.763	8.011	33.859	2.323	5.632	8.444	2.806	2.469
F(0.1)=	0.886	6.126	27.335	1.313	4.669	7.038	2.014	1.574

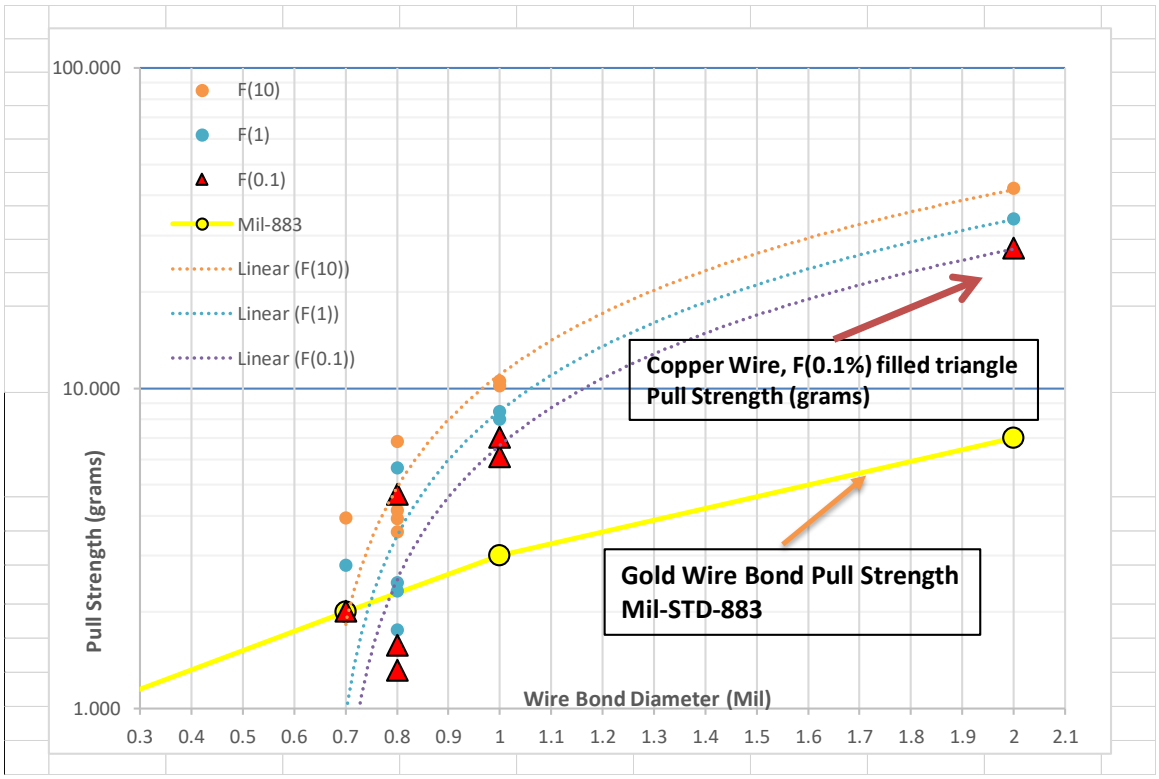

Figure 7.4-6. Mil-STD-883 for Au Wire Bond Pull Strength in Comparison to Cu Wire Bond Strength at F(0.1) , F(1), and F(10) Percentages vs. Wire Diameter (mil)

The inconsistency for Cu pull strengths for 0.7 and 0.8 mil diameters results from the strengths of wire bonds at the tail of Weibull plots. This is shown in Figure 7.4-7, where only the tail of Weibull plots for 0.7, 0.8, and 1 mil diameter parts are shown. The 1 mil diameter wire for the two parts shows higher values than 0.7 and 0.8 mil diameters, but the tails of strengths for 0.7 and 0.8 mil are inconsistent. They show either higher or lower values, which are in agreement with previous plots. Pad cratering for three parts with 0.8 and 0.7 mil diameters is one possible reason for such inconsistencies. The previous discussion regarding overall reduction in strength for commercially available bond wires at reduced diameters compared with the MIL-STD-883 plot [ref. 4] and the impact of diameter effects should be considered.

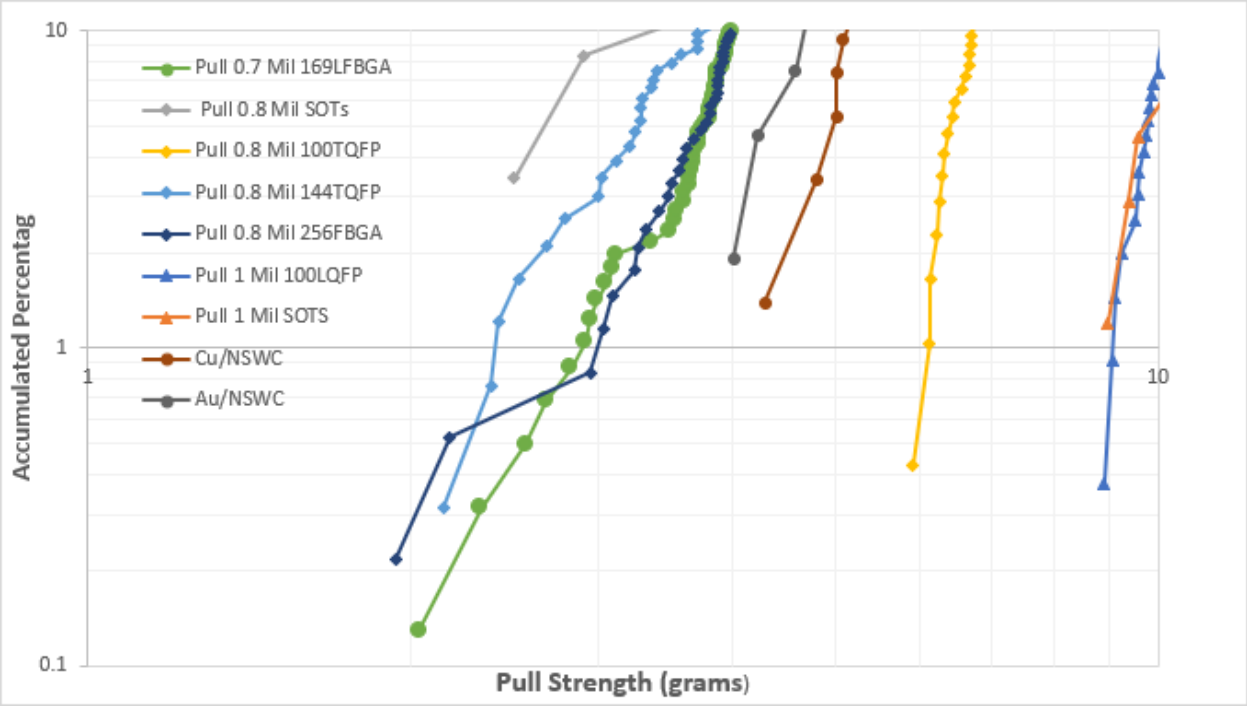

Figure 7.4-7. Tail of Weibull Plots for Cu Wire Bond Pull Strength for 0.7, 0.8, and 1 mil Diameter. Inconsistency in strength values for 0.7 and 0.8 mil diameter is apparent. Strengths increase or decrease with increasing wire bond diameter

In addition to industry, the Naval Surface Warfare Center (NSWC) documented pull and shear strength values in a different plot type for a number of packages with Cu wire bonds [ref. 28]. From one plot (see Figure 7.4-8, top left) comparing pull strengths for Cu and Au wire bonds, values for several parts were identified as 1–15. For comparison, these values were graphed in accumulated percentiles (bottom plots). The tail end of pull strength values is shown in the top right of this figure. The wire diameter is not given, but the data show a straight line for the Au value, referencing MIL-STD-883 [ref. 4]. Using this value, the diameter was estimated to be 0.8 mil if post-seal condition was considered. Also, the package types are not given; it is unknown whether parts had only four wire bonds or only four wire bonds were tested from each package type. The Au wire bonds show narrower Weibull distribution parameters, whereas this is not the case for Cu wire bond strengths. The tail end of Cu wire bond strengths at less than 10 percentiles is closer to those values from this assessment. However, at higher percentiles it shows higher values because of its wider Weibull distribution. This suggests variability in the bonding process for the Cu wire bonded parts evaluated.

Similar to the table for pull strength values, Table 7.4-2 lists shear strengths, wire diameters, and Weibull parameters for all part types, as obtained from the Excel data fit. From these parameters, the NESC assessment team estimated strength values for 0.1, 1, 10, 50, and 63.2 percentiles. Figure 7.4-9 shows the F(t) values in log-linear plots for 0.7, 0.8, 1, and 2 mil diameters.

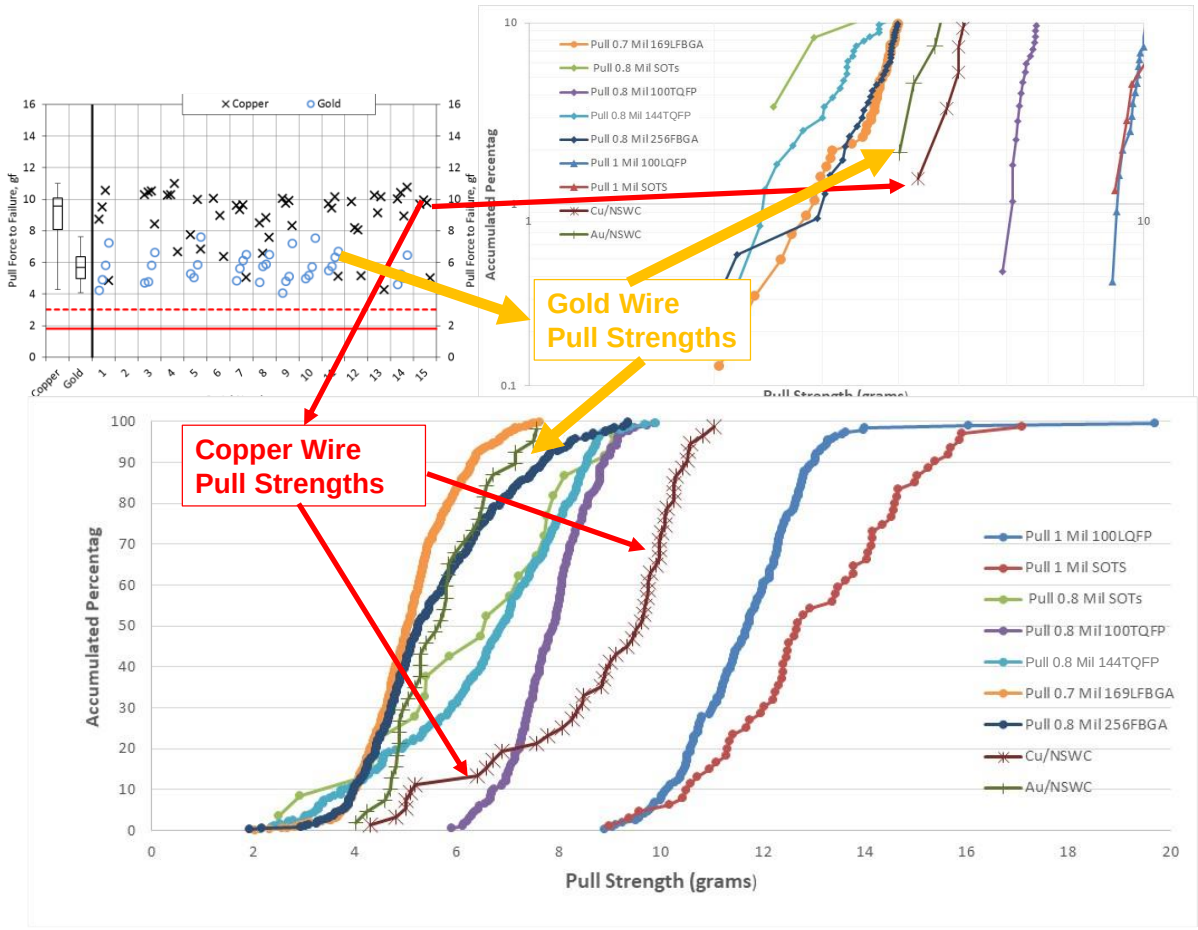

Figure 7.4-8. NSWC Pull Strength Test Data for Cu and Au Wire Bonds (top left), Weibull Plot Tail for Cu Wire Bond Pull Strength and NSWC (top right), and Weibull Plots from This Investigation and NSWC for Comparison. NSWC diameter is estimated at 0.8 mil f or post-seal condition.

Table 7.4-2. Weibull Parameters for All Parts, Used to Calculate Cu Shear Strengths for Various Percentages, e.g., F(1%)

Weibull Parameters F(X)	Shear for SOTs 0.8 mil	Shear for SOTs 1 mil	Shear for SOTs 2 mil	Shear for 144TQFP 0.8 mil	Shear for 100TQFP 0.8 mil	Shear for 100LQFP 1 mil	Shear for 169LFBGA 0.7 mil	Shear for 256FBGA 0.8 mil
β=	4.289	6.082	11.585	8.667	32.530	25.057	9.701	17.591
η=	42.124	39.610	127.409	22.711	19.203	42.004	14.027	25.129
R^2=	0.8594	0.9556	0.1935	0.5663	0.9693	0.8840	0.8117	0.9846
D=	0.8	1	2	0.8	0.8	1	0.7	0.8
F(63.2)=	42.121	39.608	127.406	22.710	19.203	42.003	14.027	25.129
F(50)=	38.674	37.293	123.442	21.770	18.988	41.394	13.507	24.611
F(10)=	24.927	27.359	104.916	17.518	17.920	38.396	11.123	22.112
F(1)=	14.412	18.591	85.656	13.358	16.671	34.959	8.730	19.347
F(0.1)=	8.416	12.722	70.190	10.236	15.530	31.884	6.883	16.969

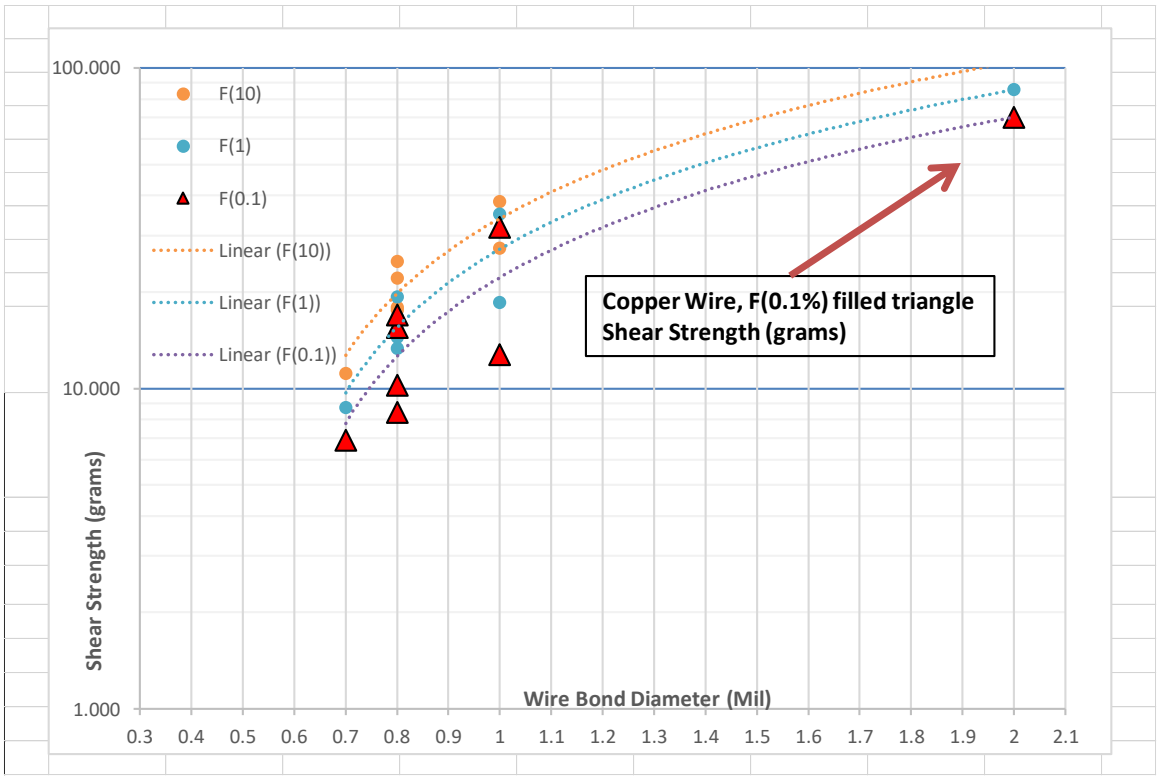

Figure 7.4-9. Cu Wire Bond Shear Strength (F(0.1), F(1), and F(10) Accumulated Percentages) vs. Wire Bond Diameter (mil)

Weibull parameters and η and β values, and the fit correlation R (R^2) for SOT parts are shown in Appendix C.4. This includes shear and pull strength of various projected percentiles, e.g., F(1%), for as-received and after-environmental exposures. Strength results for parts with 0.8, 1, and 2 mil diameters are given for 1000 TC, 2000 TC, and 500 hr HAST. Figure 7.4-10 shows pull strengths for SOTs at selected F(10), F(1), and F(0.1) percentiles. Strength values are plotted for as-received, 2000 TC, and 500 hr HAST for three diameters (0.8, 1, 2 mil) for comparison. From this plot, it appears that the 2000 TC parts for 0.8 and 2 mil diameters generally exhibit greater degradation than 500 hr bHAST. The results do not show a trend for 1 mil diameter wires. Figure 7.4-11 shows shear strengths for SOTs at selected F(10), F(1), and F(0.1) percentiles. Strength values are plotted for as-received, 2000 TC, and 500 hr HAST for three diameters (0.8, 1, 2 mil) for comparison. For shear strength, no apparent trend was observed.

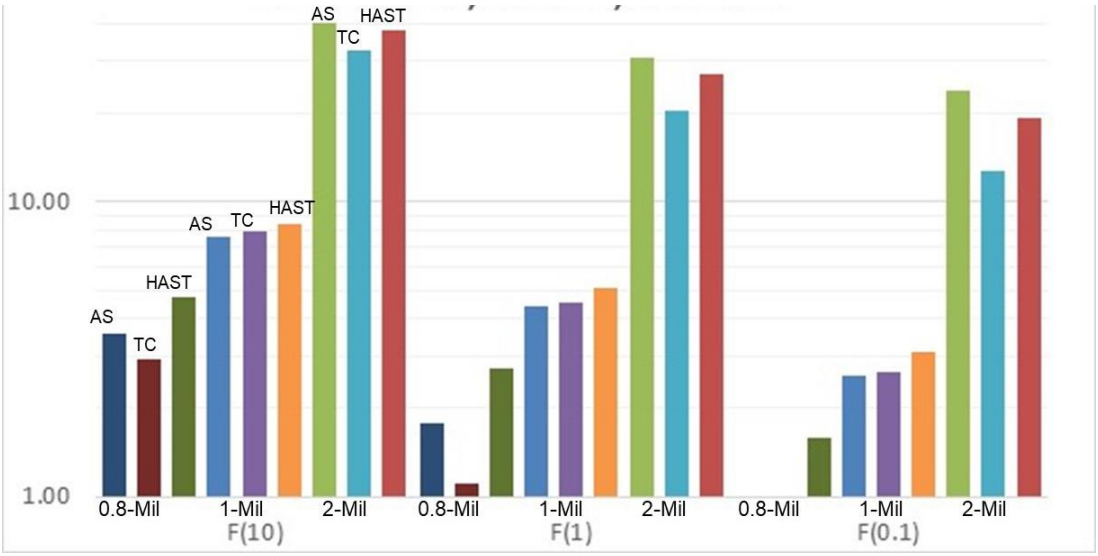

Figure 7.4-10. Cu Wire Bond Pull Strength F(10), F(1), and (F(0.1) Percentages) vs. Wire Bond Diameter (mil) for As-received, 2000 TC, and 500 hr HAST for Combined SOTs

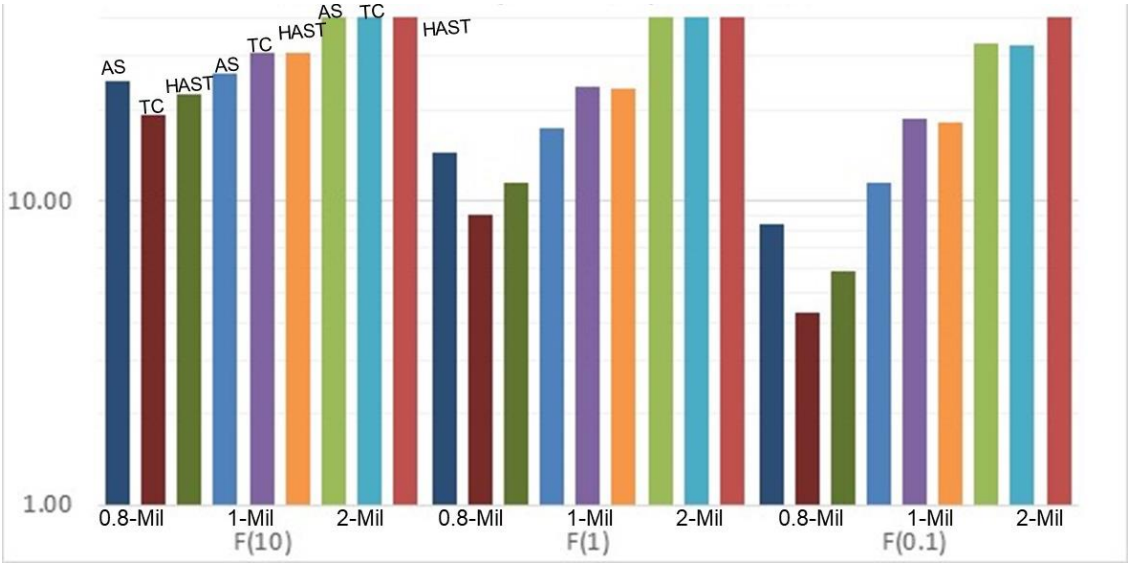

Figure 7.4-11. Cu Wire Bond Shear Strength F(10), F(1), and (F(0.1) Percentages) vs. Wire Bond Diameter (mil) for As-Received 2000 TCs, and 500 hr HAST for Combined SOTs

Appendix C.4 lists Weibull parameters, η and β values, and fit correlation R (R^2) for LFBGA with 169 balls and FBGA with 256 balls. It includes shear and pull strength of various projected percentiles, e.g., F(1%), for as-received and after-environmental exposures. Strength results for the two BGA parts with 0.7 and 0.8 mil diameters are given for 2000 TC, 500 hr HAST, and 400 hr HAST, plus 1000 TC for LFBGA. Figure 7.4-12 shows the two BGA pull strengths for selected F(10), F(1), and F(0.1) percentiles. Strength values are plotted for as-received, 2000 TC, and 500 hr HAST for the two BGA assemblies. It is apparent that 256FBGAs exhibit improved strength following 2000 TCs. There is no clear trend for other conditions. Figure 7.4-13 shows the two BGA shear strengths for selected F(10), F(1), and F(0.1) percentiles. Strength values are plotted for as-received, 2000 TC, and 500 hr HAST for the two BGA assemblies. There are no significant changes in shear strength due to the two exposures.

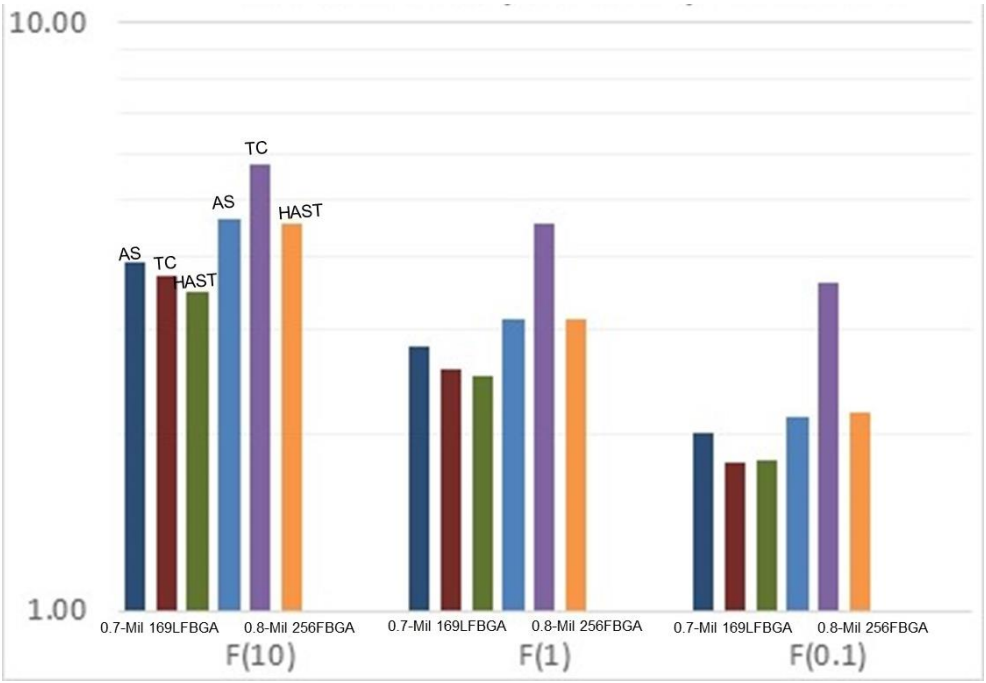

Figure 7.4-12. Cu Wire Bond Pull Strength F(10), F(1), and F(0.1) Percentages vs. Wire Bond Diameter (mil) for As-Received, 2000 TCs, and 500 hr HAST for 169LFBGA and 256FBGA Assemblies

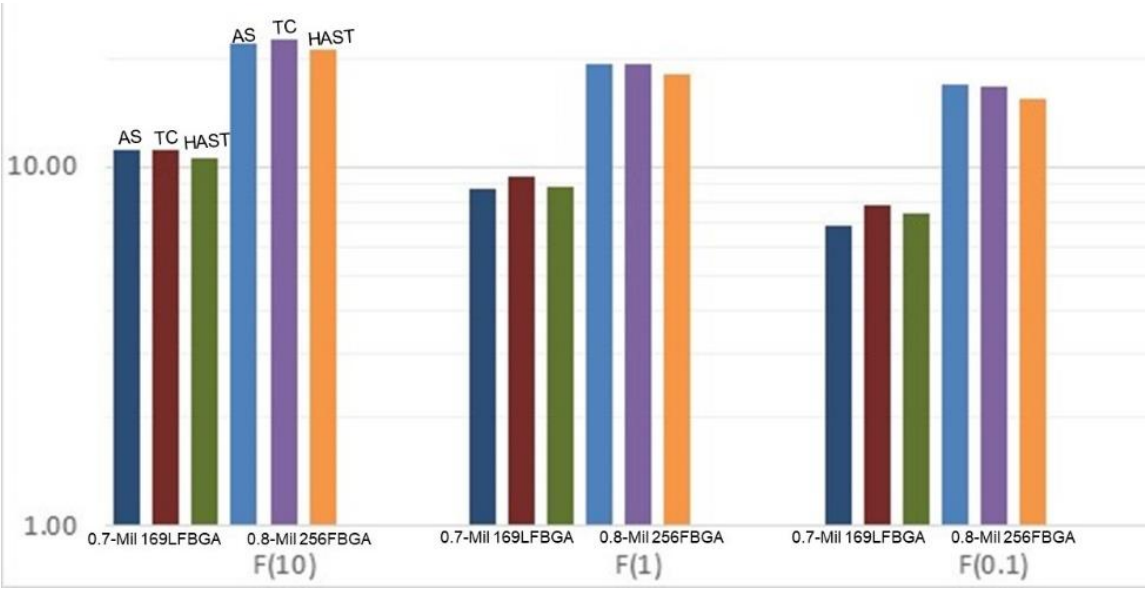

Figure 7.4-13. Cu Wire Bond Shear Strength F(10), F(1), and F(0.1) Percentages vs. Wire Bond Diameter for As-Received, 2000 TCs, and 500 hr HAST for 169LBGA and 256FBGA Assemblies

7.4.4 Acceptance Criteria for NASA Missions

Since Cu wire bonded parts are not yet available as military specified components, only COTS parts from known manufacturers were evaluated. Therefore, the criteria for acceptance provided herein are closely related to the guidance for selecting and using COTS parts in NASA missions provided within the NESC Technical Assessment Phase II report, "Recommendations on the Use

of Commercial-Off-The-Shelf (COTS) Electrical, Electronic, and Electromechanical (EEE) Parts for NASA Missions" [ref. 2]. The relationship between the two NESC assessments is summarized in Figure 7.4-14. This assessment focuses on providing evaluation criteria and selective testing approaches for the boxes highlighted in red.

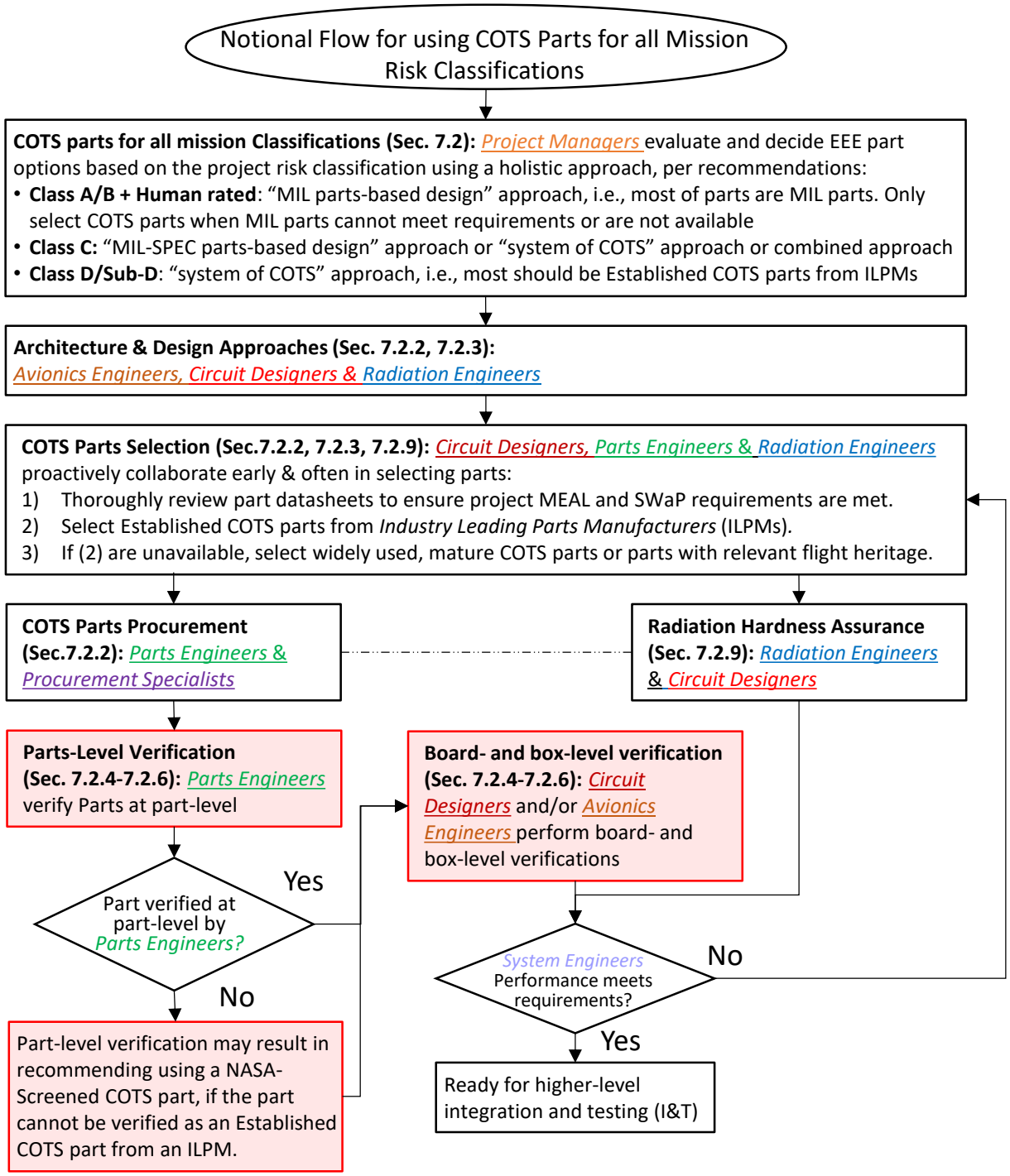

Figure 7.4-14. NESC Cu Wire Bond Assessment Relationship with NESC Recommendations on COTS Parts

The NESC Cu wire bond assessment team agrees with the NESC COTS Parts assessment Phase II report recommendations regarding COTS parts selection for NASA missions with risk classifications of A through D and human-rated missions. Mission classification and COTS parts selection are discussed briefly in section 7.4.4.1. MEAL definition guidelines for the evaluation of COTS parts with Cu wire bonds, as discussed in section 7.4.4.2, are centered around thermal extremes, thermal differentials and the number of cycles. The Cu wire bond assessment builds upon the recommendations for using COTS parts for NASA Missions and provides criteria for part and board level verification of COTS parts with Cu wire bonds. These evaluation process guidelines are detailed in section 7.4.4.3.

7.4.4.1 Mission Classification and Parts Selection Guidelines for Parts with Cu Wire Bonds

For COTS implementation into NASA missions as defined in NPR8705.4A – Risk Classification for NASA Payloads, numerous aspects of packaging technologies, including the presence of Cu wire bonds, should be identified and selected based on specific mission requirements and assessments. Implementation necessitates the definition of overall NASA mission environmental requirements, including radiation, mechanical, thermal, life cycle, mechanical shock, and vibration. In addition, it must be determined whether package properties are within the envelope of mission environmental requirements to avoid early overstress failures.

The NESC Cu wire bond assessment team concurs with the following recommendations regarding COTS parts selection for NASA missions with risk classifications of A through D and human-rated missions. [ref. 2]

- Recommend Class A/B and human-rated missions to consider a "MIL-SPEC parts-based design" approach (i.e., most of the parts are MIL-SPEC parts, and only select COTS parts when equivalent MIL-SPEC parts do not meet functional or SWaP requirements or are not available).
- Recommend Class D/Sub-D missions to consider a "system of COTS" approach (i.e., most parts should be Established COTS parts from ILPMs).
- Recommend Class C missions to determine which approach is the best for the programs/projects (i.e., "MIL-SPEC parts-based design" approach, a "system of COTS" approach, or a combined approach).

The NESC Cu wire bond assessment team applied these recommendations to all of the part acceptance criteria discussed in section 7.4.4.3 and Table 7.4-3, Cu Wire Bond Parts Evaluation Process. As an example, COTS parts with Cu wire bonds in the column Class A + Human rated should only be selected when MIL parts cannot meet requirements or are not available.

Although the selection of parts for the Cu wire bond assessment predates the recommendations provided by the NESC COTS parts assessment team, the selection process was in line with that discussed for Established COTS parts. The Cu wire bond assessment team identified hundreds of parts from well-known manufacturers following discussions with representatives from each NASA center, interested groups in various government agencies, and commercial aerospace companies. Several of the parts evaluated were being considered for use in high reliability applications. The team thoroughly reviewed all datasheets and down selected components on the basis of part type, package type, manufacturer, wire diameter, wire material, and wire count. Based on the selection and evaluation process, the guidelines provided for this assessment are focused on evaluation criteria for Established COTS parts with Cu wire bonds.

7.4.4.2 MEAL Definition Guidelines

For the Cu wire bond assessment, accelerated TC and bHAST were used to determine whether Cu wire bonds at the part level or solder joints at the board level were the weakest link in the assembly of selected packages. This approach is in-line with the global NESC COTS Parts Assessment recommendations [ref. 2].

The NESC Cu Wire Bond Assessment team considered four environmental conditions and mission durations, irrespective of NASA mission class, to address TC life requirements for various NASA missions. The four categories include the approximate equivalent accelerated TCs (e.g., -55/125 ℃) to be performed in a laboratory chamber for an assumed flight temperature fluctuation (ΔT). If failure occurs under these laboratory TCs, then a specific flight mission environment ΔT (e.g., -35/70 ℃) can be used. The number of equivalent TCs for the example ΔT is provided.

- Low ΔT and low number of thermal fluctuations: ΔT ~ 15 ℃ with short mission duration requiring lower number of cycles, <2500 cycles, within the -35/70 ℃ temperature range.
  - MEAL: ~ 150 cycles (-35/70 ℃) or ~ 50 cycles (-55/125 ℃)
- Low ΔT and moderate number of thermal fluctuations: ΔT ~ 15 ℃ with moderate mission duration requiring high number of cycles, 2500-7500 cycles, within the -40/85 ℃ temperature range.
  - MEAL: ~ 100-300 cycles (-40/85 ℃) or ~ 50-150 cycles (-55/125 ℃)
- Moderate ΔT and high number of thermal fluctuations: ΔT ~ 25 ℃ or 35 ℃ with long mission duration requiring 5000-10000 cycles within the (-55/100 ℃) or (-55/ 125 ℃) temperature range.
  - MEAL: ΔT ~ 25 ℃, ~ 400-800 cycles (-55/100 ℃) or ~ 300-600 cycles (-55/125 ℃)
  - MEAL: ΔT ~ 35 ℃, ~ 800-1500 cycles (-55/100 ℃) or ~ 600-1,100 cycles (-55/125 ℃)
- Extreme conditions: ΔT mission specific, hot bias with a maximum temperature higher than 100 ℃ or cold bias with minimum temperature less than -55 ℃ and duration short to long, to 100 cycles or to 1000 cycles. These cases have specific conditions and are beyond the scope of this reliability evaluation.

The ΔTs and TC number are correlated via different projection models for solder joint reliability. Therefore, adjustments can be made for MEAL ΔT fluctuations. It is apparent that most MEALs, except in specific extreme conditions, will be covered by the accelerated thermal cycle selected for this investigation. Depending on cycles-to-failure for a specific packaging technology, MEAL could be limited. This investigation did not address environmental requirements that exceed those evaluated (-55℃ minimum temperature and +125℃ maximum temperature) in this assessment, including extreme cold exposure (e.g., NASA's Moon and Mars missions).

7.4.4.3 Evaluation Process Guidelines for Cu Wire Bonded Parts in NASA Missions

Experimental results for the Cu wire bond assessment indicated that TC and bond pull testing were the greatest differentiators for damage. Statistical and outlier analyses were additionally critical in identifying reliability issues. The Cu wire bond assessment team, therefore, builds upon global recommendations given by the NESC COTS parts assessment team in the Phase II report and provides detailed verification, screening and LAT guidelines for Cu wire bonds in COTS PEMS that are used in a range of NASA flight conditions and mission risk postures [ref. 2]. These guidelines include performing DPA/CA evaluation and failure analysis. Statistical

analyses and outlier identification of the data and results should be performed for the defined mission applications with specific focus on flight thermal fluctuation requirements.

The Cu Wire Bond Parts Evaluation Process for Established COTS Parts is summarized in Table 7.4-3 with further discussion. The table leverages lessons learned from this investigation including guidelines on a combination of DPA/CA, outlier analysis, statistical analysis (e.g., Weibull), environmental testing (e.g., TC), and destructive bond pull to efficiently identify potential workmanship and reliability issues of Cu wire-bonds at the part- and board-level.

Table 7.4-3. Cu Wire Bond Parts Evaluation Process for Established COTS Parts

Flight Use Conditions[1] MEAL		Mission and Instrument Class [NPR8705.4A]			
ΔT (°C)	Condition	Class A/ Human-Rated	Class B	Class C	Class D
15	<2500 cycles and mission duration <1 year within maximum temperature range (-35 °C/70 °C)	1. Part DPA/CA/Outlier[2] 2. A qualification process is required at part-and board-level[3]	1. Part DPA/CA/Outlier[2] 2. A qualification process is possibly required at part-and board-level[3]	Use ILPM Established COTS Parts As Is, or 1. If non-Established COTS Parts are used qualification at the part- and board-level including Part DPA/CA /Outlier[2] may be required.	Use ILPM Established COTS Parts As Is, or 1. If non-Established COTS Parts are used qualification at the part- and board-level including DPA/CA may be required.
15	2500-7500 cycles and mission duration 1-3 years within maximum temperature range (-40 °C/85 °C)	1. Part DPA/CA/Outlier[2] 2a. Part Weibull F(1%) [≥ 11 wire for each wire type][4] or 2b. TC[5] 3. A qualification process is required at part-and board-level[3]	1. Part DPA/CA/Outlier[2] 2a. Part Weibull F(1%) [≥ 11 wire for each wire type][4] or 2b. TC[5] 3. A qualification process is required at part-and board-level[3]	1. Part DPA/CA/Outlier[2] 2. A qualification process is possibly required at part-and board-level[3]	N/A[6]
25 or 35	5000-10000 cycles and mission duration 3-6 years within maximum temperature range (-55 °C/100 °C)	1. Part DPA/Outlier[2] 2. TC[5] 3. A qualification process is required at part-and board-level[3]	1. Part DPA/Outlier[2] 2. TC[5] 3. A qualification process is required at part-and board-level[3]	N/A[6]	N/A[6]
Extreme Conditions: ΔT Mission-specific (hot/cold bias) or maximum temperature >100 °C/minimum temperature <-55 °C any cycle count		Part DPA/Outlier[2] Cycle: Conditions not covered in assessment.[7]	Part DPA/Outlier[2] Cycle: Conditions not covered in assessment.[7]	Part DPA/Outlier[2] Cycle: Conditions not covered in assessment.[7]	DPA (short duration) Cycle: Conditions not covered in assessment.[7]

[1] A hierarchy of temperature range limitations from part, assembly, and box level are considered in the selection of flight temperatures. Parts with flight use conditions between categories (e.g., lower temperature range, lower temperature limits, reduced number of cycles, or reduced mission duration) should use the lower level test conditions.

[2] Perform PEM DPA in accordance with NASA-STD-8739.11. Throughout this assessment, DPA performed according to the test methods and standards cited was found to be effective at

identifying workmanship issues (e.g., cratering, splash, and non-stick on pad), as well as fatigue damage and other time-dependent phenomena following environmental exposure.

- On Class A-C and/or Assurance Levels 1-3, DPA is required. Class D and/or Assurance Level 4 do not require DPA per NASA-STD-8739.11. Table 7.4-3 imposes additional DPA/CA recommendations based on the use of non-Established COTS parts versus Established COTS parts.
- DPA should be performed per S-311-M-70, which references MIL-STD-1580 for microcircuits, transistors, and diodes. Follow quantity for DPA as outlined in S-311-M-70 and MIL-STD-1580.
- Identify and address outliers in bond strength data at the test house and document in the final report.
- Currently there is no requirement for statistical bond pull data analysis in any NASA or MIL document for DPA or bond strength test (e.g., S-311-M-70, MIL-STD-1580, MIL-STD-750, MIL-STD-883). However, identifying outliers (also referred to as out-of-family or mavericks) can lead to identifying suspect wire bonding processes or materials.
- JESD-B120 emphasizes but does not specifically require identifying and resolving outlier bond pull values.
- Bond strength outliers should be identified and scrutinized.
- Best practice of understanding outliers should be implemented at the test house. One method is to plot bond strengths and break codes in a cumulative distribution function (CDF) plot and examine them for outlier data by identifying anomalous bond strength values or break codes. If there is a notable grouping of outliers (e.g., transition to a lower bond strength and change of break code) or a single bond strength value or break code significantly different from the rest of the group, then an explanation of this outlier should be pursued.

[3] Additional part-, board- or box- level mechanical and electrical testing is dependent upon specific mission requirements [ref. 2]. Part level testing may include TC, bHAST, and/or shock/vibration. At the board level, TC of the mounted part may be required to identify the weakest link among competing failure mechanisms, e.g., Cu-wire and solder joints, for the specific design and MEAL classification. MEAL qualification may be performed using representative parts assembled onto a board, COTS boards, or an EM unit. An example of a MEAL based packaging qualification plan is provided in reference 29.

[4] Perform a Weibull analysis of Cu wire bond pull strength results with a minimum sample size of at least 11 wires for each wire type (diameter and composition) on each part type to determine F(1%). If the F(1%) meets the minimum strength requirements outlined in MIL-STD-883 for Au wire in the pre-seal condition [ref. 4], then accept. If it does not, then reject the part or perform thermal cycling per item 5. Through this assessment, Weibull analysis (F(1%) limit) of bond pull results was effectively used to determine the level of bond degradation for different environmental conditions.

[5] Complete 100 component-level TCs in the temperature range of -55 ℃ to 125 ℃ at a ramp rate of less than 20 ℃/minute. Perform DPA and outlier analysis per item 2. If there are no changes in failure mechanism and minimum strengths are met, then accept. Otherwise, reject. Throughout this assessment, thermal cycling combined with bond pull testing was found to be the greatest differentiator for damage following initial inspection.

[6] These conditions are not applicable for this mission class definition [ref. 1]

[7] For extreme conditions, additional testing is required to accept the part, since these temperature ranges and cycle conditions are outside the range of those evaluated for this assessment. Different failure mechanisms may exist.

7.4.5 Future Work

Based on the results of this assessment, the following areas should be considered for future discipline enhancing work:

1. Various decapsulation methods were considered, but the following alternatives could not be evaluated because they were beyond the scope of this assessment. Their use could potentially improve the time required for decapsulation, Cu wire bond quality following decapsulation, or decapsulation process repeatability. It should be noted that mechanical test results obtained using the optimized decapsulation process for this assessment yielded reliable, repeatable results.
    a. The acids used for chemical decapsulation during the course of this assessment were fuming nitric acid with a concentration of 90% HNO_3 with up to 10% water, and fuming sulfuric acid with a concentration of 96.7% H_2SO_4 weight for weight. Due to supply limitations, nitric acids of other concentrations and compositions were not available. An alternative acid of particular interest would have been fuming nitric acid with 90% HNO_3 and 10% dissolved oxides rather than 10% water. The reduced water content may have helped further mitigate etching of Cu during chemical decapsulation.
    b. Biased chemical decapsulation equipment is available, which may help to preserve Cu wire bonds. The side effects of biased decapsulation observed during experimentation in the scope of this assessment should be reviewed if pursuing this solution.
    c. Microwave-induced plasma (MIP) equipment is available, which negates the need for acid wet-etch decapsulation. However, MIP requires significant etch times, parameters must be tailored for each part, and changes to the mold compound due to environmental testing can require additional modification of these parameters. The method used to remove ashed mold compound buildup during etching should also be considered, as various MIP models may employ solvents, ultrasonic baths, or compressed air.
    d. Laser milling as a complete decapsulation solution can be considered. Rather than a singular infrared laser, which was used in this assessment, equipment is available that uses a combination of lasers and solvents to remove mold compound without acids or plasmas while preserving wire and die features.
    e. It would be extremely useful to develop a library of decapsulation images to help failure analysts determine whether the level of etching on Cu wires is within acceptable levels.
2. Damage levels for Cu wire-bonded parts used in this assessment should be established to aid with life prediction in future NASA programs/projects.
    a. In the near term, additional failure analysis could be performed on the remaining tested assemblies from this assessment to understand the damage progression for external (e.g., solder joints) and internal Cu wire bonds and interfaces. This information can be used to project Cu wire bond life. Cross-sections for this assessment were obtained in the as-received condition, rather than following environmental exposure.
    b. In the long term, improved life prediction can be obtained by implementing the test-to-failure approach using the sequential highly accelerated life test (HALT) methodology on

Cu wire and Au wire-bonded parts with known acceptable wire-bonded joints and unacceptable ones (e.g., cratering) in the as-received condition.

c. Sequential thermal cycling to failure should be performed to establish sensitivity to temperature and cycling ranges.

d. Isothermal aging at different levels should be performed to establish whether this approach could be established for screening weak Cu wire bonds for this category of workmanship defect.

e. This assessment, NSWC, and industry establish hot bias thermal cycle reliability evaluation of Cu wire bonds. NASA applications cover cold bias in numerous exposed electronics. Feasibility of Cu wire bond for cold bias applications should be investigated.

3. A standardized method of evaluating the chemical and mechanical properties of molding compounds for commercial components in the as-received condition should be established.

4. NASA should work with manufacturers and research institutions to perform a manufacturing-based design of experiments and identify which materials properties and microstructure conditions yield optimal reliability. The NESC assessment team recognizes that much of this data is currently considered proprietary information for commercial entities.

8.0 Findings, Observations, and NESC Recommendations

8.1 Findings

F-1. As of June 2023, no NASA-wide practice addressed the use or acceptance of Cu wire bond parts, and no NASA standards specified Cu wire bonds.

F-2. Several trends were observed for the Cu wire bond pull strength and shear strength:

a. When the Weibull 1% pull strength values obtained for Cu wire bonds were compared with the MIL-STD-883, Method 2011.10, limits for Au wire (pre-seal), Cu wire bond pull strengths were significantly higher than Au limits for 2 mil and 1 mil wires (i.e., >4.8x and >2.5x, respectively), and similar to Au limits for 0.8 mil and 0.7 mil wires (i.e., ~1x and ~1.4x, respectively).

i. These results are supported by unbonded wire data plotted from literature, which exhibits a different trend than that shown for the minimum pull test plots in MIL-STD-883. Commercially available wires with diameters of 1 mil and above exhibit a higher relative strength than wires with diameters less than 1 mil.

b. NSWC Cu wire bond pull strength data exhibited a wider Weibull distribution when compared with the Au wire bonds in their published work and the Cu wire bond data in this assessment. This means that the lower pull strength values have a greater influence on the Weibull strength value of the NSWC Cu wire bond data at less than 10 percentiles. The Weibull 1% pull strength for the NSWC Cu wire bond data is comparable to that observed for this assessment.

F-3. X-ray inspection of PEMs was used effectively to determine the presence of Cu wire bonds when compared with a PEM with Au wire bonds.

F-4. Thermal cycling, combined with destructive wire bond pull testing, appears to be a greater differentiator for Cu wire bond damage than bHAST or ball shear testing.

F-5. Pull strengths for Cu wire bonds following decapsulation are dependent upon decapsulation processes. This fact does not change the NESC team recommendations for bond pull testing, since the processes used for this assessment were optimized and proven to yield reliable, repeatable results.

F-6. No corrosion-related failures of Cu wire bonded joints were observed in this assessment.

8.2 Observations

O-1. Cu wire bonds can potentially exhibit greater variability in bond pull strengths than Au wire bonds.

O-2. Manufacturers and users of Cu wire bonds are hesitant to share Cu bond pull strength data with organizations responsible for developing standards. This can be due to proprietary manufacturing process details and end-user applications.

O-3. Successfully assembled fine-pitch leaded packages exhibited solder bridges that had to be touched up after assembly. It was necessary to wick off uneven HASL finish prior to assembly. Several BGA components were off-center in the assembled state.

O-4. SAM inspection of select deadbug components on assembled boards could not be performed. There is no quick and reliable method of examining the delamination of deadbug parts. Reflow and removal of parts may yield delamination.

8.3 NESC Recommendations

The following NESC recommendations were identified and are summarized below. R-1 and R-2 are directed towards future NASA flight programs and the NASA parts and packaging community.

R-1. Guidelines for the use of ILPM Established COTS PEMs with Cu wire bonds for NASA missions include the following: ***(F-1 through F-5)***

a. Identify NPR8705.4A mission classifications and MEAL conditions.

b. Perform X-ray to determine which parts have Cu wire bonds if the lot bill of materials does not define wire bond composition. For Class C and D missions identified in row 1 of Table 8.3-1, when ILPM Established COTS Parts are used, this step is not required.

c. Evaluate parts with Cu wire bonds using the process summarized in Table 8.3-1. Details regarding implementation of this recommendation are provided in Section 7.4.4. The notes for Table 8.3-1 are provided in Section 7.4.4.

d. Verification data obtained from ILPMs for Established COTS should include pre-molded wire pull strength data and molding compound halogen/halide content or limits. This information will aid in the interpretation of pull strength data following decapsulation and limit the presence of corrosion related failures.

e. When possible, obtain process monitor practices and data regarding post-HAST or post-TC wire bond pull and/or shear testing.

Table 8.3-1. Summary of Cu Wire Bond Parts Evaluation Process for ILPM Established COTS Parts

Flight Use Conditions[1] MEAL		Mission and Instrument Class [NPR8705.4A]			
ΔT (°C)	Condition	Class A/ Human-Rated	Class B	Class C	Class D
15	<2500 cycles and mission duration <1 year within maximum temperature range (-35 °C/70 °C)	1. Part DPA/CA/Outlier[2] 2. A qualification process is required at part-and board-level[3]	1. Part DPA/CA/Outlier[2] 2. A qualification process is possibly required at part-and board-level[3]	Use ILPM Established COTS Parts As Is, or 1. If non-Established COTS Parts are used qualification at the part- and board-level including Part DPA/CA /Outlier[2] may be required.	Use ILPM Established COTS Parts As Is, or 1. If non-Established COTS Parts are used qualification at the part- and board-level including DPA/CA may be required.
15	2500-7500 cycles and mission duration 1-3 years within maximum temperature range (-40 °C/85 °C)	1. Part DPA/CA/Outlier[2] 2a. Part Weibull F(1%) [≥ 11 wire for each wire type][4] or 2b. TC[5] 3. A qualification process is required at part-and board-level[3]	1. Part DPA/CA/Outlier[2] 2a. Part Weibull F(1%) [≥ 11 wire for each wire type][4] or 2b. TC[5] 3. A qualification process is required at part-and board-level[3]	1. Part DPA/CA/Outlier[2] 2. A qualification process is possibly required at part-and board-level[3]	N/A[6]
25 or 35	5000-10000 cycles and mission duration 3-6 years within maximum temperature range (-55 °C/100 °C)	1. Part DPA/Outlier[2] 2. TC[5] 3. A qualification process is required at part-and board-level[3]	1. Part DPA/Outlier[2] 2. TC[5] 3. A qualification process is required at part-and board-level[3]	N/A[6]	N/A[6]
Extreme Conditions: ΔT Mission-specific (hot/cold bias) or maximum temperature >100 °C/minimum temperature <-55 °C any cycle count		Part DPA/Outlier[2] Cycle: Conditions not covered in assessment.[7]	Part DPA/Outlier[2] Cycle: Conditions not covered in assessment.[7]	Part DPA/Outlier[2] Cycle: Conditions not covered in assessment.[7]	DPA (short duration) Cycle: Conditions not covered in assessment.[7]

R-2. The NESC recommends consideration of the Cu wire bond evaluation process outlined in Table 7.4-3 for future versions of NASA-STD-8739.10 and NASA-STD-8739.11. ***(F-1)***

R-3. The following NESC recommendation for forward work is directed toward the NASA Electronic Parts and Packaging (NEPP) Program. Further details regarding these recommendations are provided in Section 7.4.5. ***(F-1, F-5, F-6)***

a. Develop a process to gather bond pull test data and decapsulation images from the different NASA centers to continue to refine strength limits for Cu wire bonds and improve uniformity of decapsulation processes.

b. Examine alternate decapsulation methods.

c. Using cross-section evaluation or an alternate test method, establish if there is any cracking or corrosion within the bonded joint at different stages of environmental exposure for Cu wire-bonded parts used in this assessment to aid with life prediction in future projects.

d. Develop improved life prediction models of Cu wire bonds for future NASA projects by implementing a test-to-failure approach using sequential highly accelerated life tests on Cu wire-bonded parts with known acceptable wire bonded joints and unacceptable ones.
e. Establish a standardized method of evaluating chemical and mechanical properties of molding compounds for commercial components in the as-received condition.
f. Work with manufacturers to determine an ideal manufacturing process and material conditions (properties and microstructure) for obtaining repeatable, high quality Cu wire bonds.

9.0 Alternate Technical Opinions

No alternate technical opinions were identified during the course of this assessment by the NESC assessment team or the NESC Review Board (NRB).

10.0 Other Deliverables

No other deliverables were developed during the course of this assessment.

11.0 Recommendations for the NASA Lessons Learned Database

No recommendations for NASA lessons learned were identified as a result of this assessment.

12.0 Recommendations for NASA Standards, Specifications, Handbooks, and Procedures

To address R-2, the assessment team is providing recommendations for the evaluation of Cu wire bonded components for future NASA missions to NASA for inclusion in future versions of NASA-STD-8739.10 and NASA-STD-8739.11. In additions, data will be provided to DLA to support the inclusion of Cu wire bond pull limits in future versions of MIL-STD-883, Method 2011.12.

13.0 Definition of Terms

Finding	A relevant factual conclusion and/or issue that is within the assessment scope and that the team has rigorously based on data from their independent analyses, tests, inspections, and/or reviews of technical documentation.
Observation	A noteworthy fact, issue, and/or risk, which is not directly within the assessment scope, but could generate a separate issue or concern if not addressed. Alternatively, an observation can be a positive acknowledgement of a center/program/project/organization's operational structure, tools, and/or support.
Recommendation	A proposed measurable stakeholder action directly supported by specific finding(s) and/or observation(s) that will correct or mitigate an identified issue or risk.

14.0 Acronyms and Nomenclature

ΔT	Temperature Change
Ω	Ohm
AEC	Automotive Electronics Council
Ag	Silver
Al	Aluminum
Al_2O_3	Aluminum Oxide
ANOVA	Analysis of Variance
ATC	Accelerated Thermal Cycle
Au	Gold
B	Boron
Ba	Barium
Be	Beryllium
BGA	Ball Grid Array
bHAST	Biased Highly Accelerated Stress Test
Br	Bromine
BSE	Backscatter Electron
Ca	Calcium
CA	Construction Analysis
Cd	Cadmium
CDF	Cumulative Distribution Function
Ce	Cerium
CF_4	Tetrafluoromethane
Cl	Chlorine
Co	Cobalt
COTS	Commercial Off the Shelf
Cr	Chromium
Cs	Cesium
CTE	Coefficient of Thermal Expansion
CTF	Cycles to Failure
Cu	Copper
$CuSO_4$	Copper Sulfate
DI	Deionized
DNP	Distance to Neutral Point
DPA	Destructive Physical Analysis
DSC	Differential Scanning Calorimetry
EBSD	Electron Backscatter Diffraction
EDS	Energy Dispersive X-ray Spectroscopy
EDX	Energy Dispersive X-ray
EEE	Electrical, Electronic, and Electromechanical

EEPROM	Erasable Programmable Read-Only Memory
EFO	Electronic Flame-Off
EMC	Epoxy Mold Compound
FAB	Free Air Ball
FBGA	Fine-Pitch Ball Grid Array
Fe	Iron
FEA	Finite Element Analysis
FPGA	Field Programmable Gate Array
g	Gram
Ga	Gallium
Ge	Germanium
T_g	Glass Transition Temperature
gf	Gram-force
H_2	Hydrogen
HALT	Highly Accelerated Life Cycle
HASL	Hot Air Solder Leveling
HAST	Highly Accelerated Stress Test
HAZ	Heat-Affected Zone
HCF	High Cycle Fatigue
Hf	Hafnium
HNO_3	Nitric Acid
hr	Hour
HRTEM	High-Resolution Transmission Electron Microscopy
ILC	Interlaboratory Comparison
IMC	Intermetallic Compound
In	Indium
I/O	Input/Output
IR	Infrared
JEDEC	Joint Electron Device Engineering Council
K	Potassium
kgf	Kilogram-force
La	Lanthanum
LAT	Lot Acceptance Testing
LCF	Low Cycle Fatigue
LDO	Low Dropout
LFBGA	Low-Profile FBGA
LQFP	Low-Profile Flat Pack
MEAL	Mission, Environment, Application, and Lifetime
Mg	Magnesium
MIP	Microwave-Induced Plasma

Mo	Molybdenum
MSL	Moisture Sensitivity Level
MTTF	Mean Time to Failure
N_2	Nitrogen
Na	Sodium
NBS	National Bureau of Standards
NEPP	NASA Electronic Parts & Packaging
NESC	NASA Engineering and Safety Center
Ni	Nickel
nm	Nanometer
NSWC	Naval Surface Warfare Center
Op Amp	Operational Amplifier
Pb	Lead
PCB	Printed Circuit Board
PCC	Palladium-Coated Copper
Pd	Palladium
PEM	Plastic Encapsulated Microcircuit
PEVAL	Post-Exposure Evaluation
Pt	Platinum
PWB	Printed Wiring Board
PWM	Pulse Width Modulation
QFN	Quad Flat No-Lead
QFP	Quad Flat Pack
Rb	Rubidium
RH	Relative Humidity
RIE	Reactive Ion Etcher
SAM	Scanning Acoustic Microscopy
SEM	Scanning Electron Microscopy
Sb	Antimony
Si	Silicon
SMT	Surface Mount Technology
Sn	Tin
H_2SO_4	Sulfuric Acid
SOD	Small Outline Diode
SOIC	Small Outline Integrated Circuit
SOT	Small Outline Transistor
Sr	Strontium
Ta	Tantalum
TC	Thermal Cycle
TEM	Transmission Electron Microscopy

TGA	Thermogravimetric Analysis
Ti	Titanium
Tl	Thallium
TQFP	Thin Quad Flat Pack
TVS	Transient Voltage Suppressor
V	Volt
VSSOP	Very-Thin Shrink Small-Outline Package
W	Tungsten
XPS	X-ray Photoelectron Spectroscopy
XRF	X-ray Fluorescence
Y	Yttrium
Zn	Zinc
Zr	Zirconium

15.0 References

1. NPR 8705.4A, Risk Classification for NASA Payloads. April 29, 2021.
2. Phase II, Recommendations on the Use of Commercial-Off-The-Shelf (COTS) Electrical, Electronic, and Electromechanical (EEE) Parts for NASA Missions. NESC-RP-19-01490, November 2022.
3. Guidelines for Verification Strategies to Minimize Risk Based on Mission Environment, Application, and Lifetime (MEAL). NESC-RP-16-01117, April 5, 2018.
4. U.S. Department of Defense Test Method Standard Microcircuits (MIL-STD-883L) Method 2011, Bond Strength (Destructive Bond Pull Test), 2021.
5. Joint Electron Device Engineering Council JESD22-B120, Wire Bond Pull Test Methods, 2017.
6. Joint Electron Device Engineering Council JESD22-B116B, Wire Bond Shear Test Method, 2017.
7. https://www.raypcb.com/types-of-wire-bonding/.
8. https://orbray.com/en/product/jewel/product/capillary.html.
9. https://accelonix.nl/bond-testing-pull-test-shear-test-and-more/.
10. Automotive Electronics Council, AEC Q006, Qualification Requirements for Components Using Copper (Cu) Wire Interconnections, Rev. A, July 1, 2016.
11. NIST Engineering Statistics website, https://www.itl.nist.gov/div898/handbook/eda/section3/eda353.htm.
12. Thomas J. Quirk, Excel 2019 for Engineering Statistics, A Guide to Solving Practical Problems, Second Edition, Springer Nature, Switzerland AG 2016, 2020.
13. Yang, H.; Cao, K.; Lu, J.; et al. (2019) “Effects of Pd Surface Coating on the Strength and Fracture Behavior of Cu Micro Bonding Wires,” Metall Mater Trans A 50, 3013–3018.
14. Su, P. et al. (2011) “An Evaluation of Effects of Molding Compound Properties on Reliability of Cu Wire Components,” IEEE 61st ECTC, Lake Buena Vista, FL, pp. 363-369, doi: 10.1109/ECTC.2011.5898539.

15. Rongen, R.; O'Halloran, G.M.; Mavinkurve, A.; Goumans, L.; and Farrugia, M-L. (2014) "Lifetime Prediction of Cu-Al Wire Bonded Contacts for Different Mould Compounds," IEEE 64th ECTC, Orlando, FL, pp. 411-418.
16. Lall, Pradeep; Deshpande, Shantanu; Nguyen, Luu (2018). "Comparison of Reliability of Copper, Gold, Silver, and PCC Wirebonds Under Sustained Operation at 200c." Proceedings of SMTA International, Rosemont, IL.
17. Molotnikov, A.; Lapovok, R.; Davies, C.H.J.; Cao, W.; and Estrin, Y. (2008) Scripta Mater. 59, p. 1182.
18. Miyazaki, S.; Shibata, K.; and Fujita, H. (1979) Acta Metall. 27, p. 855.
19. Janssen, P.J.M.; de Keijser, Th.H.; and Geers, M.G.D. (2006) Mater. Sci. Eng. A 419, p. 238.
20. Keller, C.; Hug, E.; and Chateigner, D. (2009) Mater. Sci. Eng. A 500, p. 207.
21. Yang, B.; Motz, C.; Grosinger, W.; Dehm, G. (2010) "Cyclic Loading Behavior of Micro-Sized Polycrystalline Copper Wires," Procedia Engineering, Volume 2, Issue 1, pp. 925-930.
22. Hou, Y.; Mi, X.; Xie, H.; Zhang, W.; Huang, G.; Peng, L.; Feng, X.; Yang, Z. (2020) Size Effect on Mechanical Properties and Deformation Behavior of Pure Copper Wires Considering Free Surface Grains. Materials (Basel), 13(20):4563.
23. Chauhan, Preeti and Choubey; Anupam and Zhong, Z.; Pecht, Michael (2013) Copper Wire Bonding. 10.1007/978-1-4614-5761-9.
24. Batdorf, S. B., and Ghaffarian, Reza. "Size Effect and Strength Variability of Unidirectional Composites," International Journal of Fracture 26.2 (1984), pp.113-123. https://apps.dtic.mil/sti/pdfs/ADA134171.pdf.
25. Ono, Kanji. "A Simple Estimation Method of Weibull Modulus and Verification with Strength Data." Applied Sciences 9, no. 8 (2019), p. 1575.
26. Abernethy, Robert, The New Weibull Handbook, Fifth Edition. "Reliability and Statistical Analysis for Predicting Life, Safety, Supportability, Risk, Cost and Warranty Claims." November 1, 2006.
27. Reliability Analytics ToolKit, https://reliabilityanalyticstoolkit.appspot.com/.
28. Pedigo, Aaron, "Construction Analysis of Plastic Encapsulated Microcircuits Containing Copper Bond Wire," June 2018, NEPP ETW 2018, https://nepp.nasa.gov/workshops/etw2018/talks/18JUNE18/1500%20-%20Pedigo%20-%20NEPP%20Workshop%20-%20Dr.%20Pedigo.pdf.
29. Ghaffarian, Reza. (2022) NASA Guidelines for Ball Grid Array (BGA) and Die-Size BGA (DSBGA) Selection and Application. NASA Electronic Parts and Packaging (NEPP) Program, Office of Safety and Mission Assurance.

Appendices

A. Background

B. Experimental Test Plan

C. Test Results

Appendix A. Background

A.1 Wire Materials Processing

Fabrication of wire for bonding applications (illustrated in Figure A.1-1) involves the use of high-purity raw material, composition optimization (e.g., doping or low alloying), casting, drawing, and annealing. Together, these processing steps are used to optimize wire properties for the desired application. Physical properties for a selection of materials used for bonding wires are summarized in Tables A.1-1 [ref. 1] and A.1-2 [ref. 2]. Although drawing and alloying can be used to optimize microstructure and the resultant properties, this methodology is limited with respect to the attainable control of mechanical properties. Wire manufacturers often consider chemical composition optimization to be the most important tool used to tailor mechanical and electrical characteristics of bonding wires [ref. 3].

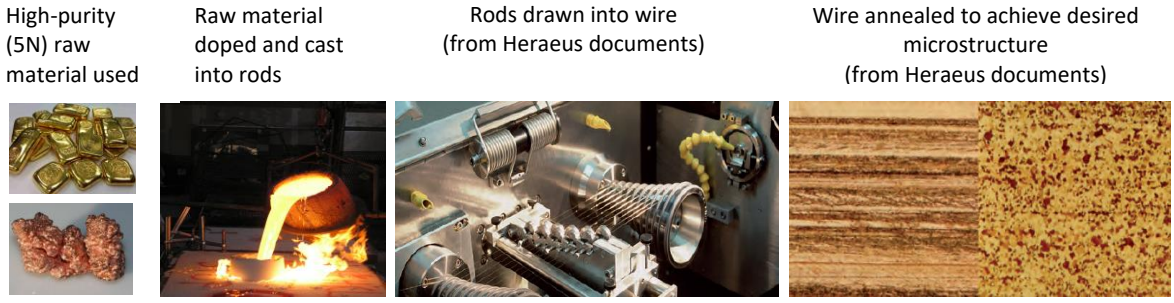

Figure A.1-1. Wire Fabrication Process

Table A.1-1. Physical Characteristics for Simulations

	Unit	Gold	Copper	Aluminum	Silver	Palladium	Platinum
Atomic symbol		Au	Cu	Al	Ag	Pd	Pt
Atomic number		79	29	13	47	46	78
Atomic weight		196.97	63.55	26.98	107.87	106.42	195.08
Crystal structure		FCC	FCC	FCC	FCC	FCC	FCC
Lattice constant	Å	4.0785	3.6147	4.0496	4.0862	3.8907	3.924
Melting point	K	1336.15	1356.45±0.1	933.25	1233.95	1825.15	2042.15±1
Boiling point	K	2983	2855	2750±50	2423±20	3150±100	4100±100
Density (20 ℃)	g/cm^3	19.32	8.92	2.70	10.50	12.02 (22 ℃)	21.45
Resistivity (20 ℃)	μΩ·cm	2.3	1.694	2.7	1.63	10.8	10.58
Heat of fusion	kJ/mol	12.37	13.1	8.40±0.16	11±0.5	16.7	19.7
Thermal conductivity (0～100 ℃)	W/m K	315.5	397	238	425	75.2	73.4
Specific heat (0～100 ℃)	J/kg·K	130	386.0	917	234	247	134.4
CTE (0～100 ℃)	x 10^{-6}·/K	14.1	17.0	23.5	19.1	11.0	9.0
Young's modulus	Gpa	88.3 (300K)	136 (298K)	69 (300K)	100.5 (300K)	121 (293K)	169.9 (293K)
Shear modulus	Gpa	29.6		26.0	31.3		
Poisson's ratio		0.440	0.343	0.345	0.367	0.393	0.377

Table A.1-2. Bulk Material Properties of Pure Materials

Properties	Units	Au	Cu	Al
Melting Point	°C	1063	1083	658
Density	g/cm^3	19.3	8.9	2.7
Lattice Constant (@20 °C)	10^{-10} m (Å)	4.079	3.615	4.049
Lattice Structure		FCC	FCC	FCC
Specific Heat (@20 °C)	J/g K	0.126	0.386	0.900
Thermal Conductance	kW/m^2 K	31.1	39.4	22.2
CTE	ppm/K	14.2	16.5	23.1
Electrical Resistivity (@20 °C)	10^{-8} Ω m	2.2	1.7	2.7
Electrical Conductivity (@20 °C)	10^7 / Ω m	4.55	5.88	3.65
Vickers Hardness	MN/m^2	216	369	167
Youngs Modulus	Gpa	78	130	70
Modulus of Elasticity	Gpa	79	123	71
Tensile Strength	N/mm^2	120 – 220	210 – 370	100 – 200

High-purity, unalloyed Au wire demonstrates excellent chemical inertness, plasticity, and softness, but its limited mechanical strength and microstructural instability can cause problems with respect to the formation of reliable, reproducible bonds. As a result, manufacturers began doping with beryllium (Be) and other alkali, alkaline earth, and rare earth elements, including potassium (K), Be, magnesium (Mg), calcium (Ca), barium (Ba), lanthanum (La), cerium (Ce), zirconium (Zr), gallium (Ga), indium (In), germanium (Ge), lead (Pb), Cu, Ag, platinum (Pt), palladium (Pd), and boron (B). Table A.1-3 illustrates the impact of various doping elements on the recrystallization temperature of Au bond wires [ref. 4]. Doping element concentrations can range from about 10 to 100 ppm. Due to the increase in strength and higher thermal stability, these doped wires are used for more difficult loop geometries. Most recently, manufacturers of Au wires began providing low-alloyed Au bonding wires with 1% to 5% alloying elements. The most important alloying elements are precious metals (Ag, Pd, Pt) but they can also include non-precious metals such as Cu, titanium (Ti), Zr, iron (Fe), nickel (Ni), cobalt (Co) or others. Through alloying, manufacturers are able to obtain significant increases in strength, enabling more difficult bonding geometries and mechanical stability for small-diameter wires. Additionally, they provide improved thermal stability. For alloying elements with high solubility in Au, mechanical improvements are often achieved via solid solution strengthening; however, the greatest increase in strength is obtained by elements with low solubility that form grain pinning IMCs along grain boundaries. The amount of alloying elements is restricted mainly by increased electrical resistivity, non-conforming ball geometries, increased oxidation during FAB formation, and decreased corrosion stability in the long-term application. More highly strengthened materials usually show a higher hardness, which might become a problem during the bonding process because good ball deformation and an appropriate soft ball are necessary to create a stable bond joint without damaging the substrate material. Figure A.1-2 shows the impact of doping and alloying on the tensile strength and elongation of Au wire [ref. 3].

Table A.1-3. Dependence on Dopant Species of Recrystallization Temperature of Au Wire

Purity of Au	99.999%	99.995%			
Dopant species		Ag, Pd, Pt	Mg, Ni, Si	Co, Cu, Fe, Ga, Ge, In	Al, Be, Ca, Pb, Sn, Ti
Recrystallization temperature*, °C	150	150	150–200	200–300	Over 300

**Degree of cold work is fixed at 99%. Temperatures quoted are those measured for continuous annealing through a ring-type furnace.*

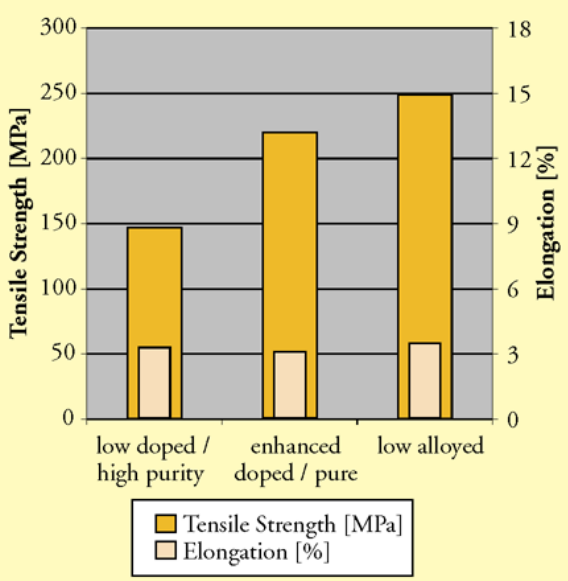

Figure A.1-2. Tensile Strength and Elongation as a Function of Doping Level of Au Wire

Although Au and Al wires typically use 2N to 4N purities (99 to 99.99%), Cu wire bonding generally uses only 4N. Dopants can be added to improve loop capabilities, reliability, bondability, and corrosion resistance. For Cu wire, dopants like Ag, Ni, Pd, Au, Pt, and chromium (Cr), can be used to improve the corrosion behavior of the base alloy. The impact of these alloying elements is greatest for higher concentration levels of 2N Cu wire alloys. However, increasing the alloying elements to this degree can increase the strength and impact bonding parameters. Various patents report the benefits of different concentration levels of dopants and low alloying elements to high-purity Cu wires. Elements were reported to improve bondability and reliability (Be, iron (Fe), zinc (Zn), Zr, Ag, tin (Sn), vanadium <2000 ppm, and B, sodium (Na), Mg, Al, Si, Ca, K, V, Ga, Ge, rubidium (Rb), strontium (Sr), yttrium (Y), molybdenum (Mo), cadmium (Cd), cesium (Cs), Ba, hafnium (Hf), tantalum (Ta), thallium (Tl), and tungsten (W) <1000 ppm), reduce ball hardness and work hardening (B, Be, Ca, and Ge with <0.5ppm S), achieve bondability equal to Au (Cr<25 ppm+Zr<9 ppm+Ag<9 ppm+Sn<9 ppm) and improve corrosion resistance while maintaining low ball hardness (Ni and Co<100 ppm and Ti, Cr, Mn, Fe, Ni, Zr, Nb, Pd, Ag, In, and Sn<150 ppm), reduce crack formation within the HAZ (400 ppm of Mg and traces of Fe and Ag), and improve storage life (La <0.002 wt %, Ce<0.003 wt %, and Ca<0.004 wt % added to 4NCu) [ref. 5]. The main disadvantages of doping are slight increases in cost and resistivity of the wire (5-15%) [ref. 6]. Eto describes an improvement in the corrosion resistance of PCC wire, specifically with respect to halide induced interface corrosion and pitting corrosion at the wedge bond under high temperature storage life

testing, through proprietary compositional modification in EX1R wire. This is achieved through the formation of a protective passivation layer on the IMC and Cu surface [ref. 7].

Following the wire drawing process, the highly deformed material contains a significant amount of residual stress and exhibits high strength, high hardness, and low ductility as well as an elongated grain structure. Through the application of heat for a specified amount of time, the material is then annealed to achieve a desired combination of strength and ductility. With increasing temperature and time, the microstructure becomes more equiaxed and the grains begin to grow. Concomitantly, residual stress, strength, and hardness are reduced and ductility increases. These changes are shown schematically in Figure A.1-3. As shown in Figure A.1-4, cross-sectioned Au wires often exhibit a fine, potentially elongated grain structure while Cu wires exhibit larger, more equiaxed grains [ref. 8]. This indicates that the Cu wires have been annealed at a higher relative temperature or a longer time at temperature to achieve greater ductility and lower relative strength and hardness when compared to the final drawn material. The combined impact of composition and microstructure result in a wide range of properties for commercially available Au and Cu bonding wires. Figure A.1-5 illustrates the relative impact of microstructure and doping for Au wires on mechanical properties by showing the drop in strength and increase in ductility with time and temperature for three levels of doping [ref. 3]. Maximum and minimum break loads and ultimate tensile strengths obtained from manufacturer specification sheets are respectively summarized in Figures A.1-6 and A.1-7 as a function of wire diameter. For each wire type, the first character refers to the manufacturer (H: Hereaus and T: Tanaka). Following are the product name, data point level (H: high/maximum, L: low/ minimum), and wire material (Au, Cu). For the 883 curve, values provided by the reference table are shown as data points, with the exception of the lowest and highest values, which were used to obtain an approximate third-order polynomial curve fit (883L). Based on this plot, one can see that the range of break loads for Cu and Au wires overlap significantly, PCC wires exhibit the highest strengths, and the general trend of wire strength as a function of diameter does not appear to follow the same trend as MIL-STD-883, 2011.10, minimum bond pull limits curve.

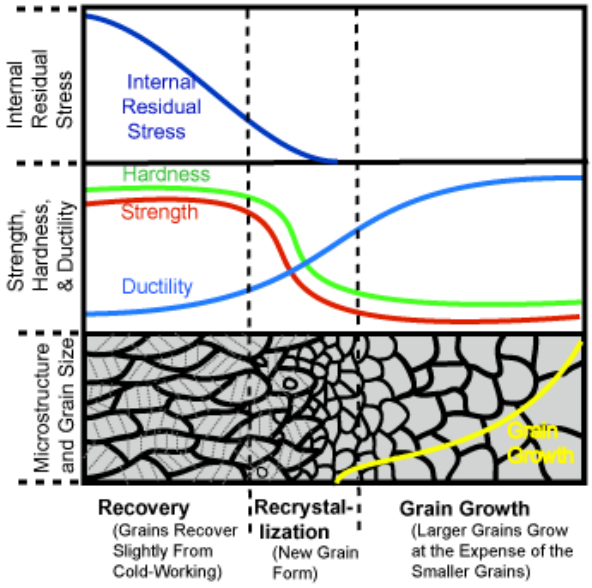

Figure A.1-3. Schematic of Annealing Process

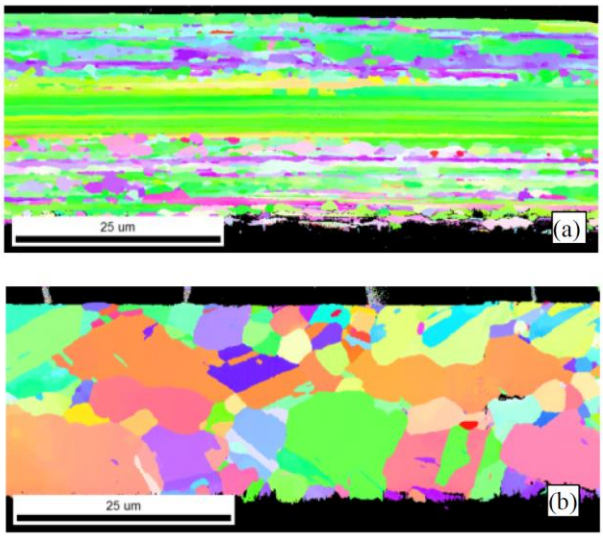

Figure A.1-4. EBSD Images of Longitudinal (a) Au and (b) Cu Bond Wire Cross-Sections
Fatigue Lifetime Modeling of Cu and Au Fine Wires

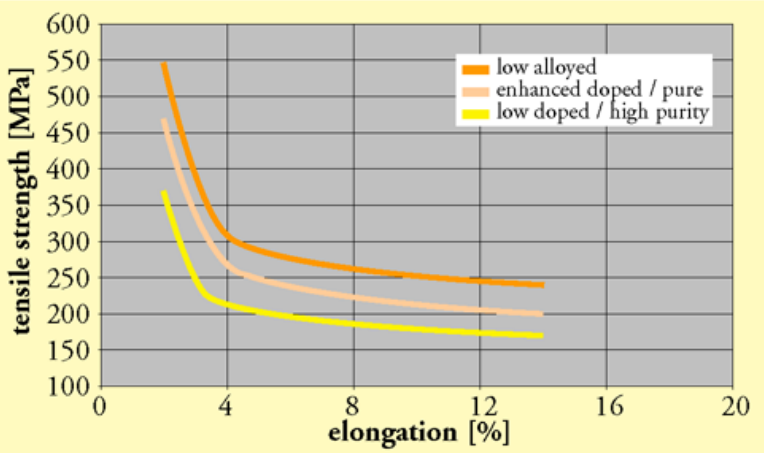

Figure A.1-5. Strength-Elongation Diagram of Au Bonding Wires.
The strength elongation curves represent microstructural states generated by a cold working process and annealing treatment. The high-strength/low-elongation ratio relates to the hard-drawn wire state; the low-strength/high-elongation ratio describes the recrystallized condition.

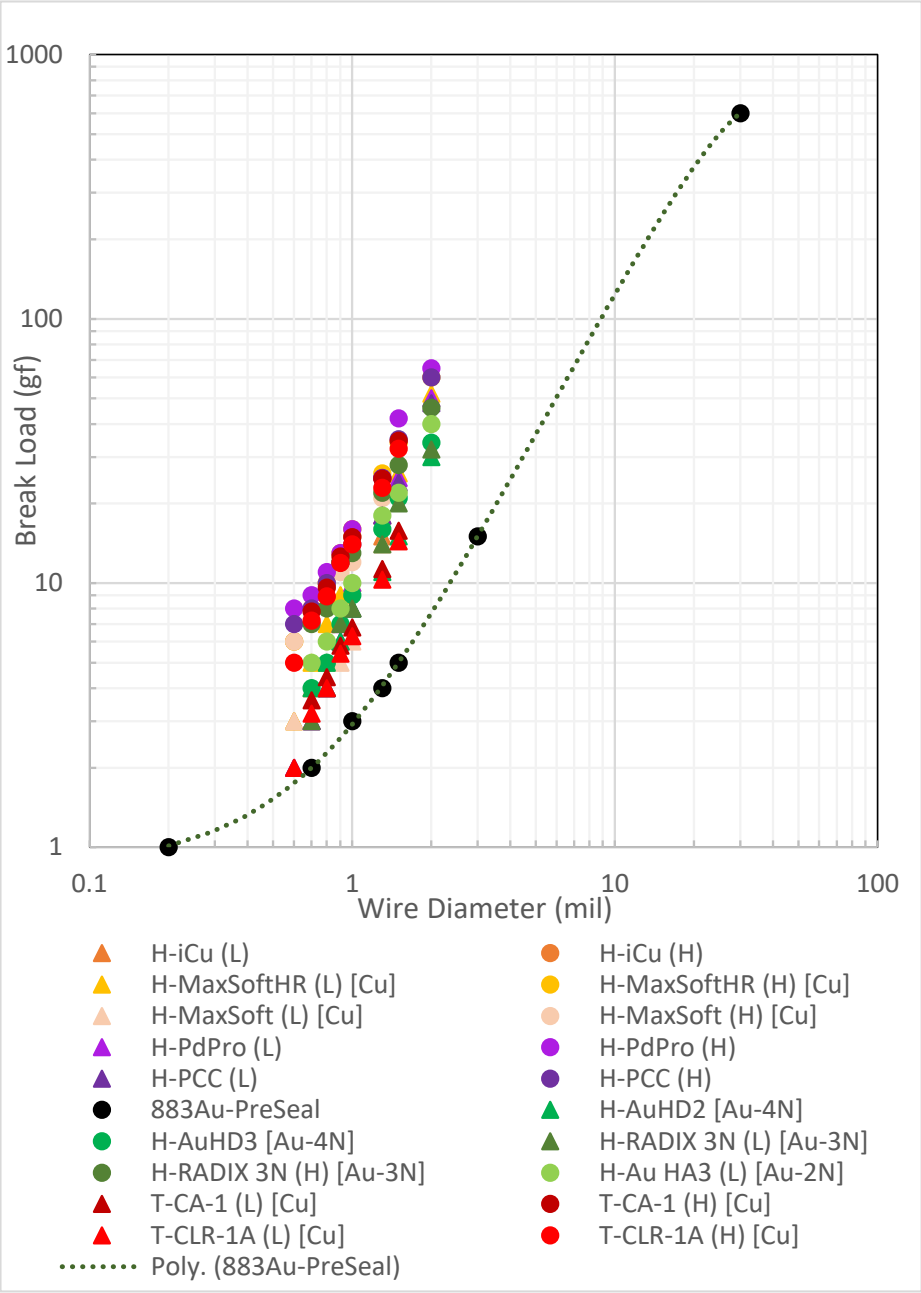

Figure A.1-6. Break Load as Function of Wire Diameter for Commercial Cu and Au Wires. Data obtained from Heraeus and Tanaka wire specification sheets.

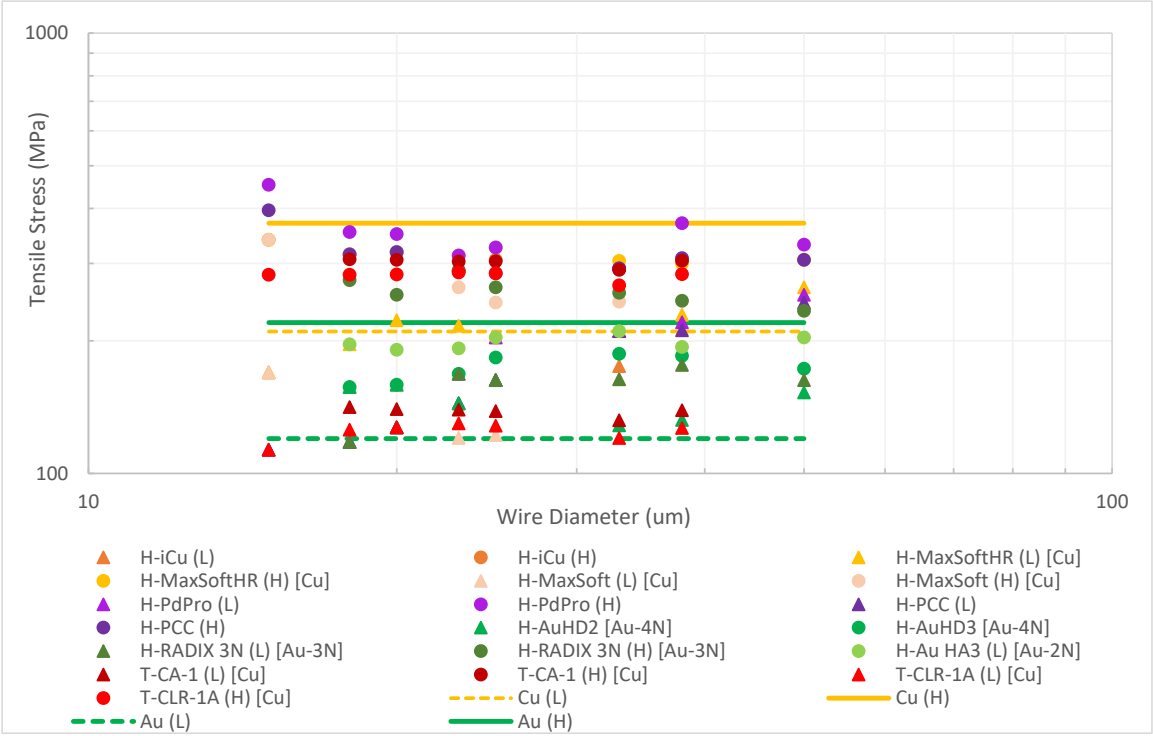

Figure A.1-7. Ultimate Tensile Strength as Function of Wire Diameter for Commercially Available Cu and Au Wires. Data obtained from Heraeus and Tanaka wire specification sheets.

A.1.1 Wire Diameter Effects

As mentioned previously, wire microstructure (grain size, shape, and orientation) influences wire mechanical behavior. It is well known that many metals exhibit an increase in yield strength with decreasing grain size due to the buildup of dislocations at grain boundaries. This phenomenon is commonly described using the Hall-Petch relationship:

$$\sigma_y = \sigma_0 + kd^{-0.5}$$

where σ_y is yield stress, d is average grain size, σ_0 is the stress required to move individual dislocations, and k the Hall-Petch slope [refs. 9, 10]. For bulk Cu, σ_0 is about 25MPa and k about 110MPa $\mu m^{-0.5}$ [Yang, 2012]. For surface grains in polycrystalline samples, however, the dislocations are only partially blocked by grain boundaries, with a portion of the dislocations able to reach the surface without impingement. This phenomenon is shown schematically in Figure A.1-8 [ref. 11].

A description of surface grains is provided in Figure A.1-9 [ref. 11]. The ratio of surface grains (r) can be described in terms of the wire diameter (D) and specimen grain size (d), where r = D/d. Various studies have evaluated the impact of specimen size on the strength of materials due to the difference in relative surface grains, where a decrease in flow stress with decreasing r was observed for Cu, Al, and Ni, below a critical value [refs. 12–15].

Three recent studies have investigated the impact of r on the strength of fine Cu wires [refs. 11, 16, 17]. Hou et al evaluated 50-500 μm wires that were annealed at different temperatures to obtain multiple grain sizes in the range of 5-55 μm. The results of tensile tests performed for this investigation are summarized in Figure A.1-10 [ref. 17]. It can be seen that wire strength

decreases with decreasing specimen size for constant grain size, and this effect is greater for larger grain sizes. Yang et al evaluated the tensile properties of polycrystalline 25, 30, and 50 μm diameter Cu wires that were annealed at temperatures from 200 °C to 900 °C to achieve an r of 1.1 to 15.6. The researchers developed and validated a composite model for this behavior and determined that yield stresses were significantly influenced by grain size and specimen thickness for r = D/d<10. Yield stress within this regime continued to drop with decreasing r (for polycrystalline samples). In a separate study, Yang investigated Cu wires annealed at 400 °C to achieve a grain size of 10 μm and selectively electropolished (with sulfuric acid) to achieve specimen sizes of 5 to 38 μm. The wires were then cyclically loaded with increasing applied stress amplitude after reaching a saturation state in plastic strain. Thicker wires were observed to exhibit smaller plastic strain at saturation and smaller creep strain compared with thinner wires. The stress strain curves shown in Figure A.1-11(a) indicate a decrease in plastic flow stress with decreasing wire thickness, and this behavior is more significant at higher plastic strains.

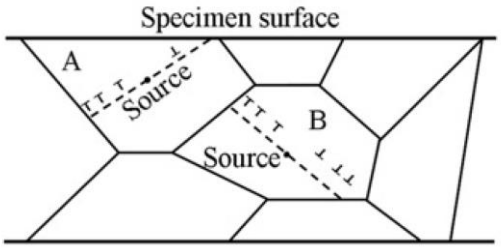

Figure A.1-8. Schematic Drawing of Dislocation Movement in Grain Intersected by Specimen Surface (A) and Inner Grain (B). In grain A, dislocations become only partly blocked by grain boundaries while other dislocations can reach the surface without impinging on a grain boundary.

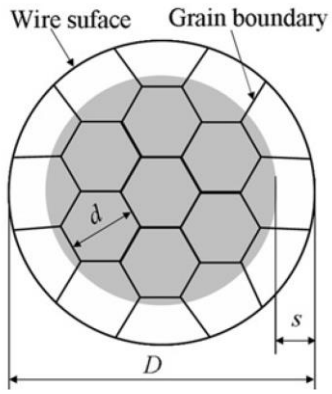

Figure A.1-9. Schematic Cross-Section of Micro-Sized Wire of Diameter D and Average Grain Size d Divided Into Two Parts: Specimen Interior (grey) and Near-Surface Zone (white) with Thickness s.

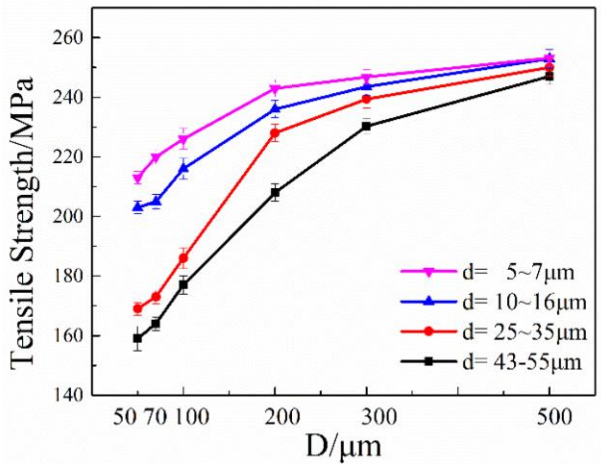

Figure A.1-10. Tensile Strength of Specimens with Different Specimen and Grain Sizes (wire diameter: 50-500 μm, grain size: 6.5-50 μm)

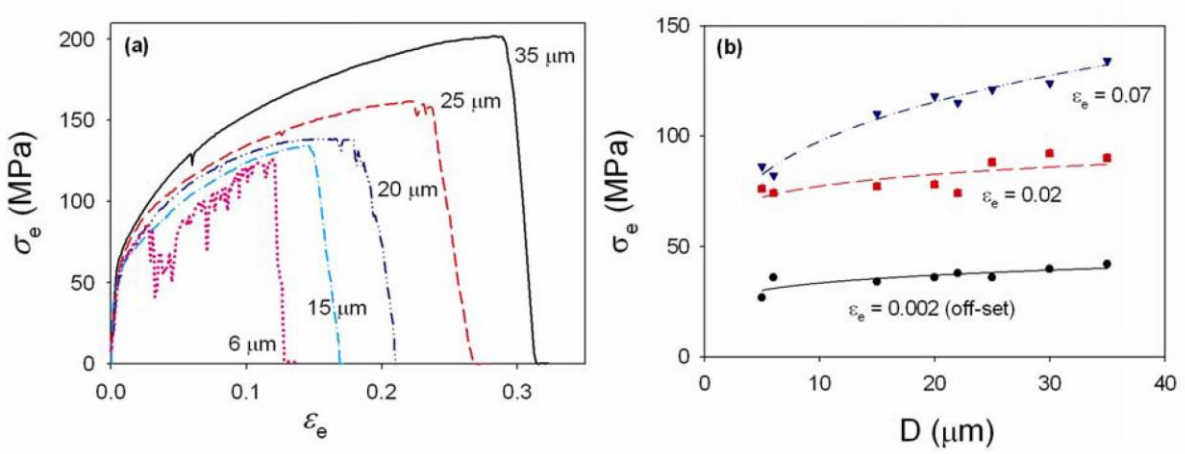

Figure A.1-11. (a) Selected Engineering Stress-Strain Curves; (b) Yield Stress and Flow Stress at Plastic Strains of 2% and 7% as Function of Wire Thickness D. A decrease in the flow stress with decreasing wire thickness can be observed, and this effect is enhanced at higher plastic strains.

Yang et al investigated the tensile behavior of 19 μm Cu wires and 22 μm PCC wires with 300 nm nanocrystalline (150 nm) Pd coatings following annealing at 200 °C to 600 °C for 60 minutes [ref. 18]. Researchers found the strength of the PCC wire to exceed that of the Cu wire and compared these results with those expected using the rule of mixtures ($\sigma_y = V_{Cu}\sigma_{y\text{-}Cu} + V_{Pd}\sigma_{y\text{-}Pd}$), where V is the volume of each phase and s is the yield strength of the corresponding element. Researchers found that the level of strengthening was greater than expected using the rule of mixtures, as shown in Figure A.1-12, and postulated that the Pd layer serves to inhibit dislocation flow for the outer grain layers, thereby counteracting the aforementioned specimen size effect with respect to fine wire samples.

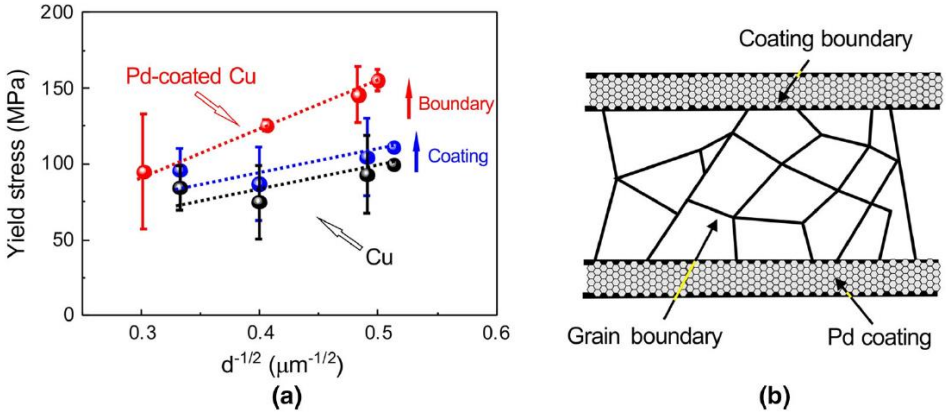

Figure A.1-12. (a) Coating and Boundary Improvement on Yield Stress; Blue Line Represents Calculated Yield Stress by Mixture Rule; (b) Illustration of Coating Boundary Effect on Hall-Petch Relation. "Boundary and "Coating" arrows in (a) represent yield stress improvement resulting from coating boundaries mechanism and mixture rule.

A.1.2 Wire Bonding Process

Wire bonds can be categorized by bond type (wedge-wedge or ball-stitch), bond technique (ultrasonic, thermocompression, or thermosonic), and materials of construction. Table A.1-4 provides an overview of wedge and ball bond types, including a description of the processes,

critical characteristics, bond techniques, and a selection of bond parameters. Representative ball bonds and wedge bonds are provided in Figure A.1-13.[1] The technology of most interest for the implementation of Cu wire bond technology is thermosonic ball bonding. The schematics in Figures A.1-14 and A.1-15 [ref. 18] illustrate the steps in the ball bonding process and details of ball bond formation. As seen in Table A.1-4, a major difference between ball and wedge bonding is the form of the primary bond. Ball bond formation begins with the creation of a symmetrical, spherical ball of precise dimensions, called a free air ball (FAB), at the end of a fine wire. This can be accomplished through a process called electronic flame-off (EFO), which involves placing an EFO wand below a length of wire and applying a high voltage to create a plasma that melts the wire. The FAB size and shape are determined by the surface tension of the molten wire material and the length of time power is applied to the plasma, as well as the propensity for wire oxidation. A combination of pressure, heat, and/or ultrasonic energy is used to form a bond between the wire and the device bond pad. The properties of the wire, device bond pad, and process parameters all influence bond quality.

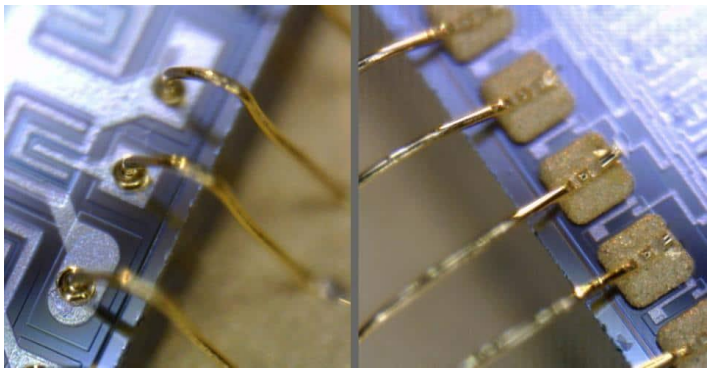

Figure A.1-13. Photographs of Chip Pad Wire Bonds Using Ball Bonding (left) and Wedge Bonding (right)

[1] https://www.raypcb.com/types-of-wire-bonding/

Table A.1-4. Comparison of Wire Bond Types

Bond Type	Wedge Bonding		Ball Bonding	
Tool	**Wedge tool**		**Capillary tool**	
Process Steps	• The bond pad (most often on the IC) is located, and the tool is positioned above this location. • Pressure and energy (and heat) are applied to form the first wedge bond. • The tool is raised and the loop is formed as the tool moves to the second bond location. • Pressure and energy (and heat) are applied to form second wedge bond • Wire is broken at heel of bond when wire clamp behind the tool closes and pulls on wire. • The tool is raised; a length of wire is exposed for the next bond.		• Free air ball (FAB) is formed. • Wire is retracted so the FAB is against the capillary. • Bond pad (most often on IC) is located; tool is positioned above this location. • Pressure and ultrasonic energy and/or heat are applied to form ball bond. • Loop is formed as tool is raised and moved above the second bond location. • Pressure and ultrasonic energy (and/or heat) are applied to form stitch bond. • The wire is broken at the stitch bond when a wire clamp above the tool pulls and breaks the wire free. • Length of wire is exposed for next bond.	
Bond Height	Low		Higher	
Bond Direction	X-Y orientation required (single direction)		All direction bonding from ball bond	
Bonding techniques	Ultrasonic	Thermosonic	Thermocompression	**Thermosonic**
Temperature	Room Temperature	120-220 ℃	Up to 300 ℃	**120-220 ℃**
Ultrasonic Power	Yes	Yes	No	**Yes**
Wire Diameter /Ribbon Size	Wide range of sizes	Wide range of sizes	< 75 μm	**< 75 μm**
Pad Size	2-3x wire ϕ or 1.2x ribbon width	2-3x wire ϕ or 1.2x ribbon width	3-5x wire ϕ	**3-5x wire ϕ**
Bonding Force	Low	Low	High	**Low**
Bonding Time	Short	Short	Long	**Short**
Wire/Ribbon Material	Au, Al	Au	Au	**Au, Cu**
Contamination Susceptibility	Medium	Medium	High	**Medium**
Cratering Susceptibility	High	Medium	Low	**Medium**

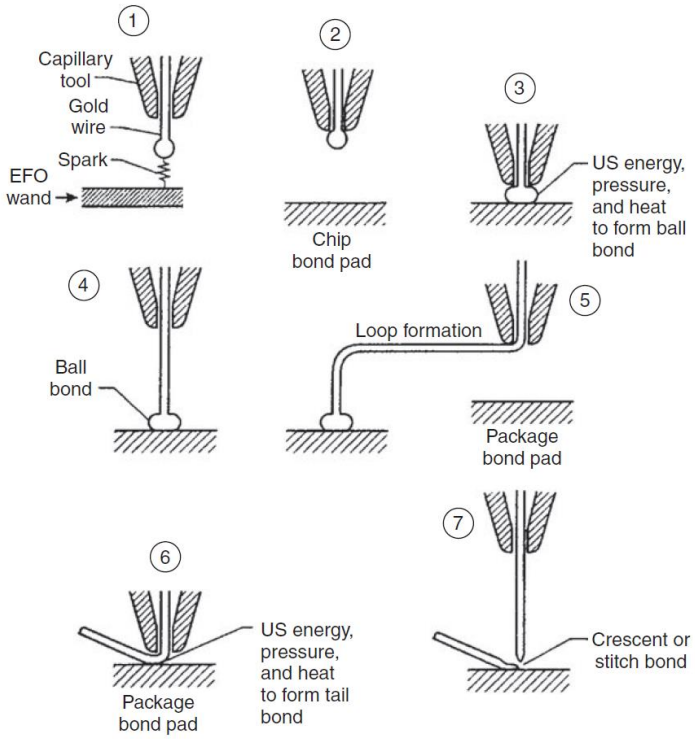

Figure A.1-14. Simplified Procedure for Ball-Stitch Wire Interconnection with Capillary Tool. (1) Au wire is fed through the capillary, and an EFO spark melts the wire. An Au ball forms at the end of the wire. (The ball typically consumes about a 300 μm length of a 25 μm diameter wire, but less for fine-pitch bonding.) (2) The wire is retracted so the ball is positioned against the bottom of the capillary. (3) The tool is lowered to the bond pad, and the Au ball is pressed against it. The interface rises to the bonding temperature (from the heated work holder), ultrasonic energy is applied, and the ball bond is formed. (4) The tool is raised, leaving the ball welded to the surface, and forming the wire loop as it moves toward the second bond position. (5) The bond pad is positioned beneath the bonding tool (or capillary). (6) The tool is lowered, as in step 3, to make a bond. This bond (and any subsequent bonds made before the wire is broken off) is called a stitch bond. Sometimes the final bond is called the crescent bond because of its shape. (7) After the stitch bond is made, the capillary tool is raised and a wire clamp above the capillary tool (not shown) pulls and breaks the wire free. The tool rises up, the clamp lowers the wire sufficiently to allow another bond to be made, and the bonder is ready to repeat the bonding cycle.

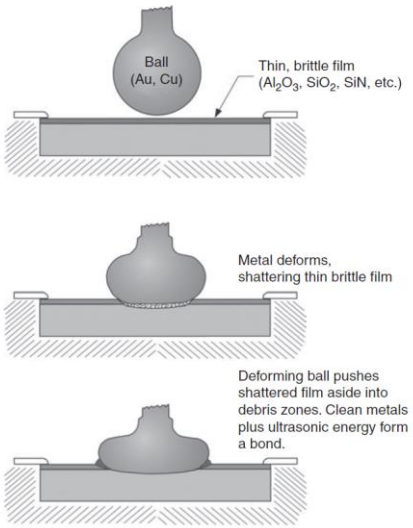

Figure A.1-15. Bonding Force and Ultrasonic Energy Break Through Thin Surface-Oxide-Films, Push Them Aside, and Form Weld

As mentioned previously, the EFO process is used to melt the wire and create a spherical ball of specified dimension for bonding. The resulting FAB generally exhibits a large equiaxed grain structure. Figure A.1-16 illustrates the FAB formation process and resulting microstructure as well as providing an optical image showing the microstructure for Au wire following EFO [ref. 19]. The portion of wire near the FAB can experience grain coarsening within the HAZ. The optical micrograph in Figure A.1-17 provides the longitudinal cross-section of an Au wire following EFO [ref. 20]. As shown in Figure A.1-18, the length of this HAZ can be modified through alloying or doping of the Au wire [ref. 3]. Figure A.1-19(a) provides a cross-sectional image for a Cu bond wire and FAB. For both images, the FAB coarse grain structure, HAZ grain growth region, and original wire microstructure can be seen. The impact of the EFO process and resulting microstructural changes on the hardness of the Cu wire is provided in Figure A.1-19(b) [ref. 21]. Maximum and minimum FAB, HAZ, and wire Vickers hardness data obtained from a selection of bond wire specification sheets is provided in Figure A.1-20. As seen in this plot, high-strength wires that rely on compositional and microstructural (fine-grain) strengthening tend to exhibit a more significant change in hardness during EFO processing and high-temperature exposure.

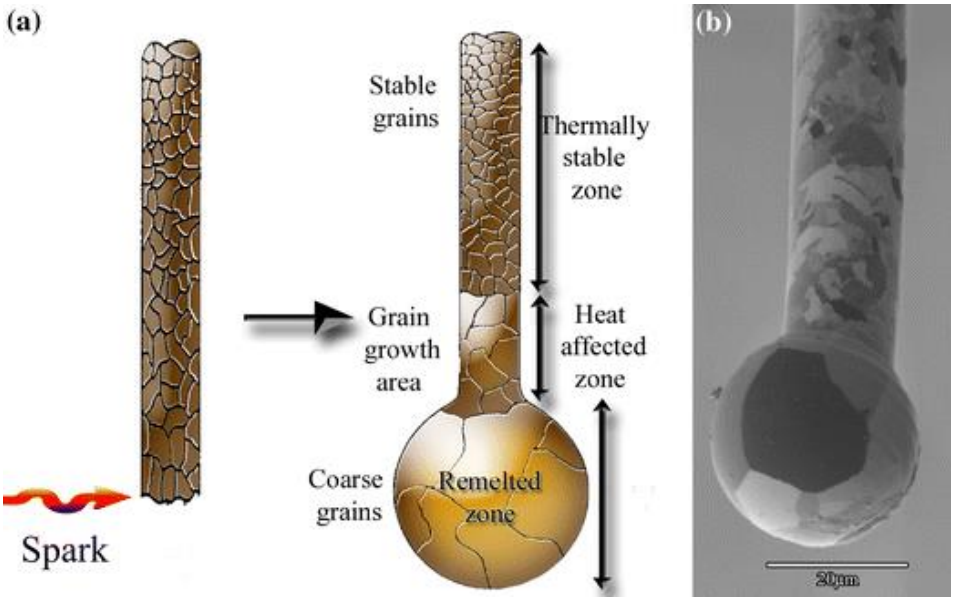

Figure A.1-16. Illustration of EFO Process and Resulting Microstructure (a) and Photograph of Au FAB and Wire, Showing Resulting Grain Structure (b)

Figure A.1-17. Micrograph of 2N Au Wire Cross-Section, Showing FAB, HAZ, and Wire Grain Structure

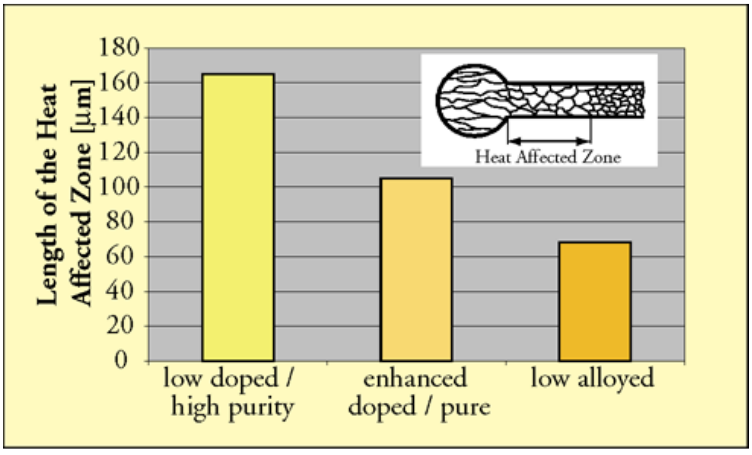

Figure A.1-18. Length of HAZ as Function of Doping Level of Au Wire

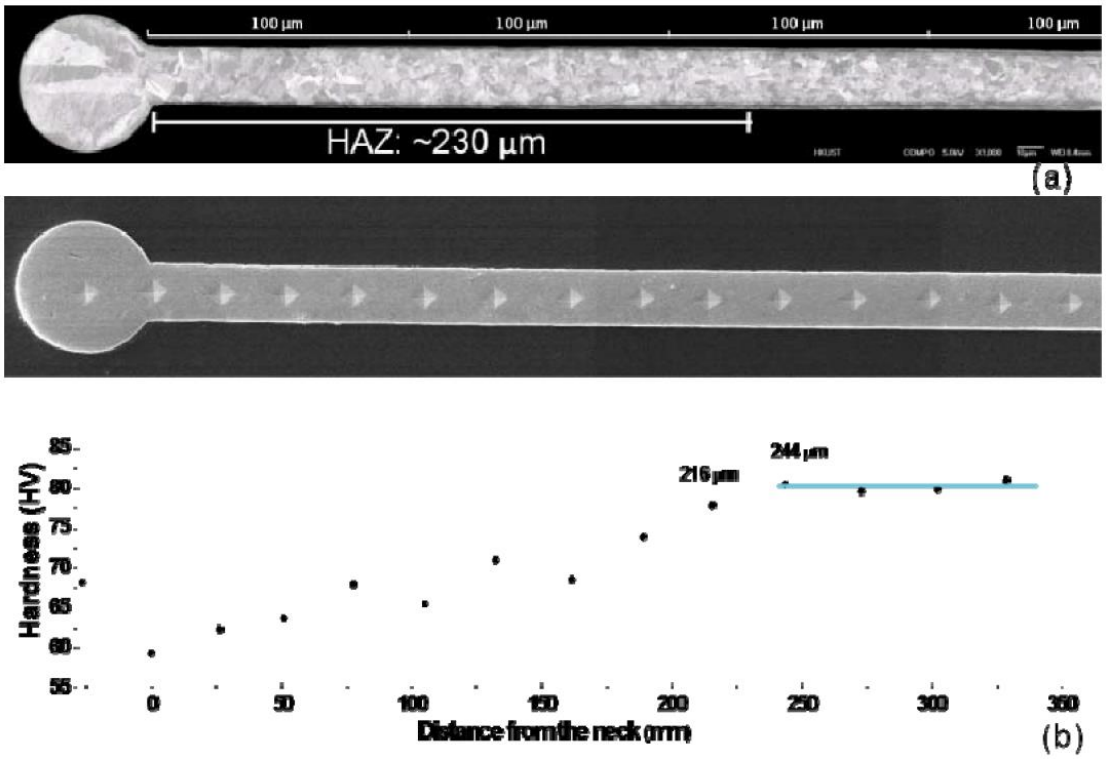

Figure A.1-19. Grain Microstructure of Cu Wire (4N 23µm) from Kulicke & Soffa (a) and its Microhardness Result (b). HAZ Length Based on Results of Microhardness.

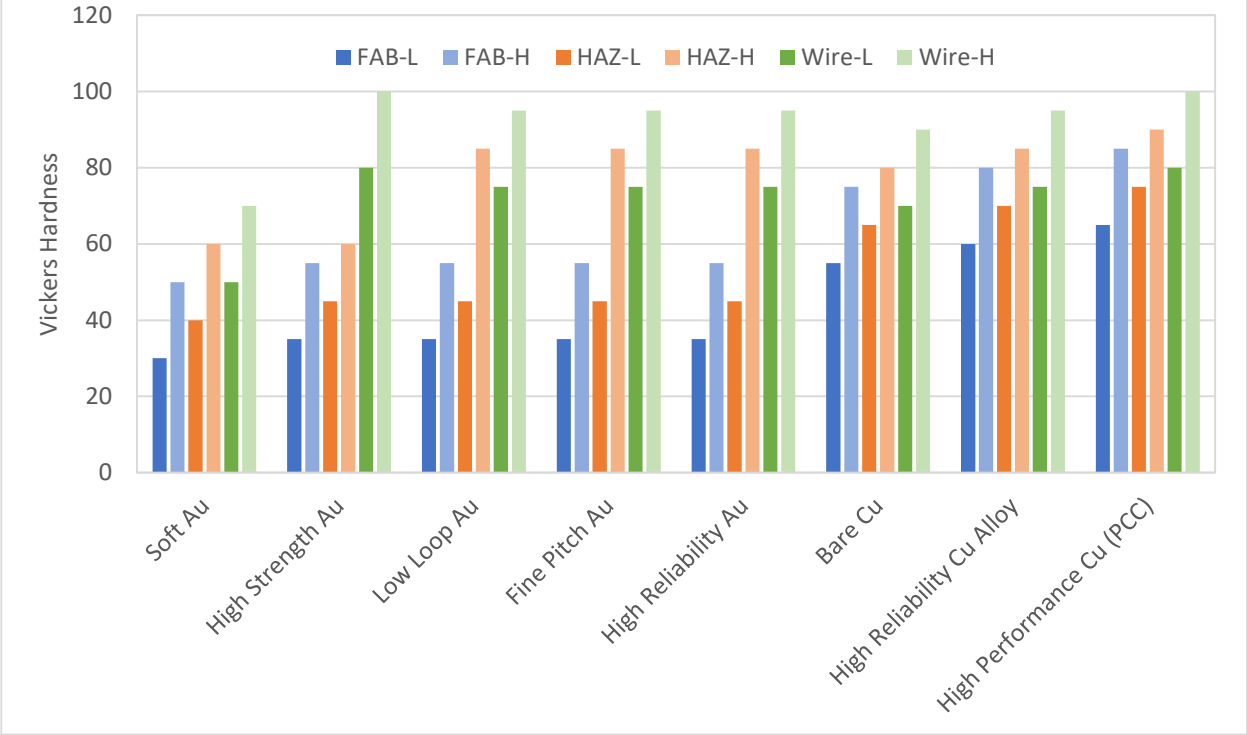

Figure A.1-20. Upper (H) and Lower (L) Limit Vickers Hardness Values for Commercially Available Au and Cu Bond Wires. Data from Tanaka specification sheets.

Due to the inert nature of Au wire, the EFO process and FAB formation can take place in air. This is not the case for Cu. Oxidation of Cu not only reduces the shelf life of Cu wire (1 week from package opening), but it also has a significant impact on FAB formation and the EFO hardware used in Cu wire bonders. Reliable ball bonding requires the formation of oxide-free, spherical FABs with predictable dimensions. Oxidation of molten Cu during EFO impacts all of these parameters and significantly affects the quality of resulting bonds. This issue represented one of the early technical hurdles for the implementation of Cu wire bonding, and it was ultimately addressed by adding a cover gas sheath to capillary tools on traditional ball bonders. Cover gas compositions include N_2 and forming gas (N_2 + H_2). Additionally, coatings such as Pd and Pd/Au have been applied to Cu wires to further limit the amount of oxidation during EFO and to reduce corrosion of the wire during use [ref. 22].

Achieving the desired FAB dimensions and HAZ length requires extensive EFO process optimization, including power, distance (between wand and wire), time, and cover gas flow rate for different wire diameters and compositions (such as Pd plating thickness). To achieve a softer FAB, a larger grain size is desired. This can be achieved with a higher heat flux (EFO current + firing time). Longer firing time can increase the HAZ length and therefore the height of the vertical wire above the ball bond. Increasing the EFO current can yield a soft FAB and shorter HAZ but can result in FABs that are not concentric with the wire. Flow gas selection can impact the shape and level of oxidation on the FAB. Oxidation can occur with low flow rates due to insufficient inert gas, and high flow rates can result in oxidation due to the transition to turbulent flow. At lower than optimal flow rates, partial oxidation can occur, yielding distorted FAB shape. Higher than optimal cover gas flow rates can also result in convective cooling of the FAB and the formation of pointed FAB. The use of forming gas can help limit oxidation and provide additional heat. It can also help reduce the required firing time to achieve the desired FAB dimensions. For PdCu wire, EFO current settings can impact the distribution of Pd within the Cu wire and influence the hardness of the resulting FAB. Lim et al. found a thin uniform Pd-rich layer along the periphery of the FAB with low EFO current, concentration of Pd at the neck for medium current and both at the neck and within the FAB for high current. The low EFO current FAB with the continuous Pd layer exhibited a 7% increase in FAB hardness when compared with the high EFO current FAB. Although this did not negatively affect reliability in this study, it could be a concern for more sensitive pad structures [ref. 23]. The optical images in Figure A.1-21 show FAB cross-sections for each of the firing conditions, and Figure A.1-22 shows an energy backscatter diffraction (EBSD) image of the PCC FAB produced with a low EFO current and forming gas. More recent work performed by the same author found that a smaller process window was observed for bonds with Pd at the interface for the researchers' bond configuration. FABs processed with a high EFO current and exhibiting a non-uniform distribution of Pd produced more bond lifts than the aforementioned joints with a uniform Pd layer at the periphery [ref. 24].

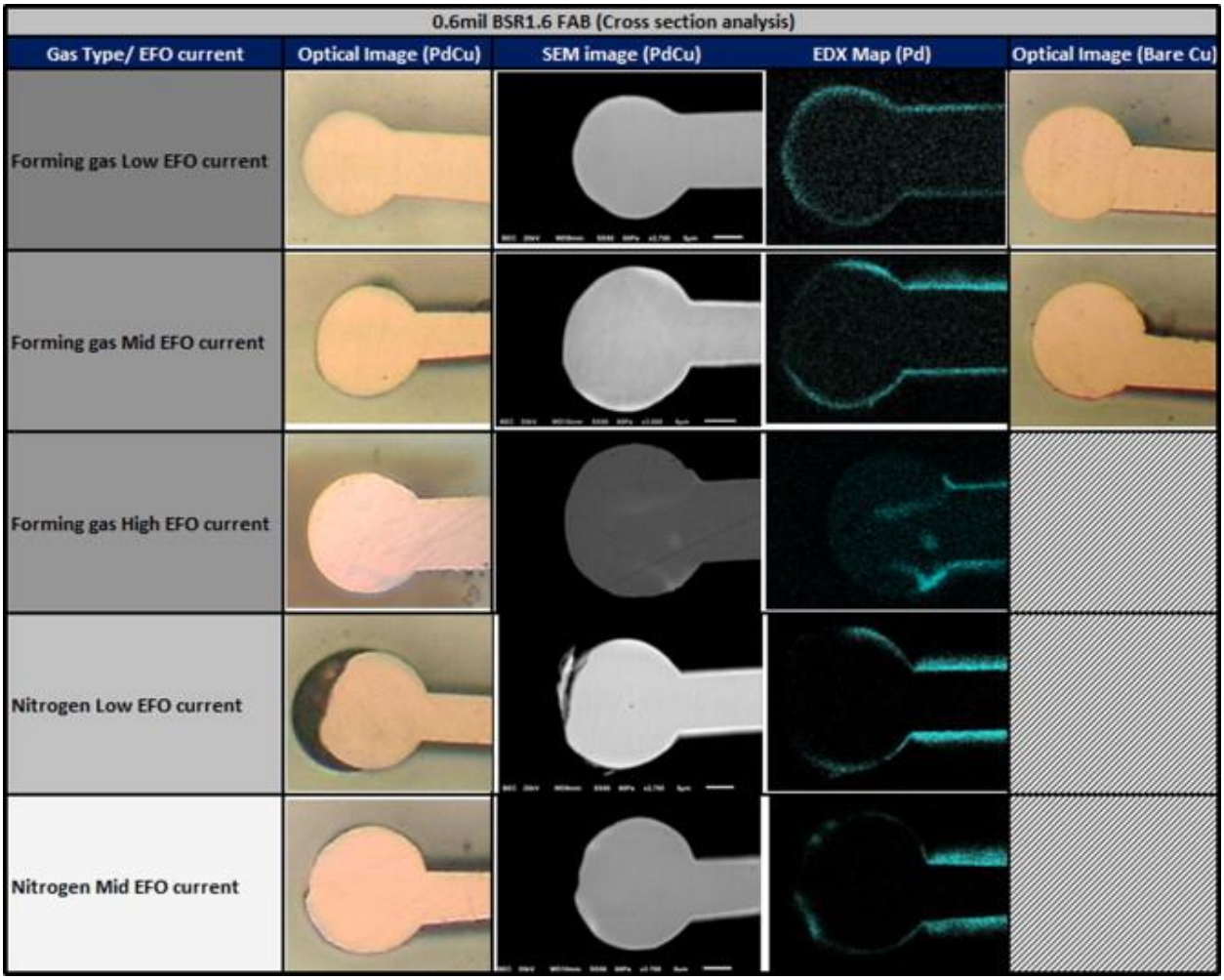

Figure A.1-21. FAB Cross-Sections for PdCu and Bare Cu Wires

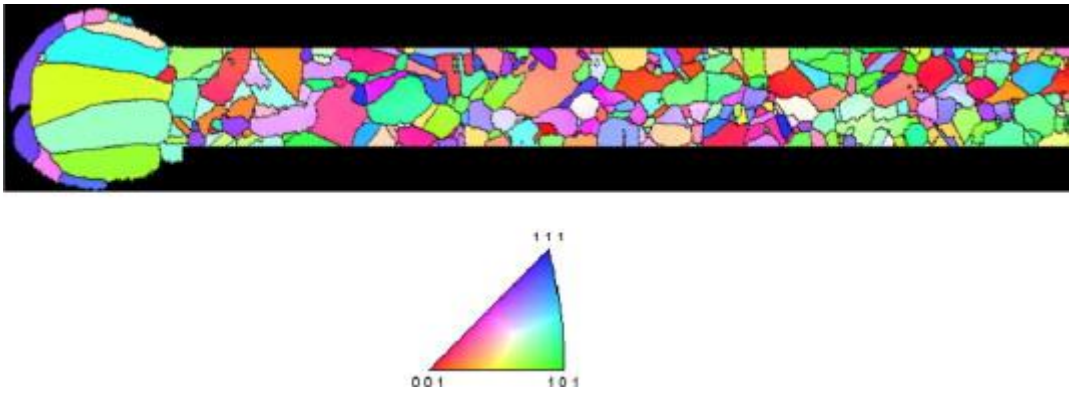

Figure A.1-22. EBSD Image of PdCu Wire at Low EFO Current in Forming Gas

As discussed previously, FAB formation is followed by bonding of the ball to the die bond pad using pressure (bond force/unit area) combined with heat and/or ultrasonic energy. Ultrasonic and thermosonic bonding are solid-state joining methods that use an ultrasonic energy source in the bonding tool to apply oscillating shears between the FAB surface and bond pad to produce a metallurgical bond. This process creates significant plastic deformation and metal turbulent flow across the interface, as well as generating heat. Oxide present on the bond pad surface is broken

and displaced by this plastic deformation and flow of metal at the bond interface. This severe local plastic deformation is believed to create the metallurgical bond via atomic forces within the areas of contact [ref. 21]. Therefore, ultrasonic and thermosonic bonding takes place in monometallic and multimetallic joints. Once bonding parameters are optimized, a bond is formed that exceeds the wire strength. Through the bonding process, IMCs begin to form at the interface due to the heat generated in the process combined with the additional applied heat. Figure A.1-23 provides a photograph of a cross-sectioned Au wire and ball bond, showing the bond, FAB, HAZ, and wire microstructure following bonding [ref. 3]. During bonding, ultrasonic coupling between the bond wire and the bond pad requires sufficient bond force and power applied to the tool, but not so much that the pressure limits tool movement or damages the bond pad. This combination of downward force and ultrasonic power (with applied heat) must be optimized to achieve a reliable bond. These parameters will rely heavily on the mechanical behavior of the wire material.

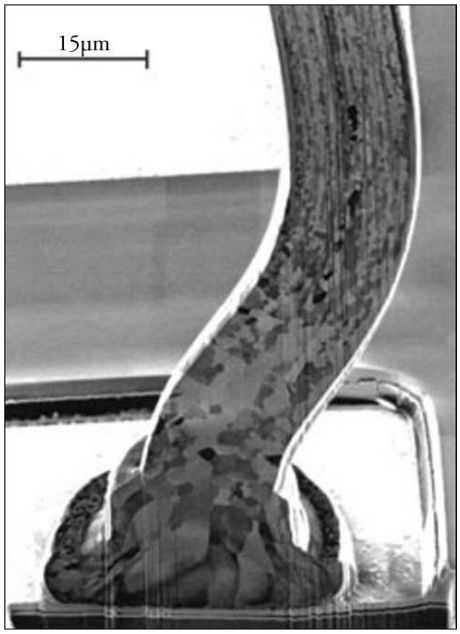

Figure A.1-23. Bonded Low Alloyed Au Wire Showing Ball Bond with Deformed Ball and HAZ.

Cu generally has a higher strength, a higher modulus of elasticity or stiffness (i.e., applied stress required to deform the material within the elastic regime), a greater degree of strain hardening (i.e., stress required to continue to deform the material once plastic deformation has begun), and a higher hardness (i.e., stress required for plastic surface deformation) than high-purity Au. Strain hardening, defined as an increase in strength with increasing plastic deformation, occurs due to the buildup of dislocations within the material and inhibition of further dislocation flow. If no strain hardening were to occur, there would be perfect plasticity or yielding. The stress strain diagram in Figure A.1-24 illustrates the difference between perfect plasticity and strain hardening [ref. 25]. Figure A.1-25 provides stress strain curves for the Cu and Au wires shown in Figure A.1-4 (initial state) and their annealed counterparts [ref. 8]. This figure clearly indicates a significantly greater increase of strength for Cu wire than for Au wire. The impact of this phenomenon for the wire-bonding process is that a higher bonding load is required to initiate deformation of the Cu FAB, and this continues to increase due to the application of load and ultrasonic energy. As a result of the higher bonding load requirements and stiffness of the Cu

wire, the bond pad Al can be displaced, referred to as Al splash. In addition, the Si and circuitry below the bond pad can be damaged, resulting in bond pad cratering. Figure A.1-26 shows an SEM image of a Cu bond with significant Al splash [ref. 26]. Manufacturers have addressed this issue by limiting the strength of the baseline Cu wire, increasing the thickness of the Al bond pad, and modifying the integrated circuit design to limit the placement of sensitive circuitry under the bond pad. If insufficient bonding force is applied, no bond will be formed and the ball will lift off the bond pad with minimal applied force. Figure A.1-27 illustrates the resulting narrow process window for Cu-Al bonds [ref. 22]. Doping and alloying of the wire can influence the resulting process window, as shown in Figure A.1-28 [ref. 27].

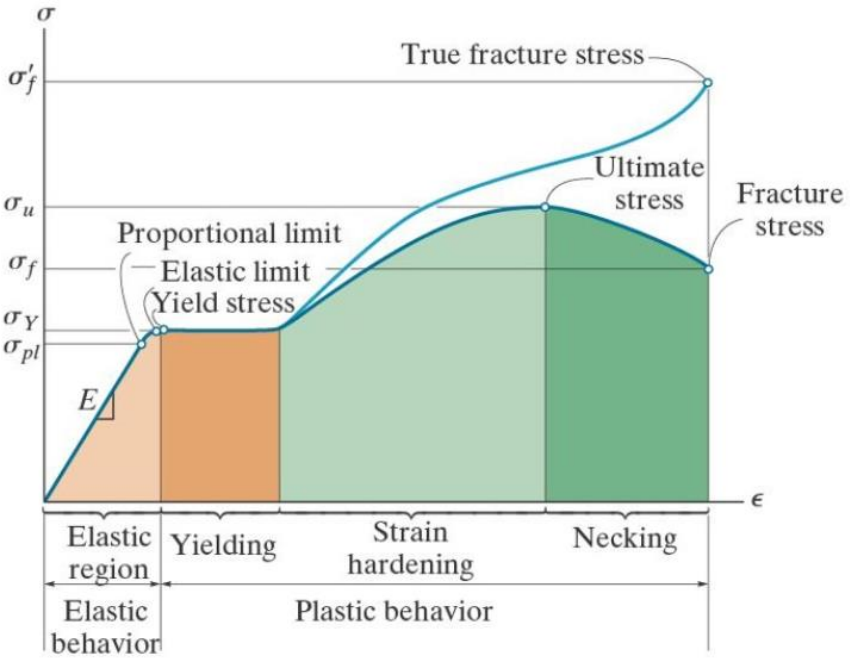

Figure A.1-24. Conventional and True Stress-Strain Diagram for Ductile Material (Steel) (Not to Scale), Illustrating Difference Between Various Deformation Regions

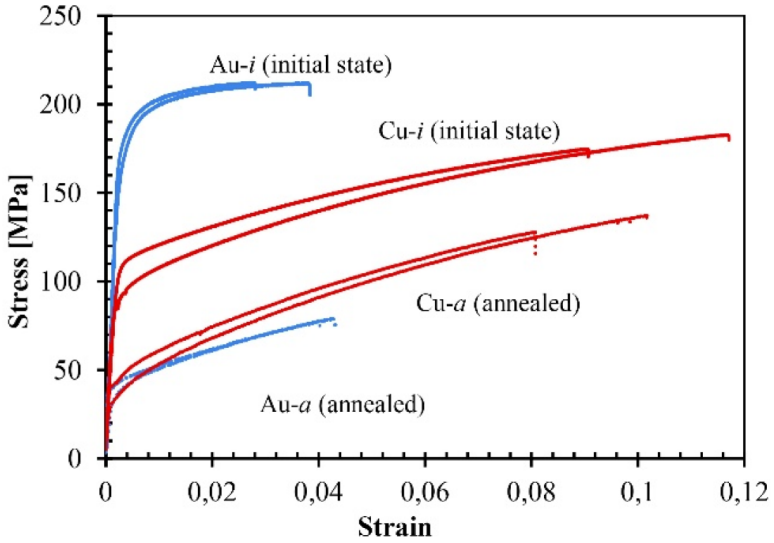

Figure A.1-25. Stress-Strain Behavior of Cu and Au Wires Before and After Annealing

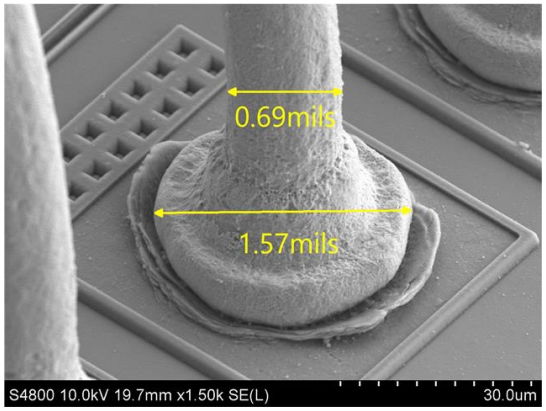

Figure A.1-26. SEM image of a Cu bond with significant Al splash

IMC coverage	Too low	Acceptable	Too high
Al splash	Acceptable		Too high
Crack	No crack		Crack
Pull test failure	Ball lift	OK	Pad peel

Narrow window

Figure A.1-27. Process Window for Cu Wire Bonding

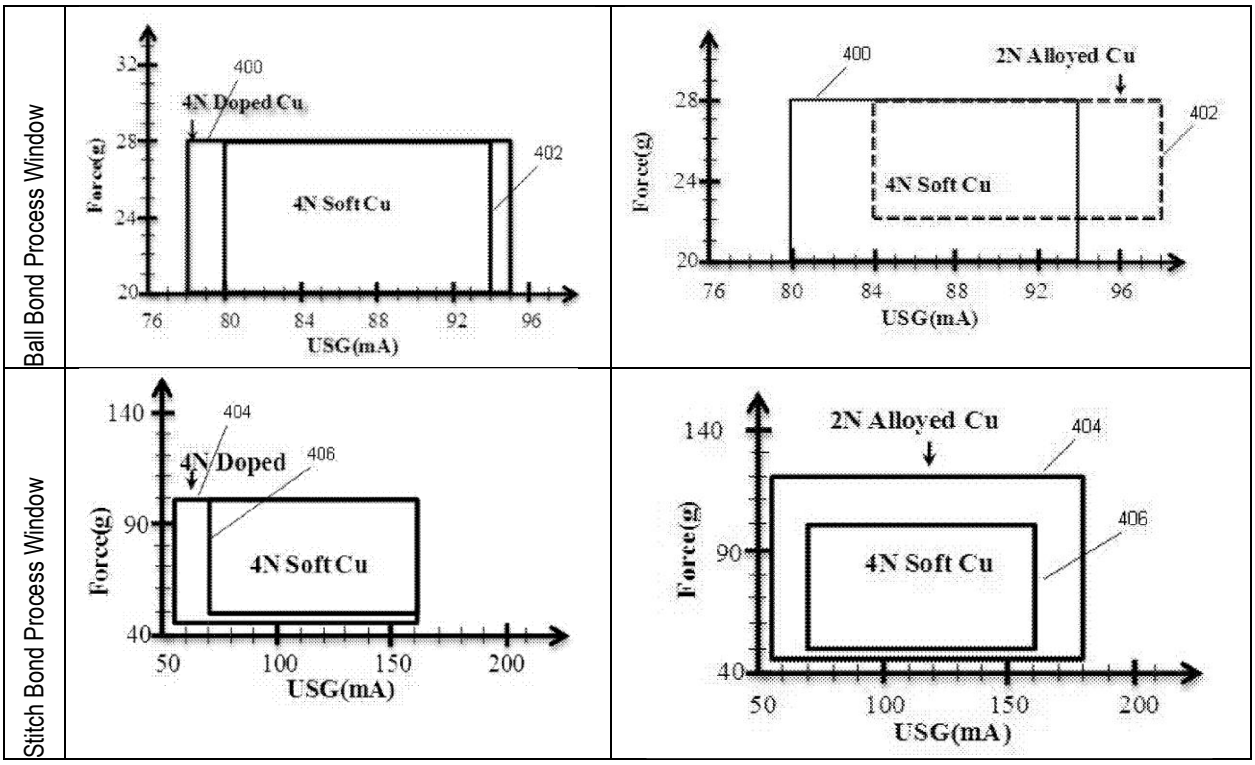

Figure A.1-28. Plots Showing Influence of Composition on Ball Bond and Stitch Bond Process Windows for 4N Doped Cu and 2N Alloyed Cu, Compared with Those of 4N Soft Cu.

A.1.3 High Wire Count

Demand for increased I/O count, reduced package size, and greater performance has resulted in a dramatic increase in fine and ultra-fine pitch wire-bonded components. Unfortunately, fine and ultra-fine pitch wire bonds exhibit more reliability issues, including non-stick and pad damage. Reduced part size and increased wire count produce multiple manufacturing challenges, requiring wires with reduced diameters to be bonded with greater accuracy onto smaller pads with a smaller pitch. To achieve this, wires require lower loop height (i.e., shorter HAZ) and increased strength to avoid shorting with nearby wires. Smaller ball sizes are required (Table A.1-5) due to the smaller pad pitch, and this can become problematic [ref. 28]. Stringent bonding parameter optimization is required, including ultra-fine tool height control to minimize damage to the bond pad and underlying circuitry. The use of lower parameter settings to avoid damage can result in non-stick on pad, and higher settings to improve bonding can result in pad peeling or cratering. This is further exacerbated by the fact that these devices may have more delicate structures for fine-pitch devices, especially for low-K device bonding. Also, pad damage following probing can cause further problems, including bond lifts and non-stick on pad, since a smaller ball is being bonded onto a smaller damaged area. In addition to ball bond challenges, significant issues can arise with stitch bonding for fine wire diameters, since the least scrubbing action is encountered at the tail bond location. Non-sticking on lead, wire opens, or low stitch pull readings can result from poor bondability on leadframes, plating thickness variation, surface roughness or hardness. Further, the required reduction in capillary tip diameter size means the second bond size is reduced. The primary challenge for fine-pitch wire bonds for aligned and staggered pads are, respectively, achieving bond strength stability at reduced ball sizes and forming low and high looping profiles without shorting [ref. 29].

Table A.1-5. Reductions in Bond Pad Pitch, Wire Size, and Ball Size

Bond pad pitch (μm)	70	60	50	45	40
Reduction in bond pad pitch (%)	0	14	29	36	43
Reduction in wire size (%)	0	0–10	10–20	20	30
Reduction in ball size (%)	0	13	31	38	46

Due to the aforementioned issues, high wire count, fine, and ultra-fine pitch bonding has a narrower processing window. Wire bonder requirements for fine-pitch, high I/O count wire bonding include increased bonding speed, Z-resolution, bond placement accuracy, FAB consistency, and improved looping algorithms, as well as requiring a significant capillary tip diameter reduction to avoid interference between adjacent bonds. This translates to ±1.5 μm bond placement accuracy (3σ), advanced Z-axis control (contact detection resolution of 0.4 μm), a dual-frequency ultrasonic transducer for optimal bonding performance, and optimal transducer and bonding-tool geometry to achieve a reliable 30 μm bond pad pitch [ref. 28].

As mentioned previously, fine-pitch wire bonding requires smaller wire diameters. For a 40 μm bond pad pitch, an 18μm diameter may be used. This 7μm reduction in size would result in a 51% reduction in strength and 76% reduction in stiffness. Due to higher strength and stiffness, fine Cu wires tends to exhibit greater loop control, reduced sagging, and improved resistance to wire sweep compared with Au wires of the same diameter. Unfortunately, the higher parameter settings required to form reliable bonds can cause damage because a smaller diameter wire is deformed on a weaker pad with a smaller capillary tip than for conventional pads with Au wires. The aforementioned stitch bond issues arise, where higher parameter settings can cause heavy cap marks and wire opens. To address these issues, wire manufacturers have developed soft Cu

wires for diameters less than 1 mil. Additionally, studies have shown that Pd coatings and Au-Pd coatings may help alleviate issues with fine Cu wire stitch bonds.

A.1.4 Mold Compound

Once the wire bonding is complete, epoxy mold compound (EMC) is applied. EMCs provide electronic devices with electrical insulation and a method of mounting a device to a PCB while protecting the device from impact, pressure, moisture, chemicals, heat, and ultraviolet rays. Such compounds are composite materials composed of 70-90% inorganic filler (silica), 5-10% epoxy resin, 5% hardener resin, flame retardant, cure promoter, mold release agent, pigments, catalysts, coupling agent, and additional proprietary elements. Tg, moisture adsorption rate, strength, CTE, thermal conductivity, and adhesive ability must all be optimized for the application.

Fused amorphous silica, which is formed by melting natural silica stone, has wide use in the electronics industry due to its low CTE, high purity, high chemical resistance, and high electrical insulating resistance. High filler loading of silica reduces the CTE, viscosity, and moisture adsorption of EMCs. Parts requiring significant heat dissipation may use higher thermal conductivity filler materials, such as crystalline silica, alumina, or silicon nitride, for greater heat dissipation. Silane coupling agents are often employed to strengthen the interface between the epoxy resin matrix and inorganic elements within the matrix, including fillers, die, passivation, wire bonds, and leadframe. These agents additionally reduce viscosity during molding. Flame retardants are used to satisfy the UL94V-0 flammability rating.

Historically, halogen-based resins, such as brominated epoxy resin, have been used in combination with antimony-based flame retardants. Due to environmental concerns regarding the generation of halogen compounds during combustion, as well as chronic toxicity resulting from antimony, new “green” EMCs have been developed that do not include halogens or antimony. Green EMCs include multi-aromatic resins with a high aromatic carbon ring content and a higher oxygen index that are resistant to combustion [ref. 30]. An alternative EMC patented flame-retardant system includes transition metal oxides, meets environmental requirements, resists cracking at higher processing temperatures, meets process demands, and maintains high molding capabilities [ref. 31].

Transfer molding is the most common process used to encapsulate microcircuits within EMCs. This process is illustrated in Figure A.1-29 [ref. 30]. EMC molding temperatures generally range from 170 to 180 ℃, and times range from 60 to 120 seconds (depending on mold configuration). During the molding process, EMC viscosity must be kept low to flow smoothly, fill the small gaps in the mold die and minimize deformation of bond wires. High EMC fluid viscosity can lead to wire sweep or fracture.

The plot in Figure A.1-30 [ref. 30] illustrates the influence of increasing EMC melt viscosity (i.e., increased plunger pressure) on Au wire deformation. Wire sweep, or the movement of wire loops during the transfer molding process, can result in wires touching and shorting to one another. Industry specifications permit loop displacement of up to 5%, a value too high for fine and ultra-fine pitch devices but normally acceptable for traditional pitch components. Therefore, more rejectable parts will be identified for fine-pitch diameter parts with small diameter wires and high and low bonds [ref. 32]. Based on manufacturer specification sheets and literature, the package is heated to 170–180 ℃ for 2–8 hr to fully cure the EMC and achieve target properties. Significant IMC growth can occur during this time.

Failure of EMCs after processing completion often occurs when parts absorb environmental humidity and are subsequently heated to high temperatures at a high rate (i.e, thermal shock). This vaporizes the moisture and generates internal pressure sufficient to reduce adhesive strength or initiate peeling and subsequent delamination. This issue is further exacerbated by the use of lead-free components that require higher operating temperatures. Higher-strength EMCs created for such applications may be prone to internal cracking when exposed to the previously described conditions. The use of flexible EMCs that are capable of expanding at higher temperatures are a second option. In cases where delamination occurs, subsequent moisture absorption can negatively impact degradation of internal wire bonded joints.

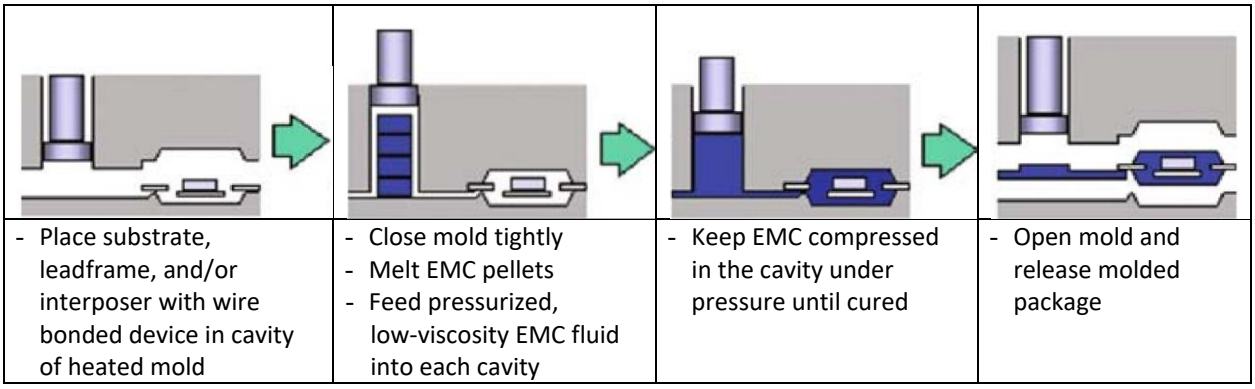

Figure A.1-29. Transfer Molding Process Schematic

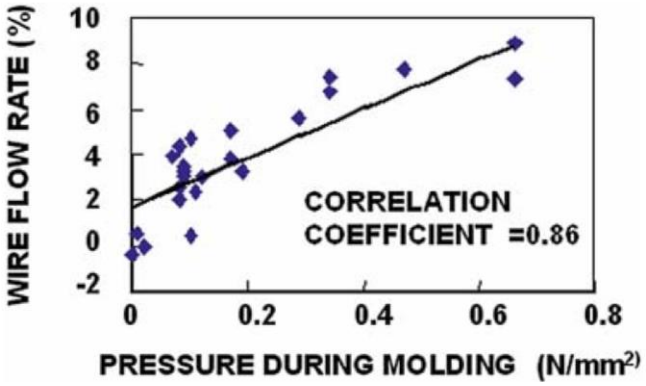

Figure A.1-30. Relationship Between Wire Deformation and Molten EMC Viscosity

A.1.4.1 IMC Formation, Growth, and Reliability

Following is a description of the bond formed at the interface, as well as the long-term reliability of this bond following high temperature exposure. Ultrasonic and thermosonic bonding are solid-state joining methods that use a bonding tool to apply oscillating shears between the FAB surface and bond pad, producing a metallurgical bond. This process creates significant plastic deformation and metal turbulent flow across the interface, as well as generating heat. Oxide on the bond pad surface is broken and displaced by the plastic deformation and flow of metal at the bond interface. This severe local plastic deformation is believed to create the metallurgical bond via atomic forces within the areas of contact [ref. 33]. Therefore, ultrasonic and thermosonic bonding take place in monometallic and multimetallic joints. Through the bonding process, IMCs begin to form at the interface due to the heat generated in the process combined with additional applied heat. A local effective temperature of 465 °C at the bond pad was reported to

occur in Cu-Al wire bond joints as a result of ultrasonic vibration; additionally, alumina fragmentation and a more uniform IMC layer were found to occur with increased bonding time [ref. 34]. Subsequent device heating during molding compound curing, part screening, qualification, and operation will lead to microstructural and phase changes within this layer of IMCs.

Philosfsky's work on intermetallic formation in the Au-Al system was performed on a butt-welded Au-Al diffusion couple at temperatures of 200 °C to 460 °C. Au_4Al, Au_5Al_2 (now known as Au_8Al_3), Au_2Al, AuAl, and $AuAl_2$ all form at sufficiently long annealing times. Significant voiding formed in Au_5Al_2 after extended exposures above 300 °C and in $AuAl_2$ after extended exposure above 400 °C, catastrophically weakening these phases and the joint [ref. 35]. Evaluating the influence of bond pad thickness on reliability of AuAl joints revealed that joint reliability increased when bond pad thickness was less than wire diameter/X and $X \geq 2.5$ [ref. 36]. This would translate to a 1μm Al bond pad for a 1 mil Au wire. The rapid growth of IMCs for Au-Al bonds at elevated temperature has resulted in the well-documented failure mechanism termed "purple plague," which receives its name due to the characteristic color of the $AuAl_2$ intermetallic along with the associated Kirkendall voids.

Originally identified by Smigelskas and Kirkendall in 1947, the Kirkendall Effect describes the voids formed in a diffusion couple as a result of one element diffusing into a second element faster than the second diffuses into the first [ref. 37]. This effect has been observed in multiple alloy systems and generally occurs when the atoms with lower melting points possess higher diffusivities [ref. 38]. The progression of phase formation as summarized by Majni is shown in Figure A.1-31 [ref. 39]. Activation energies for Au-Al IMC layers are summarized in Table A.1-6 [refs. 32, 40]. Structures and properties of each of the Au-Al intermetallics are summarized in Table A.1-7 [refs. 32, 41–43].

Harman describes the classical Au-Al bond failure modes as follows: Characterized by Kirkendall voids around the Au ball bond periphery on an Al bond pad, which restrict the conduction path, the first failure mode exhibits a high resistance and potentially high bond strength. The increase in resistance is initially slow, during initial intermetallic formation, but exhibits a rapid rate increase when Kirkendall voids begin to grow after several thousand hr at 150 °C. The second failure mode is characterized by the formation of voids under the bond (immediately inside the bond perimeter). It exhibits a mechanically weak bond and an increase in resistance. Prior to void formation, the growth of brittle Au-Al IMCs can result in early brittle fracture at the joint when exposed to TC fatigue. Exposure of Au-Al bonds to the high resin curing and post-cure conditions can drive the initial intermetallics completely through some thin Al bond pads. [ref. 32].

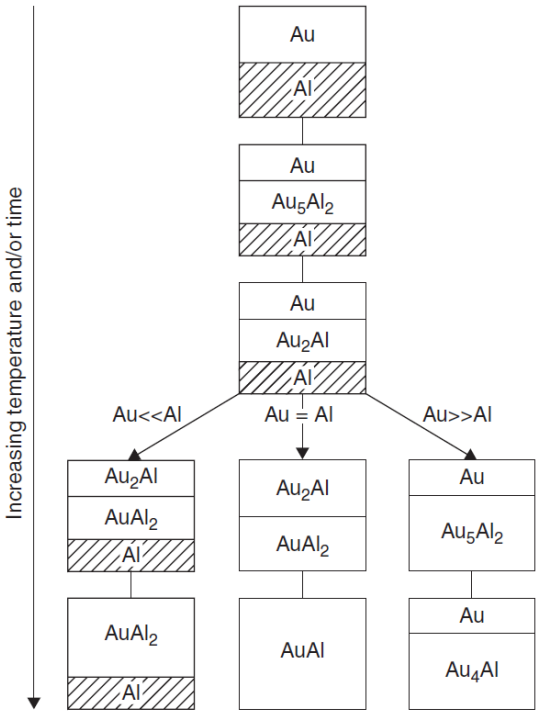

Figure A.1-31. Schematic Representation of Compound Formation in Au-Al Thin-Film Systems. The identity of the final compounds is determined by the annealing temperature and proportions of the starting materials. The final compounds result from the reaction being driven to completion (stability), with one compound being completely consumed.

Table A.1-6. Various Thermal Activation Energies Reported for Bond Failures and Growth of Au-Al Compounds

References	Specimen	Observed Quantity	Activation Energy
8	Au-Al-films	Au-Al-growth rate	1 eV
9	Au-Al-films	Sheet resistance	1 eV
10, 11	Au-Al-wire couples	Au-Al-growth rate	0.78 eV
1	Au-Al-wire couples	Au-Al-growth rate	0.69 eV
2	Au-Al-wire couples	Mechanical degradation	1 eV
12	Au-wire, Al-film	Au-Al-growth rate	0.88 eV
13	Au-wire, Al-film (1.4 μm) on Ta	Contact resistance, $\Delta R = 50\%$	0.55 eV
13	Au-wire, Al-film <0.3 μm 0.5, 1 μm	Contact resistance, $\Delta R = 1\ \Omega$ Contact resistance, $\Delta R = 1\ \Omega$ Pull strength (time to failure)	0.7 eV 0.9 eV 0.2 eV
16	Al wire, Au-film	Resistance drift to $\Delta R = 15\ m\Omega$	0.73 eV
8	Au-balls, Al-films 1 μm, Al-Si 1.3 μm, Al 2.5 μm, Al	Resistance (peripheral voiding)	0.9 eV ≥0.8 eV 0.6 eV
14, 15	Au-balls, Al-film	Ball shear strength	0.4 to 0.56 eV

Table A.1-7. Structure and Properties of Au-Al IMCs

Phase	Structure	Lattice Parameters (Å)	Composition at % Au	Vicker's Hardness (5 Kg)	Specific Resistance (Ohm–cm)	Coefficient of Linear Expansion (10^{-5})	Color of the Phase	Heats of Formation at 400K (cal +/–500)
Au	FCC	a = 4.08	84–100	60–90	2.3	1.42	Gold	
Au_4Al	Cubic	a = 6.92	80–81.2	334	37.5	1.2	Tan	
Au_8Al_3 Au_5Al_2	Rhombohedral	a = 14.68, α = 30.5	72.7	271	25.5	1.4	Tan	
	HCP	a = 7.71 c = 41.9						
Au_2Al	Orthorhombic	A = 3.36 B = 8.84 C = 3.21	65–66.8	130	13.1	1.3	Tan	–8300
AuAl	Monoclinic	A = 6.40 B = 3.33 C = 6.32 β = 92.99	50	249	12.4	1.2	White	–9200
$AuAl_2$	FCC	A = 5.99	32.33 –33.92	263	7.9	0.94	Purple	–10100
Al	FCC	A = 4.05	0–0.6	20–50	3.2	2.3	Lustrous	

Due to the impact of EMCs on degradation of intermetallics at the Cu-Al bond interface, phase transformation in the absence of molding compounds will be covered first. Au-Al and Cu-Al bonds exhibit significantly different IMC thickness immediately following bonding and long term reliability of these joints at elevated temperatures. Wei et al. found that the Au-Al intermetallic is 20x thicker than that of Cu-Al in the as-bonded condition. This is accompanied by a significantly higher growth rate during aging [ref. 44]. Researchers have found Cu–Al IMC in the as-bonded condition to be about 20 nm thick [ref. 45], as opposed to the 150-300 nm thickness observed for as-bonded Au-Al [ref. 46].

The Al-Cu binary alloy phase diagram is shown in Figure A.1-32 [ref. 47]. Funamizu et al. found the five thermodynamically stable IMCs ($CuAl_2$ (Θ), CuAl (η2), Cu_4Al_3 (ξ2), Cu_3Al_2 (δ), and Cu_9Al_4 (γ2)) highlighted in Figure A.1-33 [refs. 49, 50] following annealing of Al-Cu bulk material samples in the temperature range of 400 °C to 535 °C [ref. 48]. In this work, researchers found the IMC layer growth to obey the parabolic law and therefore to be controlled by volume diffusion. To determine the relative diffusion rate and measure the Kirkendall effect, they utilized alumina powder at the interface and plotted the marker shift as a function of the square root of diffusion time. They determined that diffusion occurred toward the Al side (Al diffuses more rapidly than Cu), and the linear relation indicated that diffusion was controlled by a vacancy mechanism [ref. 48].

Gubbels et al. evaluated bulk Al-Cu diffusion couples in the temperature range of 225 °C to 500 °C and compared those results with Funamizu's. While all five phases were identified for couples annealed at high temperatures (> 400 °C), this work determined that annealing at temperatures below 300 °C yielded only Θ ($CuAl_2$), η (CuAl) and γ (Cu_9Al_4). The researchers suggested the absence of the additional phases could be due to difficulties in nucleation or the possibility that the phase may be present in a layer too thin to be detected [ref. 50].

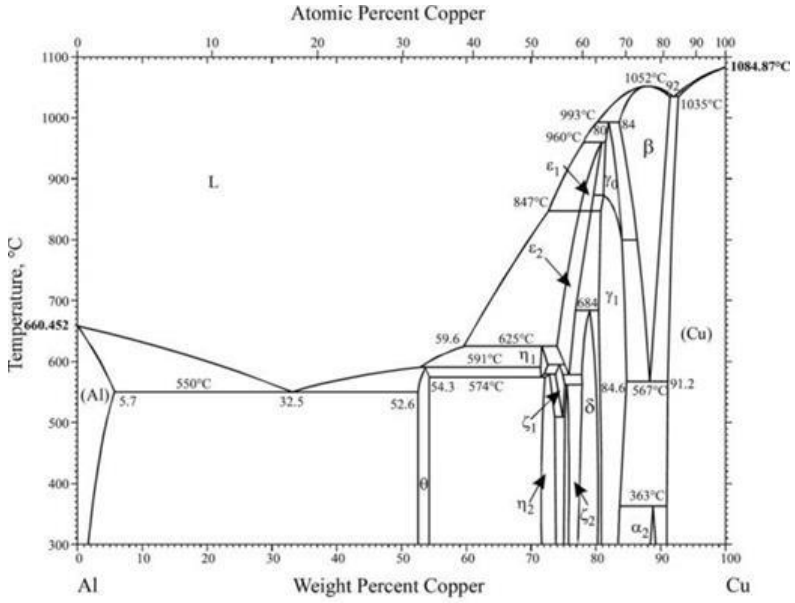

Figure A.1-32. Al-Cu Phase Diagram

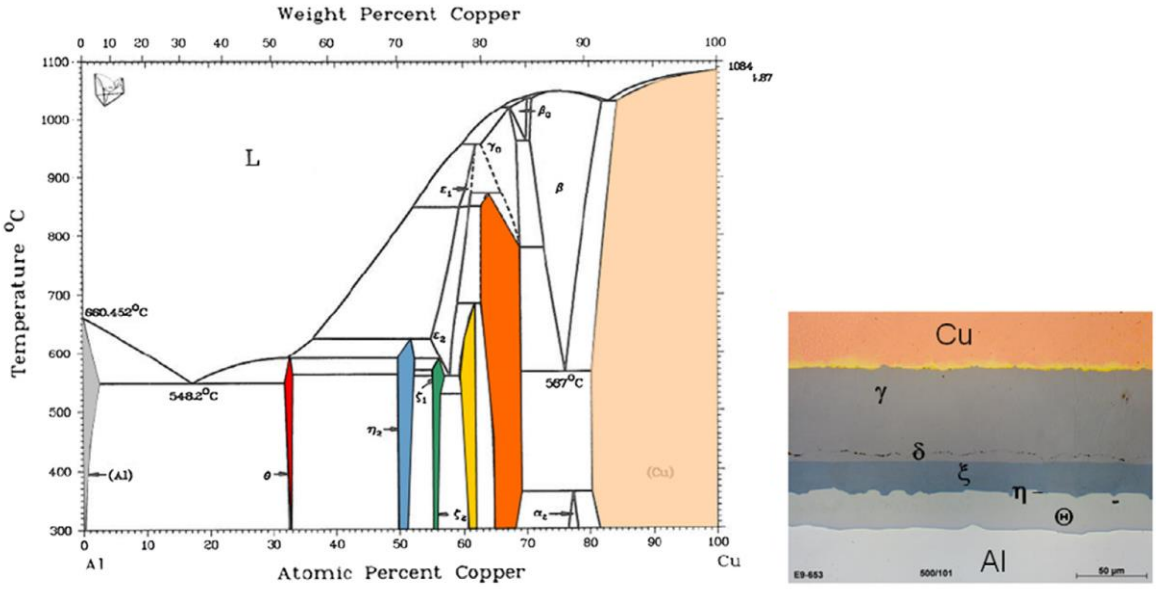

Figure A.1-33. (a) Phase Diagram of Al-Cu System with Indication of Intermetallic Phases, Al Solid Solution and Cu Solid Solution, and (b) Microscopy Images of Diffusion Zone Developed Between Al and Cu (500 °C, 100 hr in vacuum)

Kouters et al. evaluated the mechanical and physical properties of the individual Cu-Al IMCs and summarized the results as shown in Table A.1-8. This work found oxidation occurred at the interface between the Cu solid solution layer (Al in Cu) and Cu_9Al_4 and measured the highest density and greatest reduction in volume (5%) exhibited by the same Cu_9Al_4 phase. This indicates that this is likely the weakest interface link. Kouters notes that the CuAl phase mechanical properties could not be measured due to the limited thickness of this layer within the couple. Hardness was measured using nano indentation, micro-Vickers, and Vickers hardness measurement methods, and researchers found variation in values. They calculated a load-independent hardness, as shown in the table [ref. 51], and were able to resolve the variation. For

mechanical testing, the Al-rich IMCs were more sensitive to fracture than the Cu-rich IMCs, and interfacial delamination was observed to initiate in the Al-rich IMCs (CuAl and $CuAl_2$), then propagate through the other IMC layers [ref. 51]. Structure and physical properties for the Cu-Al intermetallics are provided in Tables A.1-9 [refs. 46, 52, 53] and A.1-10 [refs. 51–55].

Table A.1-8. Overview of Thermal, Mechanical and Physical Properties of Cu–Al Intermetallics

Intermetallic phase		Units	Θ-$CuAl_2$	η-CuAl	ζ-Cu_4Al_3	δ-Cu_3Al_2	γ-Cu_9Al_4
Load independent hardness	H^0_v	GPa	3.94	6.18	5.93	6.25	5.20
Indentation Young's moduli	e	GPa	123.5 ± 6.6	180.2 ± 12.5	180.2 ± 12.5	174.4 ± 19.5	186.8 ± 9.0
Indentation fracture toughness	K_{1c}	MPa √m	0.27 ± 0.06	0.20 ± 0.03	0.21 ± 0.05	0.68 ± 0.15	0.67 ± 0.10
Density	d	g/cm^3	4.27	5.31	5.60	6.25	6.65
	V	$cm^3/grat$	9.05	8.53	8.44	7.91	7.70
Specific heat capacity	C_p (20°C)	$J/kg^{-1}\ K^{-1}$		537		498	474
	C_p (100°C)			560		516	498
Thermal diffusivity	α (20°C)	m^2/s^{-1}		3.0×10^{-5}		8.4×10^{-6}	1.6×10^{-5}
	α (100°C)			2.3×10^{-5}		1.0×10^{-5}	1.4×10^{-5}
Thermal conductivity	λ (20°C)	$W/m^{-1}\ K^{-1}$		87		26	50
	λ (100°C)			69		33	46

Table A.1-9. Structure of Cu-Al IMCs in Binary System

Phase	Composition (at % Cu)	Symmetry	Space group	Atomic Packing Factor	Atoms/ unit cell	Unit cell volume ($Å^3$)	Molar volume, Vm (cm^3/mol)	ΔH_f (KJ/mol)
Al	0.0-2.8	FCC	*Fm-3m*	0.740	4	66.41	10.0	
$CuAl_2$	31.9-33.0	Tetragonal	*I4/mcm*	0.739	12	179.52	27.03	-15.036
CuAl	49.8-52.3	Monoclinic	*C12/m1*	0.739	20	280.62	16.9	-20.656
Cu_9Al_4	62.5-69.0	Cubic	*P4-3m*	0.776	52	660.05	99.37	-20.466
Cu	80.3-100	FCC	*Fm-3m*	0.740	4	47.24	7.11	

Table A.1-10. Physical Parameters of Cu–Al Intermetallics

Phase	Cu at%	HV5 kgf/mm^2	CTE ppm/°C	Density g/cm^3	Resistivity ($\mu\Omega$-cm)
Al	0–2.84	20–50	23.5	2.70	2.4
$CuAl_2$	31.9–33	324	16.1	4.38	7.0-8.0
CuAl	49.8–52.3	628	11.9	5.36	11.4
Cu_4Al_3	55.2–56.3	616	16.1	na	
Cu_3Al_2	59.3–61.9	558	15.1	na	
Cu_9Al_4	62.5–69	549	17.6	6.85	14.2-17.3
Cu	80.3–100	60–100	17.3	8.93	2.0

Xu et al. evaluated the interfacial evolution of IMCs in Cu-Al wire-bonded joints using high-resolution transmission electron microscopy (HRTEM) following annealing within the temperature range of 175 °C to 250 °C. Figure A.1-34 shows a TEM image and diffraction patterns for the IMCs observed in the Cu-Al wire bond interface following 100 hr at 175 °C [ref. 55]. Researchers found the native Al_2O_3 layer broken up during the bonding process was

initially located at the interface between Cu_9Al_4 and $CuAl_2$, was then surrounded by Cu_9Al_4 following transformation (Figure A.1-35) and was observed to migrate toward the Cu ball during annealing. This differed from the results obtained by Funamizu for bulk specimens. Xu observed that the distances between the SiO_2 layer on the device and the alumina were about 500 nm, 600 nm, and 850 nm, respectively, following 0, 1 and 100 hr at 250 ℃. Researchers determined that IMC formation within the Cu-Al ball bond is controlled by Cu diffusion, and kinetics obey a parabolic growth law until the Al pad is consumed. Figure A.1-36 illustrates the phase transformation sequence observed. Once the Al pad is consumed, $CuAl_2$ transforms to Cu_9Al_4 due to the continued supply of Cu. Unlike the void growth discussed previously for Au-Al bonds, Xu observed that only a few voids in the size range of 10s of nms nucleated in the Cu-Al bonds after long-term annealing at 250 ℃. Researchers attributed this to lower oxidation rate and volumetric shrinkage within Cu-Al IMCs, compared with Au-Al IMCs. Researchers also found that IMC growth is heavily dependent upon the distribution of IMC seed particles that are difficult to nucleate [ref. 55]. Liu et al. similarly observed the voids formed following high-temperature storage at 150 ℃ to be too small to pose a reliability concern. As described previously, researchers found the IMC reaction layer growth to occur by bulk diffusion of reactants to the interface. A parabolic reduction in film growth rate indicated that the previously formed IMC layer impeded transport of reactants. Additionally, they found activation energy in Cu-Al bonded joints was lower than observed in bulk or thin film Cu-Al couples and attributed this difference to the small bond area and availability of Al [ref. 53].

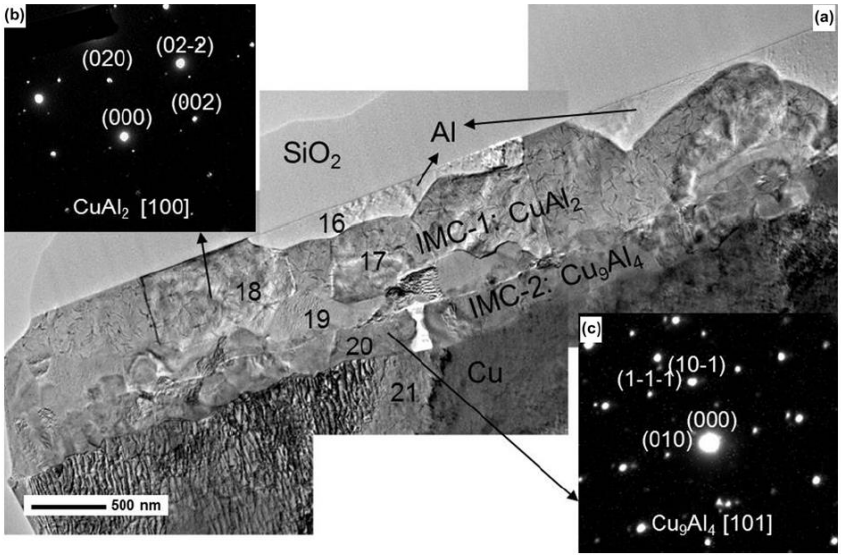

Figure A.1-34. (a) TEM Image of Cu-Al Interface After Annealing at 175 ℃ for 100 h, (b) SAED with $CuAl_2$; (c) SAED with Cu_9Al_4

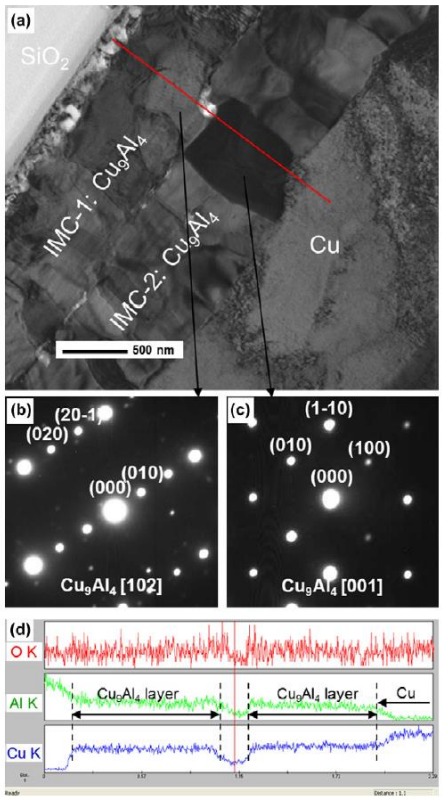

Figure A.1-35. (a) TEM Image of Cu-Al interface After Annealing at 250 ℃ for 100 hr; (b) SAED with Cu_9Al_4 [1 0 2]; (c) SAED with Cu_9Al_4 [0 0 1]; (d) Line Scanning EDX Results Along line in (a)

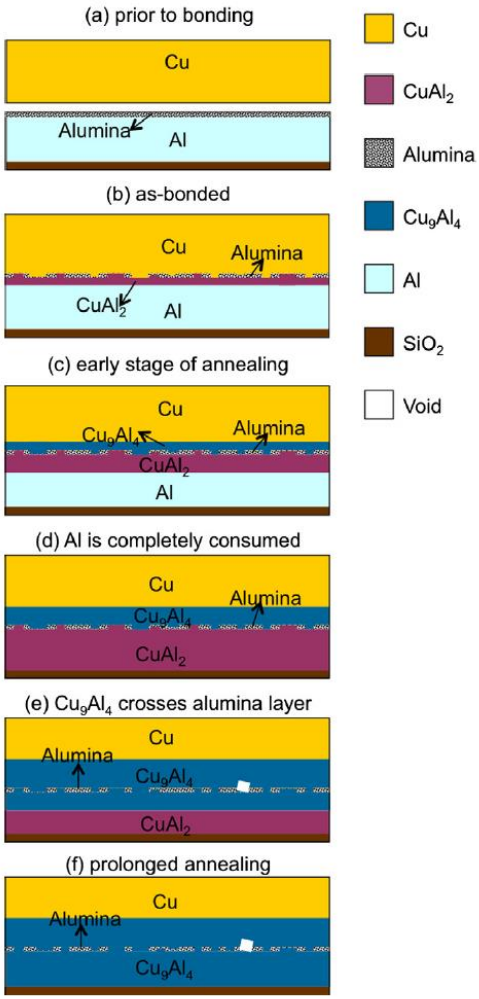

Figure A.1-36. Illustration of Phase Transformation in Cu-Al Bonds During Thermal Annealing: (a) Native Oxide Layer on Al Prior to Bonding; (b) $CuAl_2$ Formed During Bonding; (c) Cu_9Al_4 Formed at Early Stage of Annealing; (d) Both $CuAl_2$ and Cu_9Al_4 Simultaneously Grow Until Al Pad is Complete; (e) Cu_9Al_4 Keeps Growing by Consuming $CuAl_2$; (f) Cu_9Al_4 Becomes Only Final IMC After Prolonged Annealing

The growth rate of IMCs at the Cu-Al bond interface exhibited an exponential dependence with temperature, as described by the Arrhenius equation:

$$k = k_0 e^{-(E/RT)}$$

where k_0 is the growth rate constant ($\mu m^2/s$), E is activation energy (kJ/mol), R is gas constant (8.314 J/mol K), and T is the temperature (K). Activation energies from several published works are summarized in Table A.1-11, which shows a wide range of activation energies [ref. 53]. Liu suggested discrepancies could result from Cu wire material type, wire diameter, Al pad thickness, Al pad composition, EMC composition, bonding conditions, test conditions, measurement methods, and calculation methods. Molded samples, for example, would have been exposed to the molding cure and post-cure operations, resulting in a thicker IMC initial

condition. Researchers also noted that IMC growth rates for smaller-diameter Cu wires were dominated more by Al pad thickness than by bond area. This was due to the energy barrier increase resulting from the limiting material effect. Additionally, smaller Cu-Al interface area availability for the diffusion reaction may reduce activation energy and result in faster IMC growth than that observed for bulk systems. Mass transfer and the resulting defect densities, such as grain boundaries, vacancies, and dislocations, that occurs during the thermosonic bonding process could additionally increase IMC growth rate for Cu-Al wire bonds. Liu postulated that this may be the reason for the reduced individual IMC activation energies reported by Xu et al., compared with those seen by Koerner et al.

The presence of Pd on PCC wires has been shown by several researchers to reduce diffusion and IMC growth rate of Cu-Al wire bonds during high temperature storage and HAST, thereby prolonging life of the bonds [refs. 56–60]. Lim et al. found bonds with Pd exhibited nano-scaled voids at the interface that appeared to be strongly related to Pd content but did not appear to negatively impact bond pull strength. Additionally, Pd at the bond interface appeared to slow IMC growth rate to a greater degree than distributed Pd for PCC-Al bonds wires compared with Cu-Al ones [ref. 60].

Table A.1-11. Summary and Comparison of Cu-Al Intermetallic Growth Rate Constants and Activation Energies Used in Thermosonic Wire Bonded Samples for Different Testing Conditions and Materials Selection

Cu wire dimension (μm)	Al pad thickness (μm)	Aging time (h)	Aging temp. (°C)	Growth Rate, k (μm²/s)	Growth rate constant, k_0 (μm²/s)	Activation energy, E (KJ/mol)	Ref.
20.3 (0.8mil) (4 N purity)	1.0	0–100 0–100 0–25 0–100 0–100 0–25	175 200 250 175 200 250	3.60×10^{-7} 7.80×10^{-7} 3.67×10^{-6} 8.01×10^{-8} 2.10×10^{-7} 1.44×10^{-6}	4.14 (for $CuAl_2$) 49 (for Cu_9Al_4)	60.66 [0.629 eV] (for $CuAl_2$) 75.61 [0.784 eV] (for Cu_9Al_4)	Xu et al. (2011b) [w/o EMC]
22	1.5	5.7–7.8 3.5–8.3 2.5–6.4	150 175 220	3.76×10^{-8} 1.66×10^{-7} 1.91×10^{-6}	6.45×10^{4}	99.65 [1.033 eV] (23.7 Kcal/mol)	Yang et al. (2015), [TEM in-situ w/o EMC]
50.4 (2mil) (4 N purity)	2.0 (Al-1%Si-0.5%Cu)	2–300 2–300 2–300	150 250 300	1.878×10^{-8} 6.833×10^{-6} 6.027×10^{-5}	4.66×10^{5}	108.46 [1.124 eV] (26Kcal/mol)	Kim et al. (2003) [w/o EMC]
25	0.6 (Al-0.5%Cu)	0–1000 0–1000	150 175	5.56×10^{-6} 1.49×10^{-5}	1.898×10^{2}	60.9 [0.63 eV]	England and Jiang, (2007) [w/EMC]
50.4 (2mil) (4 N purity)	3.0 (Al-1%Si-0.5%Cu)	0–225 0–169 0–16	200 250 300	2.27×10^{-6} 2.46×10^{-5} 1.67×10^{-4}	1.21×10^{5}	97.1 [1.01 eV]	Hui et al., 2008, Xu et al. (2010) [w/EMC]
50.4 (2mil)	3.0 (Al-1%Si-0.5%Cu)	0–170	250	6.2×10^{-6}	–	–	Hang et al. (2008) [w/EMC]
25.0 (4 N purity)	3.0 (Al-1%Si-0.5%Cu)	1000–10,000 1000–10,000 1000–10,000 1000–10,000	125 150 175 200	5.52×10^{-4} 8.35×10^{-4} 1.31×10^{-3} 2.13×10^{-3}	5.76×10^{-2}	22.19 [0.230 eV]	Amistoso and Amorsolo, (2010) w/EMC

Cu wire dimension (μm)	Al pad thickness (μm)	Aging time (h)	Aging temp. (°C)	Growth Rate, k (μm²/s)	Growth rate constant, k_0 (μm²/s)	Activation energy, E (KJ/mol)	Ref.
20 (4 N purity)	0.6 (Al-1%Si)	100–1000 100–1000 100–1000	150 200 250	2.15×10^{-8} 2.56×10^{-8} 1.08×10^{-7}	6.36×10^{-2}	44.77 [0.464 eV] (10.71Kcal/mol)	Na et al. (2011) [w/EMC]
50 (4 N purity)	5.0 (Al-0.5%Cu)	50–1000 50–1000 25–1000 100–1000 50	175 200 225 250 300	– – – – –	3.7×10^{7}	121.8 [1.262 eV]	Pelzer et al. (2012) [w/EMC]
25.0 (4 N purity)	1.2 (Al-0.5%Cu)	120–480 120–480 120–480	175 200 225	3.57×10^{-7} 6.26×10^{-7} 7.15×10^{-7}	3.52×10^{-4}	25.47 [0.264 eV] (6.1 Kcal/mol)	Goh et al. (2013) [w/EMC]
22.0 (5 N purity)	_	0–5000 0–2000 0–1000	125 150 175	– – –	–	101.31 [1.05 eV]	Koerner et al. (2014) [w/EMC]
20.3 (4 N purity)	1.0 (Al-0.5%Cu)	2–3000 2–2000 2–200	150 200 250	2.09×10^{-8} 1.38×10^{-7} 1.35×10^{-6}	46.47	76.13 [0.789 eV]	Lui 2019 [w/EMC]
20.3 (0.8mil) (Pd coat Cu) (4 N purity)	_	0–2000 0–2000 0–2000	150 175 200	9.63×10^{-10} 2.08×10^{-9} 2.02×10^{-8}	1.43×10^{4}	104.21 [1.08 eV]	Chong et al, (2013) [w/EMC]
20.3 (0.8mil) (Pd coat Cu) (4 N purity)	2.0 (Al-0.5%Cu)	0–2000	175	7.74×10^{-8}	_	_	Kim et al. (2014), [w/o EMC]
20.3 (0.8mil) (Pd coat Cu) (4 N purity)	_	0–2000 0–2000 0–2000 0–2000 0–2000 0–2000	150 175 200 150 175 200	9.63×10^{-10} 2.08×10^{-9} 2.02×10^{-8} 4.92×10^{-9} 6.65×10^{-9} 8.51×10^{-9}	1.43×10^{4} (EMC A) 5.78×10^{4} (EMC B)	104.21 [1.08 eV] 100.35 [1.04 eV]	Gan et al. (2014) [w/EMC]

A.1.4.2 Impact of Molding Compound on Corrosion

Since Cu wire bonding is generally associated with commercial PEMs, several researchers have investigated the influence of EMC chemistry, configuration on the reliability of Cu wire bonds. One fact became clear early in the use of this technology: The presence of Br- or Cl- ions in the molding compound significantly increases corrosion issues for Cu wire bonded joints. Su et al investigated the influence of pH levels and Cl- content on the reliability of Cu wire bonded joints under high temperature storage and bHAST conditions. The researchers did not observe corrosion of the Au wire bonded parts, regardless of molding compound composition. The Cu wire bonds began to exhibit failures (defined as resistance increase of more than 20% on a daisy chain test device) after 120 hr (130 °C 85% RH 20V bias). Microstructural analysis following failure indicated that crack formation and growth occurred due to corrosion within the IMC layers. All failures were observed in the positively biased daisy chains. The researchers suggested that the electrical potential may help drive the negatively charged Cl- ion to these regions, thereby increasing the acidity of the environment surrounding the ball. Failure rates observed following 360 hr of HAST are shown in Figure A.1-37 for all of the mold compound conditions. The low pH acidic environment and increased Cl- concentration exacerbate

corrosion. The most significant corrosion occurred in the Cu_9Al_4 phase, with consumption of this phase initiating cracks that led to opens. This result is clearly illustrated by Figure A.1-38, where energy dispersive X-ray (EDX) performed in the vicinity of the crack at each of the locations shown indicated the presence of Cu (X1), a near-amorphous layer of corrosion product with Cu, Al, and O (X3 and X4), $CuAl_2$ (X2), and Al (X5) but no Cu_9Al_4 phase. [ref. 61]

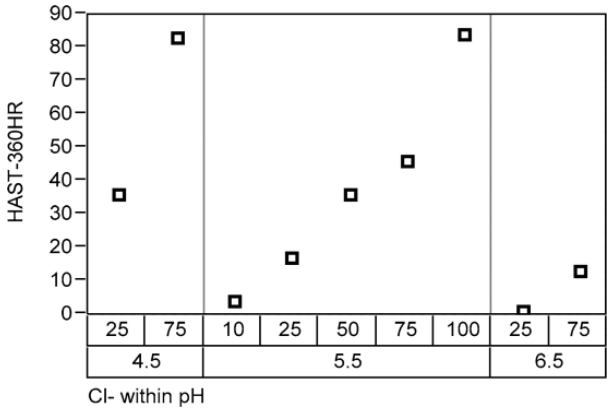

Figure A.1-37. Variability Plot of Failure Rates at 360-hr Read Point of bHAST. The data show failure rates increase as pH value decreases and CI-content increases.

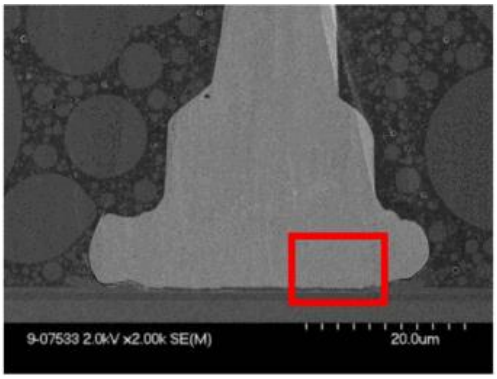

(a) An overview of the ball bond

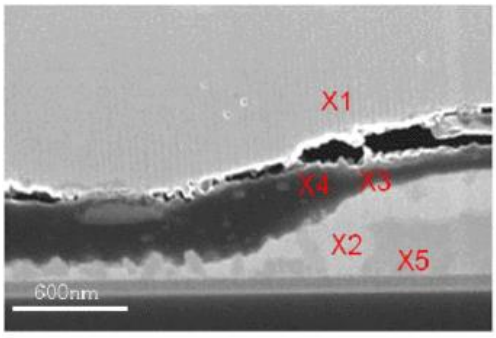

(b) Close-up view of the interface

Figure A.1-38. IMC Layers at Cu/Al Interface for Leg 6, from the 120-hr Read Point

Rongen et al. evaluated four commercial components with different EMCs, as summarized in Table A.1-12, from two different manufacturers. Only type A compounds were known to have halogens. The researchers evaluated the degradation in terms of crack length as a function of time at temperature (150 °C to 225 °C) and as a function of time under unbiased HAST conditions (110 °C/85% RH and 130 °C/75, 85, 95% RH). The researchers identified three sequential corrosion mechanisms whose chemical reactions were catalyzed by halogen ions in the vicinity of the bond and IMC.

The first mechanism is corrosion along the interface between the Cu ball and the IMC layer, within the solid solution layer (Al in Cu at concentrations below the solid solution limit). Corrosion is initiated by a low concentration of halogen ions and associated with a fine gap or crack at the interface. The researchers postulated that the small concentration (few at.%) of Al within the solid solution layer increases corrosion susceptibility. The TEM image of the Cu-Al IMC layer following 100 hr of aging at 300 °C and the associated compositions at the positions shown (Figure A.1-39) indicate the presence of this solid solution region [ref. 62].

Researchers then suggested that the second mechanism, bulk corrosion of the IMC layer beginning with the Cu-rich Cu_9Al_4 layer, was initiated once the halogen concentration at the corrosion front reached a critical threshold. When the halogen concentration exceeded a third threshold, the final mechanism occurred in the form of bond pad corrosion.

Table A.1-12. Overview of Used Molding Compounds

Type	Characteristic Description	Package Type
A	Brominated OCN-PN based epoxy from Supplier 1	DIP16, HSOP
B	Halogen-free multiaromatic epoxy from Supplier 1	HSOP
C	Halogen-free multiaromatic/ biphenyl epoxy from Supplier 2	DIP16
D	Halogen-free multiaromatic from Supplier 2	DIP16, HVQFN

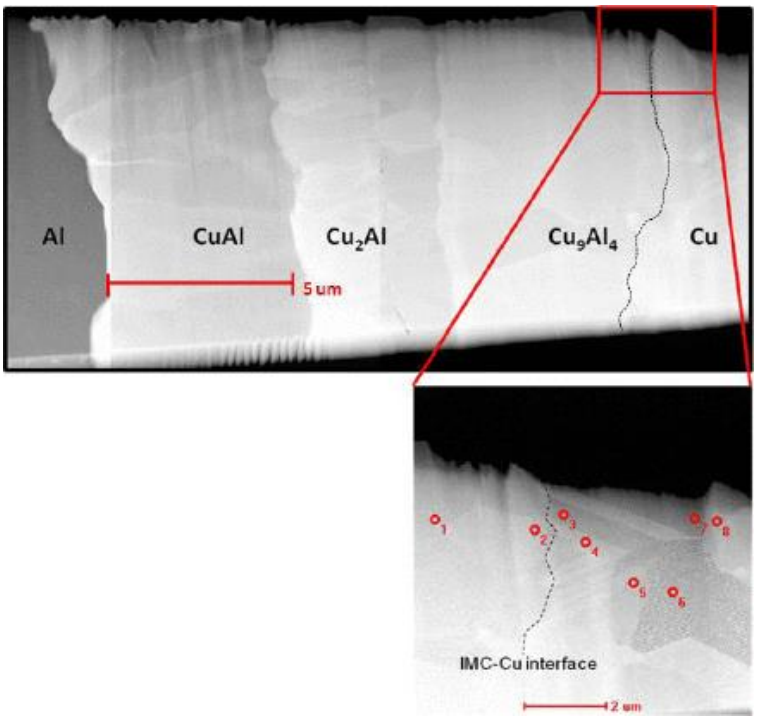

	At% @ location No.											
	CuAl	Cu_2Al	Cu_9Al_4	O_1	O_2	O_3	O_4	O_5	O_6	O_7	O_8	O_9
Cu	46	62	73	78	78	94	94	98	99	98	99	100
Al	54	38	27	22	22	6.1	6.2	2.3	0.9	2.0	1.4	0

Figure A.1-39. TEM Micrograph and Location Compositions Within Cu-Al IMC Layer

Following high temperature exposure, Cu-Al bonds encapsulated within compounds A and B exhibited significantly greater degradation (crack length of about 20-25μm) than those encapsulated in compounds C and D (5-10 μm). These results are shown in Figure A.1-40. Following unbiased HAST exposure, the bonds in compound A exhibited significant crack growth, with this effect occurring more quickly at 130 ℃ than 110 ℃. Bonds encapsulated within compounds B, C, and D did not exhibit significant degradation.

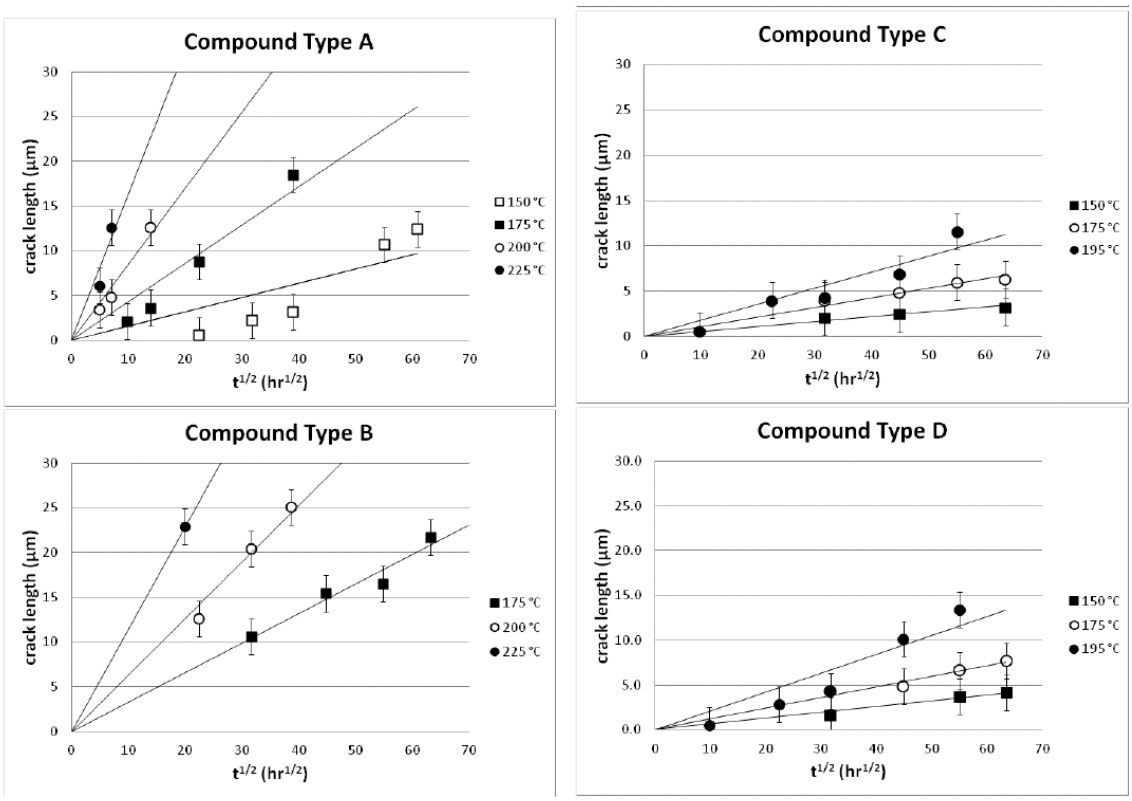

Figure A.1-40. Square Root Over Time Plots of Crack Length "x" for 4 Compound Types at Different Temperatures (measurement uncertainty is ± 2 μm)

A.1.5 Bond Material Chemical Reliability Comparison

Lall et al. performed a detailed study regarding the degradation in electrical and mechanical properties of Au, Ag, Cu, and PCC wires (all 1 mil except for 0.8 mil PCC) bonded to 1 μm Al pads following high temperature storage at 200 °C. Packages and EMCs (5 ppm Cl-, pH of 6, T_g of 150 °C, cured for 4 hr at 175 °C) were the same for all parts. Electrical failure was defined as a 20% change in resistance. The researchers found that prolonged aging resulted in degradation of IMCs along the periphery of the wire bonds, which led to the initiation and propagation of cracks to the center of the bond. This culminated in the eventual bond separation.

As stated previously, degradation of the Cu-Al and PCC-Al bonds was dominated by corrosion of the Cu-rich Cu_9Al_4 phase. Figures A.1-41 and A.1-42 illustrate the change in resistance with aging time and the associated IMC thickness for each of the aforementioned bonds. Cu, Ag, and PCC each exhibited slower degradation than Au. IMC thickness for Cu and PCC wires each exhibited an initial rapid rise in IMC thickness that slowed after a 10% change in resistance was exhibited. The Au bond failed due to Kirkendall voiding, as discussed previously. Pd at the bond interface was observed to slow the growth of IMCs. Following shear testing, Au bonds exhibited detachment at the center of the bond and brittle fracture at the periphery. Cu and PCC bonds instead exhibited peripheral cracking due to corrosion, with significantly thinner IMC and partial cracking at the center. Complete consumption of the Al pad following extended aging resulted in random ball detachment of Cu and PCC bonds from the Si device. A comparison of the performance of Cu and PCC bonds as a function of time at 175 °C is provided in Figure A.1-43 [ref. 63].

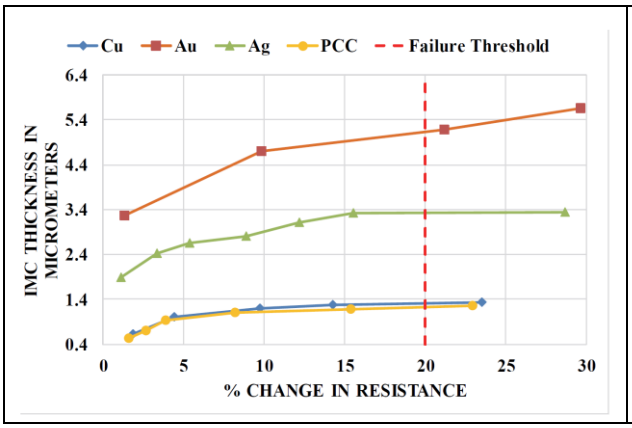

Figure A.1-41. Change in Package Resistance vs. IMC Growth

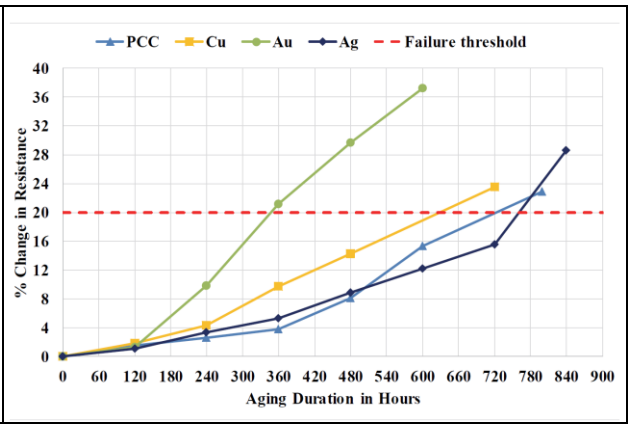

Figure A.1-42. Change in Wire Bond Resistance Due to High-Temperature Exposure

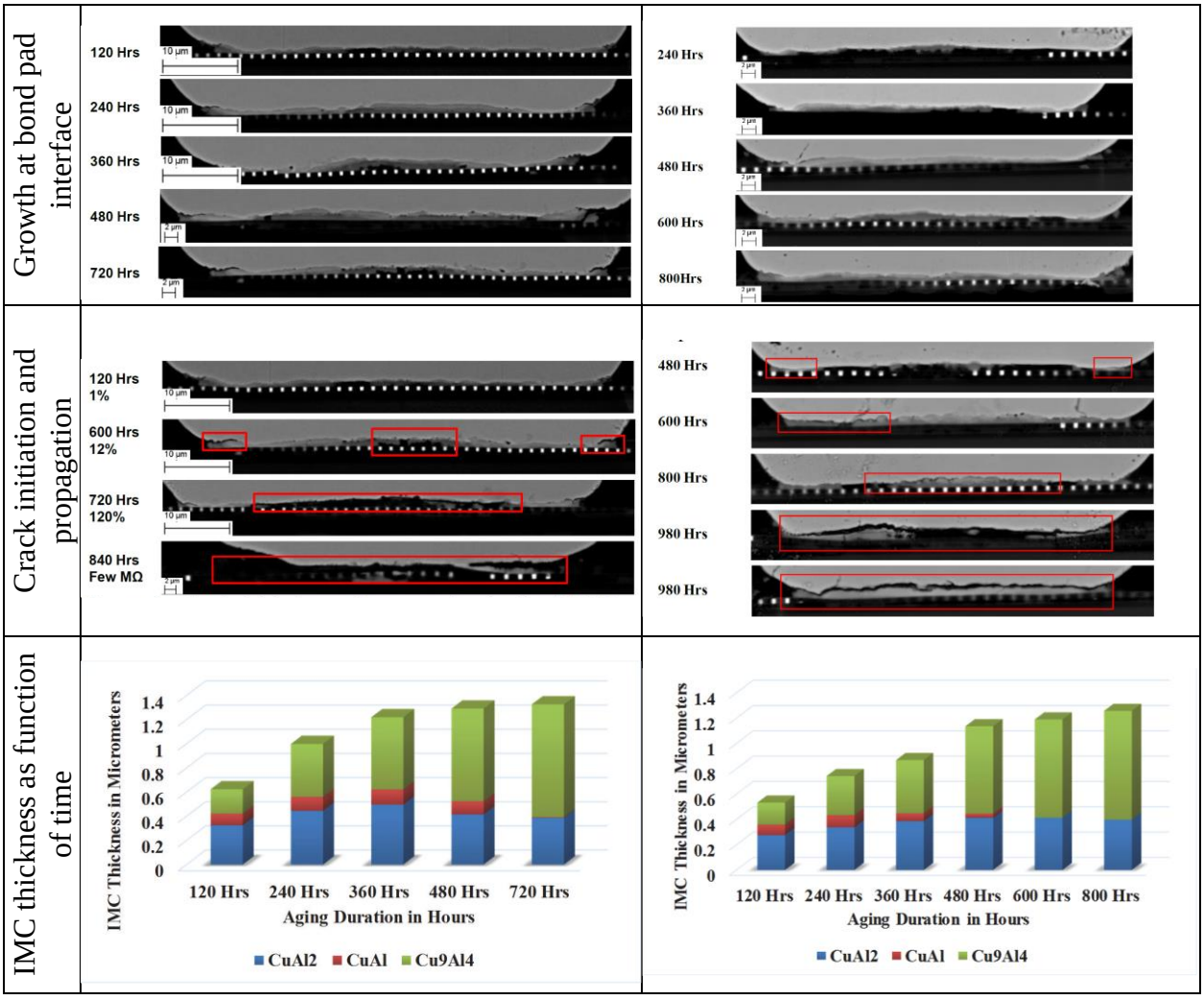

Shear failure mode	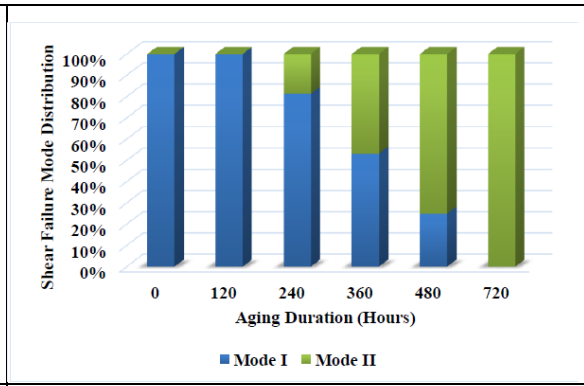	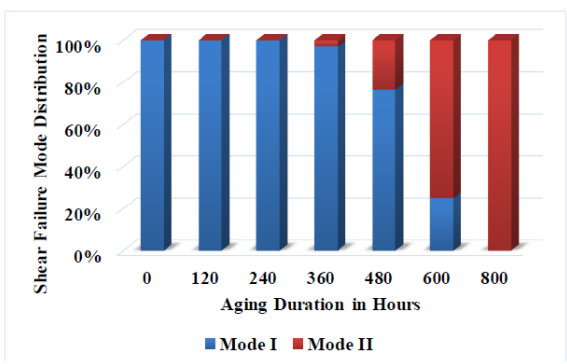
	Cu-Al wire bond system	PCC-Al wire bond system

Figure A.1-43. Comparison of Cu and PCC Bond Performance as Function of Time at 175 ℃

A.2 Wire Bond Testing

The mechanical quality and robustness of wire bonded joints are most commonly assessed using destructive bond pull testing and wire ball shear testing. These tests can be performed during process development, during part qualification, following environmental exposure, or during quality assurance. Bond pull testing for space applications is described in MIL-STD-883L, Method 2011.12. This standard is currently applicable only for Au and Al bond wires. This section will also discuss JESD22-B120, Wire Bond Pull Test Methods, since this test method is applicable to pre-encapsulated and post-encapsulated devices as well as Au alloy, Cu alloy, and Ag alloy bonds. Wire ball shear testing is performed based on JESD22-B116B, Wire Bond Shear Test Method. This method is also applicable to pre-encapsulated and post-encapsulated devices as well as Au alloy, Cu alloy, and Ag alloy bonds.

A.2.1 Bond Pull Test

The impact of various mechanical parameters on the pull strength of a wire-bonded interconnection can be understood by performing a resolution of forces for the bond [ref. 64]. A diagram defining the geometrical variables is provided in Figure A.2-1, along with the image of a cross-sectioned wire bond joint obtained for this project. The forces applied at the terminal (upper bond) F_{wt} and the device bond pad (lower bond) F_{wd} are provided in equations 1 and 2, respectively. The plots in Figures A.2-2 through A.2-5 illustrate the impact of horizontal and vertical position of the bond hook, bond height differential, and bond length on the forces at the wire for both the upper and lower bond [ref. 64]. Flat bonds that have a much longer length (d) than height (h) will have a lower θ and a much higher load at the bond, F_{wt} or F_{wd}, than applied at the hook (F). This is addressed in MIL-STD-883L, Method 2011.10, using equation 3 [ref. 1]. Additionally, the load distribution between the two bonds will be significantly influenced by the pull angle and the relative position of the hook between the two bond pads. To minimize the influence of such factors, MIL-STD-883L specifies that the force be applied perpendicularly (ϕ=0) and that the hook be located at the midpoint between the two bonds, ϵ=0.5, for most cases. As noted by Harman, wires for Al ball bonds normally break within the HAZ and the break load for the wire is near 90% of the manufacturer-specified breaking load. For Al wedge bonds, the bond breaking load is 60 to 75% of that specified by the manufacturer due to heel deformation and metallurgical overworking [ref. 65]. Details of the wire bond pull test method implementation for this project are provided in Appendix C.3.2.

a) 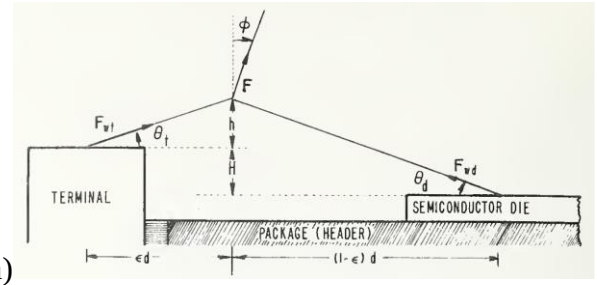

b) 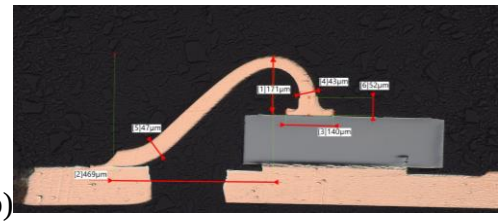

Figure A.2-1. a) Schematic Showing Resolution of Forces for Wire Bond Interconnect and b) Optical Micrograph of Cross-Sectioned Wire Bond

$$f_{wt} = F\left[\frac{(h^2+\epsilon^2 d^2)^{1/2}\left((1-\epsilon)\cos\phi+\frac{(h+H)}{d}\sin\phi\right)}{h+\epsilon H}\right] \quad (1)$$

$$f_{wd} = F\left[\frac{\left(1+\frac{(1-\epsilon)^2 d^2}{(H+h)^2}\right)^{1/2}(h+H)\left(\epsilon\cos\phi-\frac{h}{d}\sin\phi\right)}{h+\epsilon H}\right] \quad (2)$$

$$V1 = V2 \sin \Theta \quad (3)$$

where V1 = New value to pull test, V2 = bond limit value for size wire tested, and Θ = the greatest calculated wire loop angle.

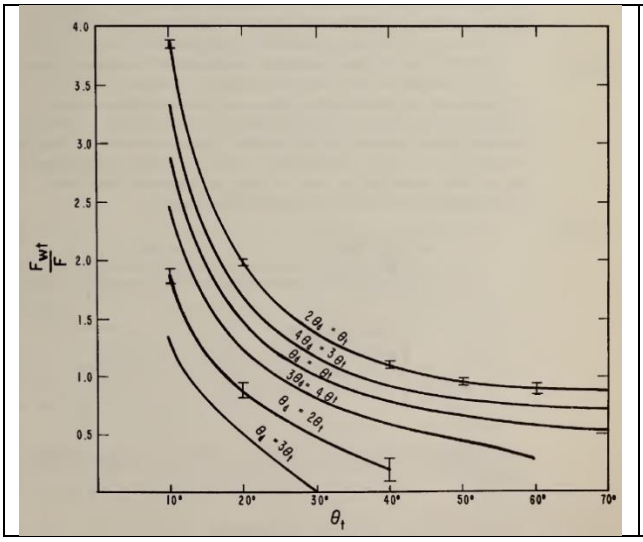

Figure A.2-2. Dependence of F_{wt}/F on ϑ_t for Various Ratios ϑ_d to ϑ_t. Curves are for $\varphi=0$

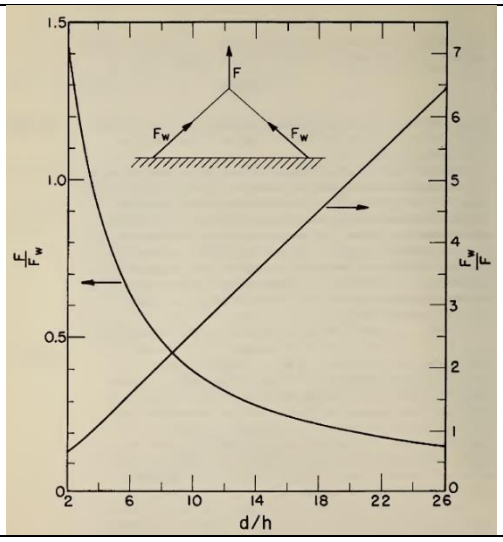

Figure A.2-3. F/F_w and F_w/F as Functions of d/h Graphed for Single-Level Double-Bond Pull Test

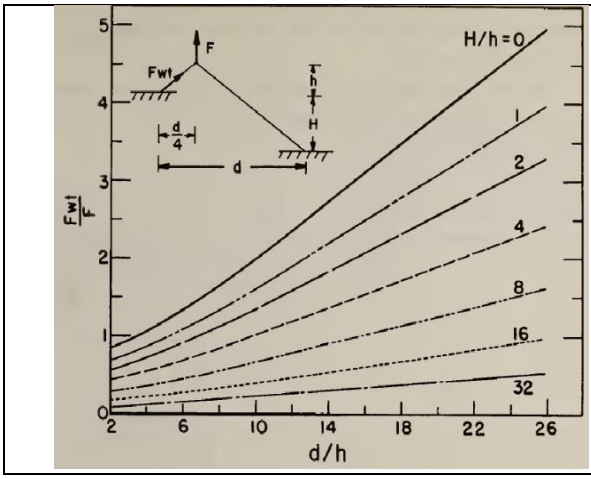

Figure A.2-4. F_{wt}/F as Function of d/h for Different Values of H/h and for Hook Position of 1/4d Graphed for Two-Level Double-Bond Pull Test

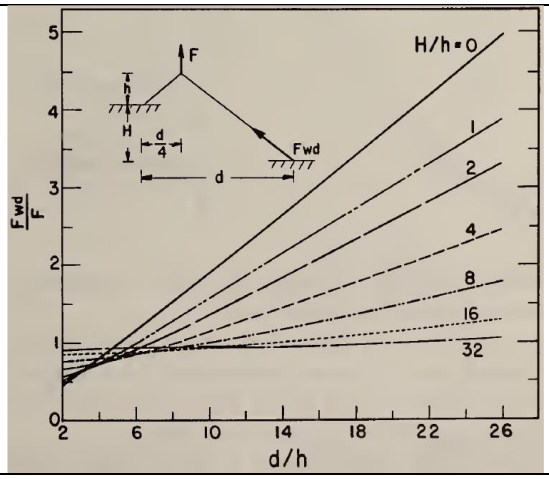

Figure A.2-5. F_{wd}/F as Function of d/h for Different Values of H/h and for Hook Position of 1/4d Graphed for Two-Level, Double-Bond Pull Test

A.2.1.1 Pull Test Limits

Pull tests have been used to evaluate wire bonds since thermocompression bonding was first developed at Bell Laboratories in 1957. During the development of the specification, pull test data, including mean range charts and acceptance criteria, were obtained from multiple semiconductor plants and device manufacturers to develop a realistic standard that offered a level of quality control that was acceptable to manufacturers and customers. Wire tensile strength, elongation, and additional metallurgical information was provided by three bonding wire companies. Finally, in-house bond pull data was obtained for different wire sizes and a limited number of device types. In 1975, the National Bureau of Standards (NBS) initiated an interlaboratory comparison (ILC) to verify accuracy of the bond pull method and provide data on reproducibility before establishing the test method as a standard.

To minimize variables, all bonds for this study were made with the same bonding machine and operator. Evaluation details can be found in the referenced reports [refs. 65–70]. A time line of the bond pull test, including materials and values, is provided in Figure A.2-6. During round-robin evaluation of wedge-bonded Al wires, multiple test structures were analyzed with controlled configurations. Measured results were compared with theoretical values calculated using the aforementioned equations to determine the sensitivity to various parameters. Selected results for 1 mil ultrasonically bonded unannealed Al-1% Si wires are provided in Figure A.2-7 [ref. 64].

The team found that the pull test results were most sensitive to pull angle due to a change in failure mode (tearing rather than heel failure resulting from tensile loading). Results of the sensitivity analysis are provided in Figure A.2-8 [ref. 64] and Table A.2-1. This example illustrates the controlled method used to determine the influence of various factors on identified pull strength values. Unfortunately, as stated in JESD22-B120 [ref. 2], the three curves generated for MIL-STD 883, Method 2011 were based on a limited data set obtained from a few diameters of Au and Al wire bonds that were predominantly ultrasonically wedge-bonded. The curves were then extrapolated using engineering judgement. The team found no evidence that the curves were

modified over the following 50 years as bonding technology (e.g., thermosonic bonding) and materials advanced.

Since the electronics industry began using Cu wire bonding, the Au minimum pull values from MIL-STD 883 have been used for Cu wires, regardless of coating or formulation. Due to this fact and the significant overlap of pull strength values for commercially available Au and Cu bond wires (Figure A.2-6), the committee recommended that the minimum pull strength for Au wire be used for Cu wire. It should also be noted that the JEDEC standard does not cover post-encapsulation or post-stress pull strength recommendations. This will be covered by JEDEC Committee JC-13 Government Liaison when it proposes an update to MIL-STD 883. Finally, the standard stresses the need to perform statistical process control (SPC) and maverick product management procedures as stated in JESD557 and JESD50 because the distribution of pull values can be much higher than the minimum pull values and some pull values may be much lower than the distribution but higher than the stated minimum.

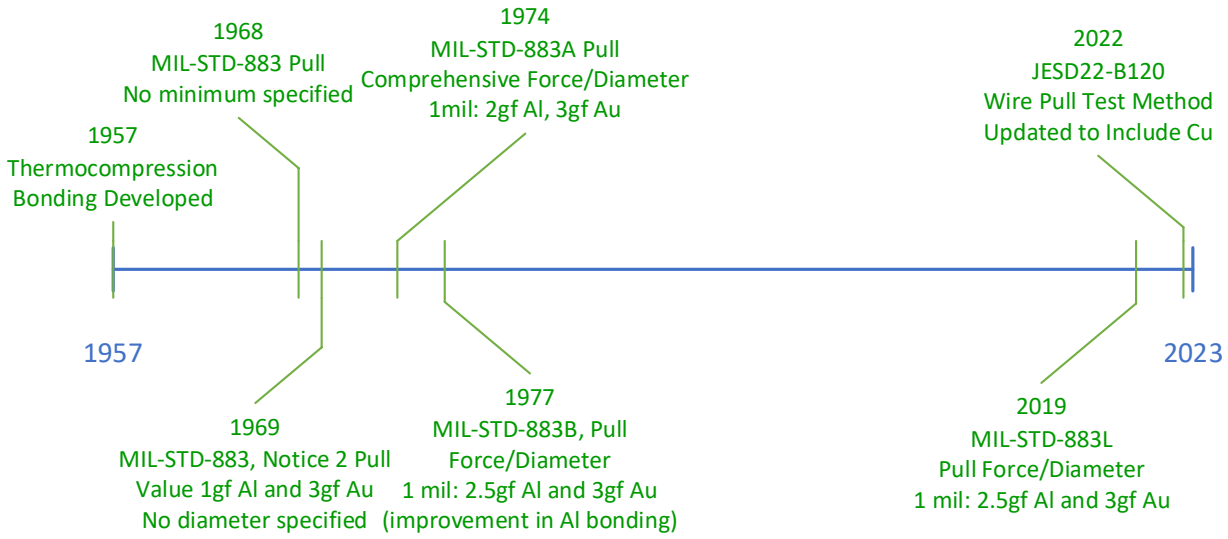

Figure A.2-6. Time Line of Bond Pull Test Modifications

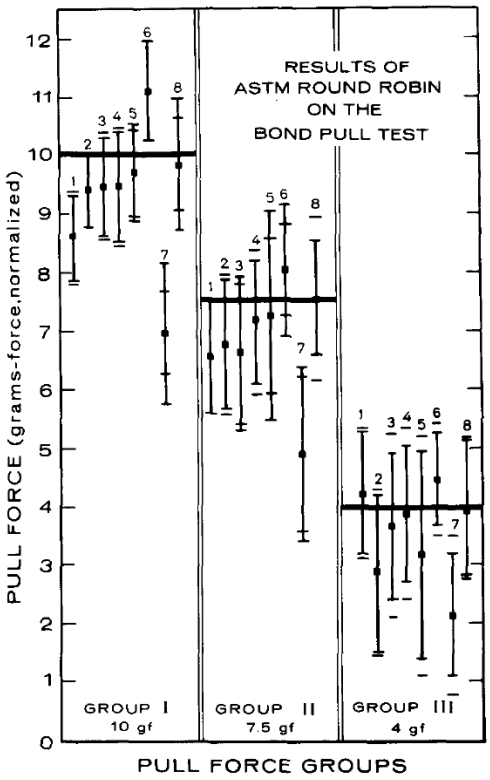

Figure A.2-7. Graphical Presentation of Pull Test ILC (round robin) Data. Numbers represent various participating laboratories, except 8, which is NBS retest. Error bars represent ±1 standard deviation of original NBS data on the laboratory specimen. Group I data were normalized to 10-gf, II to 7.5-gf, and III to 4-gf pull force.

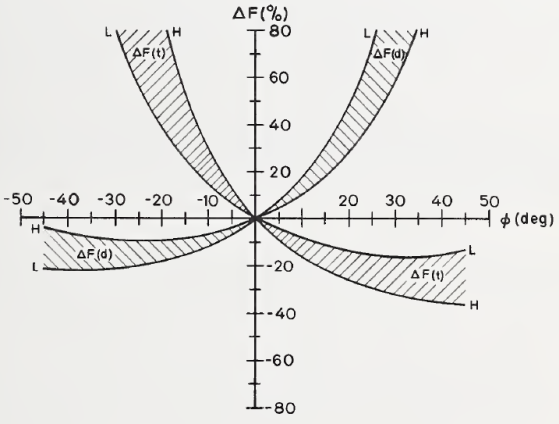

Figure 22. Normalized variation in calculated pull strength for the terminal bond, ΔF(t), and die bond, ΔF(d) as a function of pull angle ϕ.

(For case L:
d = 38.5 mils (0.98 mm);
h = 11.6 mils (0.29 mm);
ε = 0.375; and
H = 3.5 mils (0.09 mm).)

(For case H:
d = 41.5 mils (1.05 mm);
h = 12.4 mils (0.31 mm);
ε = 0.625; and
H = 6.5 mils (0.17 mm).)

Figure A.2-8. Normalized Variation in Calculated Pull Strength for Terminal Bond, ΔF (t) and Die Bond, ΔF(d), as Function of Pull Angle φ.

Table A.2-1. Calculated Dependence of ΔF (t) and ΔF(d) on Pull Test Conditions for TO-18 Transistor

Quantity	Change	ΔF(t)	ΔF(d)	Change	ΔF(t)	ΔF(d)
ϕ	+10 deg	-11%	+14%	+20 deg	-19%	+37%
	-10 deg	+20%	-8%	-20 deg	+50	-13
d	+10%	-7%	-6	+20%	-13	-11
	-10%	+8%	+6	-20%	+16	+13
h	+10%	+5%	+5	+20%	+11	+10
	-10%	-5	-5	-20%	-12	-10
ε	+10%	+4	-3	+20%	+9	-5
	-10%	-3	+4	-20%	-6	+9
H	+10%	+2	+0.5	+20%	+3	+1.0
	-10%	-2	-0.5	-20%	-3	-1.0

A.2.2 Wire Bond Shear Test

The JESD22-B116B Wire Bond Shear Test Method can be used to determine the strength of a ball bond to a die or package bonding surface. The test method provides significant detail regarding shear failure modes but does not discuss minimum shear forces. It may be used on wire bonded devices either pre-encapsulation or post-encapsulation. Toward that end, both JESD22-B116B and JESD22-B120 provide helpful guidelines regarding the decapsulation of PEMs prior to mechanical evaluation. Such guidelines include general description regarding the acceptable level of damage to Cu wires following decapsulation as well as the removal of encapsulant under wedge bonds and over-etching of Ag plating on leadframes. In addition, the importance of decapsulation on shear and pull strength results is highlighted, as well as the importance of bond and wire inspection before and after testing to ensure material removal during the etch process has not been excessive. Shear testing of bonds and acquisition of bond strength is needed to determine the integrity of the metallurgical bond and the quality of the ball bond to the die or package. Details of the wire bond shear test method implementation for this project are provided in Appendix C.3.3.

A.2.2.1 Comparison of Au and Cu Bonded Joints-Pull and Shear

In discussing the relative applicability of wire bond pull and ball shear testing for Au ball bonds, Harman stresses that the pull test is valid for wedge bonds but states that a shear test (or thermal stress test) is required to evaluate Au ball bonds [ref. 65]. He points out that placement of the hook at the peak of the bond would result in most of the stress being applied to the stronger ball bond (due to the greater cross-sectional area), and the weaker crescent bond would not be adequately stressed. Failure would most often occur within the ball bond HAZ. Shear tests, however, are a direct measure of the quality of the ball bonded joint, and studies performed on Cu ball bonded joints yield different results.

Due to the reliance on grain size for strengthening within Au wires and the temperature distribution during the EFO process, Au wire FABs and HAZs tend to exhibit much lower strength than the wire. The result is that bonds will tend to fail within the HAZ during pull testing due to the greater diameter of the FAB, as stated by Harman. Additionally, the bond will tend to shear within the ball for a well-formed joint. Cu wires, on the other hand, tend to be annealed to a greater degree in the initial condition to achieve the hardness required for bonding. Cu wires also have a higher thermal conductivity. The result is that the HAZ for Cu wires is less

dramatic with respect to grain size differences between the HAZ and the wire. This leads to a less significant reduction in strength. Due to the stiffness and strength of the Cu ball, a greater load is applied to the joint and the pad metallization. During shear testing, a greater portion of failures occurs within the pad metallization for well-bonded joints. The impact of these differences is shown below. Figure A.2-9 [ref. 71] illustrates this phenomenon, and Figures A.2-10 through A.2-14 provide ANSYS FEM models of the shear test on as-bonded Au and Cu wire bonds [refs. 71, 72]. An atomic-level schematic of the resulting failures is shown in Figure A.2-15 [ref. 71].

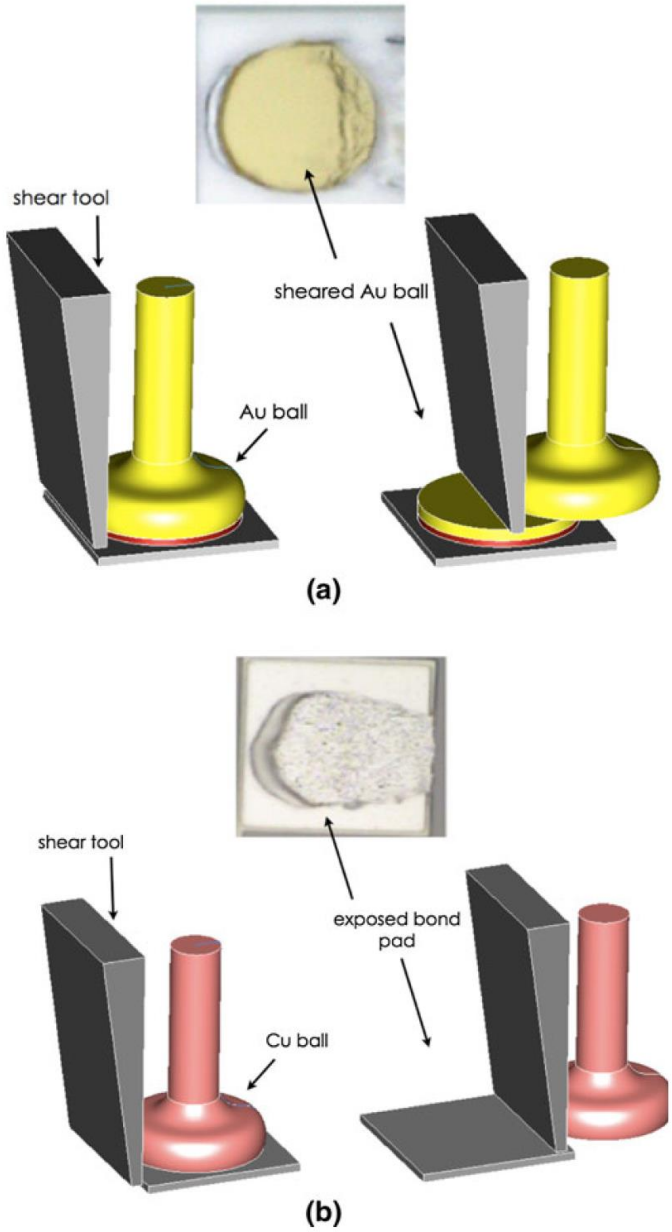

Figure A.2-9. Illustrations of Shear Test for As-Bonded or Aged Balls (a) plastic deformation and shearing of Au balls; (b) plastic deformation in aluminum and complete removal of Cu balls from the bond pad; illustrations not to scale

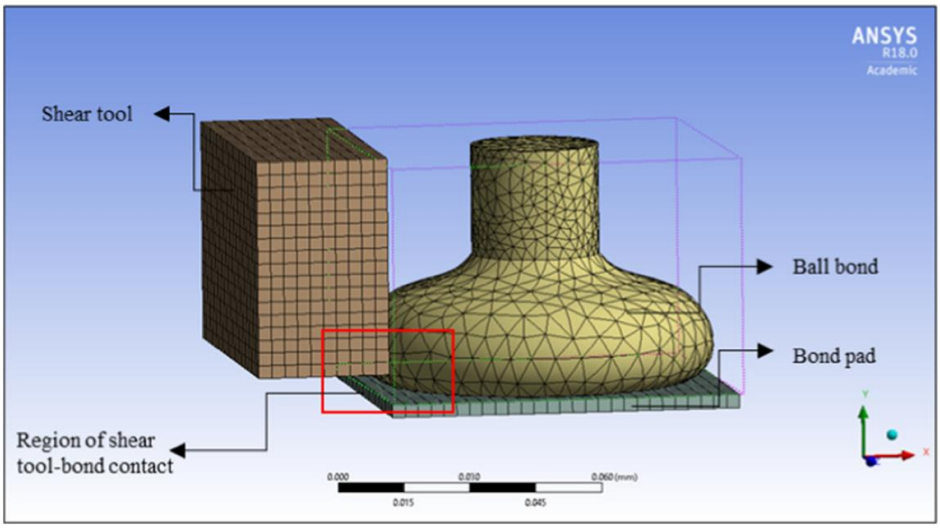

Figure A.2-10. Bond Shear Test – FEA Model

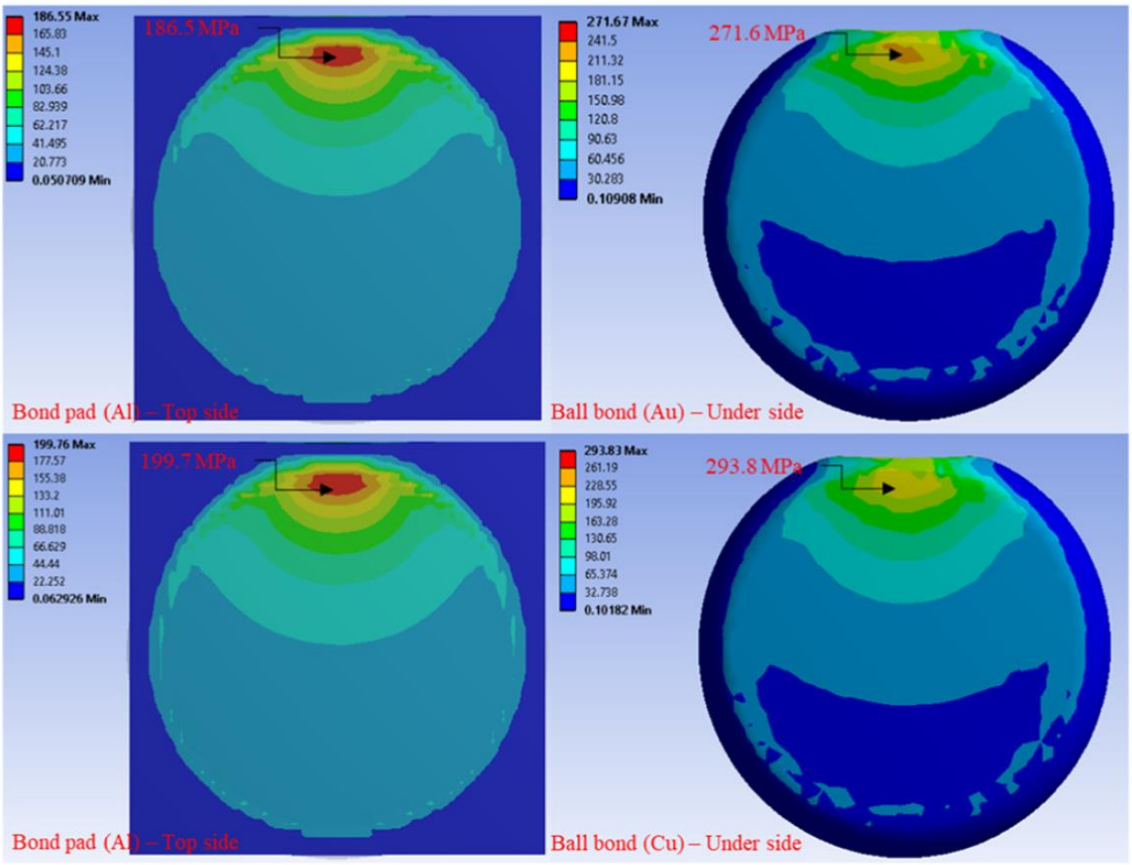

Figure A.2-11. Stress in Au-Al (top) and Cu-Al (bottom) System During Shear Testing

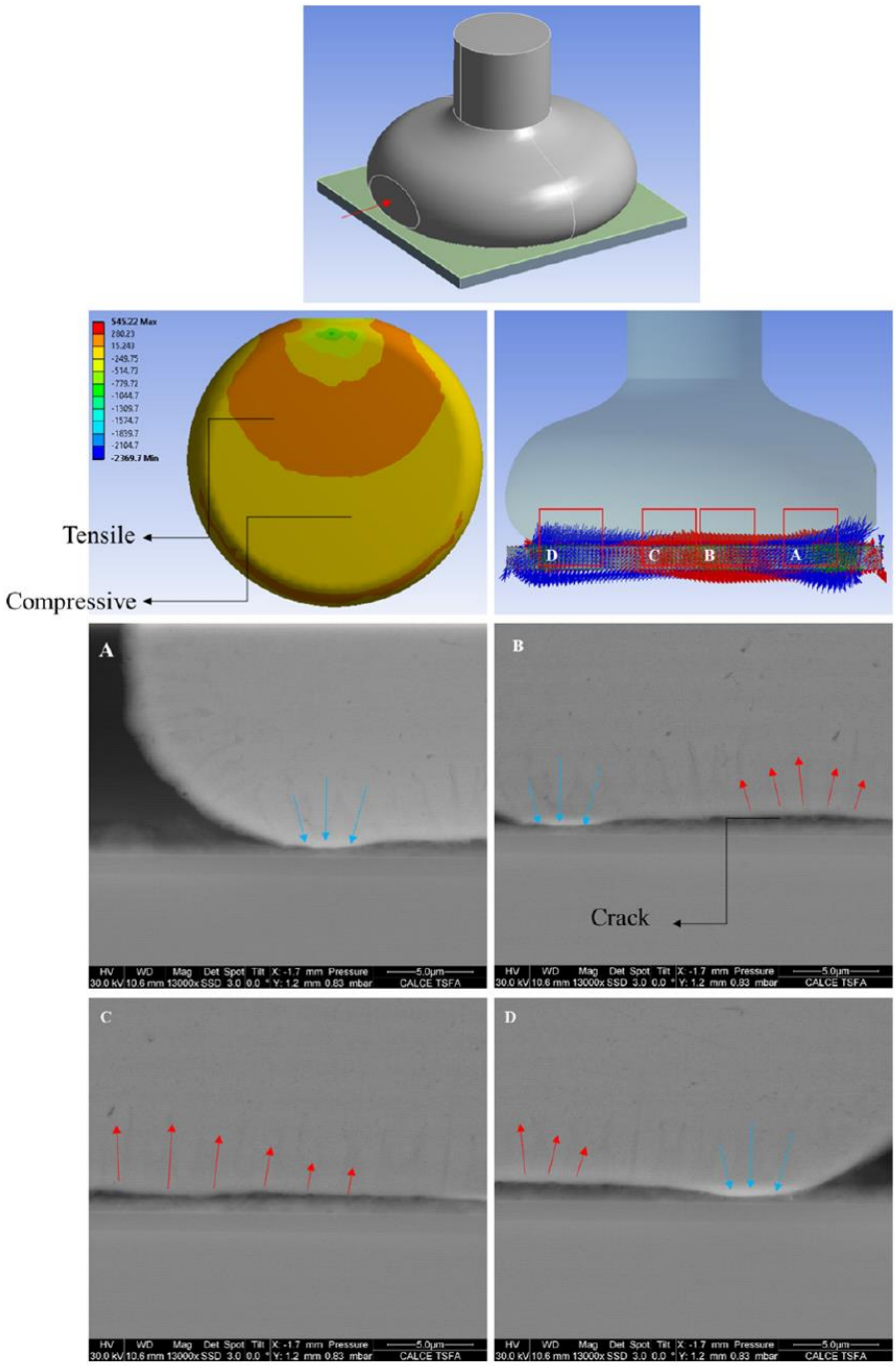

Figure A.2-12. Bond Shear FEA (top) Partial Shearing, Showing Result of Combination of Tensile and Compressive Stress (bottom)

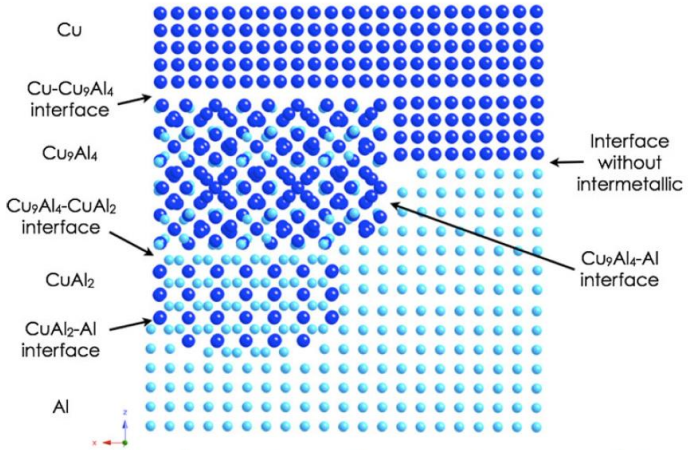

Figure A.2-13. Illustrations of Some Interfaces That May Exist in Cu Ball Bonds. Large spheres are Cu; small spheres are Al. Intermetallics have been drawn with a certain orientation for illustration purposes; actual orientations may differ.

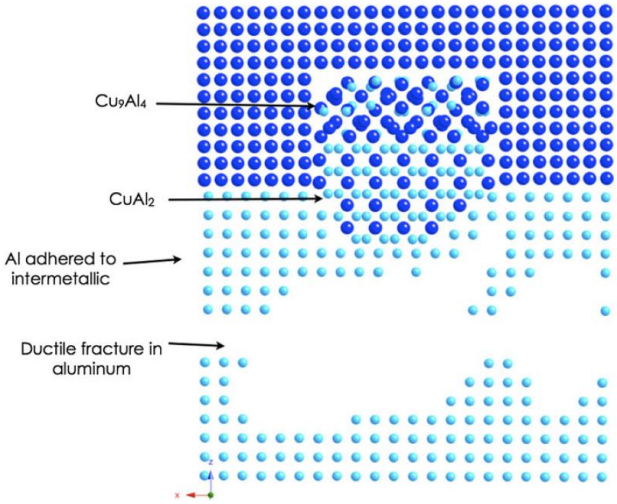

Figure A.2-14. Illustration of Ductile Fracture (tearing) of Al Strongly Bonded to Intermetallics

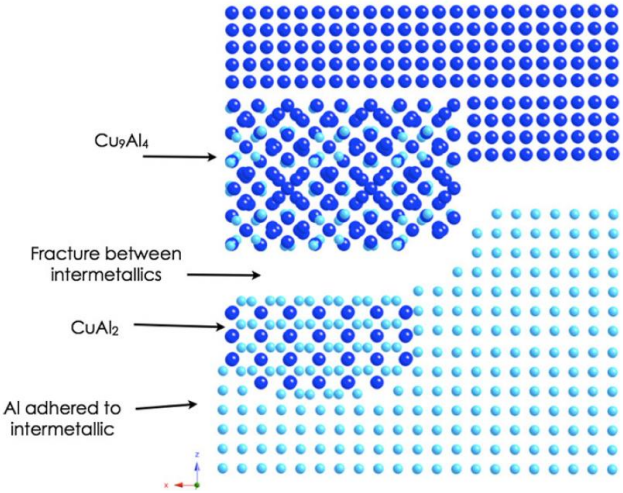

Figure A.2-15. Illustration of Brittle Fracture Between Intermetallics in Cu Ball Bond

Mazzei et al. performed a detailed evaluation of Cu wire pull and shear failure modes, including finite element modeling and crack propagation, analysis of Cu-wire pull and shear test failure modes under aging cycles, and finite element modeling of Si-crack propagation [ref. 73]. The researchers performed ball shear and wire pull testing on 2.5 mil Cu wire bonds in the unmolded, molded, post-TC, and post-high-temperature storage combined with TC conditions. As shown in Figure A.2-16, wire pull testing was more effective than ball shear for detecting mechanically weak joints between Cu wires and Al bond pads. Due to the greater stiffness of Cu compared with that of Au, the researchers stressed the importance of understanding crack propagation mechanisms and developed an FEM model and simulated crack path using stress intensity factors from linear elastic fracture mechanics. Defects that occurred during bonding tended to concentrate around the greatly deformed zone that correlated to the capillary deformation region and lowest Al pad thickness following ball bonding (Figure A.2-17). Such defects served as stress intensifiers during subsequent operations and could facilitate crack propagation through the device. The model parameters used for this assessment are shown in Figure A.2-18, indicating that a vertical pull direction was assumed. Due to the relative weakness of the bond pad compared with the Cu ball, the crack exhibited a mixed mode (Mode I-opening and Mode II-sliding) propagation and growth at a downward angle into the bond pad. These results are shown in Figure A.2-19. It was found that high bond-pad metal deformation with residual Al thickness less than 1 μm, even in the absence of defects, resulted in a greater incidence of unacceptable failure modes during pull and shear testing. The worst case occurred when the Al bond pad was completely displaced, leaving the Cu ball in direct contact with the underlying dielectric, and the bonding load was applied directly to substrate.

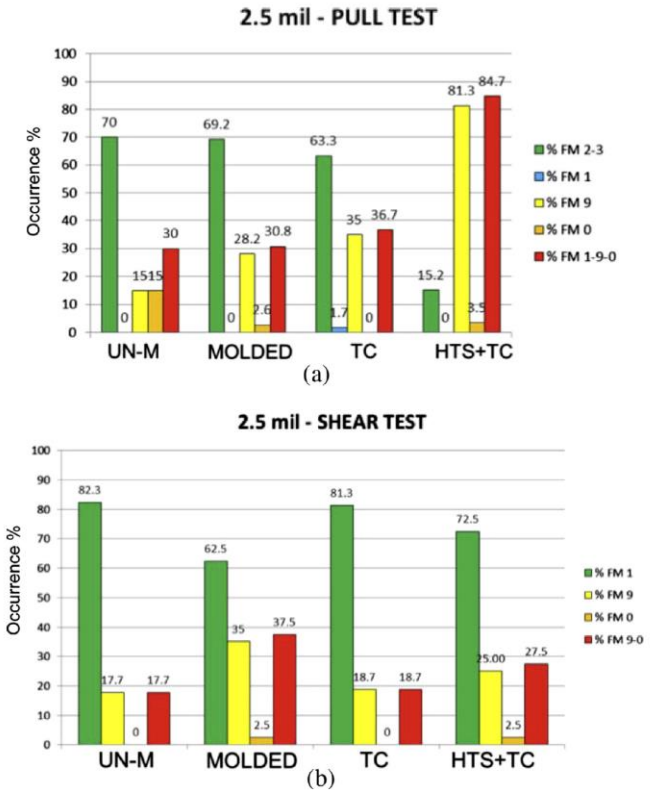

Figure A.2-16. Occurrence Frequency for Each Failure Mode During (a) Pull Test and (b) Shear Test of 2.5 mil Devices. The last column of each group clusters all the non-acceptable failure modes. Data are presented in increasing order of stress condition.

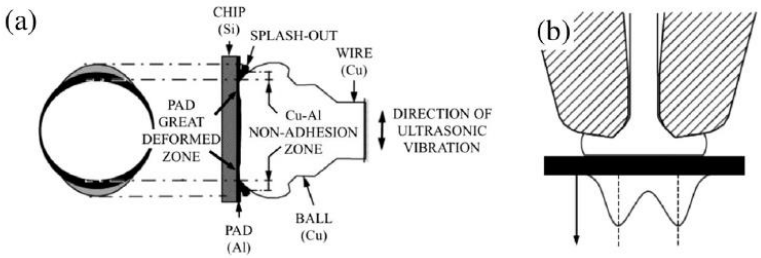

Figure A.2-17. (a) Geometry of Bond [ref. 74] and (b) Stress Distribution [refs. 75, 76] During Wire Bonding [ref. 73]

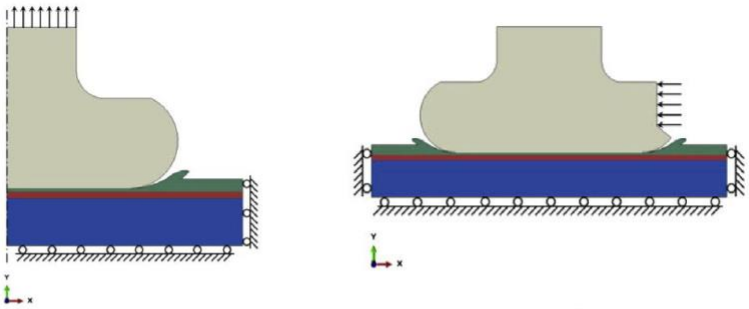

Material	Colour	*E* (GPa)	*v*	Thickness (μm)
Copper		130	0.36	(Ball)
Aluminium		73	0.334	1.53
Oxide		75	0.2	2.7 (dielectric)
Silicon		188	0.3	20

Figure A.2-18. Layout of Geometry, Load, and Boundary Conditions in Finite Element Models (a) Pull Test, (b) Shear Test, and (c) Characteristic of Modeled Layers in Terms of Thickness and Elastic Properties of Materials [ref. 73]

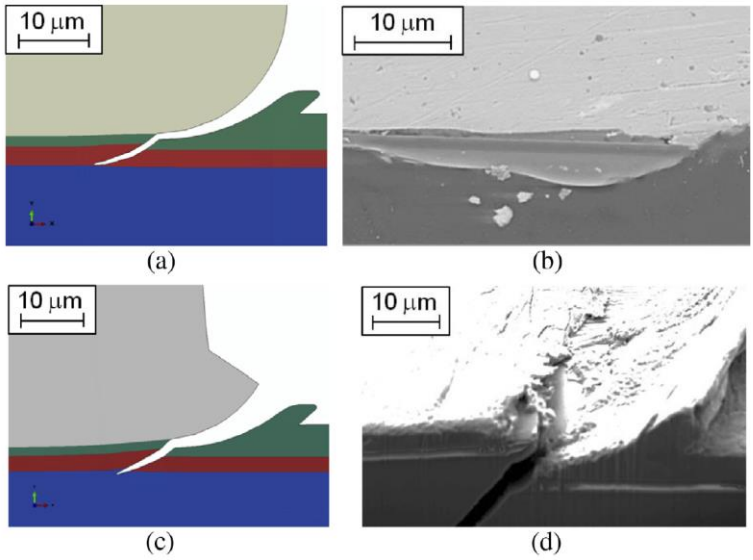

Figure A.2-19. Comparison Between Numerical Predicted and Experimental Crack Path in Tests (a) Pull Test Simulation; (b) Experimental Pull Test; (c) Shear Test Simulation; and (d) Experimental Shear Test [ref. 73]

A.2.3 Reliability Parameters

A.2.3.1 Packaging Technologies Trends

Reliability at the system level covers various interconnects from within package to solder joints at assembly level, as well as degradation due to various environmental exposures and functional processes. This section addresses reliability with consideration of the competing weakest link within package, e.g., failures from Cu-wire bond as opposed to assembly-level failure from solder joint interconnections. Since Au wire bonds are generally robust, the solder joints are considered the weakest link in the corresponding systems. This may not be the case for Cu wire bonds. Therefore, the reliability of COTS packaging technologies with internal Cu wire bond interconnections were evaluated and compared to parts having Au wire bonds.

A.2.3.2 Thermal Fatigue

Reliability under thermal stress for package and assembly depends on the reliability of constituent elements and global/local interfaces (e.g., attachments). Conventional packages have many elements, including Cu wire bonds, that become potential sources of the weakest link for reliability and also act as local conduits for heat dissipation. At the assembly level, solders in surface mount assemblies are unique in providing both electrical interconnections and mechanical load-bearing elements for attaching packages onto PCBs; they may also function as critical heat conduits. A package in isolation is neither reliable nor unreliable; second-level reliability has meaning only in the context of assembly-level interconnections, either within or outside the package onto PCB. There is a competition for failure among the various interconnections: failure potential is addressed first at the package level, with extensive stress testing, then at the assembly level for thermal and mechanical integrity. However, interaction effects on failures are not considered in such an approach.

Figure A.2-20 schematically shows three critical elements that play key roles in defining reliability of a package at assembly level: global, local, and solder alloy. For example, in quad flat no-lead (QFN) packages, solder is located at the periphery and castellated Cu finish acts as both electrical connection and loading element, with the additional benefit of a heat-sink attachment at the package bottom [ref. 77]. In ball grid arrays (BGA)s, solder balls also act as load carrying elements between packages and boards, in a manner similar to metallic leads on ceramic quad flat packs (CQFP)s. The characteristics of these three elements — package (e.g., Cu wire bond, die attach), PCB (e.g., polyimide, Cu, plated through hole, microvia), and solder joints (e.g., via balls, leads) — together with the use conditions, the design life, and acceptance failure probability for the electronics assembly will determine the reliability of package assemblies.

A.2.3.3 Mechanical Fatigue

Large surface mount technologies (SMTs) and area array packages, such as the aforementioned BGAs, lack the thermal and mechanical resistance generally observed for plated through-hole and small leaded package assemblies that are soldered with Sn63Pb37 alloys. Lack of reliability resistance is further aggravated by the use of Pb-free solder alloys, especially under harsh thermal cycling and dynamic loading, such as drop and vibration. For these reasons, corner staking for large packages and underfills for area array may be required to improve solder joint reliability under mechanical fatigue at the assembly level but may have negative effects under accelerated TCs (ATC) [ref. 78].

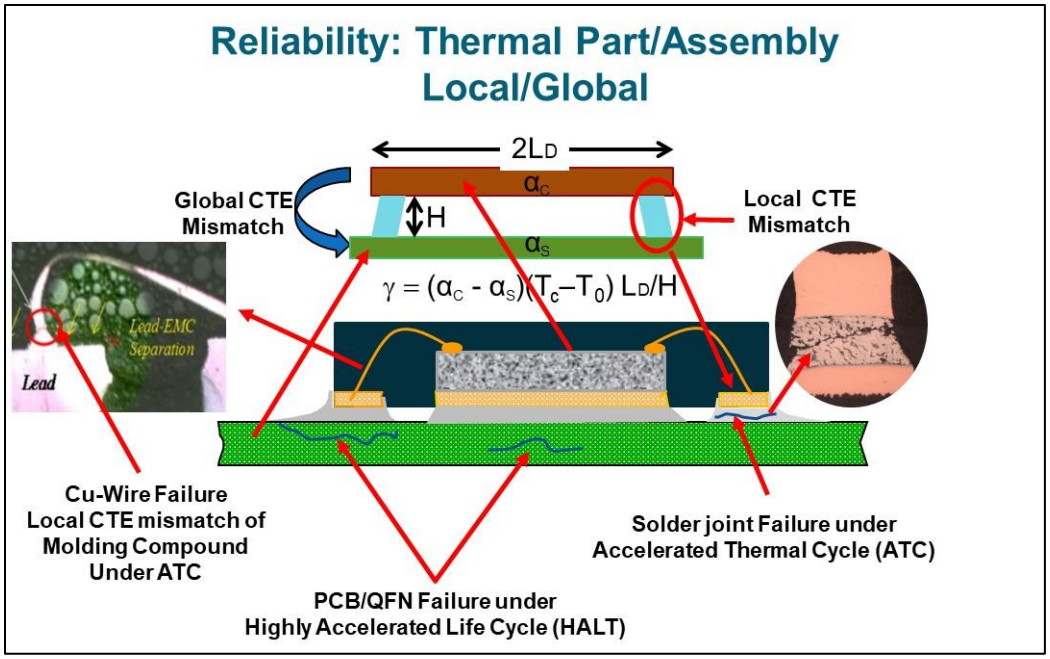

Figure A.2-20. Schematic Representative of Failure Mechanisms Within Package and at Assembly due to CTE Mismatches Under Accelerated Thermal Cycling for QFN Assembly.

A.2.3.4 Failure Mechanisms Under Fatigue

Failure mechanisms are different under thermal stress and thermal fluctuation and under mechanical stress and fatigue cycling environmental conditions. For example, underfill failure mechanisms are different under mechanical repeated drop and thermal cycling and are affected by different parameters. Under repeated drop, failure mechanisms are dominated by failures at interfaces or cohesive failures within the adhesive. However, failure mechanisms under thermal cycling are complex and a combination of parameters, including Tg, CTE mismatches, and modulus affect failure and mechanism. It is shown that a low Tg with high CTE mismatch and a low fracture toughness could lead to early underfill cracking, both cohesively and through adhesive failure in the underfill fillet. Fillet cracking causes delamination between the underfill and the die passivation and/or between the underfill and the board, while bulk cracking can initiate solder joint cracking and solder bridging.

Appendix A References

1. Tanaka, https://tanaka-preciousmetals.com/en/products/detail/bonding-wires/
2. Heraeus Technical Datasheet, “Bonding Wires for Semiconductor Technology.”
3. Simons, C.; Schräpler, L.; and Herklotz, G. (2000) “Doped and Low-Alloyed Gold Bonding Wires,” Gold Bull 33, 89–96. https://doi.org/10.1007/BF03215484.
4. Tomiyama, S., Fukui, Y. (1982) “Gold Bonding Wire for Semiconductor Applications,” Gold Bull 15, 43–50. https://doi.org/10.1007/BF03214605.
5. Gan, C.L., Hashim, U. (2015) Evolutions of Bonding Wires Used in Semiconductor Electronics: Perspective Over 25 Years. J Mater Sci: Mater Electron 26, 4412–4424. https://doi.org/10.1007/s10854-015-2892-8.

6. Sarangapani, Murali; Yeung, Ping Ha; Milke, Eugen (2013) “Doped 4N Copper Wires for Bonding in Microelectronics Devices,” Heraeus Materials Technology GmbH & Co. KG (Hanau, DE), U.S. Patent No. 20130142567.
7. Eto, M.; Araki, N.; Yamada, T.; Klengel, R.; Klengel, S.; Petzold, M.; Sugiyama, M.; Fujimoto, S. (2020) “Effects of Alloying Elements in High- Reliability Copper Wire Bond Material for High- Temperature Applications,” Microelectronics Reliability, Volume 114, 113819.
8. Khatibi, Golta; Mazloum-Nejadari, Ali; Lederer, Martin; Delshadmanesh, Mitra; and Czerny, Bernhard (2018) Fatigue Life Time Modelling of Cu and Au Fine Wires. MATEC Web of Conferences 165, 06002. https://doi.org/10.1051/matecconf/201816506002.Hall, E.O. (1951) Proc. Phys. Soc. Lond. B 64, p.747.
9. Petch, J. (1953) Iron Steel Inst. 174, p. 25.
10. Yang, B.; Motz, C.; Rester, M.; Dehm, G. (2012) “Yield Stress Influenced by the Ratio of Wire Diameter to Grain Size—A Competition Between the Effects of Specimen Microstructure and Dimension in Micro-Sized Polycrystalline Copper Wires,” Philosophical Magazine, 92:25-27, 3243-3256.
11. Molotnikov, A.; Lapovok, R.; Davies, C.H.J.; Cao, W.; and Estrin, Y. (2008) Scripta Mater. 59, p. 1182.
12. Miyazaki, S.; Shibata, K.; and Fujita, H. (1979) Acta Metall. 27, p. 855.
13. Janssen, P.J.M.; de Keijser, Th.H.; and Geers, M.G.D. (2006) Mater. Sci. Eng. A 419, p. 238.
14. Keller, C.; Hug, E.; and Chateigner, D. (2009) Mater . Sci. Eng. A 500, p. 207.
15. Yang, B.; Motz, C.; Grosinger, W.; Dehm, G. (2010) “Cyclic Loading Behavior of Micro-Sized Polycrystalline Copper Wires,” Procedia Engineering, Volume 2, Issue 1, pp. 925-930.
16. Hou, Y.; Mi, X.; Xie, H.; Zhang, W.; Huang, G.; Peng, L.; Feng, X.; Yang, Z. (2020) Size Effect on Mechanical Properties and Deformation Behavior of Pure Copper Wires Considering Free Surface Grains. Materials (Basel), 13(20):4563.
17. Yang, H.; Cao, K.; Lu, J.; et al. (2019) “Effects of Pd Surface Coating on the Strength and Fracture Behavior of Cu Micro Bonding Wires,” Metall Mater Trans A 50, 3013–3018.
18. Harman, G., Wire Bonding in Microelectronics, McGraw Hills, Third Edition, 2010.
19. Karpel, A.; Gur, G.; Atzmon, Z.; et al (2007) Microstructural Evolution of Au–Al Wire-Bonds. J Mater Sci 42, 2347–2357. https://doi.org/10.1007/s10853-007-1593-y.
20. Heraeus Technical Datasheet, “FP2 2N Gold Wire for Proven Ultimate Reliability.”
21. Liu, D.; Chen, H.; Wong, F.Y.; Lee, K.; Shiu, I.; and Wu, J. (2011) “Effect of Heat Affected Zone on the Mechanical Properties of Copper Bonding Wire.” IEEE 6 1st Electronic Components and Technology Conference (ECTC), 1523-1528.
22. Chauhan, Preeti and Choubey; Anupam and Zhong, Z.; Pecht, Michael (2013) Copper Wire Bonding. 10.1007/978-1-4614-5761-9.
23. Lim, Adeline B.Y.; Chang, Andrew C.K.; Yauw, Oranna; Chylak, Bob; Gan, Chee Lip; Chen, Zhong (2014) “Ultra-Fine Pitch Palladium-Coated Copper Wire Bonding: Effect of Bonding Parameters,” Microelectronics Reliability, Volume 54, Issue 11, pp. 2555-2563.
24. Lim, Adeline B. Y., et al. (2016) “Interfacial Evolution and Bond Reliability in Thermosonic Pd Coated Cu Wire Bonding on Aluminum Metallization: Effect of Palladium Distribution.” Microelectron. Reliab. 63, pp. 214-223.

25. Hibbeler, Russell C. (2023) Mechanics of Materials, 11th edition, Pearson.
26. K. Soffa (2012) Presentation, cited in Chauhan, Preeti and Choubey; Anupam and Zhong, Z.; Pecht, Michael (2013) Copper Wire Bonding. 10.1007/978-1-4614-5761-9.
27. Sarangapani, Murali; Yeung, Ping Ha; Milke, Eugen (2013) "Alloyed 2N Copper Wires for Bonding in Microelectronics Devices," Heraeus Materials Technology Gmbh & Co. KG (Hanau, DE), U.S. Patent No. 20130140084.
28. Goh, K.S., Zhong, Z.W. (2007) "Two Capillary Solutions for Ultra-Fine-Pitch Wire Bonding and Insulated Wire Bonding," Microelectronic Engineering, Volume 84, Issue 2, pp. 362-367.
29. Zhong, Z.W. (2009) "Fine and Ultra-Fine Pitch Wire Bonding: Challenges and Solutions," Microelectronics International, Vol. 26 No. 2, pp. 10-18.
30. Komori, S., Sakamoto, Y. (2009). "Development Trend of Epoxy Molding Compound for Encapsulating Semiconductor Chips." Lu, D., Wong, C. (eds), Materials for Advanced Packaging. Springer, Boston, MA. https://doi.org/10.1007/978-0-387-78219-5_10
31. Henkel Corp.: Nigel Hackett, global director of business development, and Dan Loskot, global product manager of semiconductor liquids, may be contacted through Douglass Dixon, marketing manager. 15350 Barranca Parkway, Irvine, CA 92618; 949-789-2517; doug.dixon@us.henkel.com.
32. Harman, G. (1997) "Gold-Aluminum Intermetallic Compounds and Other Metallic Interface Reactions Encountered in Wire Bonding," Wire Bonding in Microelectronics Materials, Processes, Reliability, and Yield, 2nd ed., New York: McGraw-Hill, pp. 115-159.
33. Li, Leijun, and Zhang, Chunbo (2011) "Fundamentals of Ultrasonic Welding, Welding Fundamentals and Processes," ASM Handbook, vol. 6A, edited by T. Lienert, T. Siewert, S. Babu, V. Acoff, ASM International, pp. 201–208.
34. Xu, H.; Liu, C.; Silberschmidt, V.V.; Pramana, S.S.; White, T.J.; Chen, Z.; Acoff, V.L. (2011) "Behavior of Aluminum Oxide, Intermetallics and Voids in Cu–Al Wire Bonds," Acta Materialia, vol. 59, iss. 14, pp. 5661-5673.
35. Philofsky, E. (1970) "Intermetallic Formation in Gold-Aluminum Systems," Solid-State Electronics, vol. 13, no. 10, pp. 1391-1399.
36. Philofsky, E. (1971) "Design Limits When Using Gold-Aluminum Bonds," Proc. IEEE Reliability Physics Symp., Las Vegas, Nevada, pp. 11-16.
37. Smigelskas A.D., and Kirkendall, E.O. (1947) "Zinc Diffusion in Alpha Brass," Trans. Met. Soc. AIME, vol. 171, pp. 130-142.
38. Porter, D.A., and Easterling, K.E. (1992) Phase Transformations in Metals and Alloys, London: Chapman & Hall, p. 89.
39. Majni, G. and Ottaviani, G., "AuAl Compound Formation by Thin Film Interactions," J. Crystal Growth, Vol. 47, 1979, pp. 583–588.
40. Gerling, W., "Electrical and Physical Characterization of Gold-Ball Bonds on Aluminum Layers," IEEE ECC, New Orleans, Louisiana, May 14–16, 1984, pp. 13–20.
41. Noolu, N.J.; Murdeshwar, N.M.; Ely, K.J.; Baeslack W.A.; Lippold, J.C. (2004) "Phase Transformations in Thermally Exposed Au-Al Ball Bonds," J. Electronic Materials, vol. 33, no. 4, pp. 340–352.

42. Noolu, N.J.; Murdeshwar, N.M.; Ely, K.J.; Lippold, J.C.; Baeslack, W.A. (2004) “Partial Diffusion Reactions and the Associated Volume Changes in Thermally Exposed Au-Al Ball Bonds,” Met. Matls Trans. A, vol. 35, pp. 1273–1280.
43. Noolu, N.J.; Murdeshwar, N.M.; Ely, K.J.; Lippold, J.C.; Baeslack, W.A. (2004) “Degradation and Failure Mechanisms in Thermally Exposed Au-Al Ball Bonds,” J. Materials Research, vol. 19, no. 5, pp. 1374–1385.
44. Wei, T.C., and Daud, A.R. (2003) “Mechanical and Electrical Properties of Au-Al and Cu-Al Intermetallics Layer at Wire Bonding Interface.” ASME. J. Electron. Packag. pp. 617–620.
45. Xu, H.; Liu, C.; Silberschmidt, V.V.; Pramana, S.S.; White, T.J.; Chen, Z. (2009) Scripta Mater; 61:165.
46. Xu, H.; Liu, C.; Silberschmidt, V.V.; Pramana, S.S.; White, T.J.; Chen, Z., et al. (2010) J Appl Phys;108:113517.
47. Okamoto, H. (2013) ASM Handbook of Alloy Phase Diagram, J. Phase Equilib. Diff., vol. 34, no. 6, pp. 493–505.
48. Funamizu, Yasuhiro; Watanabe, Katsuya (1971) “Interdiffusion in the Al–Cu System,” Transactions of the Japan Institute of Metals, vol. 12, iss. 3, pp. 147-152.
49. Massalski, T.B. (1986) Binary Alloy Phase Diagrams, ASM.
50. Gubbels, G.H.M.; Kouters, M.H.M.; O’Halloran, O.; and Rongen, R. (2010) “Growth and Properties of Intermetallics Formed During Thermal Aging of Cu-Al Ball Bonds,” 3rd Electronics System Integration Technology Conference ESTC, Berlin, Germany, pp. 1-6.
51. Kouters, M.H.M.; Gubbels, G.H.M.; Dos Santos Ferreira, O. (2013) “Characterization of Intermetallic Compounds in Cu–Al Ball Bonds: Mechanical Properties, Interface Delamination And Thermal Conductivity,” Microelectronics Reliability, vol. 53, iss. 8, pp. 1068-1075.
52. Wulff, F.W., Breach, C.D., Stephan, D., Saraswati, Dittmer, K.J. (2004) “Characterisation of Intermetallic Growth in Copper and Gold Ball Bonds on Aluminium Metallization,” Proceedings of 6th Electronics Packaging Technology Conference (EPTC), pp. 348–353.
53. Liu, Chien-Pan; Chang, Shoou-Jinn; Liu, Yen-Fu; Chen, Wei-Shou (2019) “Cu-Al Interfacial Formation and Kinetic Growth Behavior During HTS Reliability Test,” Journal of Materials Processing Technology, vol. 267, pp. 90-102.
54. Rabkin, D.M.; Ryabov, V.R.; Lozovskaya, A.V.; et al. (1970) “Preparation and Properties of Copper-Aluminum Intermetallic Compounds.” Powder Metall Met Ceram 9, 695–700.
55. Xu, H.; Liu, C.; Silberschmidt, V.V.; Pramana, S.S.; White, T.J.; Chen, Z.; Acoff, V.L. (2011) “Behavior of Aluminum Oxide, Intermetallics and Voids in Cu–Al Wire Bonds,” Acta Materialia, vol. 59, iss. 14, pp. 5661-5673.
56. Kaimori, S.; Nonaka, T.; and Mizoguchi, A. (2006) “The Development of Cu Bonding Wire with Oxidation-Resistant Metal Coating,” IEEE Transactions on Advanced Packaging, vol. 29, no. 2, pp. 227-231.
57. Lim, A.; Chang, A.; Lee, C.; Yauw, O.; Chylak, B.; Chen, Z. (2013) “Palladium-coated Copper Wire Study for Ultra-Fine Pitch Wire Bonding,” Transactions of Electro-Chemical Society, vol. 52, pp. 717-730.

58. Tang, L.; Ho, H.; Zhang, Y.; Lee, Y.; Lee, C. (2010) “Investigation of Palladium Distribution on the Free Air Ball of Pd-coated Cu Wire,” Proceedings of 12th Electronics Packaging Technology Conference (EPTC), pp. 777-782.
59. Abe, H. et al. (2012) Cu Wire and Pd-Cu Wire Package Reliability and Molding Compounds,” Proc. IEEE ECTC, San Diego. pp. 1117-1123.
60. Lim, Adeline B.Y., et al. (2016) “Interfacial Evolution and Bond Reliability in Thermosonic Pd Coated Cu Wire Bonding on Aluminum Metallization: Effect of Palladium Distribution.” Microelectron. Reliab. 63: 214-223.
61. Su, P. et al. (2011) “An Evaluation of Effects of Molding Compound Properties on Reliability of Cu Wire Components,” IEEE 61st ECTC, Lake Buena Vista, FL, USA, 2011, pp. 363-369, doi: 10.1109/ECTC.2011.5898539.
62. Rongen, R.; O’Halloran, G.M.; Mavinkurve, A.; Goumans, L.; and Farrugia, M-L. (2014) “Lifetime Prediction of Cu-Al Wire Bonded Contacts for Different Mould Compounds,” IEEE 64th ECTC, Orlando, FL, USA, pp. 411-418.
63. Lall, Pradeep; Deshpande, Shantanu; Nguyen, Luu (2018). “Comparison of Reliability of Copper, Gold, Silver, and PCC Wirebonds Under Sustained Operation at 200c.” Proceedings of SMTA International, Rosemont, IL, USA.
64. NBS 400-18, The Destructive Bond Pull Test (1976), John Albers. doi:10.6028/NBS.SP.400-18
65. Harman, G.G., Ed. (1974) “Semiconductor Measurement Technology. Microelectronic Ultrasonic Bonding,” NBS Spec. Pub. 400–2.
66. Albers, J.H., Ed., (1976) “Semiconductor Measurement Technology: The Destructive Bond Pull Test,” NBS Spec., Pub. 400-18.
67. Hoffman, G.; Johnson, R.; Straub, R. (1971) “Qualification Procedures for Hybrid Circuits,” Final Technical Report, RADC-TR-71-107, General Motors Corporation, Delco Electronics Division.
68. Schafft, Harry A. (1972) “Testing and Fabrication of Wire-Bond Electrical Connections-A Comprehensive Survey,” NBS Technical Note 726.
69. Mirth, Lee (1982) “Quality Assurance Procedures for LSI,” Final Technical Report, RAD-TR-82-43, Martin Marietta Corporation.
70. Ebel, G.H.; Jeffery, J.A.; Engleke, H.A.; Ossenkopp, B.D.; and Glick, D.J. (1983) “Application Guidelines for Quality Assurance Procedures for Hybrid Microcircuits,” Final Technical Report, RADC-TR-83-74, The Singer Company.
71. Breach, C., Lee, T. (2012) “Shear Strength and Failure Modes of As-Bonded Gold and Copper Ball Bonds on Aluminum Metallization,” J. Electron. Mater. 41, 2018–2028. https://doi.org/10.1007/s11664-012-1923-y
72. Manoharan, Subramani; Patel, Chandradip; Hunter, Stevan; McCluskey, Patrick (2018) “Mechanism of Wire Bond Shear Testing,” Microelectronics Reliability, vols. 88–90, pp. 738-744.
73. Mazzei, S.; Madia, M.; Beretta, S.; Mancaleoni, A.; Aparo, S. (2014) “Analysis of Cu-Wire Pull and Shear Test Failure Modes Under Aging Cycles and Finite Element Modelling of Si-Crack Propagation,” Microelectronics Reliability, vol. 54, iss. 11, pp. 2501-2512.

74. Shah, A.; Rezvani, A.; Mayer, M.; Zhou, Y.; Persic, J.; Moon, J.T. (2011) “Reduction of Ultrasonic Pad Stress and Aluminium Splash in Copper Ball Bonding.” Microelectronics Reliability, Elsevier, pp. 67–74.
75. Hang, C.J.; Wang, C.Q.; Mayer, M.; Tian, Y.H.; Zhou, Y.; Wang, H.H. (2008) “Growth Behaviour of Cu/Al Intermetallic Compounds and Cracks in Copper Ball Bonds During Isothermal Aging.” Microelectronics Reliability, Elsevier, pp. 416–24.
76. Anand, T.J.S.; Yau, C.K.; Huat, L.B. (2012) “Oxidation Study on As-Bonded Intermetallic of Copper Wire-Aluminium Bond Pad Metallization for Electronic Microchip.” Mater Chem Phys;136(2–3):638–47.
77. Anselm, M.K.; Ghaffarian, R. (2017) “QFN Reliability, Thermal Shock, Lead-Free vs. SnPb, Microstructure.” Thermal and Thermomechanical Phenomena in Electronic Systems (ITherm), 16th IEEE Intersociety Conference, pp. 422-427.
78. Ghaffarian, R. (2013) “Damage and Failures of CGA/BGA Assemblies under Thermal Cycling and Dynamic Loadings,” ASME International Mechanical Engineering Congress and Engineering (IMECE), San Diego, California.

Appendix B. Experimental Test Plan

In the following sections, detailed information on PCB design, assembly processes, inspection approaches, TC condition and monitoring, as well as failure analyses and characterizations are presented. Statistical analyses were performed to determine whether changes due to thermal cycling and HAST are significant relative to baseline or within environmental conditions. Baseline results for Cu wire pull strengths were also be compared with MIL-STD-883 graphs for Au wire bond pull strengths. Finally, from TC and HAST data and failure mechanisms and Cu-wire COTS packaging technologies will be categorized based on mission applications (MEAL). As mentioned previously, part selection for this investigation included a variety of Cu wire-bonded COTS PEMs packaging technologies, including BGA, QFP, and SOT. Details of CA test methods will be outlined, as will decapsulation and mechanical analysis methods, including pull and shear testing. Large components have sufficient wire bonds to achieve an acceptable reliability and confidence level, but smaller diodes and transistors require decapsulation of multiple components to achieve adequate reliability and confidence levels. This aspect was also considered during selection and design of the PCBs for environmental analysis. The test matrix for board-level evaluation will be discussed, along with process variation to replicate flight assembly processes and variation in assembly processes.

B.1 Specifications, Standards and Test Methods

The current NASA practice of **using** parts with Cu wire bonds is described below.

1. There is no NASA-wide practice for addressing use of Cu wire bond parts. However, currently, there are no MIL-PRF-38534 or MIL-PRF-38535 products with Cu wire bonds. DLA commercial item descriptions (CIDs) do not mention Cu wire bonds, and CID products may or may not have Cu wire bonds. DLA 5962 vendor item drawings (VIDs) are discussed below.
    a. Enhanced Product VID (EP VID) does not allow Cu wire bonding and it has a requirement where Sn solder shall be alloyed with Pb.
    b. Next Generation Enhanced Product VID (NEP VID) allows the use of Pb-free bumps, Pb-free solders, Pb-free finishes, or Cu wire bonding. DLA has not yet received devices proposing Cu wires.
2. For programs that use commercial parts, NASA-STD-8739.10 para 5.1.1.4 requires the designated EEE parts authority to determine if any mitigating actions are required for approval based on the requirements stated in the program or project EEE Parts Management and Control Plan – which may include destructive physical analysis (DPA) that check wire bond integrity [ref. 1].
3. Several NASA centers use EEE-INST-002 (https://nepp.nasa.gov/pages/EEE-INST-002.cfm) as the basis for EEE Parts Management and Control Plans
4. Program assurance levels 1, 2, 3 submit parts for DPA, where per MIL-STD-1580 material of the wire is identified, and bond pull strength for Cu wire is judged against MIL-STD-883 limits for Au.

The current NASA method for **evaluating** parts with Cu wire bonds is described below.

1. If a NASA project requires a destructive physical analysis (DPA), it is done per S-311-M-70 or MIL-STD-1580. Both documents require identification of wire material and performance

of bond strength tests. Currently the Cu wire is judged against pull requirements per MIL-STD-883 limits for Au. For PEMs, a bond shear test is required per JESD22-B116/JESD47

2. GSFC projects will evaluate parts per EEE-INST-002. For non-QML microcircuits and diodes used for class A, B and C programs there will be a DPA conducted per S-311-M-70 (which in turn references MIL-STD-1580)
3. JPL uses a modified version of EEE-INST-002.
4. There is no requirement or effort to collect bond pull/shear data internal to NASA centers, or across programs.

The current state of **standards** on Cu wire bond evaluation is described below.

1. NASA: No NASA standards call out anything related to Cu wire bonds, including the not-yet-released NASA-STD-8739.11 "Electrical, Electronic, Electromechanical, And Electro-Optical (EEEE Or Quad-E) Parts Selection, Testing and Derating Standard." Although NASA-STD-8739.11 does not address Cu wire bonds, it does stipulate DPA for program assurance levels 1, 2, and 3, but not 4.
2. Commercial: Manufacturers can perform qualification per AEC Q006: Qualification Requirements for Components Using Copper (Cu) Wire Interconnections.
3. Multiple documents reference Cu wire bond use for avionics or space applications site compliance with AEC Q006, including:
    a. MIL-STD-1580 "Destructive Physical Analysis for Electronic, Electromagnetic, and Electromechanical Parts" para 16.5.1.8 AS6294 "Requirements for Plastic Encapsulated Microcircuits in Military and Avionics Applications"
    b. IEC 62239-1 "Process management for avionics – Management plan – Part 1: Preparation and maintenance of an electronic components management plan - Edition 1.0"
    c. SAE ARP6379 "Processes for Application-Specific Qualification of Electrical, Electronic, and Electromechanical Parts and Sub-Assemblies for Use in Aerospace, Defense, and High Performance Systems"
4. JESD22-B120 Wire Bond Pull Test Methods is applicable to pre-encapsulated and post-encapsulated devices as well as Au alloy, Cu alloy and Ag alloy bonds. JESD22-B116B Wire Bond Shear Test Method is also applicable to pre-encapsulated and post-encapsulated devices as well as Au alloy, Cu alloy and Ag alloy bonds.
5. Work in progress for standards on Cu wire bond evaluation is described below.
    a. A JC-13 led Task Group TG-22-04 is working on adding Cu wire bonds to MIL-STD-883, Test Method 2011, Title: Bond Strength (Destructive Bond Pull Test)

B.2 Part Inspection and Analysis

Incoming inspection was performed on each of the 18 part types received. CA was performed as outlined in Section 7.2.2.1. Although low-CTE molding compounds can contain up to 85% silica inclusions within the epoxy matrix, the epoxy matrix Tg can affect the stress transmitted to the wire interconnect during thermal cycling. Therefore, the molding compounds were further assessed using thermogravimetric analysis (TGA) and DSC to determine the decomposition temperature and Tg, respectively. The analysis was performed as outlined in Section 7.2.2.2. Since the amount of material available for evaluation was insufficient to perform

thermomechanical analysis, nano-indentation was used to understand the relative mechanical strength of the molding compounds. Following material inspection and CA, components were decapsulated to reveal the bare wires. Section 7.2.2.3 describes the decapsulation methods used.

B.2.1 Construction Analysis

Baseline CA (S-311-M-70, MIL-STD-1580, Requirement 16 for guidelines) was performed on each of the 18 components in the as-received condition. The following tests were performed:

1. External visual examination of the package was performed with HIROX KH-7700, HIROC RH-2000 and Keyence VHX-7000 Digital Microscopes.
2. X-ray fluorescence (XRF) of the external package to document all metal surfaces was performed using a Fischerscope X-ray XDAL XRF.
3. Radiographic (X-ray) examination was performed using a GE Phoenix X-ray to confirm the presence of Cu wire bonds and document the device construction.
4. SAM was performed using a Sonoscan Gen 5 C-mode reflected scanner to detect any delamination within the package construction.
5. Components were cross-sectioned to determine internal device construction. Every effort was made to expose at least one ball bond and one crescent bond. As part of the cross-section analysis, internal features of the wire bond system were clearly identified. This included wire diameter, bond pad metallization thickness (below and near the bond), and splash height.
6. SEM secondary electron imaging, EDS and dot maps of the representative joints were performed using a ThermoFisher Apreo S SEM (60 mm^2 Bruker EDS detector) and a ThermoFisher Phenom XL Desktop SEM (25 mm^2 Oxford EDS detector) to identify:
    a. Composition of bond wires and any coatings on the wire (such as PCC wire and Au/Pd-coated Cu wire).
    b. Structure of bond pads, such as pillars or underlayers present under the top layer.
    c. Presence of halides (e.g., Br, Cl, iodine, fluorine) within the mold compound in quantities detectable with EDS at 2,000X.
    d. Presence of fillers such as glass beads within the mold compound.

B.2.1.2 Thermophysical Evaluation of Molding Compound

Thermal analysis was carried out via DSC, using a thermal “heat-cool-heat” cycle over a temperature range of 40 °C to 200 °C to yield the Tg. DSC was carried out using a TA Q100 DSC instrument configured in standard DSC mode with a refrigerated cooling system accessory. The PEMs were fractured/cut/crushed (using wire clippers) to allow the black epoxy pieces to be isolated (using brass tweezers) from the rest of the chip components (a single part/chip generated epoxy pieces used for both DSC and TGA, except where noted in Table B.2-1). Epoxy pieces isolated from above were placed into a tared Al DSC pan, along with a crimp-sealed Al DSC sample lid. The “heat-cool-heat” DSC scan in standard DSC mode was carried out by heating from 40 °C to 200 ºC at a rate of 10 °C/min. Upon reaching 200 °C, the sample was cooled to 40 °C at 10 °C/min, followed by immediately heating to 180 °C at 10 °C/min. The DSC sample compartment was purged with nitrogen gas (50 mL/min) during the entire DSC experiment. The purpose of this scan is twofold: 1) the Tg of the as-is epoxy may be measured, and 2) a complete cure of the material can be carried out (i.e., any residual cure can be finished curing). Once the first scan was completed, a cooling process commenced where the sample was cooled to 40 °C at a rate of 10 °C/min. Finally, the second heating scan was carried out under the same DSC

conditions as the first heat scan, but up to 180 ºC, where the absence of any residual cure exotherm verified the cure was completed during the first heat scan. Additionally, the Tg of the completely cured sample could be observed. A typical DSC thermogram is shown in Figure B.2-1. For clarity, an enlarged portion (Figure B.2-2) highlights the Tg and possible residual cure information.

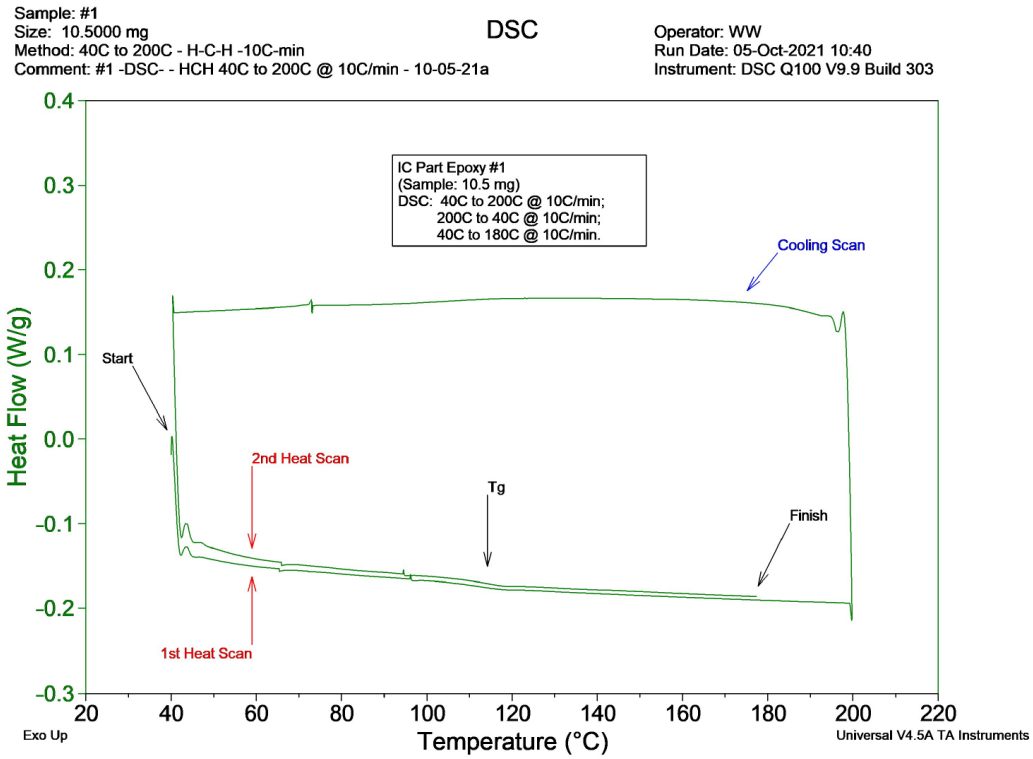

Figure B.2-1. Representative DSC Result for IC Part Epoxy

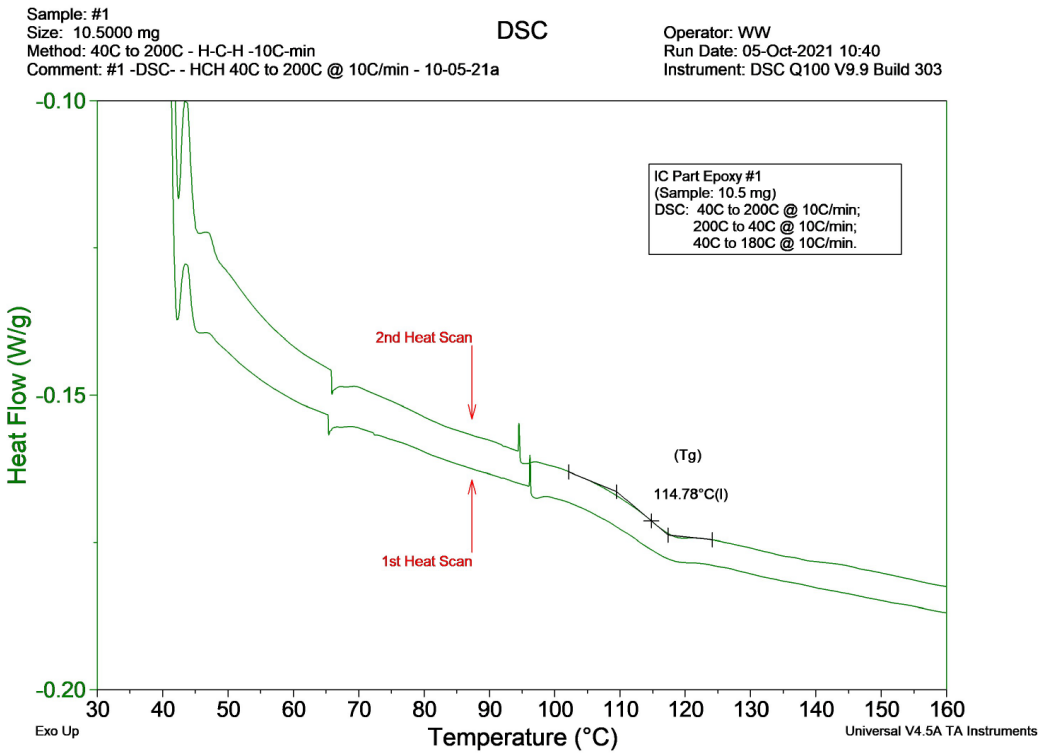

Figure B.2-2. Expanded View of DSC Result from Figure B.2-1.

The onset of thermal decomposition was measured by TGA, carried out using a TA Q500 TGA instrument configured in the standard mode. The parts were fractured as described above, and a single sample was used for both TGA and DSC analyses). Typically, one to three epoxy pieces were placed in the Pt hang-down pan and loaded into the TGA furnace. In the three instances where an intact chip was analyzed by TGA, the parts were placed with the black epoxy side facing down on the TGA sample pan. The sample was heated to 800 °C from room temperature at a ramp rate of 20 °C/min. The sample compartment was purged with nitrogen gas at 100 mL/min throughout the experiment. TGA of the epoxy molding compound found the temperature of the extrapolated onset of thermal decomposition (as seen by a significant loss in sample weight), as well as the remaining sample weight at 500 ºC and 750 ºC (Figure B.2-3).

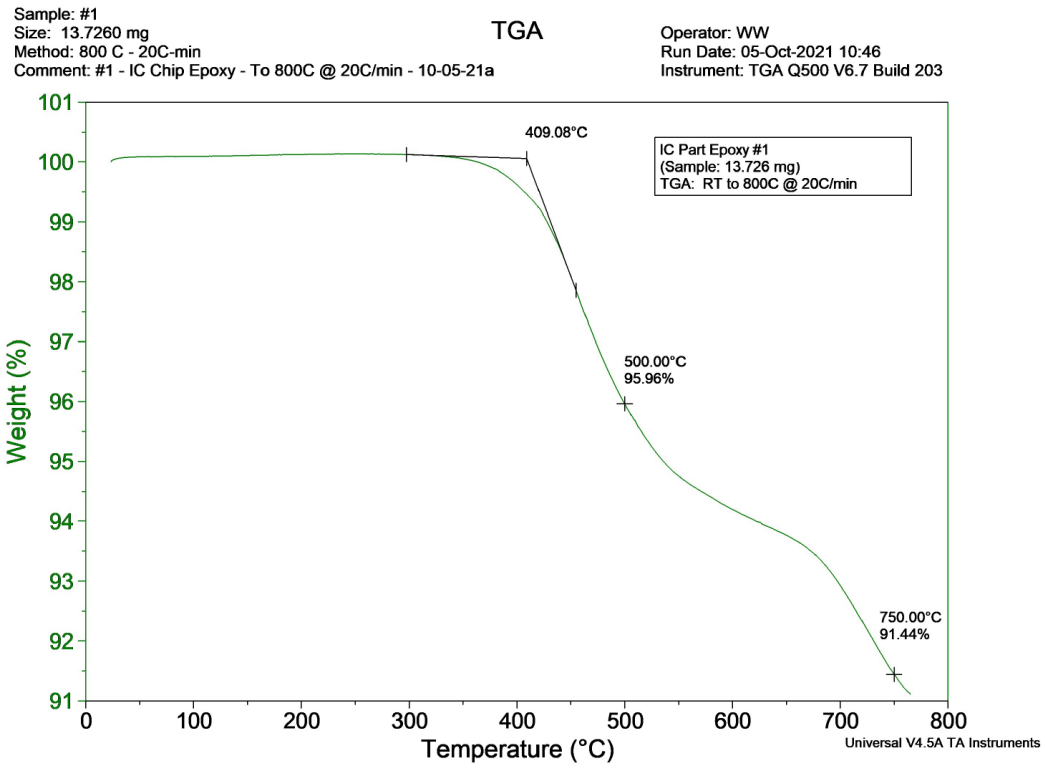

Figure B.2-3. Representative TGA Result for IC Part Epoxy

B.2.1.3 Decapsulation

Proper decapsulation is critical to the evaluation of PEMS Cu wire-bonded parts. As part of this assessment, the team used a combination of laser milling, with a CLC FALIT laser decapsulation system, and chemical decapsulation methods. Laser milling parameters, as well as chemical exposure times, temperatures, and agitation methods, were optimized to fully remove the plastic molding compound while minimizing damage to the wire and bond pads. Multiple experiments were conducted for each condition. Following exposure, parts were inspected using an optical microscope (HIROX KH-7700, HIROC RH-2000, or Keyence VHX-7000), and/or an SEM to measure wire thickness and composition. Following decapsulation, wire pull and ball shear experiments were performed. To determine the quality of the decapsulated bond wires used in this assessment, the following criteria were used:

- Wire spans, ball bonds, and stitch bonds are fully exposed.
- Wire span diameters appear consistent by optical examination.
- Leadframe at stitch bonds appears intact by optical examination.
- Wire pull break forces fall within generally expected values.
- Wire pull break locations are not obviously skewed by decapsulation processes.

Similarly, the quality of decapsulated ball bonds for ball shear data was determined using the following criteria:

- Ball bonds are fully exposed.
- Ball bonds and bond pads appear intact by optical examination.
- Ball shear failure forces fall within generally expected values.
- Ball shear failure locations do not seem to be obviously skewed by decapsulation processes.

B.3 Wire Bond Mechanical Testing Methods

B.3.1 Wire Pull

Wire pull testing for this project was performed using a Royce Instruments Model 650 multi-functional bond tester. The wire pull module selected is capable of drawing 100 g of pull force with a measuring resolution of ±0.1%. Test hooks are available in diameters between 1 and 32 mils; the test hook to be utilized is dependent on the diameter of the bond wire to be pulled.

MIL-STD-883 Method 2011, Bond Strength (Destructive Bond Pull Test), outlines the procedures for measuring the bond strengths and break locations of wires of various configurations within wire-bonded microelectronic devices. For this project, all wires were standard thermosonic double bonds, secured by a ball bond and a stitch bond, represented by Test Condition D. Wire diameters ranged from 0.7 mils to 2 mils. The entire spans of pull-tested wires were exposed through decapsulation of the surrounding plastic package material. A test hook with a diameter greater than the wire to be pulled was selected when possible. If the desired hook would not fit under a wire (e.g., due to limited clearance between tiers of multiple rows of bond wires), then the next available size down was used.

In accordance with Test Condition D, the targeted placement for the test hook was between the wire loop apex and the center of the midspan, as shown in Figure B.2-4. The intention of this placement was to distribute the pull force evenly between the ball bond and stitch bond of a wire.

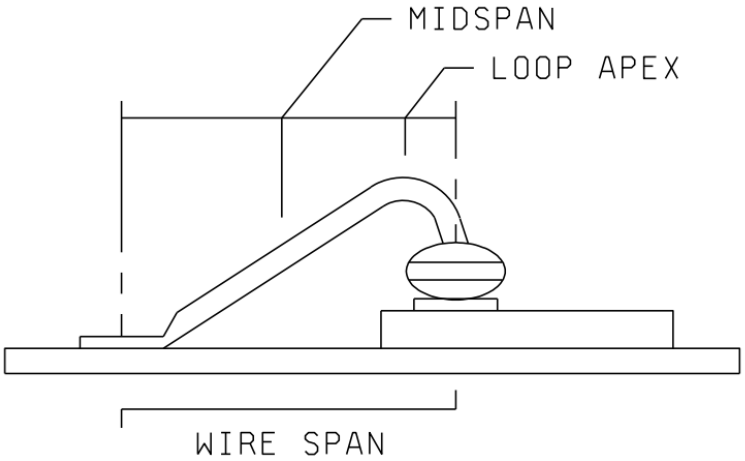

Figure B.2-4. Diagram from MIL-STD-883 Method 2011 Depicting Bond Wire Reference Locations for Hook Placement

Individual bond wires were pulled to failure, and the break forces and location of the breaks were recorded. Wire images were captured when deemed appropriate (e.g., out-of-family low break forces, anomalous break locations). Wire pull test results from bond wires partially occluded by residual mold compound or affected by operator error were not included among the data in the final report.

B.3.2 Ball Shear

Ball bond shear testing for this project was performed using a Royce Instruments Model 650 multifunctional bond tester. The ball shear module selected is capable of projecting 250 g of lateral force with a measuring resolution of ±0.1%. Shear tools are available for this module in

widths between 2 and 50 mils; the shear tool to be utilized is dependent on the diameter of the ball bond to be sheared.

MIL-STD-883 instructs an operator to perform ball shear in accordance with JESD22-B116. For this project, all ball bonds were symmetrical (basically round). Statistically representative ball bond diameters were measured optically for each part. The ball bonds of sheared wires were exposed through decapsulation of the surrounding plastic package material. A shear tool with a width greater than the ball diameter to be sheared was selected, taking care that the shear tool did not come into contact with adjacent ball bonds. The height of the shear tool's placement on a ball bond was targeted at or below the centerline, as guided by JESD22-B116 and shown in Figure B.3-1. The location of the centerline was measured using statistically representative data from cross-sectioned ball bonds or through examination of the tool's impression on ball bonds after preliminary shear testing at various tool lift heights.

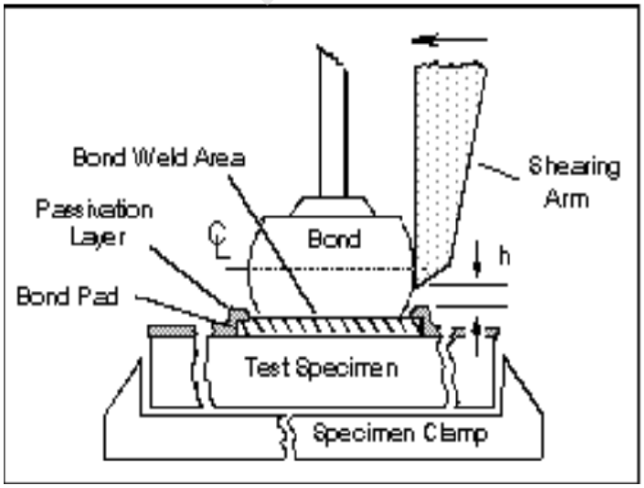

Figure B.3-1. JESD22-B116 Diagram Depicting Intended Shear Tool Placement on Ball Bond

For some parts in this project, a polyimide layer was present over the die passivation overcoat, the thickness of which may hinder appropriate placement of the shear tool at or below the centerline of the ball bond (Figure B.3-2). JESD22-B116 considers this specific circumstance, recommending that shear test results be used for qualitative rather than quantitative assessment since the torque force imparted by tool placement above the centerline can alter the correlation between test setups from ball-to-ball and unit-to-unit and change the resultant bond fail mode. JESD22-B116 does not recommend removal of the polyimide layer prior to shear testing.

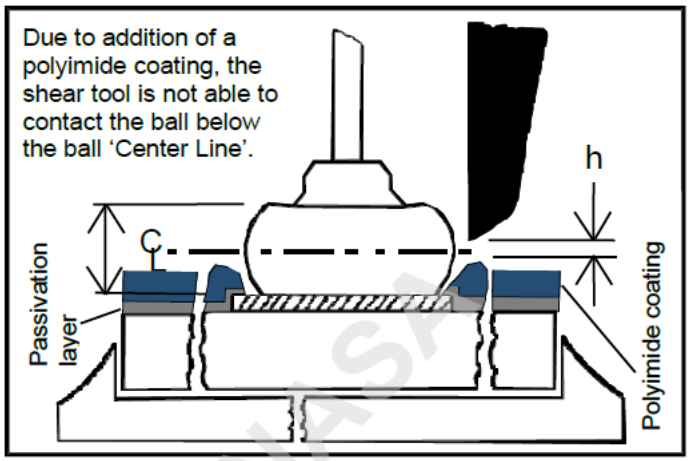

Figure B.3-2. JEDEC JESD22-B116 Diagram Depicting Polyimide Layer Restricting Appropriate Shear Tool Placement with Respect to Centerline

Individual ball bonds were sheared to failure, and the bond failure forces and locations were recorded. Images were taken of the shear tool imprint on representative ball bonds, of bond failure locations representative of each type on a given part, and when anomalous results were obtained (e.g., out-of-family shear forces, failure locations deemed to indicate potential manufacturing issues). Ball shear test results from ball bonds partially occluded by residual mold compound or affected by operator error were not included among the data in the final report.

B.4 Environmental Test

Packaging qualification, irrespective of internal configurations (e.g., Au or Cu wire bond), has been performed to determine robustness for space, military, and industry applications. The qualification tests are selected to be significantly harsher than most applications meeting the hierarchy of package, subsystem (module/assembly), and system (box). However, most tests are performed to determine comparison to their previous test versions or develop new screening approaches. Construction physical analysis has been proposed for Cu wire bond evaluation for military applications. A number of specifications for qualification of PEMs with internal Cu wire bonds were reviewed to narrow selection with consideration applicability for wider NASA missions. However, the results should be reviewed for each specific project's MEAL requirements

The characteristics of three elements—package, PCB, and solder joint interconnections—together with the mission environmental conditions, design life, and acceptance failure probability for the electronic assembly determine the reliability of various electronics assemblies. Thermal stress and cycling at package and assembly level with predication models are briefly discussed in the following sections.

B.4.1 Thermal Stress for Packaging

Packaging materials and structures are chosen to meet the demands of devices used in conventional environments. Cu wire bonding is rapidly replacing Au wire bonding for commercial applications with application history and a well-established reliability. The encapsulation in COTS is replacing the metal seal. Encapsulants are selected based on their ability to encase and protect the die over commercial temperature ranges, and the metal seal selected according to how well they conduct current into and out of chips. In addition to their

electrical conduction function, metals are used in packaging as mechanical supports, to conduct heat away (i.e., heat sinks), and to seal internal contents. Ceramics like aluminum oxide (Al_2O_3) also serve as containers for chips and often substrates for mounting semiconductor devices. Polymers are used to encase chips and are employed in PCBs for mounting the packages.

Si devices inside packages degrade under thermal stresses. Many Si device degradation mechanisms are thermally activated, and the device reliability is a strong function of temperature and operating voltage. The higher the temperature, the greater the degradation mechanisms, such as interdiffusion through interconnection, latch-up, noise, and heat. For thermally activated failure mechanisms, relative improvement in mean time to failure (MTTF) with reduction in temperature is proportional to a temperature-dependent term expressed by the Arrhenius relation

$$\text{MTTF} \sim \exp\left(E_a / K\,T\right) \qquad (1)$$

where E_a is the activation energy of a given thermal process, T is absolute temperature, and K is Boltzmann's constant. E_a will typically range between 0.3-1.2 eV. A lower value of E_a implies that the temperature effect is less significant for a failure mechanism than the one with higher E_a.

B.4.2 Thermal Stress for SMT Assembly

A majority of fatigue failures of solder joints in surface mount assemblies are due to global CTE mismatch induced damage while early premature failure may be due to workmanship anomalies and local interfacial integrity deficiencies [ref. 2]. The global expansion mismatches result from differential CTE of a package and the PCB assembly. These stem from differences in the CTEs and thermal gradients as a result of heat dissipation from functional die within the package.

Global CTE mismatches typically range from $\Delta\alpha$~2 ppm/°C ($2x10^{-6}$) for CTE-tailored high reliability assemblies to $\Delta\alpha$ ~14 ppm/°C for ceramic packages on FR-4 PCBs. The shear strain representative of the global CTE mismatch due to thermal excursion is given as:

$$\gamma = (\alpha C - \alpha S)\,(Tc - T0)\,L/H = (\Delta\alpha)\,(\Delta T)\,LD/H \qquad (2)$$

Global CTE mismatches typically are the largest, since all three parameters determining the thermal expansion mismatch, i.e., the CTE mismatch ($\Delta\alpha$), the temperature swing (ΔT), and the largest acting package length (L_D), also known as distance to neutral point (DNP), can be large. In thermal cycling, this global expansion mismatch will cyclically stress, and thus fatigue, the solder joints.

The cumulative fatigue damage will ultimately cause the failure of one of the solder joints, typically a corner joint in a ceramic package, causing permanent functional electrical failure that initially may be intermittent. The shear strain representing damage in each cycle is proportional to $\Delta\alpha$, ΔT, and L_D, and inversely proportional to the package/PCB separation height (H).

The local expansion mismatch results from differential thermal expansions of the solder and the base material of the package or PCB assembly. These thermal expansion differences result from differences in the solder CTE and those of the base materials together with thermal excursions. Local CTE mismatches typically range from $\Delta\alpha$ ~7 ppm/°C with Cu to ~18 ppm/°C with ceramic. Local thermal expansion mismatches typically are smaller than the global expansion mismatches, since the acting distance, the maximum wetted area dimension, is much smaller in the order of tens of mils, e.g., 20 mils for a typical column diameter.

Solder alloy CTE mismatch covers microstructural changes due to the solder alloy being a mixture of two or more elements. The grain structure of Sn63Pb37 solder is inherently unstable. The grains will grow in size over time as the grain structure reduces the internal energy of a fine-grained structure. This grain growth process is enhanced by exposures at elevated temperatures and strain energy input during cyclic loading. The grain growth process is thus an indication of the accumulating fatigue damage.

Interconnection failure within the package should also be considered in the overall system life cycle projection. The weakest link among the interconnections defines the CTF. In most cases, solder joints onto a board constitute the weakest link under TC fatigue. Further discussion on this topic is presented in subsequent sections.

B.4.2.1 Thermal Stress and Fatigue for Cu-Wire Bond

For certain Cu wire bond COTS packages, failure mechanisms may be affected significantly by chip-level local heat dissipation. The heat stresses on wire bond interconnections and stresses due to local CTE mismatch between Cu and EMCs may also become significant. In addition, for no-lead packaging configurations (e.g., QFN, BGA) there is a global interaction that also affects failure type at the wire bond within package or solder joint at the board assembly level.

Even though failure mechanisms for Cu wire COTS packages under thermal stress are complex to predict, mechanical fatigue characteristics and life projection for Cu wire bonds alone are similar to other metallic elements and is well understood. Figure B.4-1 shows an example of such characterization for Cu wire bonds [ref. 3]. The total fatigue life plot is for a symmetrical loading condition (R = -1) based on test data for high cycle fatigue (HCF) and using the Goodman equation for projecting low cycle fatigue (LCF) data. There are two distinct regions, LCF and HFC, with a sharp transition for as-received and with reduction in annealed condition, representative of Cu-wire bond HAZ.

Figure B.4-2 shows a minimum pull-strength reduction in Au wire bonds on pure Al pads, whereas a significant reduction in shear strength with aging time at 200 ℃ occurs due to Au-Al intermetallic formation and possibly some Kirkendall voiding [ref. 4]. It appears that for the Au wire bond, shear strength integrity of the bond, which depends on ball bond area, is the most critical parameter under isothermal heat exposure or temperature rise, due to power dissipation from the die. This trend is yet to be verified for Cu wire bond, for which isothermal annealing and corrosion could further exacerbate strength reduction. In addition, failure mechanisms may change from shear to tensile under thermal cycling condition. One of the objectives of the assembly thermal cycling tests under this task is to determine the failure mechanisms for various Cu wire bond COTS packaging technologies and find the weakest failure between local and global thermal stress conditions.

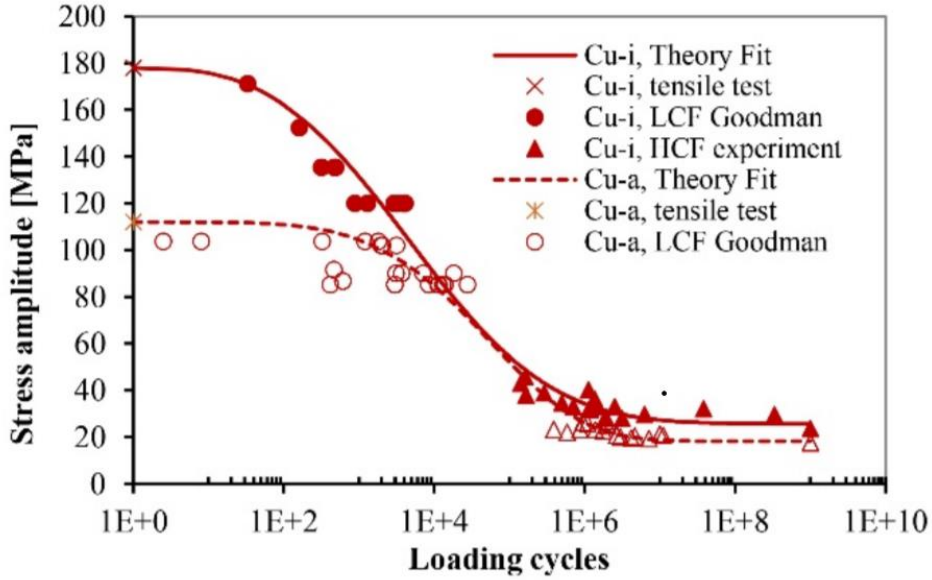

Figure B.4-1. LCF and HCF Test Data for Cu Wire Bond for As-Received and Annealed Conditions

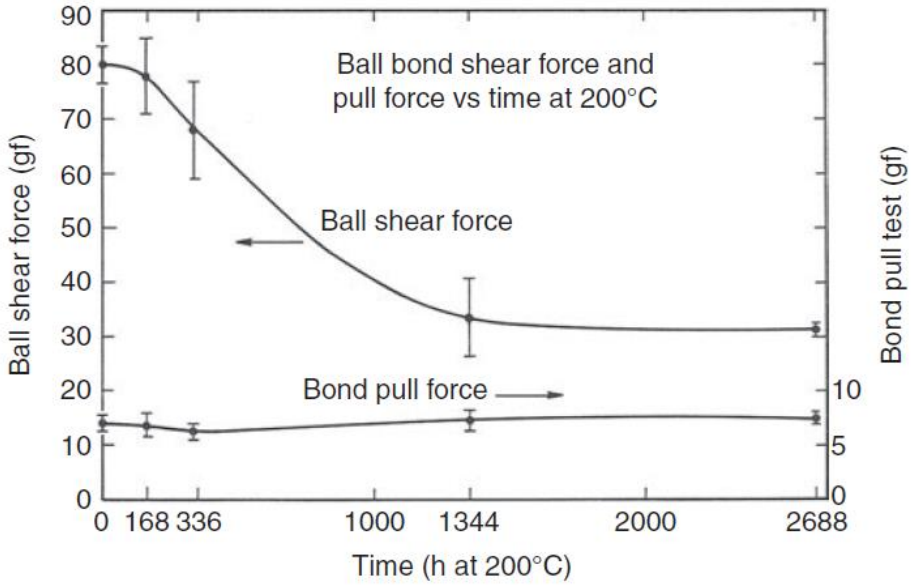

Figure B.4-2. Au-Ball Reduction in Shear and Stabilization in Pull Force With Exposure Time at 200 ℃ for 1 mil Diameter Au on Pure Al.

B.4.2.2 Thermal Fatigue Prediction Models for SMT Assembly

Predicting solder joint fatigue failure under thermal cycling stress has been one of the challenging problems for microelectronic packaging and assembly. Early solder joint fatigue models were developed based on experimental thermal cycling tests using strain gauges, therefore, mostly correlated to strains. As package size decreased, finite element analysis (FEA) became a more popular approach for estimating strains for SMT assemblies. The Coffin-Manson relationship, perhaps the best known and most widely used model, was developed for aerospace

metals and was considered for SnPb solder. The model relates total CTFs to the plastic strain amplitude and the fatigue ductility coefficient and exponential.

Many fatigue models are based on modification of the Coffin-Manson relationship. One of the long-standing models used in solder fatigue analysis is the Norris and Landzberg model. This relationship has been applied to project thermal CTFs for a number of conventional and advanced packaging assemblies based on accelerated test data. It is one of numerous parametric modeling analysis methods that have been proposed and used by industry to project CTFs from one TC condition to a field application. A number of models for life extrapolation of SnPb solder-joint attachments were summarized in reference 5.

In the Coffin-Manson relationship, CTF is inversely proportional to the creep strain. Its modified version includes the effects of frequency and the maximum temperature. The Norris Landzberg relationship is given by:

$$(N_1/N_2) \propto (\Delta\gamma_2/\Delta\gamma_1)^{\theta} \ (f_1/f_2)^{\kappa} \exp\{(1414\ (1/T_1 - 1/T_2)\} \qquad (3)$$

N_1 and N_2 represent CTF under two plastic strain conditions. θ is the fatigue exponential and is generally assumed equal to 1.9.

- $\Delta\gamma$ is proportional to (DNP/h) $\Delta\alpha\ \Delta T$, where *DNP* is the distance from the neutral point at the center of the package, *h* is equal to the solder joint height, $\Delta\alpha$ is the difference in the CTE of the package and PCB, and ΔT is the cycling temperature range, as described in equation 2.
- f_1 and f_2 are fatigue frequencies. κ is the frequency exponential varying from 0 to 1, with value 0 for no frequency effect and 1 for the maximum effect, depending on materials and testing conditions. A value equal to 1/3 is commonly used to extrapolate the laboratory accelerated TCs-to-failure data having short duration (high frequency) to on/off field operating cycles having long duration (low frequency), i.e., a shorter field cycles-to-failure projection.
- T_1 and T_2 are maximum temperatures (in degrees Kelvin) under the two cycling conditions such as field and use conditions.
- The Norris-Landzberg model was developed for controlled collapse connections from thermal cycling data over a variety of temperature ranges for alloys consisting of high Pb content solder.

B.4.2.3 Test Matrix and Key Parameter Considered for Testing

As mentioned previously, part selection for this investigation included a variety of Cu wire-bonded COTS packaging technologies, including BGA, QFP, and SOT. Large components have sufficient wire bonds to achieve an acceptable reliability and confidence level, but smaller diodes and transistors require decapsulation of multiple components to achieve adequate reliability and confidence levels. This aspect was also considered during parts selection and PCB design.

The test matrix also includes variation in assembly processes. First, an assembly process profile was developed using a spare board, parts, thermocouples, and a thermal profiler for monitoring temperature variation. Once the reflow profile was established, an assembly was built for functional verification. As part of the test matrix, to represent a flight condition, even a single-sided board went through one additional reflow cycle to represent a double-sided assembly condition. In addition, two leads from each corner of each leaded part were reflowed with a soldering iron to capture the effect of rework on internal Cu-wire bond interconnections.

The TC profile was developed using representative scrap boards with thermocouples attached to optimize the profile for various board locations in a chamber. A number of trial runs were carried out to tailor the profile with a compromise between desired ramp rate, dwell time and chamber location.

B.5 Test Board Design

The 18 part numbers used in this investigation were designed to be powered up on boards with DC bias to assess the reliability of wire bonds under electrical stresses. For simplicity of exercising 18 part numbers at the same time, the parts were not intended to be switched during environmental testing. To facilitate powering of the components, additional passive devices were designed into the circuit to simulate loads.

In total, 4535 parts across 18 part numbers were assembled on 20 boards for this investigation—see Table B.5-1 for a list of parts and what boards they were assembled on. Due to low quantity of PN M4-MCK-FBGA256-01, only 7 boards were assembled with this part, with 5 components on each board. The rest of the part numbers had 100-400 units assembled in total. The table also notes bias applied to power pins.

Table B.5-1. List of 18 Parts Distributed Among Boards

Part Number	PCB #	PCB Qty	Parts/PCB	MSL	Bake (C)	Bias on Board (V)
M1-MCK-SOIC8-01	1	10	20	1	-	3.3
M5-MCK-SOIC8-01	1	10	20	1	-	18
M5-MCK-VSSOP8-01	1	10	20	1	-	18
M5-MCK-WSON6-01	1	10	40	1	-	3.3
M5-MCK-SOT235-01	1	10	20	1	-	3.3
M5-D-SOT-233-01	1	10	40	1	-	3.3
M4-MCK-FBGA256-01 (only sublot 1)	1	7	5	3	125	3.3
M3-MCK-TQFP100-01	1	10	10	3	125	3.3
M7-MCK-LFBGA169-01	1	10	10	3	125	3.3
M2-D-SOT233-02	2	10	40	1	-	18
M2-D-SOT233-01	2	10	40	1	-	18
M6-D-SOT-235-01	2	10	40	1	-	3.3
M9-D-CUSTOM-01	2	10	40	1	-	18
M10-D-SOD323-01	2	10	40	1	-	18
M10-D-SOT1061-01	2	10	40	1	-	18
M1-MCK-LFBGA144-01	2	10	10	3	125	3.3
M8-MCK-LQFP100-01	2	10	10	3	125	3.3
M11-MCK-TQFP144-01	2	10	10	3	125	3.3 and 1.2

Includes moisture sensitivity level (MSL), bake-out information and biasing voltage during test.

B.5.1 Assembly Process and Touch-Up

Printed Wiring Boards (PWBs) were built at an outside board house using polyimide cores, 1 oz Cu, total of 6 layers, hot air solder leveling (HASL) finish, and with final board thickness of 0.062 inch. Upon examining boards after delivery, the HASL finish was noted to be uneven, and excess solder was manually wicked off the pads of BGA components to allow BGA components

to sit evenly on the board. Boards were baked out at 93 °C for 2 hr to remove moisture, then placed in dry nitrogen storage until needed for assembly.

Parts used in the study are a mix of moisture sensitivity levels (MSL), including MSL1 and MSL3. All original packages were opened for more than a year prior to assembly and intermittently taken out of dry nitrogen storage to separate parts for baseline CA. Prior to board assembly, all parts labeled as MSL3 (PNs M4-MCK-FBGA256-01, M3-MCK-TQFP100-01, M7-MCK-LFBGA169-01, M1-MCK-LFBGA144-01, M8-MCK-LQFP100-01, M11-MCK-TQFP144-01) were baked out for 49 hr at 125 °C to avoid popcorning during assembly. Afterwards, all parts were stored in dry nitrogen purge. For kitting, parts were removed for several hours from dry nitrogen storage and returned to dry nitrogen storage after kitting.

For assembly, solder (Sn63-Pb37) was added to the pads through a stencil, and parts were placed on boards using a pick-and-place machine. Boards were reflowed in a belt oven twice to simulate two-sided assembly. Figure B.5-1 shows an exemplar reflow temperature versus time profile captured during board assembly. Each board had a serial number and a traveler for traceability.

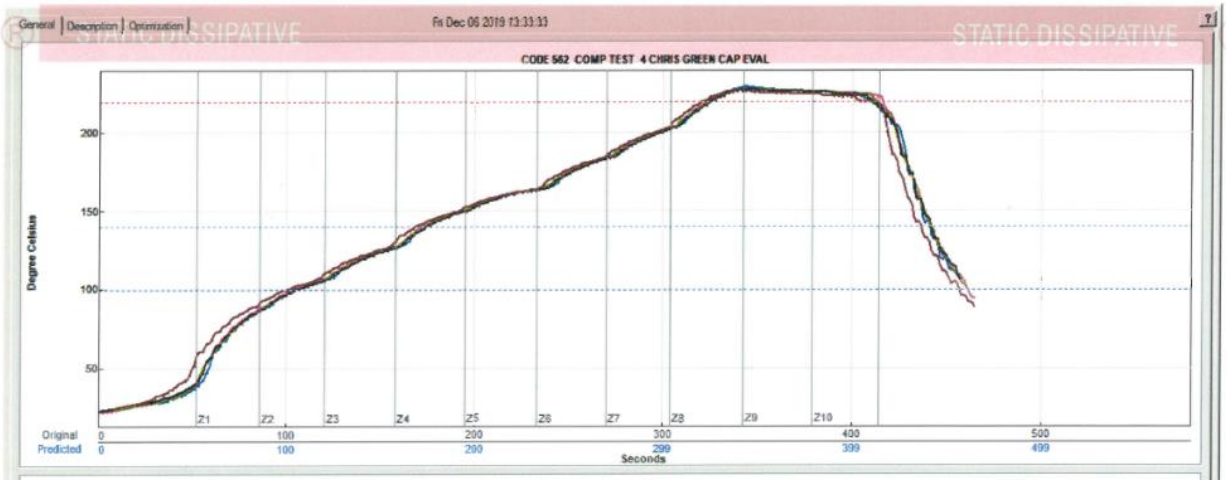

Figure B.5-1. Example of Reflow Profile Used for Boards in This Study

After two reflow cycles, boards were cleaned in an automated board cleaning machine using:

- 4-minute wash cycle with Axarel 2200 @ 29 ℃
- 60-second drip time
- 60-second rinse with deionized water
- 120-second water knife up/down
- Hot air for 6 seconds stepped for every half-inch @ 120 ℃

Boards were then dried in an oven at 60 ℃ for 4 hr.

After assembly, boards were inspected, and touch-up performed using a soldering iron to (1) separate any bridging pins and (2) simulate touch-up on one unit for each leaded part on board. See Figure B.5-2 for touch-up locations on both boards.

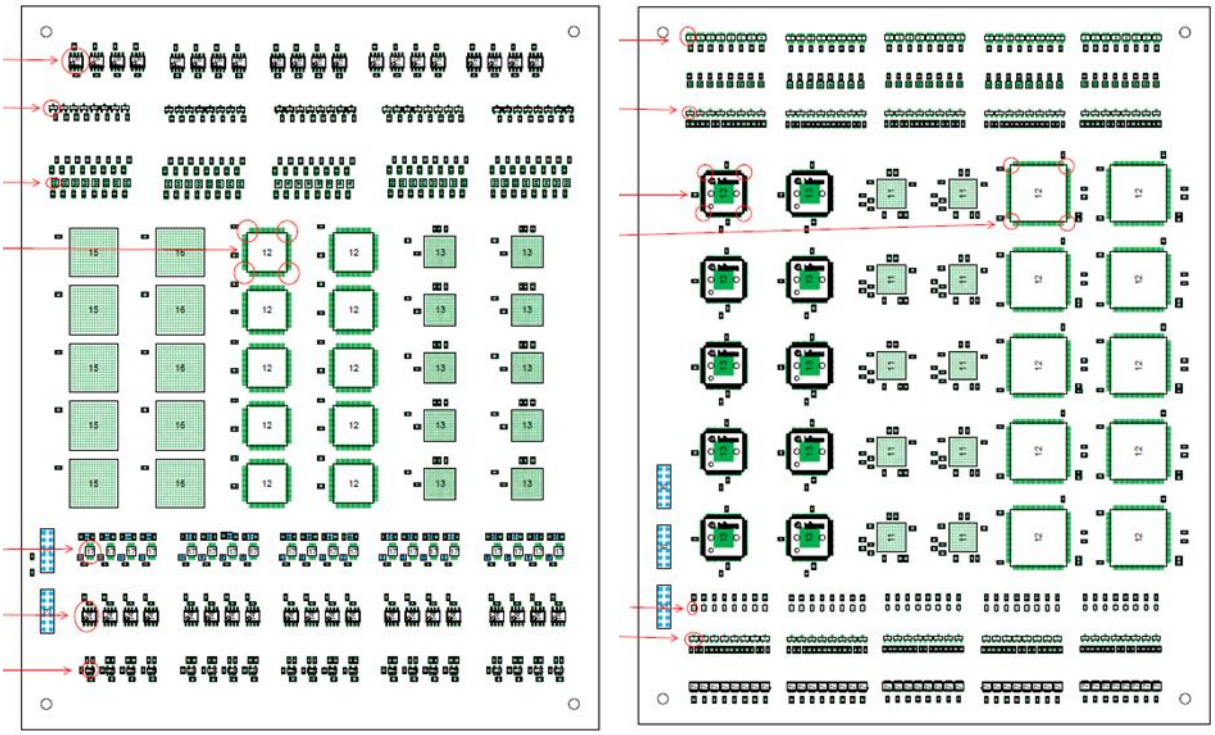

Figure B.5-2. Touch-Up Areas Highlighted in Red on PWB1, left, and PWB2, right

B.5.2 Post-Assembly Inspection: X-ray and Infrared

After assembly, boards were X-rayed to judge the quality of solder joints under BGA components that could not be visually inspected. A total of three part numbers with BGA configuration are present across the boards. Examples of X-ray images indicating the presence of defects are shown in Figures B.5-3 and B.5-4. Inspection results are provided in Table B.5-2.

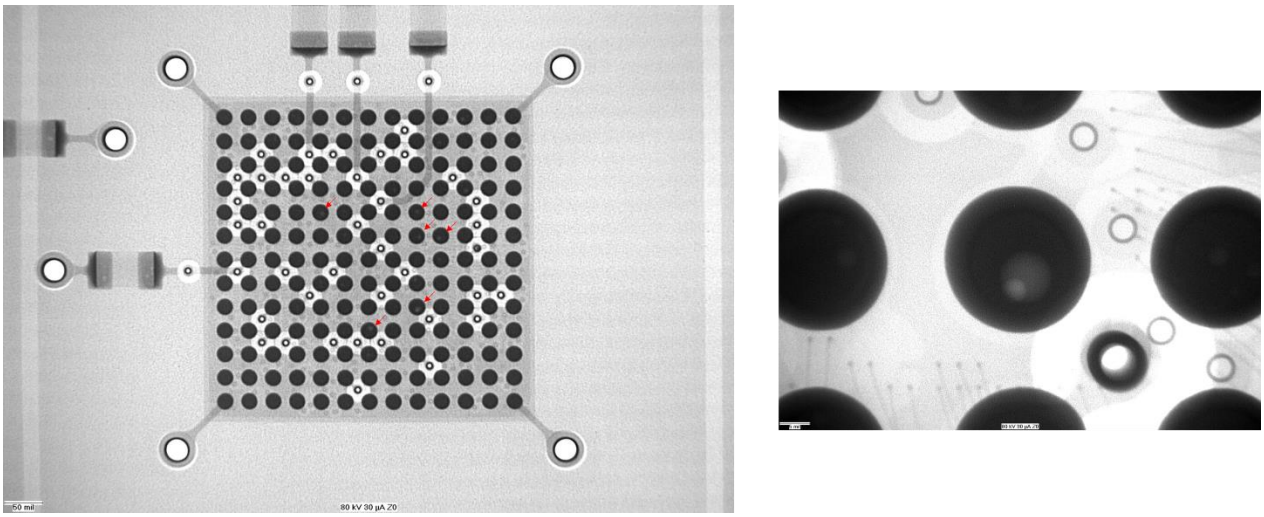

Figure B.5-3. Example of Voids Seen, from PCB1-S1-SN4 M7-MCK-LFBGA169-01 SN B21. Left, overview of device with arrows pointing to voids in solder balls. Right, close-up view of void.

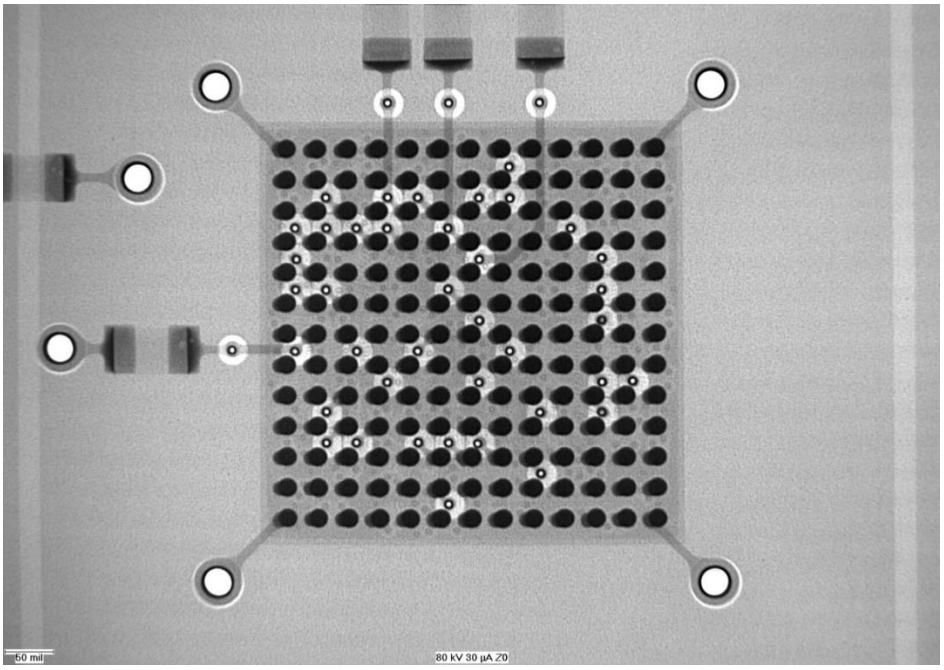

Figure B.5-4. Example of Skewed Component Observed During X-Ray Example from PCB1-S1-SN4 PN M7-MCK-LFBGA169-01 SN B14

Table B.5-2. Summary of X-ray Inspection of BGA Components

PCB#	Inspection comments	Board Used for pull/shear analysis after environmental exposure?
PCB1-S1-SN2	No bridging; M7-MCK-LFBGA169-01 SN B12 skewed/misaligned	
PCB1-S1-SN4	No bridging; a few voids in solder balls for PN M7-MCK-LFBGA169-01 SN B21; SN B14 skewed	Yes, after 1000 temperature cycles. Units with X-ray anomalies not examined.
PCB1-S1-SN5	No bridging; no other anomalies	Yes, after 2000 temperature cycles.
PCB1-S1-SN6	No bridging; no other anomalies	
PCB1-S1-SN7	No bridging; noticeable voids in solder balls	Yes, after 500 hr of HAST.
PCB1-S1-SN9	No bridging; PN M7-MCK-LFBGA169-01 SN B24 skewed; SN B21 and SN B25 slight misalignment	
PCB1-S1-SN10	No bridging; no other anomalies	
PCB1-S2-SN12	No bridging; no other anomalies	
PCB1-S2-SN13	No bridging; no other anomalies	
PCB1-S2-SN15	PN M7-MCK-LFBGA169-01SN B21 small spurious solder ball splash; no other anomalies	
PCB2-SN2	No bridging; PN M1-MCK-LFBGA144-01 SN35, SN34, SN45 slightly skewed	
PCB2-SN3	No bridging; PN M1-MCK-LFBGA144-01 SN35, SN32, SN45, SN41 slightly skewed	
PCB2-SN4	No bridging; PN M1-MCK-LFBGA144-01 SN31, SN45, SN44 slightly skewed, SN41 minor skew	
PCB2-SN7	No bridging; PN M1-MCK-LFBGA144-01 SN35, SN33, SN44, SN41 slightly skewed, solder ball voids noted in SN33 and SN42	
PCB2-SN9	No bridging; PN M1-MCK-LFBGA144-01 SN44 slightly skewed	Yes, after 2000 temperature cycles. Units with X-ray anomaly not examined.
PCB2-SN10	No bridging; no other anomalies	
PCB2-SN11	No bridging; PN M1-MCK-LFBGA144-01 SN 43 and SN41 skewed, several very small solder splash balls	
PCB2-SN18	No bridging; PN M1-MCK-LFBGA144-01 SN33 skewed and voids in the solder balls	
PCB2-SN19	No bridging; PN M1-MCK-LFBGA144-01 SN41 slightly skewed, minor solder ball voids	
PCB2-SN20	No bridging; PN M1-MCK-LFBGA144-01 SN42 slightly skewed, minor solder ball voids, one very small solder ball splash	Yes, after 500 hr of HAST. Units with X-ray anomaly not examined.

Several anomalies noted related to solder voids and skewing of parts.
None of the parts identified as anomalous were used in further inspection.

After board assembly and X-ray, infrared inspection was used to check the temperature parts would reach when powered up. A FLIR A8580 mid-infrared camera was used to examine the boards, as they were powered at intended voltages. See Table B.5-3 for a summary of maximum temperatures observed on the boards along with current levels. On PCB1, PN M5-MCK-SOIC8-01 showed a temperature rise of 33 ℃. All other components showed temperature rises of 5 ℃ or less. See infrared images in Figure B.5-5. On PCB2, PN M1-MCK-LFBGA144-01 reached the highest temperature on the board at ~30 ℃, or ~3 ℃ above ambient. This is considered to be a negligible temperature rise. See infrared image in Figure B.5-6.

The temperature rise on PN M5-MCK-SOIC8-01 was the deciding factor for the maximum temperature of HAST exposure, limiting it to 110 °C/85% RH to avoid running the part above its maximum operating junction temperature of 150 ℃. However, for temperature cycling, the maximum temperature was kept at 125 ℃, despite the possibility to be above the maximum operating junction temperature for PN M5-MCK-SOIC8-01.

Table B.5-3. Temperature Rise and Current Levels on Boards Powered on Bench at 27 ℃ Ambient Temperature Under Intended Bias

Board	Max temp rise (℃)	Relative temp rise (℃)	Current on 3.3V (Amp)	Current on 18V (Amp)	Current on 1.2V (Amp)
PCB1-S1-SN2	60	33	0.55	0.38	
PCB1-S1-SN7	60	33	0.28	0.38	
PCB2-SN10	45	18	0.8	0.8	0.0999
PCB2-SN20	32	5	0.797	0.8	0.0999

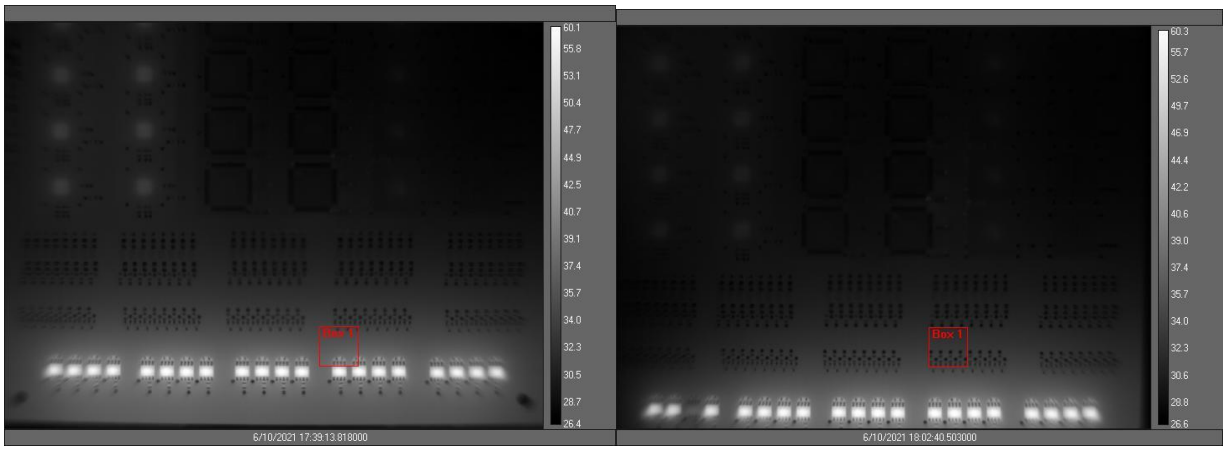

Figure B.5-5. Infrared Images of PCB1-S1-SN2 (left) and PCB1-S1-SN7 (right) of Areas on Board with PN M5-MCK-SOIC8-01 Heating Up to ~60 ℃ (or ~33 ℃ above ambient). Note that on PCB1-S1-SN7 (right image) one unit of PN M5-MCK-SOIC8-01 appears to be disconnected and not drawing power. PN M5-MCK-SOIC8-01 is connected only to 18V supply and did not show noticeable difference in current draw between the two boards.

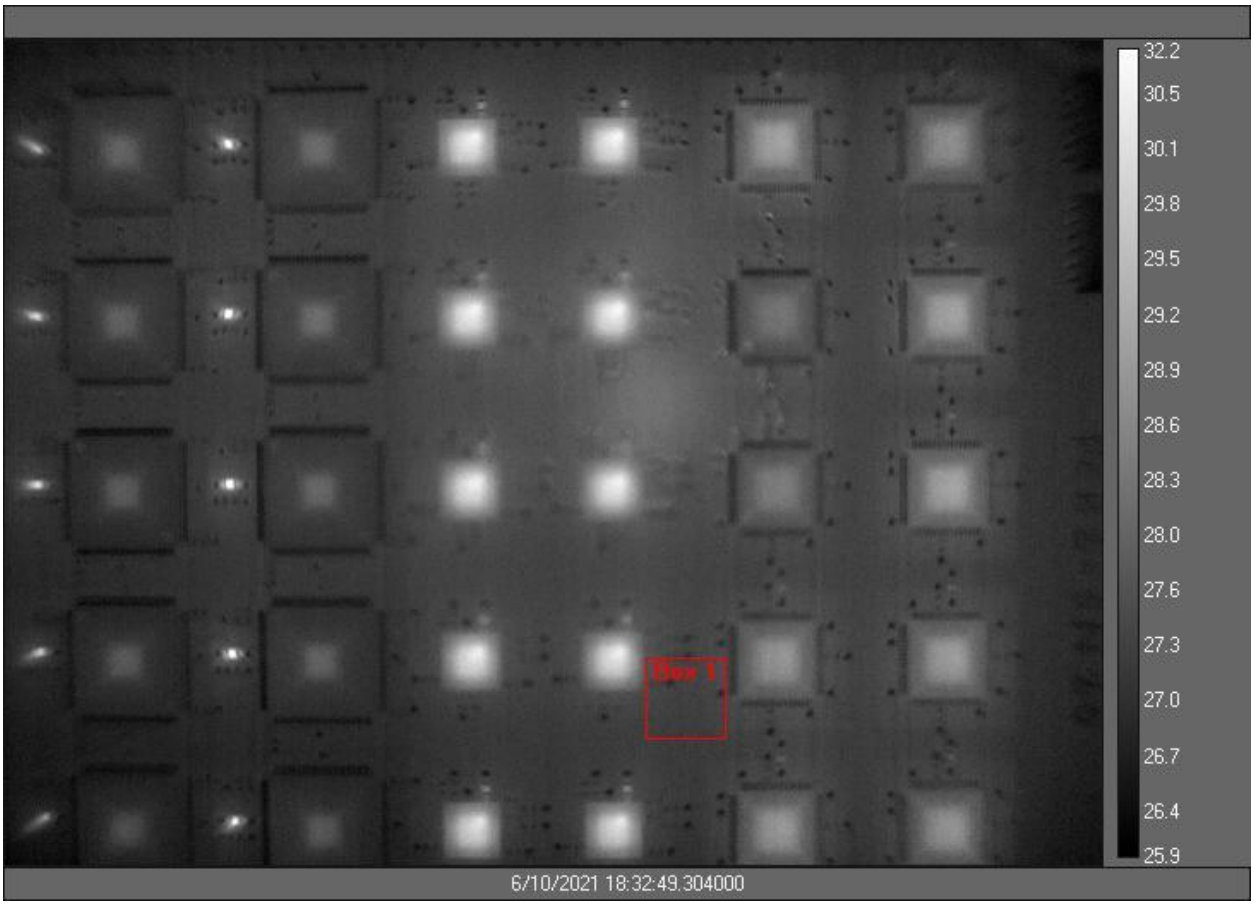

Figure B.5-6. Infrared Image Showing PCB2-SN20 with Warmest Components Being PN M1-MCK-LFBGA144-01 (two columns in center) and Resistors for PN M8-MCK-LQFP100-01 (two columns on the left), both reaching ~30 ℃, or ~3 ℃ above ambient

B.6 Test Matrix for Cu-Wire Bond Reliability Evaluation

The overall test plan was developed based on tailoring test types at package level (e.g., HAST) and at assembly level (e.g., solder joint reliability) to envelop most NASA MEAL requirements. Synergism of HAST and TCs was evaluated by subjecting a limited number of assemblies to thermal cycling and HAST. Surface mount reflow was considered since there were a number of BGAs. For leaded parts, touch-ups with a soldering iron were performed at selective critical leads to determine the effect of local soldering touch-up, a normal process for rework of leaded parts for high-reliability applications. Required sample size, especially for low lead counts, e.g., SOTs, was another aspect of the test plan that was considered for providing adequate reliability and confidence levels, which became a challenge for select parts with only one or two bonds.

B.6.1 HAST for Cu-Wire Bond Assemblies

Although the evaluation was performed at the assembly level, AEC (automotive) and IBM (commercial) specifications were considered in the test matrix development for HAST. Table B.6-1 presents a brief comparison of the two industry specifications covering biased/unbiased HASTs for Cu wire bond COTS/PEMS. None of the specifications considers the effect of soldering touch-up, which is applicable at assembly level. This test matrix could implement such evaluation.

Table B.6-1. Summary Comparing HAST and TC Tests Proposed by AEC and IBM

AEC: Integrated IC TC= -55C/150C, 1000, RH85%/85C, 110C, 130C 1000, 264, 96 hr, -40/125C, 1000 hr, HTS 150C, 175C, 1000hr **IBM: 57G9271** BHAST, 85RH/85,110 or 130, 1000,200 or50, -55/125C, 700 cy, 2nd level, 0/100C, 1000, HTS 125C, 150, 200C, 2000,1000,72 hr BHAST, 85RH/85,110 or 130, 1000,200 or50, -55/125C, 700 cy, 2nd level, 0/100C, 1000, HTS 125C, 150, 200C, 2000,1000,72 hr

Figure B.6-1 presents the HAST matrix. Synergism of HAST and TC is shown with two red arrows indicating that after 100 hr of HAST, two PCBs (as identified) were removed and added to the thermal cycling chamber. This approach also accommodated the chamber size limitation. At the end of testing, two sets of PCBs completed 400 and 500 hr of bHAST. HAST was performed at 85% RH and 110 ℃. Refer to test implementation in Section B.7 for more detailed information.

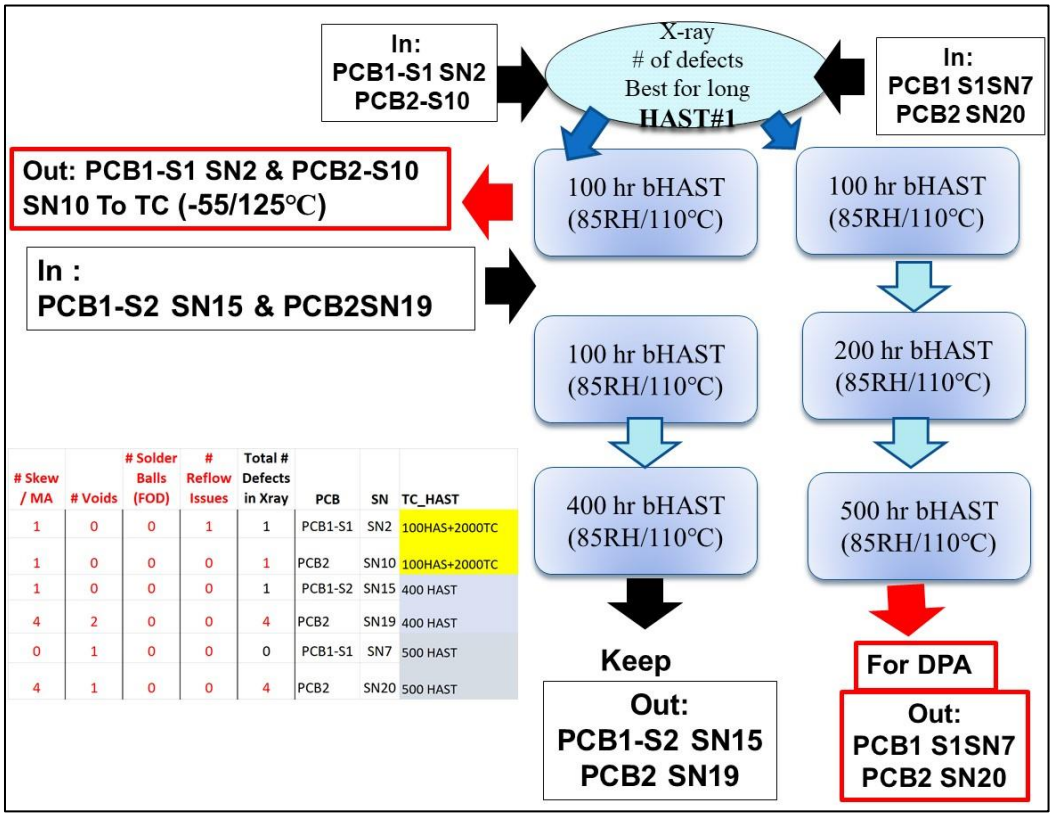

# Skew / MA	# Voids	# Solder Balls (FOD)	# Reflow Issues	Total # Defects in Xray	PCB	SN	TC_HAST
1	0	0	1	1	PCB1-S1	SN2	100HAS+2000TC
1	0	0	0	1	PCB2	SN10	100HAS+2000TC
1	0	0	0	1	PCB1-S2	SN15	400 HAST
4	2	0	0	4	PCB2	SN19	400 HAST
0	1	0	0	0	PCB1-S1	SN7	500 HAST
4	1	0	0	4	PCB2	SN20	500 HAST

Figure B.6-1. Schematic of HAST Plan of Cu-Wire COTS Packages. Red Arrows Show PCBs Removal After HAST Exposure for Adding to Thermal Cycling Chamber.

B.6.1.1 Assembly: Accelerated Test for Cu-Wire Bond/Solder

Tailoring the Cu-wire COTS test plan to achieve the project task goal of obtaining MEAL projections for various NASA missions was not straightforward, since it depended on packaging technologies and robustness under thermomechanical conditions if other parameters, e.g., radiation, were considered acceptable. For standard packaging technologies, MEAL projections are simpler because of the general robustness of solder joints at the assembly level. However, there is no established reliability for high-density packaging technologies, specifically for an internal Cu-wire-bond interconnection having many unknown failure mechanisms.

If it is assumed that the solder joint at assembly level becomes the weakest link in failure, then MEAL can be projected for various NASA missions. If Cu wire bond interconnections become the weakest link, however, then correlations for HAST/CTFs are to be established internally within chip-level interface and externally for packaging material characterizations. The relationship between the internal shear/tensile strengths of Cu wire bonds and associated IMCs and external packaging materials, including the Tg and chemical composition of molding compounds, must be established.

Figure B.6-2 shows a test matrix that was developed to address the MEAL consideration. As such, this matrix includes the evaluation of TC behavior of various packaging assemblies and addresses the synergism between a priori HAST condition and subsequent TCs. Samples are to be removed at specific cycles to track back initial failures, if observed, after 2000 TC. Thermal cycling is performed in the range of -55 ℃ to 125 ℃.

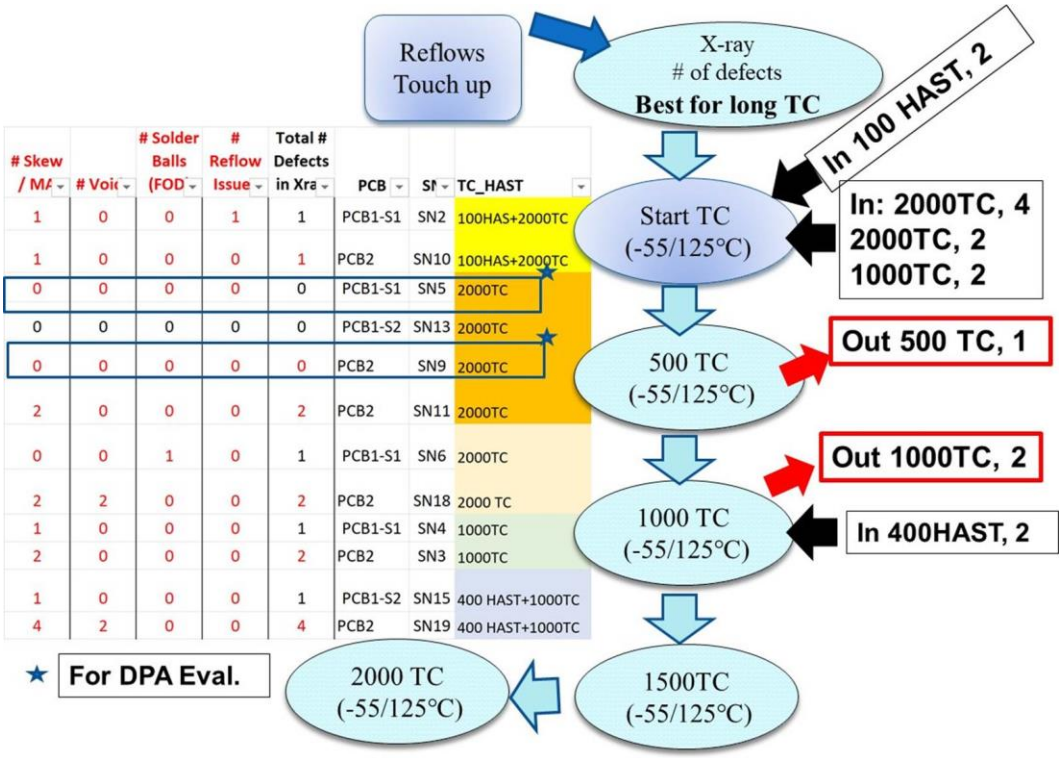

# Skew / MA	# Voi	# Solder Balls (FOD	# Reflow Issue	Total # Defects in Xra	PCB	SN	TC_HAST
1	0	0	1	1	PCB1-S1	SN2	100HAS+2000TC
1	0	0	0	1	PCB2	SN10	100HAS+2000TC
0	0	0	0	0	PCB1-S1	SN5	2000TC
0	0	0	0	0	PCB1-S2	SN13	2000TC
0	0	0	0	0	PCB2	SN9	2000TC
2	0	0	0	2	PCB2	SN11	2000TC
0	0	1	0	1	PCB1-S1	SN6	2000TC
2	2	0	0	2	PCB2	SN18	2000 TC
1	0	0	0	1	PCB1-S1	SN4	1000TC
2	0	0	0	2	PCB2	SN3	1000TC
1	0	0	0	1	PCB1-S2	SN15	400 HAST+1000TC
4	2	0	0	4	PCB2	SN19	400 HAST+1000TC

Figure B.6-2. MEAL Test Matrix Showing TC Test Plan with HAST Added Assemblies

B.6.1.2 NASA Environmental Requirements

For COTS implementation into NASA missions, numerous aspects of packaging technologies, including those with internal Cu wire bonds, should be defined and tailored for specific mission requirements and assessments. It requires the definition of overall NASA MEAL requirements, including radiation, mechanical, thermal, life cycle, mechanical shock, and vibration. In addition, it must be determined whether package properties are within the envelope of mission environmental requirements to avoid early overstress failures. Examples include radiation capability of die, temperature limits of package materials, including softening temperature (glass transition temperature, Tg), and junction temperature. Finally, special handling, bake out, assembly process, and tools requirements must be addressed.

For the Cu wire bond task, the team reviewed hundreds of packaging types, wire-bond types and sizes, and TC resistance limitations. To narrow the scope of evaluation having a significant number of variables, the team decided to concentrate on assessment of the TC life requirement for the various NASA missions. For the purpose of further narrowing package selection, the team considered the four MEAL conditions outlined in section 7.4.4.2.

Table B.6-2 lists approximate equivalent TCs for flight thermal fluctuation ΔTs of 15 ℃ and 25℃ and Laboratory ΔTs of 125 ℃ and 180 ℃. These calculations allow determination of equivalent thermal cycles for the specified MEAL conditions using accelerated thermal cycles, e.g., -55/125 ℃, to be performed in a laboratory chamber. The ΔTs and the number of TCs are correlated via different projection models for solder joint reliability; therefore, adjustment can be made for MEAL ΔT fluctuations. It is apparent that most MEALs will be covered by the accelerated TC selected for this investigation. Depending on CTF for a specific packaging technology, its MEAL could be limited. This investigation did not address the special cases of environmental requirements, such as extreme cold exposure (e.g., Moon and Mars).

Table B.6-2. MEAL Projections for Mission Conditions With Low to High Numbers of TC Fluctuation Based on Solder Joint Life Projection of Assembled Cu-Wire COTS

MEAL-Mission Condition	ΔT ℃	Low # Cycles	Moderate # Cycles	High # Cycles	Higher # Cycles
Benign ΔT MEAL Fluctuation	*15*	*10000*	*25000*	*50000*	*100000*
~ Equivalent ATC (-40/85°C)	125	432	1080	2160	4320
~ Equivalent ATC (-55/125°C)	180	208	521	1042	2083
MEAL-Mission Condition	**ΔT ℃**	**Low # Cycles**	**Moderate # Cycles**	**High # Cycles**	**Higher # Cycles**
Moderate ΔT MEAL Fluctuation	*25*	*4000*	*10000*	*15000*	*30000*
~ Equivalent ATC (-40/85°C)	125	480	1200	1800	3600
~ Equivalent ATC (-55/125°C)	180	231	579	868	1736

B.7 Testing Configuration and Bias Condition

For biasing the circuits, PCB1s were connected to 18V and 3.3V power supplies while PCB2s were connected to 18V, 3.3V, and 1.2V. Each PCB had two to three Molex connectors, one for each voltage. Each of these harnesses were connected to four resistors. The voltage over these resistors was measured via Keysight data loggers. The voltage measurements allowed for the calculation of the current draw by each board at each voltage. Figure B.7-1 provides a block diagram showing how one Molex connector was routed to sense cards and power supplies. Each sense card (shown as a green box in the figure) had five Molex cables attached through the DB-44 port. Figures B.7-2 through B.7-4 show an overall diagram for the test setup. Each harness has five Molex connectors, though one (brown) is unused—this cable is not shown in the diagram. Each purple “voltage sense” line coming from the sense cards represents 16 wires going to 16 channels on the data logger. There are 16 wires, since each resistor group connected to a Molex cable has four resistors and only four groupings were used. Therefore, only four of the five Molex cables were used per sense card. The power supply voltage readings and internal chamber temperature were also monitored by a data logger. The power supplies were turned off

when the ovens were cold and turned on to bias the parts as the oven warmed through a LabVIEW IV.

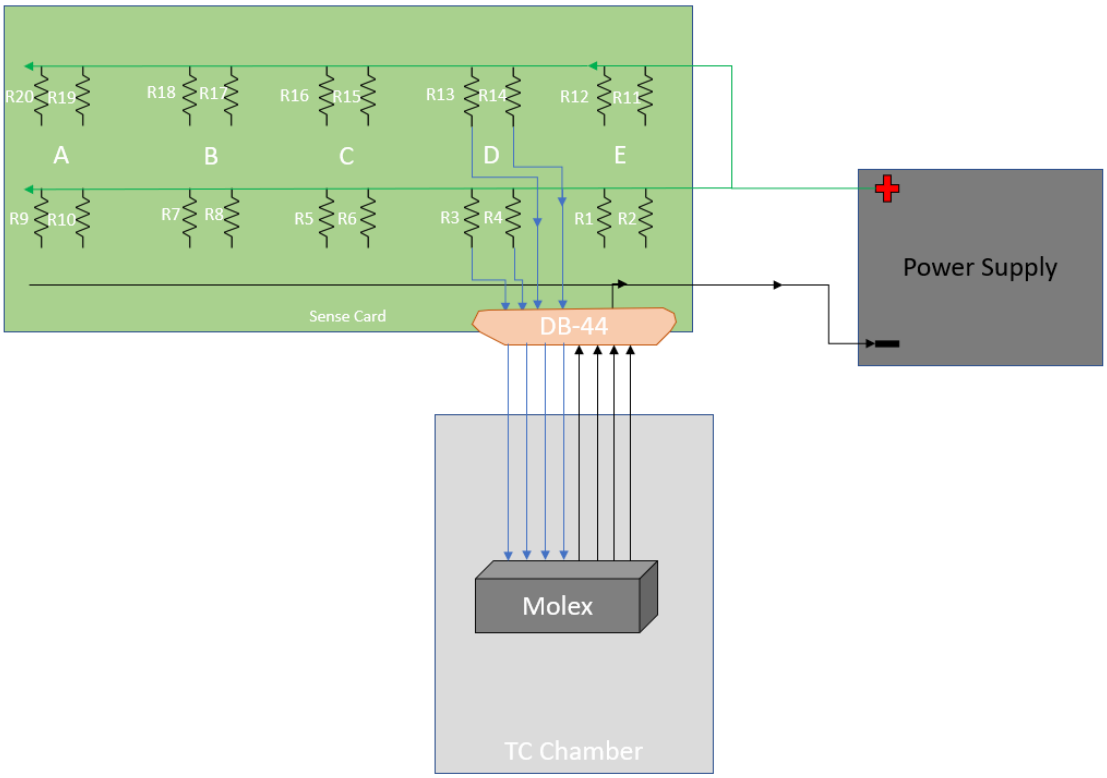

Figure B.7-1. Block Diagram Showing Wiring for one Molex Connector

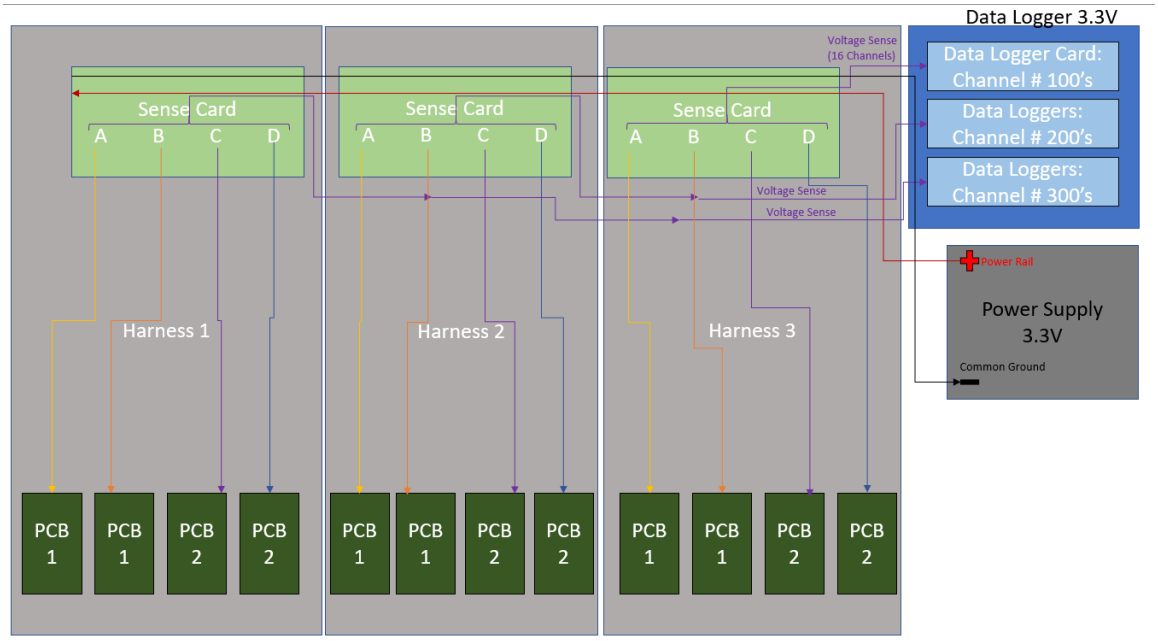

Figure B.7-2. Block Diagram Showing Full Test Setup For 3.3V

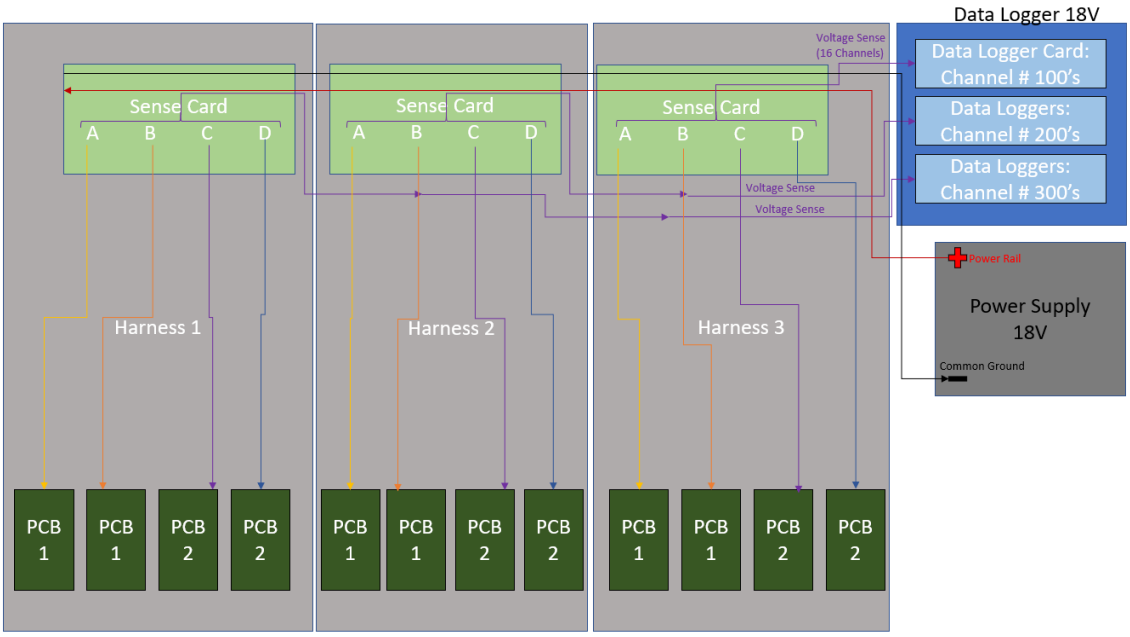

Figure B.7-3. Block Diagram Showing Full Test Setup For 18V (Same as 3.3V)

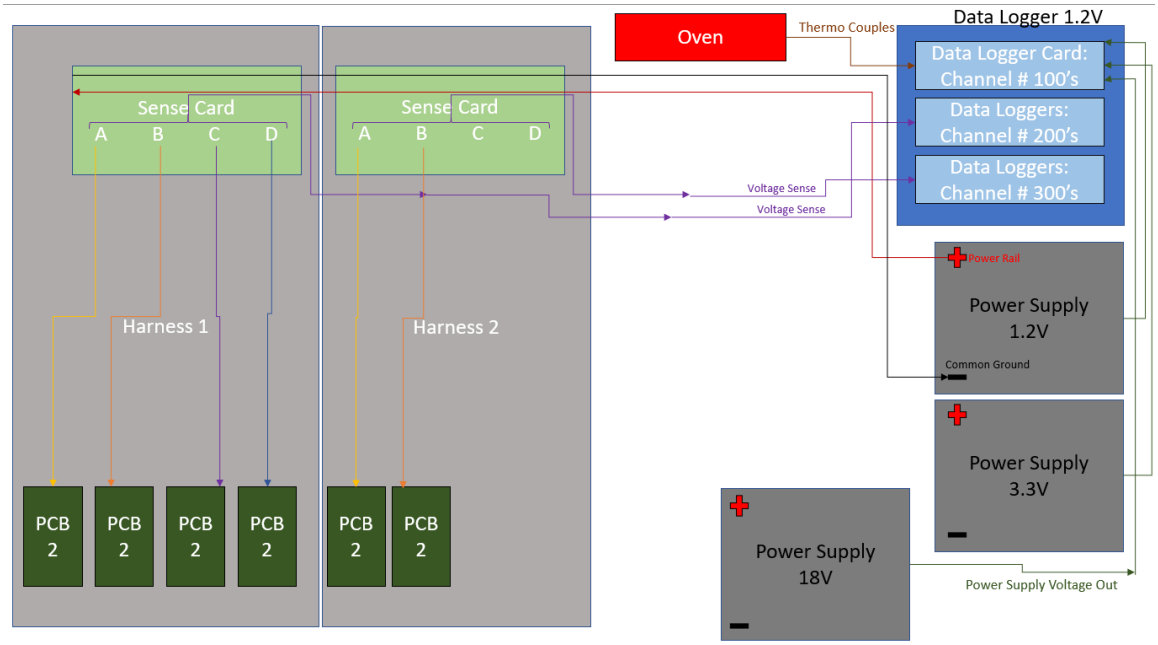

Figure B.7-4. Block Diagram Showing Full Test Setup For 1.2V, Thermocouple Readings and Power Supply Readings

B.7.1 bHAST

bHAST was performed in an Espec Corporation EHS411M HAST chamber. The test boards inside the HAST chamber were connected through sense cards to data loggers and power supplies as described above. Four boards were tested at any time, first for 100 hrs, then an additional 400 hrs of bHAST (Table B.7-1). A photograph of the assemblies within the chamber is provided in Figure B.7-5. Additionally, a set of loose unbiased parts was placed in the HAST chamber (Table B.7-2 and Figure B.7-6).

Table B.7-1. Environmental Test Summary of Six Boards After HAST

Board	HAST Exposure (110C/85%RH)	Temperature Cycle (-55/+125)
PCB1-S1-SN2	100 hr	2000 Cycles
PCB1-S1-SN7	500 hr	0 Cycles
PCB1-S2-SN15	400 hr	1000 Cycles
PCB2-SN10	100 hr	2000 Cycles
PCB2-SN19	400 hr	1000 Cycles
PCB2-SN20	500 hr	0 Cycles

Boards first completed HAST exposure before starting temperature cycling. Parts from PCB1-S1-SN7 and PCB2-SN20 were later analyzed for bond pull and shear strength.

Figure B.7-5. View Inside HAST Chamber Showing Setup.
Boards are stacked, separated by stands. Wires bring power to the boards. A metal tray with loose unbiased parts is at the bottom of the chamber.

Table B.7-2. List of Loose Parts That Underwent Unbiased 500 hr of HAST

PN	Qty
M1-MCK-LFBGA144-01	5
M3-MCK-TQFP100-01	5
M5-MCK-SOT235-01	5
M11-MCK-TQFP144-01	5
M8-MCK-LQFP100-01	5

No further testing was done on these parts.

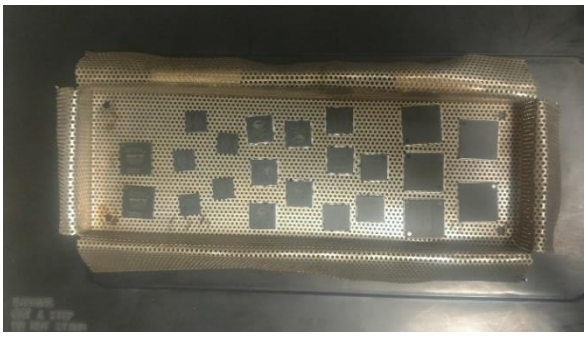

Figure B.7-6. Tray of Loose Parts Placed in Hast Chamber

HAST was marked by two incidents. The first occurred at the start of testing and was attributed to poor choice of limiting series resistors (100 Ω) that were overstressed and replaced with 2.2 KΩ. The second took place while restarting HAST for an additional 400 hr, or cumulative 500 hr. The connections of the PCB1 boards to the 3.3V and 18V power supplies were inadvertently swapped and corrected. These two incidents did not appear to affect the microcircuits and semiconductors being evaluated, because the monitored power supply currents remained fairly stable throughout the HAST. After completing 500 hr of HAST, parts from PCB1-S1-SN7 and PCB2-SN20 were analyzed for bond pull and shear strength. The rest of the boards went into temperature cycling and were stored sealed in ESD bags with desiccant at the end of the testing.

B.7.2 Thermal Cycling

Temperature cycling was performed in a Sun Systems EC12 environmental chamber. During temperature cycling, the boards were biased while the thermal chamber was soaking at the hot temperature of 132 ℃, and unbiased when soaking cold at -63 ℃. Each total cycle lasted approximately 88 minutes, with ramp rates of about 7 ℃/min and a soak time of 16.67 minutes. Photographs of the assemblies inside of the chamber and the electrical test equipment for thermal cycling are provided in Figures B.7-7 and B.7-8. Total current was monitored on each voltage line for every board.

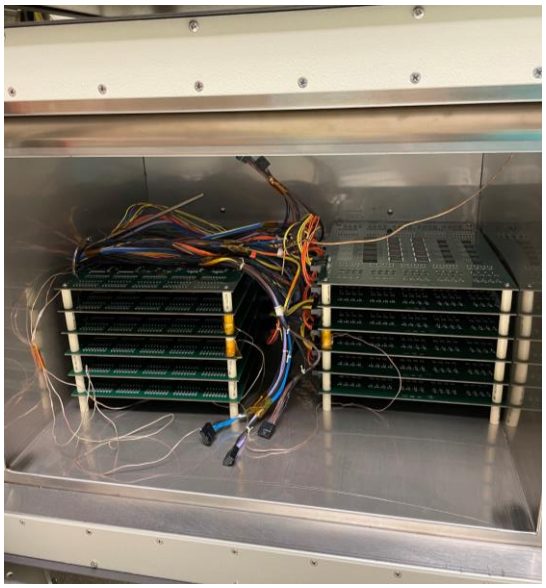

Figure B.7-7. Temperature Cycling Test Set-Up of Boards in Oven

Figure B.7-8. Electrical Power and Board Monitoring Set-Up During Temperature Cycling Test

Appendix B References

1. NASA-STD-8739.10, Electrical, Electronic, and Electromechanical (EEE) Parts Assurance Standard. https://standards.nasa.gov/sites/default/files/standards/NASA/Baseline/0/nasa-std-873910.pdf
2. Ghaffarian, R. (2016) "Update on CGA Packages for Space Applications," Microelectronics Reliability.
3. Khatibi1, G.; Mazloum-Nejadari, A.; Lederer, M.; Delshadmanesh, M.; and Czerny, B. (2018) "Fatigue Life Time Modelling of Cu and Au Fine Wires," https://www.matec-conferences.org/articles/matecconf/pdf/2018/24/matecconf_fatigue2018_06002.pdf, Accessed June, 2020.
4. Harman, G. (2010) Wire Bonding in Microelectronics, McGraw-Hill, Third Edition.
5. Tasooji, A.; Ghaffarian, R.; Rinaldi, A. (2006) "Design Parameters Influencing Reliability of CCGA Assembly and Sensitivity Analysis," Proceedings of ITherm, San Diego, CA.

Appendix C. Test Results

As shown in Figure C.1-1, parts were subjected to CA and mold compound analysis upon receipt. The results of these analyses are discussed in this section. Following fabrication and assembly, PCB assemblies were subjected to post-assembly touch-ups, X-ray inspection, and IR inspection. The assemblies were then placed in their selected environmental test condition, as described in Section 7.2. Following removal, select assemblies underwent additional destructive analysis to determine the impact of environmental exposure on Cu wire bond mechanical reliability using bond pull and ball shear testing. The results of these evaluations are provided in the following subsections.

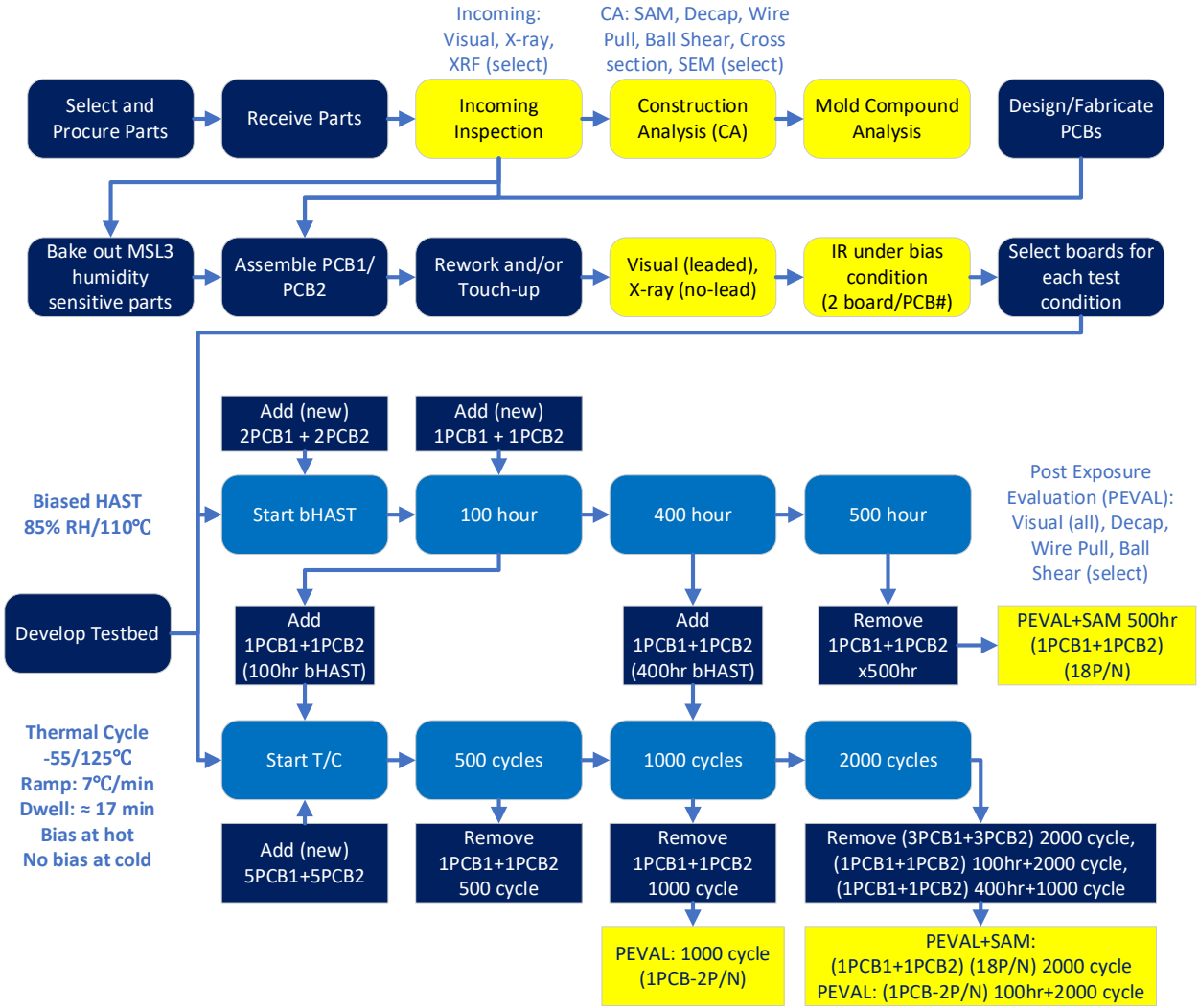

Figure C.1-1. Schematic Illustration of Cu Wire Test Plan

C.1 CA and Mold Compound Analysis

CA was performed on each of the aforementioned commercial devices prior to environmental testing. Physical properties for each device are summarized in Table C.1-1. Figures C.1-2 through C.1-19 provide X-ray images of the overall package from the top and side, optical micrographs and SEM micrographs of bond cross-sections, optical images with measurements of

decapsulated bond wires on the package, and SEM BSE EDS compositional maps of ball bond cross-sections, stitch bond cross-sections, and decapsulated bond wires.

Table C.1-1. Part CA Summary

Part Number	Package Size (mm^3)	Wire Count	Wire (mil)	Ball Area (mil^2)	Bond Pad (um)	Splash (um)	Under Ball (um)	Wire Type	Lead Frame metallization
M10-D-SOD323-01	1.251.7x0.95	1	2.00	23.20	1.30	4.00	0.60	Cu	Ag/Cu
M2-D-SOT233-01	1.3x2.9x1	2	0.80	5.37	2.60	5.07	1.00	Cu	Cu/FeNi
M5-D-SOT233-01	1.3x2.9x0.95	2	1.00	3.06	1.43	2.33	0.28	Cu	Ag/Cu
M2-D-SOT233-02	1.3x2.9x1	2	0.80	7.38	2.00	5.50	0.90	Cu	Cu/FeNi
M10-D-SOT1061-01	2x2x0.65	2	2.00	18.60	1.72	4.88	0.68	Cu	Pd/Ni/Cu
M5-MCK-SOT235-01	1.6x2.9x1.1	4	0.80	4.44	1.40	2.80	1.50	Au	Ni/Cu
M6-D-SOT235-01	1.6x2.9x1.15	5	1.00	6.63	4.00	9.00	0.00	PCC (Pd/Cu)	Ag/Cu
M5-MCK-WSON6-01	2.02x2.5x0.8	6	0.80	2.56	1.10	3.40	0.00	PCC (Au/Pd/Cu)	Ag/Cu
M1-MCK-SOIC8-01	3.9x4.9x1.25	7	1.00	5.4	0.54	3.05	0.91	PCC (Au/Pd/Cu)	Ni/Cu
M5-MCK-VSSOP8-01	3x3x1.1	8	1.00	3.84	1.46	1.54	0.50	Cu	Ag/Cu
M9-D-CUSTOM-01	3x3x1	9	2.00	21.20	4.00	8.00	2.00	Cu	Ag/Cu
M5-MCK-SOIC8-01	3.9x4.9x1.5	11	1.00	4.70	2.9	8.80	0.70	Cu	Ni/CuFe
M3-MCK-TQFP100-01	14x14x1.4	108	0.80	2.56	0.85	4.00	0.50	PCC (Pd/Cu)	Ag/Cu
M8-MCK-LQFP100-01	10x10x0.96	144	1.00	3.28	2.80	0.00	2.80	PCC (Au/Pd/Cu)	Ag/Cu
M11-MCK-TQFP144-01	20x20x1.4	151	0.80	2.07	1.50	3.30	0.50	PCC (Au/Pd/Cu)	Ag/Cu
M1-MCK-LFBGA144-01	11x11x1	198	0.70	1.92	1.68	3.37	0.51	PCC (Au/Pd/Cu)	Au/Ni/Cu
M4-MCK-FBGA256-01	11x11x1	272	0.80	3.21	0.97	2.20	0.50	Cu	Au/Ni/Cu
M7-MCK-LFBGA169-01	14x14x1.4	332	0.70	1.42	2.70	5.10	0.90	PCC (Pd/Cu)	Au/Ni/Cu

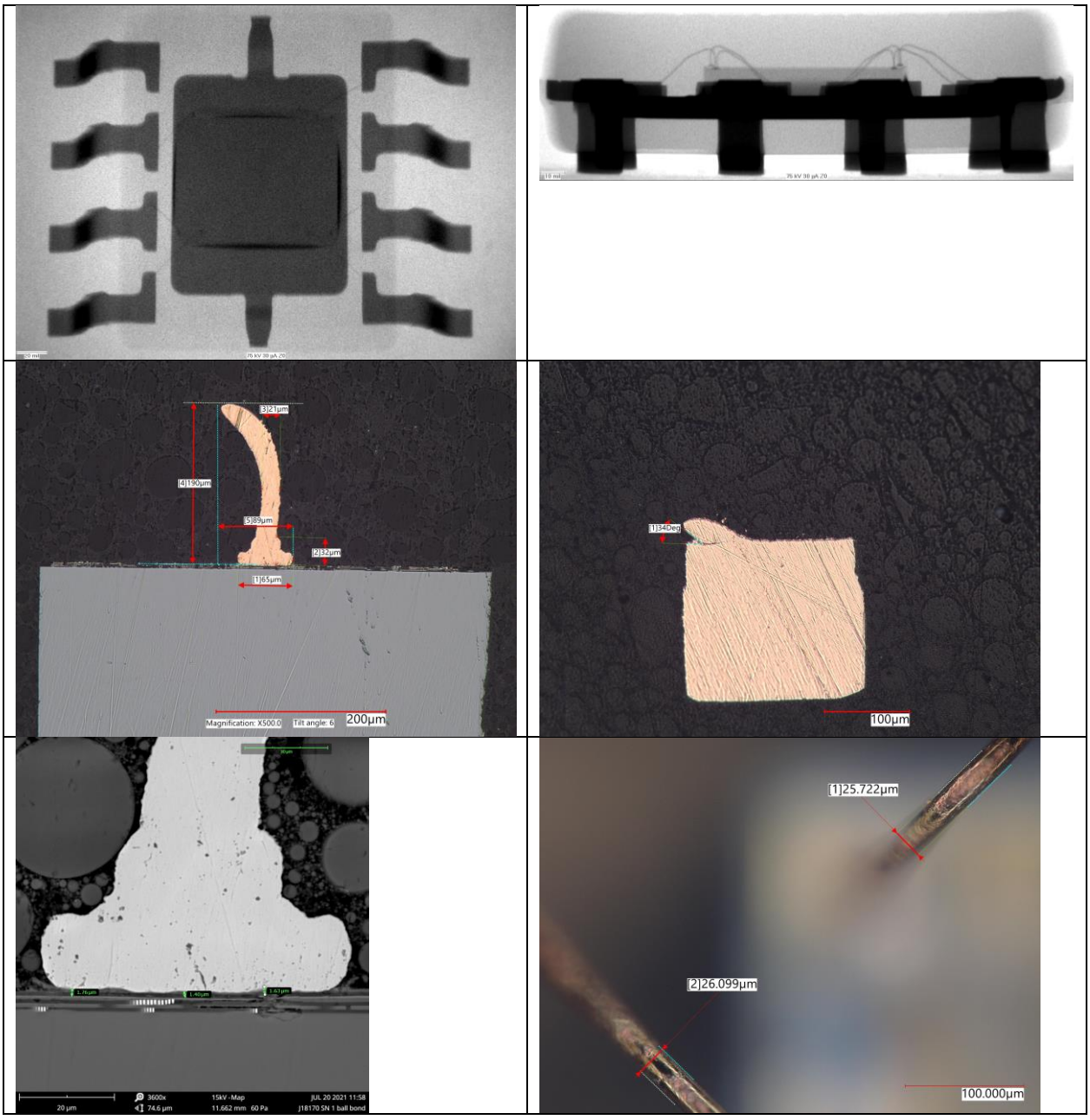

Figure C.1-2a. CA Images for Part M1-MCK-SOIC8-01.
Component X-ray, ball bond cross-section optical image, stitch bond cross-section optical image, ball bond cross-section SEM micrograph and optical image of decapsulated wires with dimensions.

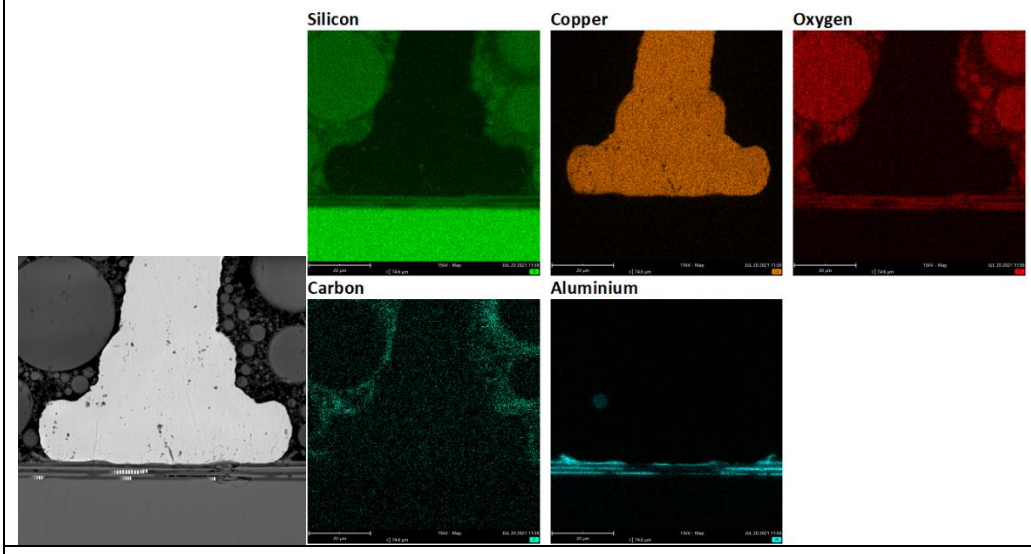

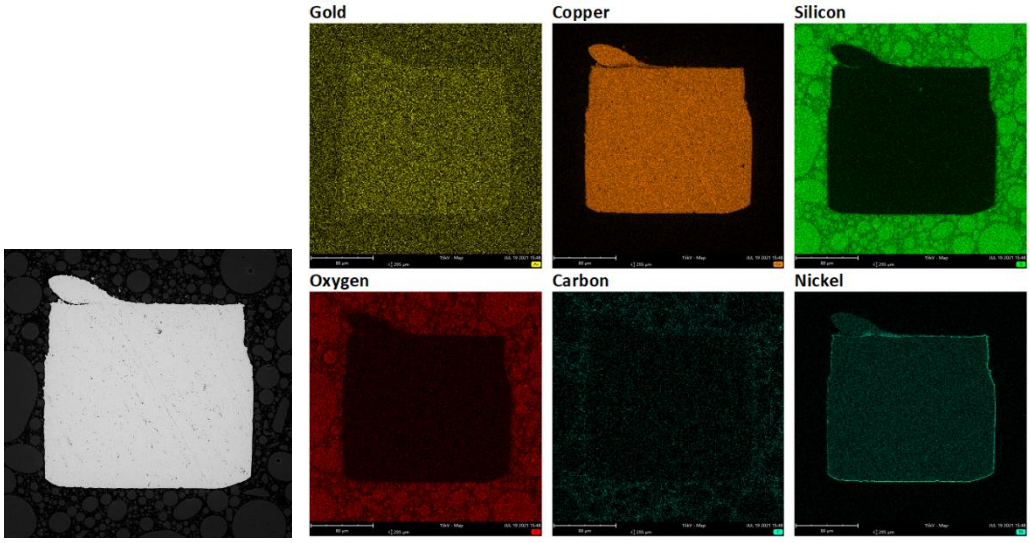

* Gold applied for SEM examination was likely the source for the above signal.

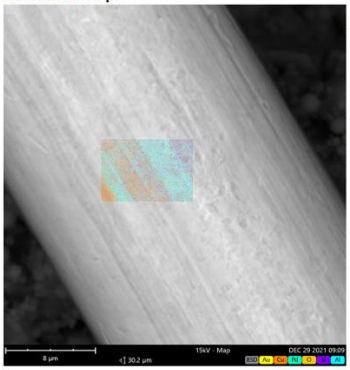

Element Number	Element Symbol	Element Name	Atomic Conc.	Weight Conc.
79	Au	Gold	14.81	38.41
29	Cu	Copper	33.76	28.25
46	Pd	Palladium	17.51	24.54
8	O	Oxygen	23.49	4.95
14	Si	Silicon	10.15	3.75
13	Al K	Aluminium	0.28	0.10

Figure C.1-2b. SEM EDS Composition Maps of Ball Bond Cross-Section, Stitch Bond Cross-Section and Decapsulated Wire Bond for Part M1-MCK-SOIC8-01

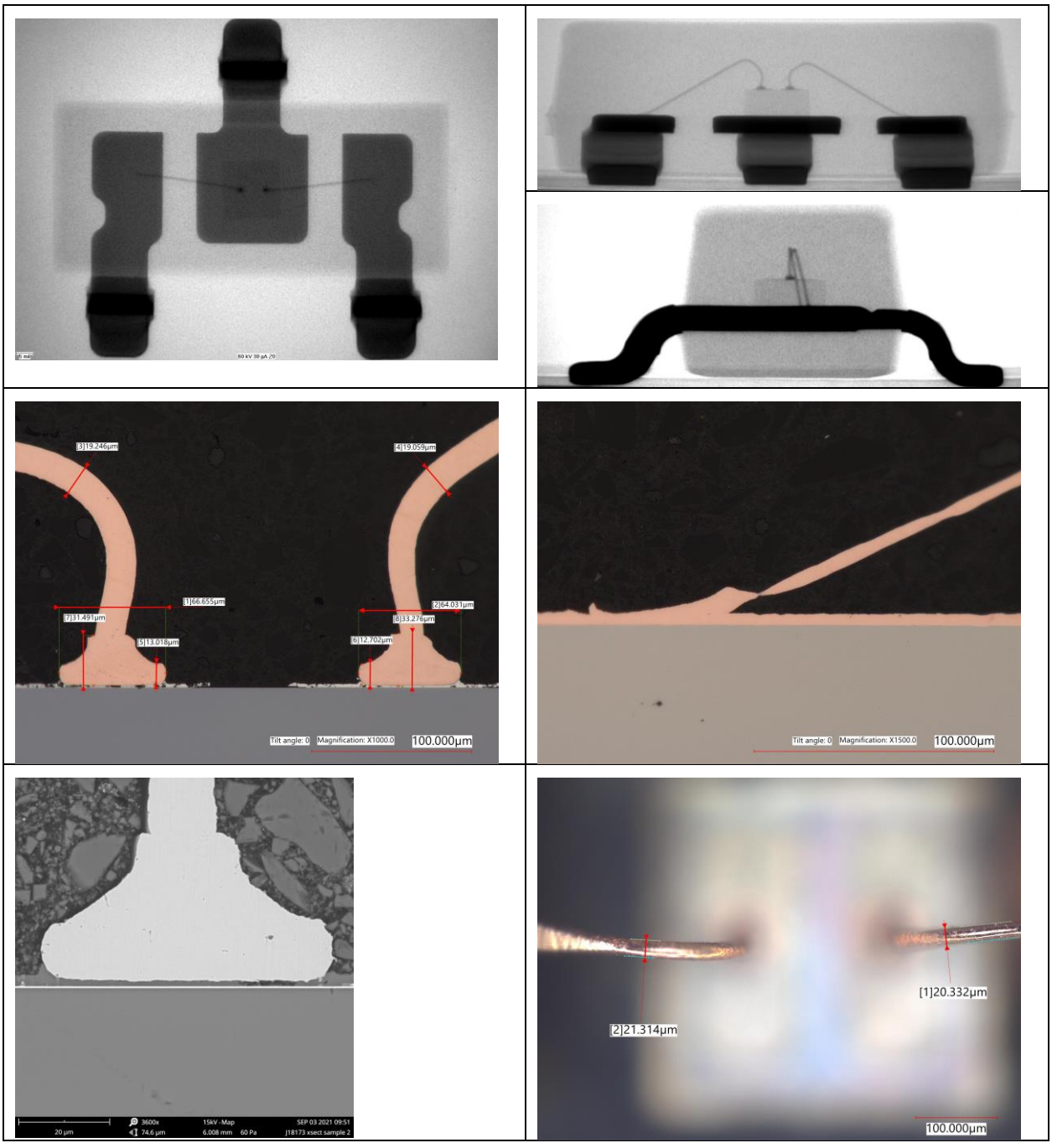

Figure C.1-3a. CA Images for Part M 2-D-SOT233-01.
Component X-ray, ball bond cross-section optical image, stitch bond cross-section optical image, ball bond cross-section SEM micrograph, and optical image of decapsulated wires with dimensions.

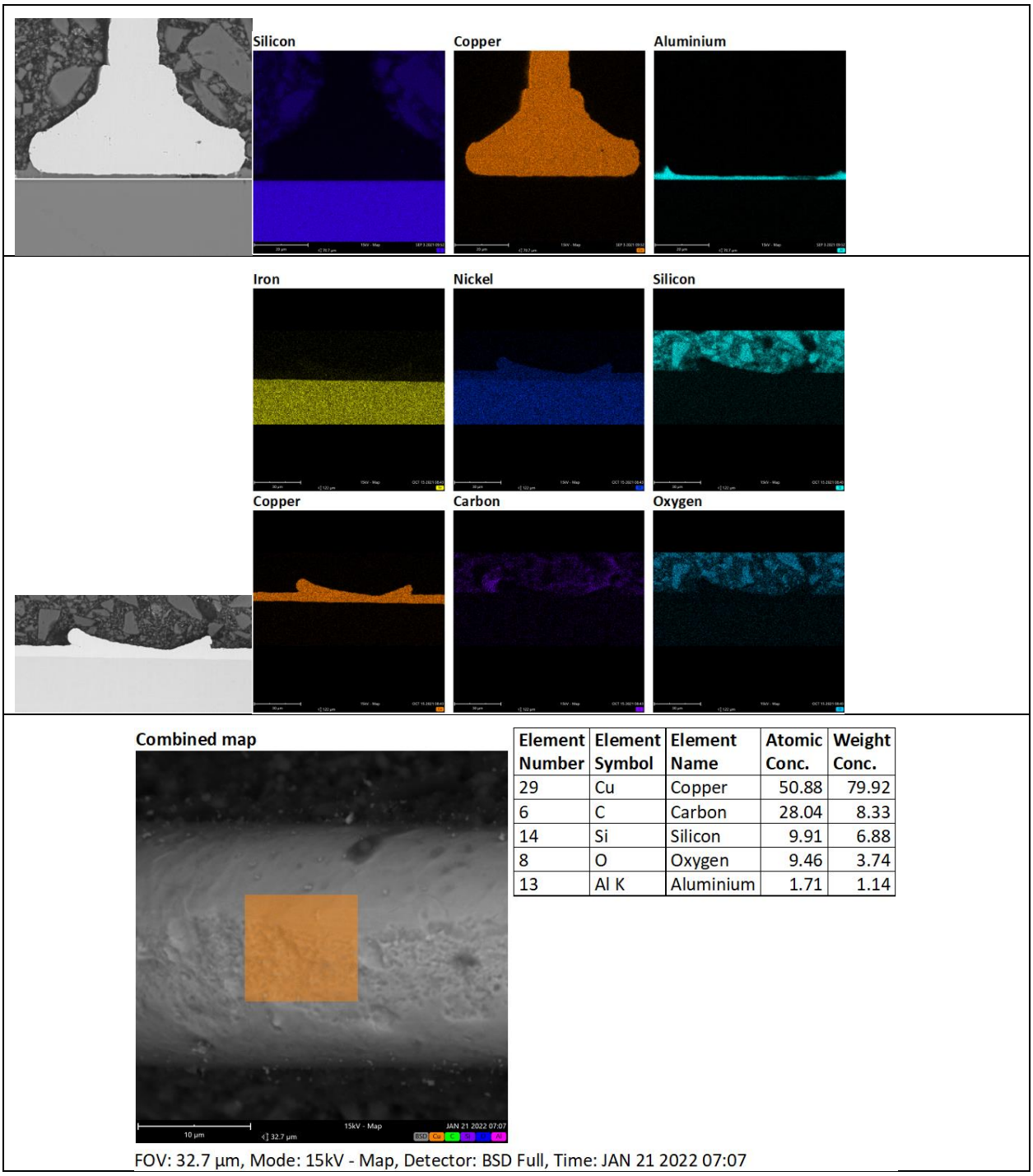

Element Number	Element Symbol	Element Name	Atomic Conc.	Weight Conc.
29	Cu	Copper	50.88	79.92
6	C	Carbon	28.04	8.33
14	Si	Silicon	9.91	6.88
8	O	Oxygen	9.46	3.74
13	Al K	Aluminium	1.71	1.14

Figure C.1-3b. SEM EDS Composition Maps of Ball Bond Cross-Section, Stitch Bond Cross-Section and Decapsulated Wire Bond for Part M2-D-SOT233-01

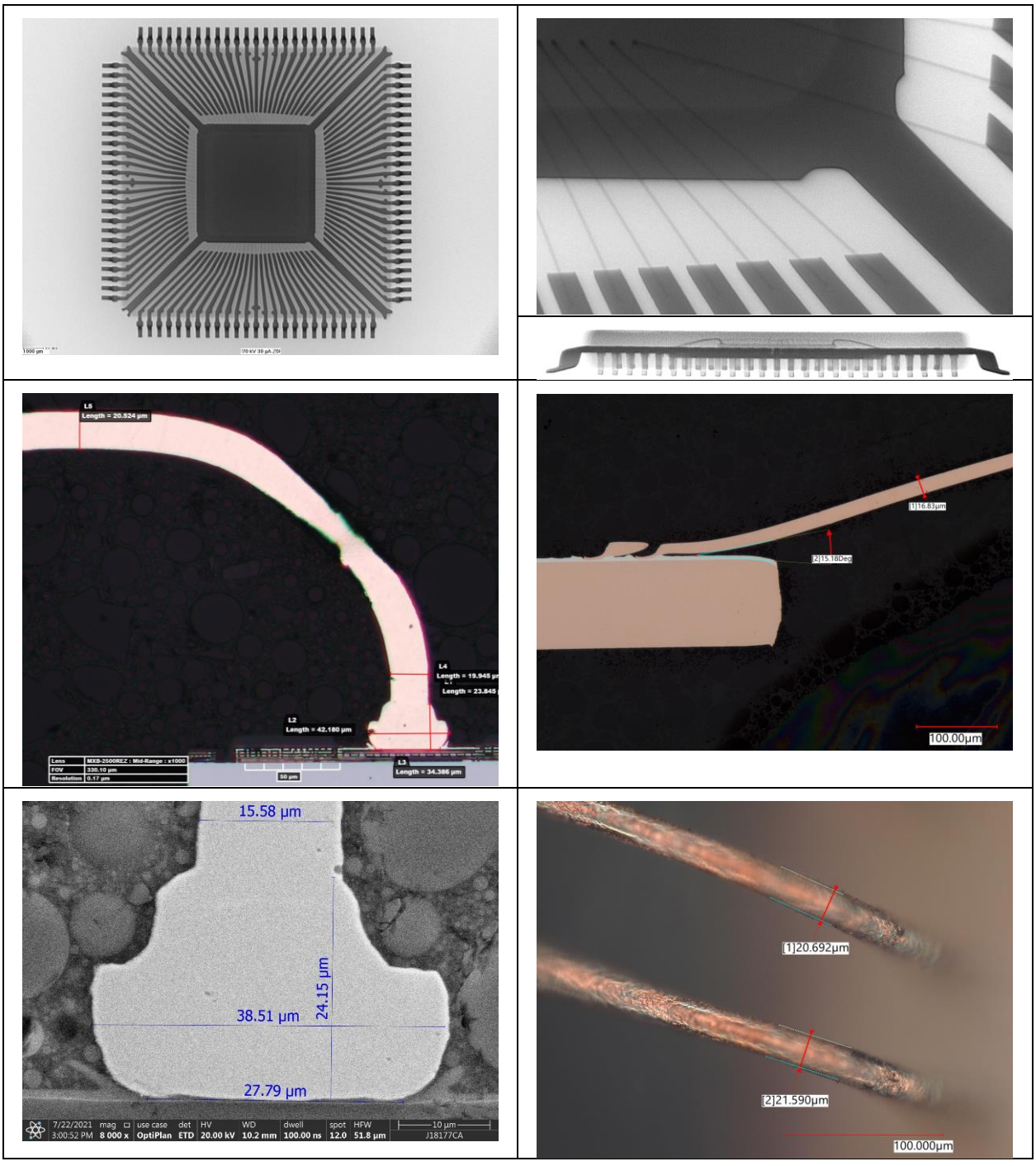

Figure C.1-4a. CA Images for Part M3-MCK-TQFP100-01.
Component X-ray, Ball Bond Cross-Section, Stitch Bond Cross-Section, Ball Bond Cross-Section SEM Micrograph and Optical Image of Decapsulated Wires with Dimensions.

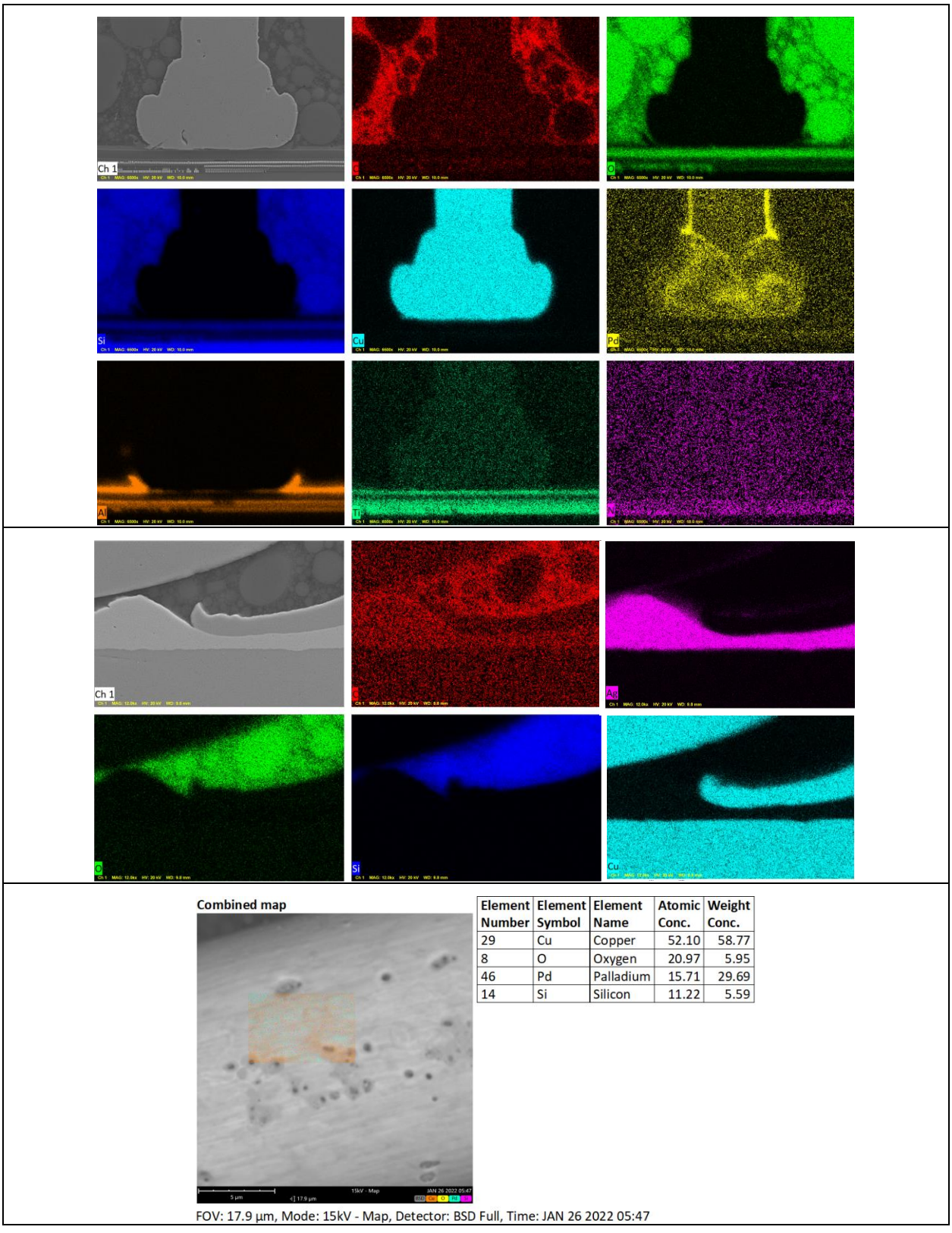

Element Number	Element Symbol	Element Name	Atomic Conc.	Weight Conc.
29	Cu	Copper	52.10	58.77
8	O	Oxygen	20.97	5.95
46	Pd	Palladium	15.71	29.69
14	Si	Silicon	11.22	5.59

FOV: 17.9 µm, Mode: 15kV - Map, Detector: BSD Full, Time: JAN 26 2022 05:47

Figure C.1-4b. SEM EDS Composition Maps of Ball Bond Cross-Section, Stitch Bond Cross-Section, and Decapsulated Wire Bond for Part Number M3-MCK-TQFP100-01

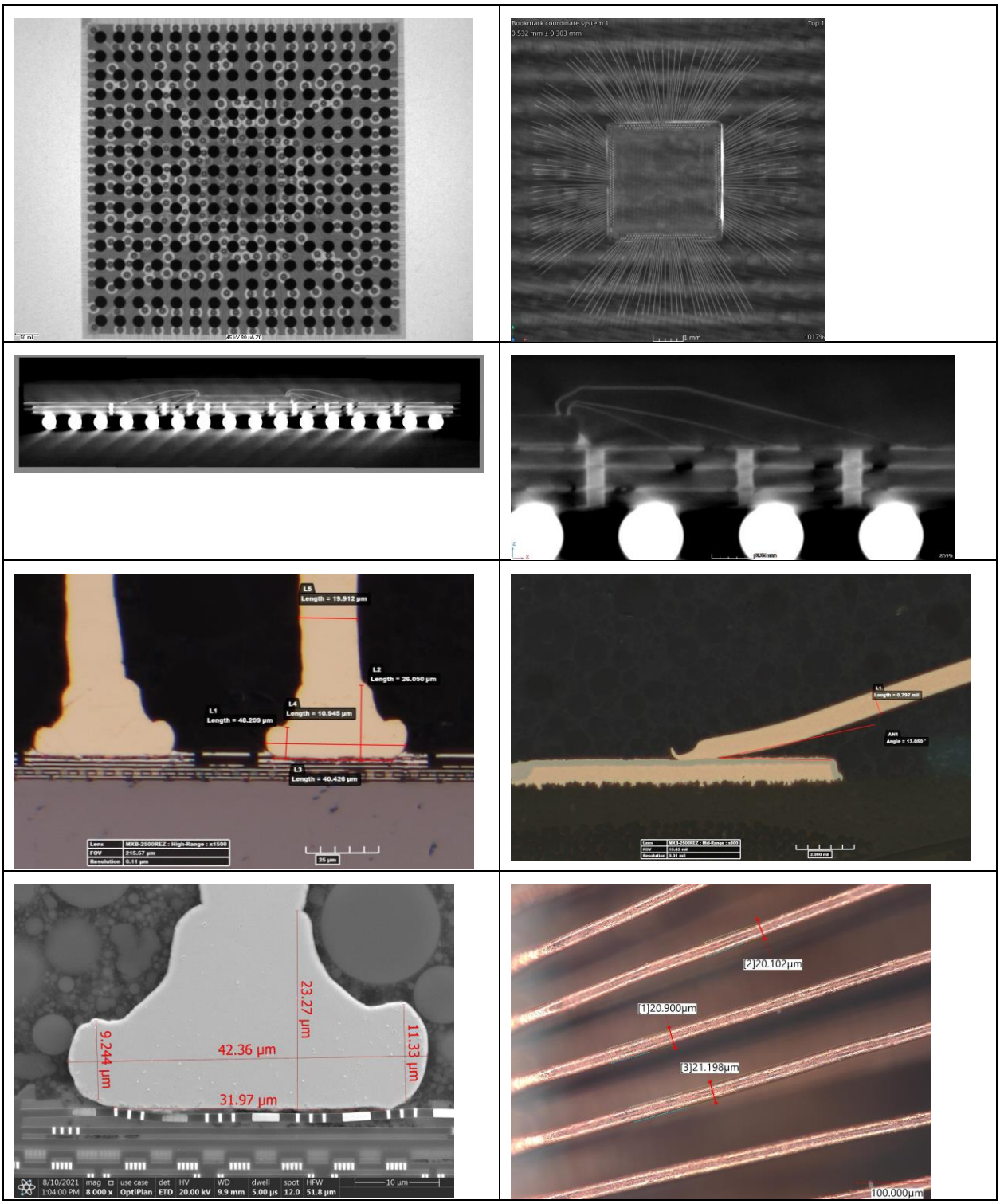

Figure C.1-5a. CA Images for Part M4-MCK-FBGA256-01. Component X-ray and CT images, ball bond cross-section, stitch bond cross-section, ball bond cross-section SEM micrograph and optical image of a decapsulated wire with dimensions.

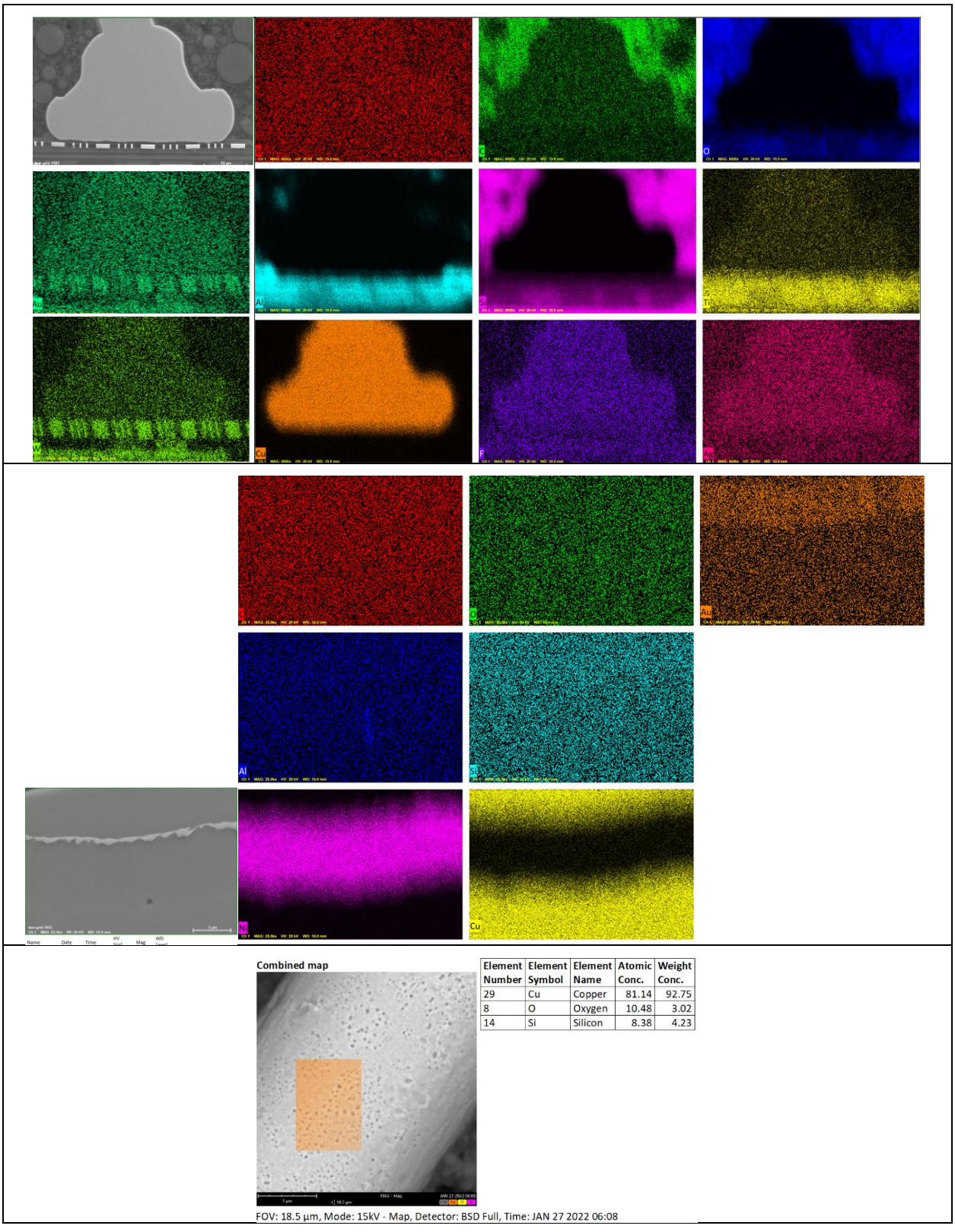

Element Number	Element Symbol	Element Name	Atomic Conc.	Weight Conc.
29	Cu	Copper	81.14	92.75
8	O	Oxygen	10.48	3.02
14	Si	Silicon	8.38	4.23

Figure C.1-5b. SEM EDS Composition Maps of Ball Bond Cross-Section, Stitch Bond Cross-Section, and Decapsulated Wire Bond for Part M4-MCK-FBGA256-01

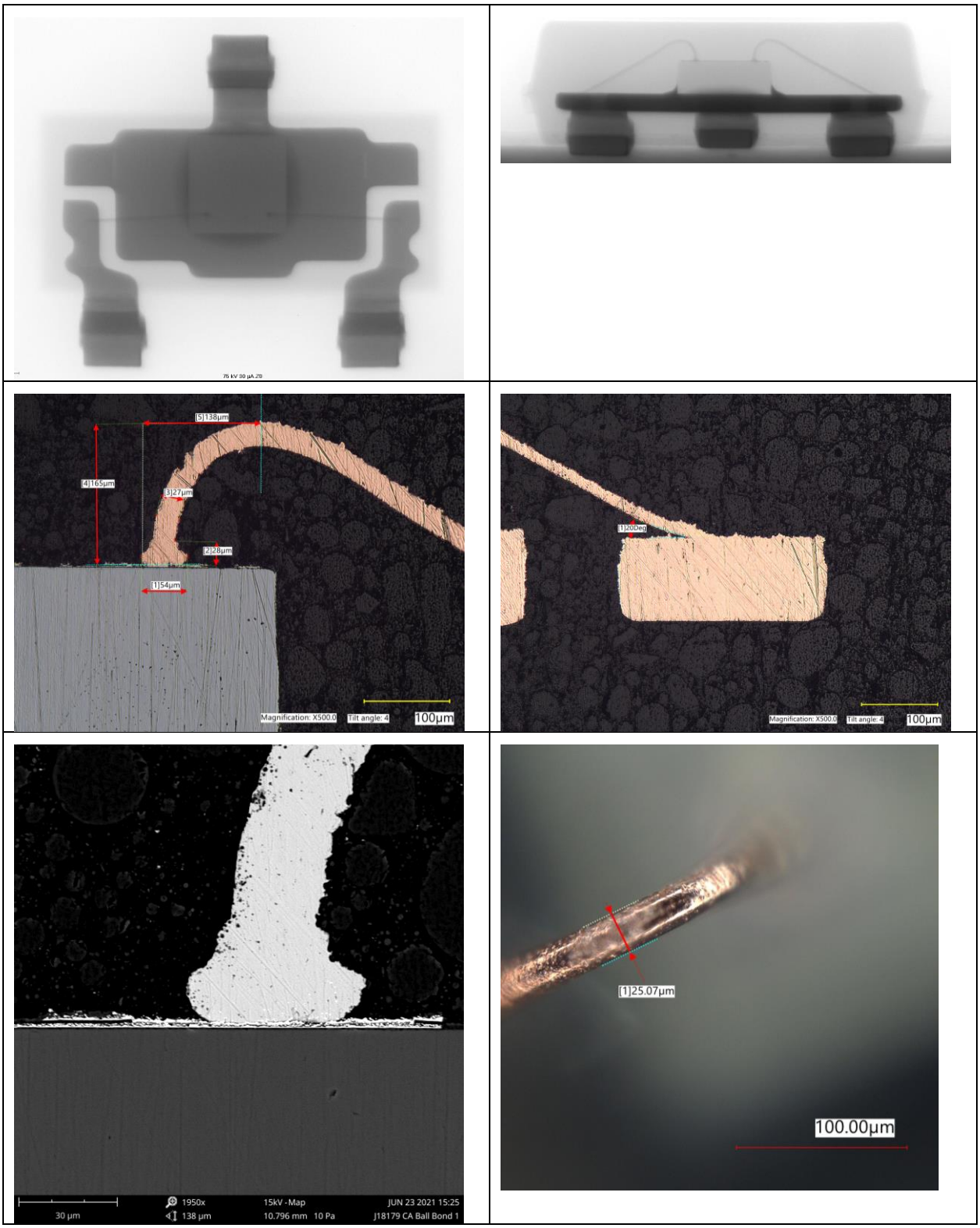

Figure C.1-6a. CA Images for Part M5-D-SOT233-01.
Component X-ray, ball bond cross-section optical image, stitch bond cross-section optical image, ball bond cross-section SEM micrograph and optical image of decapsulated wires with dimensions.

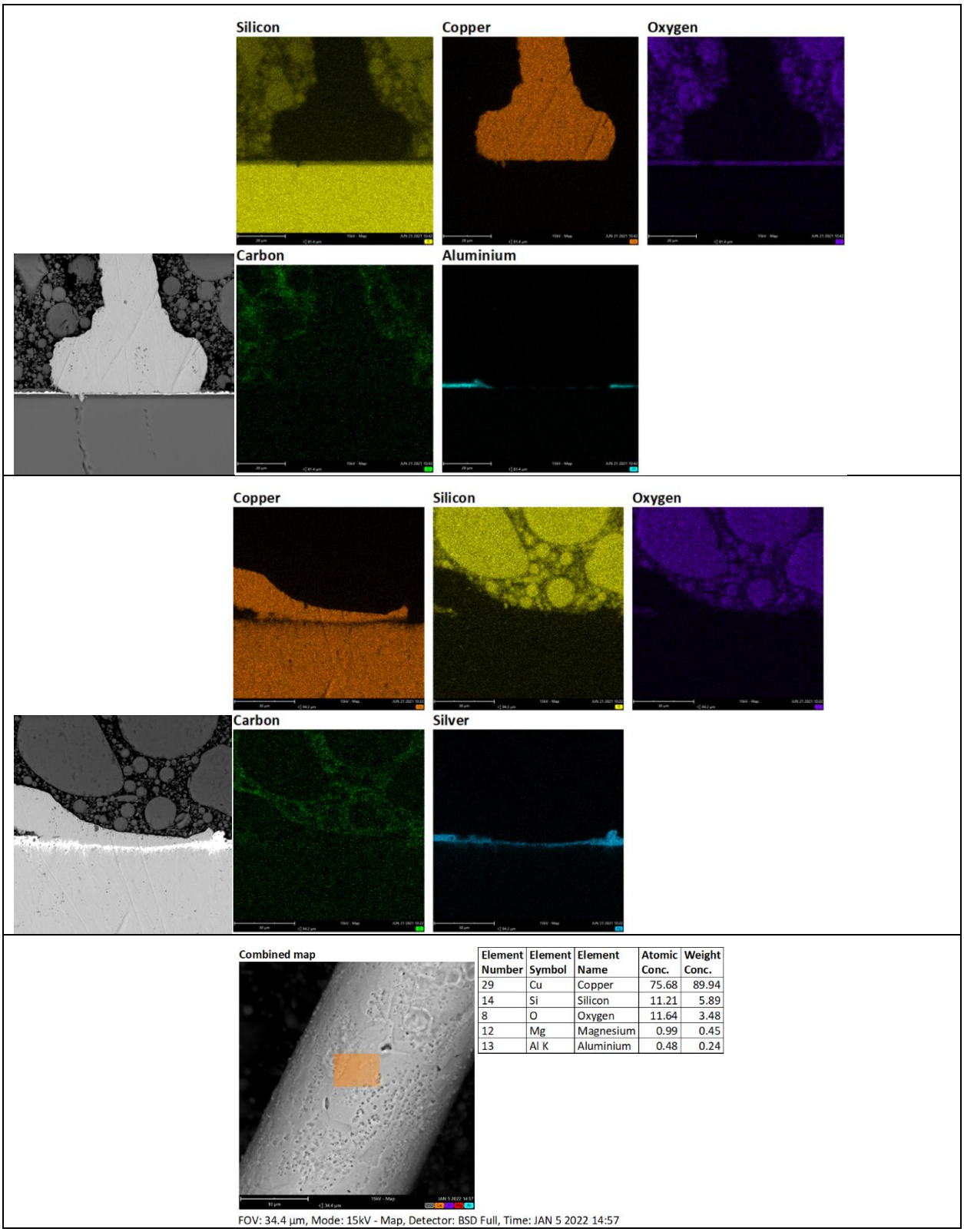

Element Number	Element Symbol	Element Name	Atomic Conc.	Weight Conc.
29	Cu	Copper	75.68	89.94
14	Si	Silicon	11.21	5.89
8	O	Oxygen	11.64	3.48
12	Mg	Magnesium	0.99	0.45
13	Al K	Aluminium	0.48	0.24

Figure C.1-6b. SEM EDS Composition Maps of Ball Bond Cross-Section, Stitch Bond Cross-Section, and Decapsulated Wire Bond for Part Number M5-D-SOT233-01

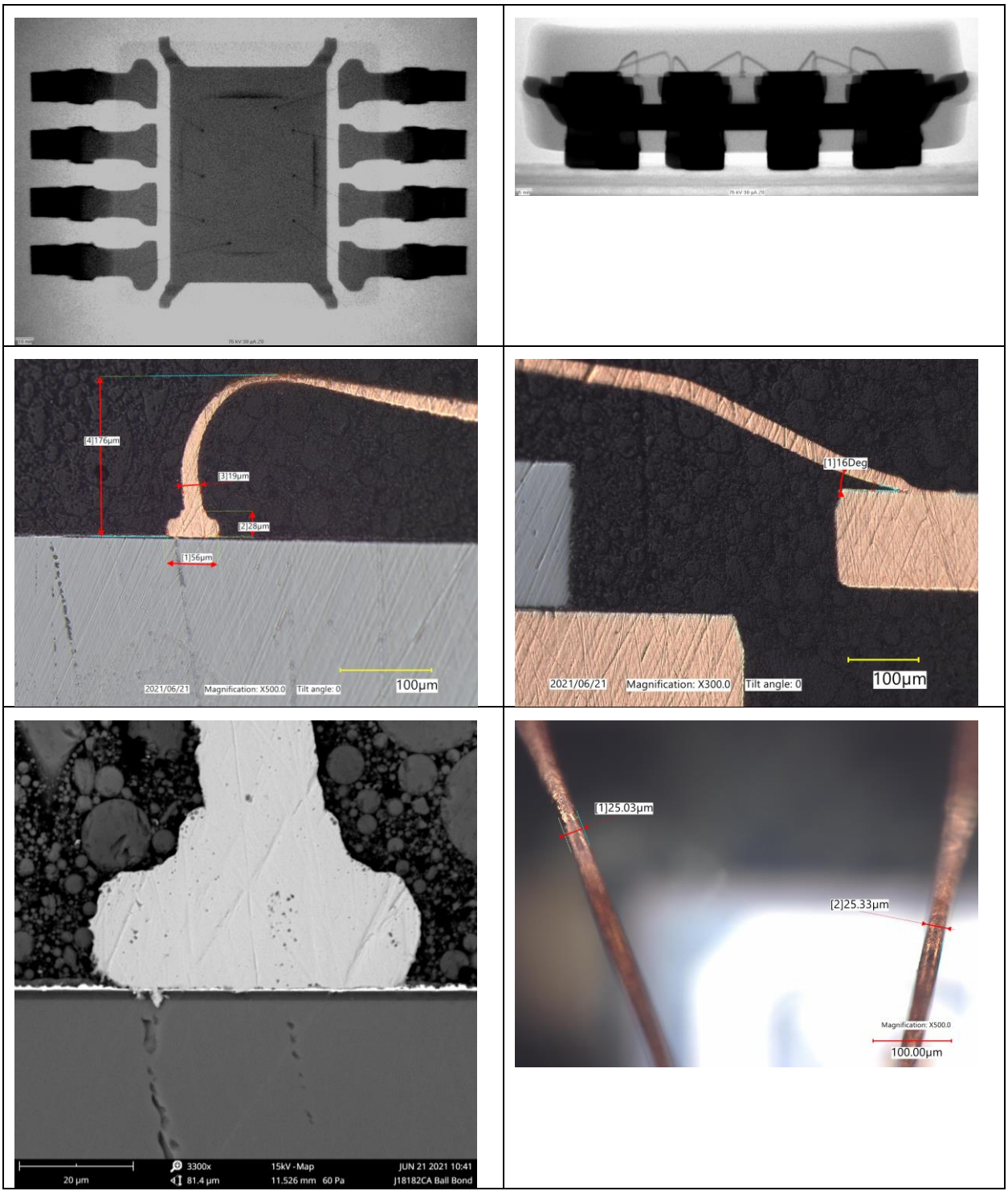

Figure C.1-7a. CA Images for Part Number M5-MCK-VSSOP8-01. Component X-ray, Ball Bond Cross-Section, Stitch Bond Cross-Section, Ball Bond Cross-Section SEM Micrograph, and Optical Image of Decapsulated Wires with Dimensions.

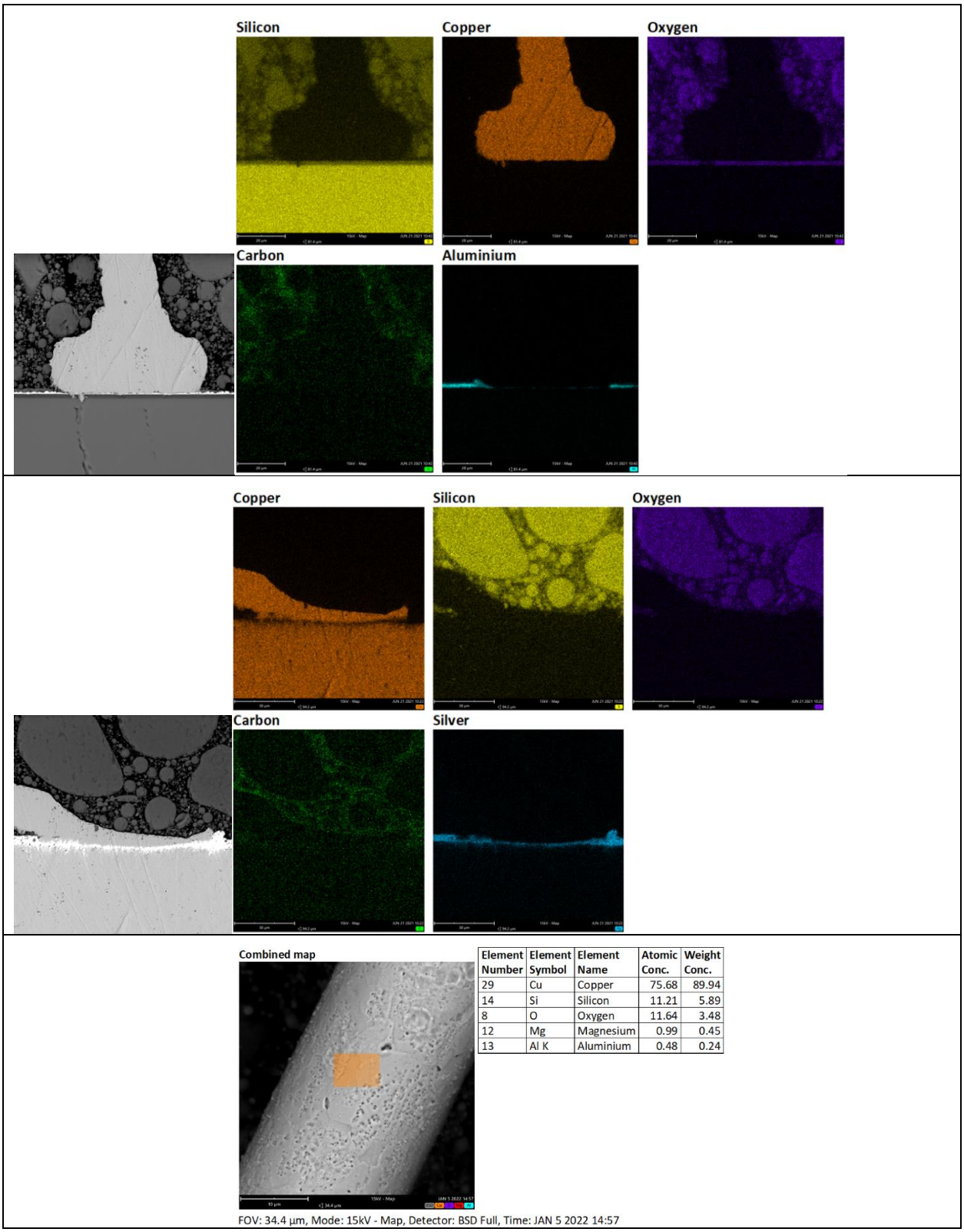

Element Number	Element Symbol	Element Name	Atomic Conc.	Weight Conc.
29	Cu	Copper	75.68	89.94
14	Si	Silicon	11.21	5.89
8	O	Oxygen	11.64	3.48
12	Mg	Magnesium	0.99	0.45
13	Al K	Aluminium	0.48	0.24

Figure C.1-7b. SEM EDS Composition Maps of Ball Bond Cross-Section, Stitch Bond Cross-Section, and Decapsulated Wire Bond for Part M5-MCK-VSSOP8-01.

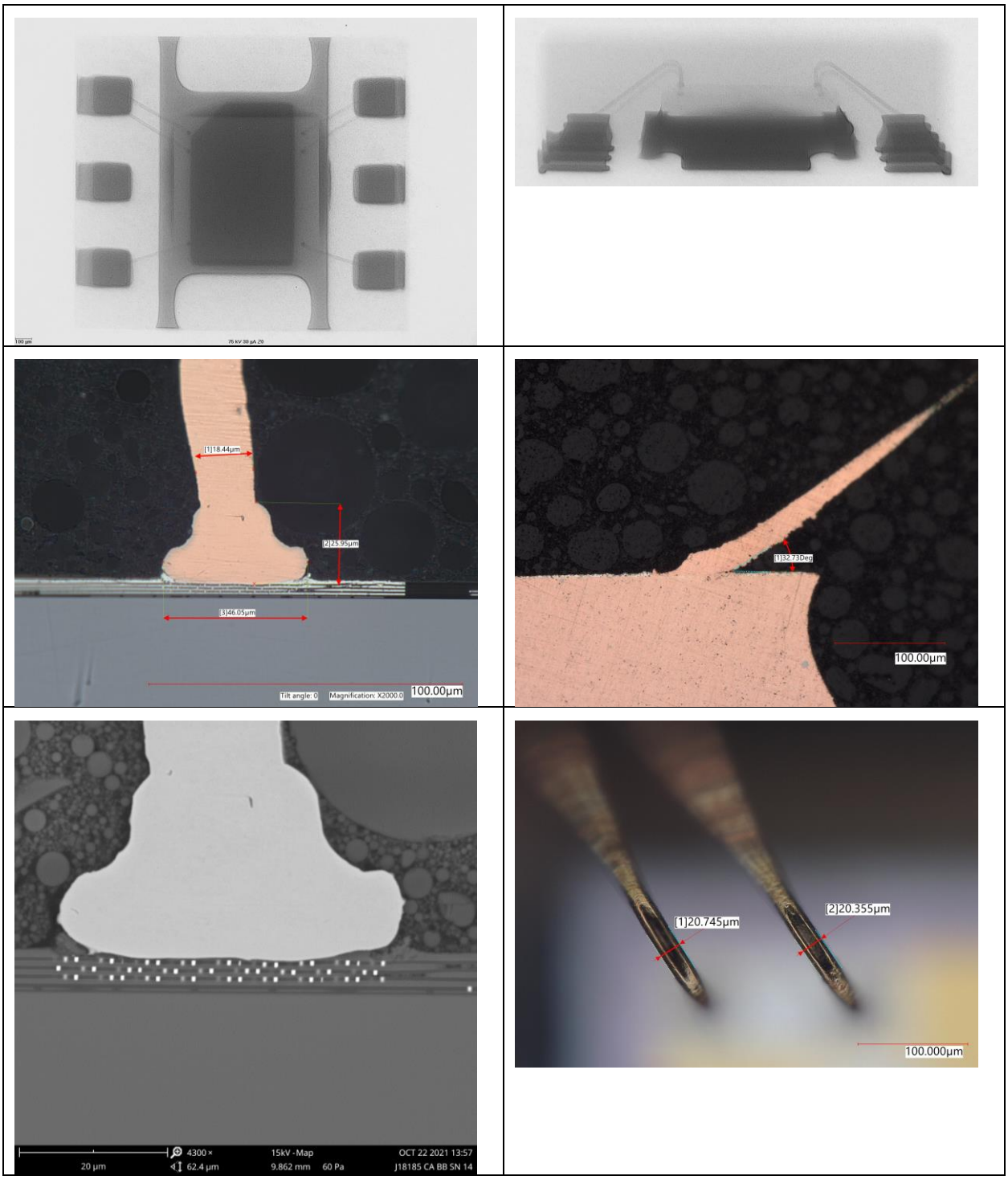

Figure C.1-8a. CA Images for Part M5-MCK-WSON6-01.
Component X-ray, ball bond cross-section optical image, stitch bond cross-section optical image, ball bond cross-section SEM micrograph, and optical image of decapsulated wires with dimensions.

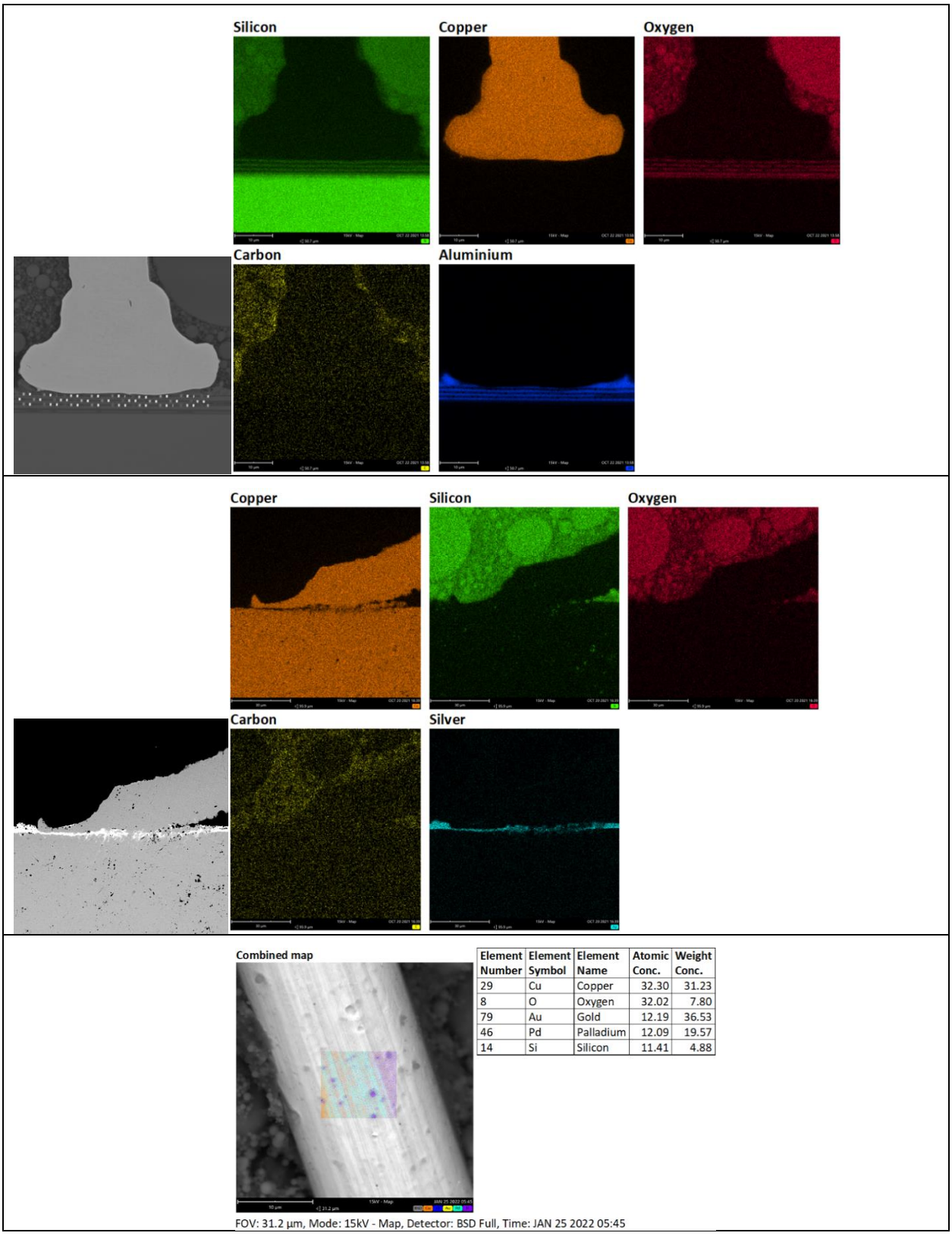

Element Number	Element Symbol	Element Name	Atomic Conc.	Weight Conc.
29	Cu	Copper	32.30	31.23
8	O	Oxygen	32.02	7.80
79	Au	Gold	12.19	36.53
46	Pd	Palladium	12.09	19.57
14	Si	Silicon	11.41	4.88

Figure C.1-8b. SEM EDS Composition Maps of Ball Bond Cross-Section, Stitch Bond Cross-Section, and Decapsulated Wire Bond for Part M5-MCK-WSON6-01

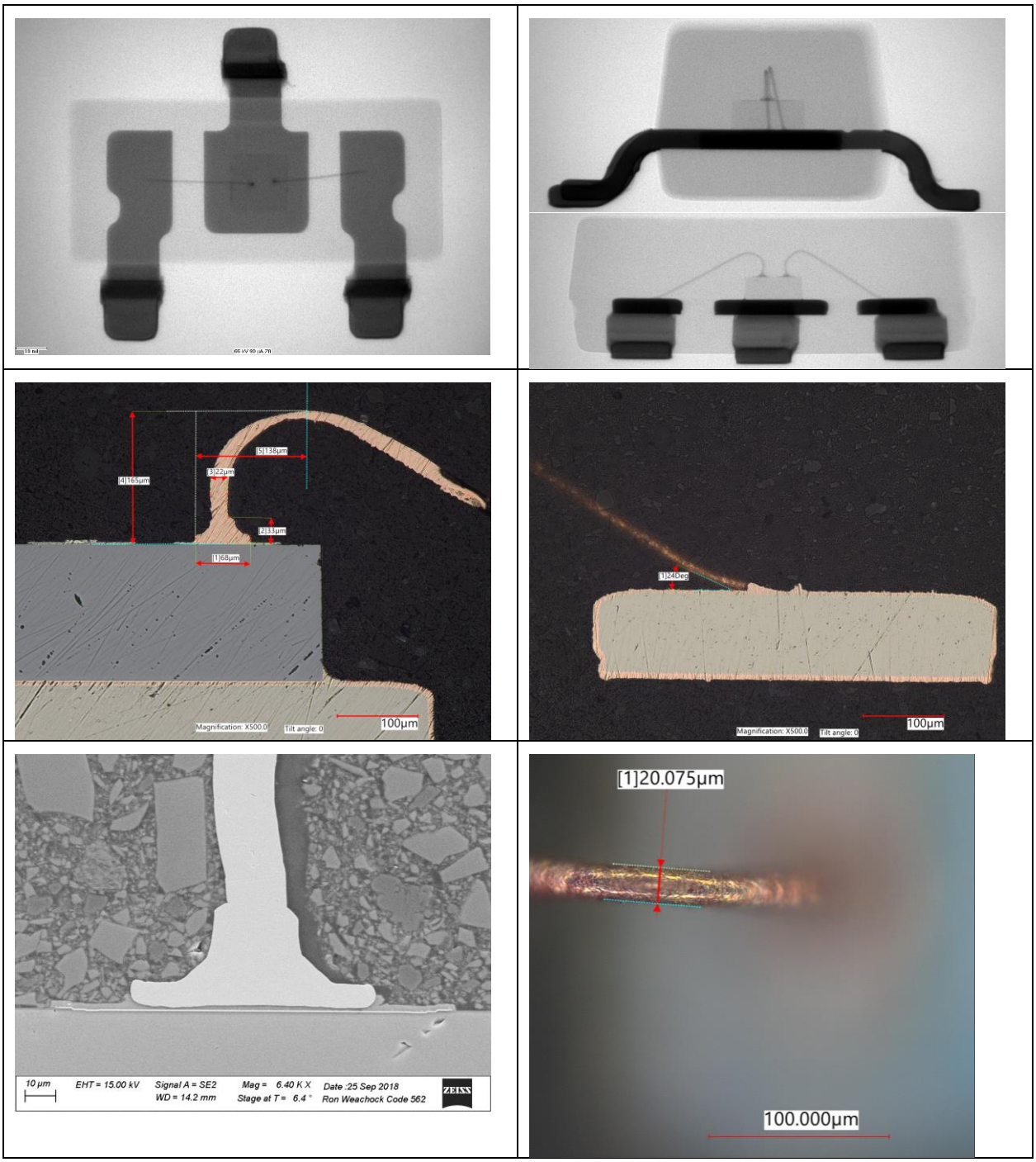

Figure C.1-9a. CA Images for Part M2-D-SOT233-02.
Component X-ray, ball bond cross-section optical image, stitch bond cross-section optical image, ball bond cross-section SEM micrograph, and optical image of decapsulated wires with dimensions.

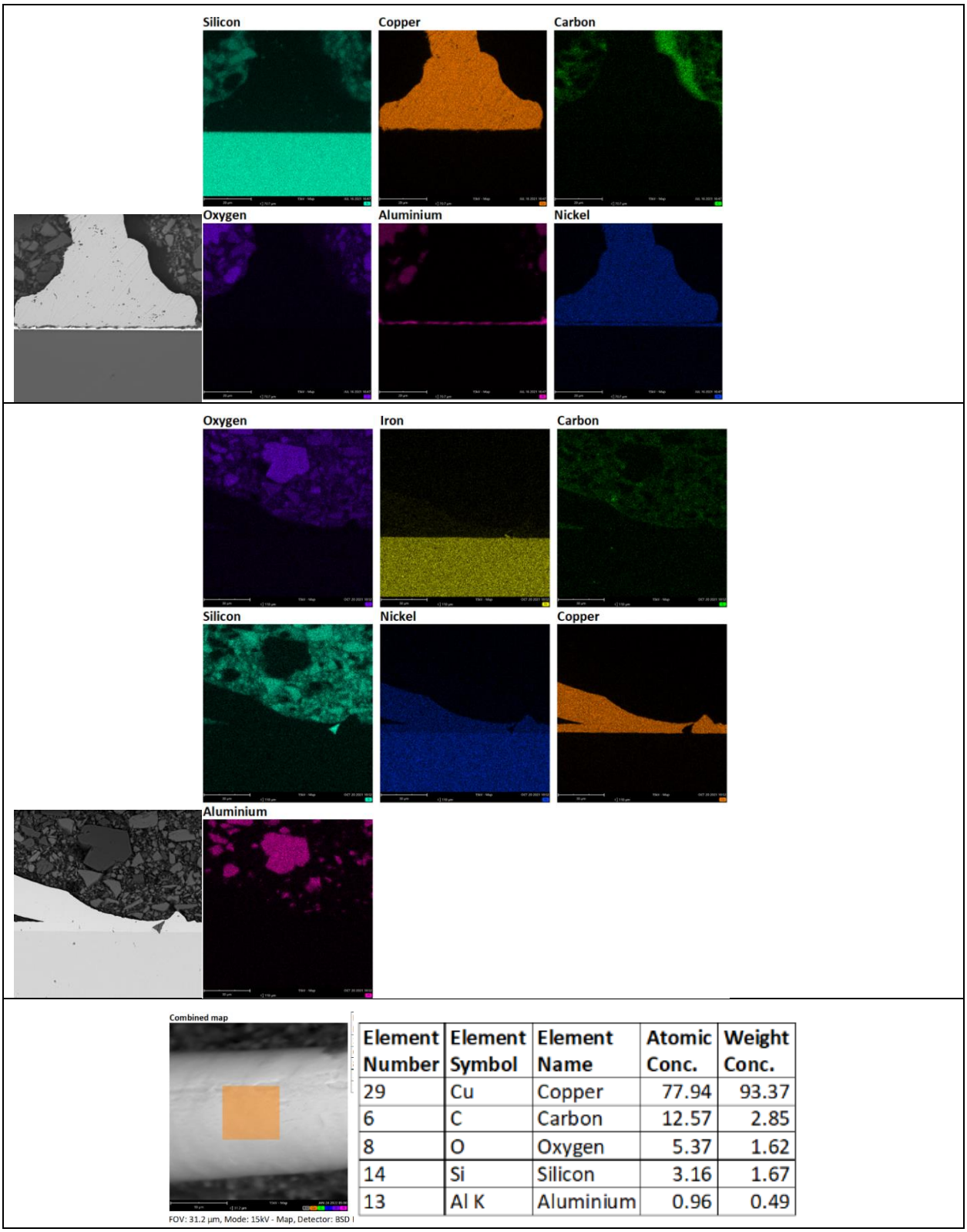

Element Number	Element Symbol	Element Name	Atomic Conc.	Weight Conc.
29	Cu	Copper	77.94	93.37
6	C	Carbon	12.57	2.85
8	O	Oxygen	5.37	1.62
14	Si	Silicon	3.16	1.67
13	Al K	Aluminium	0.96	0.49

Figure C.1-9b. SEM EDS Composition Maps of Ball Bond Cross-Section, Stitch Bond Cross-Section, and Decapsulated Wire Bond for Part M2-D-SOT233-02

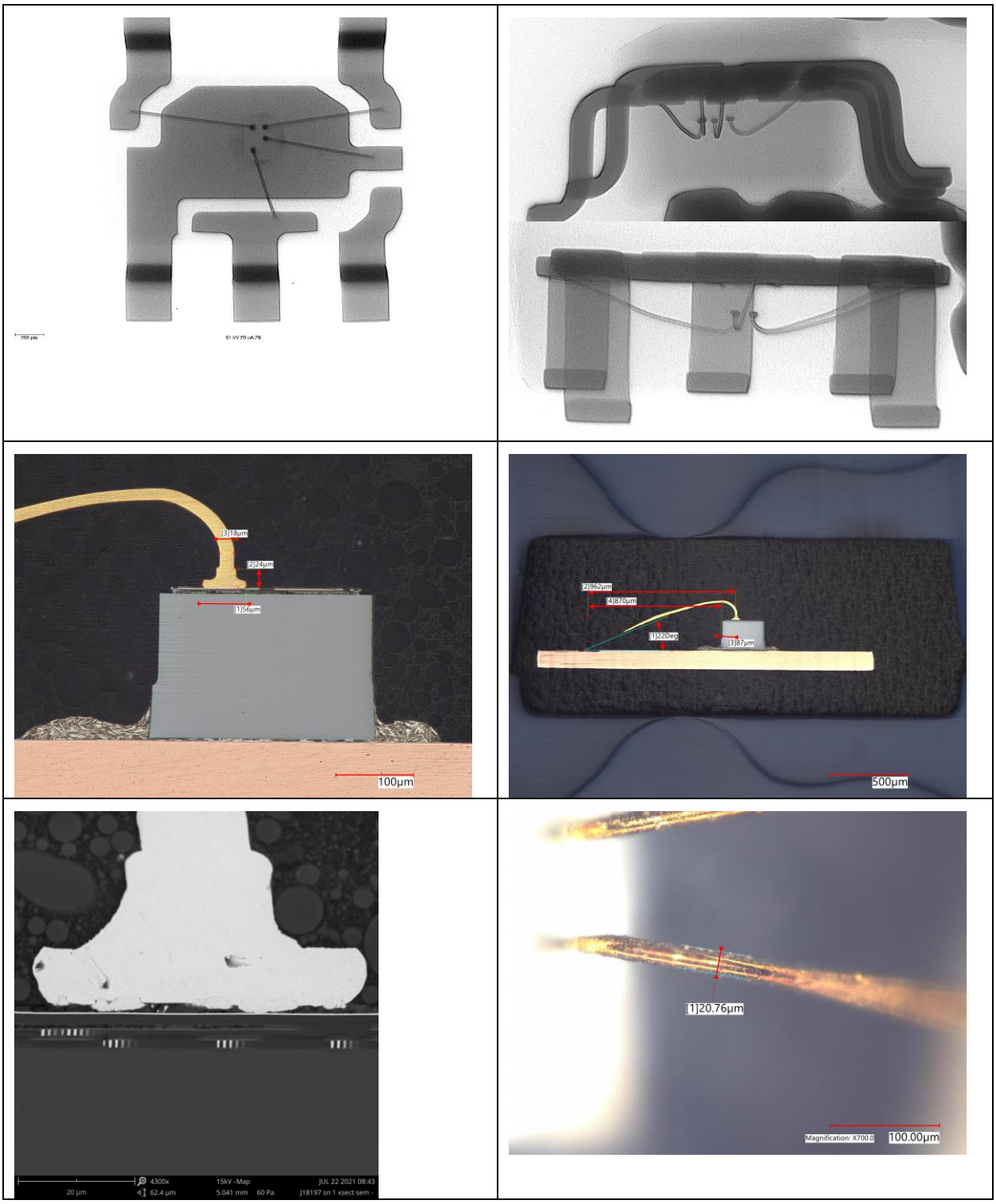

Figure C.1-10a. CA Images for Part M5-MCK-SOT235-01.
Component X-ray, ball bond cross-section optical image, stitch bond cross-section optical image, ball bond cross-section SEM micrograph, and optical image of decapsulated wires with dimensions.

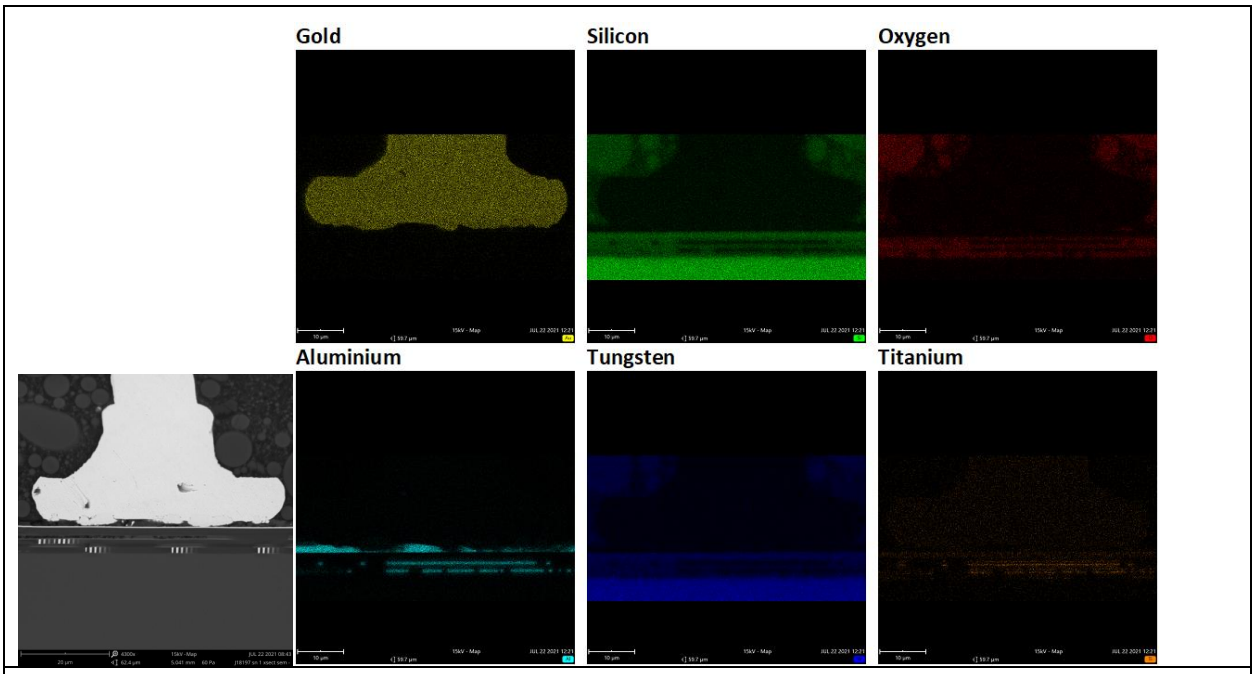

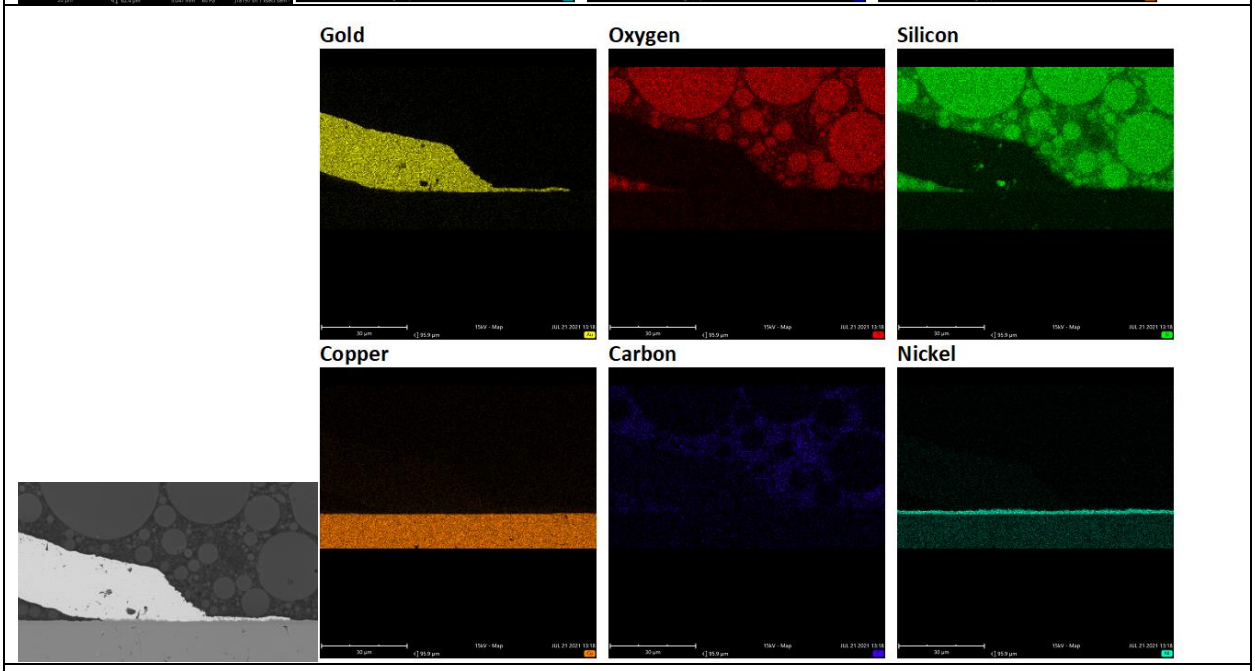

*Gold Wire-No Bare Wire EDS

Figure C.1-10b. SEM EDS Composition Maps of Ball Bond and Stitch Bond Cross-Section for Part M5-MCK-SOT235-01. No decapsulated wire compositional analysis was performed because this is Au wire.

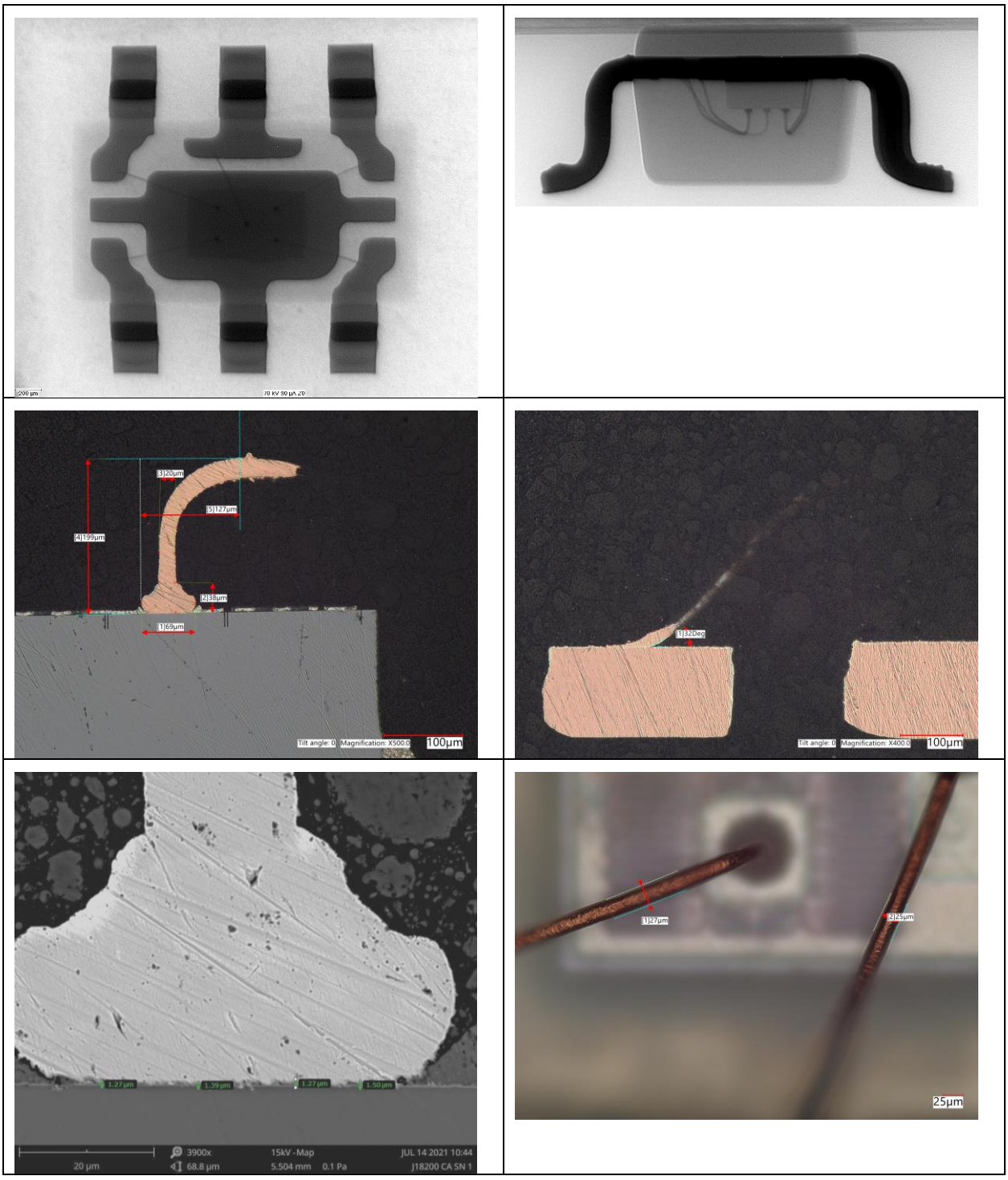

Figure C.1-11a. CA Images for Part M6-D-SOT235-01.
Component X-ray, ball bond cross-section optical image, stitch bond cross-section optical image, ball bond cross-section SEM micrograph and optical image of decapsulated wires with dimensions.

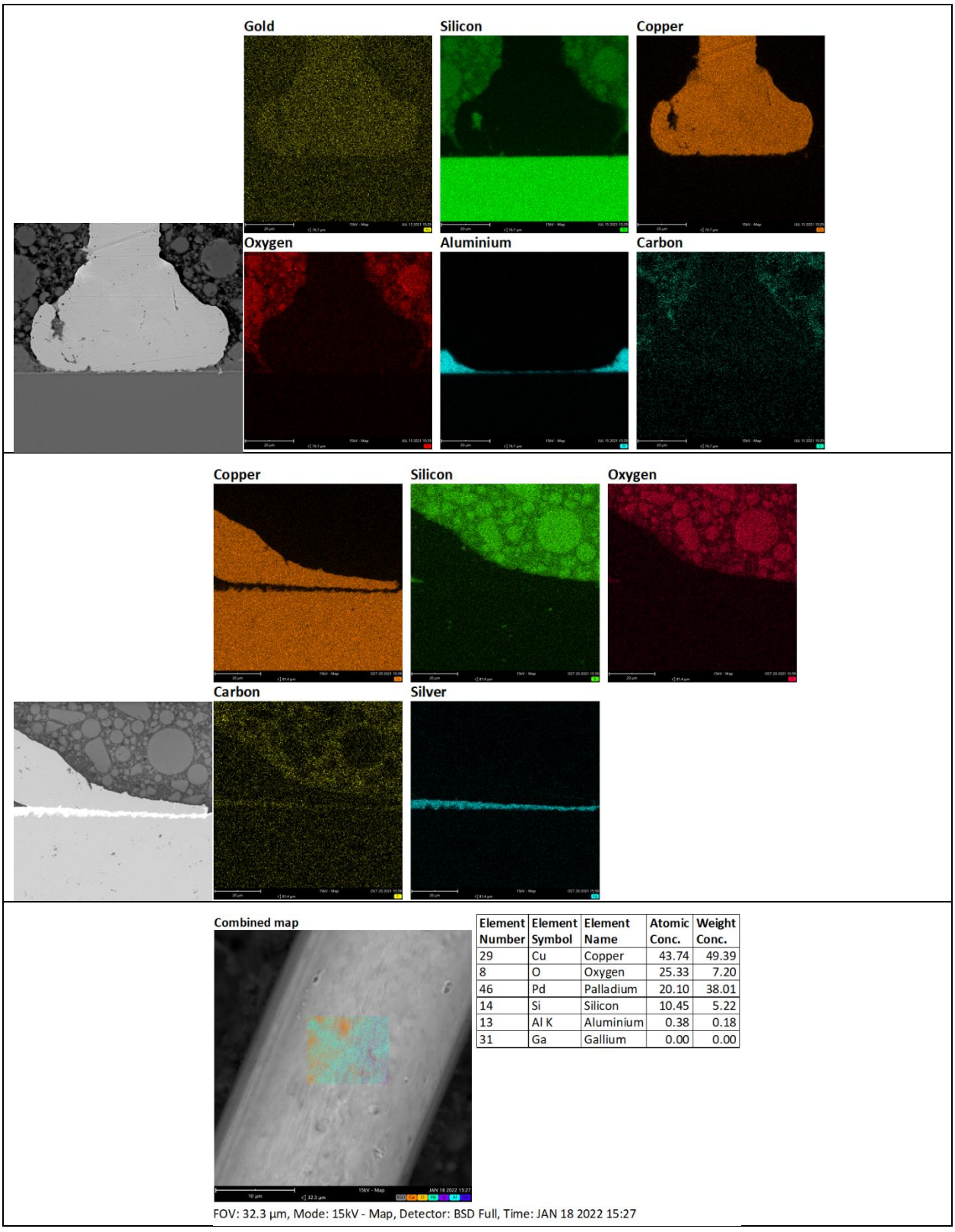

Element Number	Element Symbol	Element Name	Atomic Conc.	Weight Conc.
29	Cu	Copper	43.74	49.39
8	O	Oxygen	25.33	7.20
46	Pd	Palladium	20.10	38.01
14	Si	Silicon	10.45	5.22
13	Al K	Aluminium	0.38	0.18
31	Ga	Gallium	0.00	0.00

Figure C.1-11b. SEM EDS Composition Maps of Ball Bond Cross-Section, Stitch Bond Cross-Section, and Decapsulated Wire Bond for Part M6-D-SOT-235-01

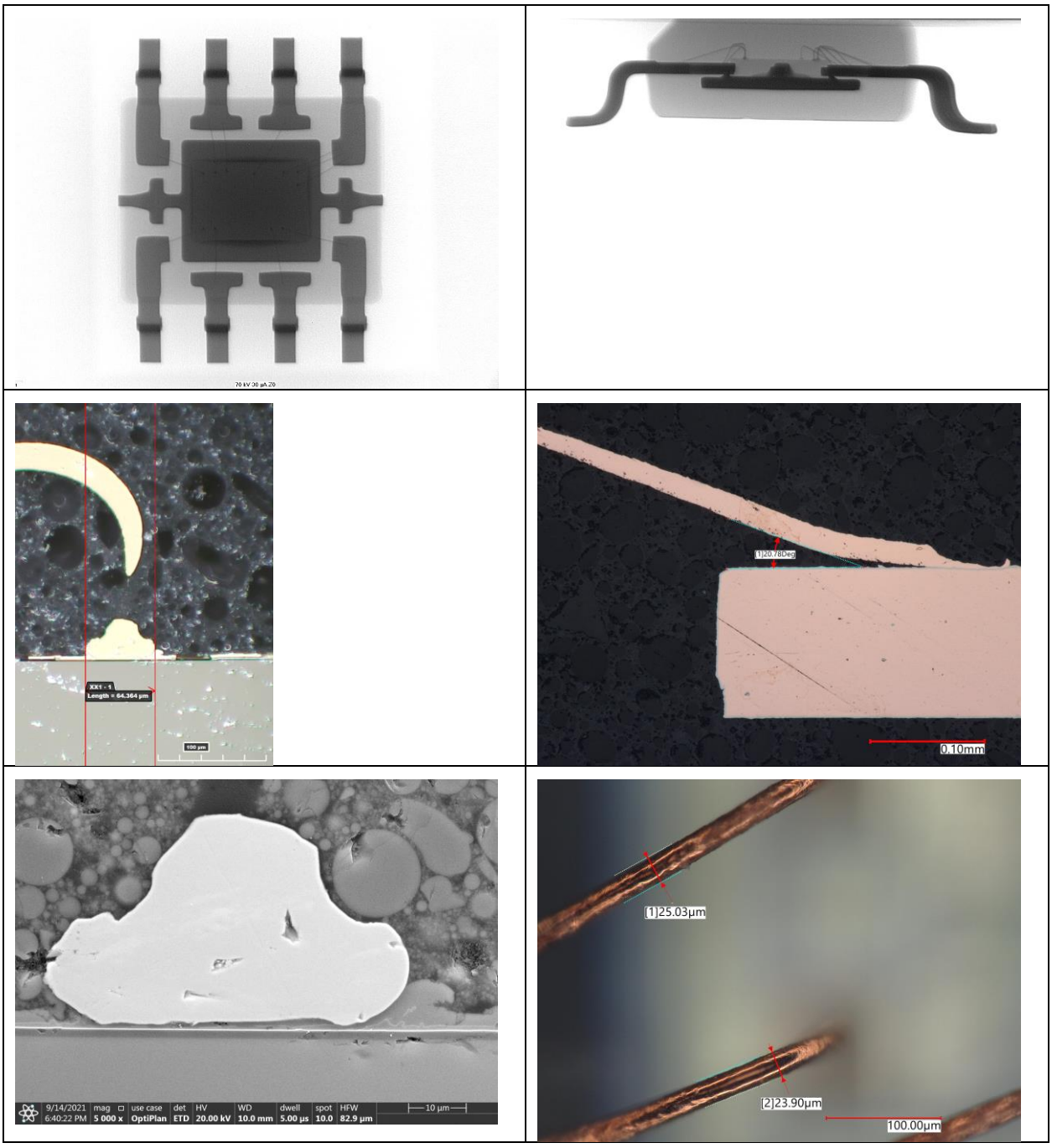

Figure C.1-12a. CA Images for Part M5-MCK-SOIC8-01.
Component X-ray, ball bond cross-section optical image, stitch bond cross-section optical image, ball bond cross-section SEM micrograph, and optical image of decapsulated wires with dimensions.

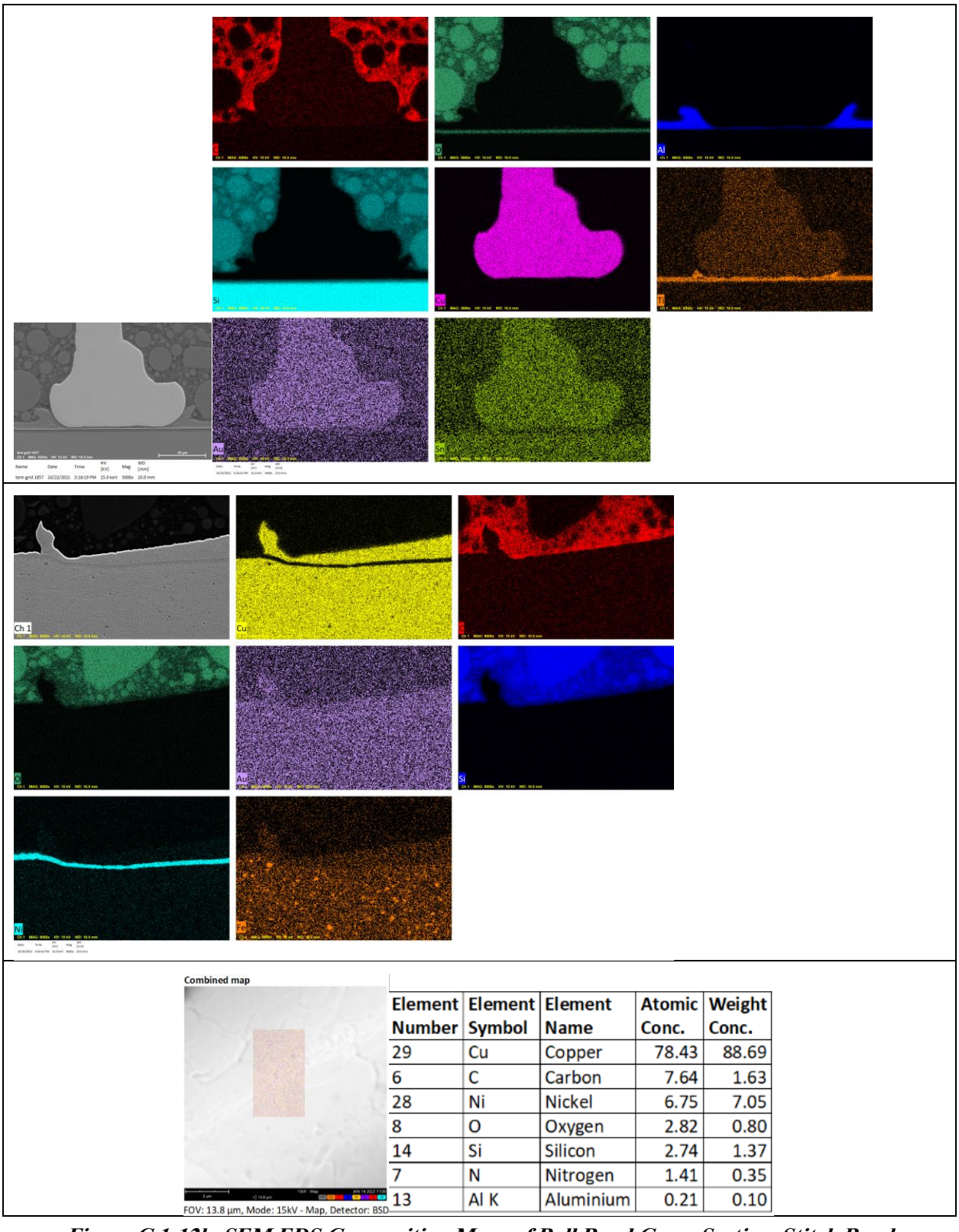

Element Number	Element Symbol	Element Name	Atomic Conc.	Weight Conc.
29	Cu	Copper	78.43	88.69
6	C	Carbon	7.64	1.63
28	Ni	Nickel	6.75	7.05
8	O	Oxygen	2.82	0.80
14	Si	Silicon	2.74	1.37
7	N	Nitrogen	1.41	0.35
13	Al K	Aluminium	0.21	0.10

Figure C.1-12b. SEM EDS Composition Maps of Ball Bond Cross-Section, Stitch Bond Cross-Section, and Decapsulated Wire Bond for Part M5-MCK-SOIC8-01

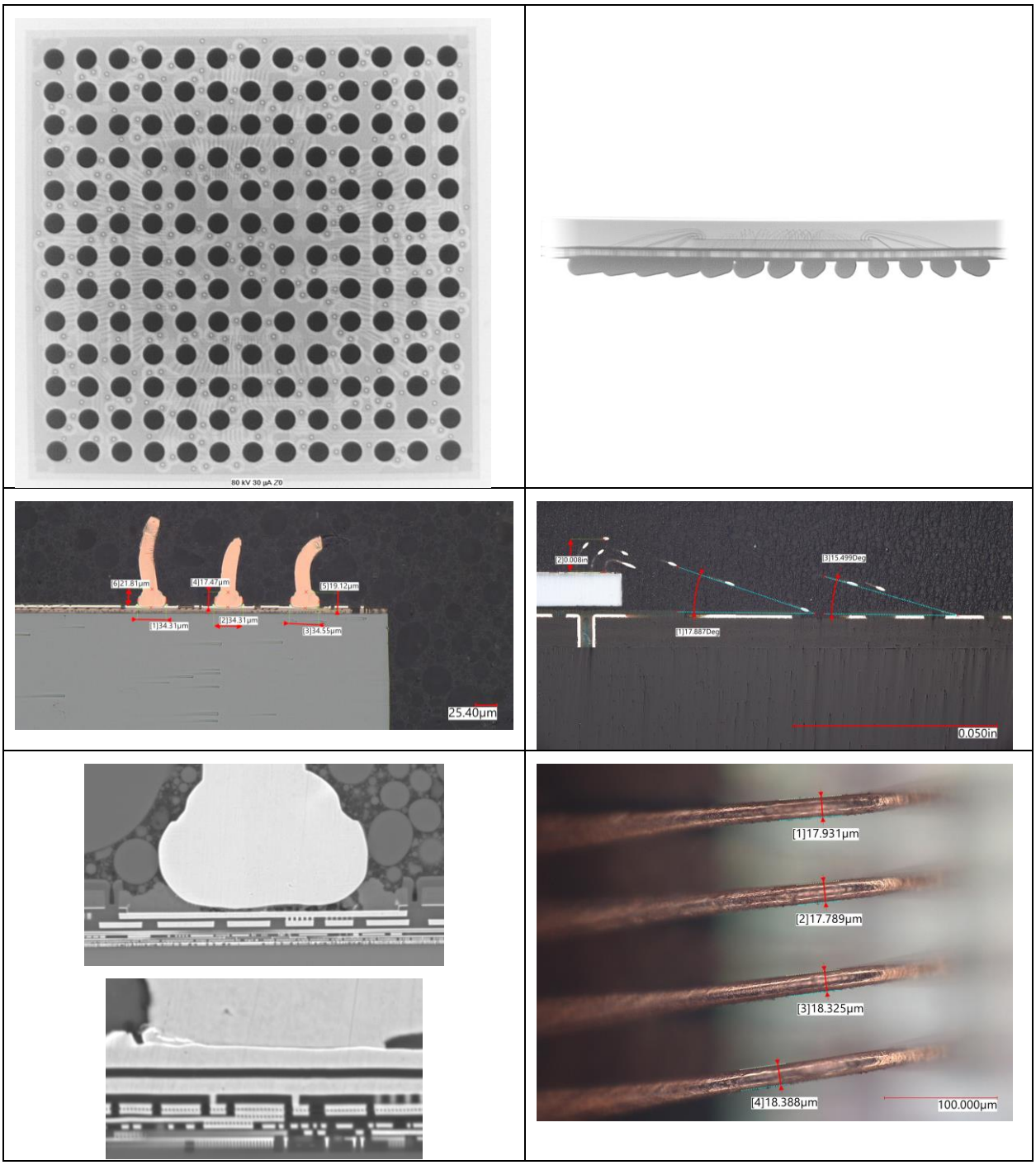

Figure C.1-13a. CA Images for Part M7-MCK-LFBGA169-01.
Component X-ray, ball bond cross-section optical image, stitch bond cross-section optical image, ball bond cross-section SEM micrograph, and optical image of decapsulated wires with dimensions.

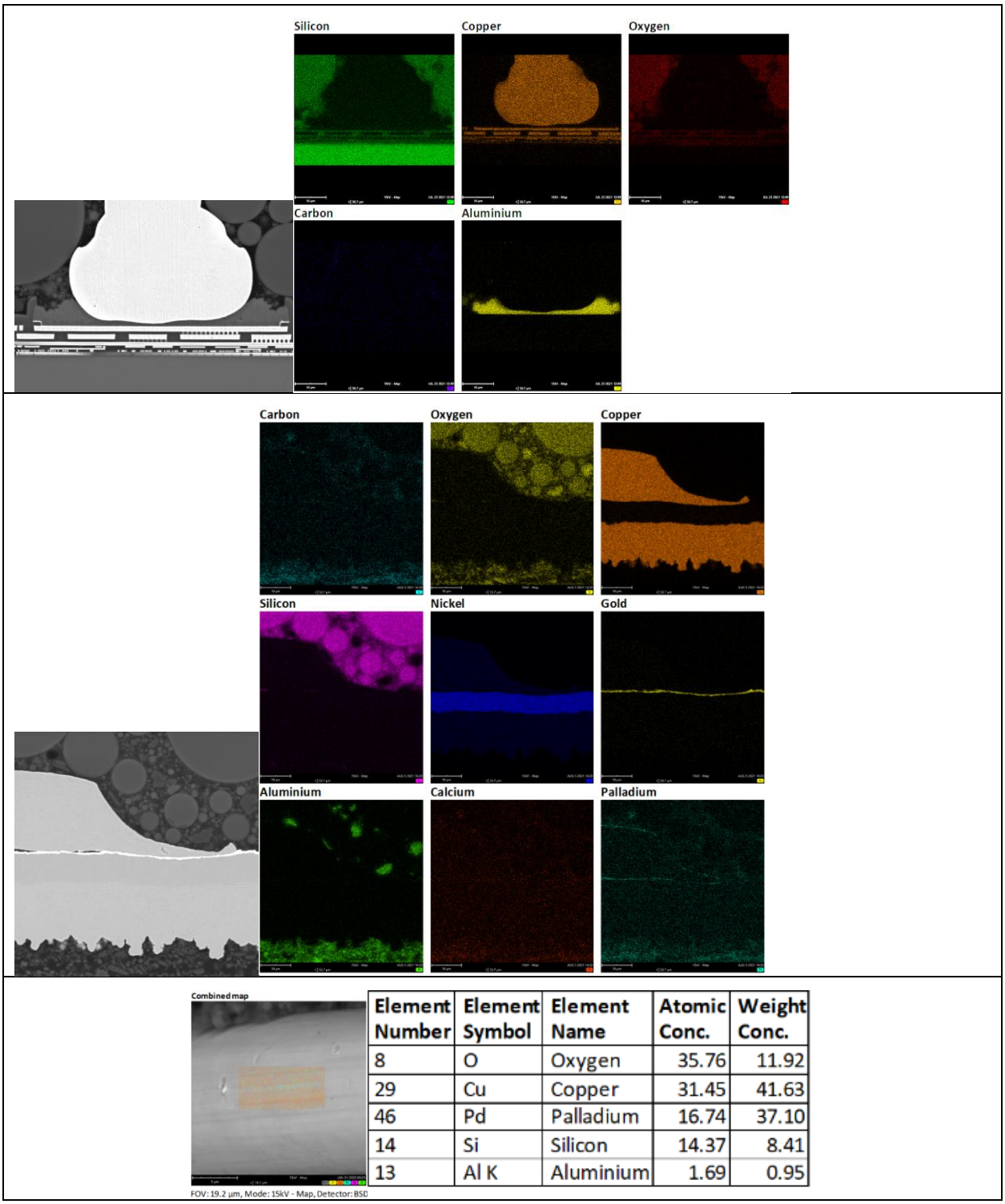

Element Number	Element Symbol	Element Name	Atomic Conc.	Weight Conc.
8	O	Oxygen	35.76	11.92
29	Cu	Copper	31.45	41.63
46	Pd	Palladium	16.74	37.10
14	Si	Silicon	14.37	8.41
13	Al K	Aluminium	1.69	0.95

Figure C.1-13b. SEM EDS Composition Maps of Ball Bond Cross-Section, Stitch Bond Cross-Section, and Decapsulated Wire Bond for Part M7-MCK-LFBGA169-01

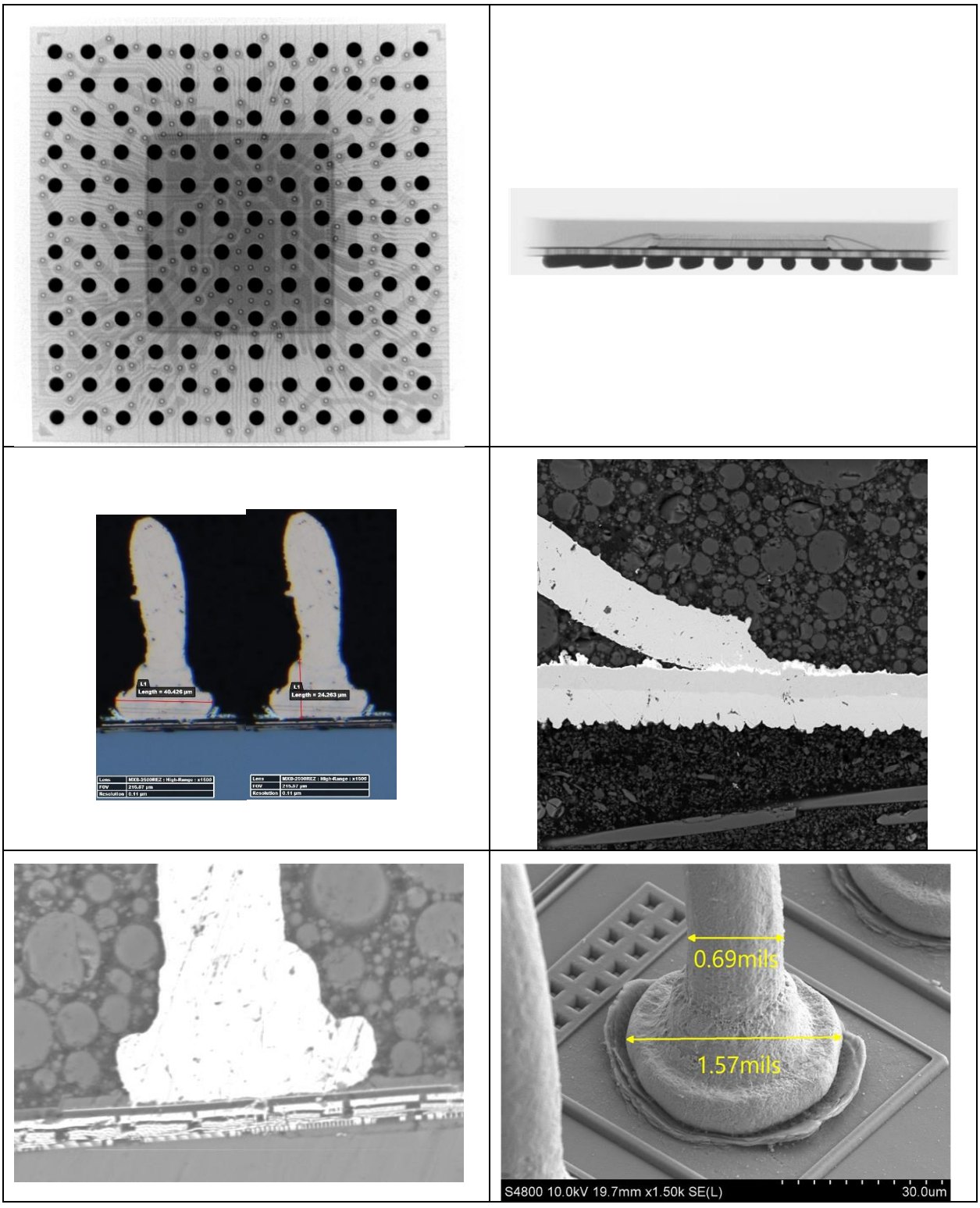

Figure C.1-14a. CA Images for Part M1-MCK-LFBGA144-01.
Component X-ray, ball bond cross-section optical image, stitch bond cross-section optical image, ball bond cross-section SEM micrograph, and optical image of decapsulated wires with dimensions.

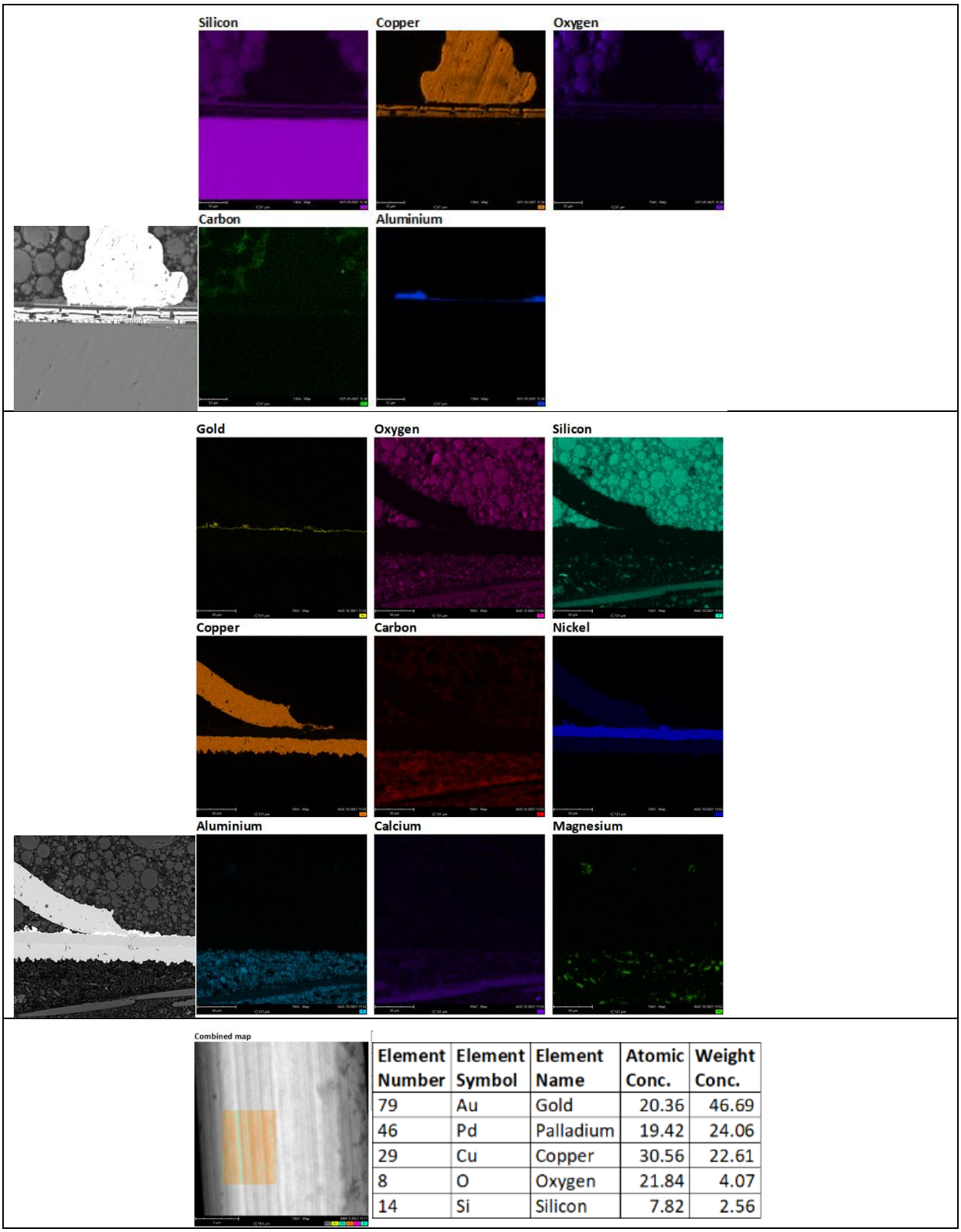

Element Number	Element Symbol	Element Name	Atomic Conc.	Weight Conc.
79	Au	Gold	20.36	46.69
46	Pd	Palladium	19.42	24.06
29	Cu	Copper	30.56	22.61
8	O	Oxygen	21.84	4.07
14	Si	Silicon	7.82	2.56

Figure C.1-14b. SEM EDS Composition Maps of Ball Bond Cross-Section, Stitch Bond Cross-Section, and Decapsulated Wire Bond for Part M1-MCK-LFBGA144-01

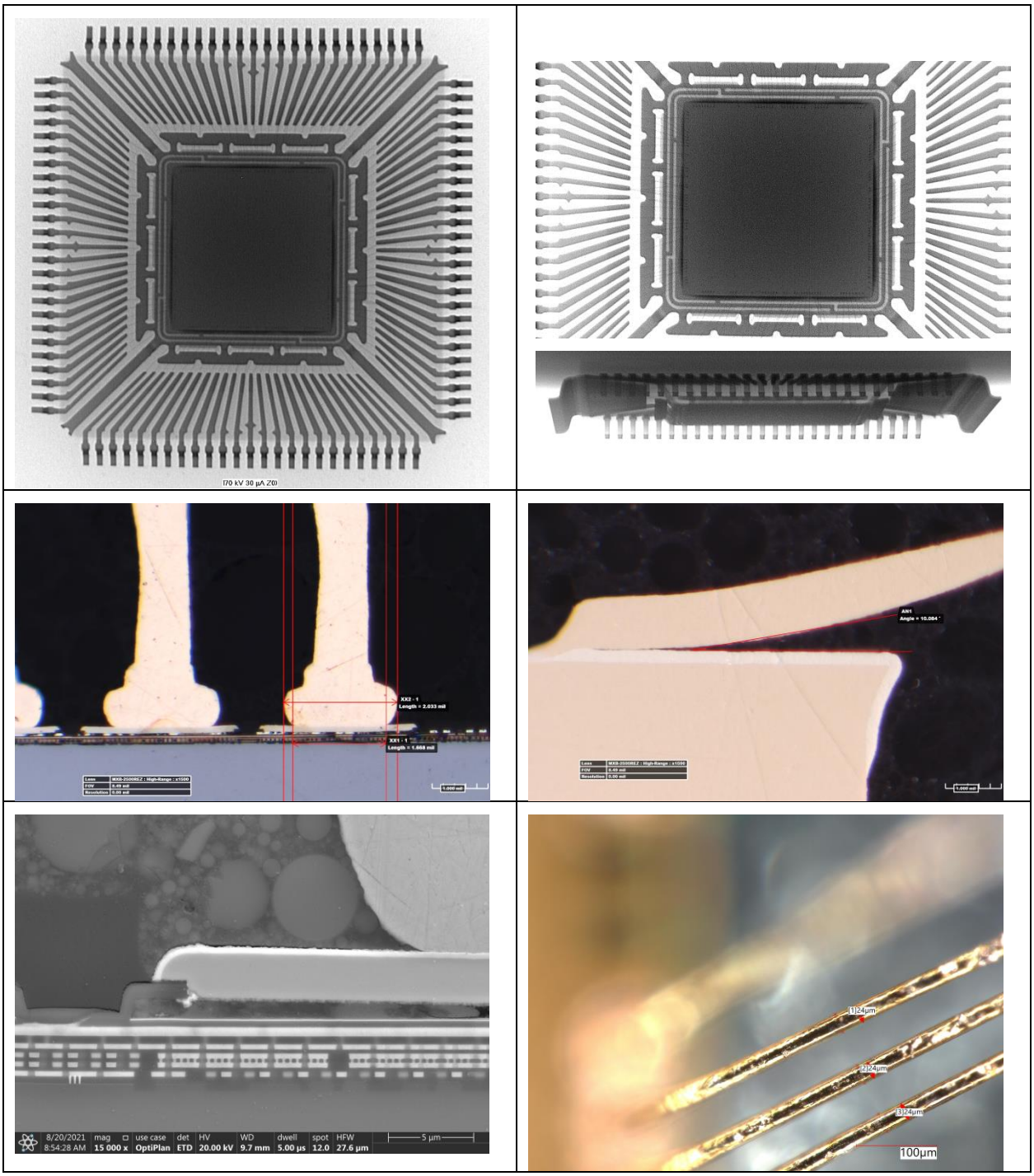

Figure C.1-15a. CA images for part number M8-MCK-LQFP100-01. Component X-ray, ball bond cross-section optical image, stitch bond cross-section optical image, ball bond cross-section SEM micrograph, and optical image of decapsulated wires with dimensions.

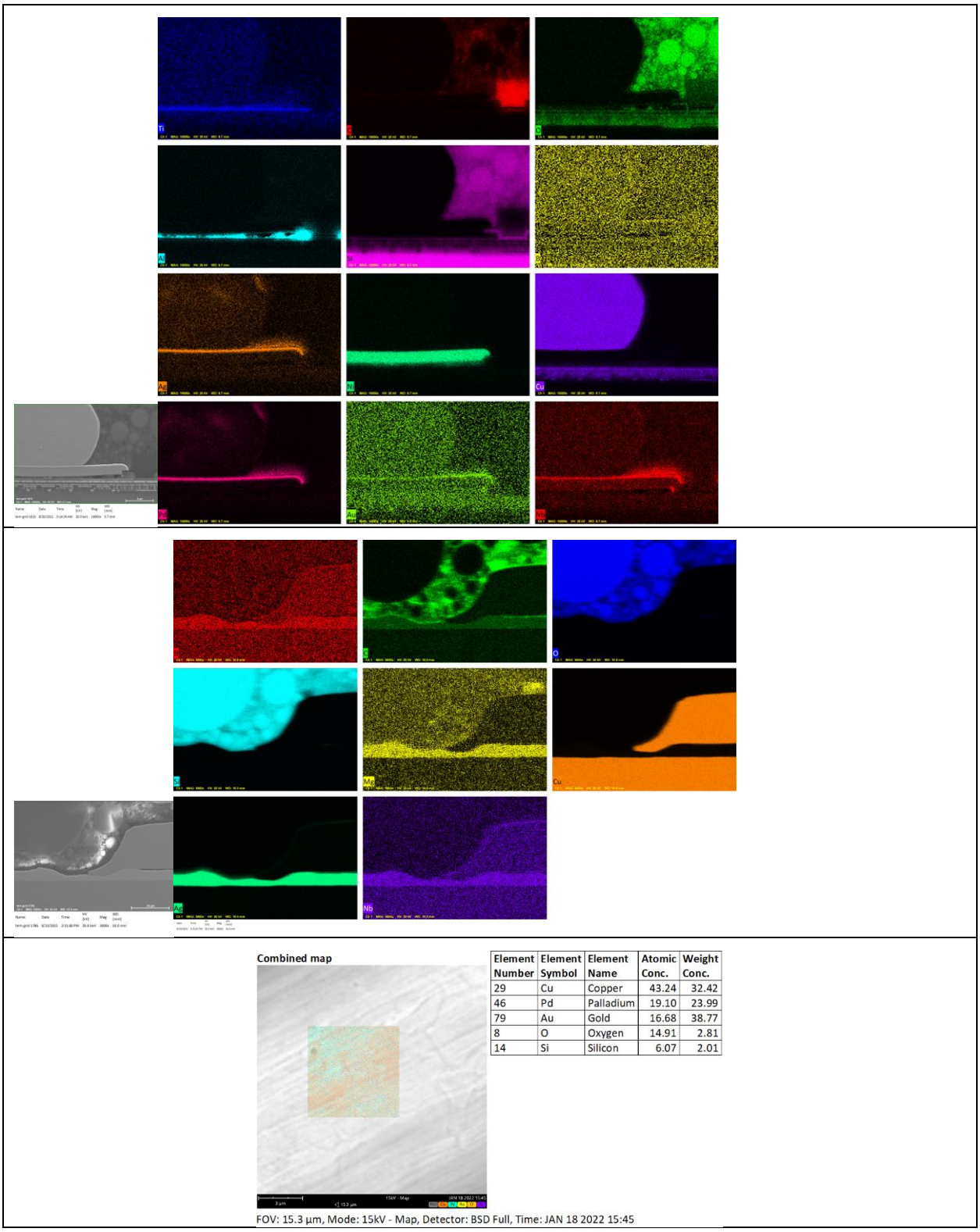

Element Number	Element Symbol	Element Name	Atomic Conc.	Weight Conc.
29	Cu	Copper	43.24	32.42
46	Pd	Palladium	19.10	23.99
79	Au	Gold	16.68	38.77
8	O	Oxygen	14.91	2.81
14	Si	Silicon	6.07	2.01

Figure C.1-15b. SEM EDS Composition Maps of Ball Bond Cross-Section, Stitch Bond Cross-Section, and Decapsulated Wire Bond for Part M8-MCK-LQFP100-01

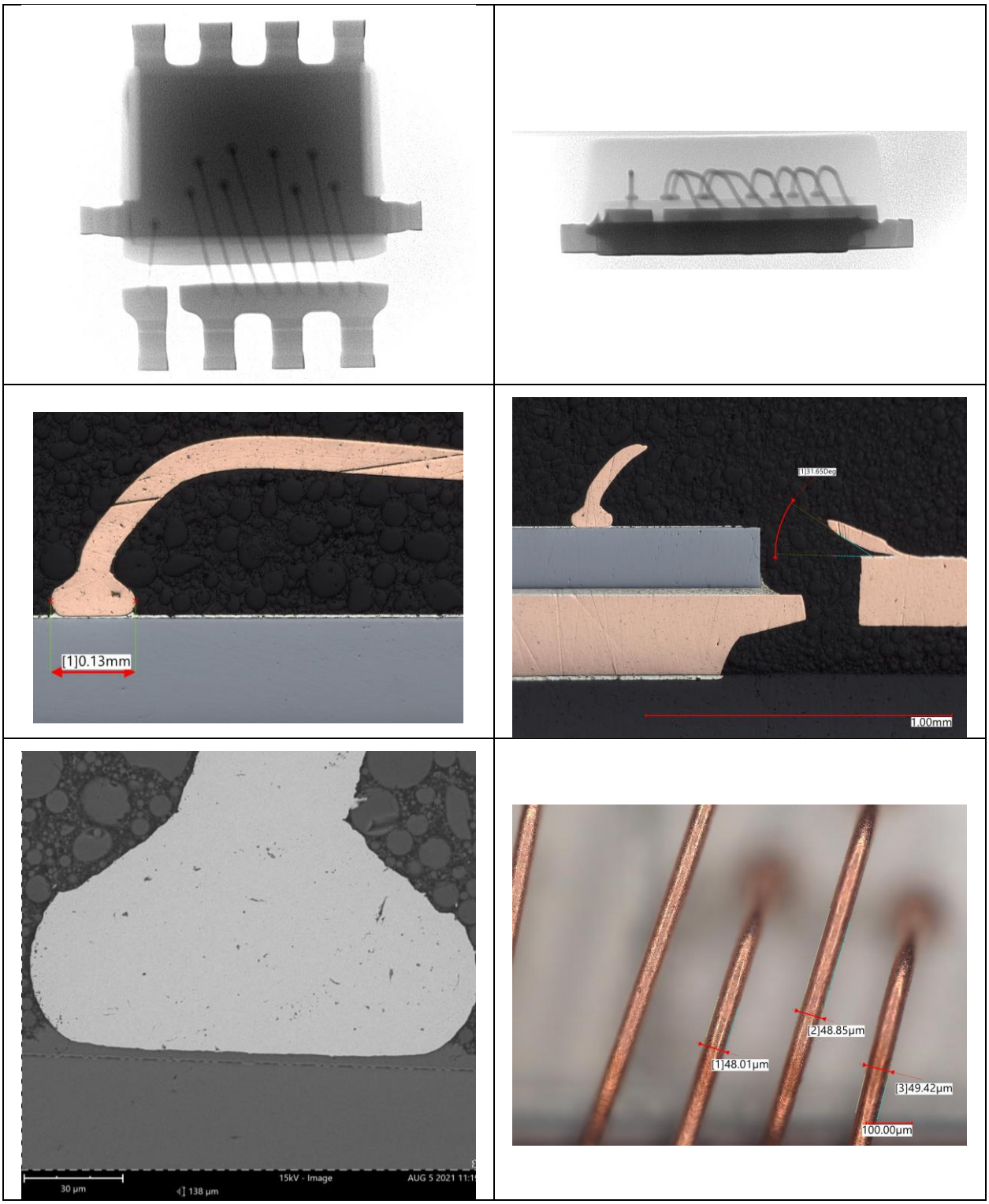

Figure C.1-16a. CA Images for Part M9-D-CUSTOM-01.
Component X-ray, ball bond cross-section optical image, stitch bond cross-section optical image, ball bond cross-section SEM micrograph, and optical image of decapsulated wires with dimensions.

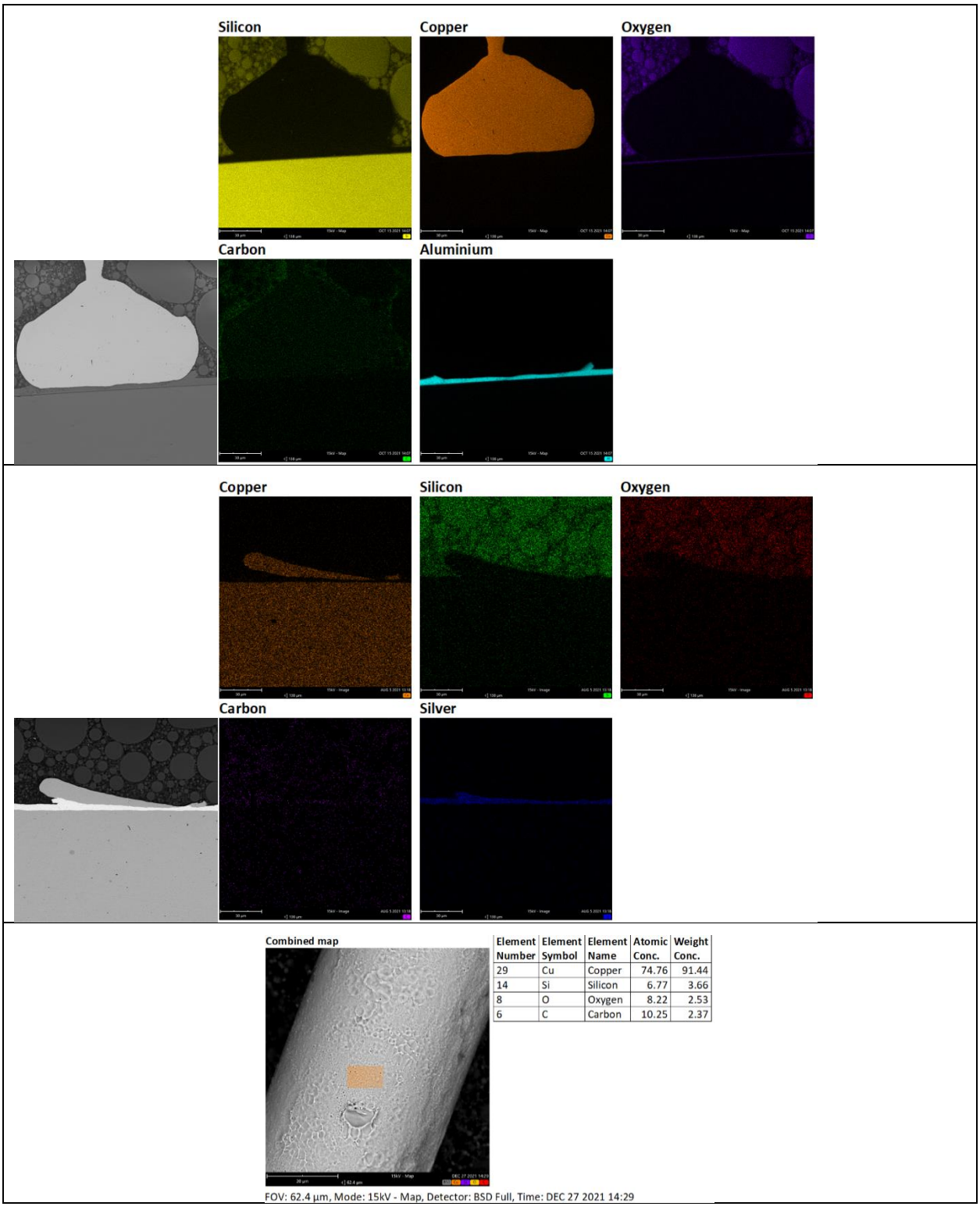

Element Number	Element Symbol	Element Name	Atomic Conc.	Weight Conc.
29	Cu	Copper	74.76	91.44
14	Si	Silicon	6.77	3.66
8	O	Oxygen	8.22	2.53
6	C	Carbon	10.25	2.37

Figure C.1-16b. SEM EDS Composition Maps of Ball Bond Cross-Section, Stitch Bond Cross-Section, and Decapsulated Wire Bond for Part M9-D-CUSTOM-01.

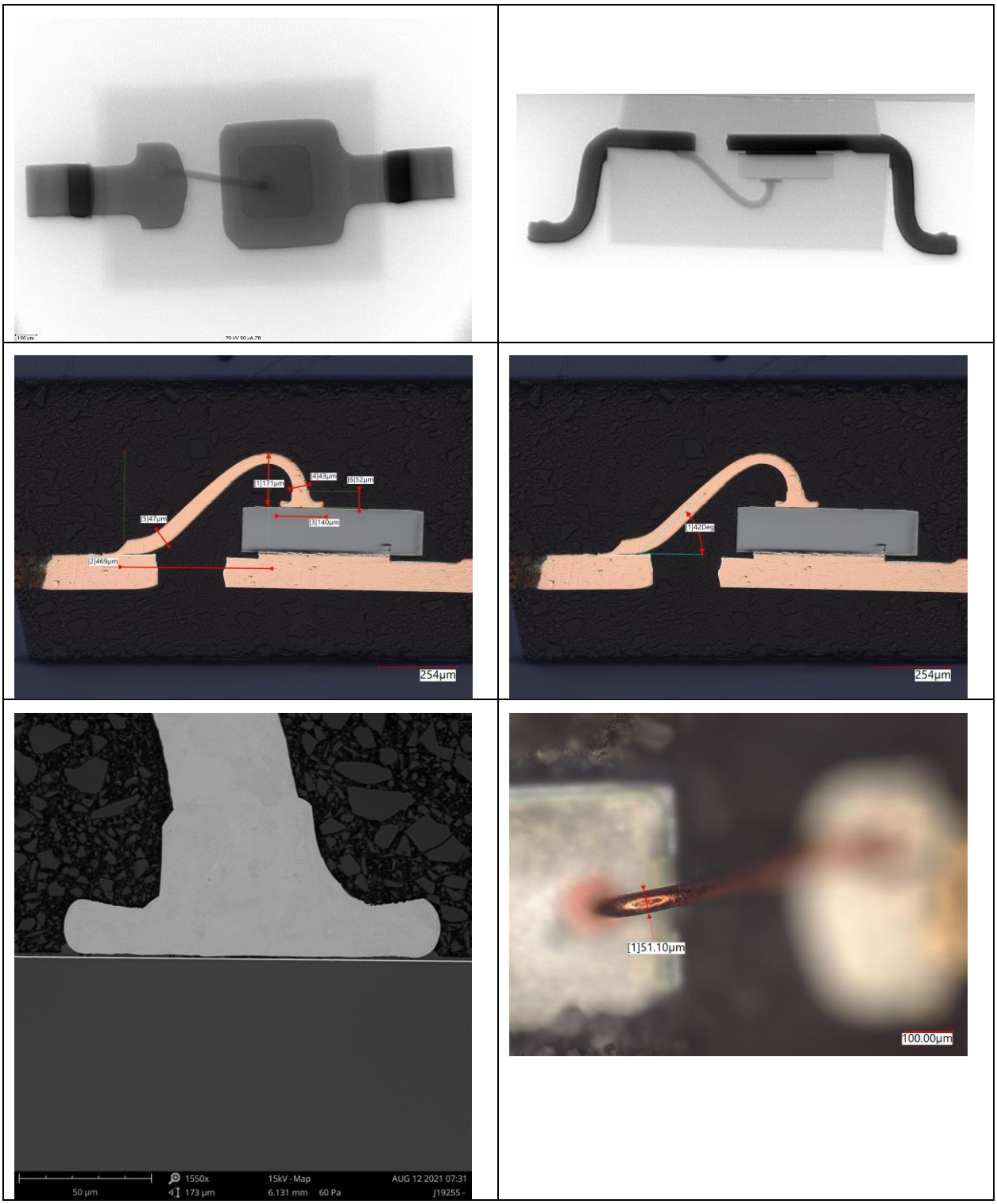

Figure C.1-17a. CA Images for Part M10-D-SOD323-01.
Component X-ray, ball bond cross-section optical image, stitch bond cross-section optical image, ball bond cross-section SEM micrograph, and optical image of decapsulated wires with dimensions.

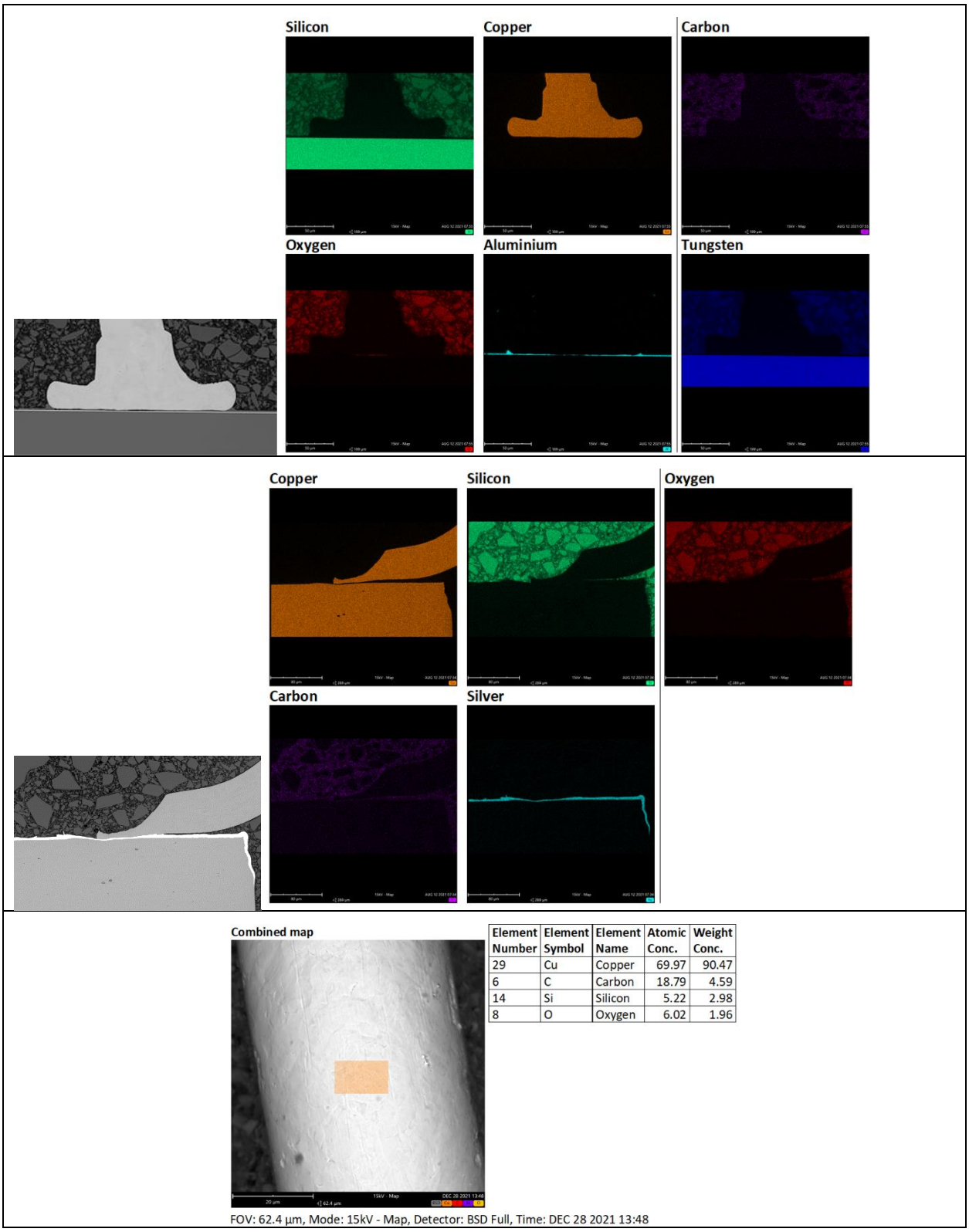

Element Number	Element Symbol	Element Name	Atomic Conc.	Weight Conc.
29	Cu	Copper	69.97	90.47
6	C	Carbon	18.79	4.59
14	Si	Silicon	5.22	2.98
8	O	Oxygen	6.02	1.96

Figure C.1-17b. SEM EDS Composition Maps of Ball Bond Cross-Section, Stitch Bond Cross-Section, and Decapsulated Wire Bond for Part M10-D-SOD323-01

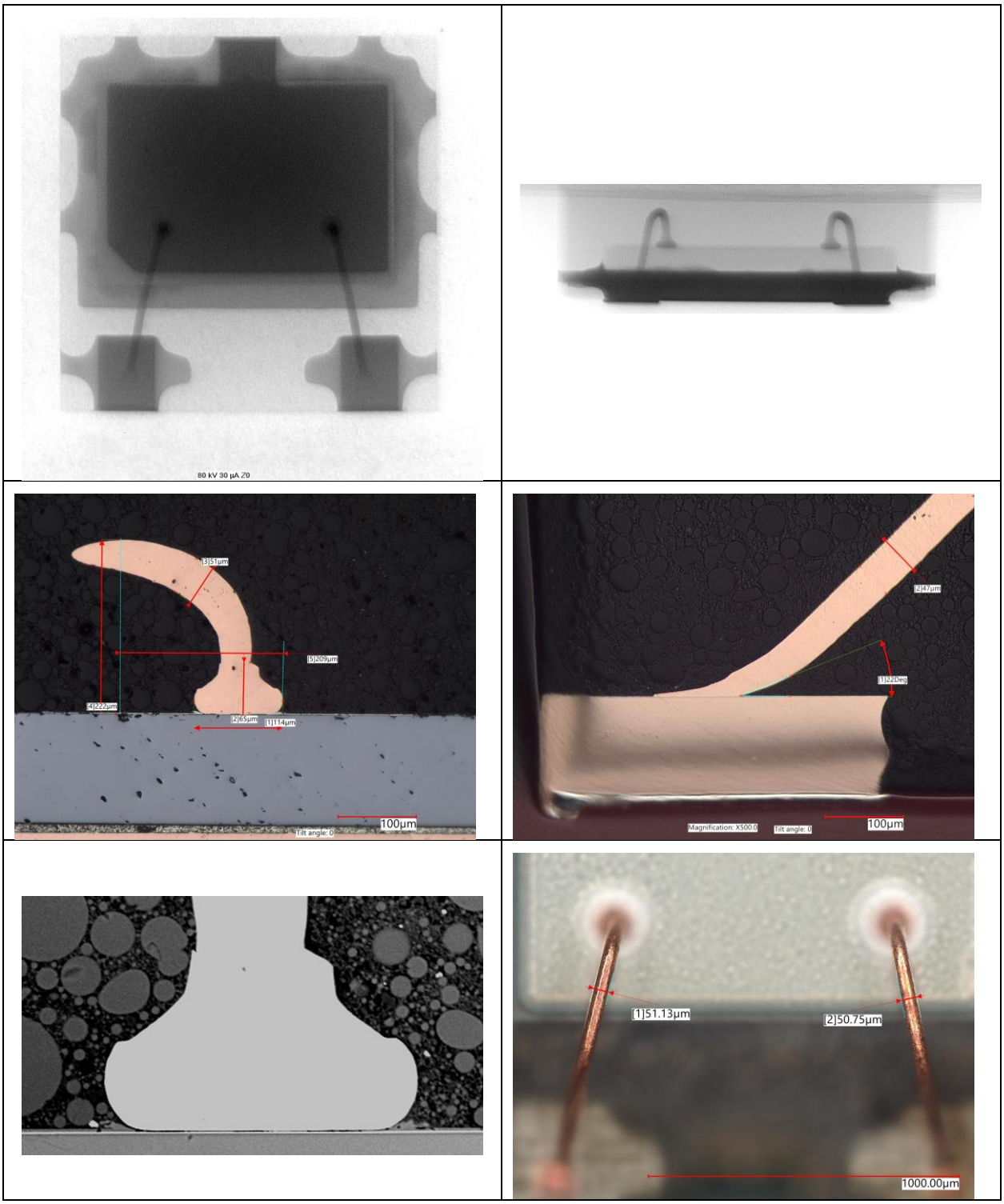

Figure C.1-18a. CA Images for Part M10-D-SOT1061-01.
Component X-ray, ball bond cross-section optical image, stitch bond cross-section optical image, ball bond cross-section SEM micrograph, and optical image of decapsulated wires with dimensions.

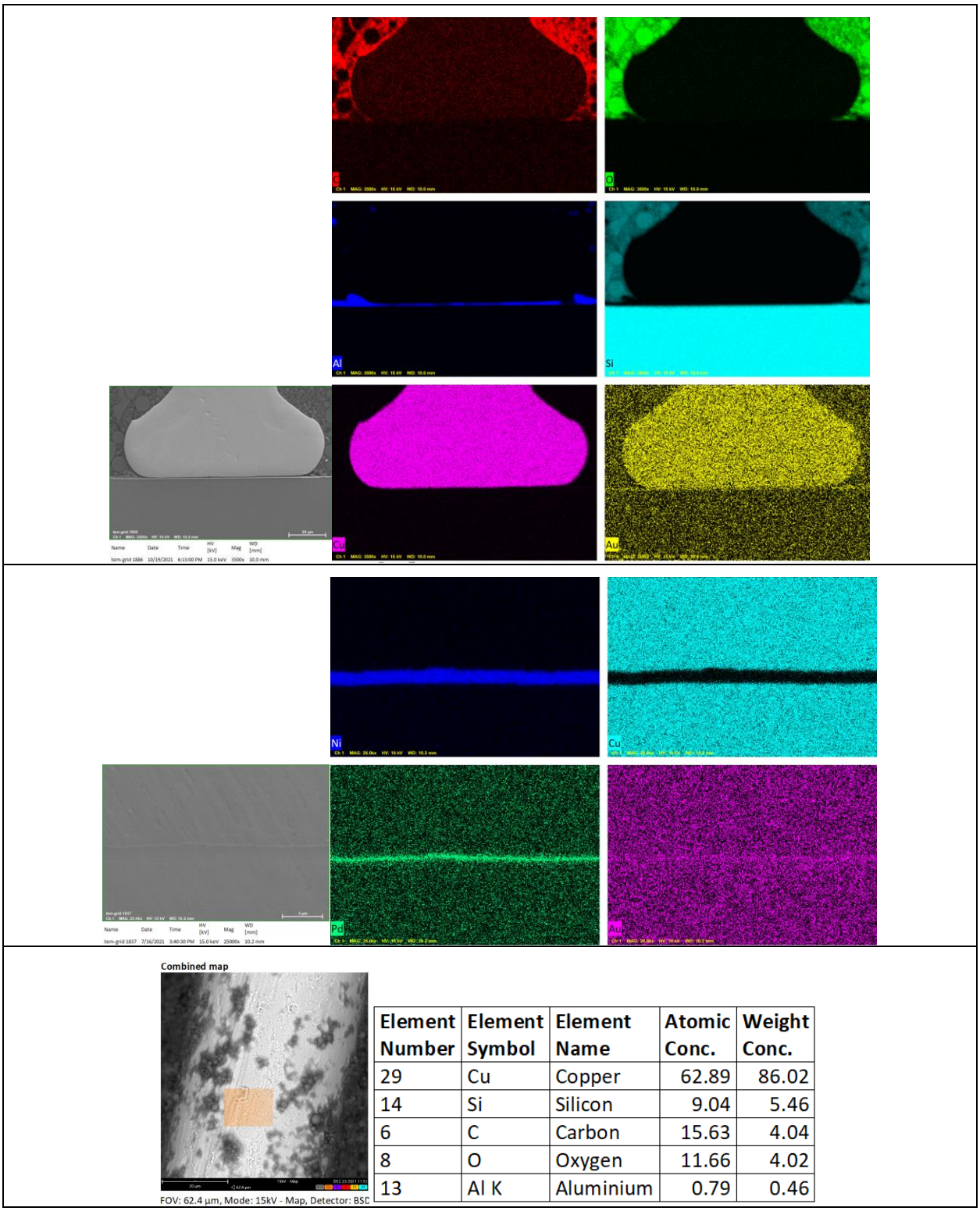

Element Number	Element Symbol	Element Name	Atomic Conc.	Weight Conc.
29	Cu	Copper	62.89	86.02
14	Si	Silicon	9.04	5.46
6	C	Carbon	15.63	4.04
8	O	Oxygen	11.66	4.02
13	Al K	Aluminium	0.79	0.46

Figure C.1-18b. SEM EDS Composition Maps of Ball Bond Cross-Section, Stitch Bond Cross-Section, and Decapsulated Wire Bond for Part M10-D-SOT1061-01.

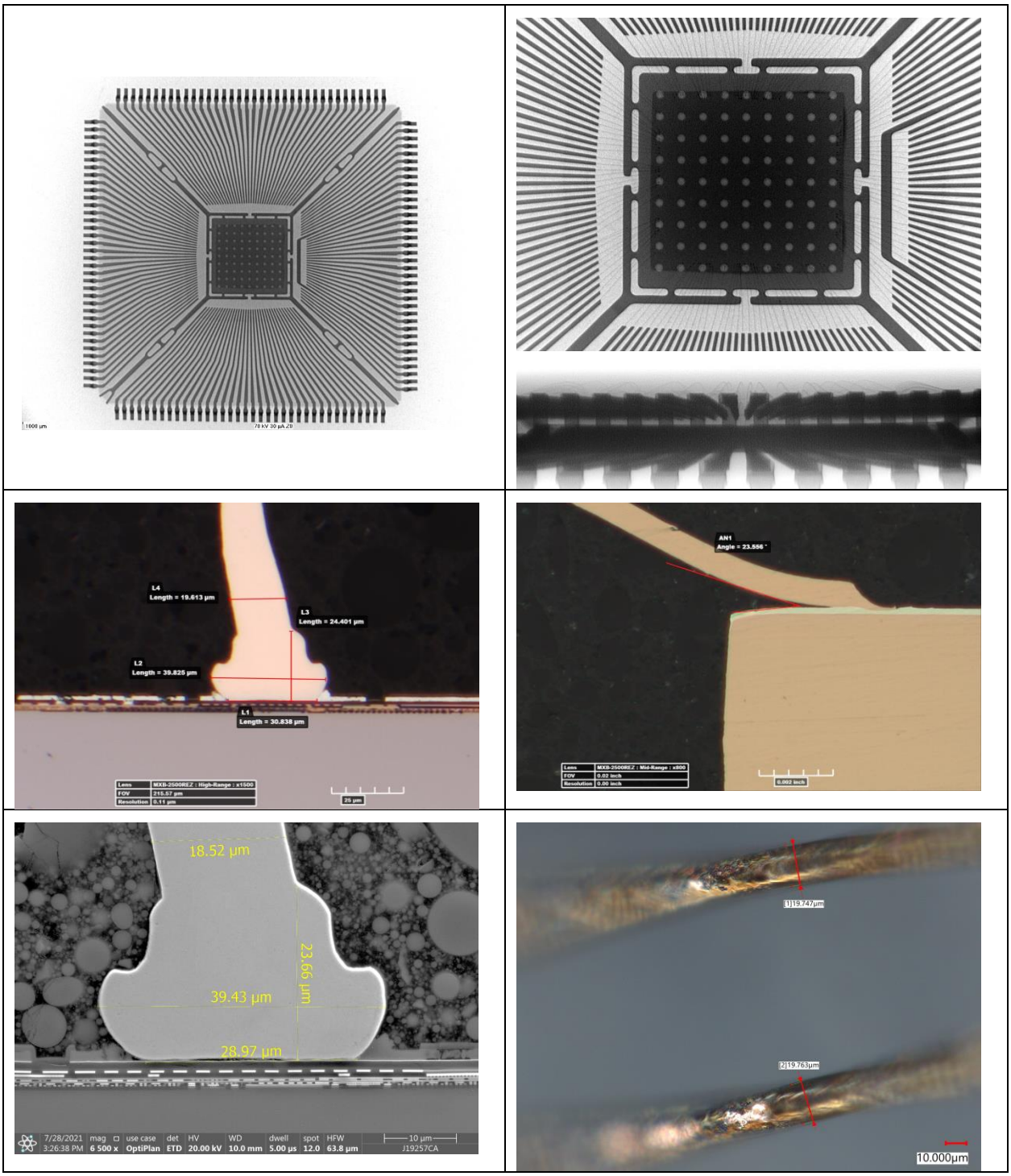

Figure C.1-19a. CA Images for Part M11-MCK-TQFP144-01.
Component X-ray, ball bond cross-section optical image, stitch bond cross-section optical image, ball bond cross-section SEM micrograph, and optical image of decapsulated wires with dimensions.

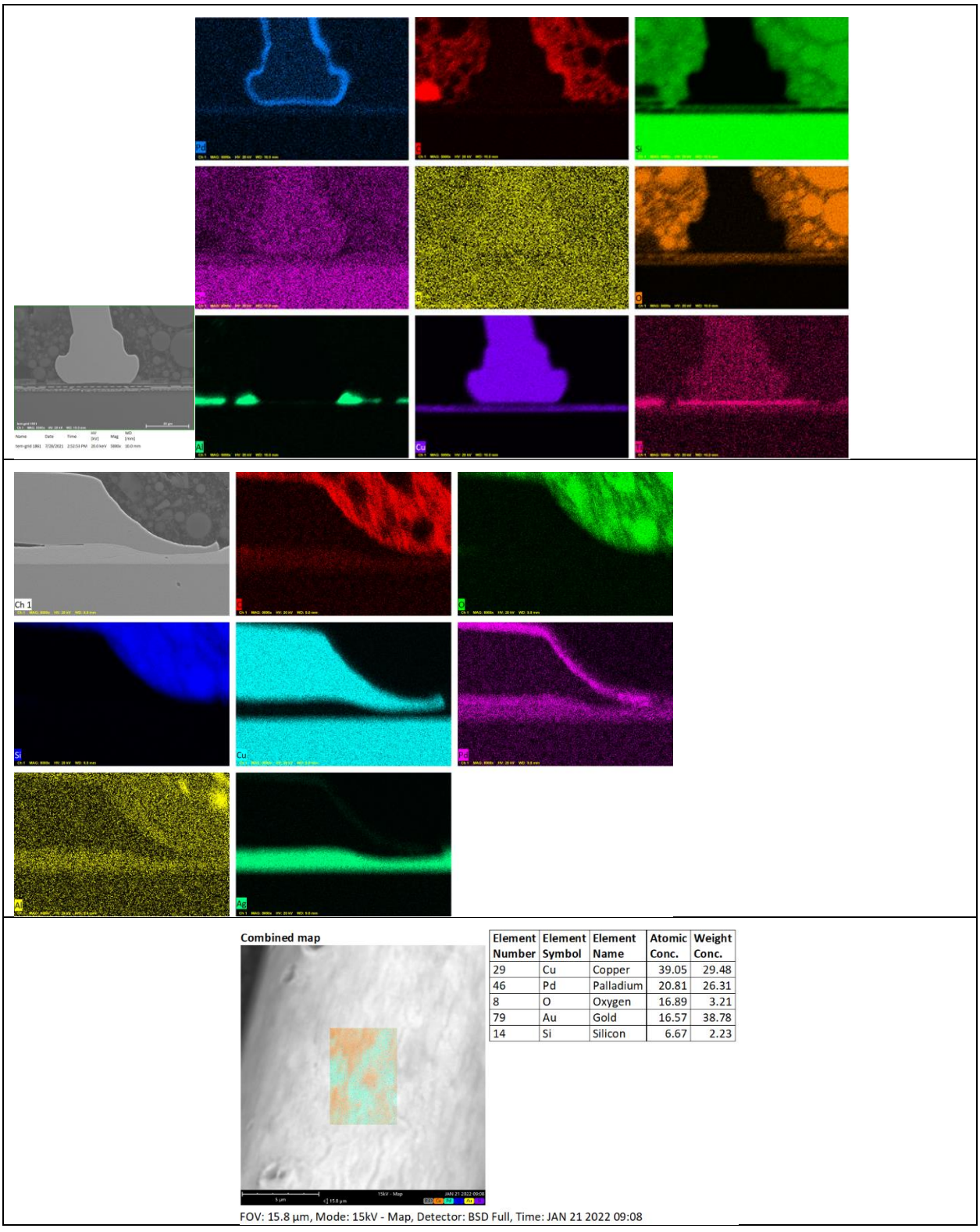

Element Number	Element Symbol	Element Name	Atomic Conc.	Weight Conc.
29	Cu	Copper	39.05	29.48
46	Pd	Palladium	20.81	26.31
8	O	Oxygen	16.89	3.21
79	Au	Gold	16.57	38.78
14	Si	Silicon	6.67	2.23

Figure C.1-19b. SEM EDS Composition Maps of Ball Bond Cross-Section, Stitch Bond Cross-Section, and Decapsulated Wire Bond for Part M11-MCK-TQFP144-01.

Supplemental compositional analyses were performed using a Bruker X-flash 6-60 60 mm^2 Energy Dispersive X-ray Spectrometer on a ThermoFisher Apreo S SEM for select components (M3-MCK-TQFP100-01, M4-MCK-FBGA256-01, M5-MCK-SOT235-01, M10-D-SOT1061-01 and M11-MCK-TQFP144-01) to confirm the presence or absence of halides in the molding compound, since preliminary assessment results were unclear. Analyses were performed using a 30kV e-beam to enable generation of characteristic X-ray peaks for Br (K emission lines at 11.88, 11.92, and 13.29keV). These conditions were used to distinguish between Br and Al, since Al has no emission lines in this region. No Br or other halides were detected in the mold compounds of these samples. Figures C.1-20 through C.1-24 provide the energy spectra, SEM images, composite energy elemental maps, and individual energy maps for the molding compounds of each part inspected. Characteristic energy levels for Al, Br, and Au are provided in Table C.1-2. Note that among the L-series, Lα is the dominant peak, followed by Lβ. It is clear from these energy levels that the L-series of Br is very close to the K-series of Al. For elements with Z between 19 and 59, Kβ is about 10-20% the magnitude of Kα.

Table C.1-2. Detectable Characteristic Energy Levels for Al, Br, and Au that EDS on ThermoFisher Apreo SEM Can Detect Using 30kV Electron Beam

All energies keV	Al (Z=13)	Br (Z=35)	Au (Z=79)
Kα	1.486	11.904	68.804 (not detectable in EDS)
Kβ	1.553	13.296	78.095 (not detectable in EDS)
Ll		1.293	8.492
Ln		1.339	10.305
Lα1		1.480	9.710
Lβ1		1.526	11.439
Lβ2			11.580
Lγ1			13.376
Lγ2			13.705
Mz			1.660
Mα			2.120
Mβ			2.204
Mγ			2.409
M2N4			2.797
N			0.258

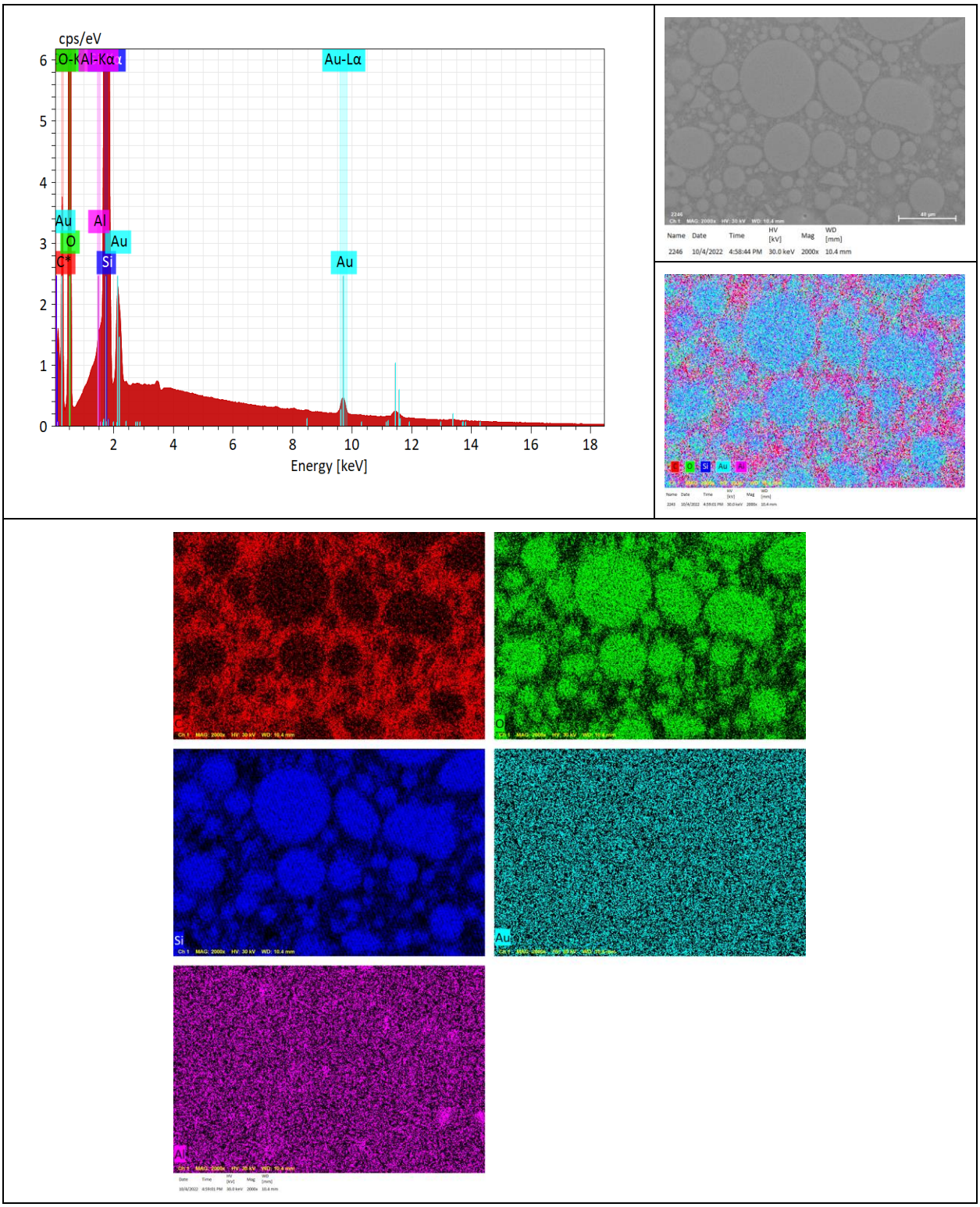

Figure C.1-20. Detailed EDS Results for M3-MCK-TQFP100-01, Including Energy Spectrum, SEM Image, Composite Energy Elemental Map, and Individual Energy Maps for Elements

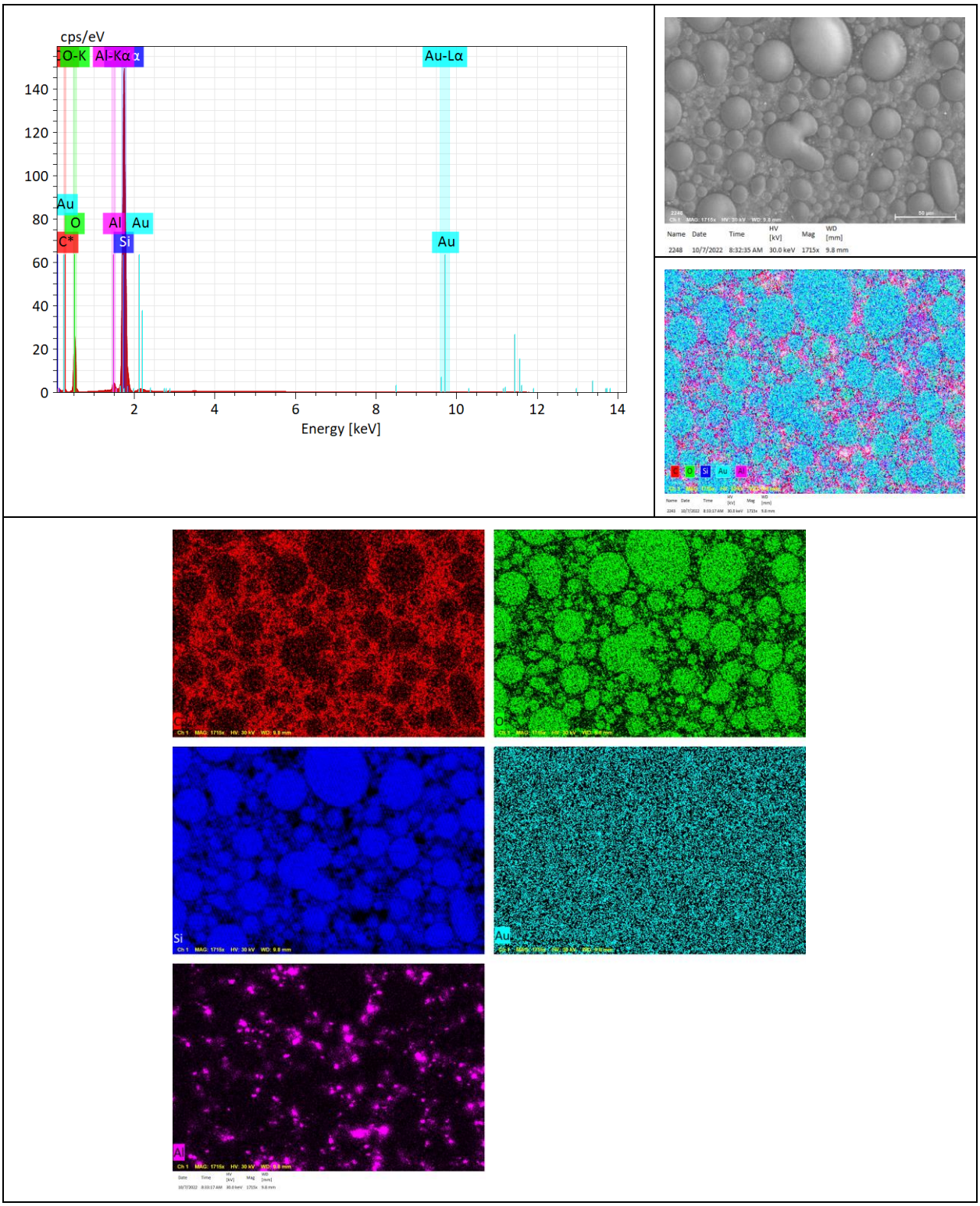

Figure C.1-21. Detailed EDS Results for M4-MCK-FBGA256-01, Including Energy Spectrum, SEM Image, Composite Energy Elemental Map, and Individual Energy Maps for Elements

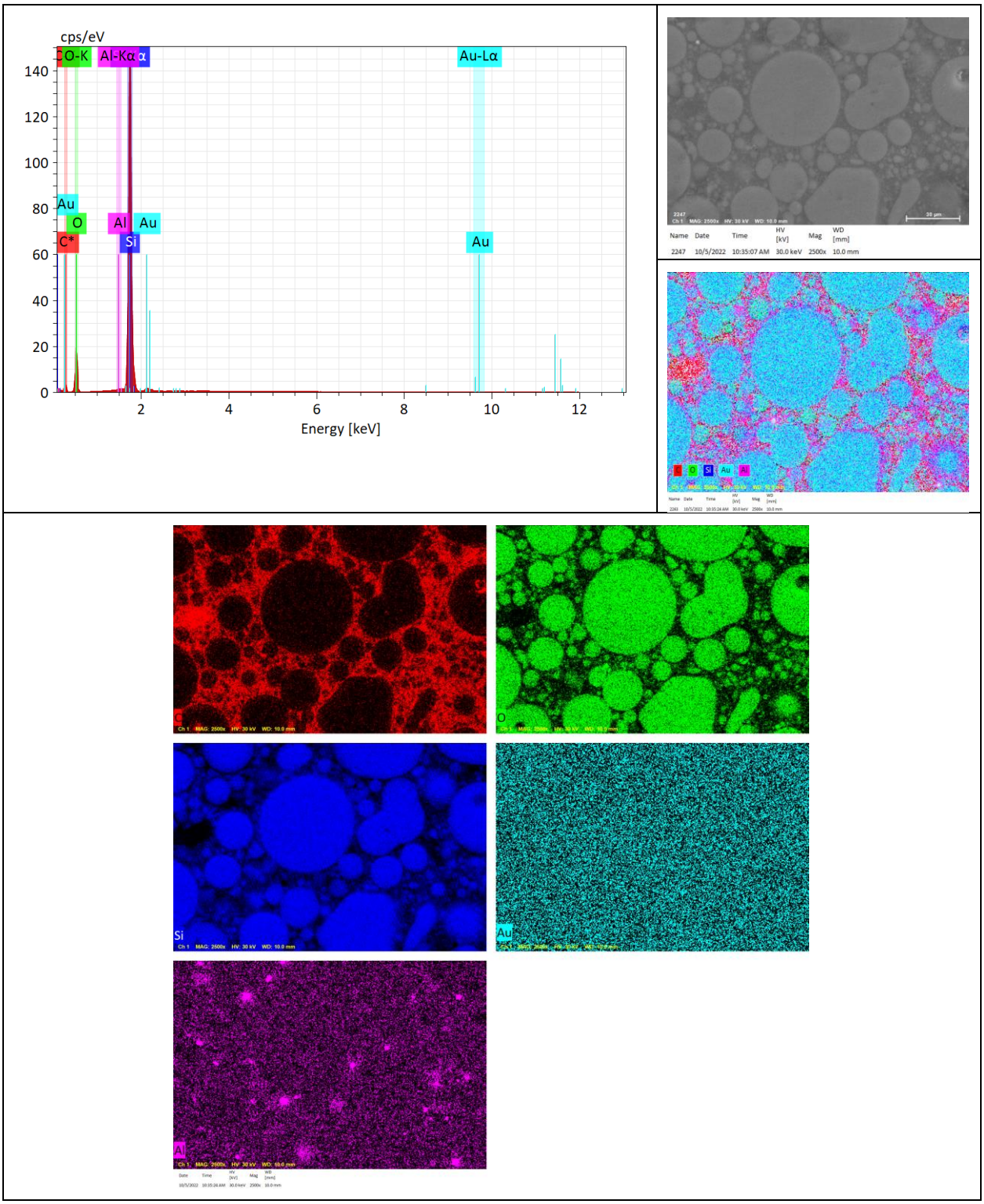

Figure C.1-22. Detailed EDS Results for M5-MCK-SOT235-01 Including Energy Spectrum, SEM Image, Composite Energy Elemental Map, and Individual Energy Maps for Elements

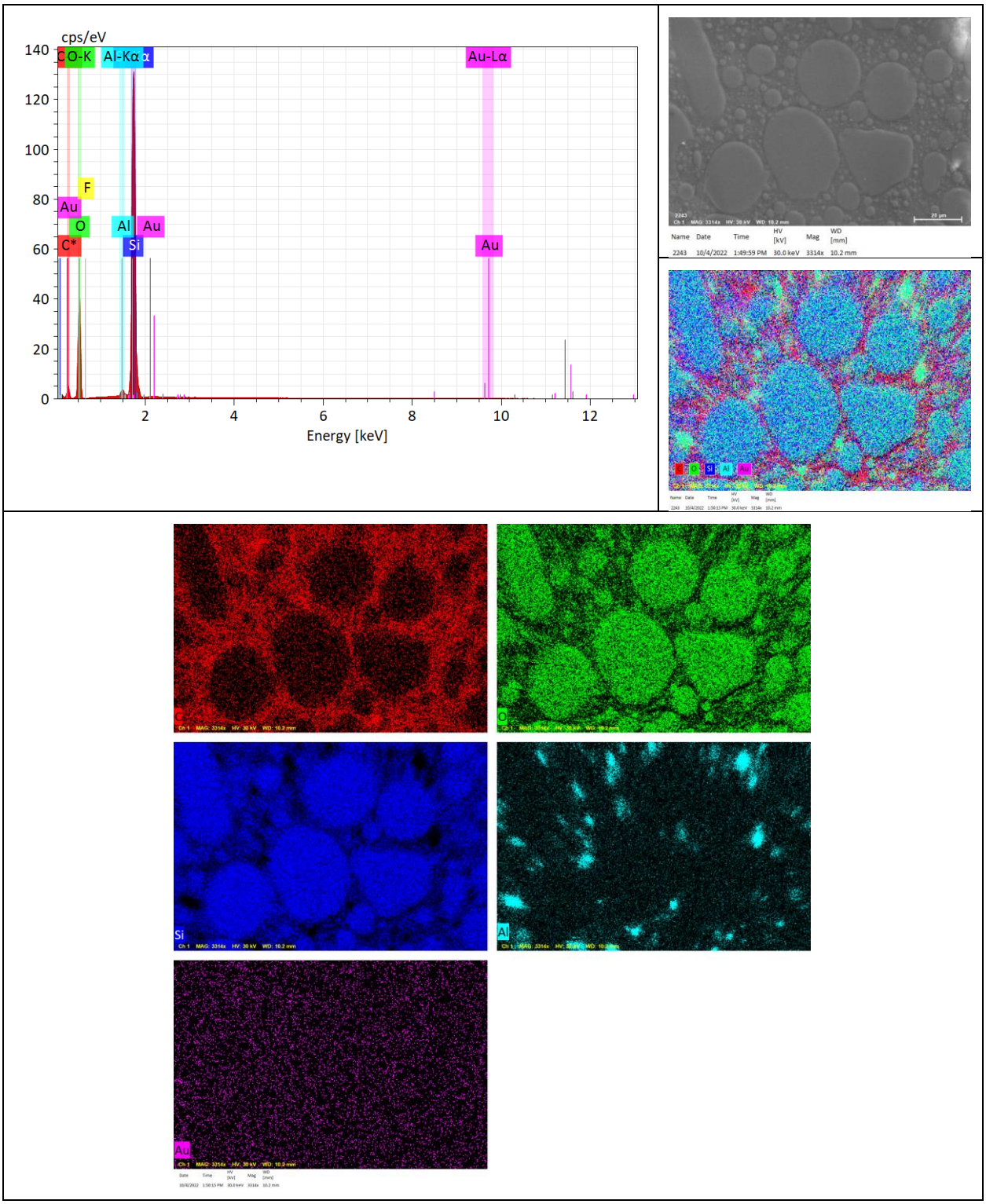

Figure C.1-23. Detailed EDS Results for M10-D-SOT1061-01 Including Energy Spectrum, SEM Image, Composite Energy Elemental Map, and Individual Energy Maps for Elements

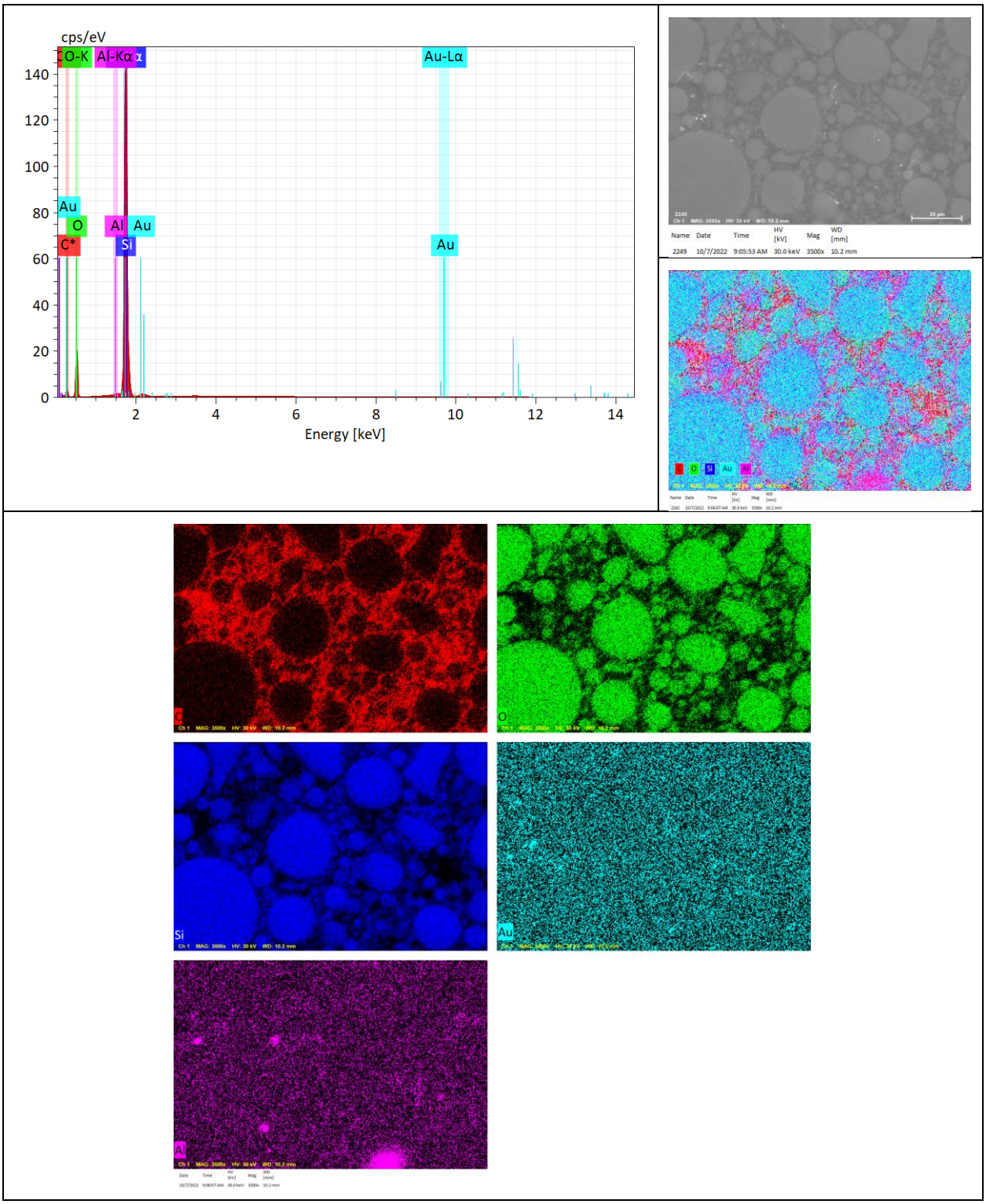

Figure C.1-24. Detailed EDS Results for M11-MCK-TQFP144-01, Including Energy Spectrum, SEM Image, Composite Energy Elemental Map, and Individual Energy Maps for Elements

C.2 Thermophysical Evaluation of Molding Compound Results

A summary of the onset of thermal decomposition and Tg obtained for each part type using TGA and DSC is provided in Table C.2-1. Results from M6-D-SOT235-01 were inconclusive.

Table C.2-1. Thermal Decomposition Temperatures and Tg

Component	TGA-Onset of Thermal Decomposition (°C)	DSC-Tg (°C)
M5-MCK-SOIC8-01	409.1	114.8
M5-MCK-VSSOP8-01	366.8	111.8
M5-D-SOT233-01	374.5	109.0
M2-D-SOT233-01	353.9	126.0
M2-D-SOT233-02	310.3	140.0
M3-MCK-TQFP100-01	382.6	121.0
M1-MCK-SOIC8-01	389.9	115.6
M4-MCK-FBGA256-01	342.0	130.6
M1-MCK-LFBGA144-01	382.7	153.7
M6-D-SOT235-01	-	123.3
M5-MCK-SOT235-01	386.4	121.7
M10-D-SOT1061-01	366.3	126.9
M9-D-Custom-01	361.6	120.1
M10-D-SOD323-01	383.3	155.8
M5-MCK-WSON6-01	390.6	139.8
M7-MCK-LFBGA169-01	364.2	110.3
M8-MCK-LQFP100-01	390.5	119.6
M11-MCK-TQFP144-01	392.8	111.2

C.2.1 Decapsulation Assessment

As mentioned previously, a combination of laser milling and chemical decapsulation was used for this investigation the results are provided in the subsequent sections.

Laser Milling

An IR laser decapsulation system was used to anisotropically disintegrate the plastic mold compound above or around features of interest, particularly die surfaces, bond wires, and leadframes. Laser decapsulation was used to reduce the amount of mold compound left to be removed by chemical decapsulation, which also helped mitigate undesired etching of key metallic features. A typical laser milling procedure involves lasing a rectangular pattern over part or all of the package surface. Custom laser parameters (e.g., high power and speed) were developed to help preserve bond wire integrity during laser milling. The infrared laser was not used as the sole method for decapsulation because laser application to Si die surfaces caused damage to die features and bond pads, even though the wires and leadframe metals were largely immune to the IR laser. Figure C.2-1 illustrates the difference in damage to the die surface and Cu bond wires for parts decapsulated using laser decapsulation alone and laser decapsulation combined with chemical decapsulation to minimize damage to the die surface. Since the focus of

this assessment was the evaluation of Cu wire bonds (including die and leadframe bonding surfaces), a combination of laser and chemical decapsulation was used with the focus of avoiding damage to the die bond pads. Some damage to the die surface was allowed since no electrical evaluation of the parts was intended to be performed post-decapsulation. This allows more laser passes to remove a greater amount of molding compound and reduced chemical degradation of wires.

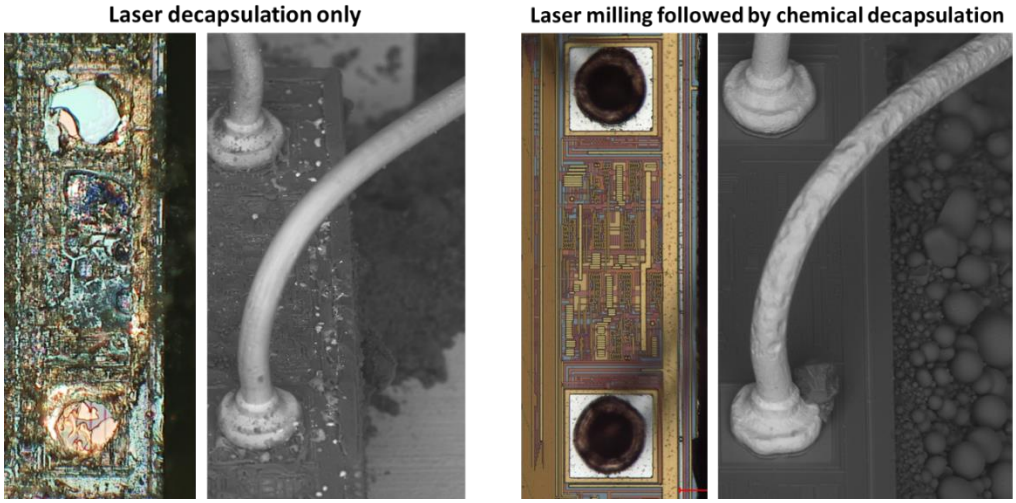

Figure C.2-1. (Left) Using an IR Laser Decapsulation System to Fully Decapsulate a Sample Protects Cu Wires but Causes Severe Damage to Die Features. (Right) Using a Laser to Reduce Mold Compound, Then Finishing with Acids, Protects Die, but Can Affect Cu Wires.

Modifications to the laser milling procedure and parameters occurred over the course of the project. The laser can be used to expose the wire bonds at the leadframe after chemical etching of the die is complete, so acids do not contact the leadframe coating and potentially affect stitch bond integrity (Figure C.2-2). Mold compound remaining under wire spans can be removed by incrementally tilting and rotating the position of the sample under the laser.

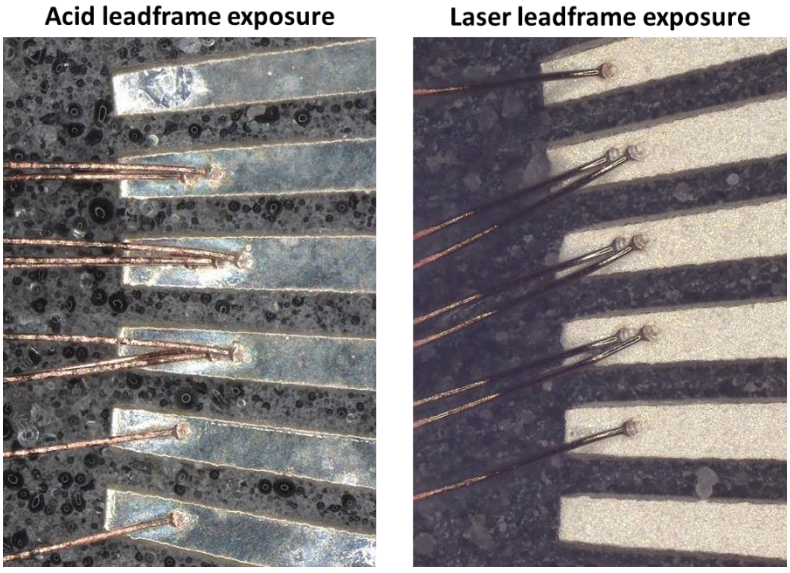

Figure C.2-2. (Left) Exposure of Silver-Coated Copper Leadframe by Chemical Decapsulation, Some Coating is Etched by Acid. (Right) Exposure of leadframe by laser only; coating intact.

Drip Chemical Decapsulation

Drip decapsulation (Figure C.2-3) is the term used to refer to application of acid from a pipette directly onto a package, usually while the unit is maintained at an elevated temperature on a hot plate. A lased well will hold the acid as it works to break down the mold compound epoxy bonds. An acid ratio of 2:1 nitric to sulfuric acid, which is common for decapsulation of PEMs with Cu wire, was used for this assessment. This ratio was not altered over the duration of the testing. Increasing the amount of nitric acid would be expected to accelerate etching not only of the mold compound, but also the Cu wire. Increasing the amount of sulfuric acid risks selective etching of Al bond pads. A small bulb pipette with a narrow tip is recommended to apply acid to the unit to be decapsulated. The number of drops to apply to the unit will depend on the size of the well.

After a certain duration of acid exposure, the sample was rinsed with acetone. If further etch cycles were possible or expected, the sample was dried directly after the acetone rinse and placed back on the mounting disc to warm up to temperature once again. If no more etching was necessary, a complete rinse and clean cycle was performed (described later). Note that even stored in a pipette, acids can weaken over time and mixed acids can separate. Releasing and redrawing the acid from the small bulb pipette between applications helped to alleviate separation. Weakened acid reduces the mold compound etching rate and accelerates etching of Cu. When there was a concern that acid was at risk of aging due to a long decapsulation process, fresh acid was used.

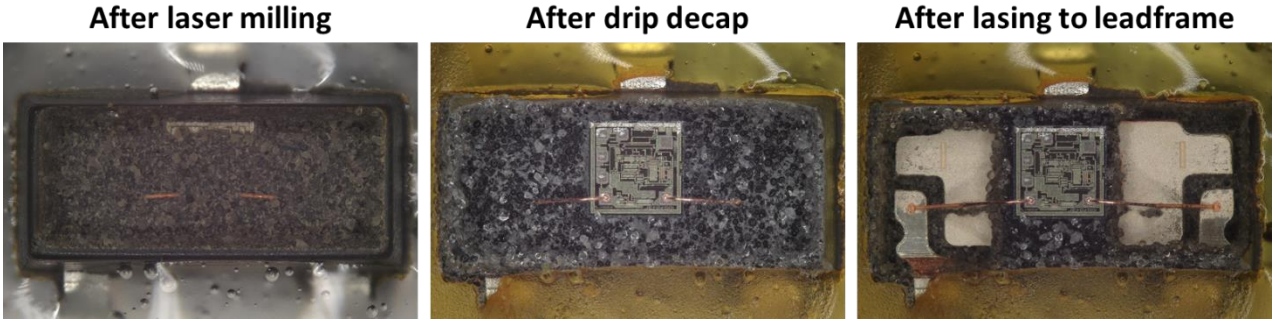

Figure C.2-3. Images Representing Stages of Decapsulation Involving Drip Decapsulation

Submerged Chemical Decapsulation

Submerged decapsulation (Figure C.2-4) is the term used to describe a sample that is completely immersed in a beaker of acid for a period of time. This technique was used for larger parts, for which the time required for acids to dissolve mold compound at elevated temperature during drip decapsulation would excessively harm the Cu bond wires. For this project, the acid in the beaker was kept at room temperature and formed into a vortex with a stir plate and a stir bar. The constant movement of acid in the vortex helps to etch some of the mold compound occluded under groupings of bond wires in large wire count parts. Using room temperature, rather than warm, acid attempts to preserve metallic features of interest (e.g., bond wires) during the long-duration chemical etch typically required for large surface area parts. For this procedure, a 400-mL beaker was found to be a good size for submerged decapsulation. A Teflon stir bar was placed in the beaker, and the stir function of the plate was activated—450-550 rpm was found to be a good range.

After a certain duration of acid exposure, determined by trial and error on practice parts, the part was removed and rinsed completely with acetone. If further etch cycles were possible or expected, the unit was dried directly after the acetone rinse. If no more etching was necessary, a complete rinse and clean cycle was performed (described later). Note that the acid in the beaker will begin to weaken as it is stirred and remains exposed to air. After 5-10 minutes, the acid's ability to remove mold compound is reduced and the etching rate of some metals, such as Cu, increases. If there was a concern that the acid was aging, fresh acid was used.

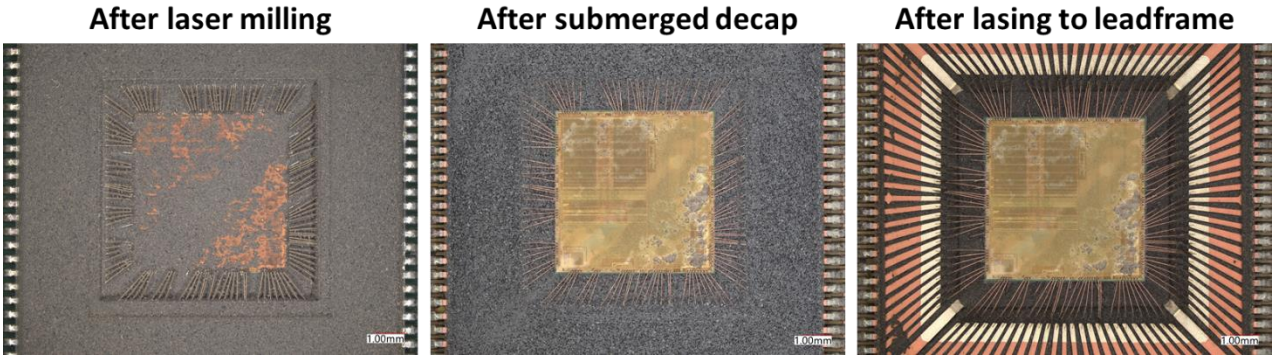

Figure C.2-4. Images Representing Decapsulation Stages Using Submerged Decapsulation

Fine-Pitch Multi-Tier Wire Bonded Part Challenges

Unintended chemical etching of Cu wire occurs, to varying extent, based on several parameters, including the procedures used. For high wire count and multiple wire tier parts, large segments of mold compound are blocked from quick laser or chemical decapsulation due to occlusion from densely packed wires. It was determined early on that drip decapsulation was not a viable method for parts of this type, since the duration of acid exposure required to completely etch the mold compound to fully expose dense groupings of wires, or lower tiers of wires, was detrimental to the integrity of wires already exposed.

The submerged acid vortex decapsulation method was attempted to alleviate the consequences of long duration acid exposure by maintaining a constant flow of acid over the device, with the goals of limiting sites of localized stationary aging acid and to continuously wash away dissolved mold compound. This solution proved effective, though not without complication. As shown by the representative SEM image (Figure C.2-5) from M7-MCK-LFBGA169-01 PEVAL (post-ball shear), which underwent submerged decapsulation in a room-temperature 2:1 acid vortex, the full diameters of the innermost/highest tier of wires are largely intact, whereas the conditions of middle and lower tier wires are seen to have degraded. For this result, the innermost wires appear to have been the first to be fully exposed and then no longer subjected to stationary pockets of acid. Lower tier wires, however, remained in mold compound that dissolved over a longer period. While in the submerged vortex, acid can seep into mold compound that has not yet been completely dissolved, during which etching of Cu wire occurs before that mold compound finally dissolves and washes away. The wire segments with the best appearance were those exposed by laser decapsulation beforehand.

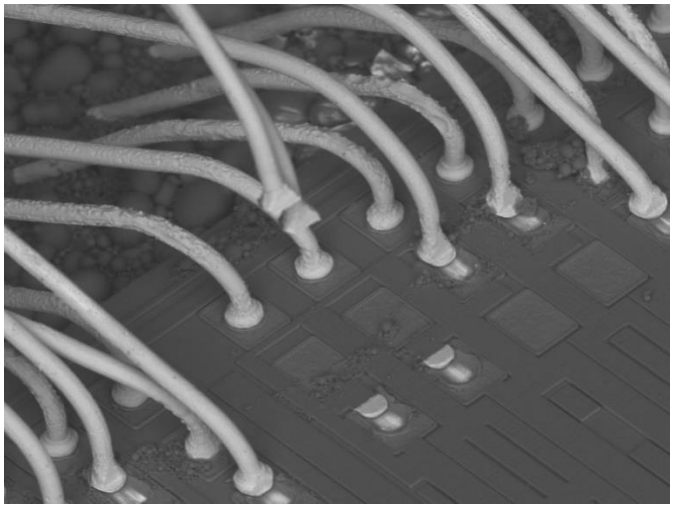

Figure C.2-5. SEM Image of Decapsulated M7-MCK-LFBGA169-01

Rinsing and Cleaning

If a unit had undergone acid etching and additional cycles of etching were possible or expected, the unit was rinsed with acetone, then dried with compressed air for interim inspection. The acetone neutralized the acid while preserving much of the copper sulfate ($CuSO_4$) barrier that developed around the Cu bond wires (Figure C.2-6). The $CuSO_4$ helps protect the wires from nitric acid during subsequent acid application cycles. If chemical etching of a unit was complete, a complete rinse and clean cycle was performed, which involved rinsing with acetone, rinsing with deionized (DI) water, spraying with methanol, then drying with compressed air. The DI water breaks down $CuSO_4$ crystals on the bond wires. The methanol displaces the DI water and allows for faster, cleaner drying. The methanol was sourced from an airbrush, rather than a rinse bottle, to generate a higher velocity stream that helped remove debris and decapsulation residue. Testing had shown that neither the methanol nor the compressed air from the airbrush had an observable effect on wire condition. The only exception was when the airbrush nozzle was very close to the wires. Ultrasonic baths were not used on final wire-tested units, due to the potential risk of sympathetic vibration along exposed bond wires.

After rinsing and drying were complete, the unit was suspended in an acetone vortex bath for an hour. This process was developed because the Cu bond wires of some parts used in this assessment exhibited a tendency to absorb acid, causing continued etching of the Cu over hours or days, despite being rinsed and cleaned after decapsulation. Testing was performed to determine how to best preserve these wires after decapsulation, including various durations of baking, soaking in still acetone, and soaking in stirred acetone. Results are shown in Figure C.2-7. The best results were obtained by soaking the decapsulated units in a stirred acetone bath. The acetone neutralized and dehydrated the acids, while the stirring vortex continuously displaced acids released from the wires during the soak. Testing suggested that the units should remain in the acetone vortex for no less than 1 hr. After this time, the units underwent the complete rinsing and drying cycle again. Examination and bond testing of the units was performed within one day of decapsulation.

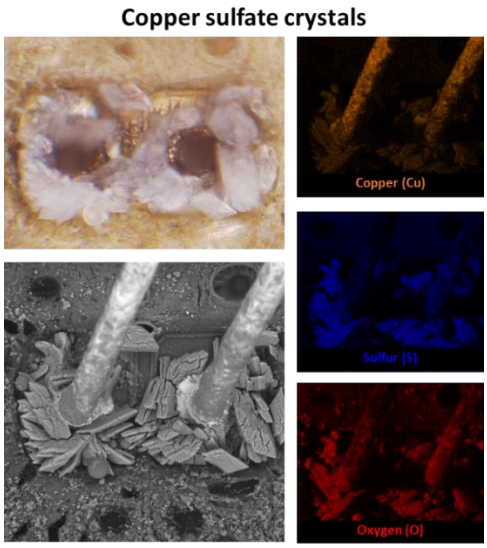

Figure C.2-6. Cu Sulfate Crystals Present at Cu Bond Wires After Acetone Rinse and Drying

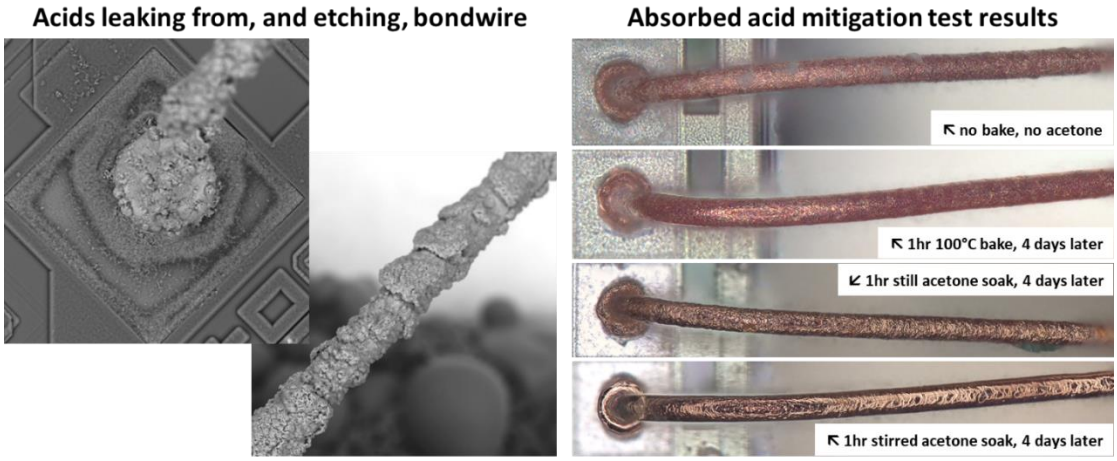

Figure C.2-7. (Left) Images of Representative Bond Wire from Part that Absorbed Acid During Decapsulation and Continued Etching Over Time. (Right) Examination and Bond Testing of Units After a Variety of Mitigation Techniques Indicated Stirred Acetone Yielded Best Results.

C.2.2. Other Attempted Decapsulation Techniques

Biased Chemical Decapsulation

Biased decapsulation, as shown in Figure C.2-8, was attempted on high wire count parts in an attempt to further limit Cu etching during submerged decapsulation. A positive voltage on the Cu wires within a negatively charged acid attracted negatively charged sulfate ions to the wires, which form a protective coating against nitric acid. For this experiment, all test unit leads were soldered to a Cu substrate along with acid-resistant insulated wire. Biasing voltage and acid temperature parameters were varied. Two consistent problems were observed: First, the biasing of the Cu wires accelerated mold compound etching around the wires, creating a physical "tunneling" effect into the mold compound. This resulted in uneven etch rates of the mold compound and sites around wires where acid could not be as easily displaced by the vortex. Second, the biasing appeared to immediately eject, or otherwise remove, coating material on Cu features. This affected not only the Pd coating of the wires, but also the Pd or Ag coating over

Cu leadframe surfaces, which became undesirably exposed due to the tunneling of mold compound described in the first instance. These two complications were not overcome, and biased decapsulation as a method of bond wire exposure for use in this project was abandoned.

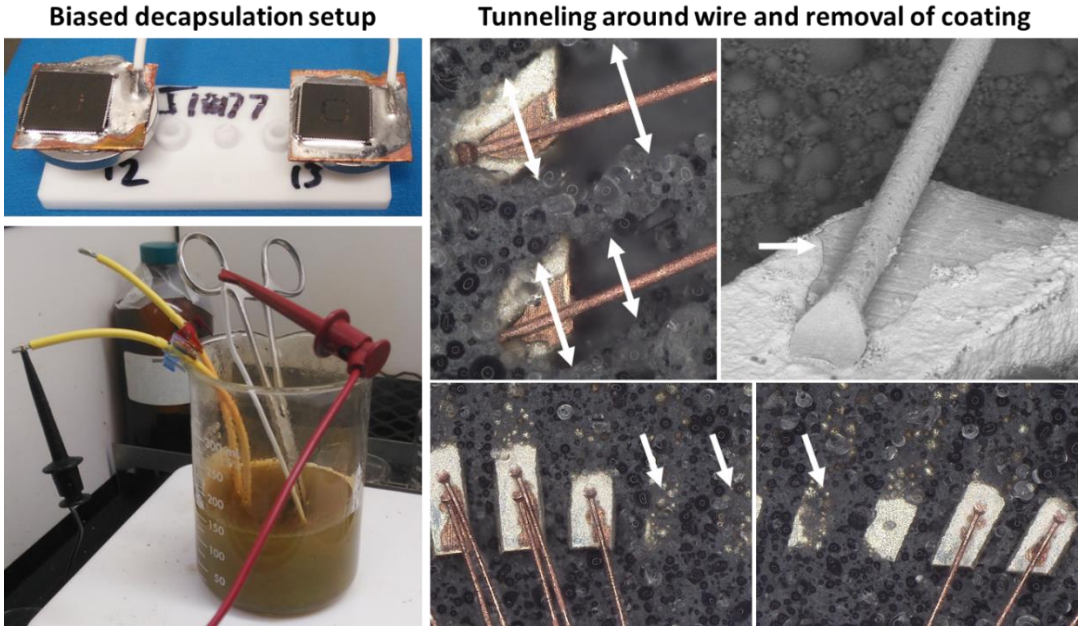

Figure C.2-8. (Left) Example of Preparation and Test Setup for Biased Decapsulation; (Right) Undesired Consequences of Biased Decapsulation: Accelerated Etching of Tunnels into Mold Compound Around Wires and Removal of Coating over Cu Features. Note reduced etch rate of mold compound over unconnected package leads in lower right images.

Plasma Decapsulation

Certain plasmas are also capable of etching and ablating mold compounds. The mold compound of one particular part was found to be particularly acid-resistant, and thus underwent experimentation with the goal of removing mold compound while preserving the bond wires, leadframe, and die. In the industry, microwave-induced plasmas (MIP) are often employed for this procedure. No MIP was available at this time, so experiments were performed with plasmas generated in a radio frequency reactive ion etcher (RIE). Laser milling was used to thin the mold compound in preparation for plasma etching. Varying the power and ratio of oxygen and tetrafluoromethane (CF_4) feedstock gases in the plasma controlled the etch rate of the mold compound and mitigated etching of other materials, such as the die surface. Through trial and error, an effective procedure was developed that removed the mold compound around features of interest and preserved the die (Figure C.2-9). However, this decapsulation procedure was abandoned as a method of exposing bond wires for testing. One factor was the significant time required for this plasma decapsulation process, which took several hours and required manual blowing off of ashed mold compound at regular intervals. Another was etching of the package substrate material of the part being tested, which permitted the buried redistribution traces to lift during wire pull, preventing accurate representation of wire pull break forces and locations.

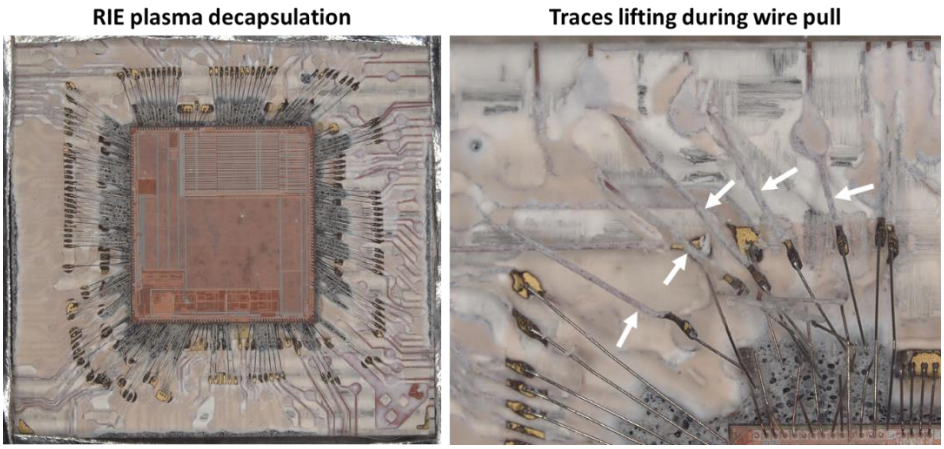

Figure C.2-9. (Left) Successful Plasma Decapsulation of Test Sample; (Right) Undesired Lifting of Buried Package Substrate Traces During Wire Pull

C.3 Environmental Test Results

TC and bHAST were monitored during testing, with no electrical failures. Examples of monitored data near the beginning and end of the 2000 cycles are provided in Figures C.3-1 and C.3-2. The levels of degradation and changes in failure mechanisms were evaluated using wire bond pull and shear strengths, as well as characterization with optical microscopy and SEM. Strength integrity is affected by decapsulation approaches; therefore, significant time was allocated to optimize mold removal, as discussed in the previous section. In weekly meetings, the team reviewed results, narrowed down methods for improvement, and discussed suspicious wire bond strengths and failure mechanisms. Raw strength data, with removal of suspicious data, are presented in this assessment. Several instrument glitches took place during temperature cycling, resulting in data anomalies that required closer investigation.

The temperature cycling test was intended to have 2000 cycles, but several instrument glitches along the way showed data anomalies that required closer investigation.

- Power applied, but no temperature cycling for ~200 cycles out of 2000 (Figure C.3-3). It should be noted that the parts did experience at least 2000 cycles.
- Data logging failure for PCB2-SN9 on 18V and 3.3V lines between cycles 525 and 1025, most likely due to connector malfunction. The problem was solved by swapping out the test connector fixture.
- Because current is calculated by measuring a voltage drop across a resistor, a change in the calculation during re-set of software resulted in different level of current being recorded.

However, several important takeaways were gained from analyzing the current monitoring of voltages supplied to the two boards:

- All notable changes in current draw occurred when switching connector harnesses or changing data logger software configurations. They did not occur mid-run.
- No gradual changes in current draw occurred over multiple cycles, such as a decrease in current draw due to an open wire bond or open solder joint, an increase in current draw as a result of die over-heating, or latent electrostatic discharge failure. During NESC testing, parts were handled with ESD precautions up to and including bond strength testing. This includes handling parts with ESD precautions prior to installation, during board installation, during

Infrared check, during loading/unloading of the boards into chambers, during decapsulation, and then during bond pull. All parts and assemblies were assumed to be Class 1A.

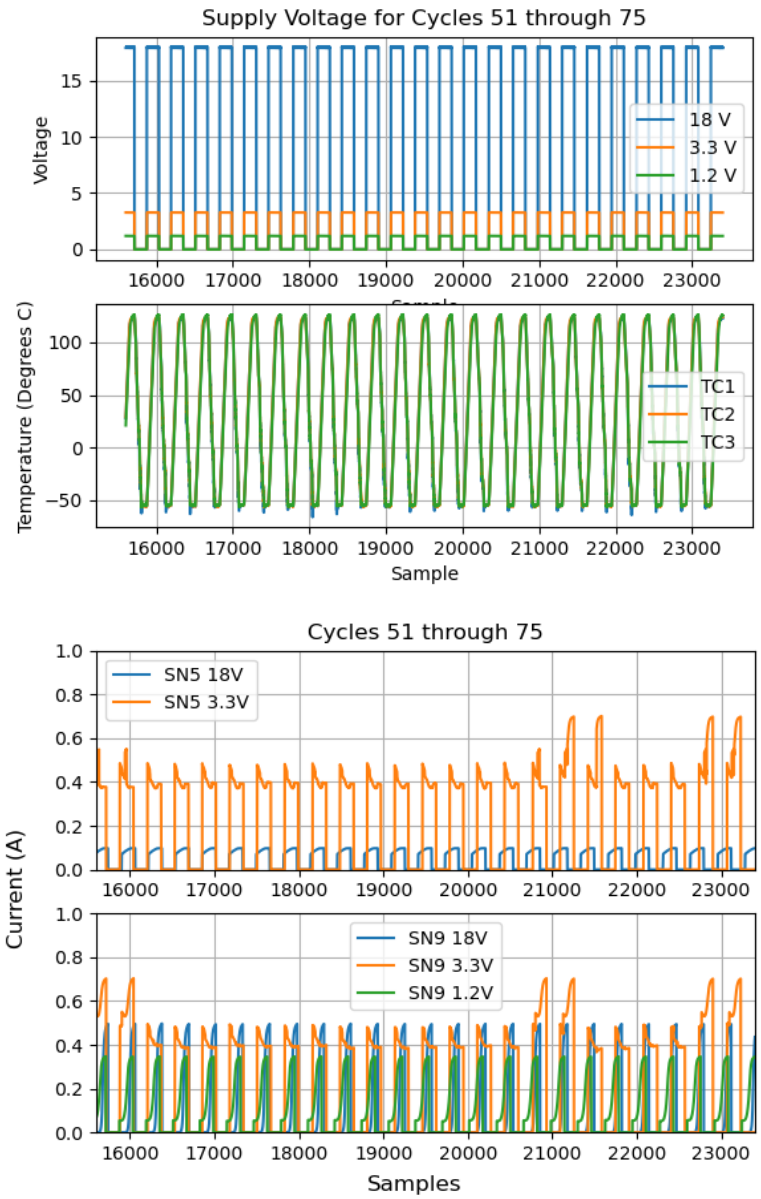

Figure C.3-1. Graphs Showing Voltage on Three Power Supplies, Temperature Inside Chamber, and Current Draws for Two Boards During Early Testing. Spikes in current draw at 3.3V supply occur on both boards and are likely not related to the boards. Board names and voltages applied: Board PCB1-S1-SN5 has 18V and 3.3V. Board PCB2-SN9 has 18V, 3.3V and 1.2V.

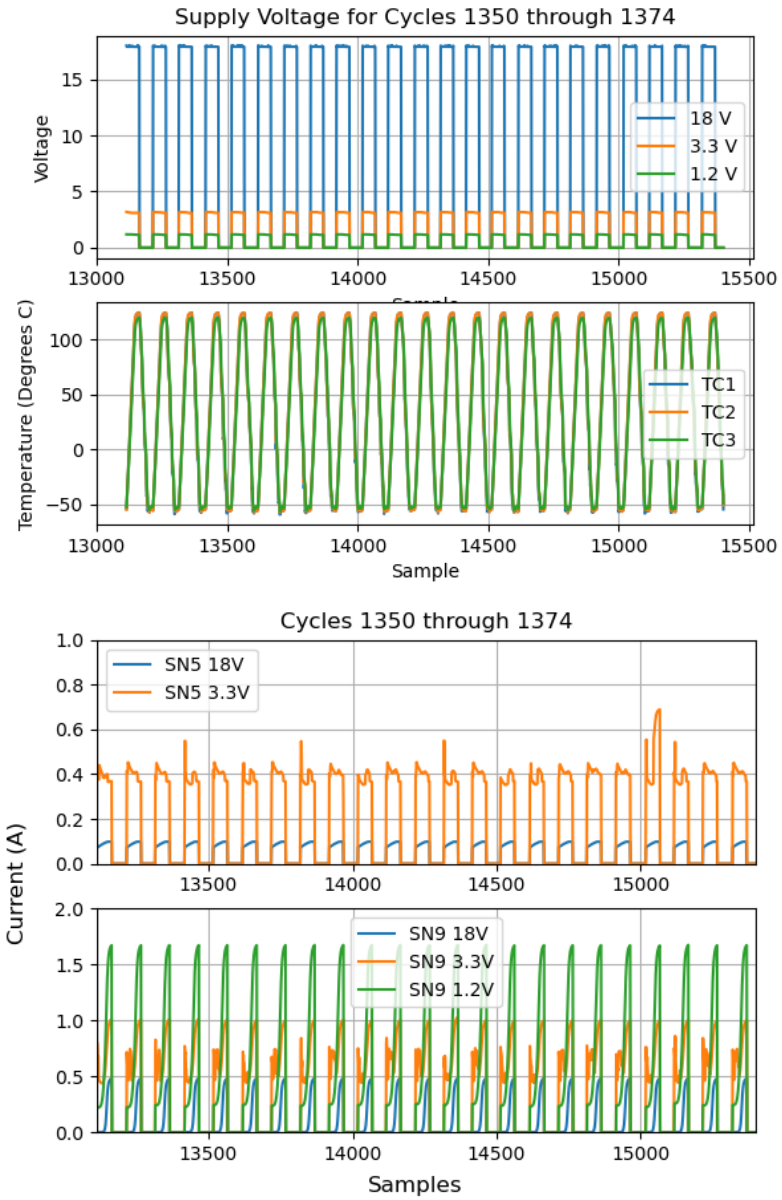

Figure C.3-2. Graphs Showing Voltage on Three Power Supplies, Temperature Inside Chamber, and Current Draws for Two Boards During Later Part of Testing. Spikes in current draw at 3.3V supply occur on both boards and are likely not related to the boards. Board names and voltages applied: Board PCB1-S1-SN5 has 18V and 3.3V. Board PCB2-SN9 has 18V, 3.3V and 1.2V. Note that there is a change in current draw on the 1.2V line for PCB2-SN9, while there appears to be a jump in current compared to Figure C.3-1. This change occurred instantaneously after datalogger software was re-programmed, and calculation for current was changed.

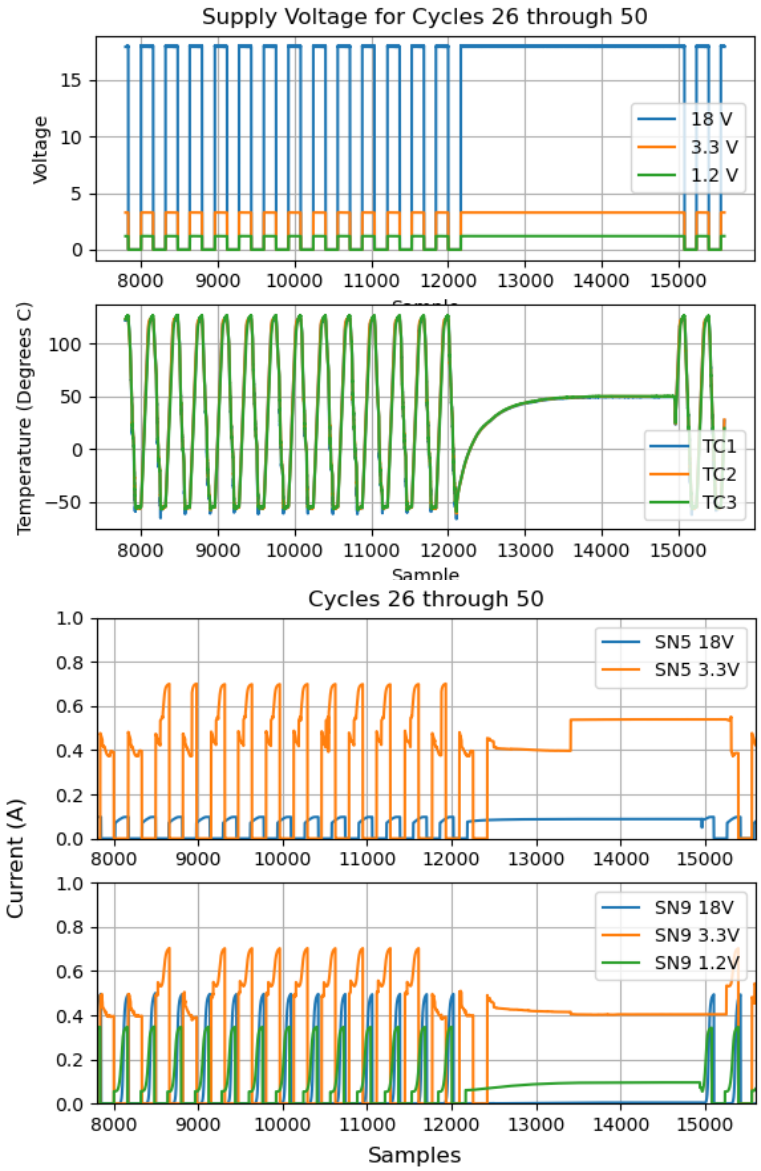

Figure C.3-3. Graphs Showing Voltage on 3 Power Supplies, Temperature Inside Chamber and Current Draws for 2 Boards During Temperature Cycling Halt That Lasted ~10 Cycles

C.3.1 SAM Results

SAM was performed on individual components in the as-received condition. Components that were exposed to bHAST or thermal cycling were mounted onto boards and tested, as described previously. Following exposure, the PCB assemblies were cut into sections and the mounted samples were inspected using SAM. Inspection results are provided in Table C.3-1, and representative SAM images are provided in Table C.3-2. The red text in Table C.3-1 refers to parts that exhibited significant delamination. In certain cases, no parts were available following exposure due to location and availability. Select components could not be inspected due to the internal configuration of the packaged part. This is the case for upside-down or “deadbug” components. Parts that were unavailable for inspection due to bond pull/ball shear test or

package configuration limitations are marked as "Y." None of the parts were subjected to dye penetrant testing following SAM to validate the results observed.

Delaminations were ranked using the following system:

- Significant = Delamination that covered an entire leadframe or die.
- Moderate = Delamination that covered part of the leadframe or die.
- Minor = Delamination that was not near a wire bond or die.
- None = No delaminations.
- N/A = SAM could not be performed because part was destroyed during processing or had "deadbug" internal construction.

Delamination is indicated during SAM inspection if there is an air gap of sufficient size between the leadframe and molding compound. Some units exhibited delamination in the as-received condition, and some after temperature cycling. CTE differences between package components could influence the occurrence of delamination. Delamination could occur rapidly during soldering if excessive amounts of moisture were absorbed by the mold compound, resulting in popcorning fractures or interfacial fractures during soldering. It could also occur slowly because of swelling from gradual moisture absorption while in service or CTE mismatch stresses. If delamination occurs, it could lead to fracture or lifting of wire bonds, ultimately resulting in open circuits. Delamination could also allow ingress of moisture or contaminants that could lead to corrosion at the bond interface or wire corrosion. Finally, it could result in current leakage as a result of mobile ions.

Table C.3-1. SAM Summary

Part Number	Notes	Condition	Sig	Mod	Min	No	N/A	Tot
M1-MCK-SOIC8-01		As-Received				5		5
		Post 2000 TC				8		8
		Post 500 hr HAST				12		12
M2-D-SOT233-01		As-Received		1		1		2
		Post 2000 TC	1	6		17		24
		Post 500 hr HAST	1		2	24		27
M3-MCK-TQFP100-01		As-Received				5		5
		Post 2000 TC				2		2
		Post 500 hr HAST	1			1		2
M4-MCK-FBGA256-01	No parts available for SAM following HAST or TC	As-Received				5		5
		Post 2000 TC					Y	
		Post 500 HAST					Y	
M5-D-SOT233-01		As-Received			6	2		8
		Post 2000 TC	1	1	5	21		28
		Post 500 hr HAST			6	22		28
M5-MCK-VSSOP8-01	Significant delamination	As-Received	2	1				3
		Post 2000 TC	8					8
		Post 500 hr HAST	11			1		12
M5-MCK-WSON6-01		As-Received				5		5
		Post 2000 TC			32			32
		Post 500 hr HAST		1	17	1		19

Part Number	Notes	Condition	Sig	Mod	Min	No	N/A	Tot
M2-D-SOT233-02		As-Received			3			3
		Post 2000 TC		28	3	1		32
		Post 500 hr HAST	11	2		11		24
M5-MCK-SOT235-01	Deadbug	As-Received			1	4		5
		Post 2000 TC					Y	
		Post 500 hr HAST					Y	Y
M6-D-SOT-235-01	Deadbug – could not be analyzed on board. Significant delamination as-received	As-Received	8	2				10
		Post 2000 TC					Y	Y
		Post 500 hr HAST					Y	Y
M5-MCK-SOIC8-01	TC Problem	As-Received				3		3
		Post 2000 TC	9	3				12
		Post 500 hr HAST				12		12
M7-MCK-LFBGA169-01	Multiple package layers inhibit delamination measurement	As-Received				10		10
		Post 2000 TC					Y	Y
		Post 500 hr HAST					Y	Y
M8-MCK-LQFP100-01		As-Received				6		6
		Post 2000 TC				2		2
		Post 500 hr HAST				2		2
M9-D-CUSTOM-01		As-Received				10		10
		Post 2000 TC				24		24
		Post 500 hr HAST				32		32
M10-D-SOD323-01		As-Received			10			10
		Post 2000 TC	1	4	4	15		24
		Post 500 hr HAST			2	20		22
M10-D-SOT1061-01	Significant delamination	As-Received		2	3	5		10
		Post 2000 TC	32					32
		Post 500 hr HAST	24	1	2			27
M11-MCK-TQFP144-01	TC Problem	As-Received				10		10
		Post 2000 TC	1					1
		Post 500 hr HAST				2		2
M1-MCK-LFBGA144-01		As-Received				10		10
		Post 2000 TC					Y	
		Post 500 hr HAST					Y	

Table C.3-2. Representative SAM Images

M1-MCK-SOIC8-01	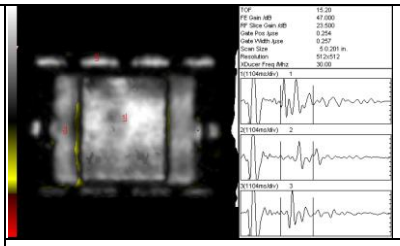	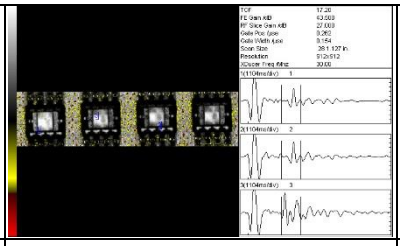	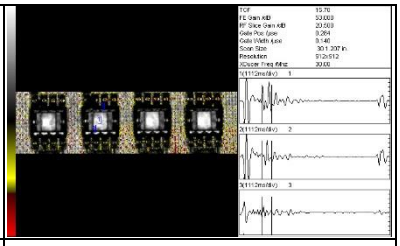
	Incoming Inspection	500 hr bHAST	2000 TCs
M2-D-SOT233-01	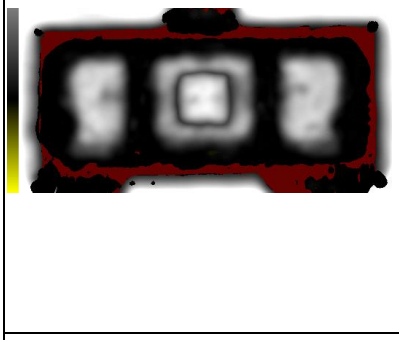	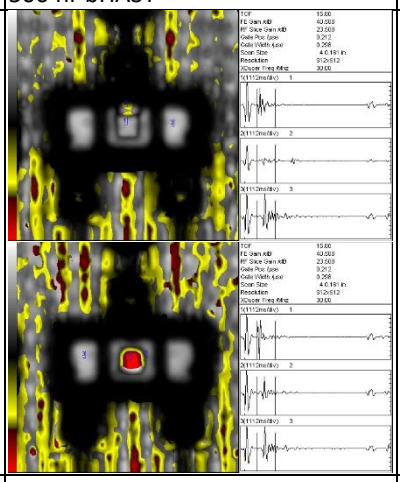	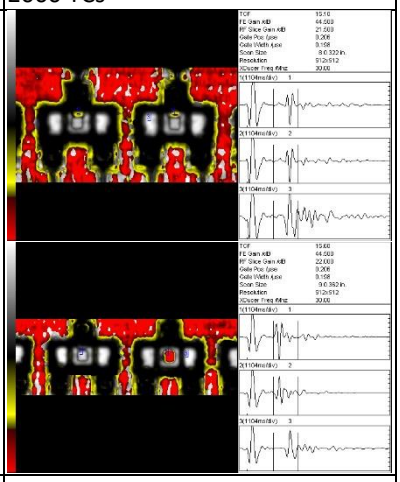
	Incoming Inspection	500 hr bHAST	2000 TCs
M3-MCK-TQFP100-01	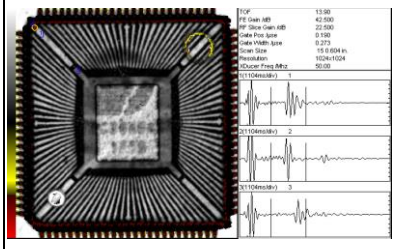	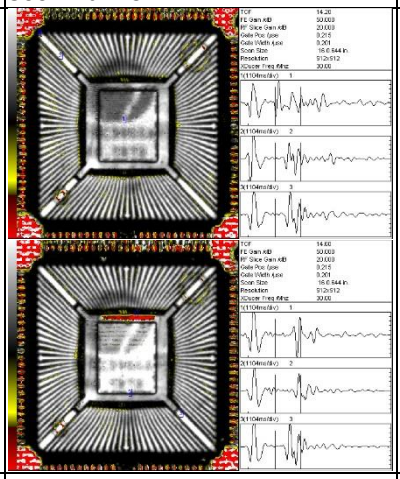	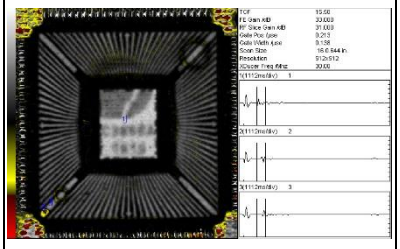
	Incoming Inspection	500 hr bHAST	2000 TCs
M4-MCK-FBGA256-01	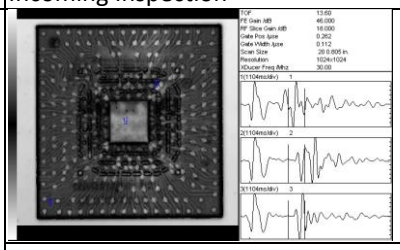		
	Incoming Inspection	500 hr bHAST	2000 TCs

M5-D-SOT233-01	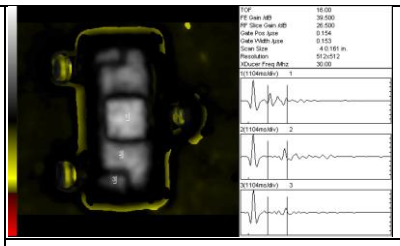	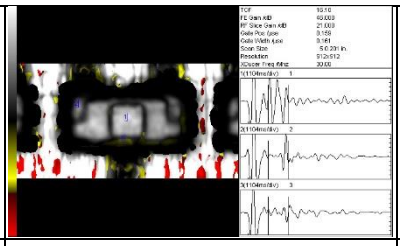	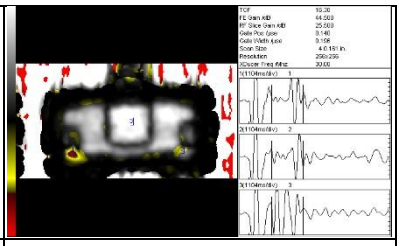
	Incoming Inspection	500 hr bHAST	2000 TCs
M5-MCK-VSSOP8-01	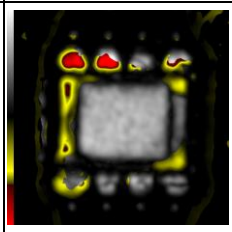	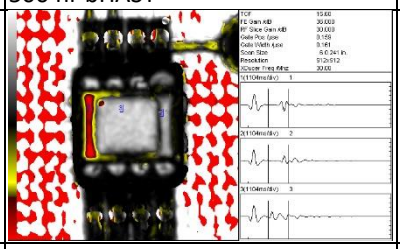	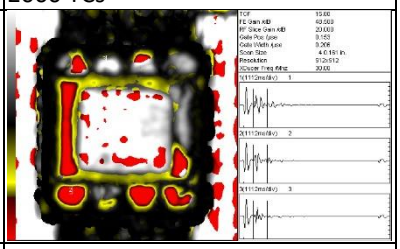
	Incoming Inspection	500 hr bHAST	2000 TCs
M5-MCK-WSON6-01	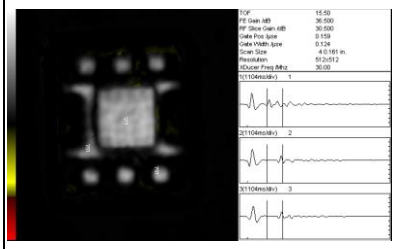	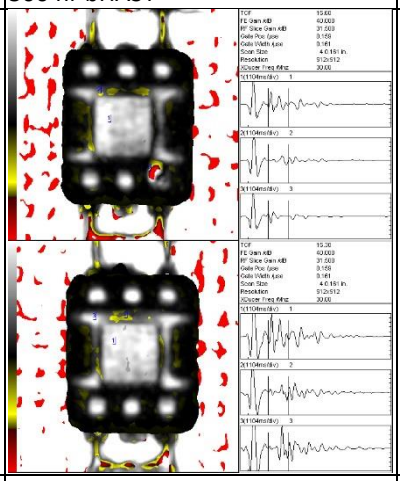	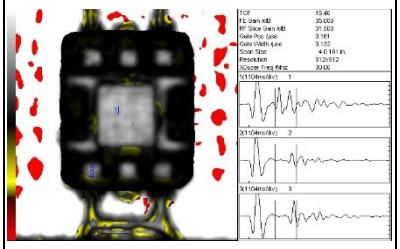
	Incoming Inspection	500 hr bHAST	2000 TCs
M2-D-SOT233-02		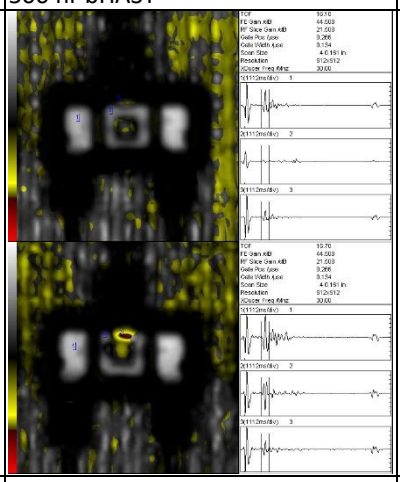	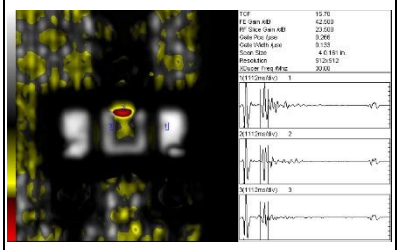
	Incoming Inspection	500 hr bHAST	2000 TCs

M5-MCK-SOT235-01	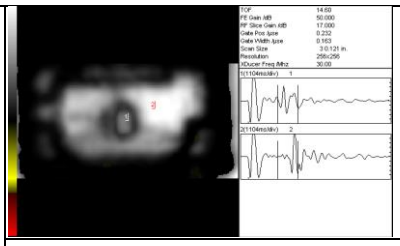		
	Incoming Inspection	500 hr bHAST	2000 TCs
M6-D-SOT-235-01	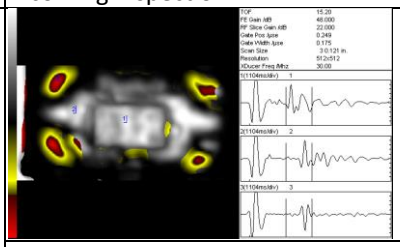		
	Incoming Inspection	500 hr bHAST	2000 TCs
M5-MCK-SOIC8-01	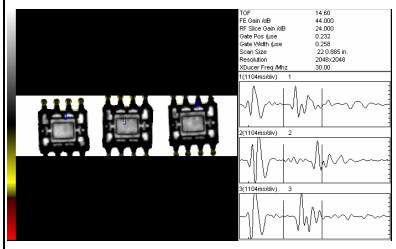	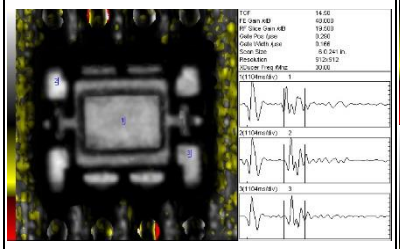	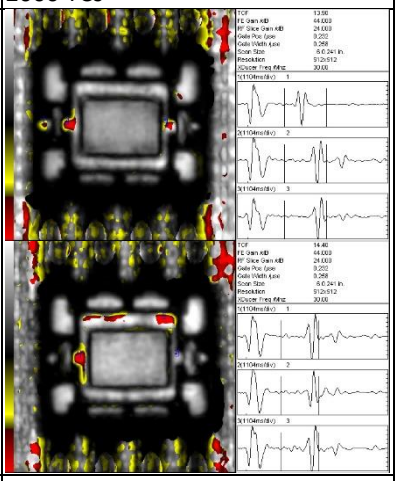
	Incoming Inspection	500 hr bHAST	2000 TCs
M7-MCK-LFBGA169-01	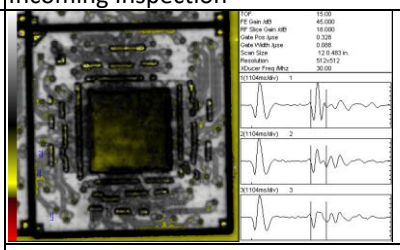	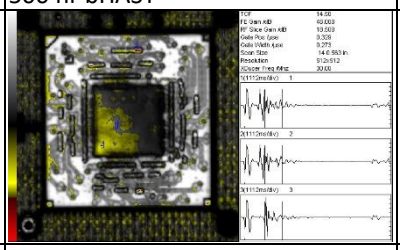	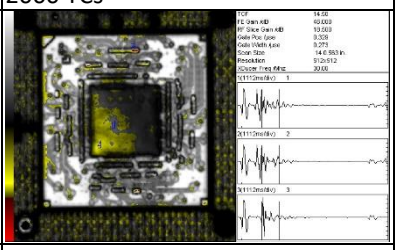
	Incoming Inspection	500 hr bHAST	2000 TCs
M8-MCK-LQFP100-01	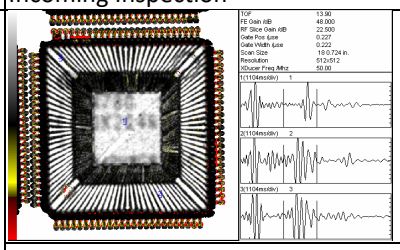	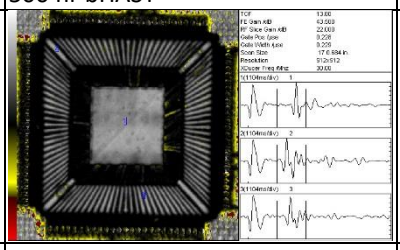	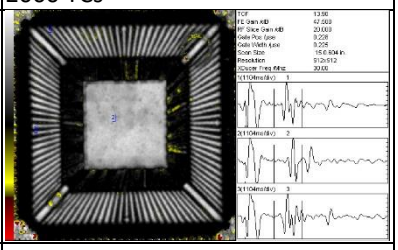
	Incoming Inspection	500 hr bHAST	2000 TCs

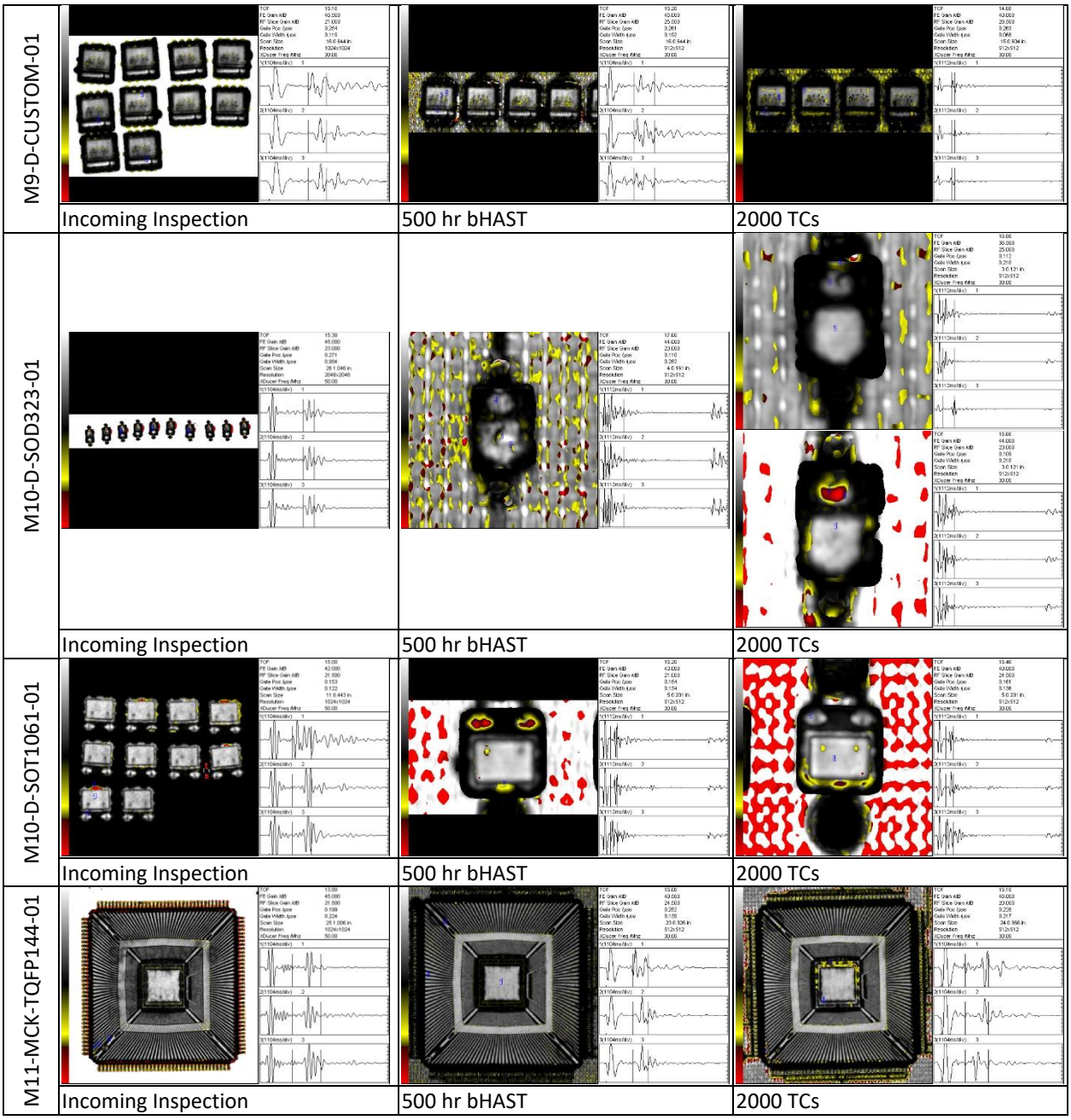

C.3.2 Cu Wire Bond Pull Test Results

Wire bond pull tests were performed in the as-received condition, after 500 hr of bHAST exposure, and after 2000 TCs for all part types. Due to indications of TC-related fatigue damage of wires, two parts were selected for decapsulation and wire pull following 1000 TCs. Additionally, two large wire count components were selected for decapsulation and wire pull following the combined exposure of 400 hr of bHAST and 1000 TCs. Figure C.3-4 and Table C.3-3 illustrate failure locations and describe the failure modes outlined in MIL-STD-883. A summary of failure categories for the parts tested is provided in Table C.3-4. Cumulative pull strengths for each component tested under each condition are provided in Table C.3-5, along with the associated failure category.

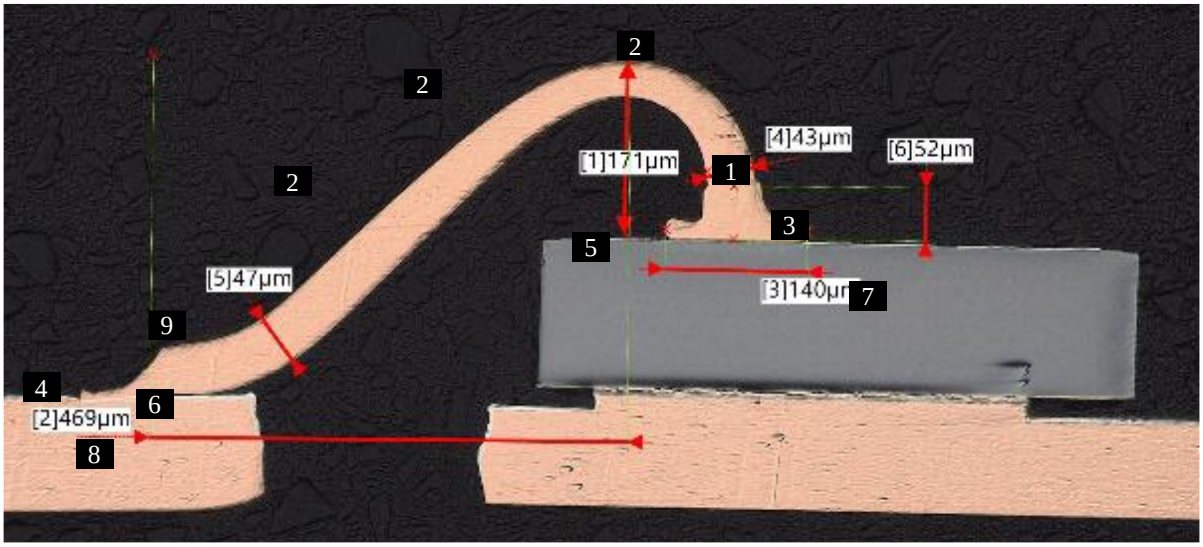

Figure C.3-4. Schematic Illustrating Location of Bond Pull Failure Codes

Table C.3-3. MIL-STD-883 Failure Categories for Internal Wire Bonds

Code	Description of Failure Code
0	Wire broken or missing prior to test.
1	Wire break at neck-down point (reduction of cross-section due to bonding process).
2	Wire break at point other than neck-down (span).
3	Failure in bond (interface between wire and metallization) at die.
4	Failure in bond (interface between wire and metallization) at substrate, package post, or other than die.
5	Lifted metallization from die.
6	Lifted metallization from substrate or package post.
7	Fracture of die (includes cratering or chip out).
8	Fracture of substrate.
9	Break in wire at neck-down on the substrate or package post.

Table C.3-4. Bond Pull Failure Category Summary for All Part Numbers and Conditions Tested

Part Number	Condition	1	2	3	4	5	6	7	8	9	Total
M1-MCK-SOIC8-01	Baseline CA	2	5							7	14
	Post 2000 TC	2	6							6	14
	Post 500 hr HAST	1	6							6	13
M2-D-SOT233-01	Baseline CA	1	3							2	6
	Post 2000 TC	1	3								4
	Post 500 hr HAST		4								4
M3-MCK-TQFP100-01	Baseline CA	49	112							2	163
	Post 2000 TC	22	84								106
	Post 500 hr HAST	53	52								105
M4-MCK-FBGA256-01	Baseline CA	94	368					1		26	489
	Post 2000 TC	146	374					2		19	541
	Post 500 hr HAST	40	358					1		15	414
M5-D-SOT233-01	Baseline CA		2							2	4
	Post 1000 TC	1	3								4
	Post 2000 TC									4	4
	Post 500 hr HAST									4	4
M5-MCK-VSSOP8-01	Baseline CA	12	3								15
	Post 1000 TC	10	2							4	16
	Post 2000 TC	2	7							7	16
	Post 500 hr HAST	3	2							11	16
M5-MCK-WSON6-01	Baseline CA	4	1							7	12
	Post 2000 TC	1	8							3	12
	Post 500 hr HAST	5								7	12
M2-D-SOT233-02	Baseline CA	3	2							1	6
	Post 2000 TC		4								4
	Post 500 hr HAST	2	2								4
M5-MCK-SOT235-01	Baseline CA	1	1							6	8
	Post 1000 TC	2								6	8
	Post 2000 TC	6								6	12
	Post 500 hr HAST	5								3	8
M6-D-SOT-235-01	Baseline CA	2	2							1	5
	Post 2000 TC	7	3								10
	Post 500 hr HAST	8	1							1	10
M5-MCK-SOIC8-01	Baseline CA	6	10							4	20
	Post 2000 TC	2	20								22
	Post 500 hr HAST	3	19								22
M7-MCK-LFBGA169-01	Baseline CA	219	299							24	542
	Post 2000 TC	383	252							15	650
	Post 400 hr HAST+1000 TC	291	369							2	662
	Post 500 hr HAST	158	358	2						18	536
M1-MCK-LFBGA144-01	Baseline CA	35	331					6		1	373

Part Number	Condition	1	2	3	4	5	6	7	8	9	Total
M8-MCK-LQFP100-01	Baseline CA	81	84							21	186
	Post 2000 TC	55	231								286
	Post 400 hr HAST+1000 TC	119	167							2	288
	Post 500 hr HAST	68	203							17	288
M9-D-CUSTOM-01	Baseline CA		16							2	18
	Post 2000 TC	1	15							2	18
	Post 500 hr HAST		7							11	18
M10-D-SOD323-01	Baseline CA		4								4
	Post 2000 TC		4								4
	Post 500 hr HAST		4								4
M10-D-SOT1061-01	Baseline CA	1	5								6
	Post 2000 TC		3							1	4
	Post 500 hr HAST		4								4
M11-MCK-TQFP144-01	Baseline CA	26	113					80		4	223
	Post 500 hr HAST	59	193			1		7			260
	Post 2000 TC	84	154					64			302
Grand Total		2076	4283	2		1		161		280	6803

Table C.3-5. Plots of Cumulative Bond Pull Results for Each Part Number

	Stress Condition	Failure Category
	CA, 500HAST, 2000TC, 1000TC, 400HAST1000TC	Pull 1, Pull 2, Pull 3, Pull 4, Pull 5, Pull 6, Pull 7, Pull 8, Pull 9
M1-MCK-SOIC8-01	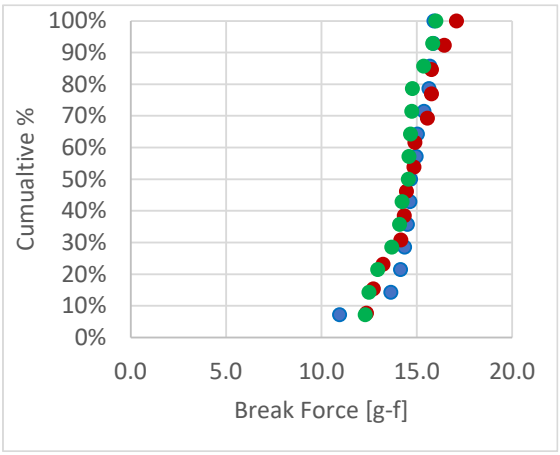	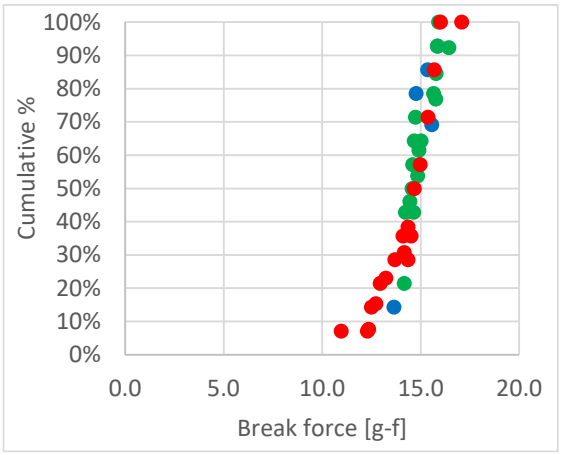
M2-D-SOT233-01	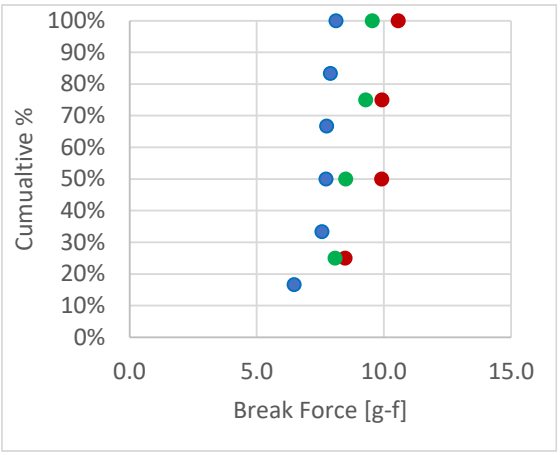	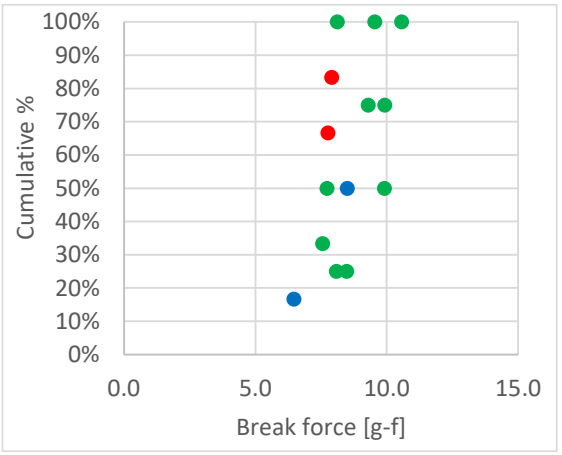
M3-MCK-TQFP100-01	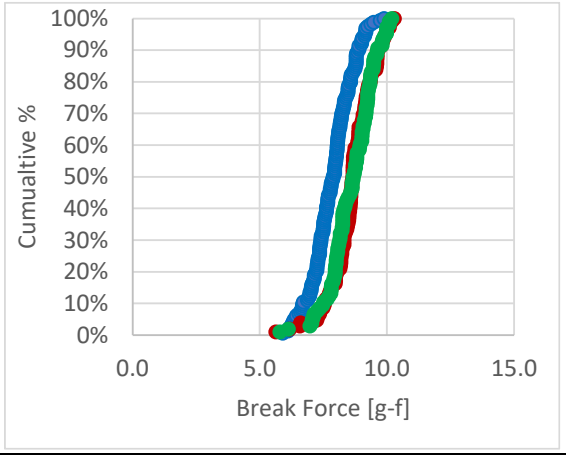	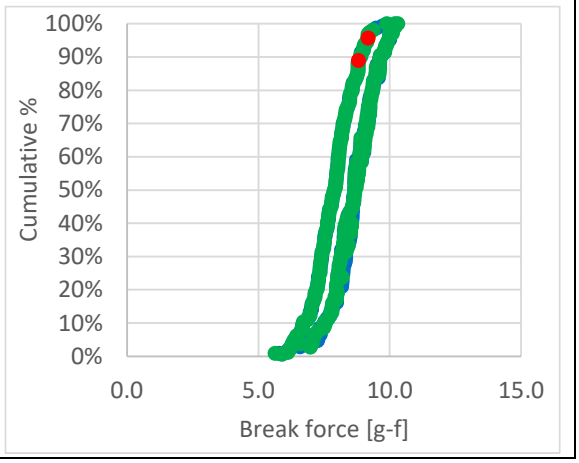

M4-MCK-FBGA256-01	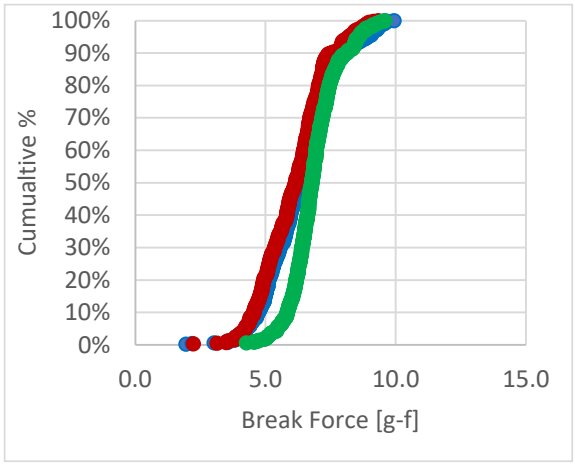	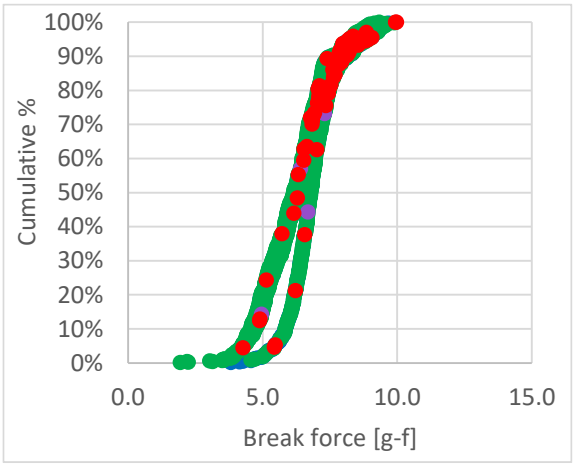
M5-D-SOT233-01	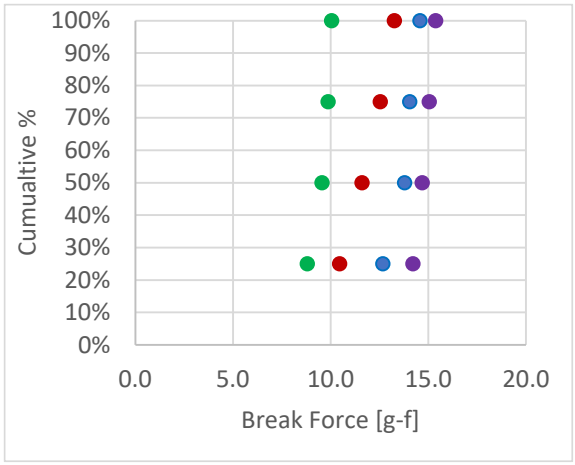	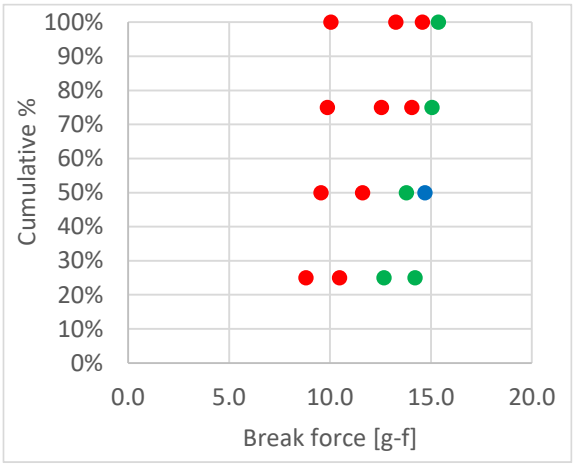
M5-MCK-VSSOP8-01	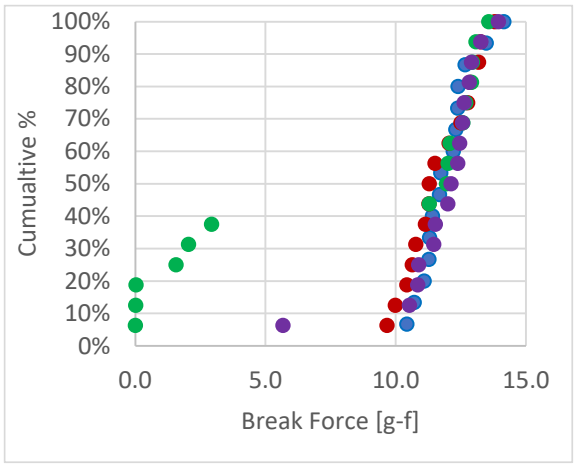	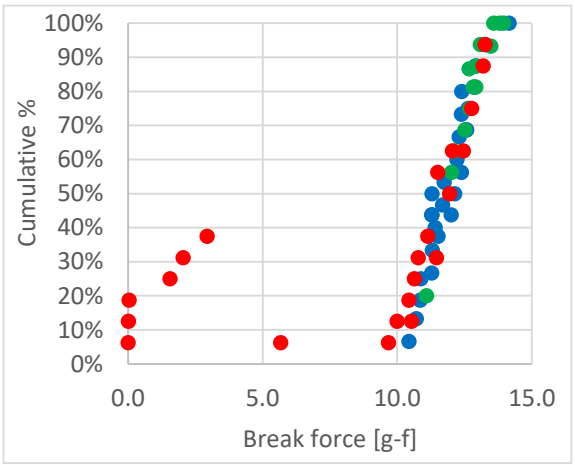

M5-MCK-WSON6-01	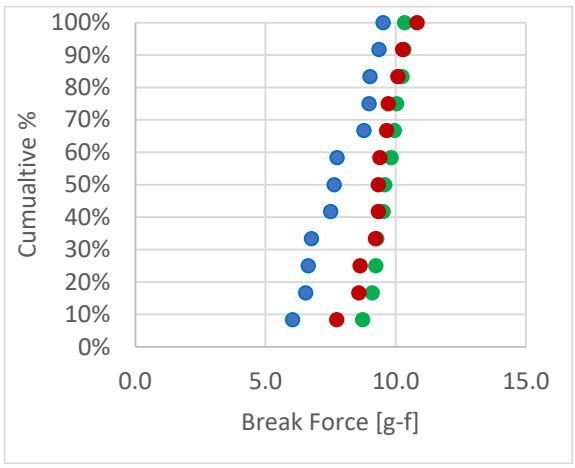	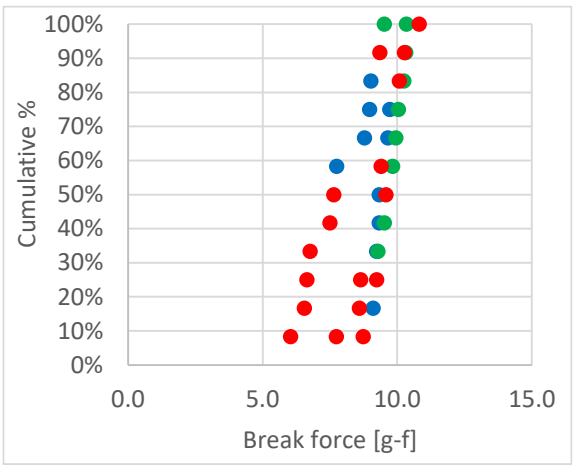
M2-D-SOT233-02	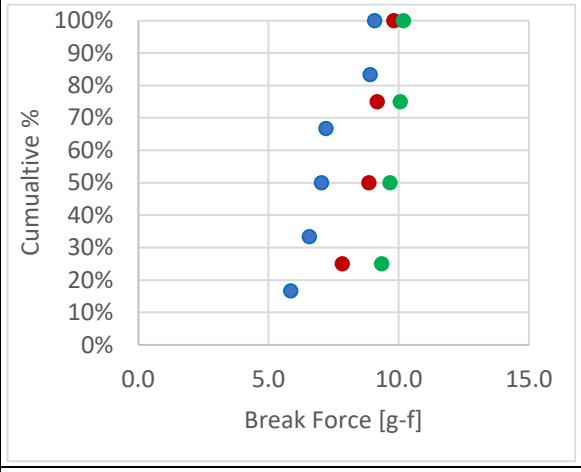	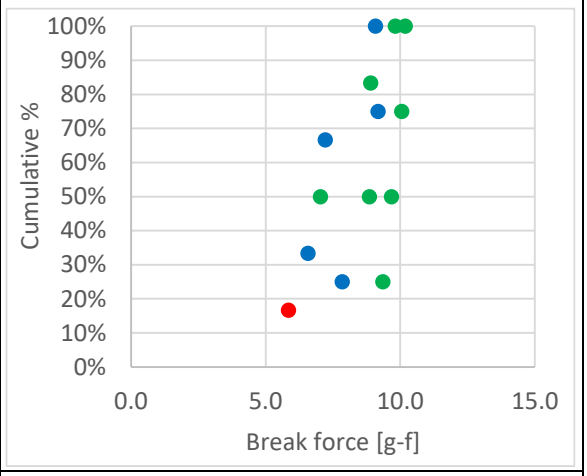
M5-MCK-SOT235-01	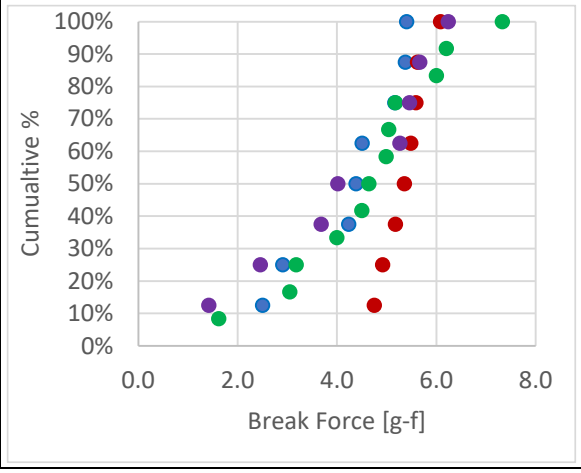	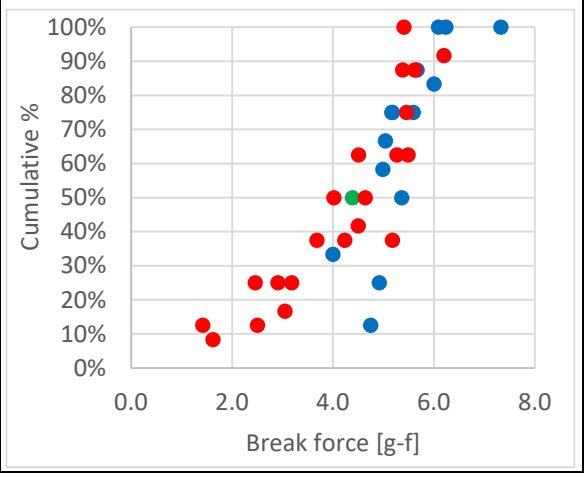

M6-D-SOT-235-01	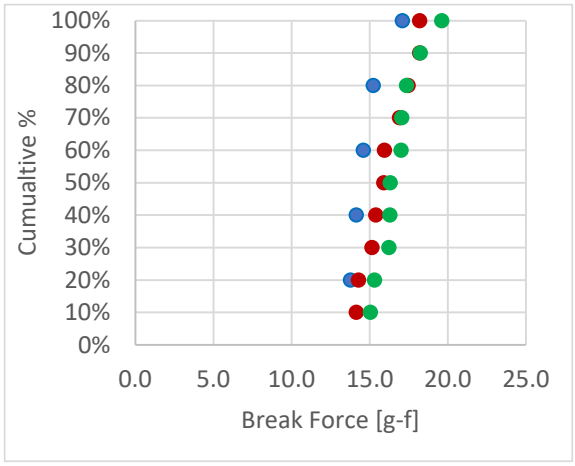	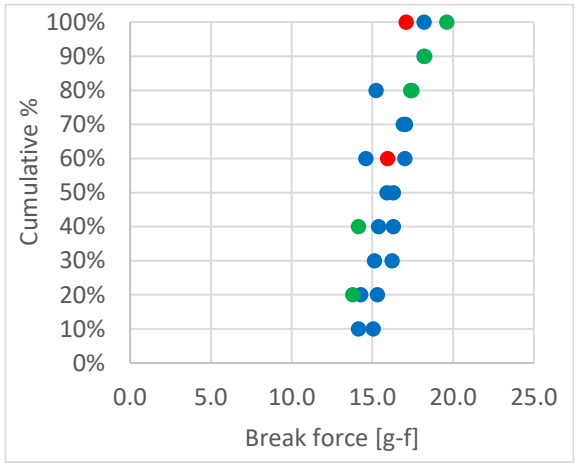
M5-MCK-SOIC8-01	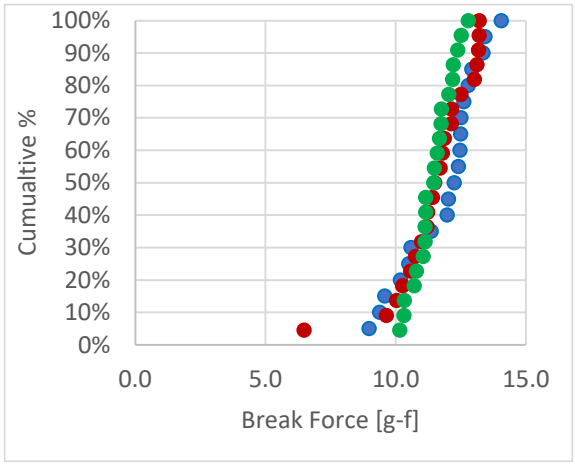	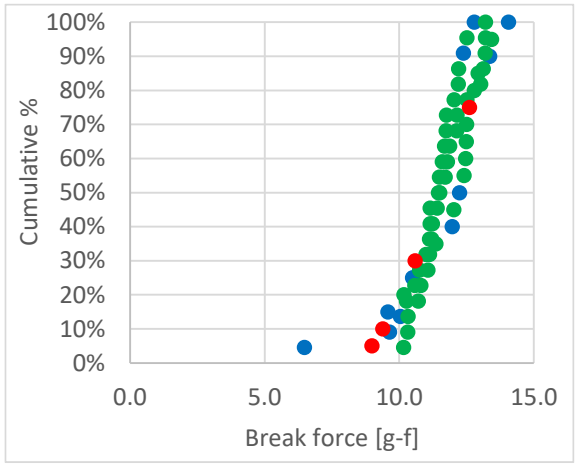
M7-MCK-LFBGA169-01	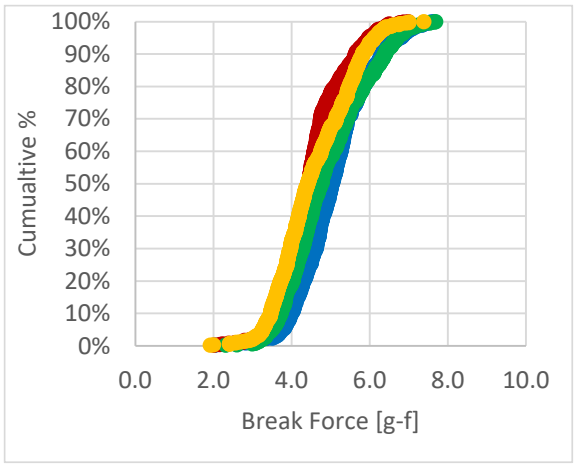	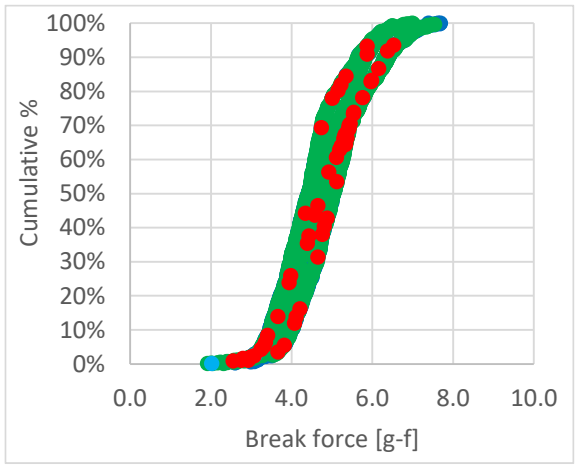

M1-MCK-LFBGA144-01	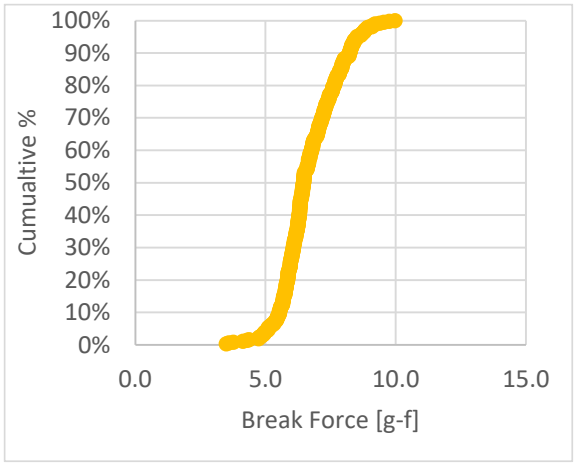	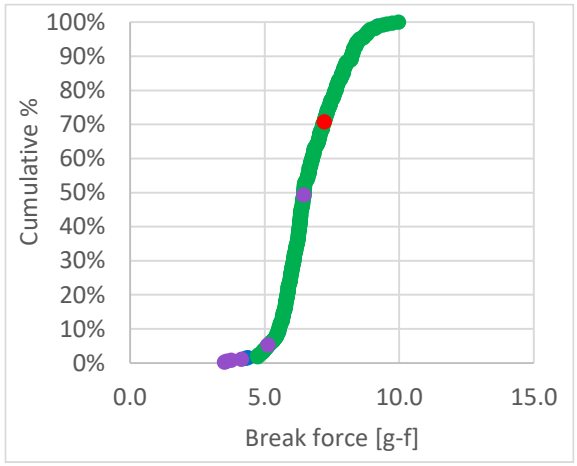
M8-MCK-LQFP100-01	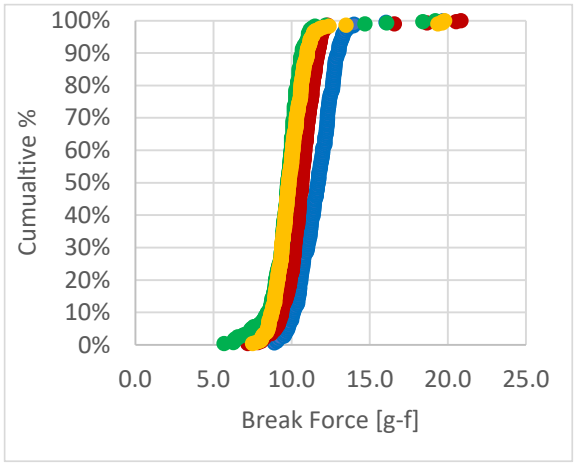	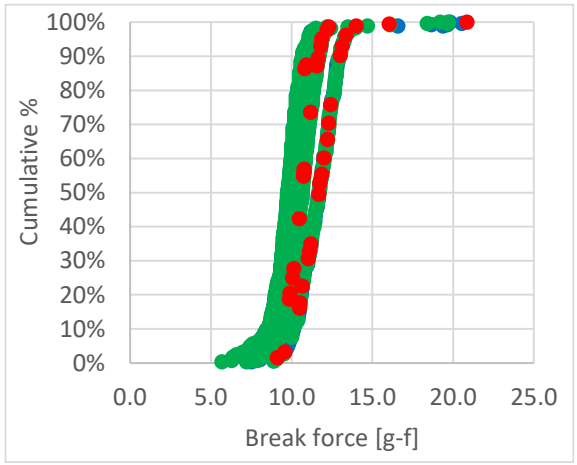
M9-D-CUSTOM-01	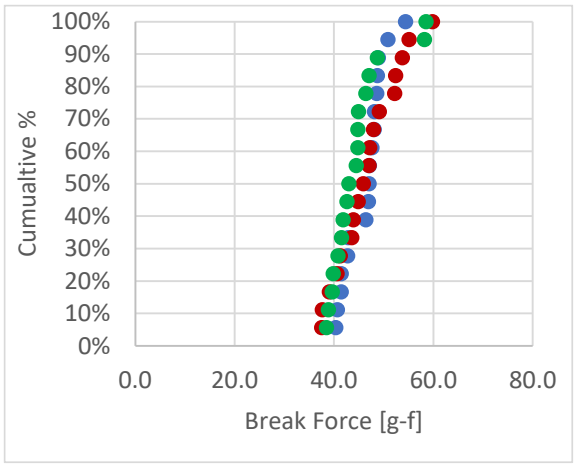	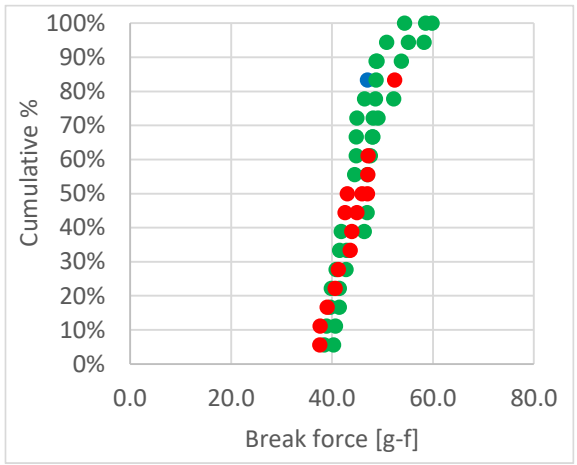

M10-D-SOD323-01	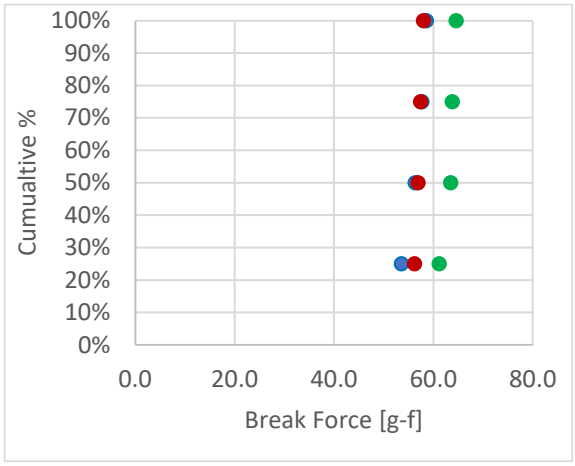	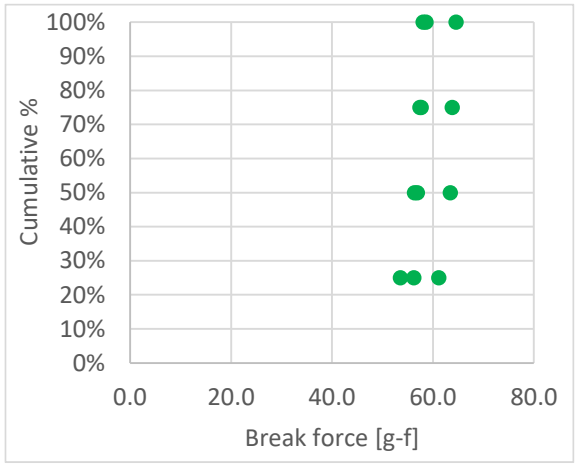
M10-D-SOT1061-01	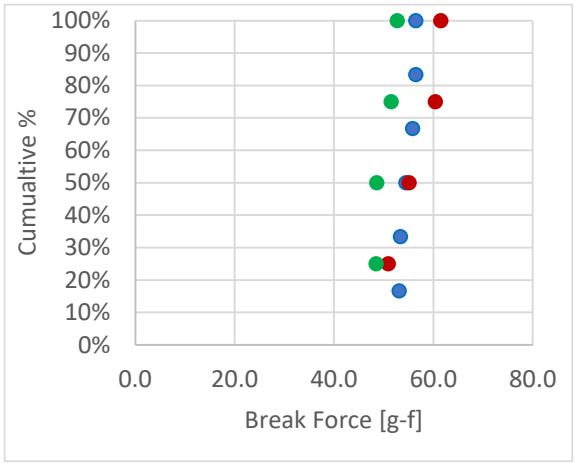	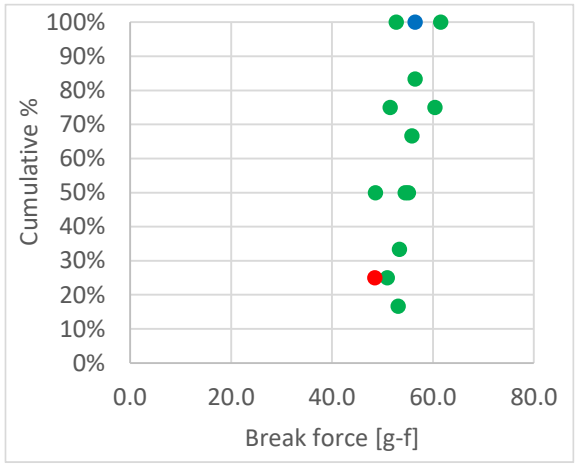
M11-MCK-TQFP144-01	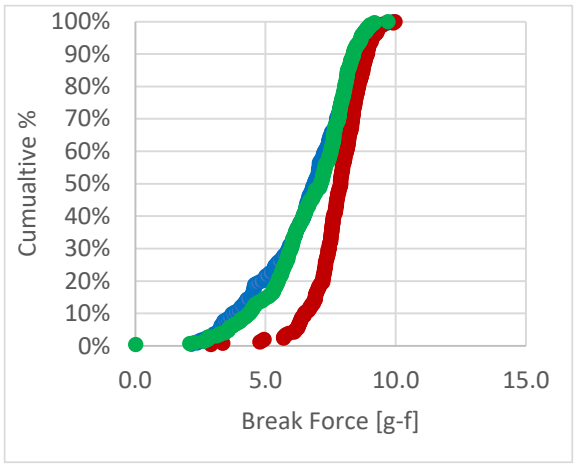	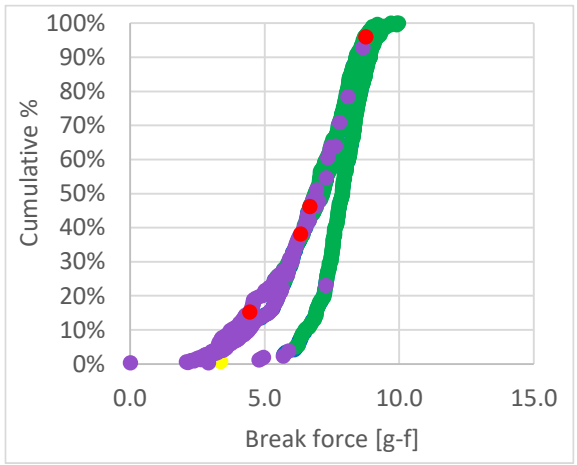

C.3.2.1 Bond Pull Issues Observed

Although most bonds exhibited wire breaks within the span or the neck-down region, select parts exhibited cratering or lifting of the die metallization. Additionally, certain wires exhibited low strengths (e.g., stitch heel break) possibly due to wire fatigue during thermal cycling. One Cu wire-bonded part and the one Au wire-bonded part exhibited this failure mode. Large parts with a large number of tiered bonds presented challenges during decapsulation. These challenges may have resulted in etch variability between the upper and lowest tiers, which could have contributed to reduced pull strength values for these parts. A discussion of these issues follows.

Cratering

As discussed in Appendix A, the higher hardness of Cu compared to Al and its propensity to increase hardness following thermosonic bonding can lead to cratering in Cu wire-bonded parts. This failure mode was observed for 3 of the 17 Cu wire-bonded parts investigated. Two parts (M1-MCK-LFBGA144-01 and M4-MCK-FBGA256-01) exhibited limited cratering (<1%), while one part (M11-MCK-TQFP144-01) exhibited significant cratering (up to 35%, depending upon condition). Each had wires in the 0.7 to 0.8 mil range. Figures C.3-5 through C.3-8 provide an overview of the parts that exhibited cratering following decapsulation and bond pull in the as-received, post-HAST and post-2000 TC conditions.

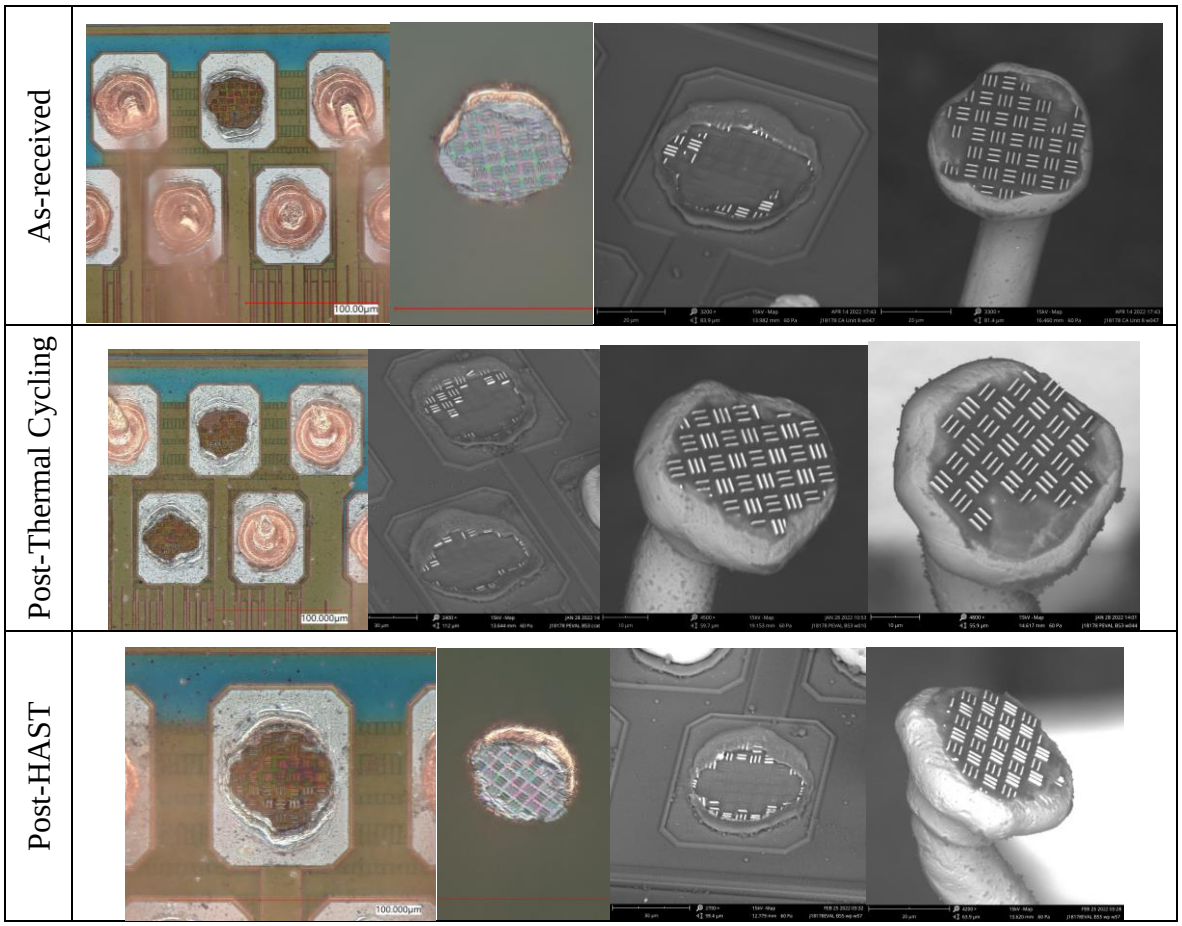

Figure C.3-5. M4-MCK-FBGA256-01 Exhibited Limited Cratering (1-2 bonds) in As-Received, Post-bHAST, and Post-TC Conditions. Representative optical and SEM images of ball bonds and bond pads exhibiting cratering following bond pull experiments are shown.

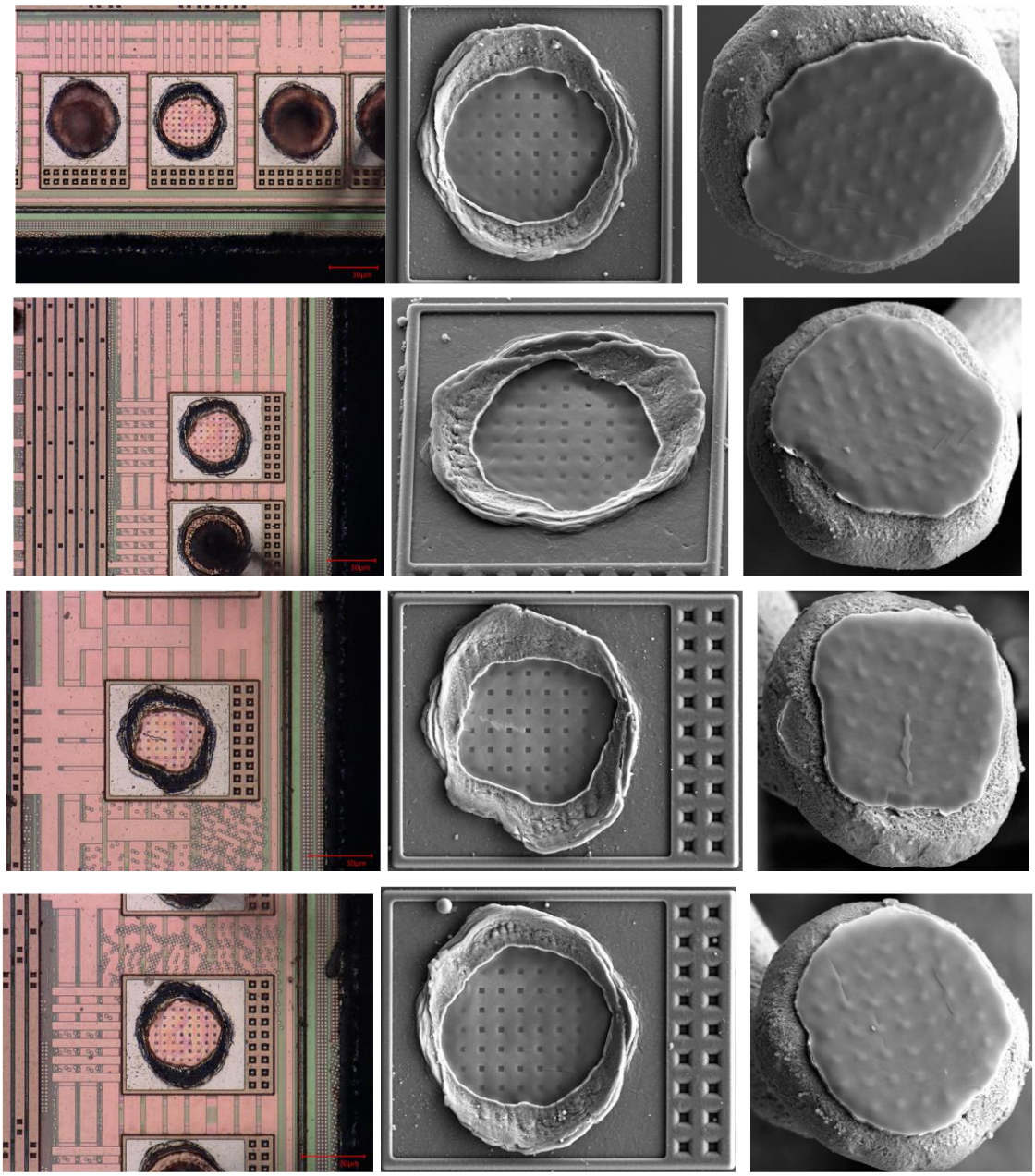

Figure C.3-6. M1-MCK-LFBGA144-01 Was Inspected Only in As-Received Condition. Limited cratering (6 bonds) was observed. Shown here: Representative optical and SEM images of ball bonds and bond pads exhibiting cratering after bond pull experiments in as-received condition.

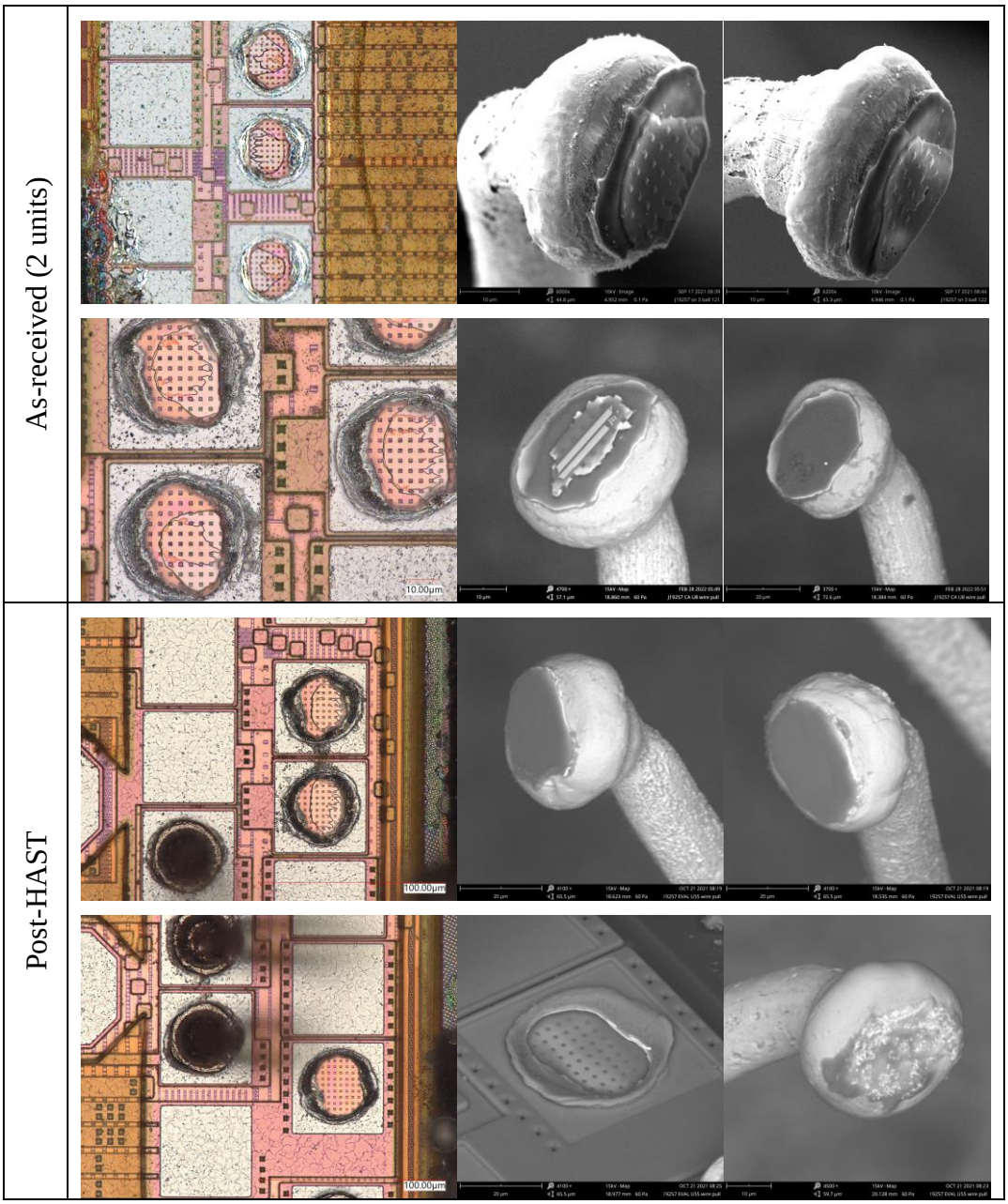

Figure C.3-7. M11-MCK-TQFP144-01 Exhibited Extensive Cratering in As-Received, Post-bHAST, and Post-TC Conditions. Shown: Representative optical and SEM images of ball bonds and bond pads exhibiting cratering following bond pull for as-received and post-HAST.

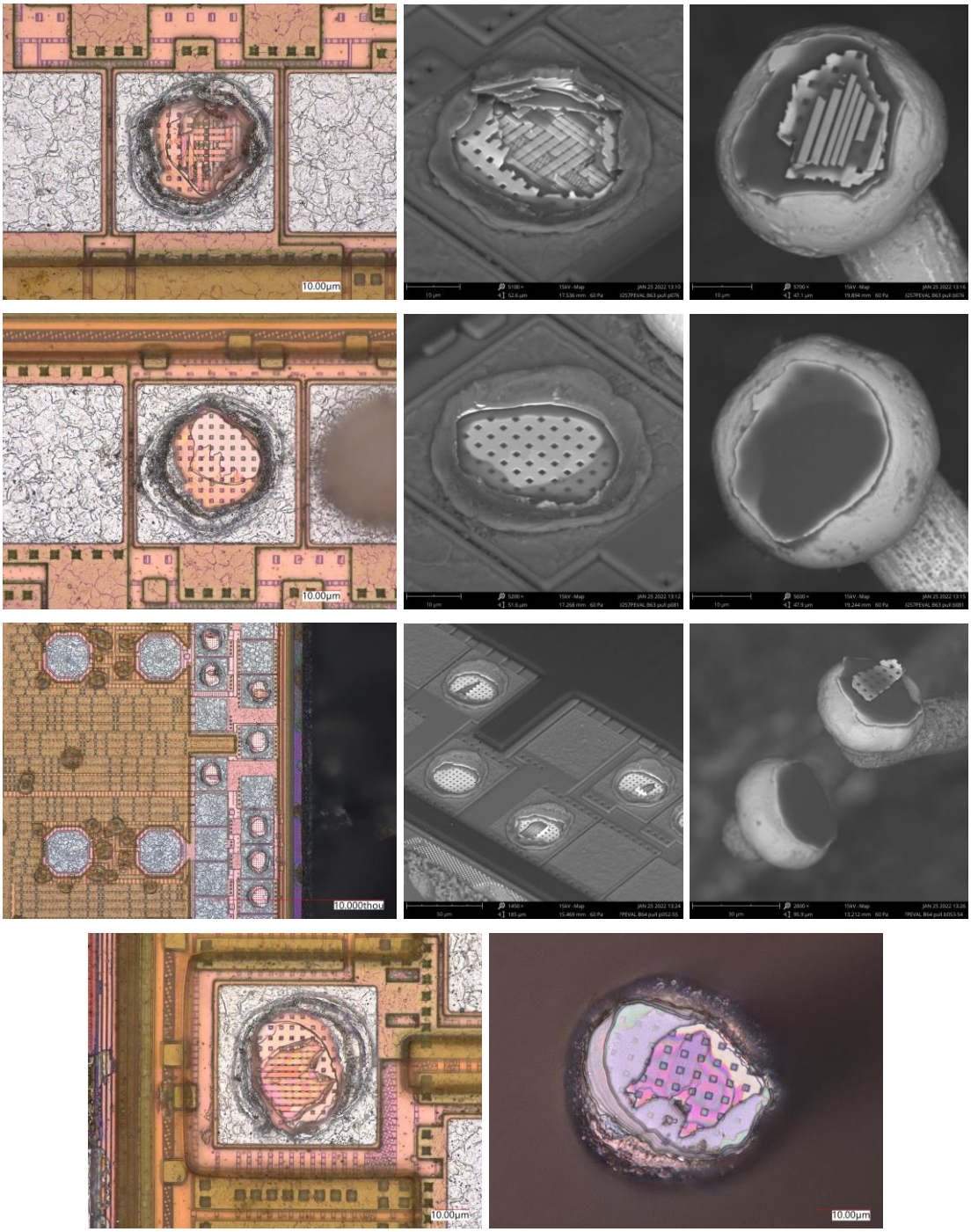

Figure C.3-8. M11-MCK-TQFP144-01 Exhibited Extensive Cratering in As-Received, Post-bHAST, and Post-TC Conditions. Shown: Representative optical and SEM images of ball bonds and bond pads exhibiting cratering following bond pull for post-thermal cycling condition.

Bond Lift

Lifted ball bonds are associated with weak bonds between the wire and the bond pad or poor adhesion between the bond pad metallization and the device below. M7-MCK-LFBGA169-01 (Figure C.3-9) exhibited a limited number of lifted ball bonds.

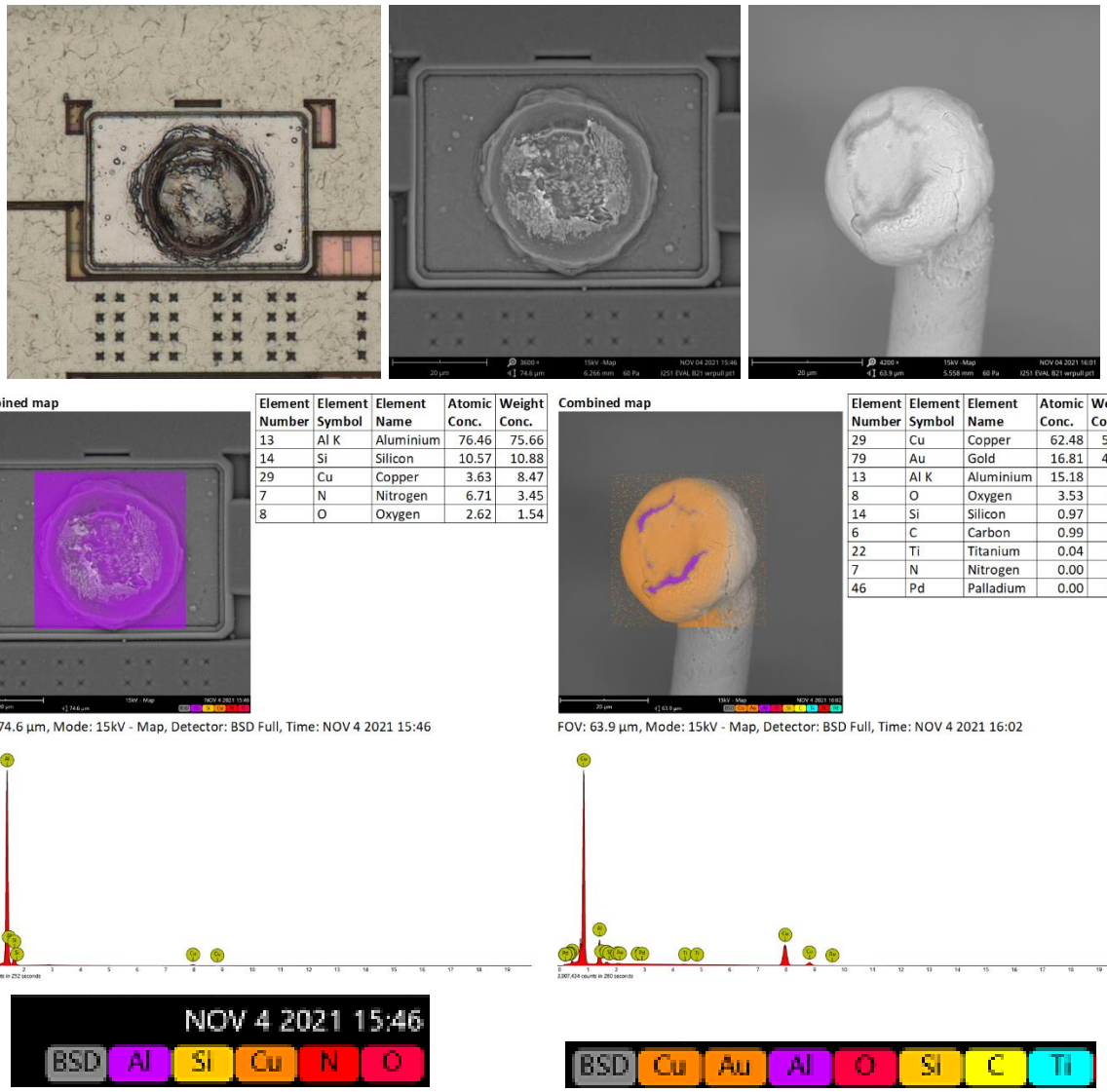

Figure C.3-9. M7-MCK-LFBGA169-01 Exhibited Lifting of Bond Pad Metallization. Optical and SEM images and energy dispersive X-ray analysis of bond composition are shown. No contamination or corrosion were detected.

Multi-Tier Package Decapsulation

Large, high-pin-count devices that use multi-tier wire bonding, such as the device shown in Figure C.3-10, are especially challenging for decapsulation. During process development, the use of laser decapsulation was maximized to reduce chemical exposure. Initial experiments resulted in broken bonds (etched wires), as indicated in Figure C.3-11. The etch process was modified to create a well for the etchant to protect the leadframe. The two highest strengths for part M7-MCK-LFBGA169-01 were leadframe-to-leadframe bonds that were never exposed to etchant but were entirely decapsulated using the laser. Laser decapsulation reduces damage to the wires but increases damage to the die. Parts were etched to remove molding compound from the entire length of the wire without over-etching the die or undercutting plating on the leadframe. Leadframe undercutting reduced the strength of both Au and Cu wires during decapsulation process development. Although every effort was made to minimize the impact of etchant on wire integrity, differences in pull strengths for different wires could be affected by etch duration and

bond geometry. Figure C.3-12 illustrates potential etch variability along the length of wires. Finally, the strengthening mechanism provided by Pd coating of Cu wire would no longer be present if the Pd coating was etched away during decapsulation.

Figure C.3-10. Representative Optical Image of Multi-Tier Component (M7-MCK-LFBGA169-01).

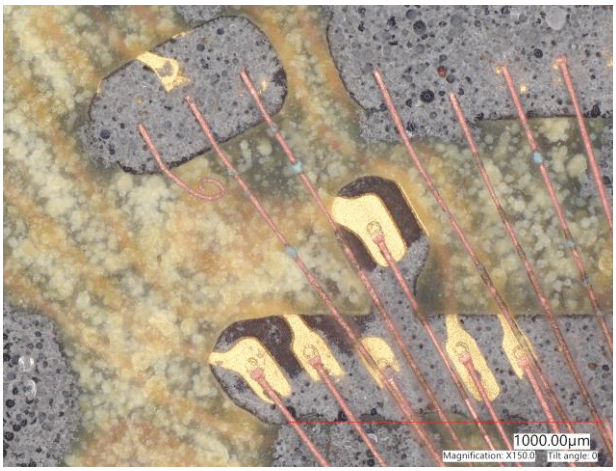

Figure C.3-11. Optical Image Showing Broken Bonds Following Decapsulation

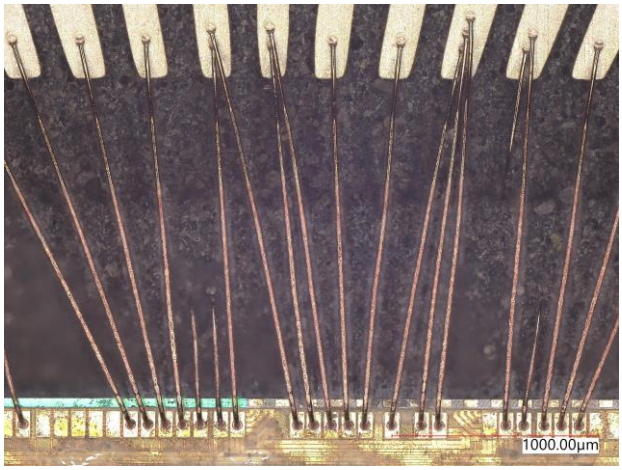

Figure C.3-12. Optical Images Showing Different Levels of Etching Along Wire Lengths

Heel Cracking

M5-MCK-VSSOP8-01 and M5-MCK-SOT235-01 (Au) exhibited cracked stitch bonds following decapsulation as well as low bond pull strength (with failure occurring in the neck-down region above the stitch bond). M5-MCK-SOT235-01 exhibited this failure mode under all conditions, whereas M5-MCK-VSSOP8-01 only exhibited heel cracking following environmental exposure. Thermomechanical fatigue of bond wires resulting from thermal cycling can lead to opens during thermal cycling or poor bond pull strength following decapsulation. Figures C.3-13 through C.3-20 provide optical and SEM images of the fatigued stitch bonds and post-bond pull fracture surfaces.

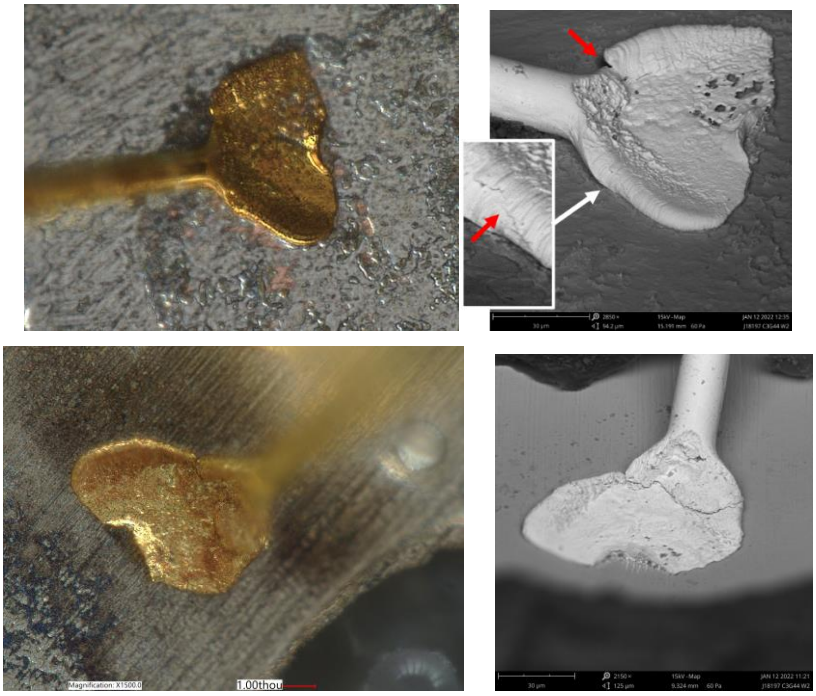

Figure C.3-13. Optical and SEM Images of Crack Forming in Fatigued Stitch Bond of M5-MCK-SOT235-01 (Au) Following Decapsulation in Post-2000 TC Condition

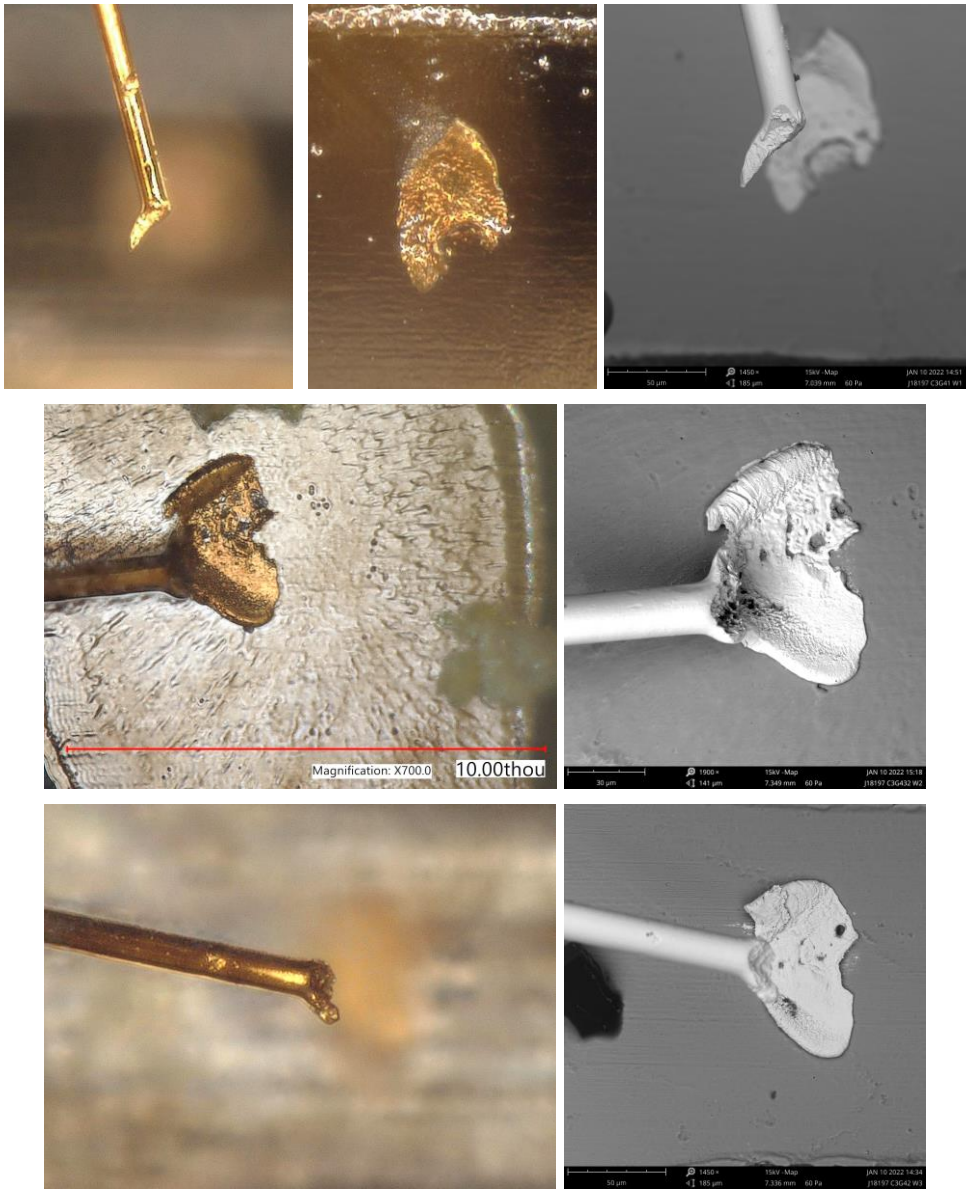

Figure C.3-14. Optical and SEM Images of Stitch Bond Wires That Broke at Low Forces Following Decapsulation and Bond Pull of M5-MCK-SOT235-01 (Au) in post-2000 TC Condition

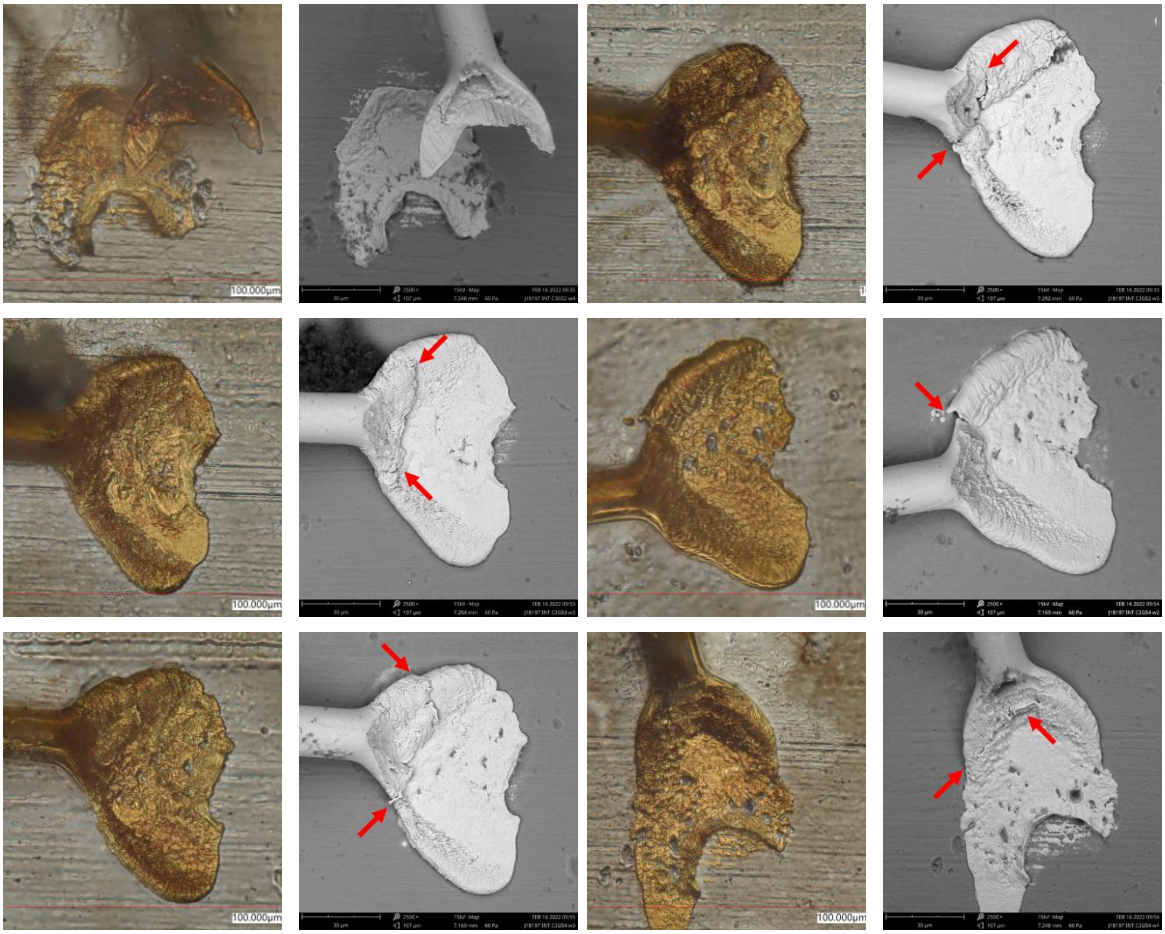

Figure C.3-15. Optical and SEM Images of Stitch Bonds Exhibiting Fatigue Crack Formation Following Decapsulation for M5-MCK-SOT235-01 (Au) in Post-1000 TC Condition

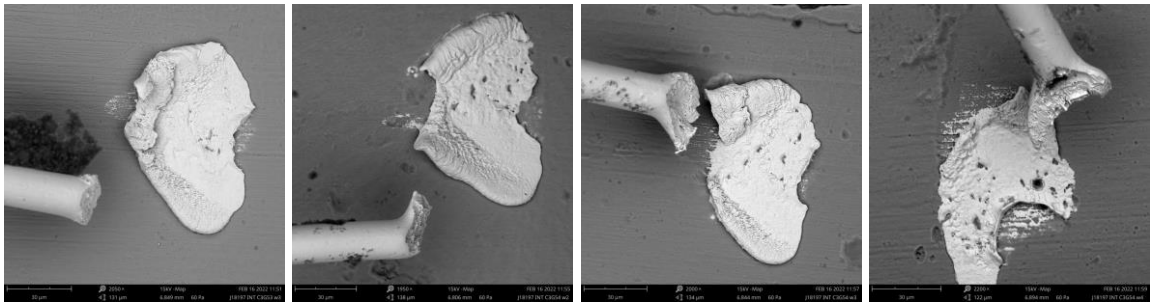

Figure C.3-16. SEM Images of Stitch Bond Wires That Broke at Low Forces Following Decapsulation and Bond Pull of M5-MCK-SOT235-01 (Au) in post-1000 TC Condition

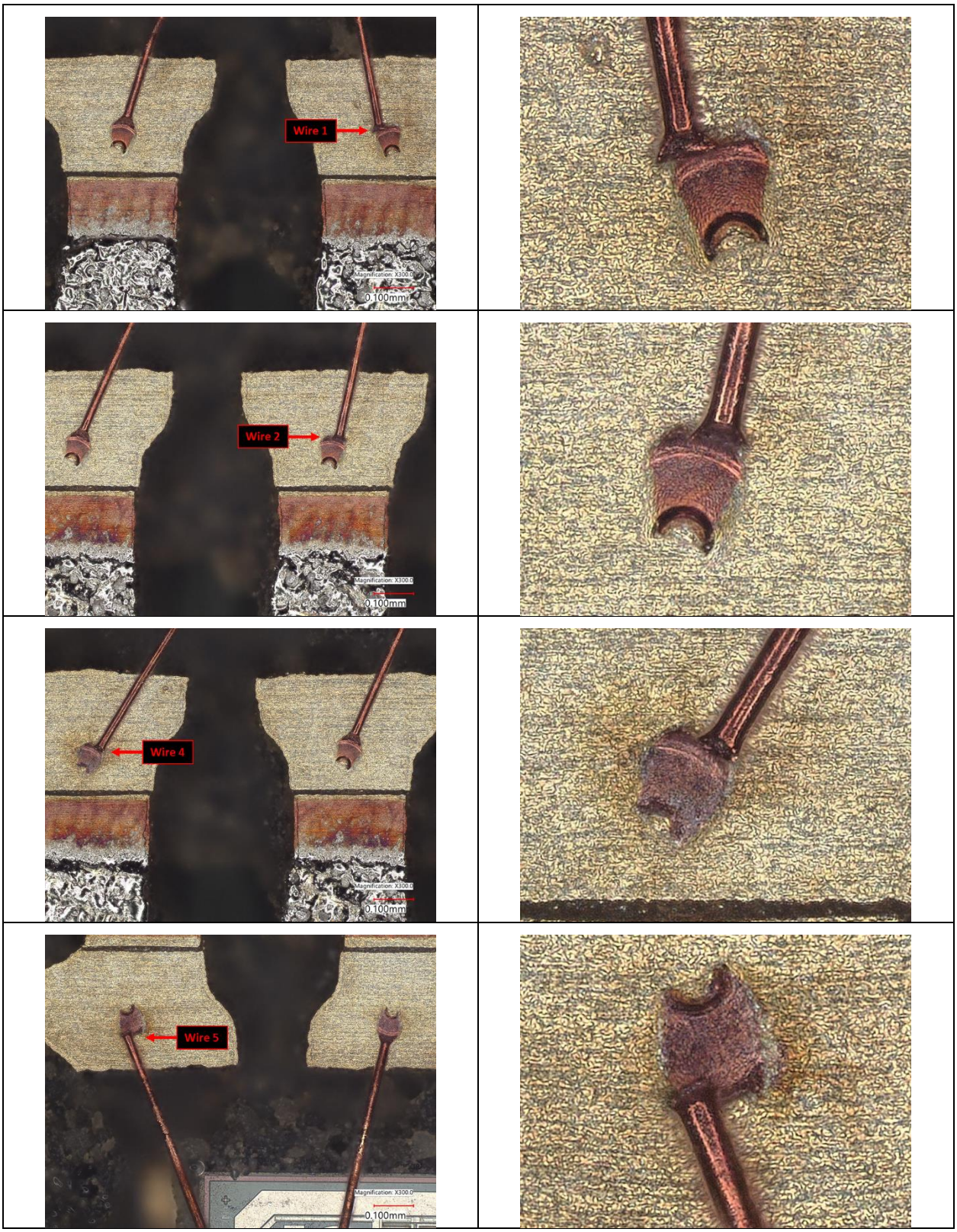

Figure C.3-17. Low- and High-Magnification Optical Images of Broken Stitch Bonds on M5-MCK-VSSOP8-01 Following Decapsulation in Post-2000 TC Condition

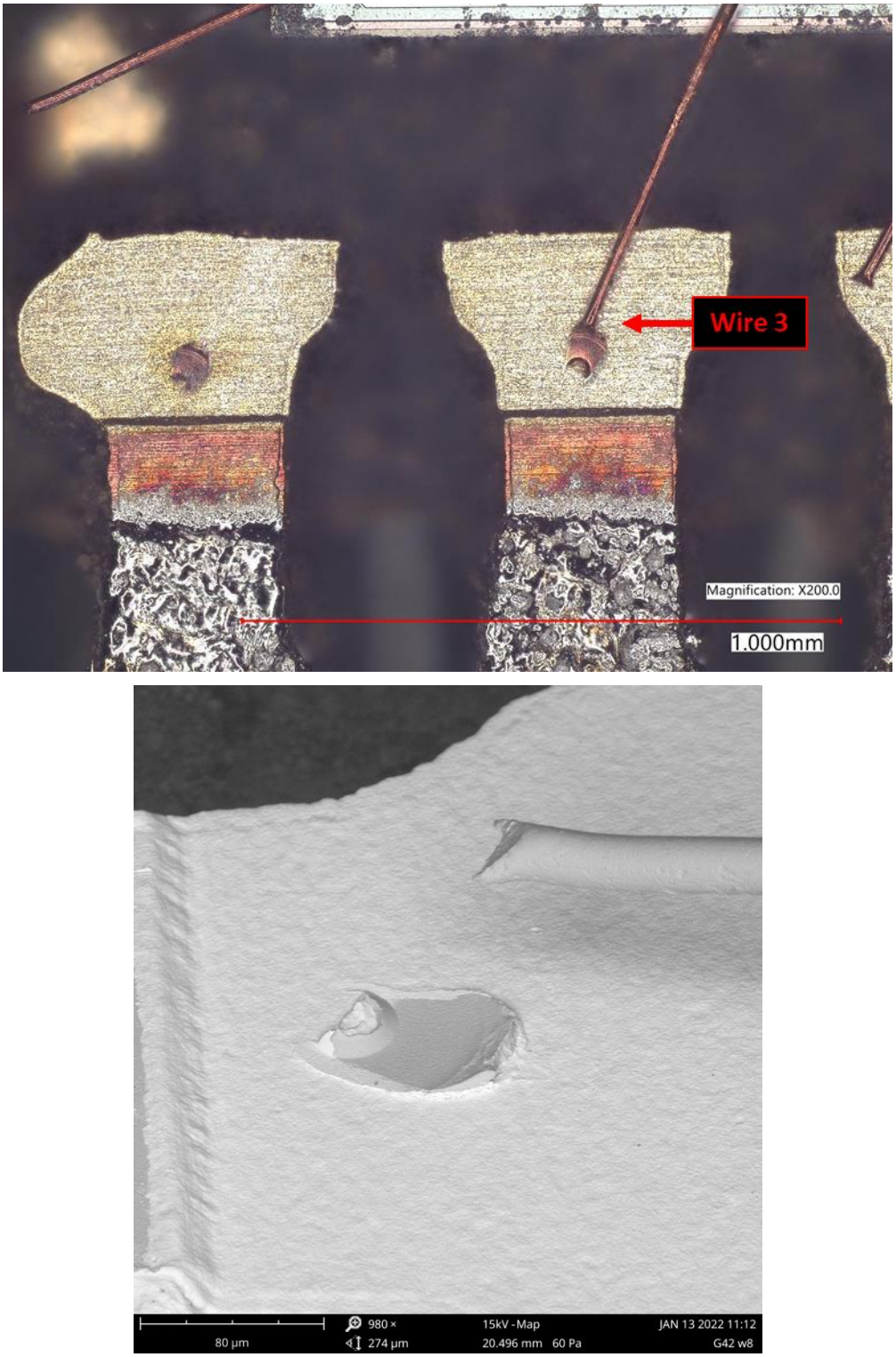

Figure C.3-18. Optical and SEM Images Showing Representative Wire That Broke With Low Force (out-of-family) on M5-MCK-VSSOP8-01 Following Decapsulation and Bond Pull in Post-2000 TC Condition

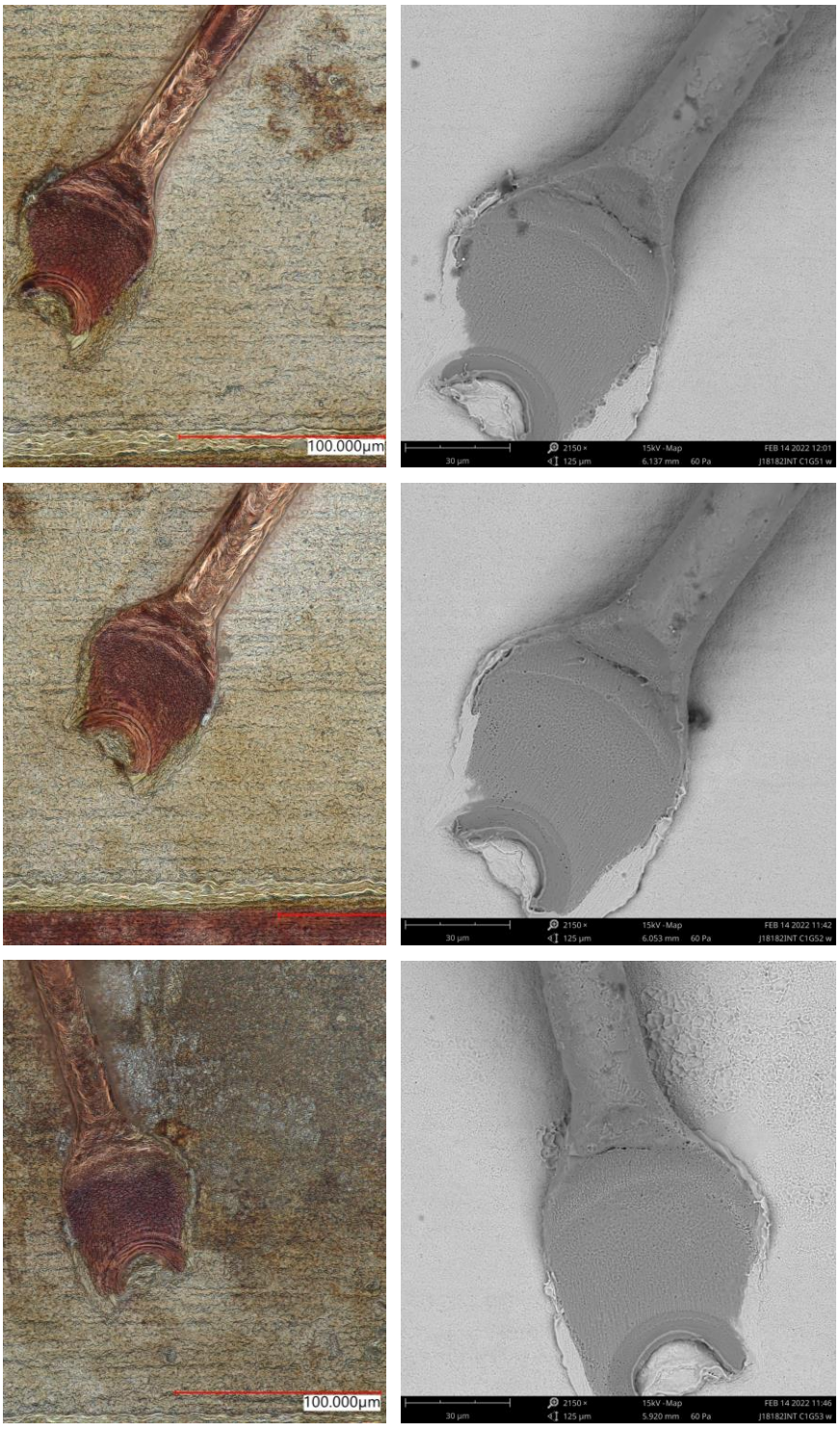

Figure C.3-19. Optical and SEM Images of Stitch Bonds Exhibiting Fatigue Crack Formation Following Decapsulation for M5-MCK-VSSOP8-01 in Post-1000 TC Condition

Figure C.3-20. Representative Optical and SEM Images of M5-MCK-VSSOP8-01 Showing Wire That Broke with Low Force Following Decapsulation and Bond Pull in Post-1000 TC Condition

C.3.3 Cu Wire Bond Shear Test Results

Wire bond shear tests were performed in the as-received condition, after 500 hr of bHAST exposure and 2000 TCs for all part types. Due to indications of TC-related fatigue damage of wires, two parts were selected for decapsulation and ball shear following 1000 TCs. Additionally, two large wire count components were selected for decapsulation and ball shear following the combined exposure of 400 hr of bHAST and 1000 TCs. Bond shear failure modes outlined in JESD22-B116B are provided in Table C.3-6. A summary of failure categories for the parts tested is provided in Table C.3-7. Cumulative shear strengths for each component tested under each condition are provided in Table C.3-8, along with the associated failure category.

Table C.3-6. Description of Failure Modes for JESD22-B116B Wire Bond Shear Test Method

Type	Name	Description for Copper/Aluminum or All Metal Systems
1	Bond Lift	Wire bond separated from bonding surface and no evidence of bond formation. Slight imprint on bonding surface.
2A	Bond Shear	Separation within bonding surface metallization. Layer of bonding surface metallization remains on wire bond. Bonding surface has some metal removed and visual evidence of metal shear.
2B	Bond Shear	Separation at bonding surface. Separation at interface with bonding surface and (mandatory) evidence of shear on surface.
2C	Bond Shear	Separation at material interface and within bulk material. Shear occurs at the material interface and within bulk material.
2D	Bond Shear	Separation within ball bond. Major portion of wire bond. Ball or wedge bonding weld area intact; visual evidence of metal shear.
3	Cratering	Residual bonding surface and substrate (bulk) material attached to wire bond. Bonding surface lifted, taking portion of substrate (bulk) material.
4	Bonding Surface Contact	Arm contacted bonding surface metallization instead of wire bond. Bonding surface separated from die surface.
5	Shear Skip	Minor portion of wire bond attached to wire. Wire bond sheared too high; only portion of wire bond removed.
6	Bond Pad Surface Lift	Underlying bonding pad metallization remains with the ball bond. Bonding surface metallization separated from die surface.

Table C.3-7. Summary of Wire Bond/Ball Shear Break Codes

Part Number	Condition	1	2A	2B	2C	2D	3	4	5	6
M1-MCK-SOIC8-01	As-received		12							
	Post 2000 TC		14							
	Post 500 hr HAST		14							
M2-D-SOT233-01	As-received		6							
	Post 2000 TC		4							
	Post 500 hr HAST		3		1					
M3-MCK-TQFP100-01	As-received			98						
	Post 2000 TC		81	8					34	
	Post 500 hr HAST		58						38	
M4-MCK-FBGA256-01	As-received			92	4		5		3	36
	Post 2000 TC			57	1		40			190
	Post 500 hr HAST			114	1		56			68
M5-D-SOT233-01	As-received		5	1						
	Post 1000 TC		1	3						
	Post 2000 TC		2	2						
	Post 500 hr HAST		2	2						
M5-MCK-VSSOP8-01	As-received		9	7						
	Post 1000 TC		7	9						
	Post 2000 TC		5	11						
	Post 500 hr HAST		5	11						
M5-MCK-WSON6-01	As-received			10			1			1
	Post 2000 TC		3	5	1					3
	Post 500 hr HAST		3	9						
M2-D-SOT233-02	As-received				5					
	Post 2000 TC				2	2				
	Post 500 hr HAST		1		3					
M5-MCK-SOT235-01	As-received		3		5					
	Post 1000 TC				7					
	Post 2000 TC				5	1				
	Post 500 hr HAST				6					
M6-D-SOT-235-01	As-received		5							
	Post 2000 TC		10							
	Post 500 hr HAST		10							
M5-MCK-SOIC8-01	As-received		17	4						
	Post 2000 TC		10	11		1				
	Post 500 hr HAST			22						
M7-MCK-LFBGA169-01	As-received		328							
	Post 2000 TC		343			2				
	Post 400 hr HAST+1000 TC		303							

Part Number	Condition	1	2A	2B	2C	2D	3	4	5	6
	Post 500 hr HAST		331							
M1-MCK-LFBGA144-01	As-received			189			6			
M8-MCK-LQFP100-01	As-received				58	54				
	Post 2000 TC					146				
	Post 400 hr HAST+1000 TC					144				
	Post 500 hr HAST				46	114				
M9-D-CUSTOM-01	As-received		17							
	Post 2000 TC		18							
	Post 500 hr HAST		18							
M10-D-SOD323-01	As-received				4					
	Post 2000 TC				4					
	Post 500 hr HAST				3					
M10-D-SOT1061-01	As-received		4	1						
	Post 2000 TC		4							
	Post 500 hr HAST		4							
M11-MCK-TQFP144-01	As-received			52	1		49		31	16
	Post 2000 TC			50	9	4	18		45	21
	Post 500 hr HAST									

Table C.3-8. Summary of Wire Bond/Ball Shear Strength

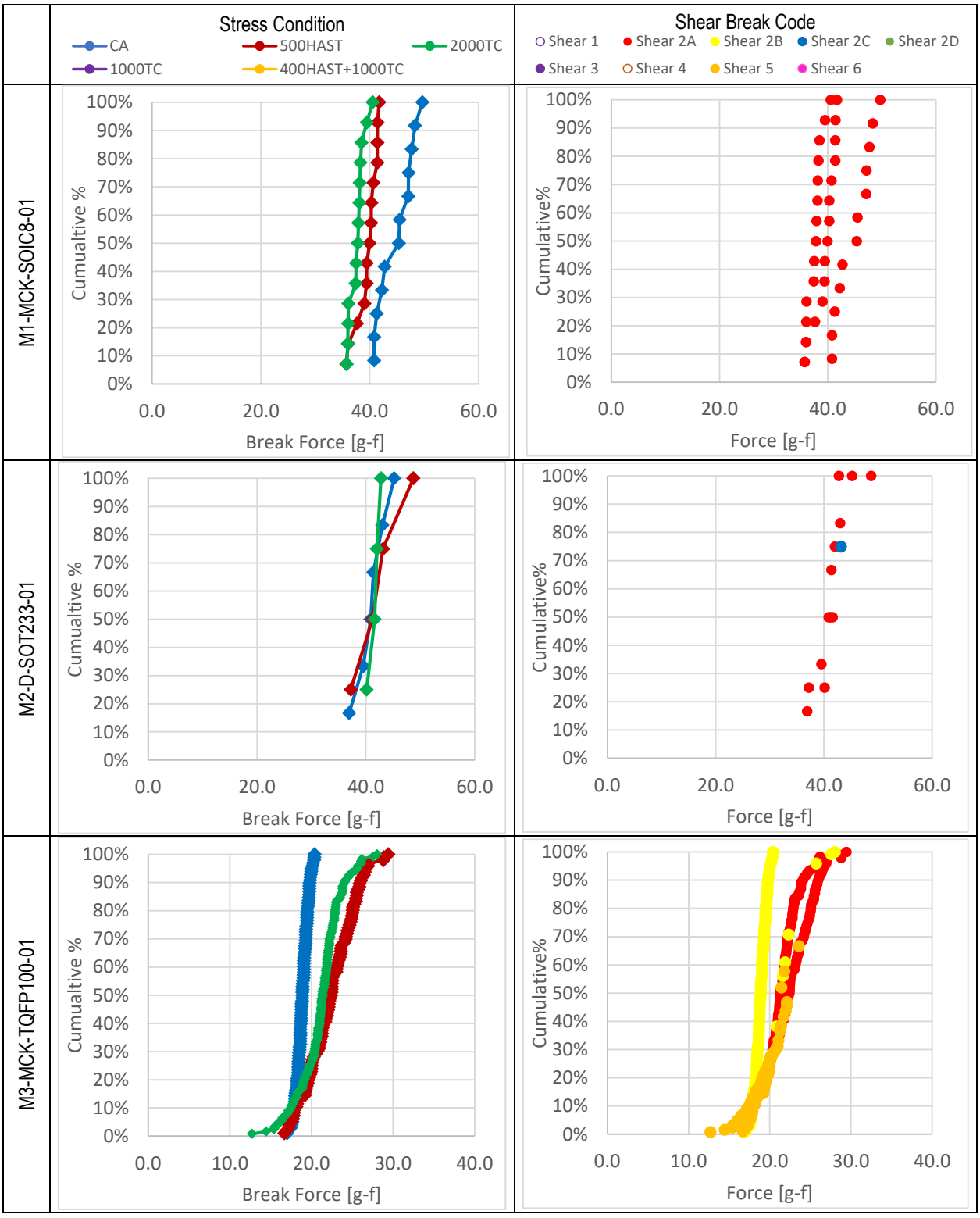

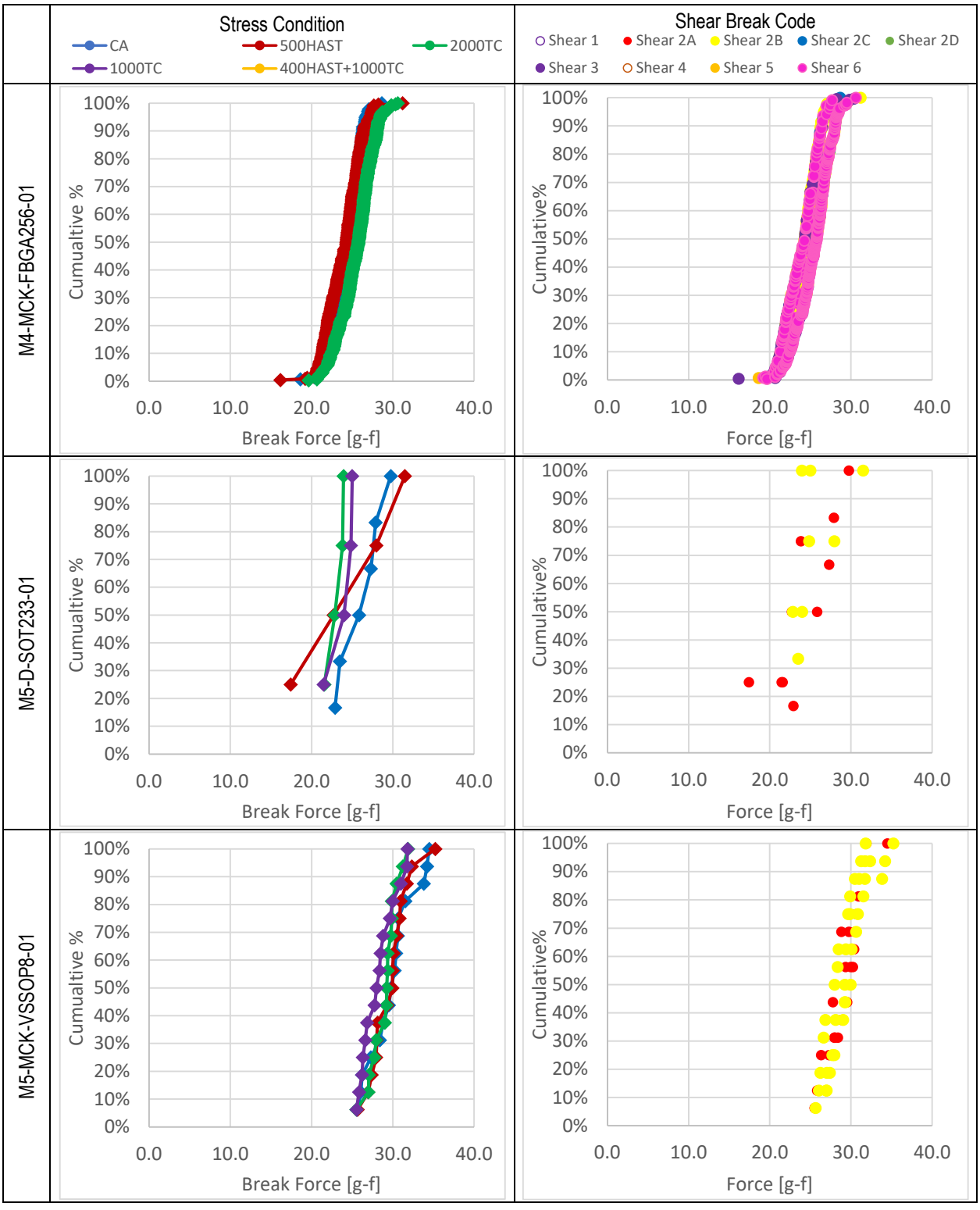
Stress Condition
CA
500HAST
2000TC
1000TC
400HAST+1000TC
Shear Break Code
Shear 1
Shear 2A
Shear 2B
Shear 2C
Shear 2D
Shear 3
Shear 4
Shear 5
Shear 6
M4-MCK-FBGA256-01
M5-D-SOT233-01
M5-MCK-VSSOP8-01
Cumulative %
Cumulative%
Break Force [g-f]
Force [g-f]
0%
10%
20%
30%
40%
50%
60%
70%
80%
90%
100%
0.0
10.0
20.0
30.0
40.0

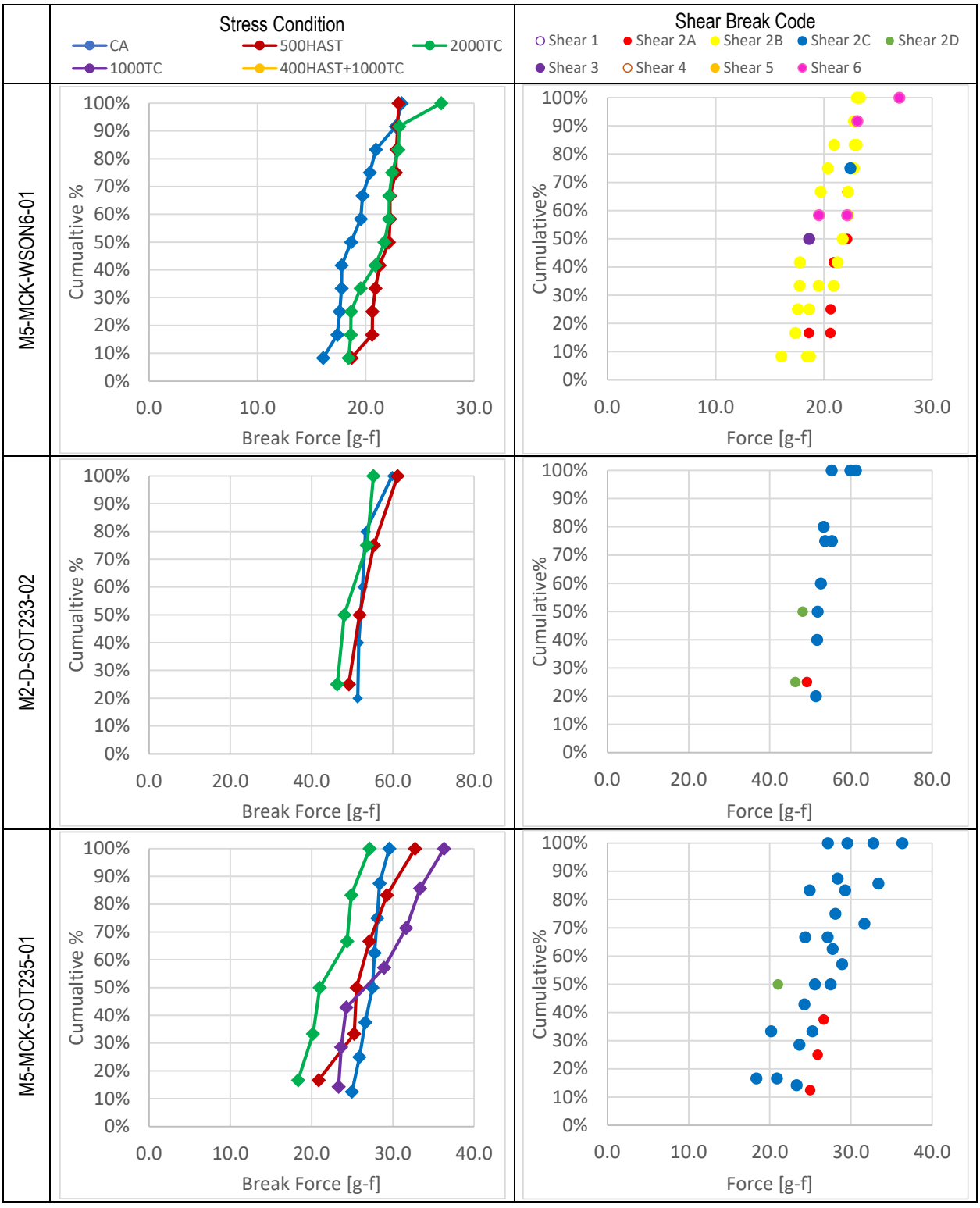
Stress Condition
CA
500HAST
2000TC
1000TC
400HAST+1000TC
Shear Break Code
Shear 1
Shear 2A
Shear 2B
Shear 2C
Shear 2D
Shear 3
Shear 4
Shear 5
Shear 6
M5-MCK-WSON6-01
M2-D-SOT233-02
M5-MCK-SOT235-01
Cumulative %
Cumulative%
Break Force [g-f]
Force [g-f]

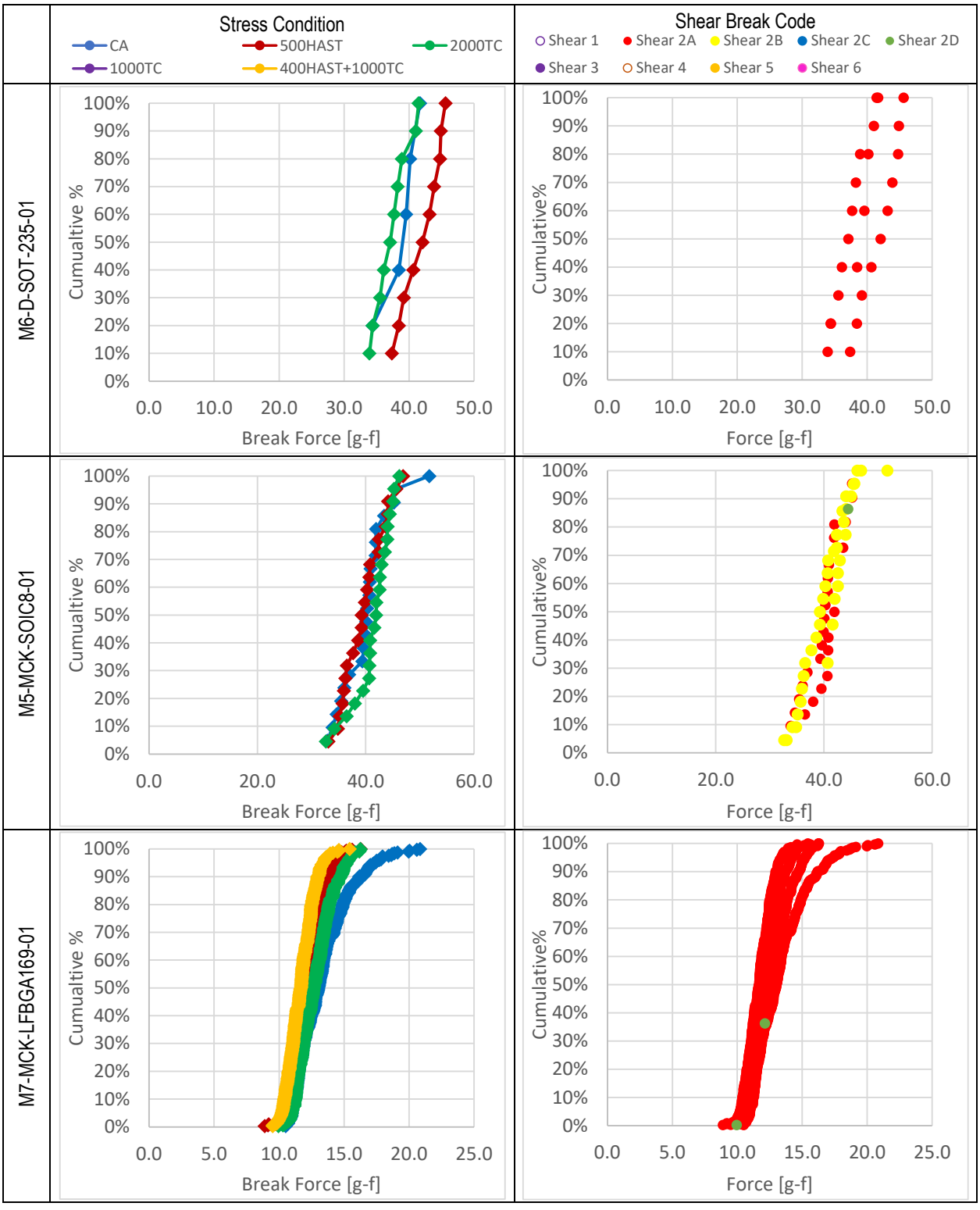
Stress Condition
CA
500HAST
2000TC
1000TC
400HAST+1000TC
Shear Break Code
Shear 1
Shear 2A
Shear 2B
Shear 2C
Shear 2D
Shear 3
Shear 4
Shear 5
Shear 6
M6-D-SOT-235-01
M5-MCK-SOIC8-01
M7-MCK-LFBGA169-01
Cumualtive %
Cumulative%
Break Force [g-f]
Force [g-f]

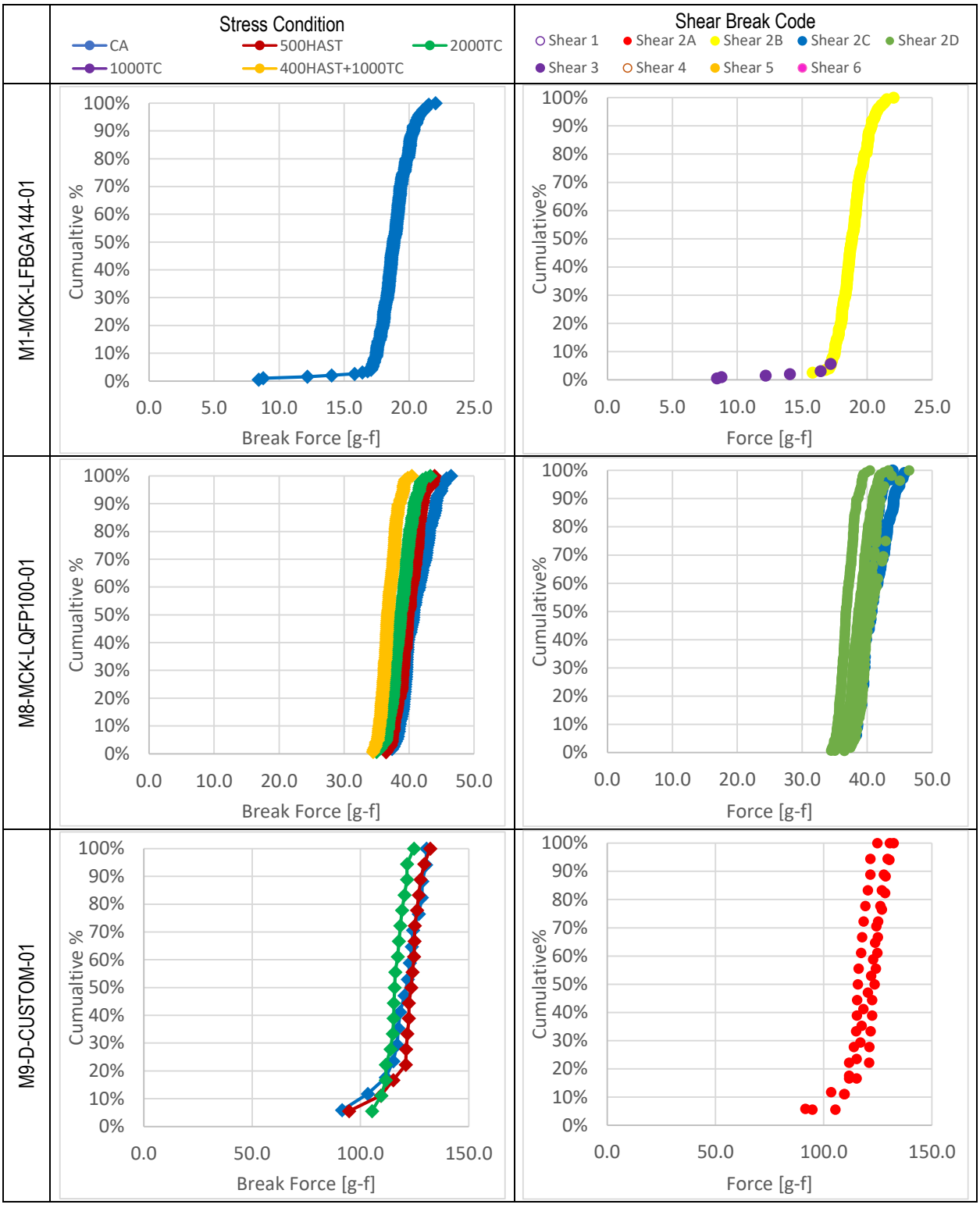
Stress Condition
CA
500HAST
2000TC
1000TC
400HAST+1000TC
Shear Break Code
Shear 1
Shear 2A
Shear 2B
Shear 2C
Shear 2D
Shear 3
Shear 4
Shear 5
Shear 6
M1-MCK-LFBGA144-01
M8-MCK-LQFP100-01
M9-D-CUSTOM-01
Cumualtive %
Cumulative%
Break Force [g-f]
Force [g-f]

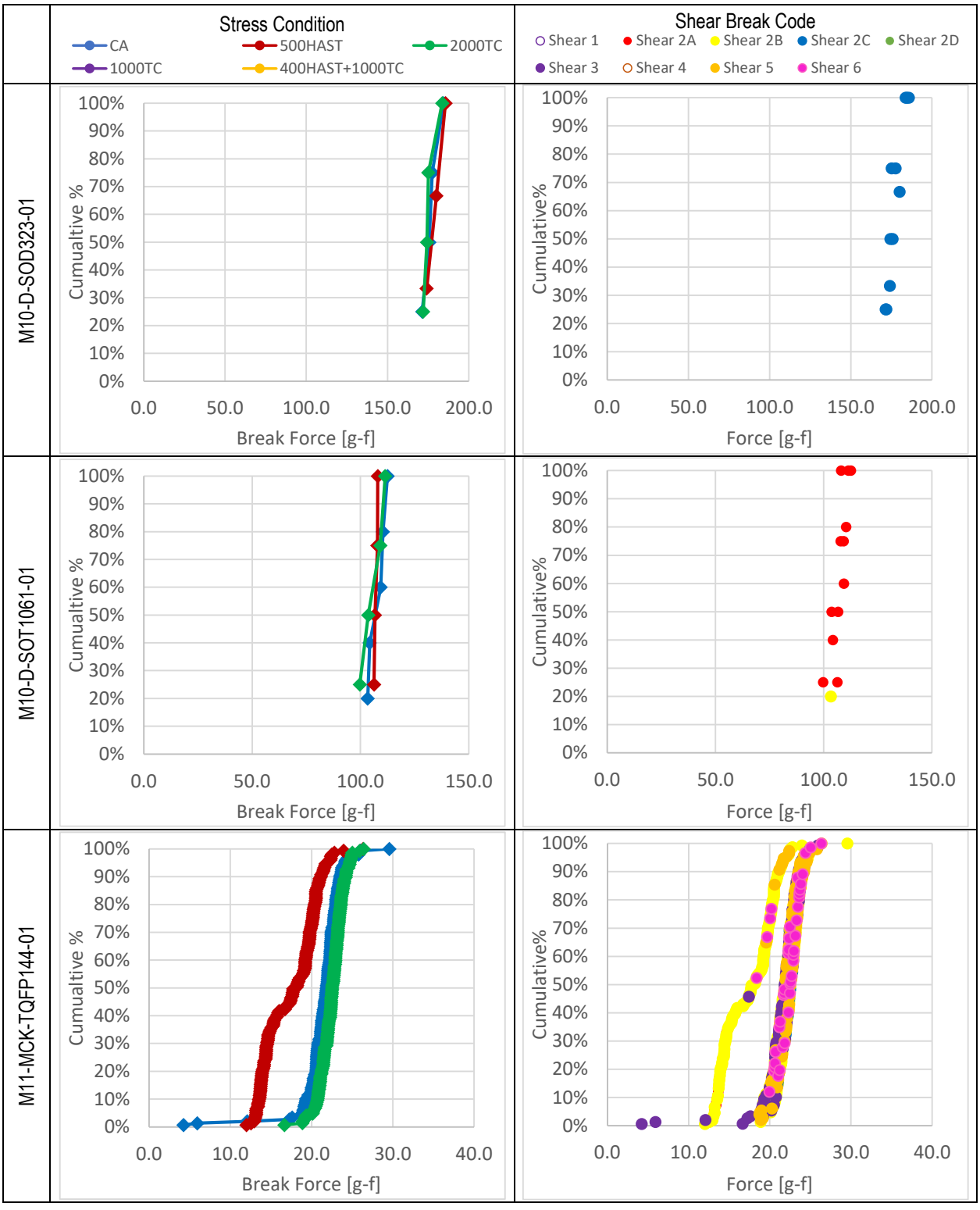
Stress Condition
CA
500HAST
2000TC
1000TC
400HAST+1000TC
Shear Break Code
Shear 1
Shear 2A
Shear 2B
Shear 2C
Shear 2D
Shear 3
Shear 4
Shear 5
Shear 6
M10-D-SOD323-01
M10-D-SOT1061-01
M11-MCK-TQFP144-01
Cumulative %
Cumulative%
Break Force [g-f]
Force [g-f]

C.3.3.1 Ball Shear Issues Observed

The main issues observed following ball shear testing of all samples included cratering and shear skipping due to polyimide passivation on certain devices.

Cratering

As with the bond pull tests, cratering was observed following ball shear for M4-MCK-FBGA256-01, M1-MCK-LFBGA144-01, and M11-MCK-TQFP144-01. One cratered bond was also observed for M5-MCK-WSON6-01. Fracture surfaces for representative cratered ball bonds are shown in Figures C.3-21 and C.3-22.

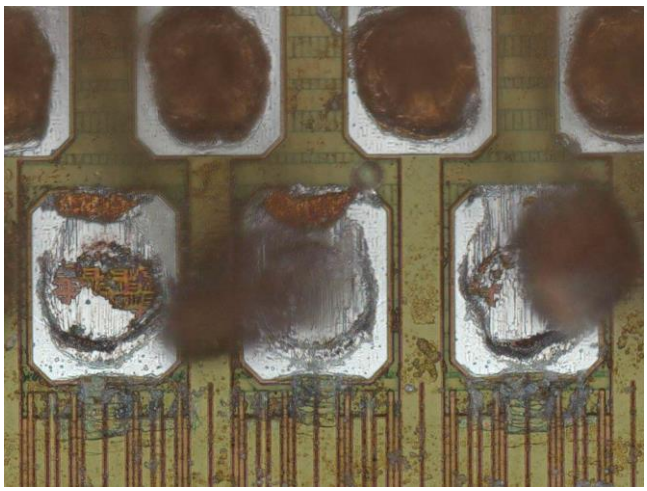

Figure C.3-21. Optical Image of M4-MCK-FBGA256-01 AR Representing Code 3 Cratering (left) and Code 6 Bond Pad Lift (right) Ball Bond Shear Results

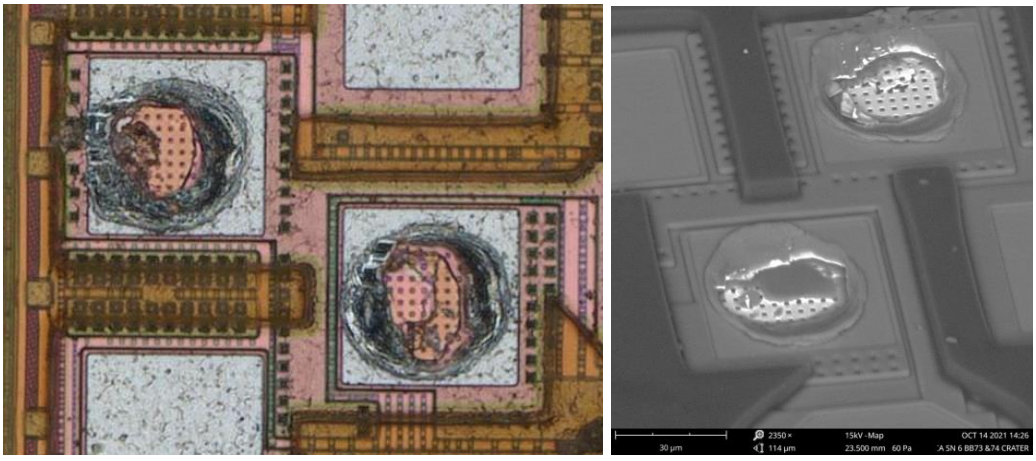

Figure C.3-22. SEM Image of Bond Pads 73 and 74 on M11-MCK-TQFP144-01AR Representing Code 3 Cratering Results

Polyimide impact on shear results

Polyimide passivation layers were present on three part types (M8-MCK-LQFP100-01, M3-MCK-TQFP100-01, and M11-MCK-TQFP144-01). The thickness of this layer requires that the ball shear tool be set to a higher position than other components to avoid contact with the polyimide surface. This causes the shear tool to contact some ball bonds at locations higher than the centerline, which can result in shear skip, as shown in Figure C.3-23. JEDEC JESD-B116

elaborates on the consequences of performing shear testing when the tool cannot reach below bond centerline, and concludes, “For these reasons, it is not recommended to attempt to perform quantitative comparisons between different shear test runs, but the results may be used for qualitative purposes.” One of the three components (M8-MCK-LQFP100-01) had consistent ball bonds with midpoints above the polyimide layer. M3-MCK-TQFP100-01 had bonds with midpoints consistently below the polyimide layer, resulting in multiple shear skips. M11-MCK-TQFP144-01 had variable ball heights, as shown in Figure C.3-24. The impact of ball height on the resulting shear strengths is illustrated in Figure C.3-25, where parts with a higher, more consistent midpoint exhibited higher shear strength.

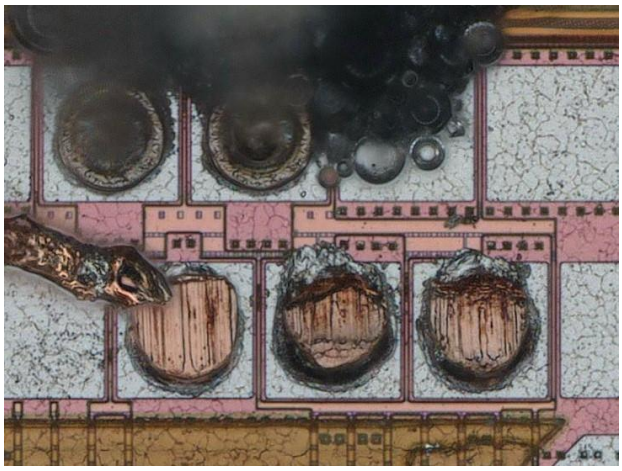

Figure C.3-23. Optical Image of Wires 63-65 on M11-MCK-TQFP144-01AR, Representing Code 5 Shear Skip Results

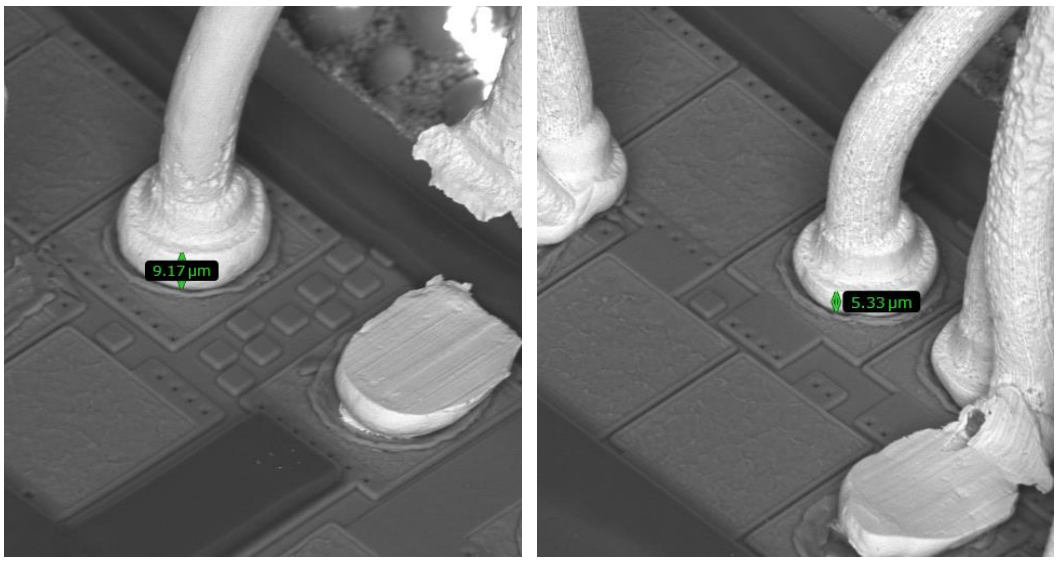

Figure C.3-24. SEM Images of Wires from B65, Illustrating Variation in Ball Bond Height. Lower height on individual ball bond can result in shear tool impacting above center line.

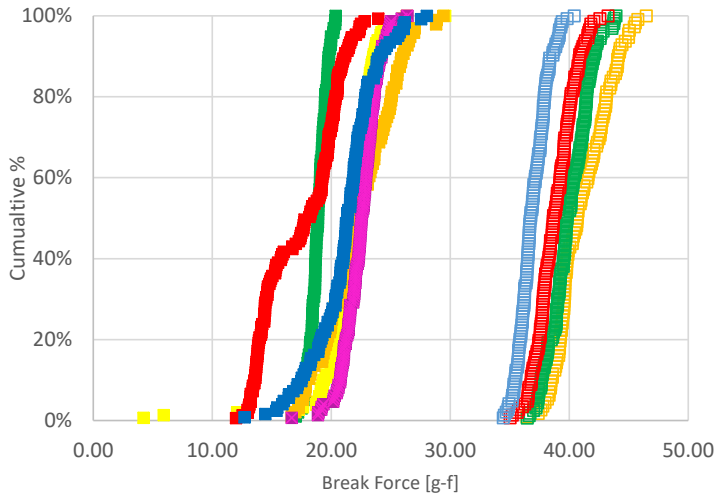

Figure C.3-25. Bond Shear Strength Comparison for All Parts with Polyimide Passivation. Filled squares represent parts with variable ball bond height or midpoints below the polyimide layer; empty squares represent parts with consistent ball bond height with midpoints above the polyimide layer.

C.4 Statistical Analysis of Bond Pull and Bond Shear

Initial data evaluation indicated trends and allowed assessment of apparent outliers, but it could not be evaluated for statistical significance. Statistical significance and trend determination was performed using ANOVA and Student's t-test [refs. 1, 2]. Initial trend analyses include all test data irrespective of as-received failure condition. Later, the team discussed the effect of unacceptable failure types identified by CA. First, statistical analyses were performed for pull/shear strengths for each part and their associated results after TC and HAST environmental exposures. Then, significance in trends were compared by combining strength values of SOT parts. Finally, the team revisited results and removed those with questionable failure to better narrow trends and comparison to Military plots and existing industry data.

Adding all SOTs with less than 20 wire bonds allowed an increase in sample size for a wire diameter and for better comparison to a single leaded part having 100 or more wire bonds. The results were then compared with the trends for each BGA having more than 100 wire bonds. These trend evaluations also allowed to fit data into a Weibull distribution for ease of data comparison for various wire bond diameter and types as well as extrapolation to a lower percentile of failures. Weibull parameters were calculated and presented. A detailed discussion of the statistical analysis methods used along with several representative examples of the analyses and their statistical significances is provided in Section C.4.1. This section provides a high-level overview and a subset of examples.

C.4.1 Statistical Analyses: Student's t-test (T test) and ANOVA

Statistical analyses were performed on pull and shear strength data for each part in the as-received condition, after thermal cycling and bHAST environmental exposures. Their significances first required analysis using ANOVA for more than two conditions, generation of statistical parameters and standard deviations, and ultimately application of Student's t-test for acceptance/rejection between two conditions using applicable standard deviation. Conditions were: (1) as-received, (2) 2000 TCs, (3) 500 hr HAST, (4) 1000 TCs, and (5) other combined conditions.

The T test is a statistical test frequently used for assessing the difference between two independent sample means. It requires definition of null and alternative hypothesis for means differences: without a priori knowledge, a non-directional (two-tailed) alternative hypothesis is selected that does not specify a direction (one-tailed) for the differences. For this condition, null and alternative hypotheses are: 1) null hypothesis, $H_0 = \mu_1 - \mu_2 = 0$, and (2) alternative hypothesis, $H_1 = \mu_1 - \mu_2 \neq 0$. Then, the level of uncertainty, Alpha (α), is considered to be acceptable. Frequently, Alpha (α) is assumed to be 0.05 with confidence of 95% (1-.05 =0.95). For rejecting or do not rejecting null hypothesis, the T test value for sample size <32 or Z score for sample ≥ 32 is calculated based on the two means and standard deviation and compared to ideal t or Z expected values. The approach is shown schematically in Figure C.4-1. If we do not reject the null hypothesis, then statistical evidence is insufficient to infer that the alternative (hypothesis) is true. If the test statistic's value is inconsistent with the null hypothesis, we reject the null hypothesis and infer that the alternative hypothesis is true.

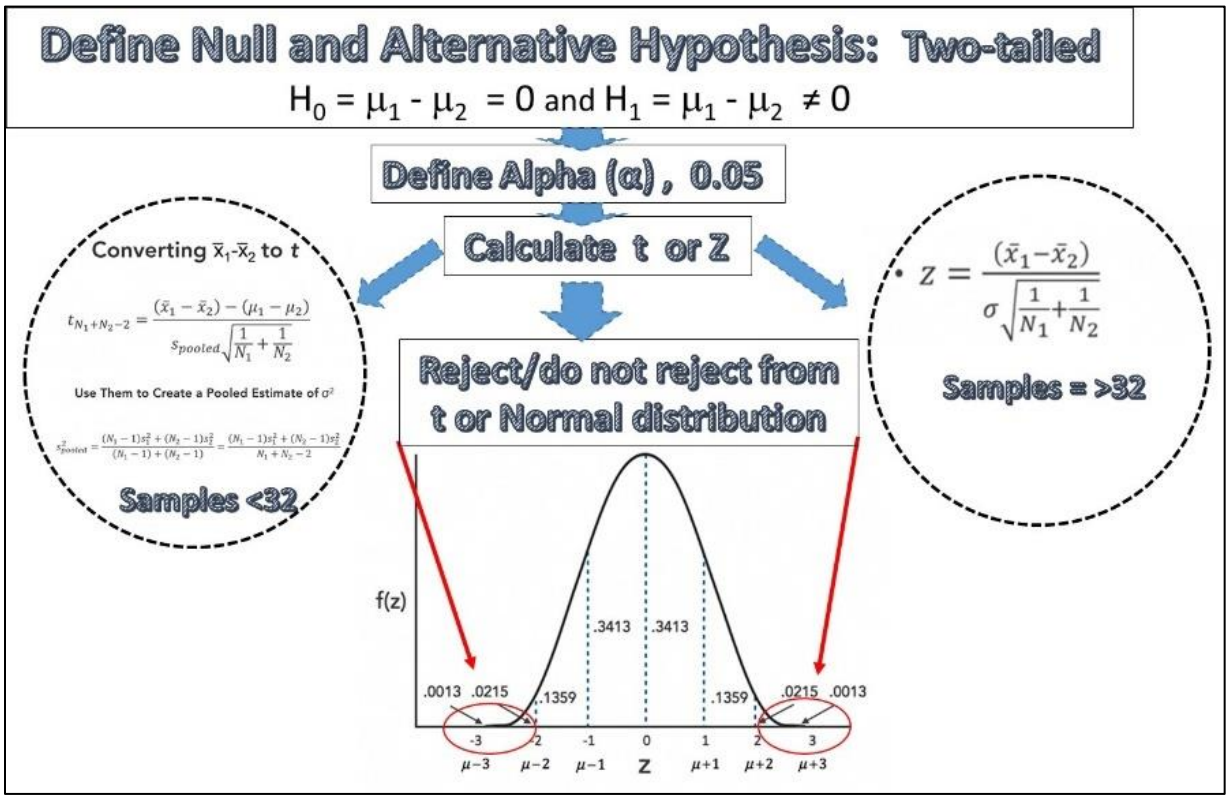

Figure C.4-1. Approach to "Reject" or "Do Not Reject" Null Hypothesis

As may be apparent, the T test calculates means from assuming "t" or normal population with a population having the same variance. For more than two parameters, however, standard deviations are compared to determine significance using F ratio— this method is called analysis of variance. If F, which is the square between divided by the mean squared within, is less or equal to one, then do not reject null hypothesis. Null hypothesis assumes all means are equal, i.e., H_0: $\mu_1 = \mu_2 = \mu_3$, whereas the alternative hypothesis assumes the means are not equal, i.e., H_1: $\mu_1 \neq \mu_2 \neq \mu_3$.

Table C.4-1 presents an example to elucidate the use of this method. An example of ANOVA analysis for wire pull strengths (e.g., baseline, post-2000 TCs, and post-500 hr bHAST) is

illustrated in the left three columns of the table. The right rows and columns show the Excel ANOVA summary results for the three values. The overall F ratio is 3.24, which is larger than one; therefore, do not reject the Null Hypothesis (H_0: $\mu_1 = \mu_2 = \mu_3$). This means that for this specific case, 2000 TCs or 500 hr of bHAST have negligible degradation effects.

Table C.4-1. Example of ANOVA Statistical Analysis *Raw Pull Strength Data (left) and Various Statistical ANOVA Parameters (right)*

Pull Strenght M1-MCK-SOIC8-01			SUMMARY: ANOVA Single Factor							
Baseline-Pull	**2000TC**	**500HAST**	*Groups*	*Count*	*Sum*	*Average*	*Variance*	*STD Error*	*Condition*	*Average*
10.96	12.3	12.36	Baseline Construction Analysis	14	205.46	14.67571429	1.608641758	0.338973425	Baseline	14.68
13.64	12.5	12.73	Post 2000TC	14	200.35	14.31071429	1.276745604	0.301986944	2000TC	14.31
14.16	12.95	13.23	Post 500HAST	13	191.7	14.74615385	1.983992308	0.390659433	500HAST	14.75
14.36	13.7	14.17								
14.52	14.11	14.35								
14.64	14.23	14.46	ANOVA							
14.67	14.56	14.85	*Source of Variation*	*SS*	*df*	*MS*	*F*	*P-value*	*F crit*	
14.98	14.6	14.91	Between Groups	1.500578545	2	0.750289272	0.464969808	0.631680491	3.244818361	
15.03	14.68	15.56	Within Groups	61.31794341	38	1.61363009				
15.38	14.74	15.77								
15.65	14.77	15.78	Total	62.81852195	40					
15.69	15.36	16.44								
15.87	15.84	17.09								
15.91	16.01									

To determine significance between two means, a T test could be used. The only difference from previous equations is the use of mean square within (different standard deviation) rather than pooled standard deviation, which assumes to have come from populations with a common standard deviation. Table C.4-2 shows the T test equation used to compare between two means of pull strength, e.g., between as-received "AS" and 2000 TCs. Then statistical significance "p" was calculated to determine hypothesis type. The "p" lower than set Alpha (α) value, i.e.,0.05, is considered to be a significant difference.

Table C.4-2. Student's t-Test Analysis to Determine Significance for Each Mean as "Reject" or "Do Not Reject" Null Hypothesis

	AS/2000TC	**AS/500HAST**	**HAST/TC**
	1	1	0
	-1	0	1
	0	-1	-1
Num	0.365	-0.070	-0.435
Den	0.480	0.489	0.489
T-Test	0.760	-0.144	-0.890
p	0.452	0.886	0.379
	Do Not Reject Null Hypothesis	Do Not Reject Null Hypothesis	Do Not Reject Null Hypothesis

$$t = \frac{(1)\bar{X}_A + (-1)\bar{X}_B + (0)\bar{X}_C + (0)\bar{X}_D}{\sqrt{MS_{Within}\left[\frac{(1)^2}{n_A} + \frac{(-1)^2}{n_B} + \frac{(0)^2}{n_C} + \frac{(0)^2}{n_D}\right]}}$$

C.4.1.1 Cu Wire Bond Pull Strengths for Different Package Types

All wire bond pull strengths were subjected to ANOVA and T test statistical analyses to determine whether "null hypothesis" could be rejected or not. Three examples are presented: (1) do not reject null hypothesis, (2) reject null hypothesis, and (3) when test results at intervals, in addition to results for 2000 TCs and 500 hr HAST, were collected.

Figure C.4-2 shows the test results for M1-MCK-SOIC8-01 with 14 wire-bond pull strength values. The bottom plot shows the strength values versus the number of wire bonds pull tested. The middle shows the average values with the assumption of normal distribution. Finally, the top table shows calculation for T test and "p" values. The statistical analysis appears to be consistent with closeness of strength distribution and average values. For all three compared cases, i.e., AS/2000TC (as-received vs. 2000 TCs), AS/500HAST (as-received vs. 500 hr of HAST), and TC/HAST (2000 TCs vs. 500 hr HAST), the "p" values are larger than 0.05; therefore, the conclusion is "do not reject null hypothesis."

Figure C.4-3 shows the test results for M5-MCK-WSON6-01 with 12 (6 wires for each part) wire-bond pull strength values. The figure is divided into section similar to the previous figure. The plots show consistently lower values for as-received strengths. For two cases of AS/2000 TC and AS/500 hr HAST, there are noticeable increases in strengths relative to as-received strengths. The values are lower than 0.05; therefore, the conclusion is "reject null hypothesis." However, this is not the case for TC/HAST (2000 TCs vs. 500 hr HAST), both showing closeness in strength. The "p" value is larger than 0.05; therefore, the conclusion is "do not reject null hypothesis."

Figure C.4-4 shows the test results for M5-D-SOT233-01 with four wire-bond pull strength values at intervals. The bottom plot shows the strength values versus the number of wire bonds pull tested. The middle shows the average values with the assumption of normal distribution. Finally, the top table shows calculation for T test and "p" values. The statistical analysis appears to be consistent with separation of strength distribution and average values. Except for AS/1000 TC (as-received vs. 1000 TCs) with the "p" value being larger than 0.05 with conclusion of "do not reject null hypothesis," the rest are opposite. For the TC case, it appears strength slightly increases at 1000 cycles and decreases at 2000 TCs.

	AS/2000TC	AS/500HAST	HAST/TC
	1	1	0
	-1	0	1
	0	-1	-1
Num	0.365	-0.070	-0.435
Den	0.480	0.489	0.489
T-Test	0.760	-0.144	-0.890
p	0.452	0.886	0.379
	Do Not Reject Null Hypothesis	Do Not Reject Null Hypothesis	Do Not Reject Null Hypothesis

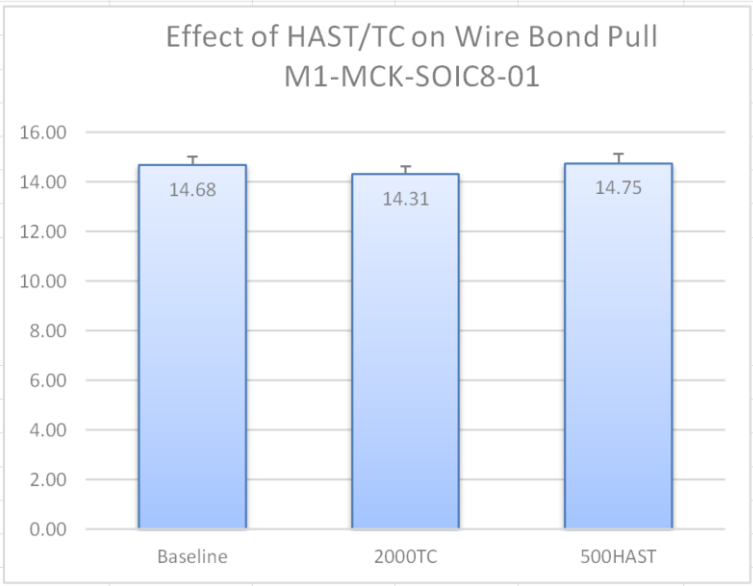

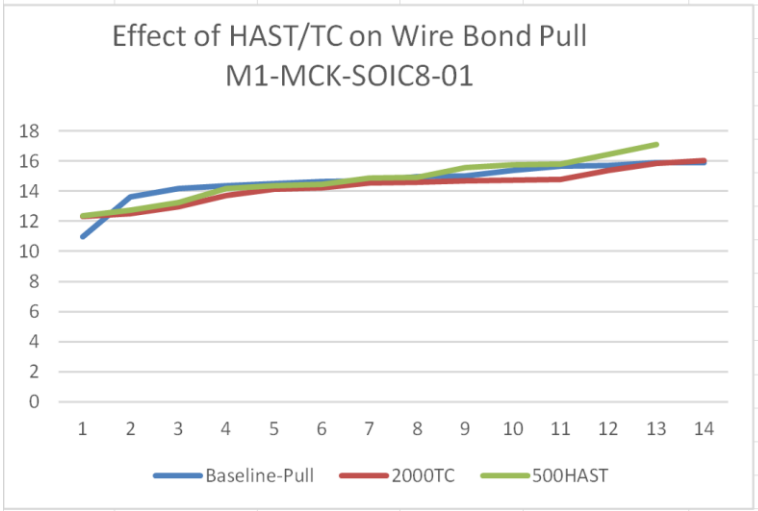

Figure C.4-2. Pull Strength Plots, Mean Value Charts, and Table Show Student's t-test Analysis for Part M1-MCK-SOIC8-01, Which Shows Statistical Significance for Each Mean as "Reject" or "Do Not Reject" Null Hypothesis

	AS/2000TC	AS/500HAST	HAST/TC
	1	1	0
	-1	0	1
	0	-1	-1
Num	-1.805	-1.524	0.282
Den	0.368	0.368	0.368
T-Test	-4.908	-4.142	0.766
p	2.42E-05	2.24E-04	0.449
	Reject Null Hypothesis	Reject Null Hypothesis	Do Not Reject Null Hypothesis

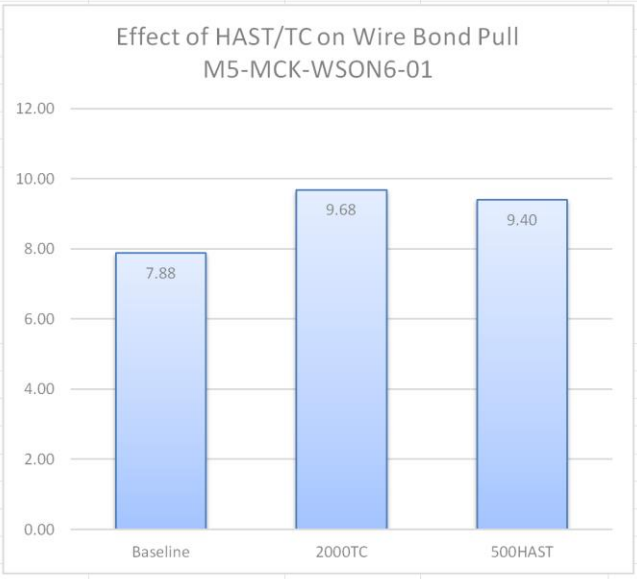

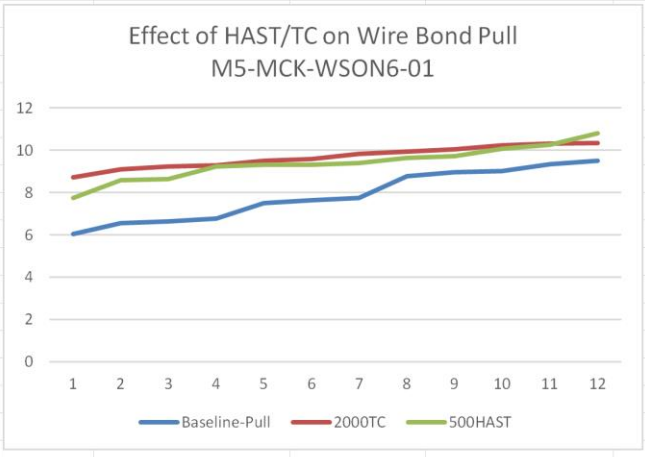

Figure C.4-3. Pull Strength Plots, Mean Value Charts, and Table Show Student's t-test Analysis for M5-MCK-WSON6-01, Which Shows Statistical Significance for Each Mean as "Reject" Or "Do Not Reject" Null Hypothesis

	AS/1000TC	AS/2000TC	AS/500HAST	500HAST/2000TC
	1	1	1	0
	-1	0	0	0
	0	-1	0	1
	0	0	-1	-1
Num	-1.063	4.203	1.803	-2.400
Den	0.575	0.575	0.575	0.575
T-Test	-1.847	7.306	3.134	-4.172
p	8.95E-02	9.40E-06	8.63E-03	1.29E-03
	Do Not Reject Null Hypothesis	Reject Null Hypothesis	Reject Null Hypothesis	Reject Null Hypothesis

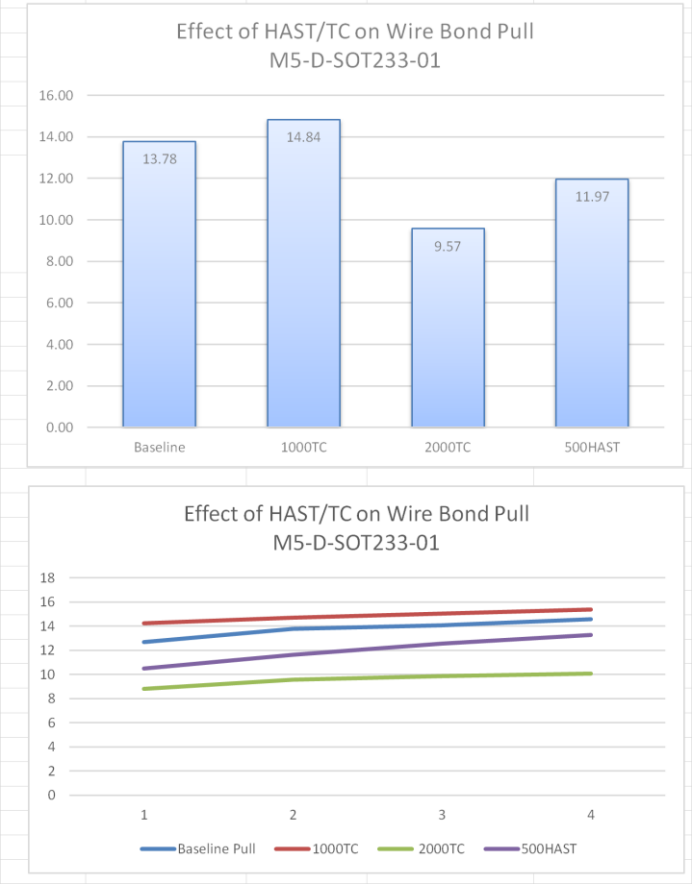

Figure C.4-4. Pull Strength Plots, Mean Value Charts, and Table Show Student's t-test Analysis for M5-D-SOT233-01, Which Shows Statistical Significance for Each Mean as "Reject" or "Do Not Reject" Null Hypothesis

Table C.4-3 provides a summary of significances, reject (Y) or do not reject (N) null hypothesis, and N/A, not applicable, for all parts with wire-bond under pull loading. Two key categories were identified. For parts with large number of wire bonds, significances are better narrowed under TC and HAST conditions. They mostly showed significances among these conditions. This is not the case for SOTs with a few numbers of wire bonds. The results for significance are mixed. This is due to the effect of variation outliers including decapsulation and wire bond length on the standard deviation. Pooled standard deviation is less affected by outliers for parts with a larger number of wire bonds whereas parts with a few wire bonds are significantly affected. In subsequent pull strength analyses, SOT parts with a low number of wire bonds, but with one wire diameter, were added together and categorized as SOTs. This allowed better comparison for Weibull and statistical analysis under various conditions.

For SOTs, 8/12 parts showed significance after 2000 TCs whereas 4/12 showed significance after 500 hr bHAST. It appears that the TC method is a better discriminator for SOTs. Note that the TC was performed at assembly level, which induces additional fatigue stress due to CTE mismatches between the part and the PCB, possibly played a role on stretching wire bond, compared to parts exposed to bHAST at lower maximum temperature (110 ℃ for bHAST vs. 125 ℃ for TC) without the additional induced CTE mismatch stresses.

Table C.4-3. Summary of Statistical Significances of Pull Strength *for All Parts with "Y" Means "Reject Null Hypothesis"*

Bond Pull Strength Part ID Test	Wire Diameter (mil)	Composition	Package Type	AS/2000TC Significance	AS/500HAST Significance	TC/HAST Significance	AS/1000TC Significance
M7-MCK-LFBGA169-01	0.7	PCC (Pd/Cu)	169-LFBGA	Y	Y	Y	
M11-MCK-TQFP144-01	0.8	PCC (Au/Pd/Cu)	TQFP144	N	Y	Y	
M3-MCK-TQFP100-01	0.8	PCC (Pd/Cu)	100-TQFP	Y	Y	N	
M4-MCK-FBGA256-01	0.8	Cu	256FBGA	Y	Y	Y	
M5-MCK-SOT235-01	0.8	Au	SOT23-5	N	N	N	N
M2-D-SOT233-02	0.8	Cu	SOT23-3	Y	Y	N	
M5-MCK-WSON6-01	0.8	PCC (Au/Pd/Cu)	6-WSON	Y	Y	N	
M2-D-SOT233-01	0.8	Cu	SOT-23-3	Y	Y	N	
M8-MCK-LQFP100-01	1	PCC(Au/Pd/Cu)	100LQFP	Y	Y	Y	
M5-MCK-SOIC8-01	1	Cu	8-SOIC	N	N	N	
M6-D-SOT-235-01	1	PCC (Pd/Cu)	SOT-23	Y	N	N	
M5-MCK-VSSOP8-01	1	Cu	8-VSSOP	Y	N	Y	N
M5-D-SOT233-01	1	Cu	SOT-23-3	Y	Y	Y	N
M1-MCK-SOIC8-01	1	PCC (Au/Pd/Cu)	8-SOIC	N	N	N	
M10-D-SOT1061-01	2	Cu	SOT1061	Y	N	Y	
M10-D-SOD323-01	2	Cu	SOD323	Y	N	Y	
M9-D-Custom-01	2	Cu	Custom	N	N	N	

C.4.1.2 Cu Wire Bond Shear Strength

Similar to the previous section on statistical analysis for wire bond pull strength, all wire bond shear strengths were subjected to ANOVA and T test evaluation. Figure C.4-5 shows the shear test results for M1-MCK-SOIC8-01 with 14 wire bonds. The bottom line plots show the shear strength values versus sample size, the middle bar chart shows the average shear values, and the top table shows calculation for T test and "p" values with the assumption of normal distribution for shear data. The statistical analysis appears to be consistent with closeness of shear strength distribution and average values. For compared three cases, i.e., AS/2000TC (as-received compared to 2000 TCs), AS/500HAST (as-received vs. 500 hr of HAST), and TC/HAST (2000 TCs vs. 500 hr HAST), the "p" values are smaller than 0.05; therefore, the conclusion is "reject null hypothesis." However, for pull strength of the same part (see previous section), for all cases conclusion was opposite to shear strengths: "do not reject null hypothesis."

	AS/2000TC	AS/500HAST	HAST/TC
	1	1	0
	-1	0	1
	0	-1	-1
Num	7.203	5.287	-1.916
Den	0.879	0.879	0.844
T-Test	8.197	6.017	-2.270
p	7.69E-10	5.96E-07	2.92E-02
	Reject Null Hypothesis	Reject Null Hypothesis	Reject Null Hypothesis

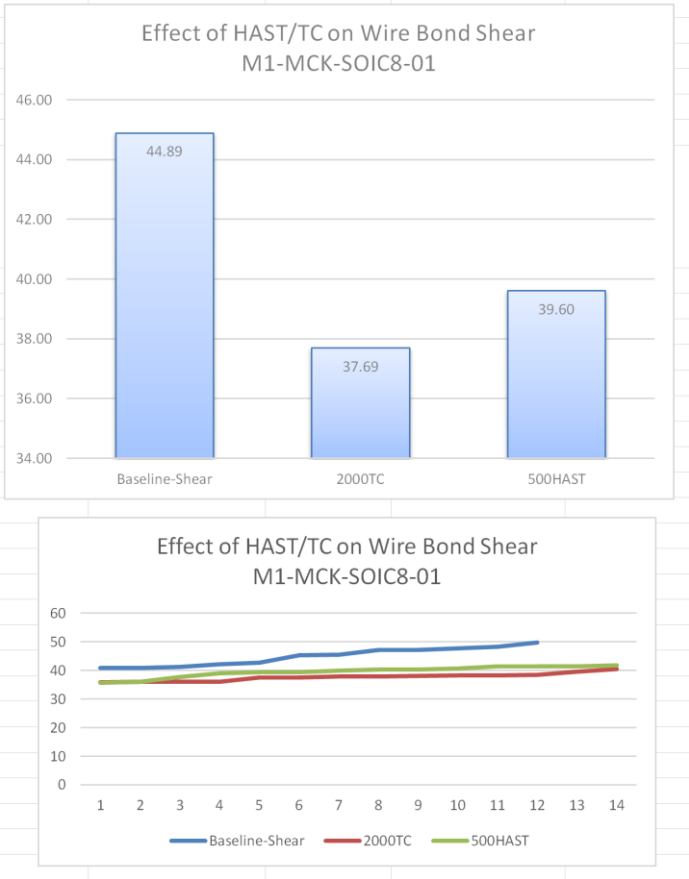

Figure C.4-5. Shear Strength Plots, Mean Value Charts, and Table Show Student's t-test Analysis for M1-MCK-SOIC8-01, Which Shows Statistical Significance for Each Mean as "Reject" or "Do Not Reject" Null Hypothesis

Figure C.4-6, similarly, shows shear test results for M5-MCK-WSON6-01 with 12 wire bonds. For two cases of AS/2000 TC and AS/500 hr HAST, there are apparent noticeable increases in shear strengths. The values are lower than 0.05; therefore, the conclusion is "reject null hypothesis." However, this is not the case for TC/HAST, with both showing closeness in strength. The "p" value is larger than 0.05; therefore, the conclusion is "do not reject null hypothesis." Compared with pull strengths, shear strengths show the same significance trends for the three conditions.

	AS/2000TC	AS/500HAST	HAST/TC
	1	1	0
	-1	0	1
	0	-1	-1
Num	-2.149	-2.370	-0.221
Den	0.841	0.841	0.841
T-Test	-2.555	-2.818	-0.263
p	1.54E-02	8.11E-03	7.94E-01
	Reject Null Hypothesis	Reject Null Hypothesis	Do Not Reject Null Hypothesis

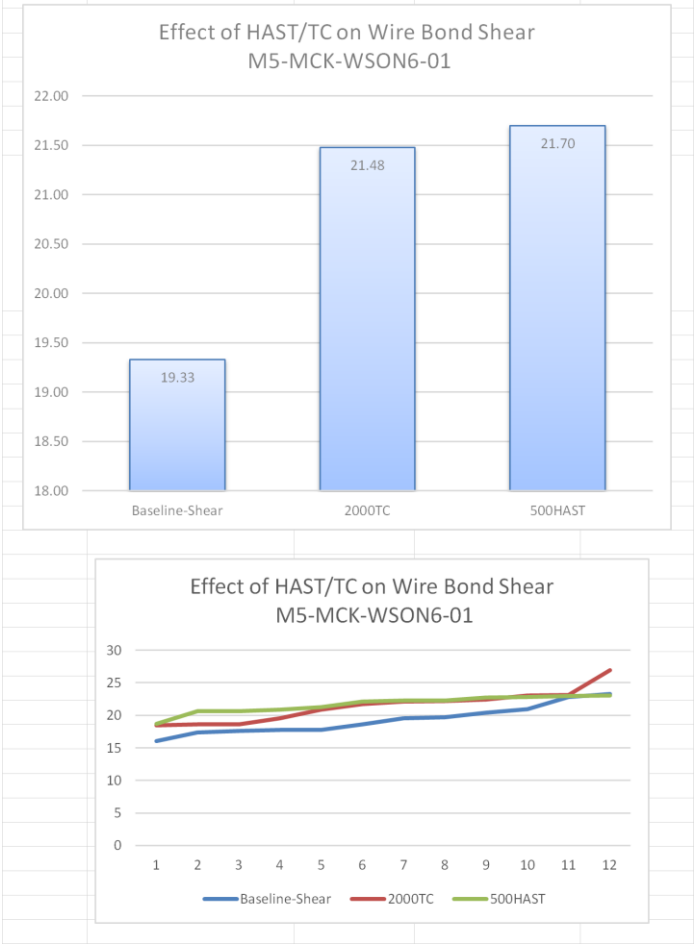

Figure C.4-6. Shear Strength Plots, Mean Value Charts, and Table Show Student's t-test Analysis for M5-MCK-WSON6-01, Which Shows Statistical Significance for Each Mean as "Reject" or "Do Not Reject" Null Hypothesis

Figure C.4-7 shows the shear test results at intervals for M5-D-SOT233-01 with four wire bonds. The plots, bar charts, and table are the same as previous ones, except this set has data for 1000 TCs. The statistical analysis may be affected by 500 hr HAST data, since it does not follow the other trends. For all cases, the conclusion is "do not reject null hypothesis," which is different from conclusions for the significances on wire bond pull strengths. Shear strengths decreased with thermal cycling, another aspect of this inconsistency in the test data trends.

	AS/1000TC	AS/2000TC	AS/500HAST	500HAST/2000TC
	1	1	1	0
	-1	0	0	0
	0	-1	0	1
	0	0	-1	-1
Num	2.372	3.153	1.297	-1.856
Den	2.184	2.184	2.184	2.393
T-Test	1.086	1.444	0.594	-0.776
p	2.96E-01	1.71E-01	5.62E-01	4.51E-01
	Do Not Reject Null Hypothesis	Do Not Reject Null Hypothesis	Do Not Reject Null Hypothesis	Do Not Reject Null Hypothesis

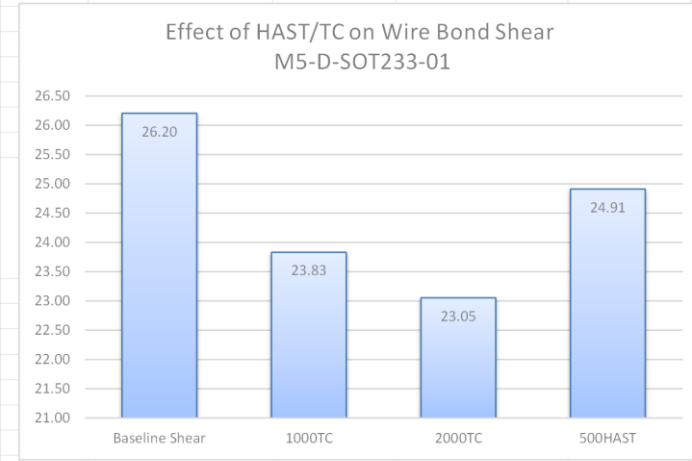

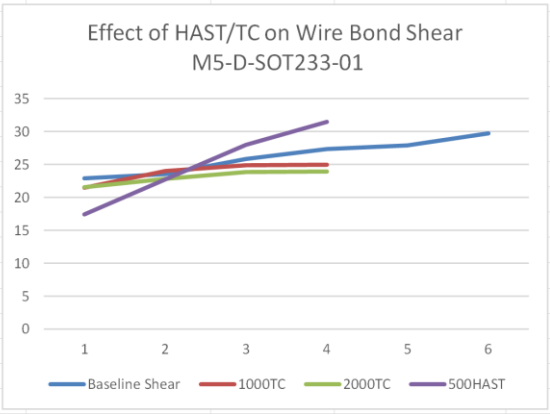

Figure C.4-7. Shear Strength Plots, Mean Value Charts, and Table Show Student's t-test Analysis for M5-D-SOT233-01, Which Shows Statistical Significance for Each Mean as "Reject" or "Do Not Reject" Null Hypothesis

Table C.4-4 presents a summary of significances, reject (Y) or do not reject (N) null hypothesis, and not applicable (N/A) for all parts under shear loading. Two key categories were identified. For parts with large number of wire bonds, all showed significances under TC and bHAST conditions. This is not the case for SOTs with a few numbers of wire bonds. The results for significance are mixed. This is due to the effect of variation outliers including decapsulation and wire bond area on the standard deviation. Pooled standard deviation is less affected by outlier for parts with larger numbers of wire bonds whereas it significantly affects parts with a few wire bonds. In subsequent pull strength analyses, parts such as SOTs which have a low number of wire bonds, were added together for a single wire diameter, in order to better compare Weibull and statistical results. Note that for SOTs, 2/12 parts showed significance after 2000 TCs

whereas 3/12 showed significance after 500 hr bHAST. So, it appears that neither 2000 TC nor 500 hr bHAST is a good discriminator for SOTs under shear testing. It appears shear strengths were not affected by PCB CTE mismatches under thermal cycling whereas this was not the case for wire bond pull strengths.

Table C.4-4. Summary of Statistical Significances of Shear Strengths for All Parts with "Y" Means "Reject Null Hypothesis." All parts with large number of wire bonds showed significance for various environmental conditions. This is not true for parts with a few wire bonds.

Shear Strength Part ID Test	Wire Diameter (mil)	Composition	Package Type	AS/2000TC Significance	AS/500HAST Significance	TC/HAST Significance	AS/1000TC Significance
M7-MCK-LFBGA169-01	0.7	PCC (Pd/Cu)	169-LFBGA	Y	Y	Y	
M11-MCK-TQFP144-01	0.8	PCC (Au/Pd/Cu)	TQFP144	Y	Y	Y	
M3-MCK-TQFP100-01	0.8	PCC (Pd/Cu)	100-TQFP	Y	Y	Y	
M4-MCK-FBGA256-01	0.8	Cu	256FBGA	Y	Y	Y	
M5-MCK-SOT235-01	0.8	Au	SOT23-5	Y	N	N	N
M2-D-SOT233-02	0.8	Cu	SOT23-3	N	N	N	
M5-MCK-WSON6-01	0.8	PCC (Au/Pd/Cu)	6-WSON	Y	Y	N	
M2-D-SOT233-01	0.8	Cu	SOT-23-3	N	N	N	
M8-MCK-LQFP100-01	1	PCC(Au/Pd/Cu)	100LQFP	Y	Y	Y	
M5-MCK-SOIC8-01	1	Cu	8-SOIC	N	N	N	
M6-D-SOT-235-01	1	PCC (Pd/Cu)	SOT-23	N	Y	Y	
M5-MCK-VSSOP8-01	1	Cu	8-VSSOP	N	N	N	Y
M5-D-SOT233-01	1	Cu	SOT-23-3	N	N	N	N
M1-MCK-SOIC8-01	1	PCC (Au/Pd/Cu)	8-SOIC	Y	Y	Y	
M10-D-SOT1061-01	2	Cu	SOT1061	N	N	N	
M10-D-SOD323-01	2	Cu	SOD323	N	N	N	
M9-D-Custom-01	2	Cu	Custom	N	N	Y	

Appendix C References

1. NIST Engineering Statistics, Website, https://www.itl.nist.gov/div898/handbook/eda/section3/eda353.htm
2. Quirk, Thomas J. (2020) *Excel 2019 for Engineering Statistics, A Guide to Solving Practical Problems*, Second Edition, Springer Nature Switzerland AG 2016.

REPORT DOCUMENTATION PAGE

Form Approved
OMB No. 0704-0188

1. REPORT DATE *(DD-MM-YYYY)*	2. REPORT TYPE	3. DATES COVERED *(From - To)*
10/05/2023	Technical Memorandum	

4. TITLE AND SUBTITLE
Assessment of Electrical, Electronic, and Electromechanical (EEE) Parts Copper Wire Bonds for Space Programs

5a. CONTRACT NUMBER

5b. GRANT NUMBER

5c. PROGRAM ELEMENT NUMBER

6. AUTHOR(S)
Hodson, Robert F.; Del Castillo, Linda Y.; Chen, Yuan; Ghaffarian, Reza; Oachs, Lyudmyla P.; Galloway, Eric M.

5d. PROJECT NUMBER

5e. TASK NUMBER

5f. WORK UNIT NUMBER
869021.01.23.01.01

7. PERFORMING ORGANIZATION NAME(S) AND ADDRESS(ES)
NASA Langley Research Center
Hampton, VA 23681-2199

8. PERFORMING ORGANIZATION REPORT NUMBER
NESC-RP-18-01317

9. SPONSORING/MONITORING AGENCY NAME(S) AND ADDRESS(ES)
National Aeronautics and Space Administration
Washington, DC 20546-0001

10. SPONSOR/MONITOR'S ACRONYM(S)
NASA

11. SPONSOR/MONITOR'S REPORT NUMBER(S)
NASA/TM-20230014536

12. DISTRIBUTION/AVAILABILITY STATEMENT
Unclassified - Unlimited
Subject Category Space Transportation and Safety
Availability: NASA STI Program (757) 864-9658

13. SUPPLEMENTARY NOTES

14. ABSTRACT
The NASA Electronic Parts and Packaging Program co-manager, requested the NASA Engineering and Safety Center (NESC) to compile a body of publicly available knowledge on copper (Cu) wire bonds and perform reliability testing and analysis on these bonds, including environment tests, sample destructive physical analysis, and bond pull/shear tests during environment test intervals. The goal was to understand the risks of using Cu wire bonds for space applications and develop guidelines on Cu bond pull/shear limits for NASA applications. This document contains the results of the NESC assessment.

15. SUBJECT TERMS
Electrical, Electronic, and Electromechanical; NASA Engineering and Safety Center; Copper Wire Bonds; Testing and Analysis

16. SECURITY CLASSIFICATION OF:			17. LIMITATION OF ABSTRACT	18. NUMBER OF PAGES	19a. NAME OF RESPONSIBLE PERSON
a. REPORT	b. ABSTRACT	c. THIS PAGE			STI Help Desk (email: help@sti.nasa.gov)
					19b. TELEPHONE NUMBER *(Include area code)*
U	U	U	UU	274	(443) 757-5802